STUDENT EEICT

BRNO UNIVERSITY OF TECHNOLOGY
FACULTY OF ELECTRICAL ENGINEERING AND COMMUNICATION

PROCEEDINGS II OF THE 31ST STUDENT EEICT 2025

ELECTRICAL ENGINEERING, INFORMATION SCIENCE,
AND COMMUNICATION TECHNOLOGIES

SELECTED PAPERS

April 29, 2025
Brno, Czech Republic

BRNO UNIVERSITY OF TECHNOLOGY
FACULTY OF ELECTRICAL ENGINEERING AND COMMUNICATION

Title Proceedings II of the 31st Conference STUDENT EEICT 2025

Editor Assoc. Prof. Vítězslav Novák

Publisher Brno University of Technology, Faculty of Electrical Engineering and Communication

Year released 2025

1st Edition

Content and language issues are the responsibility of the authors.

ISBN 978-80-214-6320-2

ISSN 2788-1334

BRNO UNIVERSITY OF TECHNOLOGY FACULTY OF ELECTRICAL ENGINEERING AND COMMUNICATION

STUDENT EEICT

SPONSORS

Diamond tier

Honeywell

Golden tier

ABB

SKUPINA ČEZ

EATON

e·on

ThermoFisher SCIENTIFIC

BRNO UNIVERSITY OF TECHNOLOGY
FACULTY OF ELECTRICAL ENGINEERING AND COMMUNICATION

SPONSORS

Silver tier

ASICentrum
A COMPANY OF THE SWATCH GROUP

Garrett
ADVANCING MOTION

resideo

NXP

Valeo

Honorary tier

SKODA

TECHNICAL SPONSORS & MEDIA PARTNERS

IEEE
IEEE Czechoslovakia Section

VERONI
kafestánek

BRNO UNIVERSITY OF TECHNOLOGY
FACULTY OF ELECTRICAL ENGINEERING AND COMMUNICATION

Contents

Foreword

Eliška Bachorecová
Forensic Verification of Author of Handwritten Character "k" Using Artificial Intelligence 9
Jevhenij Vorochta, Helena Vítková, Roman Jakubíček
Direct Gene Detection in Raw Nanopore Signals Using Transformer Neural Networks 13
Dan Nguyen
Hand gesture recognition from EMG signal using machine learning 17
Jan Kusák, Šimon Sloboda
CubeSat model for image data transmission 21
Šimon Remper, Jan Dvořák
Detection of Problems in an Industrial Network Using the Concept of Edge Computing 25
David Maňásek, Ladislav Polák
Measurement System for monitoring of LoRa Radio Links in the 2.4 GHz ISM Band 29
Michaela Tichá
Use of aerogel in combination with high entropy materials as anode material for Li-ion batteries 33
Denis Šaman, Lukáš Radil
A case study of energy community assessment in the Czech Republic 37
Tomáš Brychta, Lukáš Radil
Energy balance in water treatment plants 41
Ondřej Dušek, Kryštof Doležal, Oliver Drga, Vít Fousek
Linear Deltabot: Design, Kinematics and Trajectory Generation 45
Antonín Pospíšil, Petr Petyovsky
Display device for archery competitions 49
Michal Blažík, Matěj Kantor, Soňa Michalková, Kryštof Wojnarowský, Tomáš Janoušek, Jakub Arm
Testbed 4.0: The cooling system design 52
Jiří Strnad, Pavel Tomíček
Verification of buck converter efficency determination and its optimalization 56
Valeriia Orlova
Thermal Model of a Smart Home 60
Ekaterina Gerasina
Soil water flow modeling for irrigation control 64
Lenka Blažková
Segmentation of hip joint anatomy structures from radiographic images 68
Martina Daňková, Stanislava Košková, Filip Plešinger
Bloody Forecast: Daily Blood Demand Prediction Using Various Modeling Approaches 72
Anar Davaajargal, Krystof Novotny
Analysis of Temporal Speech Impairments in Prodromal Dementia with Lewy Bodies 76
Jakub Zdražil, Pavel Paluřík
Wildlife Tracking System 80
Alexander Bekeč, Jiří Veverka, Jan Gromeš
Design of an inter-satellite communication and ranging payload for a rendezvous and proximity operations mission 84
Ondrej Dohnal, Jan Jerabek
Tool for analysis of domain records collected from open sources 88
Radim Macho, Petr Musil
Platform for detection and monitoring of the devices connected to the power grid 92
Filip Stryk, Aleš Povalač
Evaluation of Energy Consumption in Different LoRaWAN End Device Classes 96
Marek Černý, Roman Maršálek, Radek Závorka
Experiments with the 5G beam search in millimeter waves - raytracing and practical indoor measurements 100

Tomáš Nagy, Pavel Paluřík, Lukáš Jablončík
Methods for securing Linux-based embedded systems 104
Adam Tuček, Willi Lazarov
Aggregation and Evaluation of Vulnerabilities from CVE Databases for Effective Security Assessment 108
Martina Molnárová, Willi Lazarov
Strategic Threat Intelligence in Cyberspace 112
Vojtěch Šibor, Petr Vyroubal
Digital Twin of a Lithium-ion Battery 116
Jakub Rosendorf, Petr Chmelíček, Jan Bárta
Evaluation of Eddy Effects in Winding of High-Speed Synchronous machines for EV Systems 120
Tomáš Fryšták
Availability of Railway Frequency Converter to Provide Ancillary Services 124
Josef Bartoněk, Jiří Janoušek
Vision-Based Autonomous UAV Tracking and Control 128
Tereza Havlíková
Surface Engineering of Piezoelectric Semi-Crystalline Polymer Scaffolds via Plasma Treatment for Improved Adhesion and Integration of Osteoblasts 132
Tomáš Martiník
Machine Learning-Driven Detection of Repetitive Manufacturing Processes Using Radar Sensor 136
Kristýna Heřmánková, Katarína Šlosárová, Stanislav Obruča, Karel Sedlář
Expression profiles of sRNA genes in Caldimonas thermodepolymerans 140
Michal Švento
Audio Declipping with Unfolded Douglas-Rachford Algorithm 145
David Leitgeb
Multipurpose Digital Audio Effect: Combining Different Techniques Within a Single Device 149
Pavel Palurik, Radim Dvorak, Pavel Masek
Optimized 5G-IoT Probe: Hardware Innovations and Practical Deployment 154
David Kohout, Tomas Lieskovan, Petr Mlynek
Smart Meter Emulator 159
Viet Anh Phan, Jan Jeřábek, Roman Kümmel
ptnetinspector: A Practical IPv6 Scanner for Network Reconnaissance 165
David Trochta, Ondřej Klvač, Tomáš Kazda
Investigating Battery Degradation Mechanisms by In-Situ SEM Analysis and Related Techniques 170
Hana Hálová, Ladislav Chladil, Lukáš Preisler, Pavel Čudek
Optimization of Spray Drying Synthesis of $LiFePO_4$: Effects of Calcination and Doping on Microstructure and Electrochemical Properties 175
Antonín Šimek, Tomáš Kazda, Charles Aram Hall, Ondřej Čech
Unraveling Sodium Storage Mechanisms in Carbon Anodes for Sodium-ion Batteries 180
Kipkurui Ronoh
Influence of ultrafast laser surface modification of the surface morphology, chemical composition and wettability of MONEL® alloy 400 185
Pavel Maca, Karel Katovsky
Effect of fuel assembly rotation on optimization of fuel pins burnup 190
Richard Schubert
Detection of Heavy Metal Contamination by Vibrational Spectroscopy: A Combined Theoretical and Experimental Study .. 195
Tomáš Pitner, Jan Knobloch, Jan Bárta
Current balancing in parallel structures of high-current power inverters 200
Matúš Kavec
Optimization of PMSM Control: Integrating Flux Weakening, and MTPA for Performance Enhancement 205
Jakub Súkeník, Marek Toman
Computational Fluid Dynamics Thermal Modelling of Fan-Cooled Finned Heat-sink Considering Air Temperature Rise 210
Tadeáš Zbožínek, Michal Jelínek, Josef Hynšt, Břetislav Mikel
Enhancing Signal Collection Efficiency in Liquid Scintillators via Optical Fibre End Treatments for Dosimetry Applications 215
Lukáš Zdražil, Marek Andrle, Petr Špaček
Electrical Properties Measurement of SMD Electrodes for Surface Decontamination 220

Matěj Turinský
Photovoltaic power plant source measurement system for fault detection 226
Stepan Jezek, Radim Burget
Speed Measurement from Traffic Camera Video Using Structure-from-Motion-Based Calibration 231
Jakub Čelko
Comparison of Direct and Indirect Identification of a Human Driver Model 236
Jan Klouda, Petr Marcoň
UAV platform for special operation 241

OPENING WORD OF THE DEAN

These Proceedings contain papers presented during the 31st annual STUDENT EEICT conference, held at the Faculty of Electrical Engineering and Communication, Brno University of Technology, on April 29, 2025. The fruitful tradition of joining together creative students and seasoned science or research specialists and industry-based experts was not discontinued, providing again a valuable opportunity to exchange information and experience.

The EEICT involves multiple corporate partners, collaborators, and evaluators whose intensive support is highly appreciated. Importantly, the competitive, motivating features of the conference are associated with a practical impact: In addition to encouraging students to further develop their knowledge, interests, and employability potential, the forum directly offers career opportunities through the affiliated PerFEKT JobFair, a yearly job-related workshop and exhibition complementing the actual EEICT sessions. In this context, the organizers acknowledge the long-term assistance from the Ministry of Education, Youth and Sports of the Czech Republic, which has proved essential for refining the scope and impact of the symposium.

In total, 136 peer-reviewed full papers distributed between 19 sessions were submitted and evaluated by examining boards with industry and academic specialists. The presenting authors exhibited a very high standard of knowledge and communication skills, and the best competitors received prize money and/or valuable gifts. These Proceedings comprise 54 award winning full papers, all selected by the conference's evaluation boards. Our sincere thanks go to the sponsors, experts, students, and collaborators who participated in, contributed to, and made the conference a continued success.

Considering all the efforts and work invested, I hope that the 31st STUDENT EEICT (2025) has been beneficial for all the participants.

I believe that the inspiration gathered during the event will contribute to the further advancement of open science and research, giving all the attendees a chance to freely discuss their achievements and views.

Prof. Vladimír Aubrecht
Dean of the Faculty of Electrical
Engineering and Communication

Forensic Verification of Author of Handwritten Character “k” Using Artificial Intelligence

Eliška Bachorecová
Department of Telecommunications
FEEC, Brno University of Technology
Brno, Czechia
247514@vut.cz

***Abstract*—Handwriting, as a result of the interplay of physiological and psychological factors, is considered a unique manifestation of human individuality. It carries significant information about the writer, which can be utilized across various fields, particularly in forensic science, where it is applied in forgery detection, psychological profiling, author identification and verification. Forensic handwriting analysis is currently facing a decline of handwriting. Despite the decline, its significance remains relevant as the need for higher-quality expertise is increasing. This leads to an effort to integrate modern technologies within this discipline. A major shortcoming of current studies is that analysis is performed at the sentence or word level.**

Therefore, a method was proposed for verifying authorship based exclusively on information derived from variations in the handwritten character “k”. This research was conducted in collaboration with the Institute of Criminalistics in Prague and its significance lies in its ability to analyze handwriting at the grapheme level by employing deep learning-based approaches. All models were trained and evaluated on authentic handwriting samples from criminal cases, ensuring practical applicability. The best results were achieved using a siamese network with *accuracy* of 82.8 %.

***Index Terms*—forensic handwriting analysis, artificial intelligence, deep learning, CNN, siamese networks**

I. Introduction

Forensic handwriting analysis is a criminalistic identification method based on the comparison of disputed and reference materials. Firstly, experts analyze characteristics of individual handwritten characters, such as slant, width, height and consistency. Based on this analysis, they determine whether there is sufficient similarity between the materials to confirm or reject authorship [1]. The underlying premise of this approach is that no two individuals have identical handwriting [2].

This discipline is relatively demanding, primarily due to the high variability of graphemes within an individual’s handwriting. Humans are incapable of reproducing their handwriting in an identical manner [2]. Consequently, experts can never base their conclusions on a perfect match between samples, because such exactness would suggest a forgery. Handwriting variability depends on numerous factors, such as education, nationality, psychological state and maturity. At the same time, handwriting typically carries enough unique features to allow identification, except in rare cases where the writing instrument or surface makes it impossible [3].

One of the main limitations of handwriting expertise is its subjective nature [4]. The outcomes of handwriting examinations rely solely on the cognitive and perceptual abilities of experts. Moreover, they are also time-consuming. Quantitative comparative techniques are absent [5]. The results are presented in the form of categorical conclusions, which cannot be statistically analyzed. Based on these findings, a method based on deep learning has been proposed as a supportive tool for experts, ensuring objective and reproducible results while also making their work more time efficient.

The general procedure for author verification based on handwriting using modern technologies is as follows. The first step is obtaining the dataset. For practical applicability, it is crucial that the samples are authentic and not created under laboratory conditions. This is followed by the digitization of images, during which dynamic handwriting information such as pressure, speed, or pen tilt is lost. Although these details are highly valuable to experts, this step remains necessary [6]. The preprocessing of data involves normalization, segmentation, noise reduction and data augmentation. Data augmentation techniques such as rotation, skewing or morphological operations can simulate writer variability. Finally, significant features are extracted and classification is performed using conventional or modern algorithms, followed by evaluation based on appropriately chosen metrics [7].

II. Related Works

Forensic handwriting analysis includes conventional and modern methods. Conventional methods rely on handcrafted feature extractors. An expert can manually define which handwriting characteristics will be analyzed, such as the geometric properties of a grapheme. Alternatively, automatic feature extractions can be done by algorithms like the scale-invariant feature transform (SIFT) or the local binary pattern (LBP). However, they still rely on predefined conditions, focusing on specific image aspects such as local intensity variations. Classification is often performed using methods like the support vector machine (SVM) [2], [8]. The main drawback of this approach is its reliance on the human factor and it does not always achieve the desired results [7].

Modern approaches use deep learning, where extraction and classification happen within a single unified architecture [2]. Furthermore, features are detected automatically without human involvement. On the other side, higher computational requirements can be a drawback. Convolutional neural networks (CNN) appear to be particularly suitable, as they can identify deviations even at the pixel level [9]. Additionally, siamese networks perform well even with limited data, which is crucial due to the decline in availability of handwritten texts [10]. This architecture is frequently used because it can capture fine nuances in handwriting [4]. In recent years, vision transformers (ViT) have been gaining popularity [11], as well as architectures that combine the attention mechanism with the previously mentioned approaches [12].

Recent studies show promising results, but analyses are usually conducted on entire words or longer text segments [4], [11], [12]. These sources [6], [13], [14] focus on individual graphemes. However, their practical applicability is limited because they are based on laboratory-created datasets obtained under controlled conditions. Therefore, the proposed method uses an authentic dataset containing only cursive and block variations of the letter “k”, which, due to its complex structure, is expected to carry significant information about the writer.

III. Proposed method

The general experiment scheme is shown in Figure 1. In the first phase, data is collected and then preprocessed appropriately. The next step involves training the model, which is then evaluated using assessment metrics.

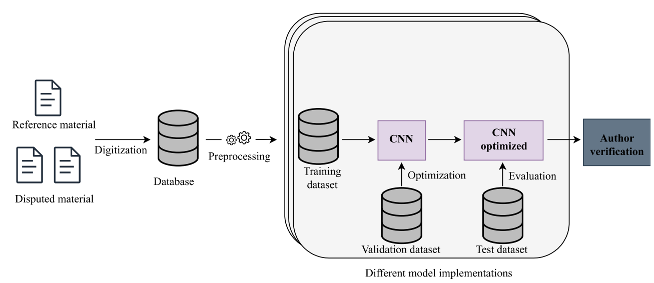

Fig. 1. Experiment scheme

A. Dataset

The dataset was provided by a consultant. It contains samples from a total of 89 individuals of Czech and Slovak nationality, which introduces certain specific characteristics. Each author provided 2–4 pages of handwritten text in A4 format. The samples are authentic and were not obtained under standardized conditions. The images were scanned at a resolution of 600 dpi. Next, they were converted to grayscale to mitigate the risk of the model learning to classify based on ink or pencil color. Connected component detection was then applied to isolate the grapheme itself and remove unwanted elements such as paper impurities or lines. Individual characters were manually selected via a convex hull. The images were centralized and resized to a uniform dimension of 229×229. In total, 2 655 samples of letter “k” were selected.

The dataset was created by first selecting a random document as the reference and another, from the same or a different author, as the disputed document. From the reference documents, 2–4 characters were selected, while 4–8 characters were taken from the disputed documents. This process resulted in the creation of training, test and validation datasets. The distribution of these datasets is shown in Table I. The datasets can be considered balanced, so minor deviations were compensated by using a simple numerical balancing method. Training data was shuffled to ensure that model performance was not dependent on the order of input data.

TABLE I
Dataset for the letter “k”

Train		Test		Validation	
Match	**No match**	**Match**	**No match**	**Match**	**No match**
809	832	180	180	139	155

B. Model based on convolutional neural network

The first model, shown in Figure 3, is based on CNN with input images capturing differences between averaged disputed and reference characters, represented in grayscale, as shown in Figure 2.

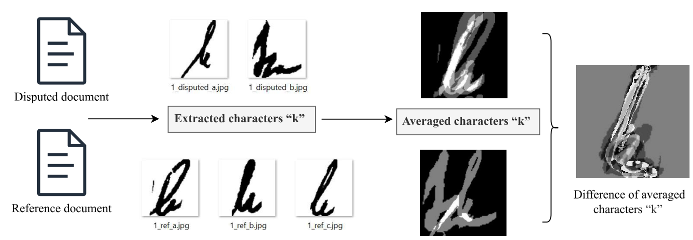

Fig. 2. Data preprocessing for the CNN

The architecture consists of four convolutional layers with a kernel size of 2×2. Their number doubles at each stage, as shown in Figure 3. These layers are followed by 2×2 MaxPool. Excessive data augmentation had a negative impact on model performance, so only rotation and horizontal and vertical shifts were used. Leaky ReLU is employed as the activation function to mitigate the risk of dying ReLU [15]. The loss function is a binary cross-entropy (BCE), defined by the following equation:

$$\mathcal{L}_{\mathrm{BCE}} = -\frac{1}{N}\sum_{i=1}^{N}\left[y_i \log(\hat{y}_i) + (1-y_i)\log(1-\hat{y}_i)\right], \quad (1)$$

where N represents the total number of samples in the dataset, y_i denotes the actual class membership of the sample and $\hat{y}_i$ represents the predicted class membership [15]. The model showed a strong tendency to overfit, therefore Batch Normalization, L2 regularization and Dropout layers were applied. For optimization, EarlyStopping and ReduceLROnPlateau mechanisms are used. The final classification is performed by the sigmoid function. The number of training epochs is 70 with a batch size of 16.

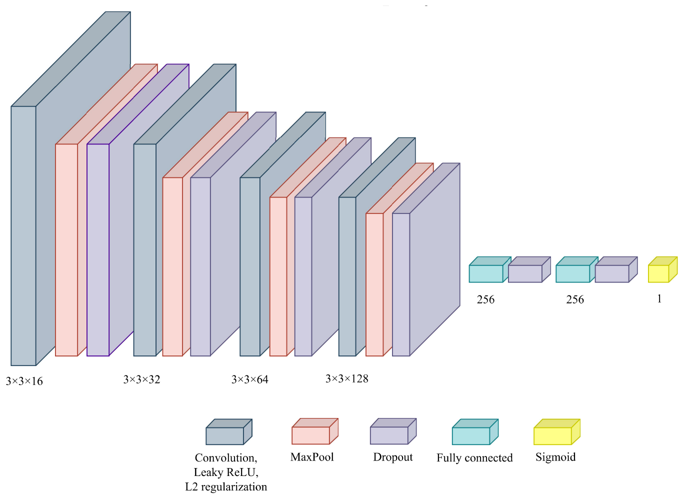

Fig. 3. The CNN architecture

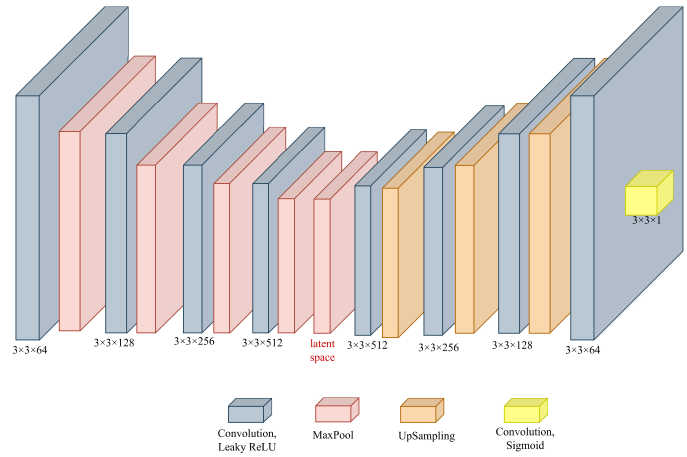

Fig. 5. Autoencoder as a part of the SCNN

C. Model based on siamese network

This model is a siamese CNN (SCNN), where the input consists of pairs of averaged disputed or reference characters. Differences or similarities between characters are highlighted in various shades of gray. An example of the input is shown in Figure 4.

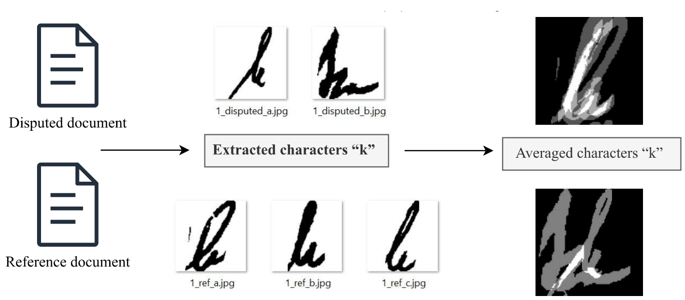

Fig. 4. Data preprocessing for the SCNN

Due to insufficient performance and a tendency to overfit when using only a CNN architecture, an autoencoder is employed, as shown in Figure 5. This type of neural network consists of an encoder and a decoder, where data is first reduced to a latent space before the model learns to reconstruct the images [15]. The number of convolutional layers with 3×3 kernels ranges from 64 to 512. MaxPool and UpSampling layers use 2×2 kernels. First four layers of the pre-trained encoder are utilized as a part of siamese network. Data augmentation did not improve results, likely due to the dataset's complexity. Leaky ReLU is used as the activation function. Finally, Lambda layer computes the absolute difference between the outputs of siamese network, followed by sigmoid classification. As in the previous case, EarlyStopping and ReduceLROnPlateau are applied. The model is trained for 70 epochs with a batch size of 16.

IV. Results

This section presents the results achieved for both models. The selected metrics include: *accuracy*, *precision*, *recall*, $F1$ score and *AUC*. These metrics were chosen considering the binary nature of the problem and the dataset balance.

Table II presents the observed metric outputs. The second column shows results for the CNN model, while the third column corresponds to the SCNN architecture. The SCNN outperformed the CNN across all evaluation metrics, achieving 82.8 % for each of *accuracy*, *precision*, and *recall*. Based on these values, the $F1$ score is 82.8 %. The CNN model achieves an *accuracy* of 73.9 %, with a *precision* of 73.6 %. *Recall* reaches 74.4 % and the $F1$ score is 74.0 %. Values of *AUC* for the CNN and the SCNN are 73.9 % and 82.8 %, respectively.

The graphs in Figure 6 shows how *accuracy* changes for training and validation data for the CNN and the SCNN, in that order. It indicates that both models do not show clear signs of overfitting.

Examples of heatmap outputs from Grad-CAM are shown in Figure 7 for the CNN and Figure 8 for the SCNN. These visualizations were created to improve the interpretability of the results. Each includes both the original image with the actual label value and its combination with the heatmap and predicted label value. The importance of different regions is represented by a color scale, where red indicates the most significant areas, while blue represents the least important ones.

TABLE II
METRICS OF THE CNN AND SCNN MODELS FOR THE LETTER "K"

Metric	CNN	SCNN
Accuracy	73.9 %	82.8 %
Precision	73.6 %	82.8 %
Recall	74.4 %	82.8 %
$F1$ score	74.0 %	82.8 %
AUC	73.9 %	82.8 %

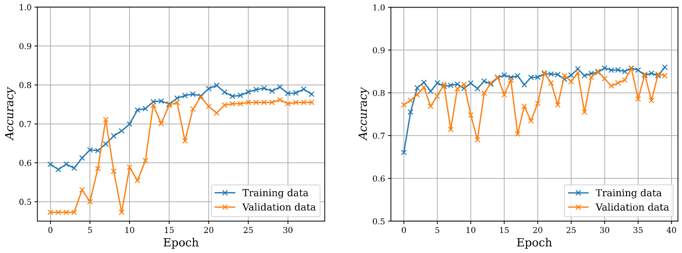

Fig. 6. *Accuracy* development for the CNN and the SCNN, respectively

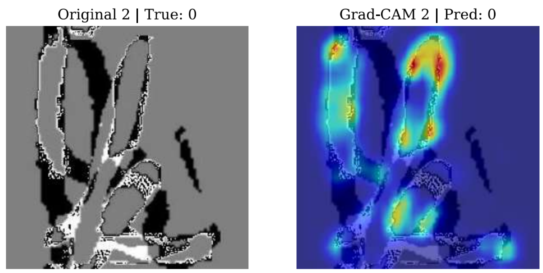

Fig. 7. Grad-CAM example for the CNN

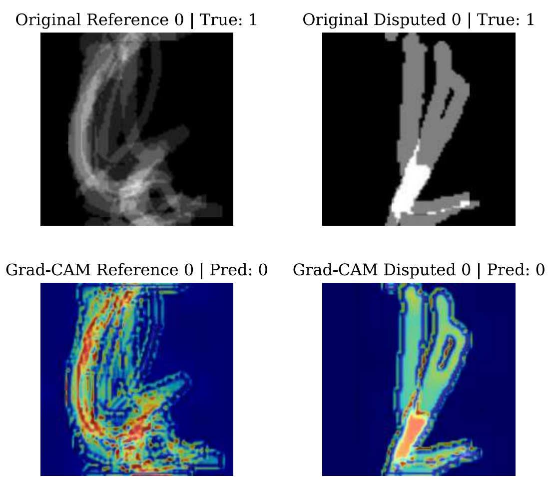

Fig. 8. Grad-CAM example for the SCNN

V. Conclusion

This study presents the design and implementation of two neural networks for verifying authorship based on the handwritten character "k". The primary goal was not to replace the human factor from handwriting analysis but to create a supportive tool for the Czech and Slovak experts. The key contribution of this work is the ability to correctly verify authorship with 82.8 % *accuracy* based on cursive and block variations of a single grapheme, reflecting the current decline in handwritten text usage. The models were trained and tested on authentic datasets, which is crucial for practical applicability. For comparsion, studies [13] and [14] focusing on graphemes achieved an average *accuracy* of 97 % and 80 %, respectively. Nevertheless, both rely on laboratory-created dataset containing only block letters, which raises concerns about models performance in real-world cases.

For future work, it would be beneficial to test the models on additional characters and evaluate their robustness. To improve result interpretability, it would be useful to consult the heatmap outputs with experts from the Institute of Criminalistics in Prague.

VI. Acknowledgement

I want to express my sincere gratitude to my supervisor doc. Ing. Radim Burget, Ph. D., for his insightful suggestions and invaluable guidance throughout my bachelor thesis. I would also like to thank Ing. Vojtěch Myška, Ph. D. for providing the dataset, which was crucial for this work.

References

[1] National Research Council et al., *Reference Manual on Scientific Evidence*, 3rd ed. Washington, DC: The National Academies Press, 2011.

[2] F. Alaei and A. Alaei, "Handwriting Analysis: Applications in Person Identification and Forensic," in *Breakthroughs in Digital Biometrics and Forensics*, K. Daimi, G. Francia III, and E. L. Hernandéz, Eds. Cham, Switzerland: Springer Cham, 2022, pp. 147–165. doi: 0.1007/978-3-031-10706-1_7.

[3] R. Morris, *Forensic Handwriting Identification: Fundamental Concepts and Principles*, 2nd ed. Cambridge, MA: Academic Press, 2020.

[4] W. Xiao, "Offline handwritten signature verification using siamese network model," in *2024 6th International Conference on Electronic Engineering and Informatics (EEI)*, 2024, pp. 1536–1539, doi: 10.1109/EEI63073.2024.10696305.

[5] A. Agius et al., "The use of handwriting examinations beyond the traditional court purpose," *Science & Justice*, vol. 57, no. 5, pp. 394–400, 2017, doi: 10.1016/j.scijus.2017.05.001.

[6] A. Hagström, R. Stanikzai, J. Bigun, and F. Alonso-Fernández, "Writer recognition using off-line handwritten single block characters," in *2022 International Workshop Biometrics Forensics (IWBF)*, 2022, pp. 1–6, doi: 10.1109/IWBF55382.2022.9794466.

[7] S. Inunganbi, "A systematic review on handwritten document analysis and recognition," *Multimedia Tools and Applications*, vol. 83, no. 2, pp. 5387–5413, 2024, doi: 10.1007/s11042-023-15326-9.

[8] K. Trehan and R. Rani, "Review on writer identification and verification methods," in *2023 14th International Conference on Computing Communication and Networking Technologies (ICCCNT))*, 2023, pp. 1–6, doi: 10.1007/s11042-023-15326-9.

[9] R. Sukhija, M. Kumar, and M. K. Jindal, "Document forgery detection: a comprehensive review," *International Journal of Data Science and Analytics*, 2025, pp. 1–23, doi: 10.1007/s41060-025-00723-0.

[10] J. J. Valero-Mas, A. J. Gallego, and J. R. Rico-Juan, "An overview of ensemble and feature learning in few-shot image classification using siamese networks," *Multimedia Tools and Applications*, vol. 83, no. 7, pp. 19929–19952, 2024, doi: 10.1007/s11042-023-15607-3.

[11] J. Kim, S. Park, and A. Carriquiry, "A deep learning approach for the comparison of handwritten documents using latent feature vectors," *Statistical Analysis and Data Mining: The ASA Data Science Journal*, vol. 17, art. e11660, 2024, doi: 10.1002/sam.11660.

[12] H. Meng, X. Lin, K. Ubul, and A. Aysa, "Multi-task interaction network based on a cross-attention fusion mechanism for offline signature verification," in *27th International Conference on Pattern Recognition*, 2025, pp. 17–31, doi: 10.1007/978-3-031-78389-0_2.

[13] V. Aubin, M. Mora, and M. Santos-Peñas, "Off-line writer verification based on simple graphemes," *Pattern Recognition*, vol. 79, pp. 414–426, 2018, doi: 10.1016/j.patcog.2018.02.024.

[14] N. Dlamini and T. L. van Zyl, "Author identification from handwritten characters using siamese CNN," in *2019 International Multidisciplinary Information Technology and Engineering Conference (IMITEC)*, 2019, pp. 1–6, doi: 10.1109/IMITEC45504.2019.9015897.

[15] S. J. D. Prince, *Understanding Deep Learning*. Cambridge, MA: MIT Press, 2023.

Direct Gene Detection in Raw Nanopore Signals Using Transformer Neural Networks

Jevhenij Vorochta
Department of Biomedical Engineering
Brno University of Technology
Brno, Czech Republic
247319@vut.cz

Ing. Helena Vítková, Ph.D.
Department of Biomedical Engineering
Brno University of Technology
Brno, Czech Republic
vitkovah@vut.cz

Ing. Roman Jakubíček, Ph.D.
Department of Biomedical Engineering
Brno University of Technology
Brno, Czech Republic
jakubicek@vut.cz

***Abstract*—Nanopore sequencing has transformed genomics by enabling real-time analysis of DNA and RNA in a compact, cost-effective device. However, conventional workflows require a separate basecalling step to convert raw electrical signals into nucleotide sequences, which can introduce errors and delay downstream analyses such as gene detection. Here, we present a novel approach that bypasses basecalling by directly analyzing raw nanopore signals using a transformer-based neural network. By adapting a model originally designed for ECG classification, we developed a system capable of detecting specific antibiotic resistance genes in *Klebsiella pneumoniae* samples. Raw signals were preprocessed through downsampling, z-normalization, and segmentation into 5,000-sample windows, yielding a dataset of 13,080 labeled segments. Experimental results demonstrate that our model effectively distinguishes gene-containing segments from non-target signals, achieving up to 80% accuracy in the "no target gene" category. In contrast, accuracy for other gene categories was lower, indicating that further optimization of the model is required. This direct-signal approach not only reduces the computational burden associated with basecalling but also streamlines the workflow, promising faster diagnostic turnaround times. These findings provide a significant step toward integrating advanced deep learning methods with nanopore sequencing for rapid, on-site genomic analysis and have potential applications in clinical diagnostics and epidemiological surveillance.**

***Index Terms*—Nanopore sequencing, transformer neural networks, gene detection, antibiotic resistance, bioinformatics, deep learning**

I. Introduction

Over the last decade, nanopore sequencing has become a prime example of third-generation sequencing technology, offering real-time analysis in a portable, cost-effective device [1]. In its early implementations, so-called "event"-based methods attempted to break the current signal into discrete transitions, each of which was assigned to a likely nucleotide by analyzing features such as the mean amplitude, standard deviation, segment length, and the difference in means across consecutive events [2]. However, these event-based approaches often struggled with noise and relatively low accuracy, limiting their utility for clinical or large-scale applications. With advancements in nanopore chemistry, hardware, and neural-network-powered basecallers, accuracy has since risen dramatically [3]. Modern pipelines typically rely on more sophisticated neural network architectures (e.g., RNNs, CNNs, LSTM/GRU models) to process raw signals directly and produce high-accuracy sequences [4].

Despite these advances, a major bottleneck remains: the conventional pipeline converts the nanopore signal into a basecalled sequence before performing higher-level analyses, such as gene detection or variant calling. This extra basecalling step can introduce errors or data loss and add significant time to the overall workflow. Inspired by the idea that DNA can be viewed analogously to linguistic data [5], we have begun exploring direct signal processing with neural networks—particularly transformers, widely used in today's large language models (LLMs) because of their ability to capture long-range dependencies and process long sequential data [6].

Motivated by these factors, our work seeks to eliminate the basecalling phase entirely by using a deep learning model that directly classifies genetic information from raw nanopore signals. The aim is to improve speed and maintain accuracy by bypassing intermediate conversion steps. In the following sections, we describe the data preparation workflow, provide an overview of our transformer-based model design, and present the experimental results along with potential applications.

II. Data Preparation and Preprocessing

Data preparation was a critical part of this project. Raw signals from nanopore sequencing of *K. pneumoniae* samples were obtained from runs performed at the Department of Internal Medicine – Haematology and Oncology, University Hospital Brno. Initially, sequencing reads stored in BAM files were converted to SAM using SAMtools (v1.13), and then a dedicated module within the NanoBlast tool [7] was employed to convert the SAM files to FASTA, thus facilitating downstream processing. Using another module of NanoBlast, the resulting sequences were compared against a reference database of selected antibiotic resistance genes. Matches that met our quality criteria (e-value, bit score, minimum matched sequence length) were located in the POD5 files, where the raw nanopore signals are stored, and the corresponding signals were extracted.

As shown in Fig. 1, these signals sometimes exceed 100,000 samples in length, while most gene segments are shorter than 20,000 samples. Based on this analysis, we first divided the signals into training, validation, and test sets in a 70:20:10 ratio

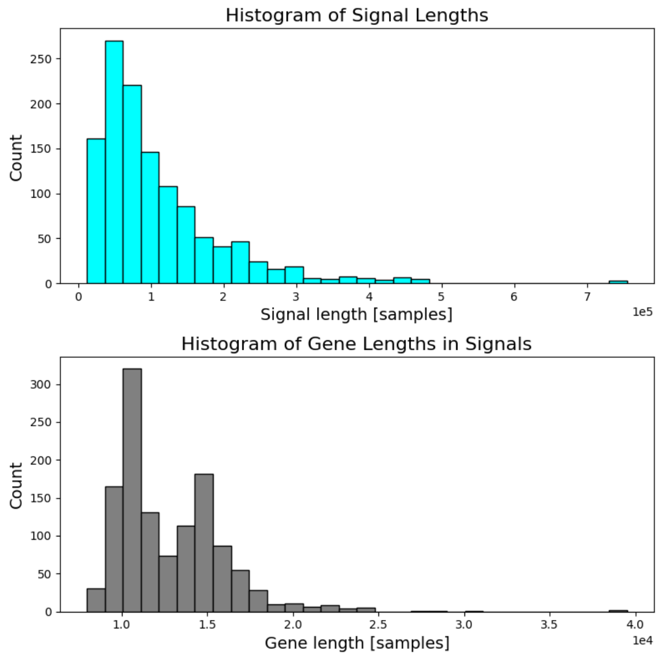

Fig. 1. Visualization of the raw signal length distribution and gene length distribution.

to ensure that segments from a single signal did not appear in multiple sets. Subsequently, we downsampled the signals by a factor of 4 and segmented them into windows of 5,000 samples, ensuring that the genes are contained within a single segment. Genes samples that were too long for one segment were not used. The segmentation was idealized so that the target gene was either fully present or absent in each segment. Additionally, one signal could be segmented multiple times by applying an offset. This form of augmentation allowed our dataset to contain thousands of labeled segments, which is essential for effective model training. Before segmentation, we also applied z-normalization to each signal to account for the variability in amplitude [8], which was necessary for more stable model training.

III. Methodology

Our approach uses a transformer-based neural network to classify the presence or absence of specific genes directly from raw nanopore signals, without the need for basecalling. The entire model was implemented in Python (v3.8.12) using the PyTorch library (v2.4.1). During implementation, we adapted a transformer model originally designed for ECG classification [9]. Nanopore signals generally have a much greater length and higher sampling frequency than ECG data, so modifications were necessary to handle more extensive sequential input.

Figure 2 presents a block diagram illustrating the architecture of our transformer model. A linear layer first embeds the one-dimensional signal into a higher-dimensional space, and positional encoding (via sine and cosine functions) preserves the order of samples. These embeddings pass through two layers of multi-head self-attention and feed-forward networks,

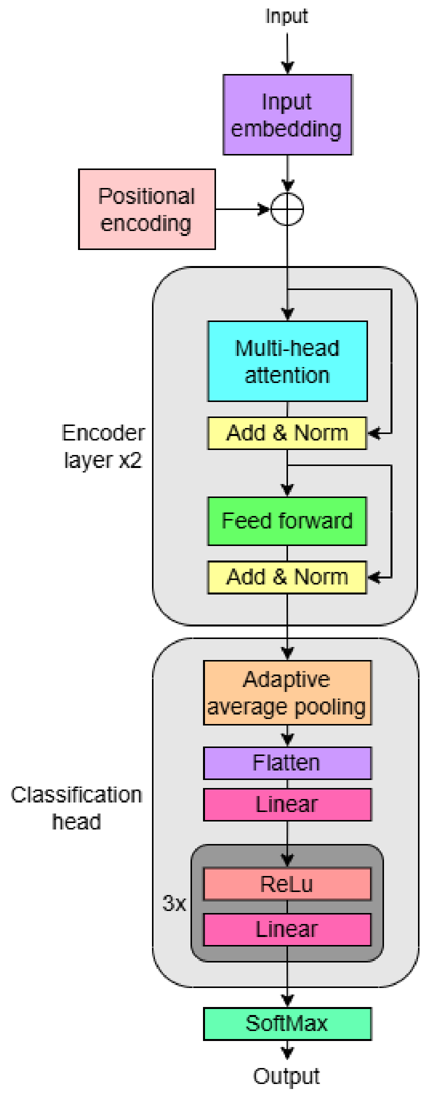

Fig. 2. Block diagram of the adapted transformer model for direct gene classification.

capturing both local features and long-range dependencies. The final classification stage uses fully connected layers to convert the encoder's output into class probabilities for multiple genes or the no-gene class [6].

During training, we encountered overfitting issues. To mitigate this, dropout was incorporated at several stages of the network, and additive Gaussian noise was applied to the input layers. These regularization strategies enabled the model to generalize more effectively, even when processing lengthy nanopore data [6] [10].

IV. Results Discussion

Our dataset consisted of 2,081 raw signals collected from 10 distinct subtypes of *K. pneumoniae*. Among these, 642 signals contained the *aac(3)-IIa* gene and 624 signals contained the *aac(3)-IId* gene—two variants conferring resistance to aminoglycosides that share 95% sequence identity—with gene lengths of approximately 1.1 kbp and 1.0 kbp, respectively.

Additionally, the *tetA* gene, associated with resistance to doxycycline, tetracycline, and minocycline, was present in 815 signals and had a length of about 1.6 kbp. Due to the variance in the raw signal sampling rate, the measured gene lengths varied from signal to signal [8]. The lengths of whole signals varied considerably, ranging from roughly 13,000 to 754,917 samples. Augmentation via segmentation (with applied offsets) increased the dataset to a total of 13,080 labeled segments. These normalized segments of 5,000 samples—typically covering the full length of the target genes—were already downsampled by a factor of 4.

Figure 3 shows the confusion matrix for the testing set, providing additional quantitative insight into the model's performance in distinguishing among the gene classes. Notably, the model achieved the highest accuracy in the "no target gene" category, with approximately 79.87% correct classifications. In contrast, the *tetA* gene was detected with an accuracy of 60.51%, while the two variants of the *aac(3)-IIa* gene were recognized with lower success rates—39.22% for *aac(3)-IIa* and 34.47% for *aac(3)-IId*. These results highlight the challenges in accurately differentiating highly similar gene variants and underscore the need for further optimization of the model.

One significant challenge remains: even after downsampling and segmentation, the input length is still too large. The computational complexity of the attention mechanism scales quadratically with the input length (i.e. $O(n^2)$) [6], which imposes memory constraints on the GPUs used for training. Future work will explore several strategies, including:

- Using convolutional layers to extract features from the signals prior to feeding them into the transformer—this approach can preserve important information better than simple downsampling.
- Altering the transformer model to use local attention mechanisms (with complexity $O(n \log n)$), as implemented in architectures like the Reformer [11] or Longformer [12].
- Incorporating statistical evaluation by combining hundreds of reads from a single run to reduce the effects of noise and artifacts.
- Employing filtering methods to reduce signal noise prior to analysis.

V. Conclusion

The primary application of this approach is the rapid detection of antibiotic resistance genes—a capability that can be crucial in emergency clinical situations. In cases where every minute counts, waiting for traditional laboratory results can have serious consequences for patient survival rates. Furthermore, in epidemiology, the method can be used for swift pathogen identification during outbreaks, thereby facilitating faster and more effective quarantine measures, especially in remote areas with limited laboratory facilities.

In conclusion, the integration of transformer-based neural networks with direct analysis of raw nanopore signals represents a promising advancement in bioinformatics. By eliminating the basecalling step, this method has the potential to significantly accelerate diagnostic processes, which are essential for both clinical decision-making and epidemiological monitoring [13]. Although the current model requires further refinement to improve its classification accuracy and generalization ability, the approach underscores the potential of combining cutting-edge deep learning methods with next-generation sequencing technologies. This work not only contributes to the evolution of bioinformatics but also lays the groundwork for future developments in rapid, on-site genomic analysis and personalized medicine.

	Target class					
Output class		**No target gene**	**aac(3)-IIa**	**aac(3)-IId**	**tetA**	**SUM** **PPV** **FDR**
	No target gene	250 19.11%	114 8.72%	123 9.40%	116 8.87%	**603** **41.46%** **58.54%**
	aac(3)-IIa	35 2.68%	111 8.49%	60 4.59%	9 0.69%	**215** **51.63%** **48.37%**
	aac(3)-IId	18 1.38%	44 3.36%	111 8.49%	29 2.22%	**202** **54.95%** **45.05%**
	tetA	10 0.76%	14 1.07%	28 2.14%	236 18.04%	**288** **81.94%** **18.06%**
	SUM **TPR** **FNR**	**313** **79.87%** **20.13%**	**283** **39.22%** **60.78%**	**322** **34.47%** **65.53%**	**390** **60.51%** **39.49%**	**708 / 1308** **54.13%** **45.87%**

Fig. 3. Confusion matrix (testing set). The colored percentage values inside each cell denote the proportion of the total samples falling into that cell. Correctly classified instances are shown in green, while misclassified instances appear in red. The last row and column present the sum of predictions for each class (row) and the sum of actual occurrences (column), together with the associated performance metrics: true positive rate (TPR), false negative rate (FNR), positive predictive value (PPV), and false discovery rate (FDR).

Acknowledgment

This work was supported by a grant project from the Czech Science Foundation [GA23-05845S].

References

[1] Heather, J. M. and Chain, B., "The sequence of sequencers: The history of sequencing DNA," *Genomics*, vol. 107, no. 1, pp. 1–8, 2016.

[2] Napieralski, A. and Nowak, R., "Basecalling Using Joint Raw and Event Nanopore Data Sequence-to-Sequence Processing," *Sensors*, vol. 22, no. 6, p. 2275, 2022. [Online]. Available: https://doi.org/10.3390/s22062275

[3] Wick, R. R., Judd, L. M. and Holt, K. E., "Performance of neural network basecalling tools for Oxford Nanopore sequencing," *Genome Biology*, vol. 20, p. 129, 2019.

[4] Wick, R. R., Judd, L. M. and Holt, K. E., "Performance of neural network basecalling tools for Oxford Nanopore sequencing,"

[5] Tsonis, A. A., Elsner, J. B. and Tsonis, P. A., "Is DNA a Language?," *Journal of Theoretical Biology*, vol. 184, no. 1, pp. 25–29, 1997. [Online]. Available: https://doi.org/10.1006/jtbi.1996.0239 *Genome Biology*, vol. 20, article 129, 2019. [Online]. Available: https://doi.org/10.1186/s13059-019-1727-y

[6] Vaswani, A., Shazeer, N., Parmar, N., et al., "Attention is All you Need," in *Advances in Neural Information Processing Systems*, 2017.

[7] M. Suriak, “Nástroj pro zpracování a konverzi nanopórových signálů,” Bachelors thesis, Brno University of Technology, 2024. [Online]. Available: https://hdl.handle.net/11012/247406

[8] Wang, Y., Zhao, Y., Bollas, A., et al., “Nanopore sequencing technology, bioinformatics and applications,” *Nature Biotechnology*, vol. 39, pp. 1348–1365, 2021.

[9] TimeSeries Classification and Forecasting, 2023. [Online]. Available: https://github.com/mselmangokmen/TimeSeriesProject

[10] Abdel-Nasser Sharkawy, “Principle of Neural Network and Its Main Types: Review,” 2020.

[11] Kitaev, N., Kaiser, Ł. and Levskaya, A., “Reformer: The Efficient Transformer,” arXiv preprint arXiv:2001.04451, 2020. [Online]. Available: https://arxiv.org/abs/2001.04451

[12] Beltagy, I., Peters, M. E. and Cohan, A., “Longformer: The Long-Document Transformer,” arXiv preprint arXiv:2004.05150, 2020. [Online]. Available: https://arxiv.org/abs/2004.05150

[13] Nykrýnová, M., Jakubíček, R., Bartoš, V., et al., “Using deep learning for gene detection and classification in raw nanopore signals,” *Frontiers in Microbiology*, vol. 13, 2022.

Hand gesture recognition from EMG signal using machine learning

Dan Nguyen
Department of Biomedical Engineering
Brno University of Technology, FEEC
Brno, Czech Republic
247280@vut.cz

***Abstract*—This work addresses the issue of upper limb gesture recognition based on the analysis of surface EMG signals recorded in the wrist area. Machine learning classification algorithms, especially LDA, are utilized for this purpose. The research focuses on future applications of this technology, particularly in the field of remote control of electronic devices in real-time, such as controlling smart home systems, robots, or other intelligent systems. In this paper, LDA machine learning classification models with different parameters were trained, achieving success rates up to 94.15% on testing data. Furthermore, a detailed analysis was conducted to examine how the specifically placed recording electrodes affected the success rate of the resulting machine learning model. This analysis can be followed to reduce the number of recording electrodes while minimizing the decrease in classification success rate.**

***Index Terms*—EMG, gestures, wrist, classification, machine learning, MATLAB**

I. Introduction

Nowadays, there are many wearable devices that make our daily lives easier. Various smart bracelets and watches are capable of giving us useful information such as daily physical activity, heart rate or stress levels. This information is obtained by the smart device from monitoring various signals, for example plethysmographic or accelerometric data. But with the help of these smart devices, it is also possible to interact more easily with other electrical devices.

The touch screen interface is still the most widely used for this purpose today. However, this method may not be applicable in all situations because of the need to use both hands. Furthermore, interacting with the small display of the device may not be comfortable for the user.

There are attempts to recognize hand gestures and use them for device control, like Apple's 'AssistiveTouch' feature, which utilizes accelerometric, gyroscopic, and photoplethysmographic data. However, this method limits the appearance of gestures, that can be recognised.

A signal that is not currently used for these purposes is surface EMG. The main reason is the complexity of acquisition, as achieving high recognition accuracy requires precise anatomical placement of electrodes over the active muscle and good conductive contact with the skin to suppress noise in the signal. However, its use could enable the classification of more complex and natural gestures, enhancing the user experience.

The focus of this paper is to develop a machine learning model capable of recognizing hand gestures in real time using EMG signals obtained from the subject's wrist. Furthermore, analysis in terms of the number of channels will be carried out. This can be used to reduce the number of electrodes, thereby simplifying data acquisition.

II. Dataset Description

For the purposes of this paper, publicly available dataset GrabMyo (Gesture Recognition and Biometrics electroMyogram) was used [1]. This database was chosen for many reasons. First of all, it was the only found database with records captured from the wrist with such a large number of participants. This brings us to the second reason for choosing this database, which is its size. The database measured 43 subjects on three different days, which, as the authors themselves state, differs significantly from other databases with a similar focus, where usually is a lack of diversity in days of records for a single subject. In this database, the lack of diversity is eliminated by measuring each subject on three different days (the first session: day 1, the second session: day 8, the third session: day 29). Other reasons include the high sampling rate, which was set here at 2048 Hz (more than enough for the EMG signal with a range of 10-500 Hz [2]).

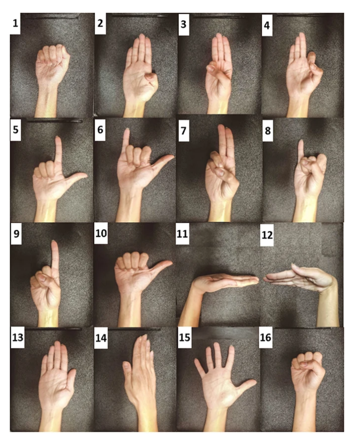

Fig. 1. Appearance of measured gestures, taken from [1]

Twenty-eight monopolar electrodes were used and were placed on the subject's arm according to the acquisition protocol . The measurement itself then consisted of 16 gestures + relaxation (gesture 17). Each gesture was measured during one session seven times, and the gestures were measured in random order. These measurements therefore resulted in 3 sessions, including 43 subjects with 7 repetitions for each gesture. Each repetition then resulted in 28 recordings (number of electrodes) lasting 5s. The authors of the study then reported that after each measurement, any errors in the recording (delay, confusion gestures) were remeasured and replaced, so the resulting recordings should capture only the required gestures. These recordings were also preprocessed with a band pass in the 10-500 Hz region, using a fourth order Butterworth filter, futhermore network noise was removed using a Notch filter at 60 Hz.

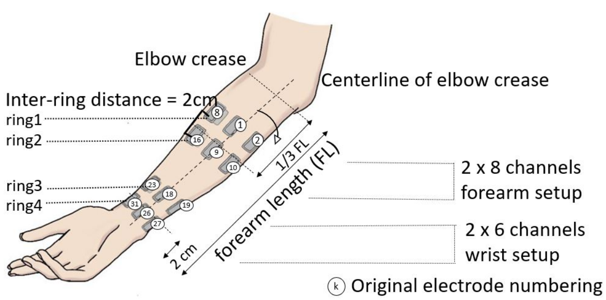

Fig. 2. Electrode location, taken from [1]

III. FEATURE EXTRACTION

Object of interest of this paper are mainly the surface EMG signals obtained from the wrist, and therefore the only signals from 6 distal electrodes (electrodes number 26-31 according to “Fig. 2”) located on the subject’s wrist were processed.

A. Preprocessing

In the block diagram in “Fig. 3”, it can be seen how the signals were processed before the actual extraction of the features. The first two steps, signal acquisition and filtering, were already performed by the authors of the database [1]. In order to achieve a higher SNR (”Signal-to-Noise Ratio”), the signals from the monopolar electrodes were referenced to the common average of all electrodes according to the formula:

$$r = x_c - \frac{1}{N}\sum_{i=1}^{N} x_i \tag{1}$$

This formula describes bringing the value x_c, captured by a particular electrode, to a common reference constructed from the average of the values of all electrodes $x_i, \quad x_i \supset x_c$. The result is processed value of r. N is the number of electrodes used.

This method, known as CAR (”Common Average Referencing”), can reduce noise by up to 30% as reported in [3]. The signal prepared in this way was further segmented into sections of 250ms in length. The segmentation was performed using the non-overlapping method to avoid repeating information in the windows. From the 5s signal, 20 non-overlapping segments were created.

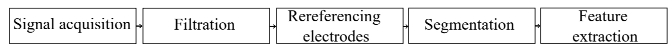

Fig. 3. Block diagram of signal preprocessing

B. Features

Features can be categorized based on the signal domain from which they extract information, namely the time domain, frequency domain, and time-frequency domain. As noted by the authors in [4], the most commonly used features for real-time gesture classification belong to the time domain. This preference is due to their lower computational complexity, which results in shorter computation time while maintaining the same recognition accuracy as features from other domains. For these reasons, this paper focuses exclusively on time-domain features.

A total of 25 features were extracted from the time domain, including Mean absolute value, Waveform length, Zero crossing, Slope sign change, etc. Most of the features used in this work are described in [4]. After extraction, statistical analysis of the features was performed, to be specific, Spearman’s correlation coefficient method was used to determine the similarities between features (the resulting coefficients can be seen in the Fig. 4). Based on the results, 6 features were eliminated from further work because they did not provide any new useful information. The eliminated features were RMS, iEMG, MNR, SD, PC and SUD.

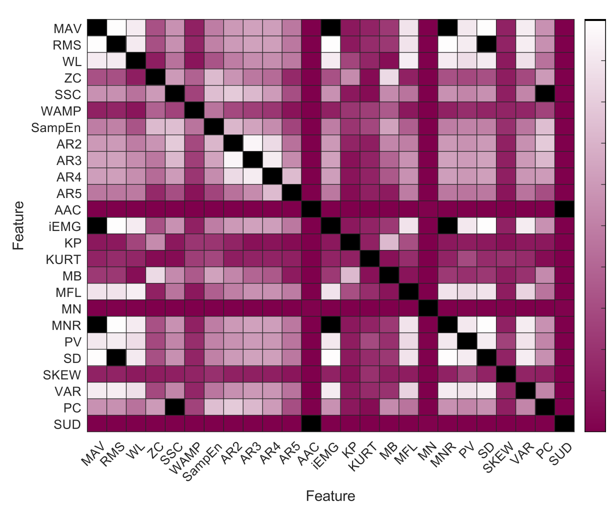

Fig. 4. Spearman correlation koeficients of features

IV. MODEL IMPLEMENTATION

There are a number of classifiers for EMG signal classification in the literature, and therefore it is very difficult to choose the best method for solving a specific problem. Studies that provide an overview of existing solutions such as [4] and [5] give the reader a slightly more detailed insight into the problem. However, it is not easy to compare the success rates and applicability of each algorithm, as each uses a different set of flags, recognizes different gestures, and is tested on a different number of subjects. Among the most frequently used classification methods are KNN (K-nearest neighbours), LDA (Linear discriminant analysis) and SVM (Support vector machine).

After initial testing of these algorithms, even though the most successful algorithm was SVM, it was decided to use the LDA algorithm for the purposes of this paper. The main reason for this is its learning rate, which is highly outperforming the other mentioned algorithms.

For the purpose of learning the algorithm, the data was divided into training and testing parts in a ratio of 35:8. This ratio was chosen because there are records from 43 participants in the dataset, therefore random 8 participants were not used for training the algorithm. The remaining 35 participants were divided into 5 random folds which were then used to perform cross-validation.

To increase the success rate of the algorithm, outliers in each feature for a particular gesture were removed from the training data. These values were replaced with the median value of the specific group. Additionally, within each feature, the data was standardized according to the following formula:

$$z_i = \frac{x_i - \mu}{\sigma} \tag{2}$$

where x_i is the original data value, μ is the mean of the data, σ is the standard deviation of the data and z_i is the standardized value.

The learning of the algorithm was performed in 6 iterations. In the first 5 iterations, the model was cross-validated with the given parameters (4 training folds and 1 validation fold). In the last iteration, the final model was trained from all available training data (35 participants). The success rate of this model is then calculated from the average success rate of the models produced in the cross-validation. At the same time, the standard deviation of the success rates is calculated to obtain information on how much the models differed from each other.

V. RESULTS AND DISCUSSION

Different testing and evaluation procedures were used to compare the models and their different parameters with each other.

At first, models were trained using all recording electrodes. This training was performed in 5 iterations, i.e. in each iteration all combinations of 2, 3, 4, 5 and 6 gestures consisting of the original 17 were tested. Of course, the training could be continued, but due to time complexity the process was stopped at 6 gestures (the number of trained models for 6 gesture combinations is 12 376). From this training the 5 most successful gesture combinations resulted, which can be seen in table I). These models were then evaluated on the testing data. It can be seen from the table that there is a decrease in success rate for the test data, but always at most in the order of one percent. These variations can be explained by outliers in the test data, for example.

TABLE I
TABLE SHOWING ACCURACY OF MODELS FOR DIFFERENT NUMBERS OF GESTURES.

Number of gestures	**Gestures number**	**Accuracy ± Standard deviation [%]**	**Test data Accuracy [%]**
2	5, 17	99.63 ± 0.33	94.15
3	15, 16, 17	98.46 ± 0.43	92.59
4	14, 15, 16, 17	95.26 ± 1.61	86.56
5	11, 14, 15, 16, 17	91.77 ± 2,29	83.28
6	7, 8, 11, 14, 15, 17	86.69 ± 2.74	74.70

In the next step, the gesture combinations from Table 1 were used. Again, the models were trained in 5 iterations, but this time, the gesture combinations used were the stable parameter, and the number and combination of electrodes used were varied. For each combination of gestures, models were trained with all possible numbers and combinations of electrodes (resulting in 5 * 63 trained models). From these models, the most successful combinations with a given number of electrodes were selected and plotted in Fig. 5 . There it can be seen how the success rate of the models changes as recording electrodes are added over time.

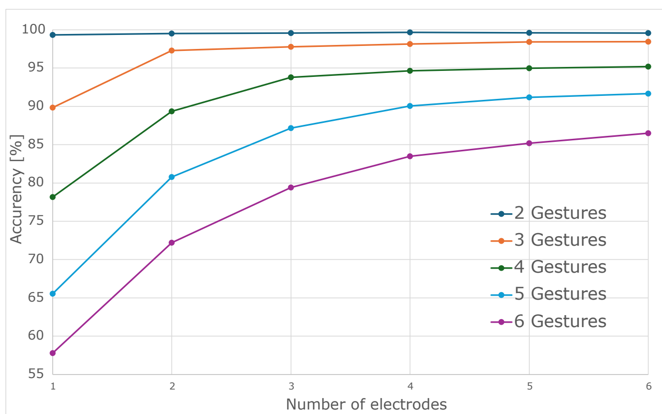

Fig. 5. Trend in success rate depending on the number of electrodes

As expected, the success rate of the model increases as electrodes are gradually added, but this rise is not linear. The graph clearly shows that as the number of electrodes used increases, the difference between the success rates of the models becomes less and less. This may be due to the fact that information from different electrodes is repeated and less and less new information is fed into the system as the number of electrodes increases, which leaves space for a reduction in the number of acquisition electrodes used. It can also be seen that the larger the number of gestures recognized by the model, the larger the number of electrodes must be for successful recognition.

However, the results in Fig. 5 do not tell us anything about which electrodes carry the most information, or whether it varies depending on the gestures. For these purposes, another series of model training was performed. This time 17 groups of models were trained specifically targeting each of the gestures (the model recognizes 2 groups : 1 - specific gesture, 0 - all other gestures). Due to the disproportion of the classification groups (1:16), some records were randomly omitted from the second group, so that this disproportion would not affect the success rates of the models.

The models were then ranked according to their success rate from highest to lowest. A scoring system based on the difference in success rates between combinations was introduced to rate the electrodes and then compare them with each other. If a given electrode was present in a combination of a certain success rate, a certain number of points was added to its score according to the following formula:

$$\text{Electrode score} = \sum_{i=1}^{N} \left(1 - \frac{\text{MaxA} - \text{CurA}}{\text{MaxA} - \text{MinA}}\right) \quad (3)$$

where N is the number of combinations where a given electrode occurs (32), MaxA and MinA correspond to the maximum and minimum success rates of the models for a particular gesture, and CurA is the currently evaluated model.

In Fig. 6, we see the percentage of points achieved compared to the maximum possible score for individual electrodes and individual gestures. Here we can see that the importance of the electrodes varies for different gestures. This fact is probably mainly due to the fact that different muscles of the forearm are involved in different gestures, and thus important information is captured in different parts of the wrist.

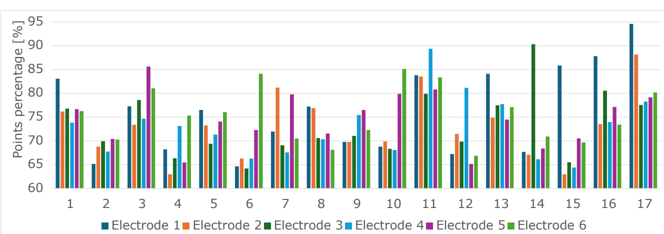

Fig. 6. Electrode scores for individual gestures

In Fig. 7 we can then observe the comparison of the individual electrodes with each other according to the averaged differences between the electrodes. It can be seen that on average electrode 1 carries the most information, followed by electrodes 6 and 5. With less information are electrodes 4, 2, and 3. According to this order, it should therefore be possible to proceed with the reduction of acquisition electrodes with the least decrease in classification success.

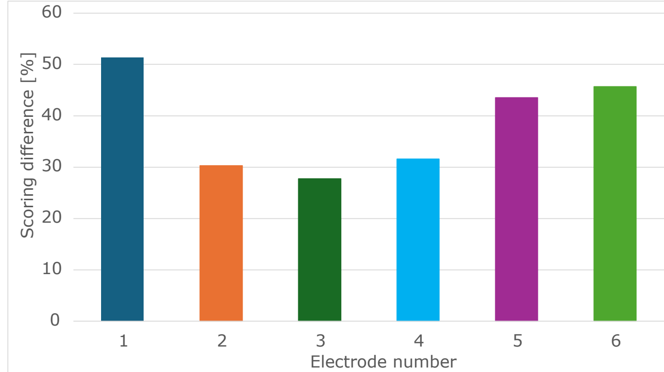

Fig. 7. Final electrode score

VI. Conclusion

The aim of this work was to create and compare machine learning classification models with different parameters. In particular, the possibility of reducing the acquisition electrodes while maintaining a high classification success rate was investigated. The trained models using all available recording electrodes achieved high success rates with a decrease on the testing data, caused primarily by the occurrence of outliers. Further analysis of the information content of each electrode then provides a detailed picture of the effect of each electrode on classification success in general and in relation to specific gestures.

References

[1] CHEN, Lin; FU, Jianting; WU, Yuheng; LI, Haochen, and ZHENG, Bin. Hand Gesture Recognition Using Compact CNN via Surface Electromyography Signals. Online. Sensors. 2020, vol. 20, no. 3. ISSN 1424-8220. Available from: https://doi.org/10.3390/s20030672. [cited 2024-11-24].

[2] KONRAD, Peter. *The ABC of EMG: A Practical Introduction to Kinesiological Electromyography*. Version 1.4. U.S.A.: Noraxon, 2005. ISBN 0-9771622-1-4. Available from: https://www.velamed.com/wp-content/uploads/ABC-of-EMG.pdf

[3] LUDWIG, Kip A.; MIRIANI, Rachel M.; LANGHALS, Nicholas B.; JOSEPH, Michael D.; ANDERSON, David J., et al. Using a Common Average Reference to Improve Cortical Neuron Recordings From Microelectrode Arrays. Online. *Journal of Neurophysiology*. 2009, vol. 101, no. 3, pp. 1679-1689. ISSN 0022-3077. Available from: https://doi.org/10.1152/jn.90989.2008. [cited 2024-12-29].

[4] JARAMILLO-YÁNEZ, Andrés; BENALCÁZAR, Marco E., and MENA-MALDONADO, Elisa. Real-Time Hand Gesture Recognition Using Surface Electromyography and Machine Learning: A Systematic Literature Review. Online. *Sensors*. 2020, vol. 20, no. 9. ISSN 1424-8220. Available from: https://doi.org/10.3390/s20092467. [cited 2024-11-24].

[5] NAZMI, Nurhazimah; ABDUL RAHMAN, Mohd; YAMAMOTO, Shin-Ichiroh; AHMAD, Siti; ZAMZURI, Hairi, et al. A Review of Classification Techniques of EMG Signals during Isotonic and Isometric Contractions. Online. *Sensors*. 2016, vol. 16, no. 8. ISSN 1424-8220. Available from: https://doi.org/10.3390/s16081304. [cited 2024-11-23].

CubeSat model for image data transmission

Jan Kusák
Department of Radio Electronics
FEEC, Brno University of Technology
Brno, Czech Repubic
246883@vutbr.cz

Šimon Sloboda
Department of Radio Electronics
FEEC, Brno University of Technology
Brno, Czech Repubic
simon.sloboda@vut.cz

***Abstract*—This work focuses on a design of nanosatellite and its communication system with use of solely Commercial Off-The-Shelf (COTS) parts. Aim is to construct an operational model according to CubeSat standard, capable of capturing and transmitting imagery along with telemetry. Satellite is expected to respond to ground station's commands. Regulations constraining satellite from the point of orbital lifetime and usage of available spectrum are being discussed here. Also requirements for suitable frequency band and transmission itself are explained, providing downlink and uplink requirements for the RF circuitry. Except transceiver, attention was paid to on-board computer, camera and power system.**

***Index Terms*—CubeSat, nanosatellite design, communication systems, data and imagery processing, RF design**

I. Introduction

The development of conventional satellites is not only astronomically expensive, but also very time consuming to ensure great longevity and reliability of the spacecraft. However, not all missions demand such qualities of their craft, nor have unlimited budget – universities, for instance. This is exactly why concept of nanosatellites rose on popularity, as many components used are Commercial Off-The-Shelf parts. Also the satellite itself is delivered to its desired orbit as secondary payload of much larger project, which lowers overall costs even more.

Point of this work is to provide reader with insight of construction processes, although durability testing, thermal control or solar panel power supply are not discussed here, as they exceed already wide scope of this work.

Many design's procedures follow its manufacturers recommendations. RF design was additionally backed up by simulations performed in ANSYS Electronics desktop environment to guarantee proper functionality of system.

II. Satellite orbit

The mechanical design was already standardized by California Polytechnic State University, San Luis Obispo and Stanford University's Space Systems Development Lab in 1999 [1], today known as CubeSat standard. *The CubeSat Handbook* [2] provides overview of standardized procedures. It is highly recommended to follow these to avoid design errors or complete system failures. Compliance with deployers' terms is another reason why standards have to be followed. Many, not if all, satellites' deployers have their dispensers constructed to contain spacecraft of standardised dimensions only. For purpose of this work, $1\,\mathrm{U}$ configuration was selected, constraining maximum mass to $2\,\mathrm{kg}$. This hypothetical mission takes place on Low Earth Orbit (LEO), for sake of simplicity.

To minimize ongoing pollution of space near Earth ("space debris") [3], the *Federal Communications Commission* (FCC) has issued a 5-year rule for deorbiting satellites [4] [5], which means that satellite has to decrease its altitude below $50\,\mathrm{km}$ within 5 years after finishing its primary mission on LEO. According to data from *Analysis and comparison of CubeSat lifetime* [6] a $1\,\mathrm{U}$ satellite orbiting at altitude of $500\,\mathrm{km}$ will comply with such a regulation only if satellite itself will not be heavier than $1.897\,\mathrm{kg}$. Such a result was deduced from the analysis by linearly approximating the data describing the effect of $1\,\mathrm{U}$ satellite's mass on its orbital lifetime. Influence of other factors, such as drag area or solar radiation reflection, is not only negligible in LEO in contrast with mass, but also they do not prolong the lifetime. More precise data could be simulated in e.g. *Systems Tool Kit* (STK) software if required.

III. Link Budget

A. Maximum transmission distance

Valid link budget has to be calculated for the least favourable conditions of transmission, i.e. the longest path. Figure (1) shows a model situation of transmission path between ground station (*GS*) and a satellite (*SAT*) with respect to the centre of the Earth (*CE*). Considering the Earth as perfect sphere of radius $6378\,\mathrm{km}$ defines distance c. Satellite's altitude was said to be around $500\,\mathrm{km}$, then distance $a = 6878\,\mathrm{km}$. Angle α represents an elevation angle, assume then an empiric value of 5° as ground station can be surrounded by obstacles blocking the signal path. Consequently, the angle between *CE* and *SAT* equals to $\alpha' = 95\,^\circ$. Finally, the maximum distance b was calculated by solving the system by applying the law of sines, resulting in distance of $2077\,\mathrm{km}$.

B. Frequency band selection

Selection of frequency band has to be done with respect to the *International Telecommunication Commission* (ITU) and in case of this work with respect to the *Czech Telecommunication Office* (ČTÚ) as well. It was found out that for a real space mission, it would be appropriate to allocate custom frequency band that would allow radiation of higher magnitudes, otherwise additional low noise amplifiers onboard the satellite would be required. Testing of this module will be measured

DOI 10.13164/eeict.2025.21

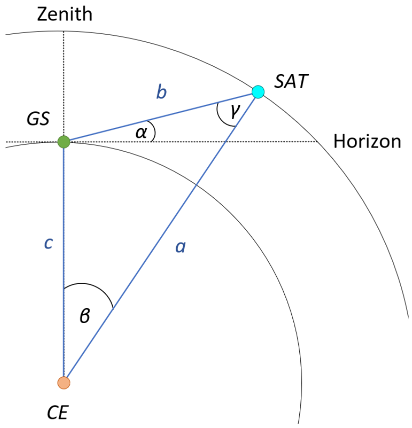

Fig. 1. Model of geometrical relation between satellite, ground station and a centre of the Earth

over relatively short distances, therefore the use of Industrial Scientific and Medical (ISM) band is convenient as it allows unlicensed operation by limiting maximum *Effective Radiated Power* (ERP) to $10\,\mathrm{mW}$, bandwidth to $250\,\mathrm{kHz}$ and duty cycle to $10\,\%$ per hour [7]. Specifically, the $434\,\mathrm{MHz}$ band was selected, because of low *Free Space Path Loss* ($FSPL$, discussed later) and also because it is recognized by ITU as radio-amateur band in all three regions [8].

C. Link budget calculation

The link budget was calculated with a guidance from *Satellite communications systems, techniques and technology* [9]. Note that calculation is performed only from a point of "gains and losses". Noise analysis is not included here, as many parameters are unknown and their rough approximation would not prove useful in broader perspective whatsoever. First, the $FSPL$ can be calculated as

$$\begin{aligned} L_{FSP} &= 10\log\left[\left(\frac{4\pi bf}{c}\right)^2\right] = \\ &= 10\log\left[\left(\frac{4\pi\cdot 2077\cdot 10^3\cdot 434\cdot 10^6}{3\cdot 10^8}\right)^2\right] = \\ &= 151.5\,\mathrm{dB}, \end{aligned} \tag{1}$$

where f is frequency and c is speed of light. Next, ERP was recalculated to *Equivalent Isotropically Radiated Power* ($EIRP$) [10].

$$\begin{aligned} EIRP &= ERP + 2.15 = 10\log\left(\frac{10\cdot 10^{-3}}{10^{-3}}\right) + 2.15 = \\ &= 12.15\,\mathrm{dBm} \end{aligned} \tag{2}$$

Magnitude of received power can be calculated by equation

$$P_{RX} = \frac{P_{TX}\cdot G_{Tmax}}{L_T\cdot L_{FTX}}\cdot\frac{1}{L_{FS}\cdot L_A}\cdot\frac{G_{Rmax}}{L_R\cdot L_{FRX}\cdot L_{POL}}. \tag{3}$$

Since this is just a prediction of system's behaviour, it is necessary to estimate losses and gains which would normally require measurement. First fraction in (3) represents already calculated $EIRP$, which on contrary will help to determine required magnitude of transmitter's input power P_{TX} later on. Aside from power requirement, also other variables are included here.

- Mismatch losses L_T are considered negligible as theoretically omnidirectional (half-wave dipole) antenna will be used,
- assume that gain of antenna is $G_{Tmax} = 0\,\mathrm{dBi}$,
- feeder loss estimated $L_{FTX} = 1\,\mathrm{dB}$.

Second fraction represents medium losses, meaning attenuation of transmission channel's environment - attenuation of the atmosphere L_A is negligible for given frequency [2].

Last fraction describes power level at receiver side, which was estimated in similar manner as for the transmitter, except polarisation losses L_{POL}. While satellite's transceiver is assumed with linear polarisation, the ground station is supposed to work with circular polarization for the best compatibility between them. This may introduce higher polarisation losses of $3\,\mathrm{dB}$ [9], but can ensure communication even if satellite starts to rotate. Of course, since a real dipole does not have perfectly omnidirectional radiation pattern, signal will be lost during times, when dipole's centreline is orthogonal to the ground station antenna's plane.

By applying said estimates and expressing (3) logarithmically, new form of equation can be obtained

$$\begin{aligned} P_{RX} &= EIRP – L = \\ &= EIRP – (L_{FTX} + L_{FSP} + L_{FRX} + L_{POL}) = \\ &= 12.15 – (1 + 151.5 + 1 + 3) = -144.35\,\mathrm{dBm}. \end{aligned} \tag{4}$$

Result of this equation dictates requirement on receiver's sensitivity, however such a low power level would be a great challenge to detect. This is the reason why a real mission would require custom frequency band allocation from a point of maximum radiated power or sophisticated low noise amplifier onboard the satellite, as mentioned earlier. Inspired by parameters of $443\,\mathrm{MHz}$ band [11], which allows maximum $EIRP$ of $42.15\,\mathrm{dBm}$. A hypothetical ground station would be constructed with antenna (or antenna array more likely) that has gain of 15 dBi, excited by power less than

$$\begin{aligned} P'_{TX} &= EIRP' + L_{FTX} - G'_{Tmax} = \\ &= 42.15 + 1 - 15 = 28.15\,\mathrm{dBm}. \end{aligned} \tag{5}$$

Which are completely feasible parameters. Such a upgrade would result in acceptable value of $P'_{RX} = -114.35\,\mathrm{dBm}$ (uplink).

IV. Transceiver design

As a transceiver, the Si4468 chip was selected. It has lower sensitivity than LoRa SX1262, but provides up to $1\,\mathrm{Mbit}\cdot\mathrm{s}^{-1}$ data rate, which is convenient for imagery data transfer. Si4468 can transmit up to $20\,\mathrm{dBm}$ and receive with sensitivity as low as $-133\,\mathrm{dBm}$ [12]. From range of modulation the Gaussian Frequency-Shift Keying (GFSK and 4GFSK) will be used. Note that the 4-level modulation exhibits lower receiver sensitivity [13]. Parameters of communication channel and their variation over the shortest and the furthest communication paths are summarized below for uplink (I, II) and for downlink (III, IV).

TABLE I
MAGNITUDE OF RECEIVED UPLINK POWER FROM DISTANCE 500KM

GFSK			4GFSK		
$Sens.$ [dBm]	R [kbit $\cdot$ s^{-1}]	P_{RX} [dBm]	$Sens.$ [dBm]	R [kbit $\cdot$ s^{-1}]	P_{RX} [dBm]
-133	0.1	31.98	-127.5	0.2	26.48
-110	40	8.979	-104.5	80	3.479
-106	100	4.979	-100.5	200	-0.5210
-98	500	-3.021	-92.5	1000	-8.521

TABLE II
MAGNITUDE OF RECEIVED UPLINK POWER FROM DISTANCE 2077KM

GFSK			4GFSK		
$Sens.$ [dBm]	R [kbit $\cdot$ s^{-1}]	P_{RX} [dBm]	$Sens.$ [dBm]	R [kbit $\cdot$ s^{-1}]	P_{RX} [dBm]
-133	0.1	19.61	-127.5	0.2	14.11
-110	40	-3.390	-104.5	80	-8.890
-106	100	-7.390	-100.5	200	-12.89
-98	500	-15.39	-92.5	1000	-20.89

TABLE III
MAGNITUDE OF RECEIVED DOWNLINK POWER FROM DISTANCE 500KM

GFSK			4GFSK		
$Sens.$ [dBm]	R [kbit $\cdot$ s^{-1}]	P_{RX} [dBm]	$Sens.$ [dBm]	R [kbit $\cdot$ s^{-1}]	P_{RX} [dBm]
-133	0.1	43.83	-127.5	0.2	38.33
-110	40	20.83	-104.5	80	15.33
-106	100	16.83	-100.5	200	11.33
-98	500	8.829	-92.5	1000	3.329

TABLE IV
MAGNITUDE OF RECEIVED DOWNLINK POWER FROM DISTANCE 2077KM

GFSK			4GFSK		
$Sens.$ [dBm]	R [kbit $\cdot$ s^{-1}]	P_{RX} [dBm]	$Sens.$ [dBm]	R [kbit $\cdot$ s^{-1}]	P_{RX} [dBm]
-133	0.1	31.46	-127.5	0.2	25.96
-110	40	8.460	-104.5	80	2.960
-106	100	4.460	-100.5	200	-1.040
-98	500	-3.540	-92.5	1000	-9.040

It is obvious that negative magnitudes of received power cannot be detected by current *Radio Frequency* (RF) circuit. Documentation states that $BER < 0.1\,\%$ (*Bit Error Rate*) for GFSK modulation and $PER = 1\,\%$ (*Packet Error Rate*) for 4GFSK modulation are achievable. Communication will be set according to situation, depending on requested channel throughput while also complying with *ECSS-E-ST-50-05C* standard [14], which states that the received signal should be having at least $3\,\mathrm{dB}$ power margin.

In terms of hardware, sharing one antenna for uplink and downlink is convenient not only from financial perspective, but also because of limited space onboard the satellite. For this purpose a pair of PIN diodes was implemented as RF switch inspired from [15]. Figure (2) shows such a switch, controlled by the SI4468's GPIO (*General Purpose Input/Output*) pin. It works in "Transceiver mode" when current flows through PIN diodes, otherwise stays in "Receiver mode", waiting for commands. Since transceiver will be receiving most of the time, this feature provides significant power savings. Transceiver's GPIOs can drive maximum current of $5\,\mathrm{mA}$, for which numerous simulations on FR4 board ($\varepsilon_r = 4.4$) were done. Circuit is adapted for possibility of higher driving current from MOSFET switch, although this feature will not be initially used. It rather serves as a reserve in case of future testing and upgrades. More importantly, specific components were used to match the system to $50\,\Omega$ impedance. Additional harmonic components generated by RF switch's nonlinearity are filtered by 3$^{\text{rd}}$ order Chebyshev low-pass filter(s) [16].

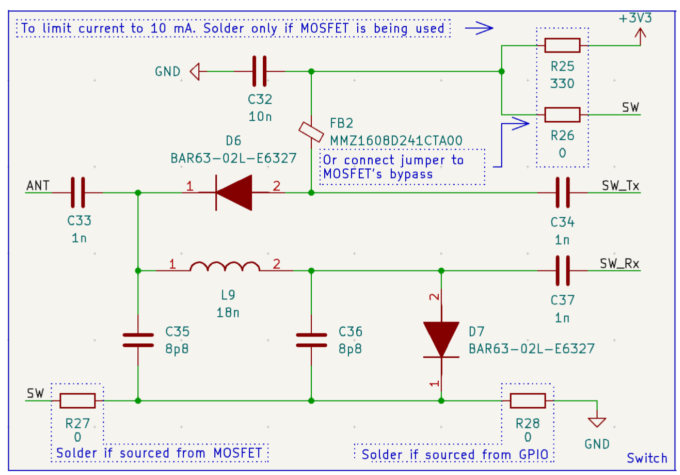

Fig. 2. Excerpt from the schematic of RF circuit, the RF switch section

Mentioned $1\,\mathrm{Mbit}\cdot\mathrm{s}^{-1}$ data rate is doable, because of the wide bandwidth available in the $434\,\mathrm{MHz}$ band. This topic is explained on *Noise, Data Rate and Frequency Bandwidth* website [17]. If bandwidth B and symbol keying M is known, then from (6) theoretical maximum data rates of GFSK (7) and 4GFSK (8) modulations in given band can be obtained.

$$R = 2B\log_2(M) \tag{6}$$

$$R_{GFSK} = 2\cdot 25\cdot 10^4\cdot\log_2(2) = 0.5\,\mathrm{Mbit}\cdot\mathrm{s}^{-1} \tag{7}$$

$$R_{4GFSK} = 2\cdot 25\cdot 10^4\cdot\log_2(4) = 1\,\mathrm{Mbit}\cdot\mathrm{s}^{-1} \tag{8}$$

V. Onboard computer

Based of its popularity and successfully passed radiation testing [18] the STM32H7 series of microcontroller (MCU) will be used as onboard computer. High clock frequency of $280\,\mathrm{MHz}$, *Integrated Direct Memory Access* (DMA), which manages data flow without extensive interruption(s) and *Digital Camera Interface* (DCMI) are major advantages as well. The STM32H7A3VIT6 model was picked for its spacious RAM of $1.4\,\mathrm{MB}$ and FLASH of $2\,\mathrm{MB}$, hence external memory is not required.

Program flashing is handled by Trace Asynchronous Serial Wire Debug by connecting external ST-Link programmer & debugger. Access to console application for direct commanding can be also done by connecting PC to USB-B micro receptacle.

VI. Camera module

An OV7670 camera module will be used to capture imagery. Camera is powered through MOSFET switch controlled by GPIO pin from MCU to provide safe current level (GPIO protection). Connection is handled by DCMI peripheral that manages image transmission – synchronisation, image storage through DMA etc. Microcontroller communicates with camera though I2C bus. After successful image capture the camera is shut down to reduce overall system consumption.

Appropriate setting is done by library, that has been written to support black-and-white (YUV) and colour (RGB565) imagery capture. This library was already tested with said camera module and NUCLEO-H7A3ZI-Q development board and proved to be fully functional. Supported resolutions are:

- VGA (640x480),
- CIF (352x288),
- QVGA (320x240),
- QCIF (176x144).

In case of YUV, only the luminescence component will be send, which significantly lowers throughput of communication channel. More information towards camera's capabilities can be found in its documentation & implementation guide [19].

VII. Power system

When all peripherals are running, consumption of major components is estimated to $268\,\mathrm{mA}$. To supply systems of the satellite a pair of 18650 batteries was implemented, as well as their protection and charging circuitry via USB-C receptacle, allowing fast battery charging with $5\,\mathrm{V}$ and $2\,\mathrm{A}$. System is then provided with voltage of $3.3\,\mathrm{V}$ regulated by switched DC/DC convertor.

VIII. Conclusion - System overview

In this work, nanosatellite systems and their constrains were discussed. Each system is constructed with respect to its manufacturer's recommendations. Additionally, all parts that are exposed to direct contact with operation personnel are provided with an *Electrostatic Discharge* (ESD) protection. Satellite itself was divided into 3 sections: onboard computer, power system and RF system. Boards following the PC/104 form factor are stacked on top of each other and connected by spacers positioned in the corners of each board. Camera and antenna are connected externally aside from boards, on opposing sides of the satellite.

References

[1] *CubeSat Design Specification: (1U – 12U)*. Online. REV 14.1. February 2022. Available from: https://www.cubesat.org/s/CDS-REV14_1-2022-02-09.pdf.

[2] CAPPELLETTI, Chantal; BATTISTINI, Simone a MALPHRUS, Benjamin K. (ed.). *CubeSat handbook: from mission design to operations*. London, United Kingdom: Academic Press, Elsevier, [2020]. ISBN 978-0-12-817884-3.

[3] ESA. Space Environment Report, Issue 8. Online. 2025. Available from: https://sdup.esoc.esa.int/discosweb/statistics/. [cit. 2024-03-10].

[4] FEDERAL COMMUNICATIONS COMMISSION. *FCC Adopts New '5-Year Rule' for Deorbiting Satellites*. Online. Federal Communications Commission. 2022. Available from: https://www.fcc.gov/document/fcc-adopts-new-5-year-rule-deorbiting-satellites-0.

[5] *State-of-the-Art of Small Spacecraft Technology: 13.0 Deorbit Systems*. Online. 2024. Available from: https://www.nasa.gov/smallsat-institute/sst-soa/deorbit-systems/.

[6] QIAO, Li; RIZOS, Chris; DEMPSTER, Andrew. *Analysis and comparison of CubeSat lifetime.* PDF. Proceedings of the 12th Australian space conference. 2013. Available from: https://citeseerx.ist.psu.edu/document?repid=rep1&type=pdf&doi=031d14751712bf202eb00cbf12e456a682d7c8d3

[7] CZECH REPUBLIC, Všeobecné oprávnění č. VO-R/10/07.2021-8 k využívání rádiových kmitočtů a k provozování zařízení krátkého dosahu. 2021, page 2-3. PDF. Available from: https://ctu.gov.cz/sites/default/files/obsah/vo-r10-072021-8.pdf

[8] *ITU: Radio Regulations*. PDF. 2020. Geneva, 2020. ISBN 978-92-61-30301-3. Available from: https://search.itu.int/history/HistoryDigitalCollectionDocLibrary/1.44.48.en.101.pdf. [cit. 2024-11-17].

[9] MARAL, Gérard; BOUSQUET, Michel a SUN, Zhilu. *Satellite Communications Systems: Systems, Techniques and Technology*. 6th edition. John Wiley, 2020. ISBN 9781119382089.

[10] THE THINGS NETWORK: *EIRP and ERP*. Online. Available from: https://www.thethingsnetwork.org/docs/lorawan/eirp-and-erp/.

[11] CZECH REPUBLIC, Plán využití rádiového spektra: Část plánu využití rádiového spektra č. PV-P/15/02.2020-2 pro kmitočtové pásmo 380—470 MHz. In: *Telekomunikační věstník*. 2020, figure 3, page 9. PDF. Available from: https://www.ctu.cz/sites/default/files/obsah/ctu/sdeleni-o-vydani-opatreni-obecne-povahy-casti-planu-vyuziti-radioveho-spektra-c.pv-p/15/02.2020-2-pro-kmitoctove-pasmo-380-470-mhz/obrazky/pvrs-15podpis.pdf

[12] SILICON LABS Si4468: *HIGH-PERFORMANCE, LOW-CURRENT TRANSCEIVER (Data Sheet*. PDF. V1. 2014. Available from: https://www.silabs.com/documents/public/data-sheets/Si4468-7.pdf.

[13] SILICON LABS Knowledge Article: 4GFSK vs. 2GFSK sensitivity on Si446x. Online. 2021. Available from: https://community.silabs.com/s/article/4gfsk-vs-2gfsk-sensitivity-on-si446x?language=en_US.

[14] EUROPEAN COOPERATION FOR SPACE STANDARDIZATION. ECSS-E-ST-50-05C, *Radio frequency and modulation.* Rev.2. 2011.

[15] VÁGNER, Petr. Vysokofrekvenční technika. PDF. 2013.

[16] AN648: Si4x6x and EZR32 High-Power PA Matching. PDF. Rev. 0.6. 2016. Available from: https://www.silabs.com/documents/public/application-notes/AN648.pdf.

[17] Noise, Data Rate and Frequency Bandwidth: *The Relationship Between Data Rate Capacity, Noise, and Frequency Bandwidth*. Online. Available from: https://mason.gmu.edu/~rmorika2/Noise__Data_Rate_and_Frequency_Bandwidth.htm.

[18] MADLE, Paul. OPEN SOURCE SATELLITE: *STM32H7 Radiation Test Report KS-DOC-01251-01*. PDF. V01. 2021. Available from: https://www.opensourcesatellite.org/downloads/KS-DOC-01251_STM32H7_Radiation_Test_Report.pdf.

[19] HAOYU Electronics: *OV7670 Implementation Guide*. PDF. V(1.0). 2005. Available from: https://www.haoyuelectronics.com/Attachment/OV7670%20+%20AL422B(FIFO)%20Camera%20Module(V2.0)/OV7670%20Implementation%20Guide%20(V1.0).pdf.

Detection of Problems in an Industrial Network Using the Concept of Edge Computing

Šimon Remper
Faculty of Electrical Engineering and Communication
Brno University of Technology
Brno, Czech Republic
240685@vutbr.cz

Ing. Jan Dvořák Ph.D.
Faculty of Electrical Engineering and Communication
Brno University of Technology
Brno, Czech Republic
dvorakjan@vut.cz

***Abstract*—This paper deals with troubleshooting and monitoring of industrial networks. It describes possible problems of deploying a network monitoring system in an industrial environment. The proposed solution, described in this paper, demonstrates the edge computing paradigm, which is also shortly introduced. The solution has been developed on the Cisco IE3400 network switch, and tested on live Profinet traffic and real industrial networking equipment.**

***Index Terms*—Edge computing, industrial networks, traffic monitoring**

I. Introduction

Industrial networks are – from a networking standpoint – a highly sensitive environment. They are very demanding, especially in terms of delay, quality of service, and reliability [1]. With the introduction and implementation of the Internet of Things (IoT) and the Industrial Internet of Things (IIoT) into industrial manufacturing, these networks are becoming more and more complex.

Consequences of a potential issue can be, in this kind of environment, quite far-reaching. Possible loss of communication between devices could lead to a shutdown of production, which could cause financial losses for a company. It is highly desirable for any issues to be solved promptly. This can put a lot of pressure on network administrators who are responsible for error-free operation.

Troubleshooting a complex network can be a challenging task. The key to a swift problem-solving process is having enough information about the issue right from the beginning. This could be achieved by deploying a monitoring system into the network infrastructure. But, as was said in the beginning, industrial production is an atypical environment.

Incorporating a new piece of hardware into an existing infrastructure often means dealing with the *SWaP* problem. The *SWaP* abbreviation stands for size, weight, and power. In this context, it means that every piece of hardware has its size and weight, and it needs its own mounting point, as well as a power source. These conditions are not met easily in an industrial hall full of production lines.

A system designated to be used in an industrial environment should be certified to work in harsh conditions, which increases the price of such hardware.

II. The Concept of Proposed Solution

The solution presented in this paper builds on the following idea: Implementing the monitoring system right into the networking infrastructure. This allows for new functionality to be added to the already existing network, without the need for new hardware. This approach avoids the SWaP problem and decreases the overall price of the solution.

There are 2 goals to be achieved:

1) Implement a simple traffic monitoring application, that uses predefined filters to generate alerts when a problem is detected and creates records of this communication for later manual analysis.
2) Give administrators a traffic capturing tool to help with network troubleshooting, e.g. detection of data flows, increasing visibility into the network.

This concept builds on the edge computing paradigm.

A. Edge Computing

The main idea behind this concept is that data are processed near their source – near the place they are generated, rather than being sent to the cloud for processing. This way allows for lower latency, faster response times, and higher reliability. Not sending data to the cloud leads to reducing network load and bandwidth requirements [2].

Edge computing is a distributed computing architecture, which involves deploying edge devices throughout the network. Edge devices do the real-time processing of the data and only send the necessary data to the cloud [2].

This concept was also implemented in the industrial environment. Smart factories can generate massive amounts of data. Sending all the data to the cloud for processing would put excessive load on the network and increase the delay [3]. That is why edge devices with sufficient computing power are used for local data processing and also immediate decision-making [3].

For example, in smart factories, the end devices can be different types of machines, robots, and other equipment. These devices use sensors to collect parameter data while in operation [4]. Smart manufacturing can benefit from local real-time data processing by having better production control and maintenance [4].

B. Solution Outline

Fig. 1 shows an example of a simplified industrial network topology. The robotic arm and sensor are examples of end devices, controlled by a programmable logic controller (PLC). Human machine interface (HMI) is a device mainly used for commissioning, diagnostics, and visual representation of data.

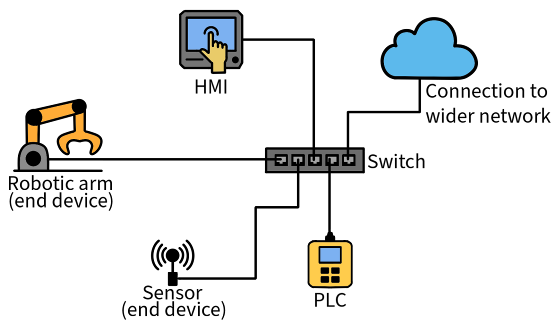

Fig. 1. Example of simplified industrial network topology.

As can be seen from fig. 1, the communication between the PLC and a device controlled by the PLC runs through the network switch. Also, the network switch is often the device nearest to the end devices. If it is powerful enough, it can be used as an edge device for some kind of data processing. The proposed solution is built on this idea.

III. The Equipment and Technologies Used

The discussed solution was developed and implemented on the Cisco IE3400 switch, which can be seen in fig. 2. Cisco is a leading vendor of networking devices, and the IE3400 is one of the most advanced switches in its Industrial Ethernet series.

It also supports an application hosting framework, which allows for external applications to be run directly on the switch, and it is powerful enough to handle both functions at the same time – network switching as well as running an application.

There are several industrial communication protocols, but the proposed solution focuses on Profinet, which is an industrial communication networking standard, built upon industrial Ethernet.

There are 2 main technologies on which the proposed solution is built – Cisco IOx and Docker.

These 2 technologies are used together to build a standalone Linux container that is deployed and run directly on the switch. A simple traffic monitoring app is then run inside the container.

A. Docker

Docker is an open platform, which allows for application management. Docker can be used to package applications and all their dependencies into an isolated container. This way, the packaged application has everything it needs to work and is not dependent on software installed on the host. Containers are a fast and lightweight means of virtualization [5].

Fig. 2. The Cisco IE3400 network switch.

B. Cisco IOx

Cisco IOx is an environment used for application development and their deployment to Cisco networking devices [6]. Most platforms supporting IOx run a newer version of operating system called IOS XE. The architecture of this system allows Linux containers and virtual machines to be hosted on the device [7].

Every IOS XE platform has specified the amount of hardware resources that are available for application hosting. These resources are reserved for applications and do not interfere with the normal operation of the device, protecting the performance [7].

IV. Container Assembly

The first step in the process of deploying a container to the switch is the assembly of the Docker container itself. Alpine Linux, which is a minimal and lightweight Linux distribution, was chosen as the base image for the container. With the help of *Dockerfile*, this image was further modified. Several packages were installed, including the Python programming language interpreter and package manager, components for Secure Shell (SSH) and Secure File Transfer Protocol (SFTP), as well as components for Network Time Protocol (NTP) and `tshark` – a terminal version of the *Wireshark* network protocol analyzer.

The container was further customized via a simple Linux script. This script was used to create a directory structure, configure NTP, and SSH access.

The container is uploaded and installed to the switch in the form of a `.tar` archive. To create this archive, one more file needs to be created.

A. The generation of archive

The file needed for the creation of a `.tar` archive from a Docker image is `package.yaml`. This file specifies an application identifier and type of application, network interfaces, CPU architecture, and hardware resources. In this case, the default resource profile was used, which allocates 20% of resources available for application hosting to the container.

The archive itself can be generated from the Docker image using the `ioxclient` command-line tool, which is available at Cisco's official websites. This tool interacts with the IOx environment on the targeted platform, in this case, the IE3400.

V. Container Deployment

After the archive is ready, it can be deployed to the switch with an enabled IOx environment. The `ioxclient` can be used to upload and install the container to the switch.

To ensure connectivity and proper operation of the container, there are 4 more things to be configured on the switch:

1) The network properties of the container itself.
2) The *AppGigabitEthernet1/1* interface, which is an internal interface used for connecting deployed containers to the network.
3) *Monitor session*, which makes the switch copy the communication on the physical interfaces, and send it to the container for analysis.
4) NTP service.

The networking configuration utilizes the concept of Virtual Local Area Networks (VLANs).

A. Container Configuration

The main goal of the container is to analyze communication and send out alerts. To do so, the container has 2 network interfaces. One of the interfaces is placed in the management VLAN and has a statically assigned IP address. This interface allows the container to actively communicate, send alerts, and make SSH or SFTP connections. The other interface is placed in the Remote Switch Port Analyzer (RSPAN) VLAN and allows the container to receive communication. This interface does not need an IP address, as it is only used to receive communication for analysis.

B. Interface Configuration

The application interface is configured as a *trunk* port, which means that it can forward traffic from multiple VLANs. In this case, the interface will be forwarding traffic from the management and RSPAN VLANs and also the VLAN that the monitored ports are assigned to.

This interface also has a native VLAN configured, so that all traffic meant for the container has a VLAN tag.

C. Monitor Session Configuration

In order for the switch to copy all communication and send it to the container, there has to be a monitor session configured. The monitor session copies traffic from a VLAN with physical ports assigned and sends it to the RSPAN VLAN.

D. NTP Configuration

The container creates records of communication and sends out alerts. All this information is timestamped, and so it is important for the container to have the accurate time set. This can be achieved with the NTP. In order for the container to be dependent only on the switch and not on other resources, a simple hierarchical architecture was implemented. The switch itself acts as an NTP client and synchronizes itself with a public NTP server. It then acts as an NTP server and allows the container to synchronize with the switch. For this reason, there is a *loopback* interface created on the switch.

VI. The Traffic Monitoring Application

The main objective of the application is to monitor communication passing through and look for issues based on predefined filters. If a problem emerges, the application will create a record of the communication and generate an operative notification.

In Profinet, the network packets warning about an issue are called *alarms*. These packets trigger the filters and cause the generation of notifications and communication records.

The idea behind the application is that when an issue occurs, a notification is generated. The operator knows about the issue and can connect to the container and, using SFTP, securely download a record of the communication. This record can then be manually analyzed, which should give valuable insight into the situation and help with the problem-solving process.

Communication records are saved in a `.pcap` file format. This format is used by the *Wireshark* network protocol analyzer. This tool is often used in network troubleshooting, especially when troubleshooting industrial networks. Notifications are sent using the *syslog* protocol to a syslog server.

To capture and analyze packets, the application utilizes the *Scapy* packet manipulation Python library.

VII. Testing

The solution discussed in this paper has been tested on real Profinet traffic in a lab, as shown in fig. 3. The IE3400 can be seen in the bottom left corner. On the DIN rail stand, there is the InduSol PROFINET-INspektor, which does a deep-level analysis of a Profinet network, as well as InduSol PROmesh switches. The other equipment is the Siemens Simatic S7-1500 and VIPA CPU M13C PLCs, the VIPA SLIO X1, which acts as a Profinet IO device, and the Weidmüller u-remote.

The test, which took place in a time window of about 2 hours, was focused on the 2 most common scenarios – an IO module disconnecting from its controller and the network being overloaded.

Disconnecting the IO module was easy to simulate. Figure 4 is a screenshot from the InduSol PROFINET-INspektor, and it shows all the devices connected to the network. The single device shown in red is the inactive (disconnected) X1 module. The application correctly generated notifications and communication records triggered by alarm packets.

Overloading the small network was achieved by broadcasting multiple multimedia streams to multicast addresses. These streams flooded the network and, together with the 1 millisecond interval of Profinet cyclic data exchange, the network was overloaded. Time requirements for Profinet communication have been breached, which caused the generation of alarm

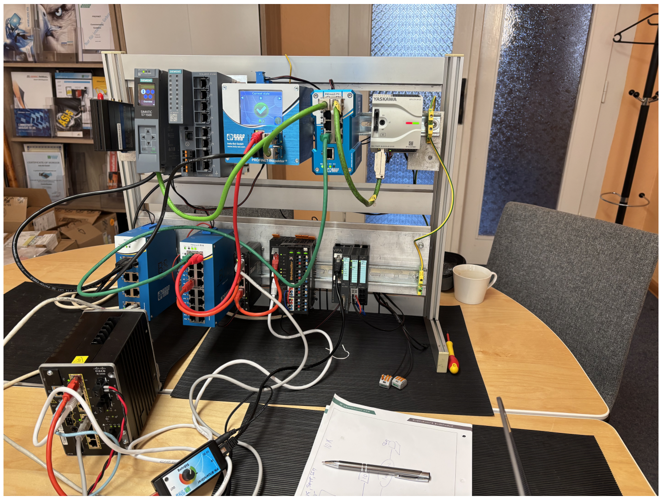

Fig. 3. The network on which the solution was tested.

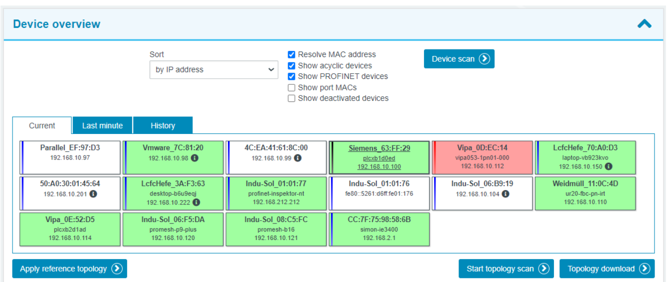

Fig. 4. Device pane from the InduSol Inspektor.

packets. The application still behaved correctly under these conditions.

An example of the communication records created by the application during testing can be seen in fig. 5. There are 3 things highlighted in the picture:

1) Name of the file includes the date and time of creation.
2) The multimedia multicast stream, used to forcibly overload the network.
3) The captured alarm packets, that triggered the creation of the file.

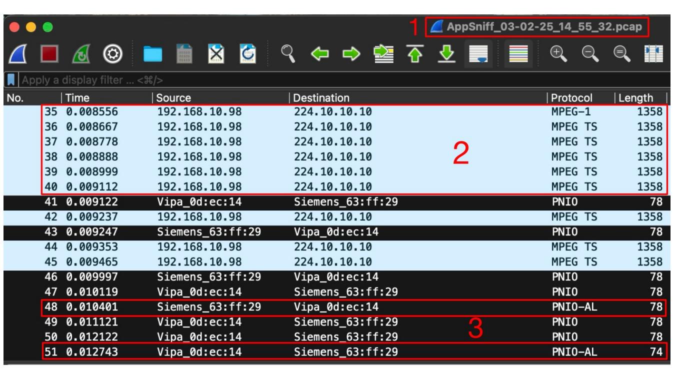

Fig. 5. Communication record example opened in Wireshark.

The hardware resources allocated to the container were sufficient for the container to analyze traffic and work properly for the whole test. The container CPU utilization did not exceed 35%, as can be seen in fig. 6, which means that the computation power reserved for the hosted application on the IE3400 is not insignificant.

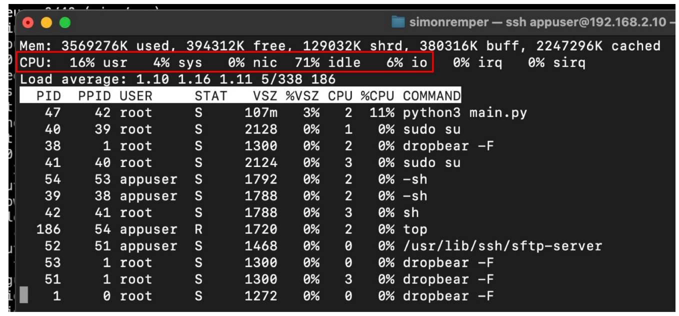

Fig. 6. Output of the `top` command executed on the container.

VIII. Conclusion

This paper describes a traffic monitoring tool, intended for industrial networks, and walks through the deployment of such a tool. The proposed solution builds on the edge computing concept and utilizes the application hosting capabilities of the IE3400 network switch. Together with the Docker platform, a lightweight container was built and deployed to the switch.

The solution described in this paper is meant to be an additional tool that helps network administrators with network visibility and troubleshooting. It utilizes and builds upon known and used tools and technologies, such as Docker, the Linux operating system, and Wireshark. The aim of this approach is to make the solution open, customizable, and easy to use.

Testing of the solution has shown that this concept is applicable, and the results achieved can be considered a success. The application worked correctly throughout the entire testing period and did not cause any problems. It also correctly identified alarm packets, and created records and notifications as intended.

References

[1] Z. Li, X. Zhou, and Y. Qin, "A Survey of Mobile Edge Computing in the Industrial Internet", in *2019 7th International Conference on Information, Communication and Networks (ICICN)*, 2019, pp. 94-98.

[2] C. Santhiya and S. Padmavathi, "Perspective Chapter: A View — Cloud-Edge Computing Technology", in *Edge Computing - Technology, Management and Integration*, IntechOpen, 2023.

[3] T. Qiu, J. Chi, X. Zhou, Z. Ning, M. Atiquzzaman, and D. O. Wu, "Edge Computing in Industrial Internet of Things: Architecture, Advances and Challenges", *IEEE Communications Surveys & Tutorials*, vol. 22, no. 4, pp. 2462-2488, 2020.

[4] X. Zhou, S. Ge, J. Chi, and T. Qiu, *Industrial Edge Computing*. Singapore: Springer Nature Singapore, 2024.

[5] "What is Docker?", *Dockerdocs*, c2013-2025.

[6] "What is IOx?", *Cisco DevNet*, c2025.

[7] A. Radford, F. Maccioni, G. Zapodeanu, I. Koren, J. McLaughlin, J. Cohoe, J. Yang, K. Kotha, N. Michraf, and R. Grasby, *Cisco IOS XE Programmability: Automating Device Lifecycle Management*.


TVOJE MYŠLENKY
OBLETÍ SVĚT
Proč čekat na budoucnost, když ji můžeš vytvářet? V brněnském R&D centru společnosti Honeywell pracujeme na technologiích, které pomáhají určovat směr celých odvětví! Zastav se na našem stánku a dozvíš se víc.
www.honeywell.com
careers.honeywell.com/Brno
THE FUTURE IS WHAT WE MAKE IT
Honeywell

PŘÍLEŽITOSTI PRO STUDENTY A ABSOLVENTY

V Honeywellu věříme, že budoucnost je taková, jakou ji společnými silami vytvoříme. V Brně se zaměřujeme na oblasti Aerospace a Industrial Automation.

KOHO HLEDÁME?

- Studenty a absolventy všech oborů FEKT VUT
- Zájem o dlouhodobou spolupráci a ochota dále rozvíjet znalosti z oboru
- Stáže: možnost pracovat 16–20 hodin týdně (flexibilní pracovní doba)
- Komunikativní znalost angličtiny

PŘÍKLADY POZIC

- Electrical/Electronics Engineer
- Hardware Engineer
- PLC Controls Engineer
- Systems Engineer
- Prototype/Test Technician
- Technical Support

careers.honeywell.com/brno
www.honeywell.com
careers.honeywell.com/EarlyCareersCZ

Measurement System for Monitoring of LoRa Radio Links in the $2.4\,\mathrm{GHz}$ ISM Band

David Manasek
Brno University of Technology
FEEC, Department of Radio Electronics
Technicka 12, 616 00 Brno, Czech Republic
246894@vut.cz

Ladislav Polak
Brno University of Technology
FEEC, Department of Radio Electronics
Technicka 12, 616 00 Brno, Czech Republic
polakl@vut.cz

***Abstract*—This paper deals with the design and implementation of a measurement system for the long-term monitoring and evaluation of a Long-Range (LoRa) radio links in the $2.4\,\mathrm{GHz}$ band. The measurement system is based on the SK-iM282A development module, which operates in the $2.4\,\mathrm{GHz}$ band. An appropriate software solution is proposed and implemented for seamless data collection and further offline data analysis. The correctness of the proposed concept has been experimentally tested for two different LoRa signal configurations in an indoor environment. Preliminary results show different performance of LoRa in different scenarios.**

***Index Terms*—LoRa, IoT, $2.4\,\mathrm{GHz}$, ISM band, transmission scenario, SK-iM282A, Raspberry Pi**

I. Introduction

Long-Range (LoRa) is a proprietary protocol that belongs to the family of Low Power Wide Area Network (LPWAN) technologies and primarily targets Internet-of-Things (IoT) applications. LoRa was developed to enable low data rate wireless communication with a high link budget, even in noisy transmission environments. Its use for various applications in the $2.4\,\mathrm{GHz}$ Industrial, Scientific and Medical (ISM) band has been reported in [1] – [4]. However, long-term monitoring and measurement of LoRa-based radio links in the $2.4\,\mathrm{GHz}$ license free band have received little attention. The main purpose of this paper is to introduce a simple measurement system suitable for this purpose.

This paper is organized as follows. Section II provides a brief description of LoRa technology, including its key properties, signal configurations, and the potential benefits of extending LoRa to the $2.4\,\mathrm{GHz}$ band. Section III describes the main hardware (HW) components used for the implementation of the measurement setup, along with the software (SW) used to configure the LoRa radio modules. In Section IV details the test measurements conducted for three different LoRa signal configurations in an indoor environment, followed by a brief evaluation of the results. Section V concludes this paper.

II. LoRa technology

LoRa utilizes Chirp Spread Spectrum (CSS) modulation. Wireless data transmission is influenced by several key factors, primarily signal attenuation and interference.

This work was supported by the BUT project no. FEKT-S-23-8191.

Signal attenuation refers to the gradual weakening of the signal as the distance between the transmitter (TX) and receiver (RX) increases, leading to a degradation in transmission quality. One of the most common causes of signal loss is free-space propagation ($FSPL$), where attenuation is quantified as [5]:

$$FSPL\,(dB) = 20 \cdot log\left(\frac{4\pi df}{c}\right), \tag{1}$$

where d is the distance between the TX and RX, f is the frequency and c is the speed of light in a vacuum. In addition to free-space loss, signal degradation can also result from reflections and diffraction caused by obstacles in the environment. Interference arises when the transmitted signal overlaps with other radio signals in the same radio frequency (RF) band or when multi-path propagation occurs [5].

A. LoRa modulation

LoRa enhances the sensitivity of RXs and improves their resistance to frequency shifts. The RX can often decode signals below the noise level and is very resistant to multi-path propagation. To establish a successful connection between two or more devices, they must have the same signal configuration. The signal configuration of LoRa is defined by parameters:

- *Bandwidth (BW)* – together with the spreading factor (SF), it influences the transmission rate and RX sensitivity. With higher BW, the transmission rate increases, but reduces both maximum communication range between TX and RX decreases, and the RX's sensitivity [7].
- *Spreading Factor (SF)* – determines the rate of frequency change in the chirp signal. As higher SF increases the maximum transmission range and RX sensitivity, but at the cost of significantly higher power consumption. The SF also represents the number of bits transmitted per symbol [7].
- *Code ratio (CR)* – LoRa uses Forward Error Correction (FEC) to enhance robustness against transmission errors. The CR is expressed as a fraction (e.g., $4/5$), where the first number represents the number of useful information bits, and the second number represents the total number of transmitted bits. A higher CR results in longer transmission times but increases the likelihood of correctly decoding the message [7].

DOI 10.13164/eeict.2025.29

B. *LoRa in the* 2.4 GHz *ISM band*

Since 2017, LoRa-based wireless links can be also operated in the 2.4 GHz ISM band. This license-free band extends the range of possible signal configurations for LoRa technology, as listed in Table I. Thanks to its flexible signal configuration, LoRa-based protocols can be applied in a wider range of fields, including industrial machinery [1]. LoRa devices operating in the 2.4 GHz ISM band are not subject to transmission time constraints. However, the higher frequency limits their suitability to shorter-range data transmissions, as higher frequencies are more susceptible to attenuation and absorption by the surrounding environment. For LoRa devices, the transmitted power is limited to $EIRP = 10\,\mathrm{dBm}$ [8].

TABLE I
POSSIBLE LORA SIGNAL PARAMETERS IN 2.4 GHz BAND

Bandwidth [kHz]	203, 406, 812, 1625
SF	5, 6, 7, 8, 9, 10, 11, 12
CR	4/5, 4/6, 4/7, 4/8

III. HARDWARE AND SOFTWARE

A. *SK-iM282A development module*

In this work, the SK-iM282A development module[1], developed by Wireless solutions, is used to create LoRa-based wireless links. The kit includes two development modules, two external antennas with SMA connector and a USB flash drive containing the necessary documentation and SW. The development module features the IM282A-L radio module, which supports Frequency Shift Keying (FSK), Long Range Communication (FLRC), and LoRa modulation [7], [9].

B. *WiMOD LR Studio*

The SK-iM282A development kit also includes configuration SW, WiMOD LR Studio, which provides a graphical user interface (GUI) [1] for setting up key parameters such as modulation type, center carrier frequency, device address, transmission power, and active receiver time. In this study, WiMOD LR Studio is specifically used to configure the individual radio modules before starting the measurements.

C. *Measurement setup*

The block diagram of the proposed and implemented measurement system for large-scale LoRa communication measurements is shown in Fig. 1. To manage the measurements, a C++ program was developed using the library provided by the SK-iM282A module manufacturer in the documentation. This library was extended with the *Radio link test* functionality, which serves as the core of the whole measurement process.

The *Radio link test* function can perform a predefined number of measurements or repeat measurements until stopped by the user. During each measurement, a device connected to a Raspbery Pi transmits a packet of a predefined size to a remote device.

[1]https://wireless-solutions.de/products/sk-im282a/

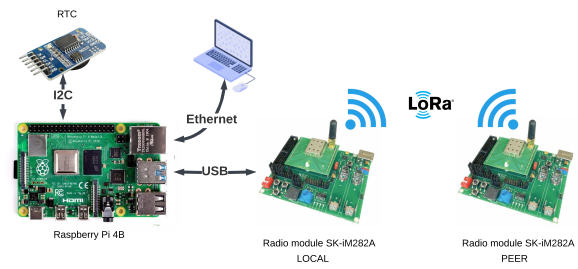

Fig. 1. Block diagram of the measurement system

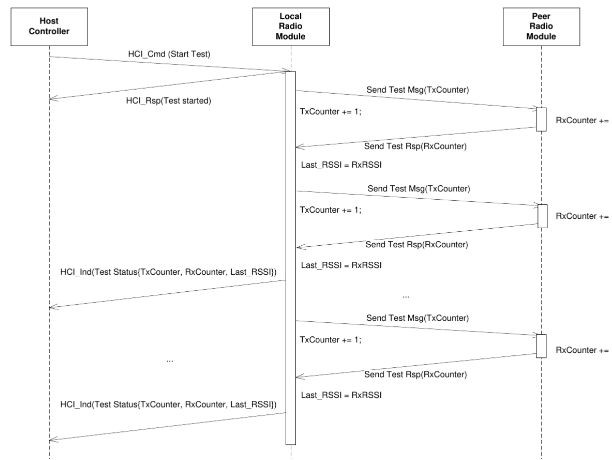

Fig. 2. Diagram of *Radio link test* [11]

Real Time Clock (RTC) module is used to automate the acquisition of the exact time for the measurement records. It is connected to the Raspberry Pi via the I^2C bus. The radio module connected by USB cable to the Raspberry Pi single board computer is called *Local*, the remote module is called *Peer*. The modules store the number of packets sent and received in their memory. Upon receiving a packet, the remote device measures the signal strength $(RSSI)$ and signal-to-noise ratio (SNR). It then responds with a packet containing its $RSSI$, SNR, and the number of packets sent and received. Once the local device receives this response, it also measures its $RSSI$ and SNR. All recorded values are then transmitted via a USB interface to the Raspbery Pi, where they are processed and saved to a file. This measurement process is repeated periodically, as illustrated in Fig. 2.

IV. TEST MEASUREMENTS

Two long-term measurements were conducted using the developed measurement system to test the functionalities of both HW and SW. These test measurements took place in an indoor environment, with the distance between the TX and RX set at $\approx 5\,\mathrm{m}$. The devices were not in direct line-of-sight (LOS). The placement of the radio modules and their labels are shown in Fig. 3.
Measurements were performed using different signal configurations, listed in Table II, representing fast and slow data

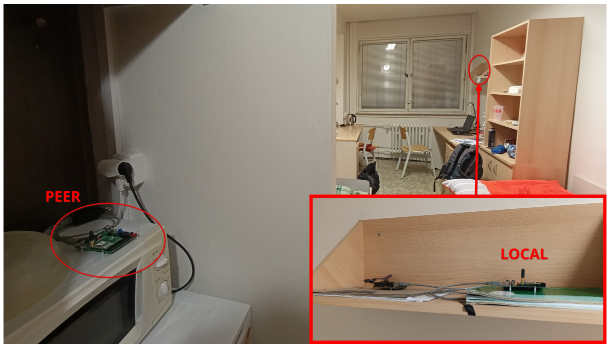

Fig. 3. Radio module locations for test measurements

TABLE II
LoRa signal configurations for test measurements

Bit-rate	SF	BW [kHz]	CR
Fast (152 kpbs)	6	1600	4/5
Slow (0.6 kpbs)	12	200	4/8

throughput for the LoRa link. The transmitted power was set to $8\,\mathrm{dBm}$, and the center frequency was $2.444\,\mathrm{GHz}$. The measurement environment (room) was also covered by a Wi-Fi signal operating on channel no. 6, corresponding to the frequency range $2.427\,\mathrm{GHz}$ to $2.447\,\mathrm{GHz}$, which could potentially interfere with the LoRa signal.

A. Slow bit-rate

Figure 4 shows the $RSSI$ values received by the module placed on a microwave oven when the signal configuration was set up for slow data throughput (see Table II). The measurement was conducted from November 21st to November 24th, 2024 (Thursday – Sunday). The random sharp drops in $RSSI$ values between 7 AM and 10 PM were caused by human movement in the room. In contrast, the periods with minimal fluctuations in $RSSI$ values, primarily during the weekend, correspond to times when the room was empty.

A similar pattern can be observed in box plots shown in Fig. 5. This figure captures data from an extended measurement period lasting eight days, from November 20th to 27th, 2024 (Wednesday - Wednesday). Once again, the $RSSI$ values remain higher from Friday to Sunday (November 22nd – 24th, 2024), when the room was empty. As a result, the data show very few outliers and minimal variations, with 99 % of the measured $RSSI$ values stabilizing at $-54\,\mathrm{dBm}$. The large number of outlying $RSSI$ values observed on weekdays and Sundays corresponds to the negative peaks seen in Fig. 4.

A similar trend is observed in the signal-to-noise ratio (SNR) values, as shown in Fig. 6. Lower SNR values can be caused not only by the presence and movement of people in the room but also by interference from Wi-Fi or Bluetooth networks operating in the same RF range as the LoRa transmission. This reduction in SNR is reflected in an increased number of outliers and shorter whiskers in the box plot. Additionally, the successful reception of several

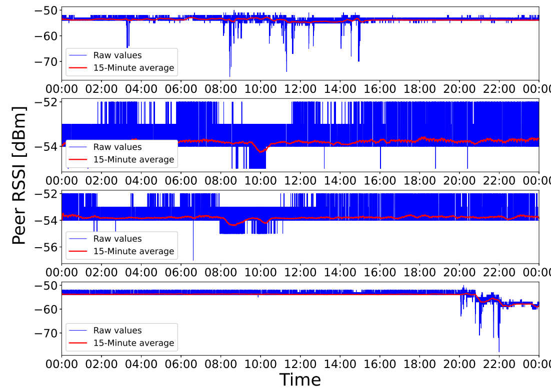

Fig. 4. $RSSI$ values (PEER side): slow bit-rate

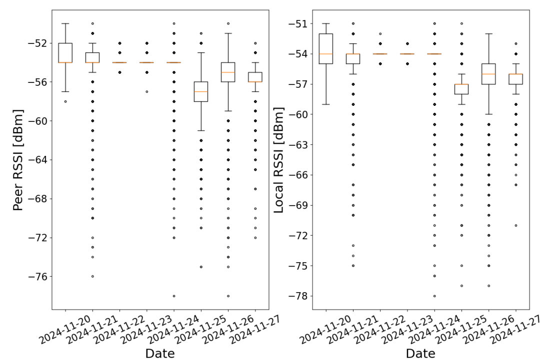

Fig. 5. Distribution of $RSSI$ values by days for slow bit-rate

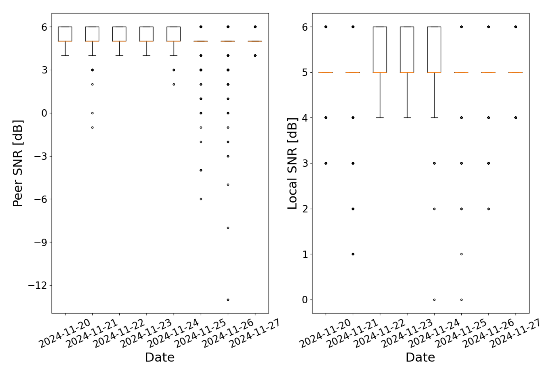

Fig. 6. Distribution of SNR values by days for slow bit-rate

packets with signals below the noise floor was observed, with a minimum SNR of $-13\,\mathrm{dB}$.

B. Fast bit-rate

The measurement for the LoRa signal configuration labeled as *Fast bit-rate* was conducted from November 13th to 19th, 2024 (Wednesday – Tuesday). Similar to the other measurement scenarios, the influence of human movement in the room is evident. The box plots in Fig. 7 show $RSSI$ values comparable to those observed in the slow data throughput scenario, but with more significant drops.

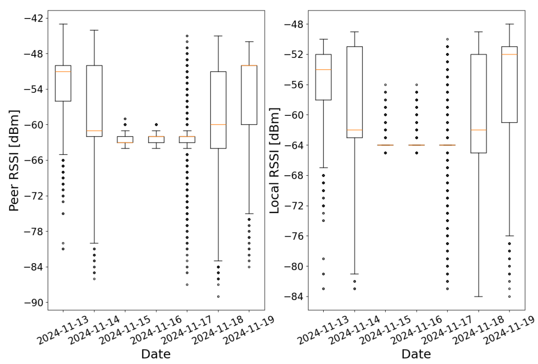

Fig. 7. Distribution of $RSSI$ values by days for fast bit-rate

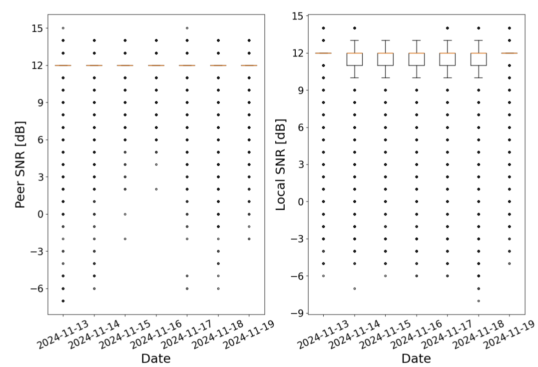

Fig. 8. Distribution of SNR values by days for fast bit-rate

The minimum obtained $RSSI$ value was $-89\,\mathrm{dBm}$. Once again, $RSSI$ values stabilized on Friday and Saturday, with a noticeable decrease in variance compared to the other days.

In Fig. 8, it can be seen that the SNR values fluctuate significantly, regardless of human presence in the room. The median SNR value remained at $12\,\mathrm{dB}$, with a whiskers spanning from $10\,\mathrm{dB}$ to $13\,\mathrm{dB}$ indicating slight fluctuations around a stable value. However, a large number of outliers were recorded, ranging from $-7\,\mathrm{dB}$ to $15\,\mathrm{dB}$. his variability is likely influenced by other wireless services operating in the $2.4\,\mathrm{GHz}$ ISM band. Due to the increase in bitrate, the RX sensitivity was reduced to a minimum, making the LoRa-based wireless link much more susceptible to interference.

V. Conclusion

This paper focused on the design and development of a measurement system for monitoring LoRa communications in the $2.4\,\mathrm{GHz}$ ISM band. The functionality of the proposed system (HW and SW design) has been validated through long-term measurements of two distinct LoRa signal configurations in an indoor environment.

The *slow bit-rate* configuration proved to be the most robust, demonstrating greater stability in both $RSSI$ and SNR values under interference. This configuration successfully decoded several packets below the noise floor with SNR values as low as $-13\,\mathrm{dB}$. The majority of the measured SNR values were in the positive range, with a stable resting value of $5\,\mathrm{dB}$.

The *fast bit-rate* configuration shown significantly higher susceptibility to interference, as evidenced by greater fluctuations in $RSSI$ and SNR values compared to the *slow bit-rate* configuration. Despite this, it was still able to receive packets below the noise floor, with SNR values as low as $-7\,\mathrm{dB}$. During the measurements, SNR values varied considerably, with negative values occurring more frequently than in the *slow bit-rate* scenario. Experimental measurements confirmed that both human movement within the room and the presence of other wireless technologies (e.g., Wi-Fi [12]) had a significant impact on the LoRa wireless link, particularly in the *fast bit-rate* configuration.

Future work will involve testing the measurement system in an outdoor environment. These experiments, in addition to measuring portable scenarios (e.g., RX in motion), will explore multiple LoRa signal configurations, including FLRC and FSK [1], [3], [4].

References

[1] M. Sinmka and L. Polak, *On the RSSI-Based Indoor Localization Employing LoRa in the 2.4 GHz ISM Band. Radioengineering*. 2022, vol. 31, no. 1, pp. 135-143. DOI: 10.13164/re.2022.0135.

[2] G. H. Derévianckine and et al., *Hate or Love in the 2.4 GHz ISM band: The Story of LoRa and IEEE 802.11g*. 2024, Available online: https://hal.science/hal-04815177v1.

[3] R.Falanji, M. Heusse, and A. Duda, *Range and Capacity of LoRa 2.4 GHz. MobiQuitous 2022*. 2023, pp. 20. DOI: 10.1007/978-3-031-34776-4_21.

[4] A. Llap and M. Nunez *Evaluating Energy Consumption and Maximum Communication Distance for SX1280 LoRa Transceiver at 2.4 GHz towards Adaptive Networks*. In: 2023 19th Int. Conf. on Wireless and Mobile Computing, Networking and Communications (WiMob), 2023, pp. 393-398. DOI: 10.1109/WiMob58348.2023.10187857.

[5] Y. Onykiienko and et al. *Using RSSI Data for LoRa Network Path Loss Modeling*. In: 2022 IEEE 41st Int. Conf.on Electronics and Nanotechnology (ELNANO), 2022, pp. 576–580. doi: 10.1109/ELNANO54667.2022.9927036.

[6] NiceRF, *What is LoRa Modulation?*, Accessed 2025-03-04. Available online: https://www.nicerf.com/news/what-is-lora-modulation.html.

[7] Semtech Corporation. *SX1280/81 Datasheet*, Accessed 2025-03-04. Available online: https://semtech.my.salesforce.com/sfc/p/#E0000000JelG/a/3n000000l9OZ/Kw7ZeYZuAZW3Q4A3R_IUjhYCQEJxkuLrUgl_GNNhuUo.

[8] G. H. Derévianckine, A. Guitton, O. Iova, B. Ning, and F. Valois. *Opportunities and Challenges of LoRa 2.4 GHz. IEEE Communications Magazine*, In press. DOI: 10.1109/MCOM.010.2200566.

[9] IMST GmbH. *SK-iM282A Module*. Accessed 2025-03-07 Available online: https://wireless-solutions.de/products/sk-im282a/.

[10] SOS electronic. *IMST SK-iM282A Module*. Accessed 2025-03-07 Available online: https://www.soselectronic.com/cz-cz/products/imst/sk-im282a-307770.

[11] IMST GmbH. *WiMOD LR Base Host Controller Interface - Specification*. Accessed 2025-03-07. Available online: https://wireless-solutions.de/downloads.html

[12] Filip Kaučiarik. *Coexistence of LoRa and Wi-Fi Systems in the RF Band 2.4 GHz*. Master's thesis. Brno University of Technology, Faculty of Electrical Engineering and Communication, Department of Radio Electronics, 2020. Supervisor: Ladislav Polák. Available at: https://www.vutbr.cz/studenti/zavprace/detail/126128.

Use of aerogel in combination with high entropy materials as anode material for Li-ion batteries

Michaela Tichá
Department of Electrical and Electronic Technology
Faculty of Electrical Engineering
Brno, Czech Republic

***Abstract*—This paper focuses mainly on Li-ion batteries in combination with an aerogel as an anode material in secondary batteries. The research then presents the fundamental principle of batteries - intercalation. At the end of the theoretical discussion, aerogel is described as a promising material not only for secondary batteries but also for technology in general. The practical part primarily focuses on the preparation of reference cells, which are used to compare key battery parameters (e.g., energy capacity, charging and discharging times, aging) to determine whether the assembled cells meet the required specifications.**

This study explores the potential of aerogel in secondary cells. It begins with a literature review and continues with a practical section describing the process of assembling reference cells and aerogel production.

***Index Terms*—Li-ion battery, electrolyte, aerogel, electrode material, secondary cell**

I. Introduction

Nowadays, it is difficult to imagine everyday life without electrical technologies. The average citizen of a civilized country uses at least one portable electronic device. Such a device could not exist without a portable energy source - a secondary battery. In recent years, the focus of development has shifted precisely to secondary batteries. These can be found not only in mobile phones but also in laptops, electric vehicles, portable medical devices, and many other applications. Aerogel represents an interesting material that could become a new component of secondary batteries. This extremely lightweight material remained outside technological development for a long time, despite its use as an excellent aid in NASA space missions. One of its great advantages is the ability to be created from various chemical compounds, such as inorganic oxides or more abundant organic substances. Aerogel is characterized by its ability to store particles, which could be utilized in secondary cells that operate on the principle of intercalation.

II. Principle of Li-ion Battery Function

A. Intercalation Reaction

As previously mentioned, the intercalation reaction is essential for Li-ion batteries. Originally, the term intercalation had a different meaning than its current technical usage; it referred to the addition of days to a standard calendar year for a certain period, such as February 29 in a leap year. Chemically, intercalation follows a similar principle. Chemical intercalation is based on storing molecules and then releasing them into the circulation. This reaction occurs not only in electronics but also in fields like biomedicine. [1]

During intercalation, both the hosting material and the ions undergo reversible changes during the merge in their chemical, electrical, optical, and geometric properties. Conductivity has a significant impact on the process, as it can influence the number of electrons flowing between the host and the ions. [1; 2]

The material used for intercalation must maintain its structure during the process to prevent mechanical collapse. Some common intercalation compounds include graphite, layered silicates, clays, and transition metal dichalcogenides. There is also ongoing research into the intercalation of alkalic metals into graphite. [2; 3]

B. Charging and Discharging

In Li-ion battery systems, the negative electrode is most commonly made of graphite, while the positive electrode consists of lithium metal oxides or phosphate-based materials. The cathode does not contain metallic lithium, as its presence could lead to dendrite formation, increasing the risk of short-circuiting. [4; 5]

During charging, lithium ions are released from the positive electrode's structure and travel through the electrolyte to be incorporated into the layers of the negative electrode. In this state, the electrode accepts electrons that move through the external circuit. [5]

The discharging process is the reverse of charging. Lithium ions exit the anode, pick up an electron flowing through the external circuit on their way to the cathode, and are subsequently incorporated into the cathode structure. The advantage of this principle is that the electrolyte does not participate in the reaction itself; it serves only as a medium for ion transport. Therefore, only a small amount of electrolyte is needed, and it does not alter the electrode structure, ensuring a longer lifespan for the cell. [5]

III. Aerogels

A gel material known as an aerogel has its liquid component replaced by gas, yet its overall structure remains intact. These materials are particularly interesting due to their low density, high porosity (which makes them transparent), and large surface area. [6]

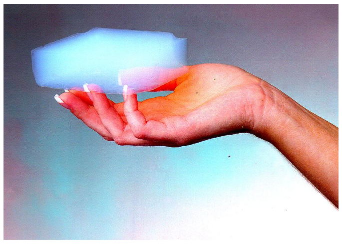

Fig. 1. Aerogel [15]

A. Characteristics

Aerogel is the lightest solid material in the world, with origins dating back 95 years when chemist Samuel Kistler developed it during his tenure at the university. Aerogels can be produced from various chemical compounds, including inorganic oxides (e.g., SiO, AlO, WO, FeO, SnO, NiO) and organic substances such as gelatin, agarose, egg albumin, or gum. Kistler used specialized methods for preparing colloidal solutions, which allowed him to control the morphology of the solid in a finely dispersed state, thereby achieving unique properties with the same chemical compounds. [7; 8]

Aerogels gained attention thanks to three key NASA missions: Mars Pathfinder, Mars Exploration Rovers, and Stardust. At the same time, experiments were conducted on aerogel production in microgravity to develop transparent aerogels suitable for insulating window glass. The first practical application of aerogel by NASA occurred in 1997, when it was used as an insulator for the electronics of the Sojourner rover during the Mars Pathfinder mission. The success of this technology led to its deployment in the Mars Exploration Rovers mission, where aerogel protected the batteries, electronics, and computers of the Spirit and Opportunity rovers. [7; 6]

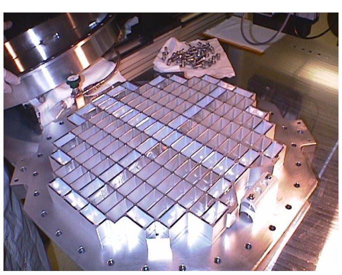

Fig. 2. Aerogel Dust Collector under construction [12]

Today, aerogels are primarily used in laboratories, with commercially available silica aerogels, as well as some organic and carbon-based variants. One of the largest consumers of aerogels is NASA, which has explored various types for a wide range of applications. A significant innovation has been the development of polymer-reinforced aerogels, which enhance material strength. [9; 10]

B. Applications

Scientists initially underestimated the potential of aerogels, but today, they are recognized for their exceptional insulating properties. Aerogels are used in construction as thermal insulation materials that are highly flexible, low in adsorption, and resistant to moisture. They are used wherever heat retention is necessary, minimizing thermal loss. For example, aerogel fibers are sewn into mountaineering gear for climbers scaling Mount Everest. [11; 12]

Aerogel also reached space under NASA's initiative in 1999 aboard the Stardust spacecraft. This mission was the first to bring comet samples (specifically from Comet Wild 2) back to Earth, made possible by aerogel. The crucial aspect was capturing comet particles without damaging them. Aerogel successfully trapped and preserved the particles while maintaining their trajectory as they penetrated deeper into the structure. [12]

IV. Supporting Experiments

There are many other studies suggesting that the use of aerogel in Li-ion batteries has great potential. Below, two studies focusing on aerogel as an electrode material are briefly introduced.

A. Aerogel as a cathode material for Li-ion

This research compared LiMO and LiMnO materials with aerogel as a cathode material. To obtain the results, X-ray analysis, Cyclic Voltammogram (CV), Galvanostatic Charge Discharge (GCD) analysis, and Electrochemical Impedance Spectroscopy (EIS) were used. The results show that aerogel enables fast charge carrier migration within its porous network while maintaining a stable capacity over a long period during multiple cycling processes. [13]

B. Aerogel as an anode material for Li-ion

In this research, the authors investigated Cobalt Carbonate and Cobalt Oxide/Graphene Aerogel Composite Anodes. Cyclic voltammetry (CV) and electrochemical impedance spectroscopy (EIS) were also performed. They demonstrated that this anode, compared to others without aerogel, exhibits higher capacity at high currents and improved stability. Additionally, it was found that the CoCO/GA anode performed better at low current densities, while the CoO/GA anode exhibited superior performance at high currents. [14]

V. The Experiment

A. Preparation

HEOs labelled CCC-A and MgCoCuNiZnO produced by CEITEC BUT was used as the active materials of the anode. The anodes were prepared from conductive carbon Super P (10% wt.), binder PVDF (polyvinylidene difluoride) (10% wt.), and active material CCC-A (80%. The resulting mixture was deposited on an Al foil by a 200 μm coating bar, dried at 60 °C under ambient atmosphere, and, after the solvent was evaporated, pressed with the pressure of 300 kg·cm^2. The discs with a diameter of 18 mm were cut out from the coated

Al foil and subsequently dried at 110 °C under the vacuum. Finally, the discs were inserted into an electrochemical cell El-

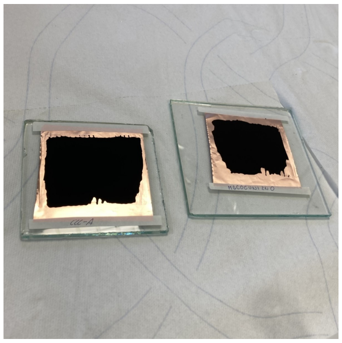

Fig. 3. The mixture applied on copper foil

Cell© ECC-Std and assembled in the argon atmosphere inside a Jacomex glove box with less than 1 ppm of oxygen and water content. For Li-ion configuration a lithium metal disc was used as the anode and 1 mol l1 LiPF6 in EC:DMC in the ratio 1:1 w/w as the electrolyte. The electrolyte was soaked into the glass fiber separator. Cyclic voltammetry (CV) were used for electrochemical characterization. All methods were performed on the VMP3 potentiostat (Bio-Logic). CV was done in the potential window from 0,01 to 2,5 V vs. Li/Li+ and scan rate were set to 0,1, 0,5, 1 and 5 mV/s.

Fig. 4. Finished electrodes

B. Results of Cyclic Voltammetry

The first graph shows the course of four cycles of cyclic voltammetry for the Li–CCC-A cell at a scan rate of 5 mV/s. During individual cycles, an increase in both anodic and cathodic currents can be observed.

In the following graph, the scan rate was reduced to 1 mV/s. Even in these cycles, the currents increase, although not as significantly as in the previous graph. The extreme potential values remain the same, but the maximum anodic current has decreased, while the corresponding potential has increased.

The first graph in the second row shows a gradual decrease in anodic and cathodic current was observed. At the same time, the individual peaks are already quite clearly visible. The maximum anodic current is half of that in the first graph,

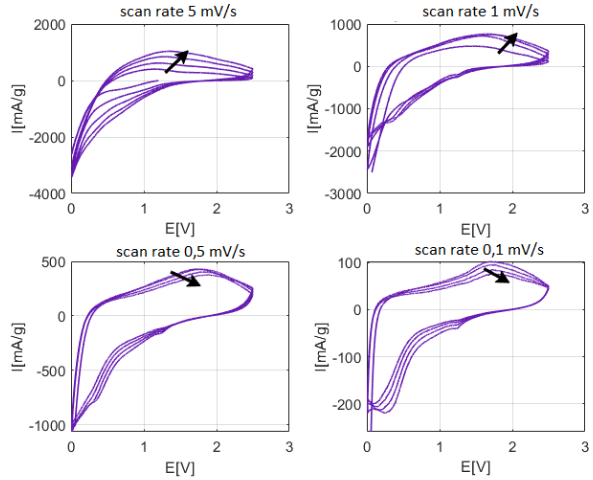

Fig. 5. CV of Li–CCC-A

reaching 430 mA/g at 1,73 V. The minimum current has also visibly decreased to -1000 mA/g at a potential of 9,87 mV

The last graph provides a highly detailed representation, as it has the lowest scan rate — 0,1 mV/s. The maximum current has dropped to 102 mA/g at 1,70 V vs. Li/Li+, while the minimum value is -978 mA/g (9,74 mV). The maximum and minimum values are therefore converging, and the overall profiles are narrowing.

In the second graph of the first row, both currents decreased compared to the previous graph. The most significant drop is in the anodic current, which decreased by nearly 1000 mA/g to 562 mA/g, with the maximum value reduced to 2,07 V.

The third graph maintains the maximum potential value at 2,07 V (as does the following graph); however, the anodic current has again decreased, this time by half, to 289 mA/g. The minimum has significantly dropped multiple times to -940 mA/g at 9,75 mV.

The last graph once again shows the lowest values. The maximum value is 73 mA/g at a constant 2,07 V, while the minimum is -417 mA/g at 9,66 mV.

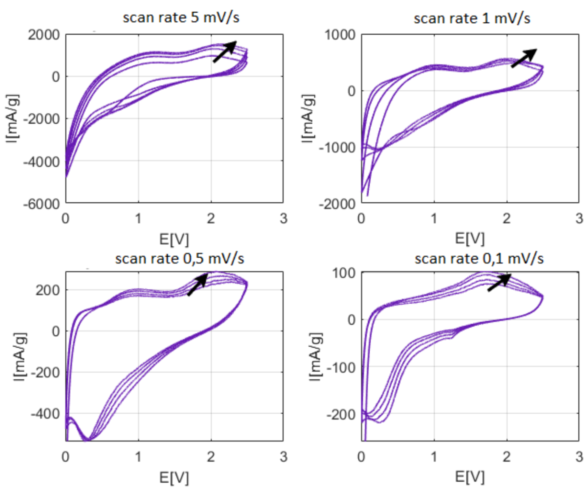

Fig. 6. CV of Li–MgCoCuNiZnO

In these results, it can be seen that the Li-CCC-A cell exhibits the best performance, as its profile is stable. Overall, cells with a lithium electrode show significant stability.

C. Aerogel production

First, 65 mg of sodium alginate was weighed. Additionally, 150 mg of sodium alginate was weighed to evaluate its properties and gelling ability. The alginate was then stirred on a magnetic stirrer in 20 ml of deionized water until fully dissolved, which took approximately 40 minutes. This mixture was poured into a Petri dish and left to further solidify.

The gel was then transferred in a plastic bag creating a vacuum atmosphere to a freezer, where it was frozen at -40 °C for 24 hours. After one day, the material was annealed at 900 °C in a nitrogen atmosphere. After this process, the aerogel was completed and ready for use in cells.

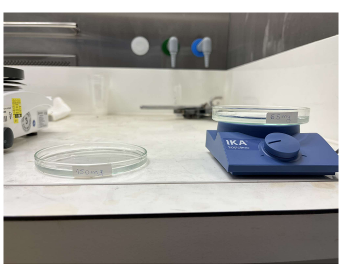

Fig. 7. Gel after stirring process

VI. Conclusion

Based on numerous studies, aerogel holds great potential in battery applications. Its exceptional properties could enable higher performance and stability in secondary batteries. In this work, we have verified the properties of two HEO-based anode materials in combination with Li anode. Both materials were found to be electrochemically active. The material labelled MgCoCuNiZnO showed good electrochemical stability at all scan rates from 5 mV/s to 0,1 mV/s, with a gradual increase in the generated current in all cases. Thus, this sample seems to be more suitable for use as Li-ion battery anodes. Initial experiments have been undertaken to prepare the aerogel and subsequently the aerogel will be modified using a selected sample of HEO based anode material to form a porous conductive matrix which should help to further improve the electrochemical properties of this anode material.

Acknowledgment

I would like to express my gratitude to my thesis supervisor, who introduced me to the methods of electrode and cell fabrication and provided invaluable guidance throughout the experiment, ensuring its smooth progression.

References

[1] WHITTINGHAM, Stanley M. Intercalation Chemistry. Academic Press, 2021. ISBN 0124120679
[2] HANDBOOK OF BATTERIES. 4. The McGraw-Hill Companies, 2011. ISBN 978-0-07-162419-0
[3] BAĎURA, David. Electron microscopy study of the processes involved in the recycling of electrode materials for Li-ion batteries. Bachelors thesis. Brno University of Technology, 2024.
[4] KAZDA, Tomáš. Materiály pro Li-ion akumulátory – porovnání. Online. TZB - info. 2022.
[5] KHAN, Anish, JAWAID, Mohammad, ASIRI, M. Abdullah, INAMUDDIN. Nanocarbon and its Composites. Online. I. Woodhead Publishing, 2019.
[6] LEVY, David, ZAYAT, Marcos. The Sol-Gel Handbook Sol–Gel Materials. Online. I. Wiley-VCH Verlag GmbH & Co., 2015.
[7] KISTLER, Samuel. COHERENT EXPANDED AEROGELS. Online. Nature. 1931, vol. 127, num. 3211, pp 13.
[8] Aerogels: Thinner, Lighter, Stronger. Online. NASA. 2011.
[9] SMIRNOVA, Irina, GURIKOV, Pavel. Aerogel production: Current status, research directions, and future opportunities. The Journal of Supercritical Fluids. vol .134, 2017
[10] HÜSING, Nicola, SCHUBERT, Ulrich. Aerogels—Airy Materials: Chemistry, Structure, and Properties. Online. Angewandte Chemie International Edition. 1998, vol. 37, num. 1-2, pp 24.
[11] GURAV, Jyoti, HYUNG-HO, Park. Silica Aerogel: Synthesis and Applications. Online. Journal of Nanomaterials. 2010, vol. 409310, pp 11.
[12] Catching Comet Dust. Online. Solarsystem NASA. 2005.
[13] MUTHU MUNIYANDI T., BALAMURUGAN S., NARESH N., PRAKASH I., VENKATESH R., DESHPANDE, Uday, SATYANARAYANA N. Li2FeSiO4/C aerogel: A promising nanostructured cathode material for lithium-ion battery applications, Journal of Alloys and Compounds, vol. 6, num. 887, 2021, 161341 ,ISSN 0925-8388
[14] GARAKANI AKBARI, Mohammad et al. Cobalt Carbonate/ and Cobalt Oxide/Graphene Aerogel Composite Anodes for High Performance Li-Ion Batteries, ACS Applied Materials & Interfaces, vol. 2014, num. 6 (21), pp 18971-18980 ,DOI: 10.1021/am504851s
[15] THOMAS, Gary P. AZO Materials. Online. Azom.com

A case study of energy community assessment in the Czech Republic

1st Denis Šaman
Faculty of electrical engineering and communication
Brno University of Technology
Brno, Czech Republic
240297@vut.cz

2nd Lukáš Radil
Faculty of electrical engineering and communication
Brno University of Technology
Brno, Czech Republic
radil@vut.cz

***Abstract*—This article focuses on a case study of an energy community assessment. Different allocation keys will be presented to ensure a fair and efficient distribution of shared energy among community members. The calculation is demonstrated using real data from an anonymized energy community. A static allocation key will be used for the calculation with repeated iterative computation.**

***Index Terms*—Allocation key; Energy community; Energy sharing; Accounting operations**

I. Introduction

In August 2024, the Czech Republic implemented electricity sharing within community energy systems, aligning with Directive (EU) 2019/944 of the European Parliament and Council, part of the Clean Energy for All Europeans (CEP) package. This initiative empowers citizens, municipalities, and businesses to actively manage energy production and consumption, fostering cost savings, energy self-sufficiency, and reduced reliance on centralized sources. Community energy plays a pivotal role in decentralization and contributes to the decarbonization of the energy sector.

To support this transition, the Czech Republic established the Energy Data Centre (EDC), tasked with collecting, analyzing, and providing energy data to stakeholders such as producers, consumers, and market operators. The EDC's online platform enables stakeholder registration for electricity sharing and community management.

Electricity sharing operates under two models:

- Active customer model
- Energy community model.

The active customer model allows individuals or groups (up to 11 members connected via the distribution network or up to 1,000 members within a single residential building) to share the electricity generated by their members. For example, photovoltaic energy generated at a cottage can be consumed in a family home with associated distribution charges. Registration on the EDC platform and ownership of the energy source is sufficient to participate, without the need to set up a legal entity. Sharing here is not territorially limited.

Energy communities, on the other hand, require formal legal structures such as associations or cooperatives and can include up to 1,000 members in 3 neighbouring municipalities or within the Prague metropolitan area. These communities benefit from subsidies, voting rights and larger investment opportunities. According to the Czech legislation, the amendment to the Energy Act 469/2023 Coll. (LEX OZE II), two types of energy communities are defined: Energy Communities (EC) and Renewable Energy Communities (REC). While ECs focus exclusively on electricity sharing, RECs include heat and biogas sharing. Both models mandate the reinvestment of at least 67% of profits in community development

A key aspect of electricity sharing is the allocation of electricity, which is determined by predefined keys for the distribution of electricity among members. This system ensures fair distribution while supporting the broader goals of sustainability and local energy independence [1]–[3].

II. Energy Data Centre

The Energy Data Centre (EDC), established as a joint-stock company, addresses challenges arising from the decentralization and digitalization of the energy system, as well as issues related to the integration of volatile energy sources. EDC achieves this by collecting and analyzing household and business energy consumption and production data at 15-minute intervals, providing these insights to relevant market participants.

In addition to data analysis, EDC facilitates the registration of off-take points (EANc) and generation transfer points (EANs) on its online platform. These points can be integrated into energy communities or active customer structures. The platform also supports the setup of allocation systems for individual off-take points and enables comprehensive management and monitoring of sharing groups [4].

III. Allocation Key

Currently, at the time of the amendment to the Energy Act Lex OZE II, the electricity produced in the Czech Republic is divided among the consumption points using a static allocation key with the possibility of repeated iterative calculation. In the following years, with the third stage of the amendment of the Energy Act Lex OZE III, the possibility of using a dynamic key is envisaged. The principle of the hybrid allocation key, which is not yet envisaged in the Czech Republic but is also used in Europe, will be described here.

A. Static Allocation Key

The static allocation key (SAC) with the possibility of iterative recalculation, as used in the Czech Republic, is defined by a fixed percentage distribution of the shared energy among the energy end-uses (EANc) in the community. However, due to the iterative calculation, energy can be allocated to a customer site up to five times in a given 15-minute interval. In the first iteration, a given percentage allocation of the total energy produced is assigned to the customer site. In each subsequent iteration, the remaining unallocated energy is then allocated by the same percentage. There is a limitation of a maximum of 5 generation sites (EANs) that can supply a single load point. The key is set in the online form during community registration and configuration in the EDC web portal. Based on the set priorities, a percentage of the shared energy from each EANs is allocated to each EANc in turn. If there is not enough energy available to cover all EANc's according to their percentage allocations, energy will only be allocated to the higher priority customer sites up to their allocation, starting with the highest priority 1.

B. Dynamic Allocation Key

The Dynamic Allocation Key (DAC) takes into account the actual electricity consumption at individual consumption points, compared to the Static Allocation Key. Whereas in SAC, the shared energy is distributed to the customer sites according to predetermined percentages, irrespective of their actual needs, and the surplus energy is returned to the grid after all iterations are completed (in case of repeated iterative calculations), DAC allows for a more flexible energy allocation. In each 15-minute interval, the largest share of energy is allocated to the customer site that shows the highest consumption. This maximizes the efficient use of available energy within the community, up to the current demand at any given time.

C. Hybrid Allocation Key

The hybrid method combines static and dynamic methods. It is built on the principle of two cycles, where in the first round the electricity is distributed by the static method according to a set percentage and the energy that is not consumed in a 15-minute interval is distributed among the other participants by the dynamic method (according to their actual consumption) [3].

IV. Data Basis for Electricity Allocation Calculation

The allocation key was processed using the MATLAB software tool, enabling efficient handling of large datasets and graphical visualization of results. This approach also facilitated the automation of calculations and their generalization for different consumption points. The computation was conducted as part of a broader study, in which I participated, aimed at assessing the benefits and feasibility of establishing an energy community for a real group of municipalities.

To comply with data anonymization requirements, specific names of municipalities and their associated data are omitted in this paper. Instead, the calculation is presented through a model scenario. The model simulates an energy community comprising six consumption points and three production points, all located within a single municipality. Electricity production is provided by three photovoltaic power plants. The parameters of the individual consumption and production sites are summarized in Tables 1 and 2.

TABLE I
Annual Energy Consumption and Tariff Rates in the Energy Community

EANc	Annual Energy Consumption (MWh)	Tariff rate	Sharing
Municipal Office	167.61	C45d	Yes
Community Centre	15.83	C02d	Yes
Nursery	37.33	C25d	Yes
Primary School	149.17	C25d	Yes
Health Centre	42.73	C02d	Yes
Collection Yard	5.06	C45d	Yes
Public lighting	4.60	C62d	No

For municipal power sharing, only objects that coincide with electricity production are suitable.For example, if we have PV generation without batteries, it is not possible to use the consumption in the form of public lighting. The use of batteries is currently not possible under the amendment to the Energy Act No. 469/2023 Coll. (Lex OZE II) as separate facilities independent of production sources, but with the forthcoming amendment to the Energy Act No. 458/2000 Coll. (Lex OZE III) their full legislative anchoring is expected, including conditions for grid connection and operation as separate storage facilities.

TABLE II
Installed Power in the Energy Community

EANs	Installed Power (kW)
Municipal Office PV	49.58
Nursery PV	29.815
Primary School PV	10.45

V. Processing Production and Consumption Data

Neither the annual consumption data nor the PV installed capacity data will be sufficient, so we will have to spread these data over suitable intervals. For simulation and community setup we need consumption data at 15 minute intervals as processed by EDC. Smart meters are used for metering and sending, which are mandatory for sharing. However, if, as in our case, we want to simulate e.g. a community that is just starting to share and we only have annual consumption data and building tariff classes, we need help by approximating the consumption pattern over the year. For this purpose, Standard Load Profiles (SLP).

A. Working with Standard Load Profiles of Electricity Supply

The electricity market operator (OTE a.s.) publishes average annual consumption profiles at 15-minute intervals, divided by typical consumption groups. These groups correspond to specific tariff classes. The sum of all the values in the corresponding column of the SLP class represents the maximum duration of Tm per year that satisfies equation (1). Based on the given annual energy consumption *E*, the maximum energy consumption *Pm* can be determined. In the next step, each value in the corresponding SLP class column is multiplied by *Pm* to obtain the profile of the annual energy consumption in hourly intervals, respecting the SLP class and the annual consumption at the point of consumption.

This method can be used for all required consumption points. For the distribution into 15-minute intervals, an even distribution of the hourly power value is assumed, i.e. one quarter of the hourly power is assigned to each 15-minute interval.

$$P_m = \frac{E}{T_m} = \frac{1}{T_m}\int_0^T P(t)\mathrm{d}t \leq T \tag{1}$$

Where:

P_m is the highest power consumption (kW),
E is the value of annual energy consumption (kWh),
T_m is the duration of the maximum (h).

B. Photovoltaic Power Generation Prediction

In order to accurately predict the amount of energy produced by PV plants in the following year, it is necessary to take into account meteorological data in addition to the installed capacity of the plants. A number of software tools and applications are available to calculate the energy production of PV systems. For our model we have chosen the Photovoltaic Geographical Information System (PVGIS), which is developed by the European Commission's Science Centre.

PVGIS allows estimating the annual electricity production of PV plants with hourly increments in a specific location. The calculation is based on an approximation based on long-term solar radiation databases since 2005. This approach allows prediction based on historical meteorological data and provides a relevant basis for modelling future electricity production from PV sources [5]. Hourly data were further interpolated to 15-minute intervals.

VI. Allocation Key Calculation

The developed MATLAB program allows to assign individual power plants to individual consumption points. In addition to the allocation, priority levels are also set. Demand points with a photovoltaic (PV) system installed on the roof have their own PV system assigned as priority 1, while all other priorities are determined according to the order shown in Table II.

Once the priorities are set, the software tool requires the selection of a specific point of consumption of interest. The software then sequentially allocates energy from available resources to this point. The process of energy allocation is governed by two key conditions:

- If the allocated shared energy exceeds the consumption of the selected point, only the amount equal to the actual consumption is shared.
- If, after sharing energy from a given source, the consumption at the selected EAN remains positive, energy from the next available source is allocated.

Once the priorities are set, the software tool requires the selection of a specific point of consumption. The software then sequentially allocates energy from available resources to this point.

The output of the programme is not only numerical values of energy surplus and unmet consumption, but also a graphical representation. The first set of graphs shows the overall energy balance of the municipality (see Figure 1), the second set of graphs visualizes the annual energy consumption of the selected EAN before and after energy sharing from individual sources (see Figure 2).

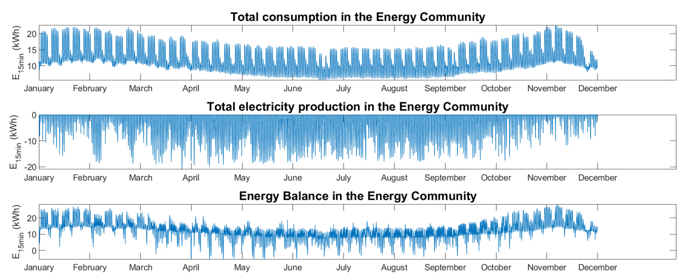

Fig. 1. Overall balance of the energy community in a 15-minute profile

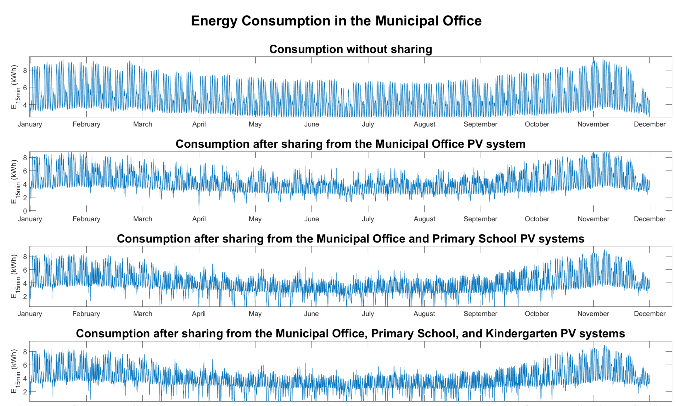

Fig. 2. 15-minute energy consumption profile at the municipal office

Table III provides a detailed financial analysis of energy sharing within the Energy Community. It shows key parameters such as consumption, generation and energy use, together with financial factors including unit electricity prices, total purchase costs and resulting savings. The data illustrates the economic feasibility of energy sharing by comparing costs with and without a sharing mechanism. The results highlight potential cost reductions for community members. The average price per MWh according to the second largest electricity supplier in the Czech Republic EG.D, a.s. is calculated here.It is further assumed that community members will not incur any costs for energy produced within the community.

TABLE III
FINANCIAL BENEFITS OF POWER SHARING WITHIN THE ENERGY COMMUNITY

Name of municipality	Energy consumption (MWh/year)	Energy production (MWh/year)	Use of energy (MWh/year)	Purchase for consumption (MWh)	Unit price of electricity (CZK/MWh)	Price for purchase without sharing (CZK)	Price for purchase with sharing (CZK)	Unit price for the purchase of shared energy (CZK/MWh)	Savings (CZK/year)
Energy Community	417,725	14,53	13,18	404,545	3,474	1,451,176	1,405,389	0	45,787

Electricity prices from community-owned sources are assumed to be 0 CZK/MWh.

TABLE IV
AVAILABILITY OF POWER SUPPLY AND OVERFLOW FOR COMMUNITY SHARING

Potential energy production (MWh)	**Unused potential of electrical energy (MWh)**	**Energy use (MWh)**
14.53	1.35	13.18

Table IV shows the balance between energy production and consumption. It shows the total potential energy production, the surplus energy produced and the proportion of energy successfully used for sharing.The amount of surplus energy is directly affected by the correct configuration of the allocation key.

TABLE V
ANNUAL BALANCE IN ELECTRICITY CONSUMPTION COVERAGE FOR THE MUNICIPALITY

Power consumption for sharing (MWh)	**Purchase of electricity for consumption (MWh)**	**Surplus energy (MWh)**
14.53	404,545	1,35

VII. CONCLUSION

This paper investigated the principle of the allocation key function in community energy and its importance for the efficient allocation of shared electricity among the members of the energy community. Different approaches to energy allocation and their implications for equity and optimization of the use of available resources were analyzed.

A custom computational model was also presented and implemented in this study, which allows iterative calculation of shared energy allocation based on predefined parameters. This model reflects the static allocation key used in the Czech Republic, while its iterative nature allows dynamic reallocation of unallocated energy at a given time interval.

Another purpose of the article was to present the real situation of some municipalities that are considering electricity sharing. It is always important to remember that electricity sharing only covers the commodity portion of the electricity price and it is not possible to avoid distribution charges unless the area owns the distribution portion. Due to the CAPEX and OPEX associated with the construction of resources, power sharing cannot be recommended to everyone, but only after careful consideration.

REFERENCES

[1] ENERGY REGULATORY AUTHORITY. Active customer or community? Online. Electricity Sharing - Energy Communities. © 2024. Available from: https://eru.gov.cz/sdileni-elektriny-energeticka-spolecenstvi. [cited 2024-10-28].

[2] ENERGY REGULATORY AUTHORITY. Active customer or community? Online. Electricity Sharing - Energy Communities. © 2024. Available from: https://eru.gov.cz/sdileni-elektriny-energeticka-spolecenstvi. [cited 2024-10-28].

[3] CZECH REPUBLIC. § 20b of Act No. 458/2000 Coll., on the conditions of doing business and on the exercise of state administration in the energy sectors and on amendments to certain acts (Energy Act) - In: Zákony pro lidi.cz [online]. © AION CS 2010-2024 [cited 28.10. 2024]. Available from: https://www.zakonyprolidi.cz/cs/2000-458#p20b-2.

[4] ELEKTROENERGETIC DATA CENTER, A.S. About us Online. Edc-cr. © 2024. Available from: https://www.edc-cr.cz/o-nas/#co-is edc. [cited 2024-10-28].

[5] EU SCIENCE HUB. PVGIS user manual. Online. EUROPEAN COMMISSION.© 2025. Available from:https://joint-research centre.ec.europa.eu/photovoltaic-geographical-information-system-pvgis/getting-started-pvgis/pvgisusermanual_en [cited 2025-01-04].

[6] COMMUNITY ENERGY UNION. Electricity sharing methods. Which one pays the most? Online. Union of Community Energy. 2023. Available from: https://www.uken.cz/blog/metody-sdileni-elektriny-ktera se-newest-payoff[cited 2024-12-12].

Energy Balance in Water Treatment Plants

1st Tomáš Brychta
Faculty of Electrical Engineering and Communication
Brno University of Technology
Brno, Czech Republic
247652@vut.cz

2nd Lukáš Radil
Faculty of Electrical Engineering and Communication
Brno University of Technology
Brno, Czech Republic
radil@vut.cz

***Abstract*—This article deals with the reduction of the energy consumption of water treatment plants through the production of their own electricity and their optimization using new, more efficient energy technologies and approaches. The main objective of the work was to present the issue of high electricity consumption of waterworks, its solution, and the technologies used for optimization. These technologies have already been proven worldwide but remain underutilized. By their extension and appropriate use, significant and proven savings can be achieved. The second task was to propose a model of a photovoltaic power plant with a battery system designed for a water pumping station, based on data obtained by monitoring electricity consumption for a whole year. The model was created using the SAM (System Advisor Model) software from the US National Renewable Energy Laboratory (NREL) and is used to demonstrate possible solutions. Basically, the aim of this work was to present the problem of high electricity consumption of waterworks and the possibilities to reduce it.**

***Index Terms*—Water treatment plant; Wastewater treatment plant; Water pumping station; Energy optimization**

I. Introduction

Reducing the electricity consumption of water supply facilities is a key issue that affects everyone. Every day, an average person uses between 120 and 150 litres of water, which is first pumped to the point of consumption using pumps in water pumping stations. Pumps consume large amounts of electricity, so we try to use the most efficient ones. Subsequently, most of this water becomes wastewater. This wastewater is discharged through waste pipes to a wastewater treatment plant where it undergoes a complex treatment process. Wastewater treatment is generally a very energy-intensive process and cannot be restricted in any way to save energy, as the quality of the treated water could be adversely affected. There are many different ways to reduce the energy intensity of pumping and treatment. This issue has already been dealt with in a number of expert articles, see [1]. One option is to generate your own electricity and thus achieve greater self-sufficiency. This can be done by using a photovoltaic power plant with a battery system that could cover part of the electricity consumption. Its main advantage is its simple and quick installation. However, the disadvantage is the uneven production. Another option is to install heat pumps. In the case of wastewater treatment plants (WWTPs), it is possible to use the biomass generated during the treatment process to produce biogas. The second way to achieve savings is to use new and more efficient technologies in the different parts of the water pumping or treatment process, which will be discussed later in this paper [2].

The solution to the energy needs of waterworks facilities can be seen on two levels:

a) in electricity savings – meaning that it is necessary to focus on the efficient use of electricity and not just electricity
b) in the resource base – meaning primarily the production of energy directly at the point of consumption.

II. New energy-saving technologies

The technological equipment of waterworks usually corresponds to the time of the establishment of these facilities. Nowadays, with advanced modeling and new materials, it is possible to replace machine technologies with newer ones that provide the same functionality, but with better energy efficiency. Furthermore, two types of main plants are distinguished, namely:

a) pumping stations (water treatment plants)
b) wastewater treatment plants

III. Pumping stations – Water treatment plants

Pumping stations are used to increase the water pressure in the system and to pump water from storage tanks or boreholes into the water reservoir. They are used, for example, to pump wastewater from households, apartment complexes, businesses, or parts of towns into sewers, which can be either pressure or gravity. They are also used for pumping drinking water and distributing it to the water supply network [3].

A. New pumps and electric motors with IE3

As standards are gradually tightened, old equipment with low efficiencies is being phased out and replaced with newer, more efficient electric motors. The efficiency classes of electric motors are denoted by IE and are divided into four classes according to EN 60034-30, namely:

- IE1 standard efficiency
- IE2 increased efficiency
- IE3 high efficiency
- IE4 very high efficiency

Currently, under EU Regulation 2019/1781, electric motors from 0.75 kW to 1000 kW must meet at least IE3 efficiency. For electric motors rated from 75 to 200 kW with a pole count of 2, 4 and 6 , which are non-braking and designed

DOI 10.13164/eeict.2025.41

for non-explosive environments, a minimum efficiency of IE4 is required. New electric motors for hazardous areas from 0.12 kW to 1000 kW nominal power shall also comply with a minimum efficiency of IE2 [4].

For an example of possible electricity savings by replacing the existing electric motor with a 55 kW four-pole electric motor, if it were loaded to 100 % of rated power every 24 hours for 251 working days, see Tab. II. The savings would be 11 424 kWh/year, so the return on investment would only take a few months.

TABLE I
EXAMPLE OF POSSIBLE SAVINGS BY USING A HIGHER EFFICIENCY ELECTRIC MOTOR, TAKEN FROM [5]

Electric motor 55 kW	IE1	IE2	IE3
Electricity consumption (MWh/year)	331.3	323.6	319.9
Saved electricity (MWh/year)	0.0	7.7	11.4

IV. WASTEWATER TREATMENT PLANTS

Electricity consumption in wastewater treatment plants varies according to their size. The published data show that the 8 monitored WWTPs of up to 500 PE (population equivalent) in size achieve an average electricity consumption of 173 kWh/PE. In contrast, WWTPs for more than 100,000 PE achieve an average consumption of 36 kWh/PE [2].

Tab. II shows the share of consumption of individual technological units in the wastewater treatment plant. It shows that it is the blowers that consume the most electricity.

TABLE II
SHARE OF CONSUMPTION OF INDIVIDUAL TECHNOLOGICAL UNITS IN WWTP, TAKEN FROM [2]

Technological unit	Share of consumption
blowers	64 %
others	15 %
screening station	13 %
drainage	5 %
thickening	3 %

A. *Screw blowers*

One of the most used technologies for reducing the power consumption of wastewater treatment plants is screw blowers.

Screw blowers are increasingly replacing existing Roots blowers. The main difference between them is in design, principle of operation, and efficiency. Blowers are generally used to create the compressed air needed to aerate and mix the waste material in the tanks. They provide access for microorganisms that remove waste substances from the water [6], [7].

These blowers consist of two screw rotors that rotate in opposite directions. This draws in air and creates many working chambers. The sucked air is compressed between the rotors and the wall, where it leaves into a pressure tank [8].

Their main advantages include high efficiency over the entire range of volumetric flow, as the tight screw profile in speed control manages an almost constant power flow in each mode of operation. Thanks to the integrated control, data can be monitored for efficient control and parameter monitoring. Another significant advantage is the long service life and low heat generation [8].

Fig.. 1 shows the power consumption of the wastewater treatment plant before and after process optimization. In the first part of the optimization, a photovoltaic plant was installed to cover part of the electricity consumption. In the second part, the replacement of the existing Roots blowers with new screw blowers was carried out. The overall optimization has thus been shown to reduce electricity consumption by almost 20 %.

V. RESOURCE BASE

The resource base can include photovoltaic power plants, heat pumps, and cogeneration units. These plants are able to use either freely available renewable sources of electricity or those that are a by-product of the process.

A. *Heat pumps*

Wastewater treatment plants in the Czech Republic have a large potential for waste heat. Their outlet temperature is almost constant all year in the range of (12-15) °C. Because WWTPs are located in almost every town or village, they are a locally available source of energy. Their use would reduce the proportion of heat for heating obtained by burning fossil fuels [9].

Heat pumps are distinguished according to the refrigerant. The refrigerants most commonly used are hydrofluorocarbons (HFC), mixtures containing HFC, and natural refrigerants. These refrigerants are being replaced by less harmful refrigerants such as R290 (propane) and R744 (carbon dioxide) [10].

TABLE III
THE MOST USED REFRIGERANTS IN HEAT PUMPS, TAKEN FROM [10]–[14]

Refrigerant	R744C	R407C	R32	R290
Type	natural	HFC blend	HFC	natural
GWP	1	1774	675	3
Safety classification	A1	A1	A2L	A3
Water temperature (°C)	65	55	55	55
SCOP	3.5	3.8	3.51	3.66
Maximum temperature (°C)	100	65	65	80

B. *Cogeneration units*

One of the other options is the use of combined heat and power (CHP) units. CHP units work by combining an engine and a generator to produce electricity and heat directly at the point of consumption. They allow the combustion of biogas containing methane, which is produced from organic waste

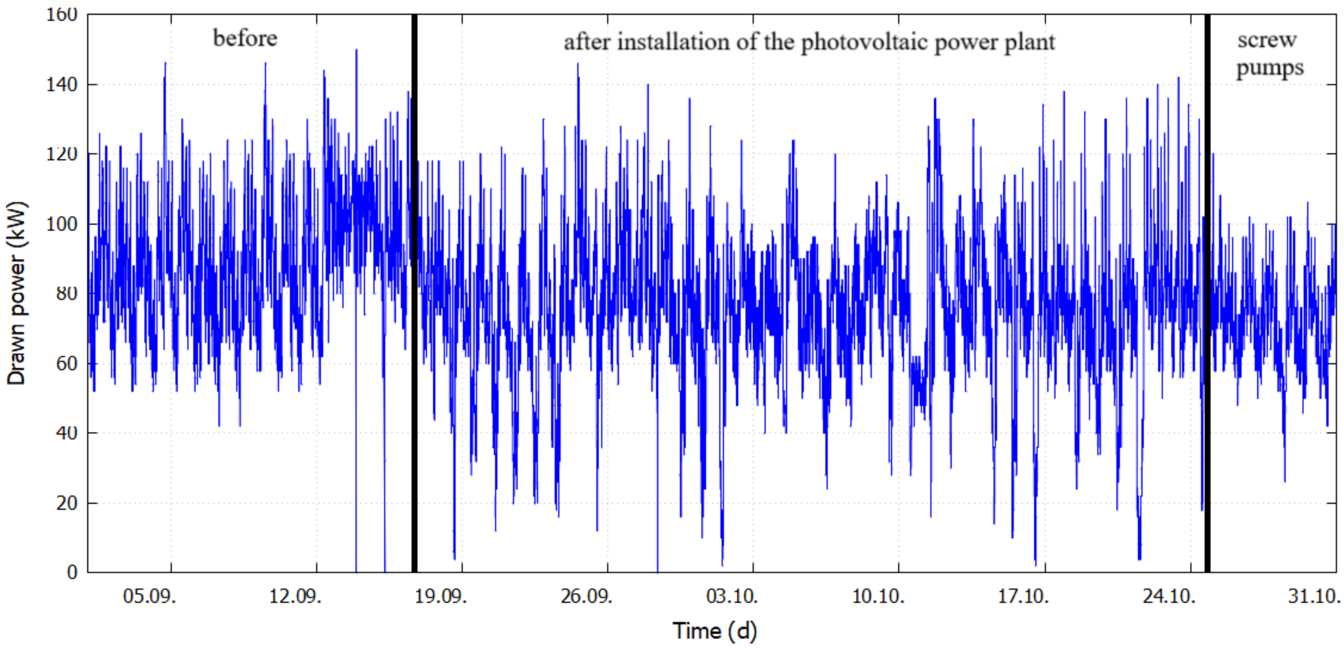

Fig. 1. Graph of electricity consumption in the wastewater treatment plant before and after optimization

accumulated during wastewater treatment. This makes it possible to generate their own energy directly in the wastewater treatment plant and to make efficient use of organic waste materials that would otherwise be wasted [15].

The installation of a cogeneration unit at the wastewater treatment plant on site in Tábor and the Klokoty wastewater treatment plant covered almost 95 % of the electricity consumption. The heat generated is used to heat all buildings on site, as well as the digestion tanks. These treatment plants produce around 8 000 tonnes of digested sludge per year. During the digestion process, biogas is released, which is used in two cogeneration units [16].

C. Photovoltaic power plant

Photovoltaic power plants are one of the most widely used ways of generating your own electricity at the point of consumption. Optimal photovoltaic design can reduce electricity consumption. The size of the photovoltaic plant must be chosen so that the solar panels themselves fit on the land and, at the same time, there are no large power flows into the grid.

In the SAM program, a photovoltaic power plant with a battery system was designed for a water pump station. The pattern of electricity consumption before and after the installation of the photovoltaic power plant is shown in Fig. 2. This represents a typical pattern for a water utility facility. The calculated output of the photovoltaic power plant is $58.888\,\mathrm{kW_{AC}}$, which will be achieved using 128 solar modules with a maximum output of $550\,\mathrm{W_{DC}}$, along with a $\mathrm{LiFePO_4}$ battery with a capacity of 12 kWh.

The share of individual sources contributing to covering the electricity consumption of the pumping station is shown in Fig. 3.

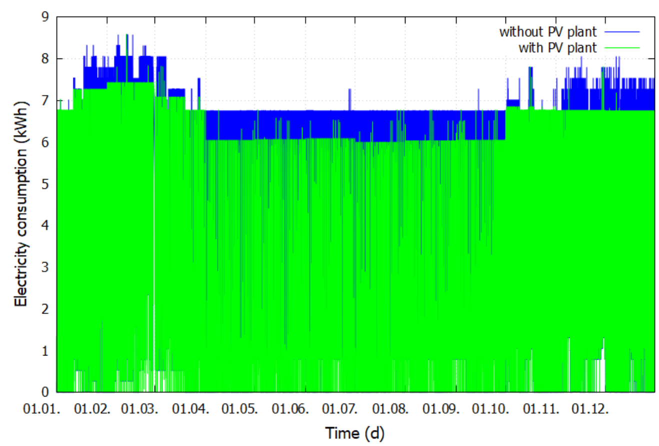

Fig. 2. Electricity consumption before and after PV installation

Fig. 4 shows the histogram of the probability density function (PDF) and the cumulative distribution function (CDF) for the electricity drawn from the grid after the installation of a PV resource.For a practical evaluation of the object under study, the following applies:

- The object has a fairly wide range of electricity consumption,
- There are distinct patterns of usage (presumably corresponding to different modes of operation),
- This type of graph is useful for planning energy needs, sizing systems, and optimizing electricity consumption.

After the installation of the additional power source, approximately 20 % of the time the consumption is less than $1\,\mathrm{kWh.h^{-1}}$, approximately 50 % of the time the consumption

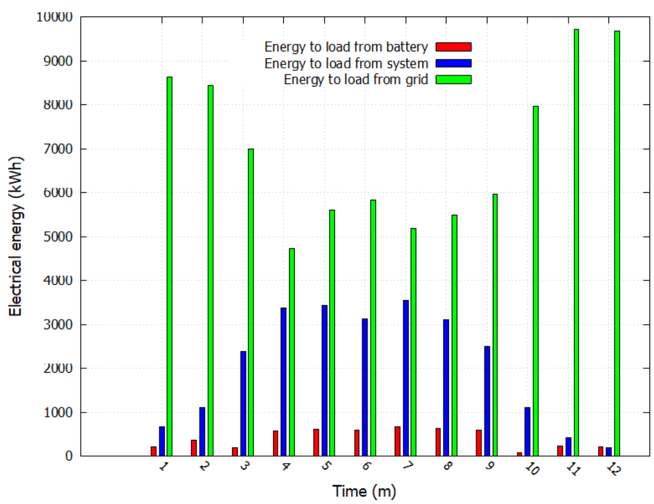

Fig. 3. Energy to Load by Source

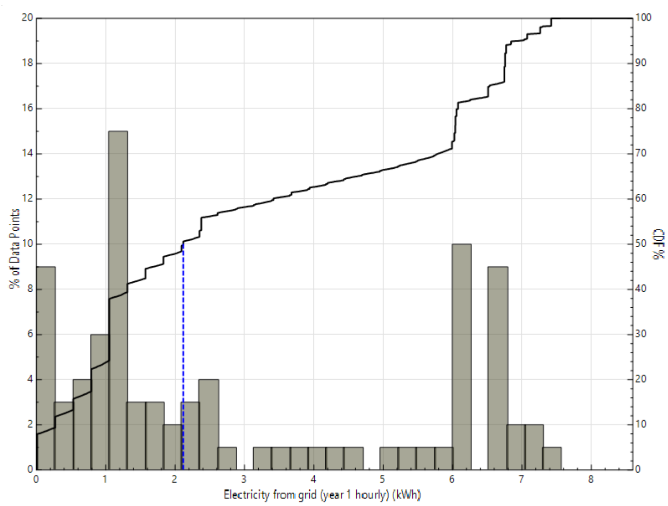

Fig. 4. Histogram showing the PFD and CDF function for electricity drawn from the grid

is less than $2\,\mathrm{kWh.h^{-1}}$, and approximately 80 % of the time the consumption is less than $6\,\mathrm{kWh.h^{-1}}$. The facility has a relatively wide range of electricity consumption. There are distinct usage patterns (which probably correspond to various operational modes). The CDF curve shows that consumption is not evenly distributed but has several typical operational levels. This regime differs from the typical household consumption pattern.

VI. Conclusion

Reducing the energy intensity of water utility facilities is a very current topic of societal importance. In most cases, these are already outdated operations with high electricity consumption. Reducing their energy demands by producing their own electricity at the point of consumption and implementing new technologies that will provide the same functionality can lead to a better energy balance. The proposed photovoltaic power plant with a battery system for the water pumping station is a demonstrative example of a possible implementation of partial optimization of these facilities. However, it is necessary to meet EU conditions with respect to the requirements of Directive 271/91/EEC on urban waste water treatment, which calls for energy neutrality by 2040. This article therefore provides a basic overview of technologies and possible directions toward fulfilling EU goals.

References

[1] MAHFUZ-UR-RAHMAN, A. M.; BUKSH, Ashif; MUTTAQI, Kashem M. a SUTANTO, Danny. *Rooftop Photovoltaic System with Battery Storage to Supply Power in a Sewage Water Pumping Station based Industrial Microgrid with Zero Grid Power*. Online. IEEE Xplore. Dostupné z: https://ieeexplore.ieee.org/document/9334832. [cit. 2025-04-02].

[2] BENEŠ, Ondřej. *Energetické požiadavky na komunálne ČOV*. Online. 2023. Dostupné z: https://acesr.sk/wp-content/uploads/2023/02/O.-Benes.pdf. [cit. 2024-11-22].

[3] PROSPECT ENERGO A.S. *Tlakové systémy kapalin*. Online. Dostupné z: https://www.prospect-energo.cz/tlakove-systemy-kapalin/. [cit. 2025-03-10].

[4] HODBOĎ, Josef. *Povinně vyšší účinnost elektromotorů sníží náklady za provoz technických zařízení budov*. Online. TZB-info. 2023. Dostupné z: https://elektro.tzb-info.cz/elektromotory-pohony-a-stroje/26137-povinne-vyssi-ucinnost-elektromotoru-snizi-naklady-za-provoz-technicky ch-zarizeni-budov. [cit. 2025-03-10].

[5] K-DRIVES A.S. *Kalkulace úspor pro výkon 55 kW*. Online. K-drives. Dostupné z: http://www.elektromotory.cz/sporte-s-novym-pohonem-55kw-24-hodin-denne. [cit. 2025-03-10].

[6] *Rootsova dmychadla (přetlaková, podtlaková)*. Online. Vakuum-bohemia.cz. Dostupné z: https://vakuum-bohemia.cz/rootsova-dmychadla-pretlak-podtlak. [cit. 2024-11-16].

[7] PUMPS AND SYSTEMS. *Čištění odpadních vod: Návrh dmychadel*. Online. Pumps and Systems Magazine. 2021. Dostupné z: https://www.pumpsandsystems.com/wastewater-treatment-design-consideration-blowers. [cit. 2024-11-17].

[8] ROBUSCHI. *Rotary Screw Blower Technology Explained*. Online. Robuschi. Dostupné z: https://www.robuschi.com/en-mc/technologies/rotary-screw-blower-technology. [cit. 2024-11-17].

[9] *Čistírny odpadních vod mají velký potenciál pro dekarbonizaci českého teplárenství*. Online. Vakinfo.cz. 2022. Dostupné z: https://www.vakinfo.cz/velka-tepelna-cerpadla-budou-v-ceske-energetice-hrat-zasadni-roli/. [cit. 2025-03-11].

[10] KRAINER, Robert a DUDA, Jiří. *Chladiva používaná v tepelných čerpadlech*. Online. TZB-info. 2015, 22.3.2022. Dostupné z: https://vytapeni.tzb-info.cz/tepelna-cerpadla/12647-chladiva-pouzivana-v-tepelnych-cerpadlech. [cit. 2024-11-23].

[11] PRECISIONHEATING. *Heat Pumps*. Online. Precisionheating.ie. Dostupné z: https://precisionheating.ie/heat-pumps-ireland/. [cit. 2024-12-09].

[12] TCL. *R32 Tri-thermal ATW Heat Pump*. Online. TCL Europe. Dostupné z: https://www.tcl.com/eu/en/heatpump/heat-pump/r32-split. [cit. 2024-12-09].

[13] POWER WORLD. *Invertorové tepelné čerpadlo R290 Full DC*. Online. Power world.com. Dostupné z: https://cz.powerworldhp.com/heat-pump/home-heat-pump/r290-full-dc-inverter-heat-pump.html. [cit. 2024-12-09].

[14] HAMWORTHY HEATING. *Tyneham CO2 and CO2Q air source heat pump*. Online. Hamworthy Heating.com. Dostupné z: https://hamworthy-heating.com/Products/Commercial-air-source-heat-pumps/Tyneham-CO2-CO2Q-air-source-heat-pump. [cit. 2024-12-09].

[15] *ČOV*. Online. Tedom.com. Dostupné z: https://www.tedom.com/cs/energetickyslovnik/cov/. [cit. 2025-03-11].

[16] TOMANEC, Lubor. *Areálová čistírna odpadních vod získá jedinečnou technologii na úpravu kalů*. Online. 2023. Dostupné z: https://www.vstab.cz/cz/aktualne/45-arealova-cistirna-odpadnich-vod-ziska-jedinecnou-technologii-na-upravu-kalu?utm_source=chatgpt.com. [cit. 2025-03-11].

Linear Deltabot: Design, Kinematics and Trajectory Generation

Ondřej Dušek
Department of Control and Instrumentation
FEEC, Brno University of Technology
Technická 12, Brno 616 00, Czech Republic
246995@vutbr.cz

Kryštof Doležal
Department of Control and Instrumentation
FEEC, Brno University of Technology
Technická 12, Brno 616 00, Czech Republic
xdolez0d@vutbr.cz

Oliver Drga
Department of Control and Instrumentation
FEEC, Brno University of Technology
Technická 12, Brno 616 00, Czech Republic
247362@vutbr.cz

Vít Fousek
Department of Control and Instrumentation
FEEC, Brno University of Technology
Technická 12, Brno 616 00, Czech Republic
247370@vutbr.cz

***Abstract*—This paper describes the design, kinematics, and control of the Deltabot, a high-speed parallel robot optimized for precision tasks such as assembly and 3D printing. The study focuses on its mechanical structure, material selection, and trajectory planning using MATLAB Simulink.**

***Index Terms*—Deltabot, Delta robot, Inverse Kinematics, Forward Kinematics, Multilateration, PLC, MATLAB Simulink, Trajectory generation**

INTRODUCTION

Deltabots are widely used in industries requiring high-speed and high-precision automation, such as packaging, assembly, and 3D printing[1]. Their parallel kinematic structure allows for rapid movements with minimal inertia, making them ideal for applications where speed and accuracy are critical [2]. One of the few major European manufacturers is Igus GmbH [3], which primarily produces linear Deltabots. These robots differ from traditional delta designs by incorporating linear actuators instead of rotational joints, making them less demanding on motor torque[4]. This paper explores the design, control, kinematics, and trajectory generation of a Deltabot, addressing its advantages and the solutions for implementing such systems in practical applications.

I. MECHANICAL DESIGN

This section delves into the design of the Deltabot, examining its physical structure and functionality.

A. Materials Used

The Deltabot is built using materials selected for their strength, low weight, and cost-effectiveness. Aluminum profiles: Provide a balance of strength and low weight for the frame and moving axes. Carbon rods: Used for the arms, ensuring a high strength-to-weight ratio for reduced inertia and faster movements. 3D-printed ASA filament: Used for structural parts, the effector flange, carriage, and mounts due to its ease of printing, machining, and light weight while maintaining reasonable strength.

B. Frame

The Deltabot has a triangular base frame with a side length of $820\,\mathrm{mm}$, made from $30\,\mathrm{mm}$ aluminum profiles. The total height, including the effector, is $834\,\mathrm{mm}$. Each corner houses a $45°$ tilted movable axis. The axes are securely fixed to a central piece for stability. See Fig.1.

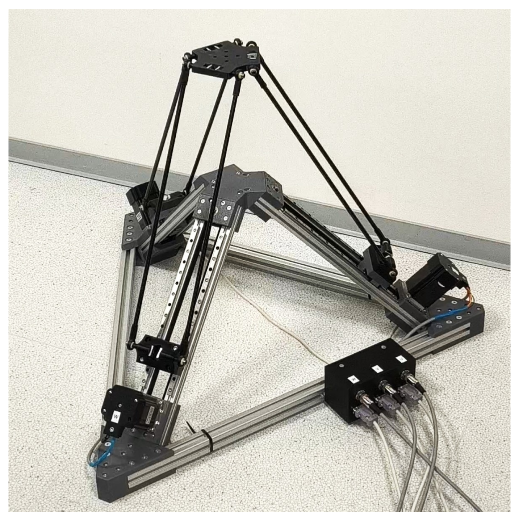

Fig. 1. Assembled Deltabot

C. Linear Axis

The moving axes use $300\,\mathrm{mm}$ linear bearing tracks mounted on $20\,\mathrm{mm}$ profiles. A 48-tooth pulley with a $15\,\mathrm{mm}$ GT2 belt connects the motor to the axle. The $440\,\mathrm{mm}$ axles link the frame to the trolley. The belt tensioning system has an adjustable motor attachment for precise tensioning.

D. Trolley

The trolley links the moving axis to the arms and consists of 3 parts. T-part: Connects to the linear bearings and holds the belt. Wedge mechanism: Secures the belt in GT2-profiled grooves. Articulated segment: Connects to the arms via ball joints, preventing collisions. The T-part includes a counterpiece to prevent deformation. It has precisely cut grooves matching the $2\,\mathrm{mm}$ GT2 belt pitch, creating a self-locking system. Its width prevents deflection.

E. Frame and Joints

Deltabot's $500\,\mathrm{mm}$ arms are made from lightweight carbon rods. Movement relies on self-lubricating Igus KRBM 06 CL ball joints with a $6\,\mathrm{mm}$ hole, handling up to $210\,\mathrm{N}$ and a $40°$ rotation.

1) Joint Restriction Issue and Solution: Initial tests showed $10\,\mathrm{mm}$ bolts limited rotation to $21.16°$. Switching to $8.5\,\mathrm{mm}$ bolts increased it to $26.13°$, but still constrained the workspace to a $225\,\mathrm{mm}$ diameter and $300\,\mathrm{mm}$ stroke. Future improvements could enhance the working area.

F. Effector - Flange

The effector serves as a universal actuator mount, connecting all arms. With a $12\,\mathrm{mm}$ thickness, it supports loads up to $1\,\mathrm{kg}$. Offset joint holes prevent collisions, and its width aligns with the trolley to keep the arms parallel.

II. PLC Programming

The PLC is programmed using ST for initialization and motion control.

A. Configuration

The X20 PLC from B&R utilizes mappMotion technology for ACOPOS motion control. Since the stepper motor cards cannot process motion directly, the PLC simulates this functionality. MappMotion includes pre-configured libraries for CNC and robotic control. Motion feedback is provided by an incremental encoder with a resolution of $4096\,\mathrm{ppt}$ and a maximum operational speed of $4000\,\mathrm{rpm}$.

B. Axis Motion

Each axis supports direct positional control. Before operation, the encoder must be zeroed relative to the actual motor position. Axes are synchronized for simultaneous initiation. Motion is controlled via ST code, internally translated into G-code.

C. Motors and Power Supplies

A Nema 23 stepper motor ($2.83\,\mathrm{N\,m}$, $2.83\,\mathrm{A}$, $36\,\mathrm{V}$) drives the system, configured for maximum torque at low speeds, enabling accelerations up to $50\,\mathrm{m\,s^{-2}}$. Power is supplied at $36\,\mathrm{V}$ with a maximum current of $12.5\,\mathrm{A}$, ensuring adequate reserves to prevent overload. PLC and power supplies are in Fig. 2.

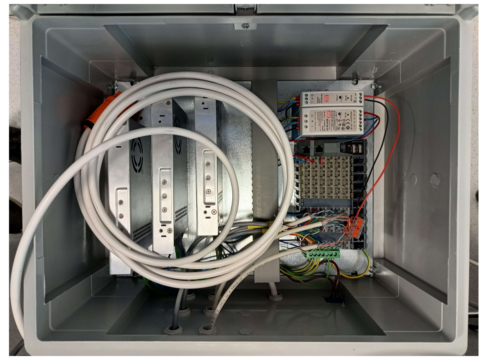

Fig. 2. PLC and Power Supplies

III. Kinematics

Before solving the kinematics, it is necessary to get familiarized with the notation for the individual parts of the arm, according to the Fig.3.

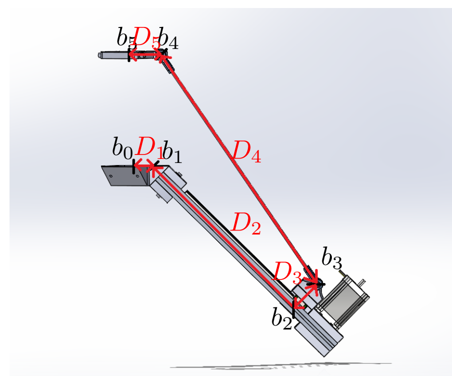

Fig. 3. Declaration of arm junctions and lengths notation

A. Inverse kinematics

Inverse kinematics for manipulators is used to calculate the necessary linear axis extension and joint rotation to achieve the desired endpoint position. Solving inverse kinematics is considerably simpler than forward kinematics, as the linear axis extensions aren't codependent for solving this problem. The intersection of the sphere and the straight line can be used to calculate the inverse kinematics of the Deltabot. The sphere, with radius D_4, is located at point b_4. The straight line is defined by the point b_3, which moves depending on the extension of the linear axis D_2.

The line can be expressed by the parametric equation

$$\vec{p} = \vec{a} + t\vec{b}. \tag{1}$$

By expressing the parameters $\vec{a}$ a $\vec{b}$ we obtain the following form

$$\vec{a} = \begin{bmatrix} \cos\gamma\,(D_1 + D_3\cos(-\alpha)) \\ \sin(-\gamma)\,(D_1 + D_3\cos(-\alpha)) \\ D_1 + D_3\cos(-\alpha) \end{bmatrix}, \tag{2}$$

$$\vec{b} = \begin{bmatrix} \cos\gamma\,(D_2\cos\alpha) \\ \sin(-\gamma)\,(D_2\cos\alpha) \\ D_2\sin\alpha \end{bmatrix}, \tag{3}$$

where γ represents the rotation of each arm: U, V, and W and $\alpha = 45°$ as specified in I-B. Arm U points in the direction of the x-axis, with rotations given by $\gamma_U = 0$, $\gamma_V = 120°$, and $\gamma_W = -120°$.

The equation of a sphere in space is of the form

$$(x-a)^2 + (y-b)^2 + (z-c)^2 = r^2, \tag{4}$$

where a, b, c are the coordinates of the center of the sphere in x, y, z coordinates. By expressing the coordinate of the point b_4, we obtain the resulting equation of the sphere in the following form:

$$\begin{aligned}(x-(x_5+D_5\cos\gamma))^2 + (y-(y_5-D_5\sin\gamma))^2 + \\ (z-z_5)^2 = D_4^2,\end{aligned} \tag{5}$$

To find the final linear axis extension, the equation of the lines 1 is substituted for the components x, y z in 5 to give three independent equations with three unknowns t_U, t_V, t_W. Each equation has two solutions. The solution is the one where values t_U, t_V, t_W lie in the interval $\langle 0; 1\rangle$.

B. Forward kinematics

For the Deltabot, the endpoint position can be determined by finding the intersection of three spheres centered at point b_3, offset toward the center of the Deltabot by the length D_5. This displacement ensures that the intersection corresponds to the position of the endpoint.

The centres of the spheres can be calculated in the form

$$\vec{S} = \begin{bmatrix} cos(\gamma)\,(D_1 + D_3\cos\alpha + t_V D_2\sin\alpha - D_5) \\ sin(\gamma)\,(D_1 + D_3\cos\alpha + t_V D_2\sin\alpha - D_5) \\ -D_3\sin\alpha + t_U D_2\cos\alpha \end{bmatrix}, \tag{6}$$

where $\gamma_U = 0, \gamma_V = 120°, \gamma_W = -120°$.

1) Forward kinematics first method: The first method involves substituting the centers 6 into 4 to obtain a system of three equations with three unknowns. Analytic formula for the solution is quite large (108,567 characters), making it impossible to include in this paper.

2) Forward kinematics multilateration method: The second method of calculation is to use multilateration. This method is most commonly used in GPS localization[5][6]. The end point can be obtained using the position of each radar and their distance to the end point. For the Deltabot case, we know the center of the sphere and the distance from the search point. To simplify the calculation, we transform the sphere centers into a simpler form, namely $S_U = [0\ 0\ 0]^T$, $S_V = [V_x\ 0\ 0]^T$, and $S_W = [W_x\ W_y\ 0]^T$. In this case, the spheres are in the same plane and the coordinate calculation is greatly simplified. Thus, the coordinates of the intersection are

$$\begin{aligned} x' &= \frac{r_1^2 - r_2^2 + U^2}{2U}, \\ y' &= \frac{r_1^2 - r_3^2 + V_x^2 + V_y^2 - 2V_x}{2V_y}, \\ z' &= \pm\sqrt{r_1^2 - x^2 - y^2}. \end{aligned} \tag{7}$$

The back-transformation is then used to obtain the position of the search endpoint.

C. Joint rotation limits

The cosine law can be used to solve the limiting joint angle problem mentioned in I-E1. However, it is necessary to know the current pose of the Deltabot (linear axis extension and endpoint position). To use the cosine theorem, the shape of the arm needs to be simplified to the shape shown in Fig. 4.

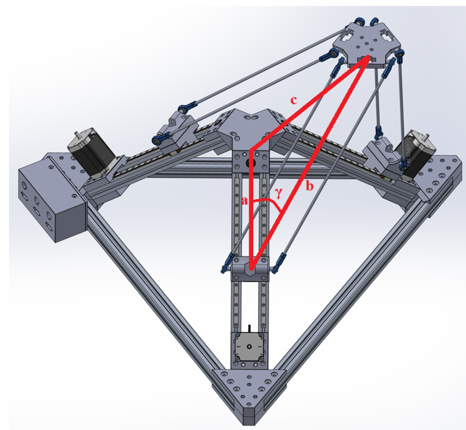

Fig. 4. Arm simplification for cosine law

The cosine law is of the form

$$c^2 = a^2 + b^2 + 2ab\cdot\cos\gamma,$$

from the original formula of the cosine law, gamma is calculated, which takes the form

$$\gamma = \arccos\frac{c^2 - a^2 - b^2}{-2ab},$$

The angle γ represents the limiting joint angle. The individual lengths a, b, c can be calculated using the standard formula for length calculation.

$$\begin{aligned} a &= \sqrt{B_{3x}^2 - B_{x1}^2} + \sqrt{B_{y3}^2 - B_{y1}^2}, \\ b &= \sqrt{B_{4x}^2 - B_{x3}^2} + \sqrt{B_{y4}^2 - B_{y3}^2}, \\ c &= \sqrt{B_{4x}^2 - B_{x1}^2} + \sqrt{B_{y4}^2 - B_{y1}^2}. \end{aligned} \tag{8}$$

These points here contain only the x and y coordinates, since changing the z coordinates does not change the angle due to the properties of the Deltabot structure.

IV. Linear trajectory generation

This chapter describes the method of trajectory generation for the digital twin of a Deltabot in the Matlab environment. The code used for trajectory generation is divided into two parts.

A. Root function Path_planer.m

In the function, the trajectory can be defined using points, between which the trajectory is subsequently generated. It is also possible to specify the speed at which the Deltabot's end-effector should move along the trajectory. Lastly, sampling period of $20\,\mathrm{ms}$ is defined. The function Func_P2P_Linear_trajectory_builder.m is called, which computes the trajectory and returns it as a precisely defined set of points that the Deltabot's end-effector follows. This set of points is then converted into a timeseries format, which is compatible with MATLAB Simulink. There is a model of the inverse kinematics in MATLAB Simulink, that calculates the positions of the linear actuators for the given end-effector trajectory.

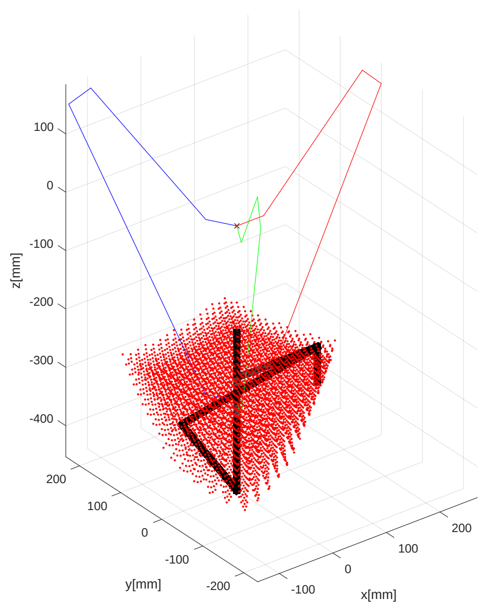

Fig. 5. Generated trajectory (black) in workspace (red grid)

B. Function Func_P2P_Linear_trajectory_builder.m

This function is used to generate a trajectory that connects multiple points in 3D space using linear motion. The trajectory is divided into discrete points to ensure that the motion adheres to the desired speed while maintaining the specified sampling period, which is practically determined by the real control system—in this case, a PLC from B&R Automation. The function always generates the trajectory sequentially between each pair of consecutive points. To maintain the desired speed, the given points must be interpolated with the appropriate number of intermediate points. This is achieved by weighting the velocities in the individual X, Y, and Z coordinates using the parameter t (see 9).

$$t = -\frac{X - \sqrt{X^2 + 4 \cdot \text{Velocity} \cdot Y^2 + 4 \cdot \text{Velocity} \cdot Z^2}}{2 \cdot (Y^2 + Z^2)}. \quad (9)$$

By multiplying the parameter t with the distance in each axis, we obtain the velocity components in the X, Y, and Z directions. Furthermore, based on the distance between the given points, the computed velocities in each axis, and the sampling period, the number of intermediate points needed to interpolate the trajectory is determined. The step size between consecutive intermediate points is then calculated. This step size is iteratively added to the given starting point until the specified endpoint is reached. In this manner, the trajectory of the Deltabot's end-effector is generated for the given speed and sampling period.

V. Conclusion

This paper presented the design, control, mechanics and kinematics of the Deltabot, focusing on its structural configuration and motion control. The analysis of inverse and forward kinematics demonstrated the advantages of the parallel mechanism in achieving precise and high-speed movements. Additionally, the implementation of trajectory generation in MATLAB Simulink proved to be an effective method for optimizing motion paths and ensuring smooth and accurate end-effector positioning. Future work could focus on refining the trajectory planning algorithms to enhance motion efficiency and minimize dynamic errors. Further improvements in kinematic modeling and real-time control strategies may also contribute to better adaptability and performance in industrial applications.

References

[1] S. Aksoy and E. Ozan, "Robots and their applications," vol. 07, pp. 2001–2009, Feb. 2020.

[2] C. R., *Conception d'un robot parallèle rapide à 4 degrés de liberté*, 1991.

[3] Igus GmbH, European manufactorer of linear Deltabots, [cit. 2025-03-16]. [Online]. Available: https://www.igus.cz/robolink/delta-robot.

[4] M. Bouri and R. Clavel, "The linear delta: Developments and applications," in *ISR 2010 (41st International Symposium on Robotics) and ROBOTIK 2010 (6th German Conference on Robotics)*, 2010, pp. 1–8.

[5] S. Bancroft, "An algebraic solution of the gps equations," *IEEE Transactions on Aerospace and Electronic Systems*, vol. AES-21, no. 1, pp. 56–59, 1985. DOI: 10.1109/TAES.1985.310538.

[6] B. T. Fang, "Trilateration and extension to global positioning system navigation," *Journal of Guidance, Control, and Dynamics*, vol. 9, no. 6, pp. 715–717, 1986. DOI: 10.2514/3.20169. eprint: https://doi.org/10.2514/3.20169. [Online]. Available: https://doi.org/10.2514/3.20169.

ABB v Brně
Lepší svět začíná s vámi

ABB je technologický lídr v oblasti elektrifikace a automatizace, který posouvá hranice průmyslových inovací už více než 140 let. Z Brna dodáváme rozváděče vysokého i nízkého napětí, modulární a digitální systémy, přístrojové transformátory a senzory. Jako hlavní partner ABB FIA Formula E ukazujeme, že budoucnost mobility je elektrická, efektivní a udržitelná. Stejně jako v závodech Formule E se i my každý den snažíme být rychlejší, chytřejší a inovativnější.

Studentům a absolventům nabízíme:
- Placené brigády
- Odborné praxe
- Stáže
- Trainee program
- Vedení balakářské nebo diplomové práce
- Hlavní pracovní poměr po ukončení studia

Buďte s námi o krok napřed.
Více na **www.abb.cz/kariera**
Kontaktujte naši náborářku:

Petra Pospíšilová
petra.pospisilova@cz.abb.com
+420 733 693 337

Lucie Vašatová
lucie.vasatova@cz.abb.com
+420 704 997 141

TOP ZAMĚSTNAVATELÉ 2025
4. místo | AUTOMOBILOVÝ & STROJÍRENSKÝ PRŮMYSL

Možná hledáme právě Tebe!

Nabídkový specialista

- Příprava nabídek v oblasti přístrojů nízkého napětí a zpracování cenových kalkulací. Návrh optimálního technického řešení pro zákazníky a aktivní účast na technických a obchodních jednáních.

R&D Simulační inženýr – brigáda

- Podpora designerů na lokálních i mezinárodních projektech vývoje plynem izolovaných rozvaděčů VN. 3D modelování v SolidWorks a SpaceClaim, příprava modelů pro simulace v ANSYS Workbench.

PLC programátor – námořní průmysl

- Vývoj PLC softwaru pro lodní automatizaci, testování a ladění systémů na palubě i v největších přístavech světa – Karibik, Jižní Amerika, Střední východ.

Projektový inženýr elektro – dlouhodobá stáž/brigáda

- Inženýrská činnost v oblasti elektro dodávek na zahraničních projektech. Možnost podílet se na inovativních technologiích, například projektu „Jansz-Io" – těžba zemního plynu s nižší uhlíkovou stopou.

Specialista řízení rozvaděčů

- Konfigurování ovládacích a ochranných terminálů v rozvaděčích VN a odzkoušení jejich správné funkčnosti

Area Sales Manager

- Zodpovědnost za prodej a koordinaci na zahraničních trzích. Péče o zákazníky a vyhledávání nových obchodních příležitostí.

Display device for archery competitions

Antonín Pospíšil
Department of Control and Instrumentation
FEEC Brno University of Technology
Brno, Czech Republic
240222@vut.cz

Petr Petyovsky
Department of Control and Instrumentation
FEEC Brno University of Technology
Brno, Czech Republic
petyovsky@vut.cz

***Abstract*—This paper presents a system designed to improve the organisation of archery competitions. The system reduces errors and delays by replacing the traditionally used paper cards with an electronic system. The basic components of the proposed system are described. The communication between the parts and the basic description of the operation of the whole system are outlined.**

***Index Terms*—display equipment for sports events, archery, e-ink display, embedded system**

I. Archery

I have been organising archery competitions for five years. Our club organises competitions for 200-300 archers, such as national championships, competitions of the Czech Archery Association Cup. In cooperation with our partner club in Slovakia, we organize a 4-round international cup, in which about 400 archers from both countries participate every year.

A. Archery competitions

In the archery competitions, the archers first shoot 72 arrows in qualification. The values of the hits are added up, the archer with the highest score wins this part. The scores are used to create a ranking for each category, and the advancement key is used to create the initial pairs for the elimination round of the competition. The winner of the duel advances to the next round of duels. Finally, two pairs remain in the semi-finals, and the winners of these duels will compete against each other for the first place, the gold medal. The less successful in the semi-finals compete together for the bronze medal.

Several categories can be competing in one round at the same time, so shooters and their coaches need to know exactly where they will be competing in the next round. Matches are shifted to make efficient use of shooting range space and to make room for new categories. However, this brings with it the need to inform shooters which target ranges will be used for their next round of matches. This information is usually posted in several places on the range, and also available online in the results system, but often shooters do not pay enough attention to this information or do not perceive this information when concentrating on their performance.

B. Paper cards

Currently, paper cards with shooter's names are used to determine where the next round of competition will take place. These are placed in front of the shooting line by the number indicating the shooting position. When the duel is over, the cards must be manually collected and moved to the appropriate location. The time between the end of the round and the start of the next is often very short, it is important that this move is done quickly and flawlessly.

Moving shooter's cards to the correct position on the range currently requires a dedicated group of people to handle the exchange and organisation of these tags. It often happens that this group is made up of different volunteers at each event, and it is therefore necessary to train and explain the principle to the new group of people each time. Initial uncertainty or lack of knowledge of the system and possible lack of coordination causes unnecessary time delays and technical complications during the eliminations.

II. Information system outline

To simplify the organization of archery competitions, especially the elimination part, I propose a system that could simplify and replace the work of several people. Important information will be shown completely on the display in front of the archer.

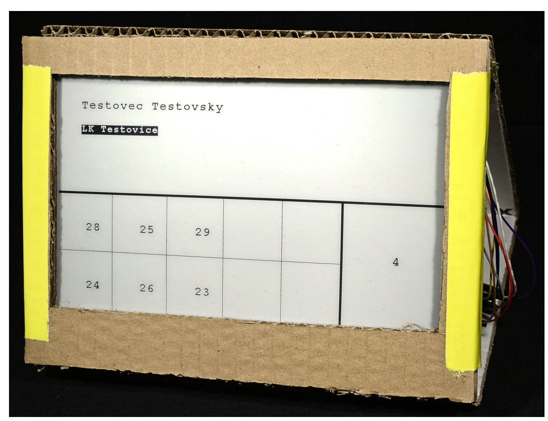

Fig. 1. First prototype

The system replaces paper cards with electronic display devices (EDD) and a central control unit (CCU), the computer. Each device will display the shooter's name and other information needed to navigate the shooting range. The data will be entered into the computer and transmitted to the display devices. Because the distance between the EDD's can exceed 100 m, the RS-485 serial standard was chosen for communication between the devices.

According to the official archery rules, the numbers indicating the shooting position must be 4 m away from the shooting line, so the EDD's must be placed at this distance. This imposes requirements on the size of the display, the size of the displayed text and the overall amount of information that will be readable at this distance.

III. Electronic display devices

Each EDD will consist of an electronic display (E-ink), a microcontroller (MCU) and an RS-485 converter.

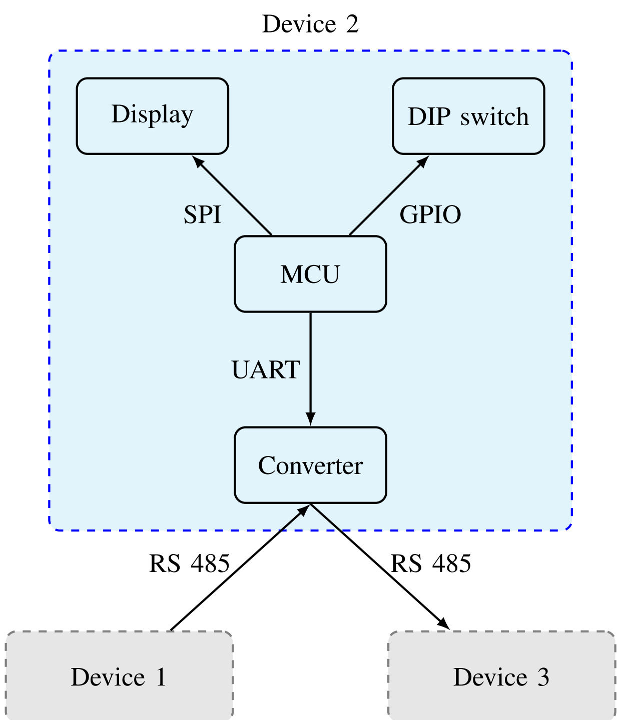

Fig. 2. Block diagram of the EDD

A. Microcontroller

The following solution was choosen. Raspberry Pi Pico microcontroller (MCU) has been selected to control the entire EDD. To operate the display, a memory is required in which the prepared image is stored before it is displayed. And also the font used occupies considerable space in the memory due to its size.

Especially because of these memory capacity requirements, it is not possible to use a simpler microcontroller such as the Arduino Nano. Increasing the memory capacity by using external memory, adds not only the cost but also the complexity of the whole system.

B. Display

Since archery is mainly an outdoor sport, it was necessary to find a display that would be easy to read even in direct sunlight. E-ink technology was chosen. It is a passive display, i.e. it does not need an internal light source to function, it reflects light from the surrounding environment.

This type of display also consumes electricity only the moment when the image on the display changes. Since the devices will be powered from a central unit this feature is not as important as if EDD's were wireless. The display of the display device consists of a black and white 7.5" display with a resolution of 800 x 480 pixels made by Waveshare company. The display driver communicates with the MCU over 4 wire SPI.

C. Device-to-device communication

The individual devices are connected in a daisy chain topology. As mentioned in the previous chapter, the RS-485 serial communication standard has been chosen. The control unit sends information about the shooters to each display unit individually. Each device has an address corresponding to the number of the target in front of which it is placed. The address of the device can be changed using the DIP switch on the back of the device.

There are also two RJ45 connectors on the rear panel for connecting the previous and next device. The connection itself is made using a UTP cable, where one pair is used for communication and the other two pairs are used to power the unit. The remaining pair will not be used in this system and is reserved for future improvements.

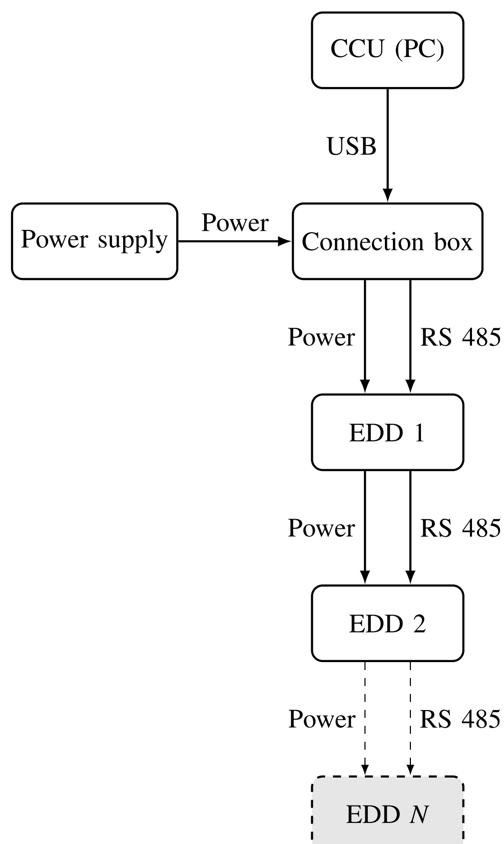

Fig. 3. Connections between devices

Data is sent from the control unit to each device individually, i.e. in unicast mode. After the transmission of the message, the display device will send an acknowledgement of receipt of the data to the control unit. CRC-16 is added to the transmitted data to ensure reliable transmission of information and to detect any errors that may occur. One round of elimination matches typically takes 20-30 minutes, so the status of the device must be monitored outside of the sequence of new data transmissions; the activity of the display device is checked approximately every 5 minutes. If the controller loses contact with one of the display devices, it makes several attempts to re-establish communication. If this fails, the user reports the disconnection of the device to the control program.

IV. The Central Control Unit

The connection between the EDD and the central control unit is made via a connection box that contains a USB to RS-485 converter and provides the connection of the display devices to the power supply. The computer is connected to the connection box via USB on one side, and the display devices are connected to the RS-485 bus via RJ45 connectors on the other side. Activity on the bus is indicated by an LED on the side of the connection box.

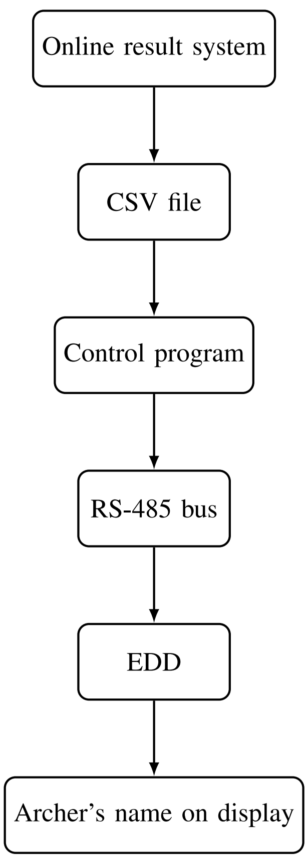

Fig. 4. Data flow from scoring application to shooter

The CCU consists of a computer running a control program. Once connected, the control program allows the user to monitor the status of the individual display devices, enter and send custom text to the displays (e.g., display of break end time, etc.). Last but not least, to confirm the sending of the next round to the display devices.

This CSV file is generated by the online results system, for display purposes it is necessary to edit the downloaded file to the desired format (change the order of the information columns) and remove redundant information. Before each round, the prepared data is presented to the user for review. Once the user has approved the data, the control unit sends the appropriate data to each of the EDDs.

In the background, the control program maintains communication with the individual display devices, monitoring their activity.

V. Future Improvements

It would be useful to further extend the control system to connect directly to the online scoring system from which it will automatically extract scorer data. This connection would allow to increasing the amount of information shown on the display of the device, for example the results of individual sets of matches.

For easier handling and preparation of the whole system, it is necessary to remove the wired connection between the devices and switch to wireless communication between all units.

VI. Conclusion

The proposed system of electronic display devices is an effective solution for simplifying the organization of archery competitions, especially in the elimination phase. By replacing paper cards with an automated electronic system, the transfer of information between organizers and archers will be significantly accelerated and made more accurate, eliminating potential errors and delays.

The use of E-ink technology ensures good display readability even in difficult lighting conditions, while the RS-485 communication bus enables reliable data transfer between the control unit and the individual displays. The system also provides the ability to monitor the connected devices and detect unit faults early.

Further development of the system should be directed towards integration with the online results system and the transition to wireless communication, thus increasing flexibility and facilitating installation and handling of the devices. These improvements could make the competition even more efficient and provide a better experience for shooters and organizers.

This system will minimize the initial delay caused by the printing and sorting of shooter's cards prior to the elimination rounds and will shorten the breaks between elimination rounds. In practice, this can save around 20 minutes of preparation time between the qualification and elimination part of competition, and around 15 minutes during the elimination rounds. It is also possible to use volunteers for other work on the range, approximately 2-6 people. The time and number of people will vary depending on the size of the event and the current operation of the eliminations in that event.

Testbed 4.0: The cooling system design

1st Michal Blažík
Dept. of Control and Instrumentation
Brno University of Technology
Brno, Czech Republic
256248@vutbr.cz

2nd Matěj Kantor
Dept. of Control and Instrumentation
Brno University of Technology
Brno, Czech Republic
247392@vutbr.cz

3rd Soňa Michalková
Dept. of Control and Instrumentation
Brno University of Technology
Brno, Czech Republic
sona.michalkova@vutbr.cz

4th Kryštof Wojnarowský
Dept. of Control and Instrumentation
Brno University of Technology
Brno, Czech Republic
krystof.wojnarowsky@vutbr.cz

5th Tomáš Janoušek
Dept. of Automation and Computer Science
Brno University of Technology
Brno, Czech Republic
239026@vutbr.cz

6th Jakub Arm
Dept. of Control and Instrumentation
Brno University of Technology
Brno, Czech Republic
jakub.arm@vut.cz

***Abstract*—The Testbed 4.0 project serves as a physical demonstrator of industrial production designed for testing advanced control strategies and algorithms. This paper focuses on the architecture of a cooling cell, one of the production units within the demonstrator. The cooling cell generates and distributes cold via a closed-loop liquid circuit to other units requiring thermal regulation. A mathematical model of the thermal system was developed in MATLAB/Simulink using measured and estimated parameters, including thermal capacities, flow rate, and heat transfer resistances. Several configurations were simulated to assess the impact of pipe insulation and geometry on temperature profiles. Results confirm that proper thermal design significantly improves cooling efficiency and the cooling aggregate is capable to meet thermal requirements of selected cells. The model will be further refined using measured data once the physical system is completed. In future work, the validated model will be integrated into a predictive control framework (MPC) and used to coordinate multiple cooling requests in a decentralized manner via Asset Administration Shell (AAS) interfaces, aligning with Industry 4.0 principles.**

***Index Terms*—Cooling system, testbed, industrial control, modeling, simulation**

I. Introduction

The Testbed 4.0 project is a modular and physical demonstrator of industrial production processes, designed to support the implementation and testing of advanced control and automation strategies. The demonstrator replicates a flexible manufacturing environment and consists of a robotic manipulator and several autonomous production cells, each equipped with a local control system based on PLC and HMI technologies. The cells are autonomous and are connected to the testbed table using a unified electrical interface connector that supplies 5 VDC, 12 VDC, and 24 VDC power.

Over the past years, production cells have been created that can be integrated into the demonstrator. There are cells for:

- glass warehouse - enables glass storing and dispatching,
- soda stream - creates a portion of soda stream,
- shaker - performs glass mixing,
- soft drinks - provides soft drinks,
- ice crusher - creates and distributes crushed ice,
- cooling - performs cooled medium.

Some of these production cells require thermal conditioning to maintain product quality and ensure correct operation. To provide cooling, a dedicated cooling cell was designed. It includes a recirculating chiller unit and a distribution system that delivers the cooling medium to the consumer cells through flexible piping.

To evaluate the behavior and performance of the updated cooling cell, a thermal model of the system could be modeled using MATLAB/Simulink. The model should incorporate physical parameters such as flow rate, pipe length and diameter, thermal capacitance, and insulation properties. Different design variants should be simulated to assess their impact on system response, energy retention, and the ability to reach target temperatures in consumer cells.

This simulation-based approach supports ongoing design refinement and serves as the basis for future implementation of predictive control strategies such as Model Predictive Control (MPC). Such strategies can enable anticipatory control based on demand forecasts and system dynamics. Although the system currently supports only a single consumer unit, the presented model prepares the foundation for scaling up the cold distribution system to multiple cells in a robust and coordinated manner.

The presented work contributes to the broader goals of Testbed 4.0, offering practical insight into simulation-driven design and energy-efficient process cooling in modular, Industry 4.0-ready manufacturing environments. One of the industrial production control algorithms for which Testbed 4.0 is designed is a distributed control method using AAS (Asset Administration Shell) technology. In this concept, each cell is wrapped in a virtual envelope created using AAS, which concentrates its data and allows it to communicate with other cells [1]

II. Related works

The first version of the cooling cell was created as part of the diploma thesis [2]. The cell was controlled using the Unipi

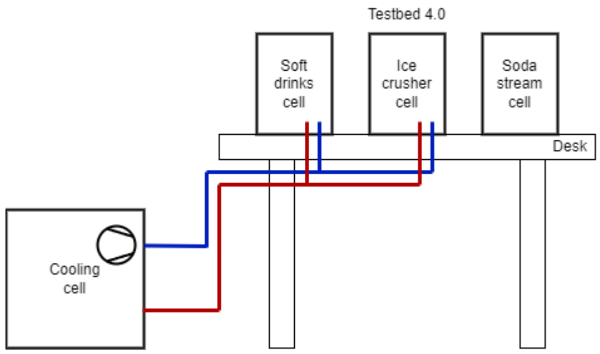

Fig. 1. The cooling system of the Testbed 4.0

control device. The created program contains its own model of the cooling apparatus, on the basis of which regulation takes place when a request arises to deliver a certain volume of cold for a defined time. The solution is close to the presented concept, but the communication interface and the method of communication between the participants are implemented using a non-standardized mechanism. The results of the work indicate that the time limitation of the regulation process to the required temperature may not be observed due to the limited performance of the available system components and its inertial nature. Another output is a model of the cooling cell based on the equations of physical heat transfer of the dominant components.

The work [3] brought about a change in the control system to a standard industrial method based on PLC (Siemens S7-1200). A digital model of the cell was also created in the 3D environment NX. An interesting conclusion of the work is also the finding of a significant negative effect of the pump on the temperature in the secondary circuit. However, the work does not discuss the possibilities of cell control.

In the article [4] a model of an exchanger station in the Matlab environment is presented, which is compared with the temperature course of a real sample. This work shows the possibility of creating a mathematical model of a cooling apparatus, or rather. an exchanger between the primary and secondary circuits, on which it is possible to simulate the course of the output temperature by setting proportional flow valves. Thanks to such a model, it is possible to predict the behavior of the cooling apparatus and train control algorithms for control. However, the model does not take into account the regulation.

The contribution [5] shows the creation of a model of an exchanger station with all its components in the OpenModelica environment. The simulations performed show the course of the outlet temperature depending on the settings of the flow valves in the primary and secondary circuits. The document also discusses the possibility of integrating this model as a simulator into the AAS and the properties of this grouping. However, the simulator no longer takes into account the regulation.

III. Architecture

The proposed architecture of the Testbed 4.0 cooling system is designed as a single-loop setup, in which the cooling unit supplies cold directly to one consumer cell using the closed primary circuit. The previous design based on secondary loop has been removed due to thermal inefficiencies and design complexity. The new design, therefore, provides more efficient cold delivery through a simplified pipeline.

Each production cell will eventually be equipped with an AAS that communicates standardized information about the cell's services, status, and requests. The cooling unit, encapsulated by an AAS, will serve as a future Service Provider (SP), while consumer cells will act as Service Requesters (SR). This interaction will be based on well-defined protocols and semantic models. The feature will provide a distributed-based control algorithms and implementation of MPC-based control algorithm for the cooling cell.

Further work will focus on expanding the physical system to support multiple concurrent cooling requests and enabling dynamic negotiation between cells based on cooling demand and aggregate capacity.

IV. Improvements of the Cooling Cell

The cooling cell, or rather the cooling apparatus, suffers from several ailments:

- insufficient cooling performance of the refrigeration unit,
- choice of medium in the secondary circuit,
- low heat exchanger effectiveness,
- unwanted heat input from the secondary circuit pump.

Problem No. 1 - Elimination of the Secondary Circuit One of the most significant design changes would be the complete removal of the secondary circuit. This decision is based on simulation results and experimental measurements that showed excessive heat gain and inefficient energy transfer. The secondary loop adds complexity and creates a thermal bottleneck, particularly due to the limitations of the transfer pump and heat exchanger. All simulations and models presented in this paper are based on a simplified, single-loop design, which significantly improves thermal responsiveness and control precision.

Problem No. 2- Medium Selection Originally, a brine solution was used in the secondary circuit as a compromise between health safety and low freezing point. However, its long-term use raised several concerns, including the risk of corrosion and leak formation due to the saline content. In contrast, the primary loop used ethylene glycol, which has better thermal properties and is more suitable for closed-loop operation. If the secondary circuit was removed, ethylene glycol would circulate directly to the consumer cells, reducing installation complexity and minimizing chemical degradation risks. Potential alternative candidates include propylene glycol, a low-concentration solution of ethyl alcohol, or glycerol, all of which have been deemed safe by the WHO [6].

-

Problem No. 3- Heat Exchanger Redesign The original spiral-type heat exchanger demonstrated low thermal efficiency due to limited surface area and poor flow characteristics. Simulation results suggested that optimizing the geometry and increasing the contact surface between the medium and the cooled area would improve performance. Additionally, improved thermal insulation around the exchanger was identified as a critical factor in reducing losses to the environment.

Problem No. 4-Pump Influence The secondary circuit pump is not thermally isolated from its motor, resulting in significant heat transfer to the coolant during operation. This issue is visualized in thermal imaging (Fig.2), where localized heating of the fluid path is clearly visible. Since the secondary circuit will be removed, this thermal interference no longer affects the system. In the current setup, a circulation pump with lower power and better thermal separation is used in the primary loop, further increasing overall system efficiency.

Problem No. 5- The updated model was used to simulate the behavior of the improved system, including various insulation qualities, pipe lengths, and heat exchanger configurations. These simulations confirmed that the current single-loop design significantly reduces the time required to reach target temperatures and increases the stability of thermal delivery. The simulation parameters were derived from available technical data and engineering assumptions and will be refined once measurement data becomes available. The simulation model also allows future implementation of predictive control (e.g., MPC) for optimized thermal management.

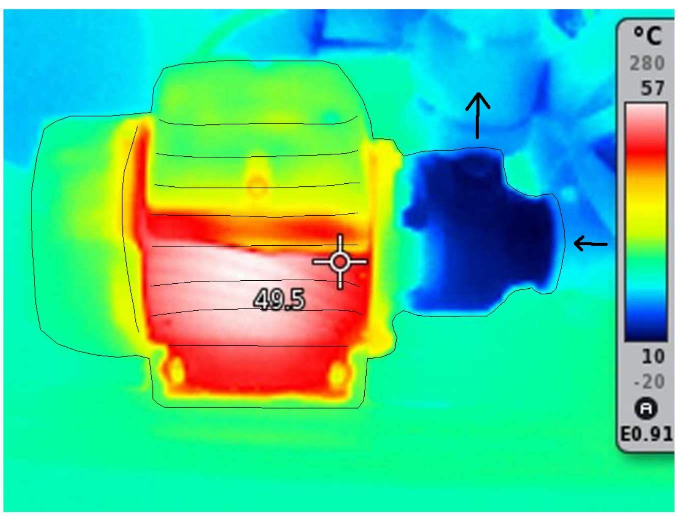

Fig. 2. The heating impact to the output temperature (pump contour is highlighted)

V. Simulations

The cooling processes were for each cell consuming the cooling energy modeled using the following equations and simulated for selected setups:

$$C_{\text{fluid}} \cdot \frac{dT_m}{dt} = \frac{T_c - T_m}{R_{\text{mc}}} + \frac{T_{\text{env}} - T_m}{R_{\text{env}}} + Q_m \cdot c \cdot (T_{\text{in}} - T_m) \quad (1)$$

and

$$C_{\text{cell}} \cdot \frac{dT_c}{dt} = \frac{T_m - T_c}{R_{\text{mc}}} + \frac{T_{\text{env}} - T_c}{R_{\text{env}}}, \quad (2)$$

where T_m is the temperature of the cooling medium [°C], T_c is the temperature of the cell [°C], C_{fluid} and C_{cell} are the thermal capacities of the fluid and the cell [J/K], R_{mc} is the thermal resistance between the medium and the cell [K/W], R_{env} is the thermal resistance to the environment [K/W], T_{in} is the temperature of the incoming coolant [°C], T_{env} is the ambient temperature [°C], Q_m is the mass flow rate of the fluid [kg/s], and c is the specific heat capacity of the fluid (propylene glycol) [J/(kg·K)].

Simulation parameters has been investigated or estimated as:

- Pipe length: 4 m (expected), 8 m (long variant)
- Inner diameter: 6 mm
- Insulation thickness: 5 mm or none
- Medium: 50% propylene glycol
- Initial temperature: 25°C
- Target temperatures: 5°C (Soft drink cell), -10°C (Ice crusher cell)
- Time span: 4 hours

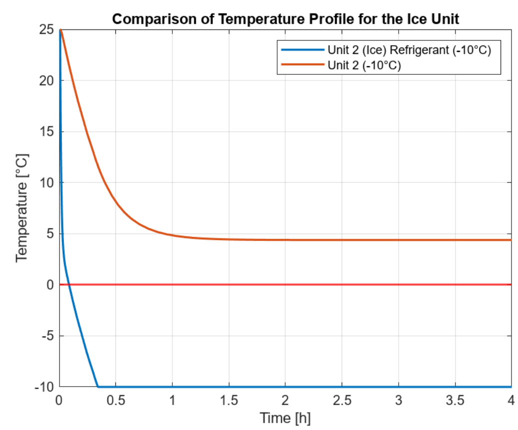

Fig. 3. The simulation of cooling process for Ice crusher cell - without isolation

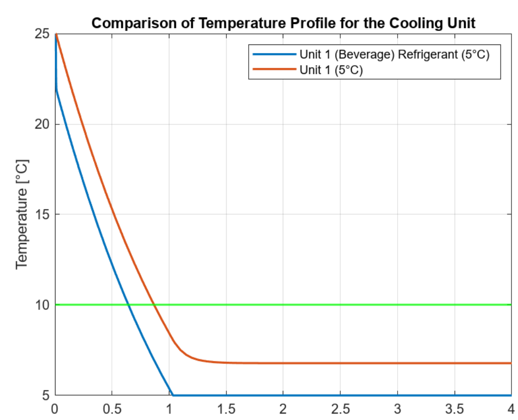

Fig. 4. The simulation of cooling process for Soft drink cell - without isolation

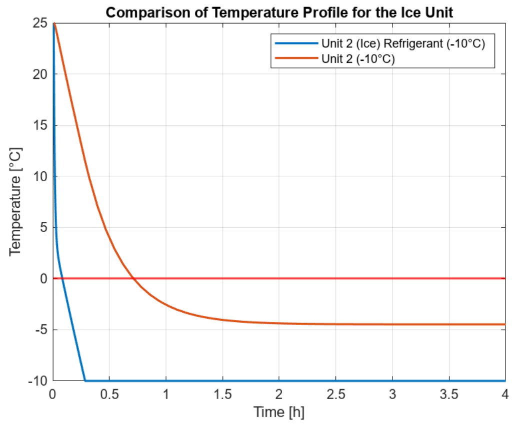

Fig. 5. The simulation of cooling process for Ice crusher cell - using isolation

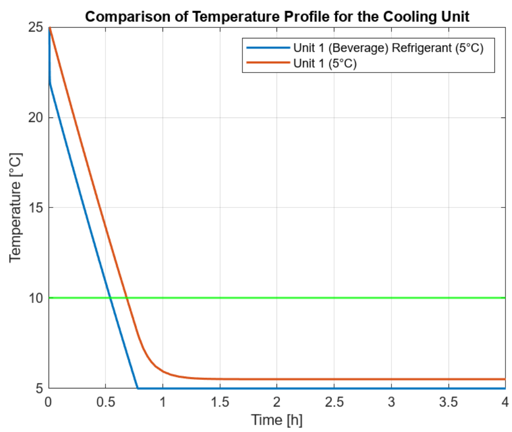

Fig. 6. The simulation of cooling process for Soft drink cell - using isolation

As can be seen from Figure 5 and 6, removing the insulation from both cells will significantly reduce the quality of cooling in both cells. Even though the cooling of the Soft drink cell would be fine if all other parameters were met, the Ice crusher cell would no longer be able to reach a temperature below 0 °C and the ice would start to heat up.

Further simulations shows that the cross-section of the pipe also plays a critical role in the dimensioning of the entire system. When it is increased, the flow capabilities of the medium improve, but the area of the pipe also increases, which increases losses. These losses are so large that they exceed the improving cooling capabilities of the medium. At the same time, it is necessary to make the entire line as short as possible, which again reduces the area of the pipe.

Conclusion

Due to the presence of several issues, it is necessary to find a solution capable of eliminating all the shortcomings of the current system without introducing any new problems. It is also essential to select a solution that does not compromise the system's regulatory capabilities. In an effort to preserve as many parts of the existing system as possible, it would be necessary to replace the system's insulation with a material that provides superior thermal insulation and to ensure that this insulation remains continuous and unbroken throughout the entire conduit. Simultaneously, it would be necessary to replace the pump of the secondary circuit with one of equivalent performance that incorporates thermal separation between the engine and pump sections. Moreover, replacing the cooling medium in the secondary circuit with a substance that is both food-grade compliant and exhibits enhanced thermal conductivity is imperative. A significant structural improvement would also be required for the heat exchanger, where substantial losses occur.

The presented approach enhancing the cooling performance rests in eliminating the secondary circuit, which is responsible for most of the issues. In this case, the only modification to the primary circuit would involve replacing the cooling medium with one of the presented substances. Although this change might reduce the thermal capacity of the primary circuit, it would overall improve the system's cooling performance as the simulations suggested.

Acknowledgment

The completion of this paper was made possible by the grant No. FEKT-S-23-8451 - "Research on advanced methods and technologies in cybernetics, robotics, artificial intelligence, automation and measurement" financially supported by the Internal science fund of Brno University of Technology.

References

[1] A. Belyaev and C. Diedrich, "Specification "demonstrator i4.0-language" v3.0," 07 2019. [Online]. Available: https://www.researchgate.net/publication/334429449_Specification_Demonstrator_I40-Language_v30

[2] O. Kupka, "Chladící jednotka pro projekt barman," in *Diplomová práce*. Brno, Česká republika: Vysoké učení technické v Brně, Fakulta elektrotechniky a komunikačních technologií, Ústav automatizace a měřicí techniky, 2020. [Online]. Available: https://www.vutbr.cz/studenti/zav-prace/detail/127022

[3] P. Cviček, "Chladicí systém pro demonstrátor i4.0," in *Bakalářská práce*. Brno, Česká republika: Vysoké učení technické v Brně, Fakulta elektrotechniky a komunikačních technologií, Ústav automatizace a měřicí techniky, 2022. [Online]. Available: https://www.vutbr.cz/studenti/zav-prace/detail/142251

[4] T. Benešl, M. Husák, O. Mihálik, R. Vancl, and Z. Bradáč, "Digital twin of heat exchange station," *IFAC-PapersOnLine*, vol. 58, no. 9, pp. 311–316, 2024, 18th IFAC Conference on Programmable Devices and Embedded Systems PDES 2024. [Online]. Available: https://www.sciencedirect.com/science/article/pii/S2405896324005044

[5] P. Černocký and J. Arm, "Integration of simulator into aas for heat transfer station," in *Proceedings I of the 30th Conference STUDENT EEICT 2024*, ser. 1. Brno, Česká republika: Brno University of Technology, Faculty of Electrical Engineering and Communication, 2024, pp. 117–119. [Online]. Available: https://www.eeict.cz/eeict_download/archiv/sborniky/EEICT_2024_sbornik_1.pdf

[6] W. H. Organization, "Evaluation of certain food additives and contaminants," in *WHO Technical Report Series No. 909*. Geneva, Switzerland, p. 105: World Health Organization, 2002.

Verification of buck converter efficency determination and its optimalization

1st Jiří Strnad
Brno University of Technology
Department of Microelectronics
Brno, Czech Republic
246941@vutbr.cz

2nd Ing. Pavel Tomíček
Brno University of Technology
Department of Microelectronics
Brno, Czech Republic
xtomic05@vut.cz

***Abstract*—This paper deals with verifying methods for determining the efficiency of buck convertor and their optimization. Various loss calculation methods are compared with simulations and experimental measurements on a realized prototype. The comparison is conducted for different values of switching frequency, duty cycle, output current, and input voltage. Based on the obtained results, the power supply is then optimized to increase its efficiency.**

***Index Terms*—switching frequency, duty, layout, buck converter**

I. Introduction

Buck converters are a crucial component of modern electronics, widely used in various applications that require efficient voltage regulation.

Unlike linear regulators, which regulate voltage at the cost of significant power losses in the form of heat, switched-mode power supplies offer considerably higher efficiency. [1] This improved efficiency leads to a more compact converter, as there is less need for cooling.

The successful implementation of a buck converter requires precise adjustment of key parameters such as duty cycle, switching frequency, and other factors. Additionally, proper placement of components on the PCB is essential to minimize losses and reduce electromagnetic interference (EMI).

Several theoretical models and equations exist for calculating losses in switched-mode power supplies, taking into account parameters such as switching frequency, input voltage, output current, and duty cycle. The objective of this study is to analyze and compare these models and their impact on converter efficiency, with a focus on simulations and prototype measurements.

II. Design of buck converters and Control Unit

A. Designs of buck convertor

For testing purposes, two main types of buck converters, A and B, were created, where the diode was replaced with transistor, making them synchronous buck converters.

Buck converter A uses two silicon N-channel MOSFETs, specifically the SIR696DP for the high-side MOSFET and the SI7336ADP for the low-side MOSFET. These transistors are controlled by the LM5109BMA gate driver. Additionally, buck converter A uses a 10 µH shielded inductor, identified as 7447709100.

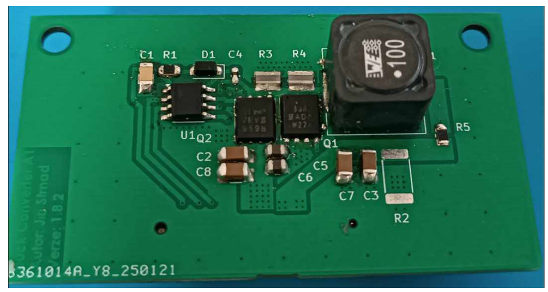

Fig. 1: PCB of buck convertor A

To achieve even greater efficiency, the silicon transistors in buck converter B were replaced with GaN FETs, specifically the EPC2111. These transistors are controlled by the LT8418ACBZ-R7 gate driver, selected along with the appropriate circuit configuration. Buck converter B has several different variants, which differ only in the inductor used. All inductors are shielded and have an inductance of 10 µH. For comparison, one of the variants uses the same inductor as buck converter A, 7447709100, while the remaining variants use the following inductors: 7443550101, 7843321000, XGL1010-103, XGL1313-103 and B82477R4103M100.

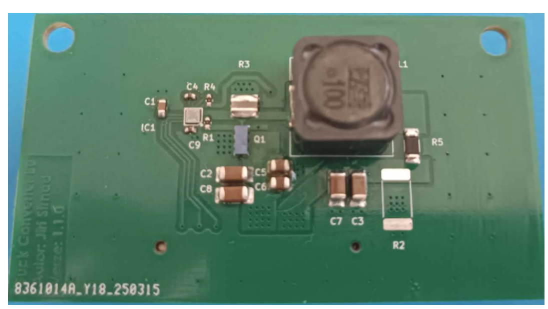

Fig. 2: PCB of buck convertor B with GaN transistors

For both configurations, the output stage includes two 47µF ceramic capacitors, while the input stage consists of two 47µF capacitors and two 22µF capacitors.

Regarding the layout, emphasis was placed on the principles of proper design, particularly on placing the capacitors as close to the input as possible, maximize the width of the conductive paths, except for the path leading to the inductor, which should only have an area sufficient for current conduction. [2]

Another principle was to create the smallest possible current loops to minimize EMI. It was also very important to ensure an adequate number of vias near components that generate significant heat for better heat dissipation. The vias also serve to provide the most efficient return path for current.

B. Control board

The control board is designed for managing the high-side and low-side transistors of the buck converter, powering the gate driver and measuring input and output data.

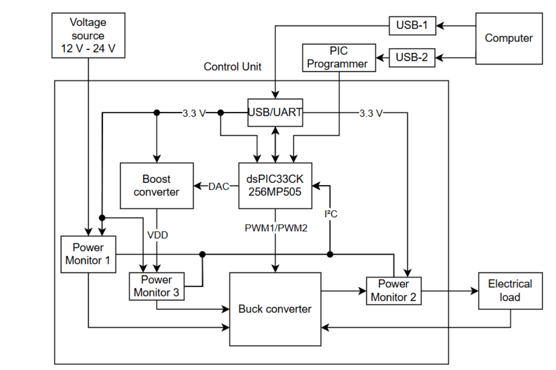

Fig. 3: Diagram of Control unit

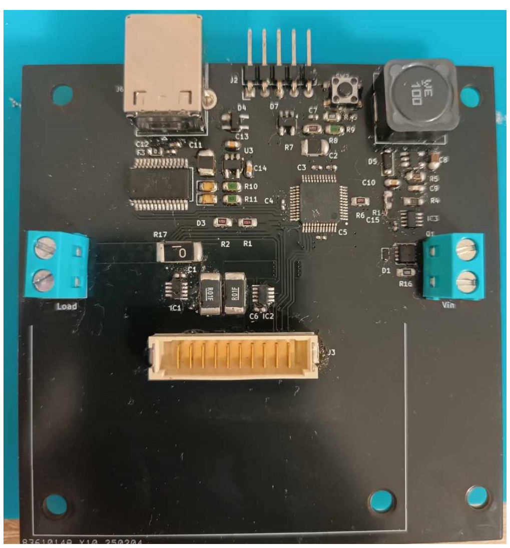

Fig. 4: PCB of Control unit

The generation of complementary signals for buck convertor transistors is handled by the dsPIC33CK256MP505 microcontroller, which provides a 3.3 V PWM signal, enabling highly precise adjustment of frequency, duty cycle, and dead time. [3]

The control board also supports an adjustable power supply via the TPS61040 boost converter, which is controlled by the DAC output of the dsPIC33CK256MP505. [4] TPS61040 supplies varying gate drivers for different types of buck converters.

Input and output measurements of the buck converter are performed using two shunt resistors connected to the INA236 power monitor. The voltage supplied to the gate driver of the buck converter is also measured by the INA236. This monitor is interfaced with the dsPIC33CK256MP505 via I²C and provides information on voltage drop across the shunt, bus voltage, current, and power. [5]

To ensure proper data processing, the microcontroller is connected to a UART/USB converter FT232RL, which transmits the acquired data to a computer. [6]

III. Optimizing of Buck Convertor

In designing the buck converter schematic and selecting components, generally known information was relied upon to ensure that the first version of the board would achieve relatively high efficiency. The first priority was to eliminate the rectifier diode, so a synchronous design was chosen. Although this slightly complicates the design, it significantly increases efficiency. [7]

Another important factor was the selection of capacitors, all of which are ceramic. This choice reduces dielectric losses, temperature dependence, and allows for a more compact board with a better layout. For the inductor, it was crucial that it be shielded to minimize EMI. These steps led to the creation of the first schematic of buck converter A. However, to achieve even better results, further modifications were necessary, including replacing silicon transistors with GaN transistors, which have lower switching losses, thereby creating buck converter B. The final improvement was the selection of five inductors, which should have lower losses, further enhancing the overall efficiency of the system.

To further improve efficiency, it is essential to select an appropriate dead time. For this purpose, LTSpice simulations were used to determine the total dead time value that provides the highest efficiency. For buck converter A, the optimal total dead time is around 140 ns, while for buck converter B, it is around 10 ns. However, a slightly higher value can be chosen to improve the margin before the transistors suffer shoot-through.

After measuring the dependence of the dead time in buck converter B, we can observe that the highest efficiency occurs with a total dead time ranging from 0 ns to 10 ns, which aligns with the simulation results. Minor inaccuracies were attributed to the effects of temperature.

For buck converter A, the optimal total dead time determined from measurements was 30 ns, which represents significant difference compared to the simulation.

Another way to increase the efficiency of the buck converter is by optimizing the switching frequency. While higher frequencies lead to greater switching losses, excessively low frequencies result in higher ripple current. Therefore, the frequency selection must align with our requirements and the chosen inductor. [8]

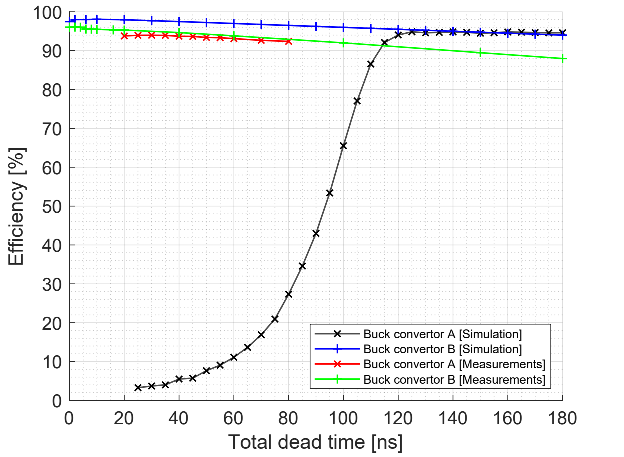

Fig. 5: Optimal dead time for buck convertors A and B for Uin = 12 V, Uout = 4 V, Iout = 1 A and fs = 500 kHz.

From the simulations, it was determined that the optimal maximum frequency is around 100 kHz, but at this value, the output ripple is still relatively high. Therefore, higher frequencies of 300 kHz and 500 kHz were selected to achieve a better balance between efficiency and output voltage quality.

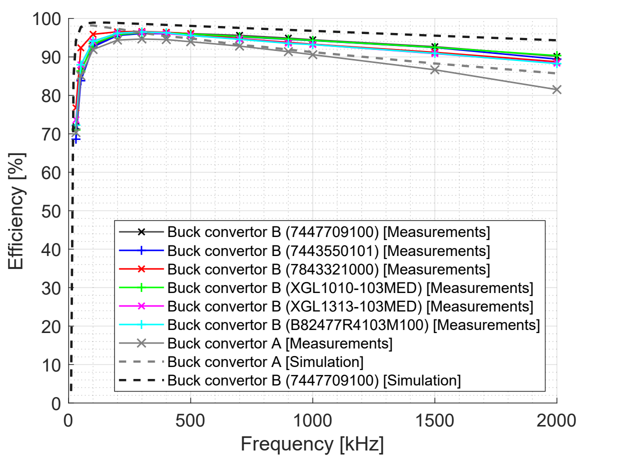

Fig. 6: The efficiency of simulated and real buck converters dependent on the switching frequency for Uin = 12 V, Uout = 4 V, Iout = 1 A.

IV. Determination of Efficiency and Comparison of Several Methods

Fig. 6 shows that in the simulation, the efficiency of the buck converter increases with frequency but begins to decline after 100 kHz. This is because, at lower frequencies, there is significant ripple current, and the circuit gradually behaves as if the inductor were not present. However, as the frequency increases, current ripple decreases, but switching losses rise, leading to a decline in efficiency at higher frequencies.

In this figure, it can also be observed that, unlike the simulation, the measured values show the highest efficiency of the buck converter at around 300 kHz.

Finally, it can be observed that the differences in the efficiency of buck converter B when using different inductors, depending on frequency, are primarily caused by core losses in the inductor. When the efficiency of buck converters A and B is compared, it becomes evident that the difference between them increases with rising frequency. This can be attributed to the poorer switching characteristics of the transistors in buck converter A compared to those in buck converter B.

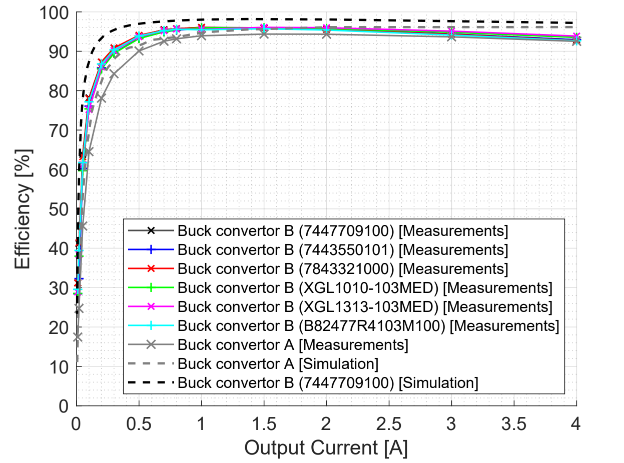

Fig. 7: The efficiency of simulated and real buck converters dependent on the output current for Uin = 12 V, Uout = 4 V and fs = 500 kHz.

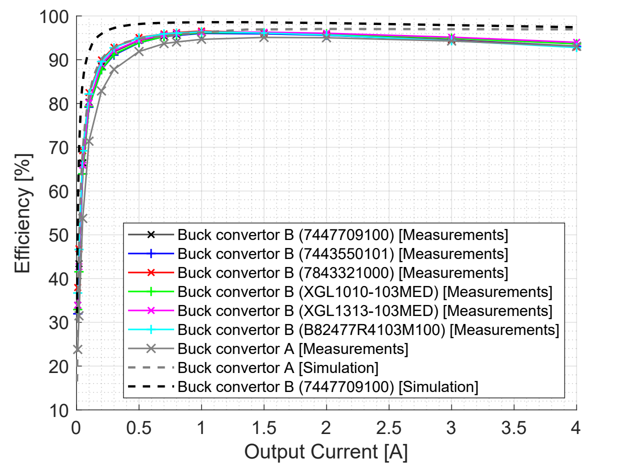

Fig. 8: The efficiency of simulated and real buck converters dependent on the output current for Uin = 12 V, Uout = 4 V and fs = 300 kHz

Fig. 7 and Fig. 8 shows that, in the simulation, as the current increases, the efficiency of buck converter A also increases. This is because losses that are independent of current, such as switching losses or gate driver losses, become less significant compared to current-dependent losses, such as conduction losses. This phenomenon occurs because the simulated model does not account for PCB conductive paths, which results in conduction losses having a less noticeable impact on the graph. To observe a decrease in efficiency, the current would need to be stepped to much higher values.

It can also be seen from the figures that the measured results are relatively similar to the simulation results. The difference can be explained by the properties of the PCB, temperature variations, and other factors present in the real environment.

When these two figures are compared, a slight increase in efficiency at 300 kHz can be noticed, which can be attributed to the reduction in switching losses due to the lower frequency.

Next, in Fig. 7 and Fig. 8, it can be observed that buck converter B is clearly more efficient than buck converter A. Regarding the inductors, it can be seen that some exhibit higher efficiency at lower currents, while others perform better at higher currents. This behavior can be explained by the characteristics of the inductors, such as series resistance and core losses. In general, higher efficiency at elevated current levels is achieved by inductors with lower resistance.

Efficiency [%]	**Buck converter A**	**Buck converter B**
Uin = 12 V, Uout = 4 V, Iout = 1 A, fs = 500 kHz		
Simulation	94,83	98,05
ROHM efficiency equations [9]	88,13	97,90
TI efficiency equations [10]	81,72	97,89
Measurements	93,94	96,06
Uin = 12 V, Uout = 4 V, Iout = 1 A, fs = 300 kHz		
Simulation	96,29	98,57
ROHM efficiency equations [9]	92,18	98,27
TI efficiency equations [10]	87,23	98,30
Measurements	94,66	96,29
Uin = 12 V, Uout = 4 V, Iout = 4 A, fs = 500 kHz		
Simulation	96,14	97,21
ROHM efficiency equations [9]	92,01	95,18
TI efficiency equations [10]	92,28	97,14
Measurements	92,52	92,92

TABLE I: Comparison of methods for determining efficiency

Next, we can see a table that compares the obtained efficiency from theoretical equations, simulation, and measurements. It is noticeable that in the case of buck converter B, the values are relatively similar. The differences can again be attributed to PCB characteristics, especially the resistance of the conductive traces, whose influence increases with current. However, in the case of buck converter A, the simulation and measurements differ significantly from the calculations based on the ROHM or Texas Instruments (TI) buck converter efficiency equations. Some values not provided by the manufacturers were replaced with suitable parameters derived from theoretical assumptions or simulation results. Additionally, since the equation for calculating core loss in the inductor, as described in the Texas Instruments application report, requires many parameters that are typically unavailable, the AC loss calculator from Würth Elektronik was used instead. [9] [10]

V. Conclusion

As part of this work, the design and production of the Control unit board were completed. This unit is capable of powering and controlling the gate driver of the buck converter. It also allows for precise measurement of power, bus voltage, shunt voltage, and current, enabling fast and accurate evaluation of the efficiency of the buck converters.

Additionally, buck converter boards were designed and built for testing, featuring an efficient layout. Buck converter A uses Si MOSFETs, while buck converter B uses GaN FETs. Several variations of buck converter B were also created, differing in the type of inductors used for further optimization. Optimization was also performed on the total dead time to achieve higher efficiency. In the case of converter B, the difference between the simulation and measurements is negligible, while for converter A, the difference reaches up to 110 ns.

Simulations were conducted to estimate the efficiency and other characteristics of the boards. The measurement results are comparable to the simulation results, with the simulations showing higher values due to the neglect of certain PCB characteristics and the absence of environmental factors, such as temperature.

Regarding the calculations, a significant difference can be observed in certain cases of buck converter A, which suggests that, in some situations, theoretical formulas used for calculating efficiency may not fully correspond to real-world results.

References

[1] *Buck converter — How it works, Application and Advantages*, 2022. Online. Electricity - Magnetism. Available from: https://www.electricity-magnetism.org/buck-converter-2/. [cit. 2025-03-05].

[2] ROHM SEMICONDUCTOR, 2024. PCB Layout Techniques of Buck Converter. Online. Available from: https://fscdn.rohm.com/en/products/databook/applinote/ic/power/switching_regulator/converter_pcb_layout_appli-e.pdf. [cit. 2025-03-05].

[3] MICROCHIP TECHNOLOGY, 2017. DsPIC33CK256MP508 Family Data Sheet DS70005349. Online. 2022. Available from: https://ww1.microchip.com/downloads/aemDocuments/documents/MCU16/ProductDocuments/DataSheets/dsPIC33CK256MP508-Family-Data-Sheet-DS70005349.pdf. [cit. 2025-03-05].

[4] TEXAS INSTRUMENTS, 2002. *TPS6104x Low-Power DC-DC Boost Converter in SOT-23 and WSON Packages*. Online. 2023. Available from: https://www.ti.com/lit/gpn/tps61040. [cit. 2025-03-15].

[5] TEXAS INSTRUMENTS, 2021. *INA236 48-V, 16-Bit, Ultra-Precise, Current, Voltage, and Power Monitor With an I2C Interface*. Online. 2023. Available from: https://www.ti.com/lit/gpn/INA236. [cit. 2025-03-06].

[6] FTDI CHIP, 2020. *Future Technology Devices International Ltd. FT232R USB UART IC*. Online. Available from: https://ftdichip.com/wp-content/uploads/2020/08/DS_FT232R.pdf. [cit. 2025-03-15].

[7] JAIN, Ajith. Synchronous vs. Aynchronous Buck Regulators. Online. Semtech Corporation. Available from: https://www.digikey.com/Site/Global/Layouts/DownloadPdf.ashx?pdfUrl=F3F58EFCE5E5498A815A2EF97F4645AA. [cit. 2025-03-05].

[8] HAUKE, Brigitte. Basic Calculation of a Buck Converter's Power Stage. Online. Available from: https://www.ti.com/lit/an/slva477b/slva477b.pdf?ts=1731735891920n. [cit. 2025-03-15].

[9] ROHM SEMICONDUCTOR, 2016. *Efficiency of Buck Converter*. Online. 2022. Available from: https://fscdn.rohm.com/en/products/databook/applinote/ic/power/switching_regulator/buck_converter_efficiency_app-e.pdf. [cit. 2025-03-15].

[10] HE, Xing; LI, Daniel a ZHANG, Vincent, 2020. An Accurate Approach for Calculating the Efficiency of a Synchronous Buck Converter Using the MOSFET Plateau Voltage. Online. Available from: https://www.ti.com/lit/an/slvaeq9/slvaeq9.pdf?ts=1732520837372&ref_url=https%253A%252F%252Fwww.google.com%252F. [cit. 2025-04-4].

Thermal Model of a Smart Home

Orlova Valeriia
Department of Control and Instrumentation
Faculty of Electrical Engineering and Communication
Brno University of Technology
Brno, Czech Republic
247590@vutbr.cz

***Abstract*—This paper focuses on developing a comprehensive thermal model of a selected smart home. Thermal behavior is derived from the 3D conceptual models of the house's interior created in SolidWorks based on personal knowledge and available blueprints. Utilizing the information about individual structural elements, their dimensions, materials, and thermal properties available in the 3D models, a thermal model of the building is developed in MATLAB Simulink using the Simscape Thermal Models. The thermal model is tested under diverse conditions through a 24-hour operation simulation using the external temperature and irradiation data from geographic information systems.**

***Index Terms*—Airflow, conjugate heat transfer, heat transfer, home automation, HVAC systems, smart home, thermal behavior simulation, thermal comfort, thermal energy storage.**

I. Introduction

Since the right home temperature is critical for a person's comfort and health, modern buildings often feature air conditioning and heating systems to provide the ideal environment. Wall thickness, type of roofing, and room layout then influence the indoor microclimate and directly determine the temperature conditions inside. Additionally, improper handling of heating, such as turning the heating system on or off at inappropriate times or improper air conditioning temperature settings, can make maintaining thermal comfort challenging and lead to various health problems. As mentioned in [1], high temperatures can cause excessive fatigue and loss of concentration, while low temperatures decrease nervous system activity, which can cause drowsiness. As a result, adequate temperature control is key to ensuring optimum thermal comfort in smart homes, and such control should consider factors related to outdoor weather and building thermal properties.

Black-box, White-box, and Grey-box models are often used to simulate ongoing thermal processes. These models differ in the amount of information about the system. When using a black-box model, the amount of system details is limited, meaning certain factors are not considered. For instance, in [2], the authors simulated the air temperature in a laboratory using a simplified model, excluding ventilation, windows, and doors. In contrast to the black-box model, the white-box approach incorporates a detailed description of the internal structure and dynamics of the system, which requires in-depth knowledge of the system being modeled. The study [3] presents the development of a white-box model for simulating the temperature in a hotel room with an integrated heating and cooling system. The research was focused on the influence of hotel personnel and guests, who can control windows, heating, and cooling. After calibration, the authors optimized the model parameters, allowing the model to predict the room temperature with a mean square error of 0.79°C. In some cases, white-box and black-box approaches are combined in gray-box models. Similarly to the black-box approach, this model avoids large amounts of data while achieving better efficiency than the black-box model. The article [4] presents a water-cooling model aimed at optimizing the cooling system with individually designed and fine-tuned coolers. The model is based on a mathematical description following physical principles, but parameters are estimated from the measured data, which is characteristic of gray-box models.

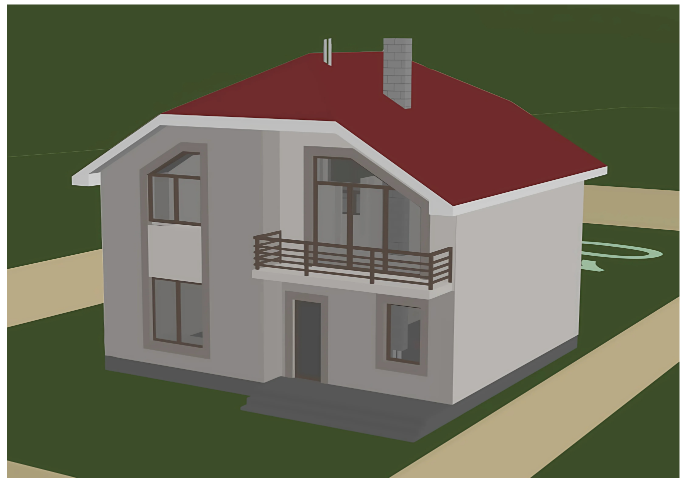

Fig. 1. Frontal view of the modeled smart home.

This paper adopts the white-box approach, chosen for our in-depth knowledge of the building's design and materials, which allowed us to use physical principles and parameters to simulate the influence of outdoor temperature, heating systems, and other factors on heat transfer within the house.

II. Selected building

The modeled building contains two floors and an attic. An image displaying the front view of the building is depicted in Fig. 1. The main entrance to the building is located on the first floor. Near the main entrance is the boiler room, which contains the primary heat source for the heating system - the boiler. This room is positioned to allow efficient heat

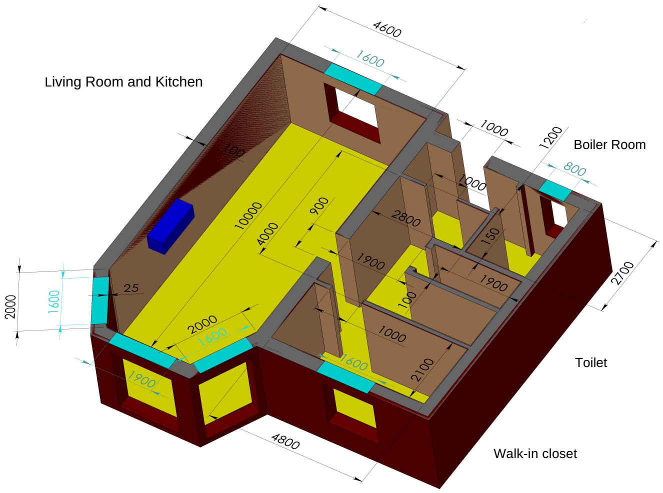

Fig. 2. 3D model of the 1st floor.

Fig. 3. 3D model of the 2nd floor.

distribution through the floor heating. Most of the first floor then comprises the kitchen, which connects to the living room. An essential factor in the distribution of cool air is the free passage into the corridor, which allows its natural circulation to other parts of the lower floor. A glass door leading to a small garden at the back of the living room is a significant part of the building's natural ventilation system; this door provides a direct path for heat transfer to the interior in summer. Conversely, heat loss through the glass doors non-negligibly decreases the indoor temperature in the winter. The illustration in Fig. 2 documents the layout of the rooms on the first floor in a more detailed way.

The second floor of the house serves primarily as a sleeping area. It contains three bedrooms and a bathroom with a separate toilet. Fig. 3 depicts the layout of the upper floor. Every room on this floor, except the toilet, features a window, and the bedrooms on the staircase's left also have air conditioning. The bedroom marked as Bedroom 3 in Fig. 3 has a large window across the entire wall, including a glazed entrance to an open, uninsulated balcony. This glazed wall significantly affects the room's temperature flows, similar to the glass living room door leading to the garden on the first floor.

The construction of the house consists of two main parts: the load-bearing structure, which includes the foundations, walls, ceilings, staircase, and roof, and the supplementary structure, which comprises partitions, suspended ceilings, floors, windows, and doors. The structural layout is of paramount importance in modeling the thermal behavior of the building. Therefore, a detailed overview has been produced, which thoroughly describes the structural elements of rooms and includes the specification of their area, thickness, and materials used. A sample section of the summary of structural elements is presented in Table I, where part of the hallway on the 1st floor is documented.

As indicated in Table I, the building has a combined insulation system for walls, employing a thicker layer of mineral wool (with thermal conductivity of 0.05 W/(m·K), heat capacity of 980 J/(kg·K), and density of 150 kg/m^3)

TABLE I
STRUCTURE AND MATERIALS FOR MODELED ROOMS

Modeled Room	Structural Component	Adjacent Room	S [m^2]	D [m]	Material
Hallway 1st Floor	East W - Structure	Toilet 1st Floor	1.500	0.150	Ytong P2-500
		Boiler Room	3.780	0.150	Ytong P2-500
	East W - Insulation	Toilet 1st Floor	1.500	0.050	Drywall
		Boiler Room	3.780	0.050	Drywall
	West W - Structure	Living Room	2.100	0.300	Ytong P2-400
	West W - Insulation	Living Room	2.100	0.100	Mineral Wool
				0.025	Drywall

as the outer layer and a thinner layer of plasterboard (with thermal conductivity of 0.25 W/(m·K), heat capacity of 900 J/(kg·K), and density of 750 kg/m^3) as the inner layer. This insulation configuration is replicated on the second floor. Ytong is then used for the building's foundation structure. Its thermal conductivity ranges from 0,08 W/(m·K) for external walls to 0,17 W/(m·K) for internal walls. In addition to the thermal conductivity, Ytong's heat capacity corresponds to 1000 J/(kg·K), and its density varies based on its type (P2-400 corresponds to the density of 400 kg/m^3 and P2-500 aligns with 500 kg/m^3).

III. THERMAL MODEL

Based on the overview of construction elements dimensions and materials prepared together with the 3D models, we formulated the thermal model in MATLAB Simulink using the Simscape extension. The Simscape allows creating complex component models based on physical interconnections and provides specific blocks for different physical domains, such as heat [5]. We utilized the "Thermal Models" library, which provides tools such as thermal energy sources, sensors, and other specialized components. Elements from the "Thermal

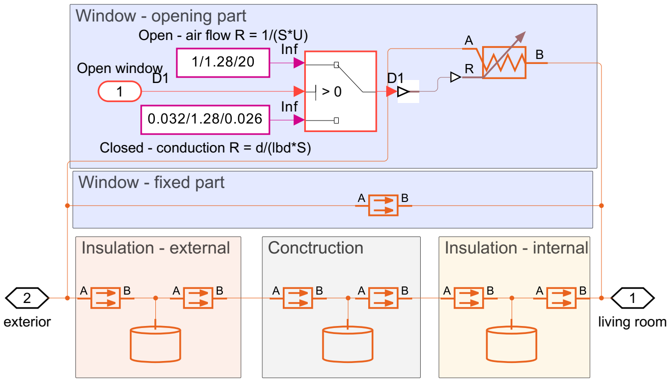

Fig. 4. Thermal model of an exterior building wall.

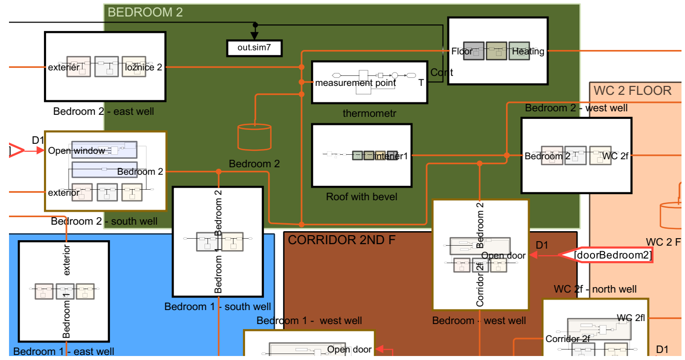

Fig. 5. Thermal model of a particular room.

Models" library represent individual structural parts of the building and their physical properties.

The fundamental part of the produced thermal model is a wall, which is realized as a subsystem containing a combination of the "Conductive heat transfer" and "Thermal mass" blocks. The wall model considers each layer separately, taking into account its specific thickness, thermal conductivity, heat capacity, and density. Each layer represents a basic thermal inertia element with two thermal resistances R_a and R_b and one thermal capacitance C, whose behavior can be described by a differential equation derived from the energy balance:

$$C\frac{dT_C}{dt} = \frac{T_A - T_C}{R_a} - \frac{T_C - T_B}{R_b} \tag{1}$$

where T_A and T_B represent the temperatures at the boundary nodes of the layer (e.g., the temperatures at the surfaces of adjacent wall layers), and T_C denotes the temperature of the thermal mass located between the resistances, representing the internal energy storage of the layer. If the wall includes windows or doors, we represent these elements in the model as extra branches connected in parallel to the wall layers. To capture the open and closed states of doors and windows, we used the "Variable Thermal Resistance" blocks. In the closed state, the heat is transferred through conduction, assuming the exact material of a particular door or window. Conversely, in the open state, the heat is transferred through direct airflow (convection). The status of each window or door can be individually controlled. Fig. 4 depicts an exampled wall model, which includes three thermal mass blocks, requiring three initial conditions to be provided. The initial conditions are computed based on initial temperatures at both sides of the modeled wall by calculating the temperature distribution over the individual thermal resistances in a steady state, employing Kirchhoff's laws. Subsequently, the individual smart home rooms are assembled from modeled walls and "Thermal Mass" blocks representing the air in the room. An example of a room model is visualized in Fig. 5. Except for the walls, separate rooms are also connected through the floor heating system. Furthermore, the irradiation incident on the roof affects the rooms on the second floor. The roof structure is divided into two parts, one directly connected to the individual rooms, where, as with the walls, the different layers of material are considered. The other part corresponds to the attic - the airy space between the ceiling of the second floor and the roof itself, which is created as a separate room. Both the parts are connected with the final layer of the roof affected by the irradiation. We modeled this layer using the "Radiative Heat Transfer" block, which is connected to the "Controlled Heat Flow Source" capturing the irradiation data obtained from the Photovoltaic Geographic Information System (PGIS) [6]. This database extracted the irradiation intensity and temperature data from one day in December in the location where the actual building is situated.

IV. Thermal Behavior Simulation

The simulations of the developed model were conducted over 24 hours, with the external air temperature varying around -7 °C. The simulations were performed under different conditions, and the outcomes are presented in Fig. **??** below.

In the first scenario, all windows and doors were closed, and the heating system was turned off. The results showed that the most significant temperature drop occurred on the first floor in the living room due to the glass doors and windows, which allow more substantial heat transfer. Only a minor temperature decrease was observed in the corridor, as none of its walls are directly exposed to the external environment. On the second floor, the temperature drop was approximately uniform across all rooms and was less pronounced overall. This can be attributed to the effect of solar heating on the roof and similar thermal insulation properties in the rooms.

In the second scenario, all doors were closed, and the heating system was activated. The heating power supplied was set to 12 kW for the first floor and 22 kW for the second floor. These values were chosen to restore the indoor temperature to approximately the same level as in the simulation's initial conditions.

In the third scenario, the interior doors were closed, but the main entrance door leading outside was opened. This resulted in a significant temperature drop in the hallway and a less pronounced decrease in other rooms. On the second floor, the results remained essentially unchanged.

In the final simulation, the interior doors were opened, which caused minor temperature redistributions on the first floor. For instance, the temperature in the corridor dropped

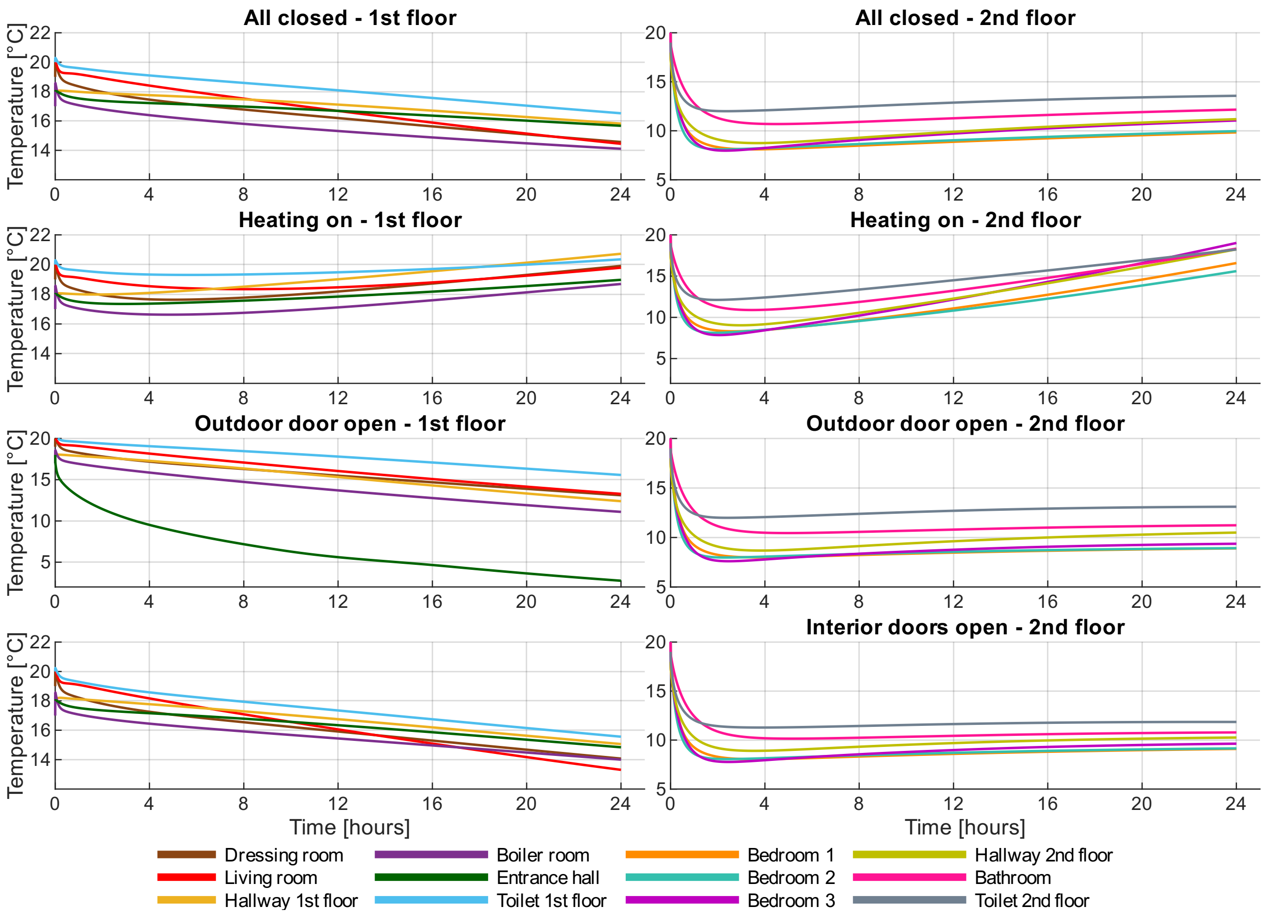

Fig. 6. Thermal behavior simulated under various conditions.

more significantly while the cooling process in the boiler room slowed down. No notable temperature changes were observed on the second floor.

V. Conclusion

In this paper, a comprehensive white-box model has been developed to describe in detail the physical reality of heating-related processes in a smart home. The model includes the representation of heating and air conditioning systems, as well as external influences such as ambient air temperature and the influence of solar heating on the roof. Its purpose is to capture the fundamental thermodynamic interactions within the building envelope and between internal zones. This enables the identification of variables with a dominant influence on the system's overall energy behavior. The subsequent research will focus on reducing the model's complexity by approximating it with lower-order descriptions and designing model-based control strategies.

The thermal model was simulated during various scenarios, including opening and closing doors and turning the heating on and off. The first floor exhibited realistic temperature behavior consistent with expected physical processes. The second floor's temperature changes due to door opening and closing were insignificant. This may be attributed to the fact that, in actual conditions, warm air rises, whereas the model lacks natural convection mechanisms, such as air circulation through the staircase opening.

Acknowledgment

The author thanks Mr. Lukáš Zezula (Brno University of Technology) for his expert guidance, valuable consultations, and constructive feedback throughout the research.

References

[1] Kotek, Lubos and Travnicek, Petr and Babinec, Frantisek and Junga, Petr and Mukhametzianova, Leisan. Impact of microclimate conditions on the control room personnel - case study. MM Science Journal. 2015, pp. 682-685. DOI: 10.17973/MMSJ.2015.10.201535.

[2] HUSSEIN, Mohd Faisal et al. Black Box Modelling and Simulating the Dynamic Indoor Air Temperature of a Laboratory Using the Continuous-Time Transfer Function Model. 2020. DOI: 10.2991/aer.k.201229.021.

[3] PALAIC, Darko and ŠTAJDUHAR, Ivan and LJUBIC, Sandi and WOLF, Igor. Development, Calibration, and Validation of a Simulation Model for Indoor Temperature Prediction and HVAC System Fault Detection. Buildings. 2023, Vol. 13. DOI: 10.3390/buildings13061388.

[4] PICÓN-NÚNEZ, Martín, POLLEY, Graham T., CANIZALEZ-DÁVALOS, Lázaro, MEDINA-FLORES, José Martín. Short cut performance method for the design of flexible cooling systems. Energy. 2011, Vol. 36, Issue 8, pp. 4646-4653. ISSN 0360-5442.

[5] The MathWorks, Inc. Simscape™ Reference. The MathWorks, Inc. Available from: https://www.mathworks.com/help/pdf_doc/simscape/simscape_ref.pdf [cit. 2024-12-28].

[6] European Commission, Joint Research Centre. Photovoltaic Geographical Information System (PVGIS). European Commission, Joint Research Centre. [cit. 2025-01-03]. Available from:https://re.jrc.ec.europa.eu/pvg_tools/en/#MR

Soil water flow modeling for irrigation control

1st Ekaterina Gerasina
Dept. of Control and Instrumentation
Brno University of Technology
Brno, Czech Republic
247372@vutbr.cz

***Abstract*—This paper focuses on developing a mathematical model for intelligent irrigation control. The model is based on the Richards equation and extended with Gardner's permeability model with the Feddes concept of root water uptake by plants. It integrates evapotranspiration, soil-water-plant interactions, water infiltration into the soil, and drainage. The model is formulated as a partial differential equation describing soil moisture dynamics and is transformed into a state-space representation for analysis and control design. Simulations illustrate the model's behavior under varying conditions, demonstrating its potential for irrigation control.**

***Index Terms*—control system model, hydraulic conductivity, irrigation, mathematical modeling, partial differential equations, Richard's equation, root water uptake, simulating, soil moisture, water flow, water use efficiency**

I. Introduction

Water is vital for agriculture, where efficient irrigation supports crop growth. However, climate change, population growth, and overuse threaten water availability. Inefficient management and outdated infrastructure worsen the problem. With over 70% of global freshwater used in agriculture, improving water management is crucial for sustainability and food security.

Automated irrigation systems offer a promising solution to address these challenges. Traditional methods, which rely on fixed timers, are inefficient as they do not account for current soil and atmospheric conditions. This paper introduces a soil-water flow model that forms the basis for developing a control system for irrigation. The model establishes the relationship between water distribution in the soil and plant water root uptake, incorporating the influence of current atmospheric conditions on transpiration rates and water uptake by the plant.

Models for predicting water flow in soil are essential in designing irrigation controllers. The models are based on the Soil-Plant-Atmosphere (SPA) concept, which describes the dynamic interactions between these components. There has been growing interest in developing mathematical models representing the water dynamics within the SPA system in recent years. Notable models include WAVE (Water and Agroecosystems Virtual Environment) [1], SPASMO (Soil Plant Atmosphere System Model) [2], MACRO (simulation of water movement through macropores in soil) [3], and SWAP (Soil-Water-Atmosphere-Plant) [4]. Models interpret the SPA concept differently, addressing various agricultural and environmental challenges. This study focuses on the SWAP concept, which was designed to simulate the interactions between soil, water, atmosphere, and plants. It combines water flow in both saturated and unsaturated zones and incorporates physically based numerical models that integrate water uptake by roots and crop growth.

The Richards equation is widely regarded as one of the most complex concepts for simulating. In this paper, we focus on simplifying the computations of the Richards equation by restricting our analysis to a single dimension. We achieve this by employing the Gardner relative permeability model and the Feddes root water uptake model, which allow us to reduce the equation to a linear form.

II. Modeling Water Flow in Soil

A. Richards equation

The Richards equation is commonly used to model water movement in porous media. Its general form for unsaturated water flow in soil can be expressed as follows:

$$\frac{\partial \theta(z,t)}{\partial t} = \frac{\partial}{\partial z}\left(K(z,t)\left(\frac{\partial}{\partial z}h(z,t)+1\right)\right) - S(z,t) \quad (1)$$

where θ is the volumetric water content [-], z is the vertical coordinate [m] (positive upward), t is time [s], h is the pressure head with $h \geq 0$ when the soil is saturated and $h < 0$ when it is unsaturated [m], S represents the root water uptake [s^{-1}].

Within the given equation, $K(z,t)$ represents a key parameter governing the system's behavior and is generally formulated as:

$$K(z,t) = K_s k_r(z,t) \quad (2)$$

where K_s is the saturated hydraulic conductivity (m/s), and $k_r(z,t)$ represents the relative permeability of the soil.

B. Modeling of Relative Soil Permeability

Hydraulic conductivity $K(z,t)$ defines a material's ability to transmit water, depending on pore size, porosity, and saturation properties. Relative permeability $k_r(z,t)$ is a dimensionless factor describing variations in hydraulic conductivity with soil moisture. Common models such as Van-Genuchten [4], Mualem [4] or Gardner [5] describing $k_r(z,t)$ rely on empirical relationships between volumetric water content $\theta(z,t)$ and pressure head $h(z,t)$. We decided to incorporate the Gardner model because it offers a simple yet effective approach to describing soil water retention and relative permeability. Despite its limitations, this model is widely used in practical applications and fundamental analyses of water

DOI 10.13164/eeict.2025.64

movement in soils. Employing exponential functions transforms the Richards equation into a linear form, making it computationally efficient and easily implementable.

$$\theta(z,t) = \begin{cases} \theta_r + (\theta_s - \theta_r)e^{\lambda h(z,t)} & h < 0 \\ \theta_s & h \geq 0 \end{cases} \quad (3)$$

$$k_r(z,t) = \begin{cases} e^{\lambda h(z,t)} & h < 0 \\ 1 & h \geq 0 \end{cases} \quad (4)$$

where θ_s is residual water content [-], θ_s is $\theta(z,t)$ at saturation [-], parameter λ is related to the pore distribution and size [m $^{-1}$].

C. The Gardner model in the Richards equation

If we limit the analysis to the unsaturated state only for $\theta(z,t)$ (3) and $k_r(z,t)$ (4), i.e. for the condition $h < 0$ we can express the pressure head and the relative permeability as follows:

$$k_r(z,t) = \frac{\theta(z,t) - \theta_r}{\theta_s - \theta_r} \quad h(z,t) = \frac{1}{\lambda} \ln\left(\frac{\theta(z,t) - \theta_r}{\theta_s - \theta_r}\right). \quad (5)$$

After computing the partial derivative of $h(z,t)$ with respect to the z axis and substituting it along with $k_r(z,t)$ into the original equation (1), we obtain the resulting form of Richards' equation as a second-order linear partial differential equation:

$$\frac{\partial\theta(z,t)}{\partial t} = \frac{K_s}{\lambda(\theta_s - \theta_r)}\frac{\partial^2\theta(z,t)}{\partial z^2} + \frac{K_s}{\theta_s - \theta_r}\frac{\partial\theta(z,t)}{\partial z} - S(z,t). \quad (6)$$

Since this model will serve as the foundation for the design of the control system, we will adhere to this linear dependency, which allows for expression of the system's transfer function.

D. Root Water Uptake

Modeling water movement in soil during crop cultivation requires describing root water uptake, which depends on temporal and spatial factors influenced by soil properties, crop characteristics, and atmospheric conditions. This study employs the Feddes reduction function $\alpha(\theta(z,t))$ [6], which represents the intensity of plant water uptake; it considers total water extraction from the root zone without detailing individual roots. Root uptake, represented by $S(z,t)$, describes the volumetric water extraction per unit of soil volume and time. Given the variability of root systems with soil type and depth, experimental determination of $S(z,t)$ is challenging. A modification of the Feddes model proposes expressing $S(z,t)$ as a function of soil water content $\theta(z,t)$ and the maximum uptake rate $S_{max}(z,t)$:

$$S(\theta(z,t)) = \alpha(\theta(z,t))S_{max}(z,t) \quad (7)$$

$$\alpha(\theta(z,t)) = \begin{cases} 0 & \text{for } \theta(z,t) \leq \theta_w \\ \frac{\theta(z,t)-\theta_w}{\theta_d-\theta_w} & \text{for } \theta_w < \theta(z,t) \leq \theta_d \\ 1 & \text{for } \theta_d < \theta(z,t) \leq \theta_{an} \\ 0 & \text{for } \theta_{an} < \theta(z,t) \leq \theta_s. \end{cases} \quad (8)$$

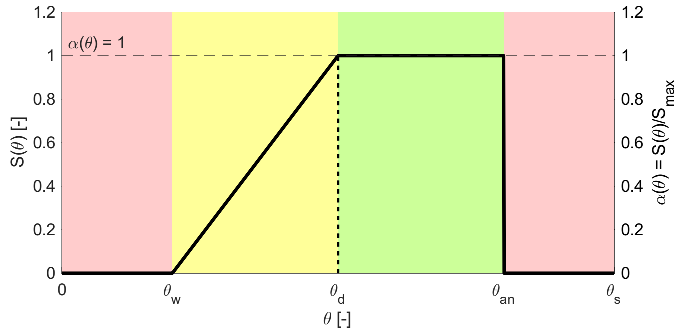

Fig. 1. The general form of the dimensionless Feddes reduction function. Red - critical soil conditions; yellow - transitional moisture conditions; green - zone of effective absorption.

The graphical representation of the Feddes function can be seen in Figure 1, where for $\theta \leq \theta_w$: no uptake (wilting point, dehydration); $\theta_w < \theta < \theta_d$: uptake increases (drainage point reached); $\theta_d < \theta < \theta_{an}$: maximum uptake (optimal moisture); $\theta_{an} < \theta < \theta_s$: uptake declines (anaerobic conditions). The maximum amount of water absorbed by the roots S_{max} is defined as $S_{max}(z,t) = \frac{2E_p(t)}{Z(t)}$, where $Z(t)$ is the depth of root [m], $E_p(t)$ represents the potential evapotranspiration [m/s] - the amount of water that would be evaporated from the soil surface and transpired by plants. This term can be calculated by various methods, including the Penman-Monteith equation, the Hargreaves method, or the Thornthwaite equation [7]. By applying the Feddes model, the time dependence of the parameters can be neglected, as the conditions under which the simulation is performed can be considered steady over short time periods. Thus, we obtain the resulting form of the root water uptake for individual regions of $\theta(z,t)$ based on the shape of the reduction function $\alpha(\theta(z,t))$.

E. Z-axis Discretization

The derivative along the z-axis was approximated using numerical differentiation, specifically through finite differences. To achieve this, centered difference approximations (which estimate the derivative by considering function values on both sides of the point of interest) (9) and (10) were employed for first and second-order derivatives, respectively. We have

$$f'(x) \approx \frac{f(x+\Delta x) - f(x-\Delta x)}{2\Delta x} \quad (9)$$

$$f''(x) \approx \frac{f(x+\Delta x) - 2f(x) + f(x-\Delta x)}{\Delta x^2}. \quad (10)$$

This approach implies that the z-axis is discretized into N sample points, where $\theta(z,t)$ values are determined. By applying this approximation to (6) and considering the range $i \in \langle 1, N\rangle$, where N is bounded by the soil depth l [m], we obtain the following result:

$$\frac{\mathrm{d}}{\mathrm{d}t}\theta(z_i,t) = \frac{K_s}{\lambda(\theta_s - \theta_r)}\frac{\theta(z_{i+1},t) - 2\theta(z_i,t) + \theta(z_{i-1},t)}{\left(\frac{l}{N}\right)^2} + \frac{K_s}{(\theta_s - \theta_r)}\frac{\theta(z_{i+1},t) - \theta(z_{i-1},t)}{2\frac{l}{N}} - S(z_i,t). \quad (11)$$

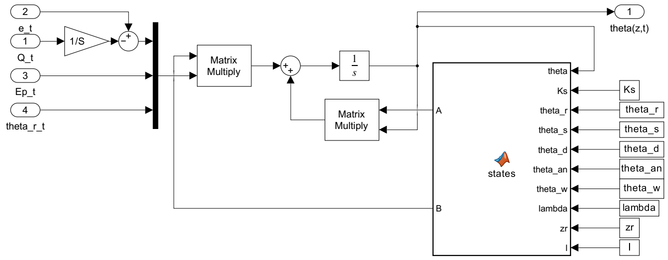

Fig. 2. Simulink scheme of the model.

F. Initial Conditions

For accurate system modeling, the initial conditions must be defined at $i = N$ and $i = 1$, which correspond to positions on the z-axis where water infiltrates into the soil and is drained out. To model the water flow, we apply Darcy's law, which accounts for the vertical movement of water through the soil:

$$q(t) = -K(z,t)\left(\frac{\partial h(z,t)}{\partial z} + 1\right) \tag{12}$$

where q is the volumetric flow rate [m^3/s]. From this equation, we determine $\frac{\partial h(z,t)}{\partial z}$ and subsequently express the partial derivative of $\theta(z,t)$ for the z-axis. Utilizing the chain rule, this relationship is given by: $\frac{\partial \theta(z,t)}{\partial z} = \frac{\partial \theta(z,t)}{\partial h}\frac{\partial h(z,t)}{\partial z}$. The term $\frac{\partial \theta(z,t)}{\partial h}$ is obtained as in (3), leading to the following derived expression:

$$\frac{\partial \theta(z,t)}{\partial z} = (\theta_s - \theta_r)\,\lambda e^{\lambda h(z,t)}\left(-\frac{q(t)}{K(z,t)} - 1\right). \tag{13}$$

By substituting for $K(z,t)$ and $h(z,t)$ as in (2) and (5), we can progressively simplify the expression to derive the final initial condition at both soil boundaries:

$$\frac{\partial \theta(z,t)}{\partial z} = -\frac{(\theta_s - \theta_r)\lambda}{K_s}q(t) - \lambda\theta(z,t) + \lambda\theta_r. \tag{14}$$

The simulation will be conducted under simplified, steady conditions using a soil sample of a given depth in a controlled environment. Thus, the boundary condition at $z \to z_1$, i.e., $z = 0$, defines the bottom of the domain, where we assume free drainage with no restriction on water outflow, meaning, $\frac{\partial h(z,t)}{\partial z} = 0$. In this case, the drain of water is determined solely by the hydraulic conductivity: $q_{out}(t) = -K(z_1,t) = -K_s\frac{\theta(z_1,t)-\theta_r}{\theta_s-\theta_r}$. By approximating the derivative (14) at $z \to z_1$ using a finite difference with the centered difference approximation (9), we obtain:

$$\frac{\mathrm{d}}{\mathrm{d}t}\theta(z_1,t) = \frac{\theta(z_2,t) - \theta(z_0,t)}{2\frac{l}{N}} \tag{15}$$

$$\frac{\theta(z_2,t) - \theta(z_0,t)}{2\frac{l}{N}} = -\frac{(\theta_s - \theta_r)\lambda}{K_s}q_{out}(t) - \lambda\theta(z,t) + \lambda\theta_r \tag{16}$$

where the point $\theta(z_0,t)$ is not part of the investigated region; therefore, this point must be expressed as:

$$\theta(z_0,t) = \theta(z_2,t) + \frac{2l}{N}\left(\frac{(\theta_s - \theta_r)\lambda}{K_s}q_{out}(t) + \lambda\theta(z_1,t) - \lambda\theta_r\right). \tag{17}$$

```matlab
function [A, B] = states(theta, Ks, theta_r, theta_s, theta_d,
     theta_an, theta_w, lambda, zr, l)
N = 20; z = l/(N-1)*(0:1:(N-1)); Ep = 7.29*10^-8;
B = zeros(N,3);B_q = zeros(N,1);
B_q(N) = -2*N/l - lambda; B_EP = zeros(N,1);
A = zeros(N,N); A(1,:) = 0;
a = Ks/(lambda*(theta_s-theta_r)); b = Ks/(theta_s-theta_r);
h=l/N;
for i = 2:N-1
        theta_i = theta(i); z_i = z(i);
        if z_i>=l-zr
            if ((theta_i>theta_an)&&(theta_i<=theta_s))||(
                 theta_i<=theta_w)
                A(i,i-1) =a/h^2 - b/(2*h);
                A(i,i) = -2*a/h^2;
                A(i,i+1) = a/h^2 + b/(2*h);
            elseif (theta_i>theta_d)&&(theta_i<=theta_an)
            A(i,i-1) =a /h^2 + b/(2*h);
            A(i,i) = -2*a/h^2;
            A(i,i+1) = a /h^2 + b /(2*h);
            B_EP(i) = -1/zr;
            else
            A(i,i-1) =a/h^2 - b/(2*h);
            A(i,i) = -2*a/h^2 - Ep/zr*1/(theta_d-theta_w);
            A(i,i+1) = a/h^2 + b / (2*h);
            B_EP(i) = theta_w/(theta_d-theta_w)/zr;
            end
        else
        A(i,i-1) =a /h^2 - b/(2*h);
        A(i,i) = -2*a/ h^2;
        A(i,i+1) = a/h^2 + b/(2*h);
    end
end
A(1,:) = 0; A(1,1) = -2*a/h^2; A(1,2) = (2*a)/h^2;
theta_i = theta(N);
if ((theta_i>theta_an)&&(theta_i<=theta_s))||(theta_i<=theta_w)
    A(N,N-1) = 2*a/h^2 - b*lambda;
    A(N,N) = -2*a/h^2 - a*(2*lambda*N)/l;
elseif (theta_i>theta_d)&&(theta_i<=theta_an)
    A(N,N-1) = 2*a/h^2 - b*lambda;
    A(N,N) = -2*a/h^2 - a*(2*lambda*N)/l;
    B_EP(N) = -1/zr;
else
    A(N, N-1) = 2*a/h^2 - b*lambda;
    A(N, N) = -2*a/h^2 - a*(2*lambda*N)/l - Ep/zr*1/(theta_d-
         theta_w);
    B_EP(N) = theta_w/(theta_d-theta_w)/zr;
end
B_theta_r = zeros(N,1); B_theta_r(1) = 0;
B_theta_r(N) = 2*a*(N/l)*lambda+b*lambda;
B=[B_q,B_EP,B_theta_r];
```

Listing 1. MATLAB function for computing state-space matrices A and B based on soil moisture dynamics.

By substituting the obtained results into (11) and progressively simplifying, we arrive at the following form of the boundary condition at $z \to z_1$:

$$\frac{\mathrm{d}}{\mathrm{d}t}\theta(z_1,t) = \frac{K_s}{\lambda(\theta_s - \theta_r)}\frac{2\theta(z_2,t) - 2\theta(z_1,t)}{\left(\frac{l}{N}\right)^2} - S(z_1,t). \tag{18}$$

In the similar manner, we express the initial condition at the point $z \to z_N$, i.e., $z = l$, which defines the soil surface. The water input to the soil will be denoted as q_{in}, representing the general flow of water entering the system. By successive calculations we achieve the following form:

$$\frac{\mathrm{d}}{\mathrm{d}t}\theta(z_N,t) = \frac{K_s}{\lambda(\theta_s - \theta_r)}\frac{2\theta(z_{N-1},t) - \frac{2l}{N}\frac{(\theta_s-\theta_r)\lambda}{K_s}q_{in(t)}}{\left(\frac{l}{N}\right)^2} - \frac{\frac{2l}{N}\lambda\theta(z_N,t) + \frac{2l}{N}\lambda\theta_r - 2\theta(z_N,t)}{\left(\frac{l}{N}\right)^2} + \frac{K_s}{(\theta_s - \theta_r)}\times \left(\frac{-(\theta_s - \theta_r)\lambda}{K_s}q_{in}(t) - \lambda\theta(z_{N-1},t) + \lambda\theta_r\right) - S(z_N,t). \tag{19}$$

III. Simulation of the Model

The model simulation was carried out in the MATLAB Simulink environment. Fig. 2 shows the Simulink scheme of the state-space representation of the soil water flow model. The system is affected by three inputs: $Q(t)$ is drip irrigation, which starts at 8:00 AM and operates for one hour. The flow rate is set to $1.61 \cdot 10^{-7}$ [m^3/s]. This input is distributed over

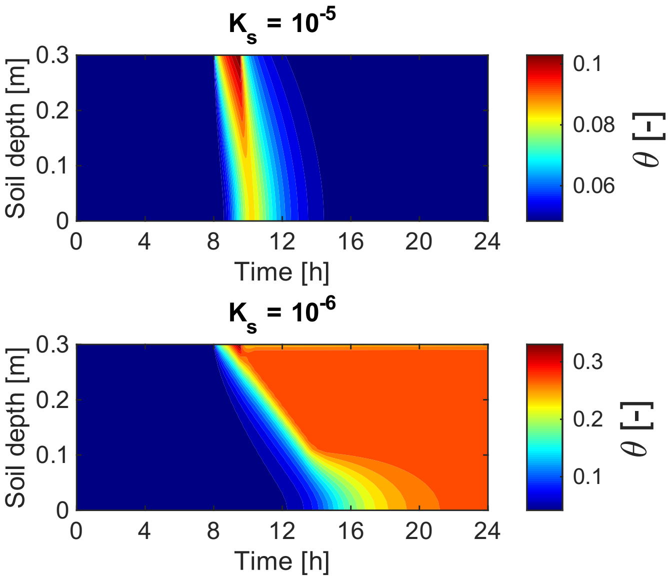

Fig. 3. Soil water flow for different values of K_s.

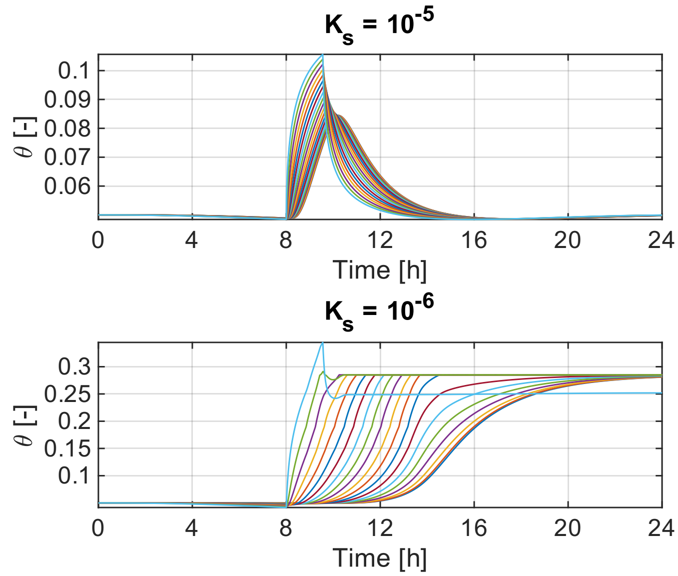

Fig. 4. Change of $\theta(z,t)$ for different value of K_s.

the irrigation area of $= 0.0707$ [m^2], with a negative sign applied as acts in the opposite direction to the defined z-axis orientation; $e(t)$ represents evaporation (water loss from the soil). The total evaporation value for the day is 0.0033 [represents the root watem]; $E_p(t)$ is assumed constant under steady conditions and set to $7.29 \cdot 10^{-8}$ [m^3/s]. The MATLAB function $states$ computes the state matrix A and input matrix B for the state-space representation, as shown in Lst. 1. The model parameters were set as follows: $l = 0.3$, $Z = 0.2$, $\lambda = 10$, $\theta_r = 0.05$, $\theta_w = 0.13$, $\theta_d = 0.19$, $\theta_{an} = 0.285$, $\theta_s = 0.35$, $K_s = 10^{-5}$ /$K_s = 10^{-6}$, $N = 20$. Fig. 3 shows the simulation results of the proposed model for different values of K_s. In soils with higher conductivity, water reaches the bottom of the soil sample relatively quickly after irrigation and then drains out, with moisture returning to its original value. Soils with lower conductivity retain water better and remain moist for a longer period. Fig. 4 illustrates the $\theta(z,t)$ distributions at different depths throughout the entire soil column. The number of curves corresponds to the system's order N, i.e. 20, with each curve representing a layer along the z-axis, spaced at intervals of l/N.

Conclusion

The paper presents a model of water flow in soil based on Richards' equation. Using the Gardner model of relative permeability, the Richards' equation is simplified into a linear form. The model also includes the Feddes function for root water uptake. The simulation was conducted under steady conditions with a fixed-depth soil sample to simplify modeling by neglecting the temporal dependence, utilizing the finite difference method with centered difference approximations for derivatives. The main advantage of the presented model is its linear form, which not only facilitates mathematical analysis but also enhances simulation efficiency. Moreover, it allows for representation in a state-space formulation in matrix form. However, the model has certain limitations resulting from its simplifications. For instance, it does not account for water flow in fully saturated conditions, and the neglect of temporal variability in certain parameters may limit its ability to accurately describe long-term dynamic effects. Nevertheless, the model helps to understand the physical principles of water flow in soil based on Richards' equation, and thanks to its linear form, it is useful for the design and simulation of irrigation control systems.

Acknowledgment

The author thanks Mr. Lukáš Zezula (Brno University of Technology) for his expert guidance, valuable consultations, and constructive feedback throughout the research.

References

[1] A. Timmerman and J. Feyen, "The WAVE model and its application; Simulation of the substances water and agrochemicals in the soil, crop and vadose environment", Ciencia & Tecnología Agropecuaria, vol. 4, no. 1, pp. 36-41, Dec. 2013.

[2] M. Hardie, S. Green, G. Oliver, N. Swarts, B. Clothier, R. Gentile, and D. Close, "Measuring and modelling nitrate fluxes in a mature commercial apple orchard", Agricultural Water Management, vol. 263, 2022.

[3] M. Larsbo and N. Jarvis, MACRO 5.0 A model of water flow and solute transport in macroporous soil. Technical description. Swedish University of Agricultural Sciences, Department of Soil Sciences, Division of Environmental Physics, 2003.

[4] M. Heinen, M. Mulder, J. van Dam, R. Bartholomeus, Q. de Jong van Lier, J. de Wit, A. de Wit, and M. Hack - ten Broeke, "SWAP 50 years: Advances in modelling soil-water-atmosphere-plant interactions", Agricultural Water Management, vol. 298, 2024.

[5] H. Suk and E. Park, "Numerical solution of the Kirchhoff-transformed Richards equation for simulating variably saturated flow in heterogeneous layered porous media", Journal of Hydrology, vol. 579, 2019.

[6] R. A. Feddes, P. Kowalik, K. Kolinska-Malinka, and H. Zaradny, "Simulation of field water uptake by plants using a soil water dependent root extraction function", Journal of Hydrology, vol. 31, no. 1-2, pp. 13-26, 1976.

[7] L. Zhaofei, "Estimating land evapotranspiration from potential evapotranspiration constrained by soil water at daily scale", Science of the Total Environment, vol. 834, pp. 2-3, 2022.

Kde nás najdete

E.ON Energie, a.s.
F. A. Gerstnera 2151/6
370 01 České Budějovice

eon.cz/kariera
E.ON Kariéra

EG.D, s.r.o.
Lidická 1873/36
602 00 Brno

egd.cz/kariera

Informace v tomto letáku platí k 1. 1. 2025.

Tvořte s námi *energetickou budoucnost*

Jsme skupina E.ON, těší nás

Jsme jedním z největších energetických koncernů u nás i ve světě. Centrálu máme v Německu, ale najdete nás už v 15 zemích Evropy včetně České republiky. Zakládáme si na tom, že naše energie můžou šetřit peníze i přírodu a čím dál víc využíváme obnovitelné zdroje.

Kdo patří do naší rodiny

E.ON Energie, a.s.
- Obchoduje s elektřinou a plynem, zajišťuje marketing a komunikaci a stará se i o výrobu energií.
- Pro zákazníky připravuje řešení na míru v oblasti fotovoltaiky, tepelné techniky a elektromobility.

EG.D, s.r.o.
- Distributor elektřiny, který vlastní a provozuje rozvodnou síť zejména na jihu Čech a Moravy.
- Zajišťuje připojení odběrných míst k síti a stará se o dopravu energií k zákazníkům.

E.ON Česká republika, s.r.o.
- Funguje jako podpora výše uvedených společností. Zajišťuje jim služby, jako jsou účetnictví, právo nebo HR, a na starost má i zákaznickou péči.

Na přírodě nám záleží

E.ON Energie je jedničkou ve výkupu zelené elektřiny v České republice.

EG.D pomocí bezpečnostních prvků na sloupech vysokého napětí chrání ptáky před úrazem.

V budovách E.ONu i ve všech dobíječkách elektromobilů využíváme zelenou energii.

Kariéra u nás

Máme téměř 3 500 kolegů, kteří nám pomáhají neustále růst a zlepšovat se.

Všem nabízíme bezpečné zázemí, férové jednání a příjemné prostředí.

Jsme pravidelně oceňováni jako TOP ZAMĚSTNAVATEL.

Koho hledáme

- Místo u nás najdou lidé s praxí i čerství absolventi středních a vysokých škol.
- Potřebujeme techniky, ekonomy i nadšence do IT, marketingu nebo obchodu.
- Kanceláře máme v Českých Budějovicích, Brně a v Praze, ale pracovní místa nabízíme i v jiných městech.

eon.cz/kariera **egd.cz/kariera**

Segmentation of hip joint anatomy structures from radiographic images

Lenka Blažková
Department of Biomedical Engineering
FEEC, Brno University of Technology
Brno, Czech Republic
xblazk01@vutbr.cz

***Abstract*—This paper deals with the problem of a hip joint segmentation in radiographic images with the use of a deep learning approach. The paper is focused on training nnU-Net models and creating an original dataset that contains 150 radiographs, 100 training and 50 test images. There are six trained models, five from cross-validation training and one trained on all training data. All models are evaluated on the test dataset using the Dice score for individual labels and the combined mean Dice score for the image. The best-performing model was the model trained on all training images. The most challenging labels for segmentation were those representing the Köhler teardrop and the space between the femoral head, teardrop and acetabulum due to their size and variability observed across the dataset.**

***Index Terms*—hip joint, femur, pelvis, radiography, radiographic image, segmentation, deep learning, convolutional neural network, U-Net, nnU-Net.**

I. Introduction

The hip joint is a critical structure in the human musculoskeletal system, essential for movement and maintaining whole-body posture, and radiography is one of the most common imaging methods used for upper femur and pelvis imaging. It is typically employed as an initial step in a joint examination due to its availability, short duration, and relatively low radiation exposure. Further procedures, surgery planning or aftercare also often rely only on it. For instance, primary hip arthroplasty is frequently performed based solely on visual assessments of X-ray images (2D radiographs) and the surgical field. However, hip preoperative planning is crucial for the success of the surgery and the patient's recovery. Planning must be precise to restore function and enhance the patient's quality of life. Therefore, accurate determination of the correct anatomical landmarks is essential to selecting the correct component type, size, or shape. [1], [2]

M. Kim et al. in [3] dealt with preoperative planning for successful total hip arthroplasty and proposed a deep-learning and rule-based algorithm for optimal hip prosthesis determination. A 2D U-Net supplemented with a classification convolutional neural network was used as a segmentation model. Another research group, led by W. Xu [4], held research regarding hip joint pathologies in infants' radiographs. The research specialized in the localization of developmental dysplasia lesions and proposed an algorithm utilizing joint segmentation via Feature Pyramid Network with ResNet50. L. Chen et al. [5] dealt with segmenting dysplasia lesions as well, specifically using 2D ultrasound images and a cascaded fully convolutional neural network.

In addition, other research groups propose hip joint segmentation approaches but from 3D data. A fully automated algorithm for hip joint segmentation was proposed by J. J. Kim et al. in [6]. It employed the complementary use of a patient-specific optimal thresholding together with a watershed algorithm. C. Chu et al. in [7] also published a fully automatic CT segmentation approach but with the integration of fast random forest regression-based landmark detection, multi-atlas segmentation, and articulated statistical shape model fitting. P. Xu et al. [8] used 3D CT scans and the MultiPlanar U-Net with transfer learning. They embraced model training on publicly available and poorly annotated data with only a few accurate training scans for fine-tuning.

II. Image Dataset

There were two datasets containing 2D radiographs found, the first one by M. Kim et al. mentioned in [3] and the second one by R. Zhao et al. from [9]. However, neither of these two datasets was publicly available and the data could not be retrieved even upon the request. Therefore, the creation of an original dataset was initiated.

83 plain anteroposterior (AP) radiographs were obtained from the DICOM database. All images were anonymised and included the entire pelvis and both upper femurs, e.g. Fig. 1a. The created original dataset itself consists of 150 images of one joint, see Fig. 1b. The remaining joints were not eligible because of already implanted hip replacement prostheses, as well as fixation components like plates and screws used for fracture and other treatments.

The dataset contains data from computed radiography acquired between the years 2010 and 2011. The image sizes range from 1223×1943 pixels to 2140×3520 pixels, and the image spacings are 0.1×0.1 mm, 0.15×0.15 mm or 0.175×0.175 mm per pixel.

Furthermore, all images in the dataset have a corresponding ground truth segmentation mask created by a non-medical health professional, according to Act No. 96/2004 Coll. [10]. Each mask includes five labels, depicted in Fig. 2. The region of the first label (L1) contains the femoral head, the medullary cavity, and the greater trochanter; the second label region (L2) includes the inferior neck, the diaphyseal cortex, and the

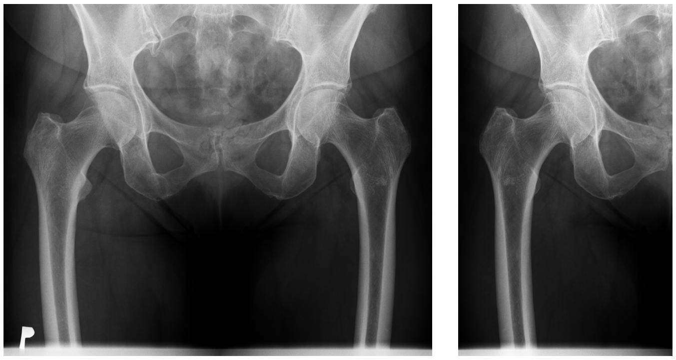

(a) (b)

Fig. 1: Example of plain AP radiography images from one patient: (a) full image showing both hip joints and (b) image of only one hip joint (image from the original dataset)

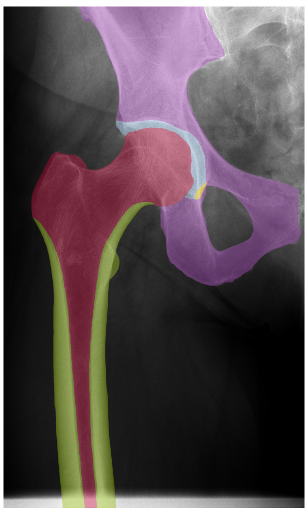

Fig. 2: Example of the segmentation mask with five labels: (L1, *red*) femoral head, medullary cavity and greater trochanter; (L2, *green*) inferior neck and diaphyseal cortex and lesser trochanter; (L3, *yellow*) Köhler teardrop; (L4, *blue*) region between femoral head, teardrop and acetabulum; and (L5, *purple*) pelvic bone

lesser trochanter; the third region (L3) is the Köhler teardrop; the fourth (L4) covers the area between the femoral head, the teardrop, and the acetabulum; and the fifth region (L5) represents the pelvic bone.

The entire dataset is divided into training and test subsets, with the training set consisting of 100 images and the test set comprising of 50 images. To ensure data integrity, images from a single patient image are not included in both subsets simultaneously.

III. Segmentation Model

The used segmentation model architecture is the nnU-Net by F. Isensee et al. [11], available at https://github.com/mic-dkfz/nnunet. It is a deep learning-based segmentation method, more specifically a convolutional neural network, comprising of an encoder-decoder U-Net architecture that automatically adapts its hyperparameters to suit diverse datasets. In this particular instance, the 2D nnU-Net model is selected, since the dataset consists of 2D images.

The data are preprocessed to the voxel spacing of $1.0\times0.15\times0.15$ mm and the shape is standardized to a size of $1\times2320\times1414$ pixels. In addition, the data processing includes Z-score normalization applied uniformly.

The specific model architecture for the used dataset is based on the plain convolution U-Net with nine stages and employs from 32 to 512 features per stage. Each stage incorporates two convolutional layers with a kernel size of 3×3. The network architecture also leverages stride adjustments in conjunction with instance normalization and the Leaky ReLU activation function. The model training is carried out with a batch size of 2, a patch size of 1536×1024 pixels and optimized using the Dice score.

IV. Results and Discussion

There are 6 trained models, five obtained via five-fold cross-validation and one trained on the whole training dataset. All the models were trained for 1000 epochs. The model performance was evaluated on the test dataset using the Dice score metric. The results of the different models were evaluated along all labels as a mean Dice score and also in the individual label categories. The mean Dice score results overview for each model can be seen in Fig. 3 and in Table I.

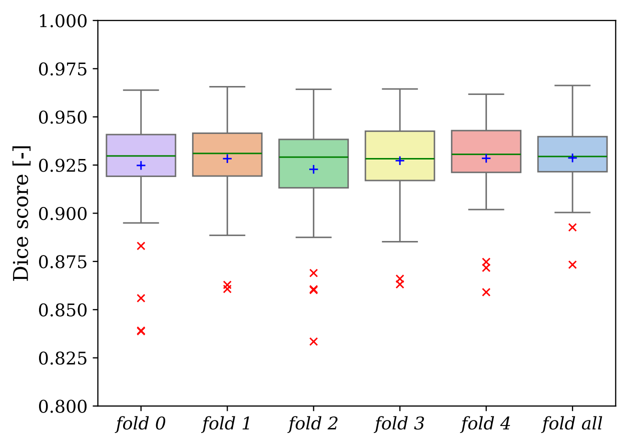

Fig. 3: Box and whisker plots of mean Dice score evaluation of different models on test dataset: mean (blue +), median (green line), 25^{th}–75^{th} percentile (coloured box), extreme values (black whiskers) and individual outliers (red $\times$)

TABLE I: Evaluation of the different models

Dice score	*fold 0*	*fold 1*	*fold 2*	*fold 3*	*fold 4*	*fold all*
mean val.	0.9248	0.9283	0.9228	0.9273	0.9285	**0.9287**
std val.	0.0263	0.0212	0.0262	0.0212	0.0207	**0.0176**
median	0.9297	**0.9310**	0.9291	0.9283	0.9306	0.9295
max val.	0.9639	0.9656	0.9643	0.9645	0.9618	**0.9663**
min val.	0.8388	0.8607	0.8334	0.8631	0.8590	**0.8733**

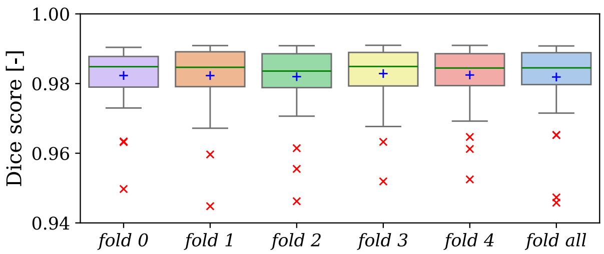

(a) Evaluation of label L1

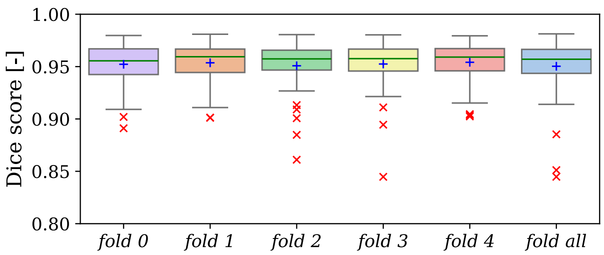

(b) Evaluation of label L2

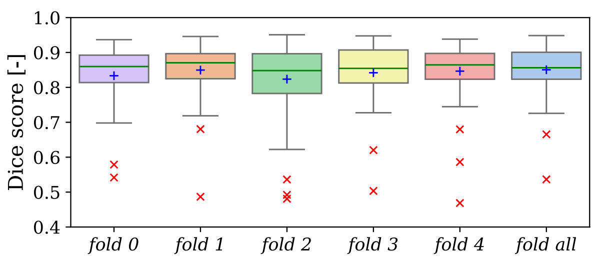

(c) Evaluation of label L3

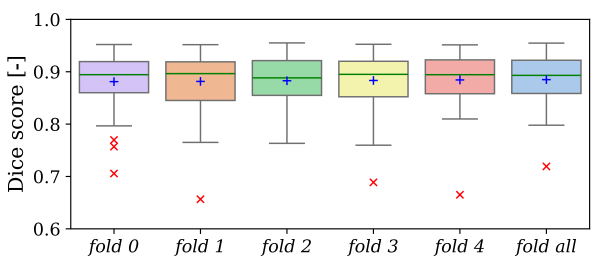

(d) Evaluation of label L4

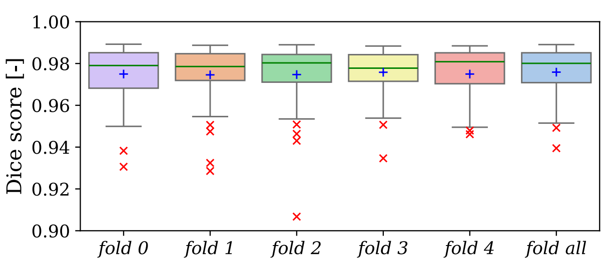

(e) Evaluation of label L5

Fig. 4: Box and whisker plots of individual labels Dice score evaluation of different models on test dataset: mean (blue +), median (green line), 25^{th}–75^{th} percentile (coloured box), extreme values (black whiskers) and individual outliers (red ×)

Individual models were also evaluated according to the different labels, and the graphical representation can be seen in Fig. 4. The best Dice score from all models has L1, above 0.94 for all data and models. L1 evaluation results are followed by L5 and L2 results. The results are connected to the sizes of the regions, which are proportionally larger than the rest of the labels. It can be assumed that they are visually simpler to be evaluated from a radiographic image.

On the contrary, L3 has the smallest Dice scores, which corresponds with the overall small label region size. L4 also has a lower Dice score, which can be a consequence of its proximity to L3. If an error is made at L3, it is likely to be made at L4. The main reasons are high variability in the region size, shape and location. Moreover, they highly depend on the positioning of the patient during the image acquisition (the rotation of the femur and the tilt of the pelvic bone) and are the most affected by joint disorders. Therefore, the ground truth annotations may vary in terms of label placement.

Fig. 5 shows two examples of the segmentation masks from the trained models, where some segmentation errors are present. Fig. 5a shows incorrect segmentation of L1 (particularly the femoral head), L4 and L3, due to the femoral head projection medial to the ilioischial line (acetabular protrusion). Another suboptimal segmentation of L1 and L4 can be observed in Fig. 5b, where the hip joint exhibits signs of osteoarthritis.

Upon further research, it was determined that the best model is the *fold all* model. Its results are shown in Table II. It has the best mean Dice score for labels L3, L4 and L5 (0.85047, 0.88497 and 0.97587). The mean Dice score for L2 is 0.9503, which is just 0.004 lower than *fold 4* model, the best for L2. The mean Dice score for L1 is only 0.001 lower than the best score from *fold 3* model. The mean Dice score of L1 is 0.9819.

TABLE II: Evaluation of the *fold all* model across labels

Dice score	*L1*	*L2*	*L3*	*L4*	*L5*
mean val.	0.9819	0.9503	0.8505	0.8850	0.9759
std val.	0.0096	0.0271	0.0741	0.0456	0.0118
median	0.9845	0.9570	0.8563	0.8931	0.9801
max val.	0.9908	0.9813	0.9484	0.9547	0.9891
min val.	0.9458	0.8448	0.5366	0.7192	0.9395

V. Conclusion

This paper aimed to train a segmentation model for key anatomical structures of the hip joints which has a high potential for hip joint analysis during medical examinations or surgery planning. The model demonstrates considerable potential for use in medical examinations, the diagnosis of hip joint disorders and the improvement of pre-operative planning.

The trained model was the nnU-Net framework by F. Isensee et al. [11] with automatically determined hyper-parameters. The training and test data were from an original radiograph dataset explicitly created for this research. A total of six models were trained, and their evaluation using the Dice score metric confirmed the effectiveness of the models.

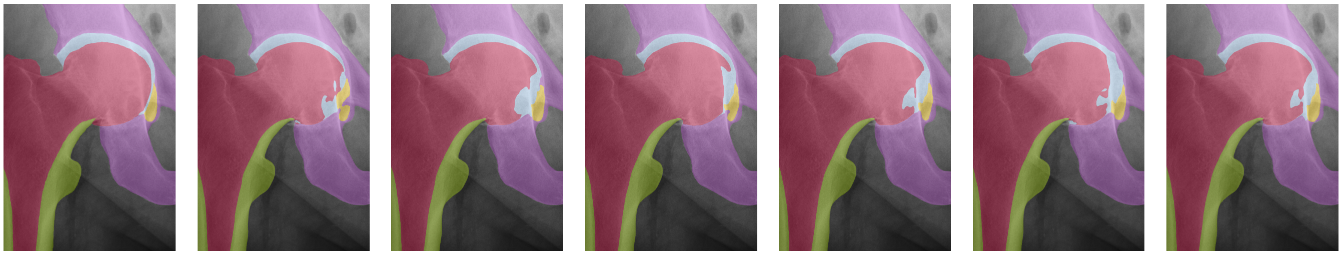

(a1) ground truth (a2) *fold 0* (a3) *fold 1* (a4) *fold 2* (a5) *fold 3* (a6) *fold 4* (a7) *fold all*

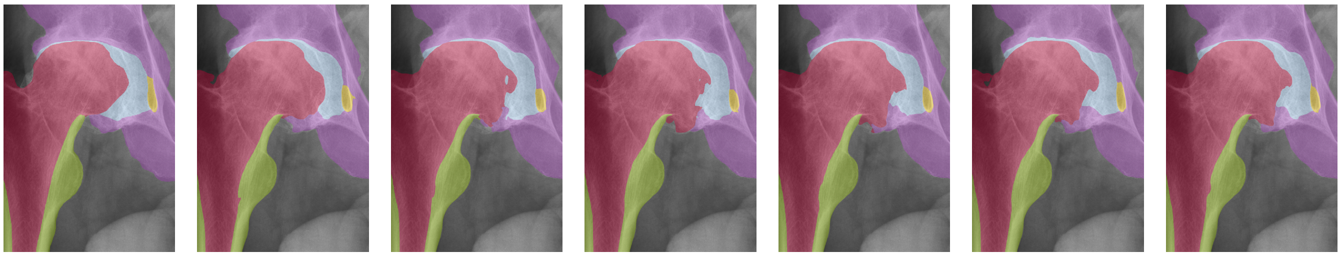

(b1) ground truth (b2) *fold 0* (b3) *fold 1* (b4) *fold 2* (b5) *fold 3* (b6) *fold 4* (b7) *fold all*

Fig. 5: Examples of predicted segmentation masks (with mean Dice score): (a) incorrect segmentation of L1 (femoral head), L4 and L3 (0.8391, 0.8886, 0.9042, 0.8852, 0.8748 and 0.9082; acetabular protrusion); (b) incorrect segmentation of L1 (femoral head) and therefore L4 (0.8831, 0.8896, 0.8888, 0.8971, 0.9067 and 0.9021; osteoarthritis)

The *fold all* model was established as the best model. Its mean Dice score is 0.9287 with a standard deviation of 0.0176 and a median of 0.9295. In addition, this model performed best on the labels L3 and L4, showing that they were the most difficult to predict overall.

Future work on this research may focus on refining the model with a larger dataset. It may also conduct a deeper analysis of pathological cases, aim for the integration of the models into clinical workflows, and explore its application in real-time diagnostics.

Acknowledgment

I would like to express my gratitude to OR-CZ spol. s r.o. for their support and for providing the essential data that made this research possible. Additionally, I would like to extend my sincere thanks to my consultant Jan Kelča and supervisor Vratislav Harabiš for their guidance throughout this project, to Michal Nohel for his insights into the nnU-Net models, and to the authors of the nnU-Net [11]. I also acknowledge MetaCentrum and the Linux Ubuntu 22.04 system running on a machine equipped with an Nvidia Titan Xp 12GB GDDR5 graphics card for providing the computational resources necessary for this work.

References

[1] V. Adukia, K. Kulkarni, and D. K. Menon, “Clinical Examination of the Hip Joint (Basic and Surface Anatomy) with Special Tests”, in *Orthopedics of the Upper and Lower Limb*, 2nd ed.Cham: Springer International Publishing, 2020, pp. 217-238. doi: 10.1007/978-3-030-43286-7_14.

[2] V. Adukia, K. Kulkarni, and D. K. Menon, “The Hip Joint”, in *Orthopedics of the Upper and Lower Limb*, 2nd ed.Cham: Springer International Publishing, 2020, pp. 239-277. doi: 10.1007/978-3-030-43286-7_15.

[3] M. Kim, I.-S. Oh, and S. -J. Yoon, “Deep Learning and Computer Vision Techniques for Automated Total Hip Arthroplasty Planning on 2-D Radiographs”, *IEEE Access*, vol. 10, 2022, doi: 10.1109/ACCESS.2022.3204147.

[4] W. Xu *et al.*, “A Deep-Learning Aided Diagnostic System in Assessing Developmental Dysplasia of the Hip on Pediatric Pelvic Radiographs”, *Frontiers in Pediatrics*, vol. 9, Mar. 2022, doi: 10.3389/fped.2021.785480.

[5] L. Chen *et al.*, “Femoral head segmentation based on improved fully convolutional neural network for ultrasound images”, *Signal, Image and Video Processing*, vol. 14, no. 5, 2020, doi: 10.1007/s11760-020-01637-z.

[6] J. J. Kim, J. Nam, and I. G. Jang, “Fully automated segmentation of a hip joint using the patient-specific optimal thresholding and watershed algorithm”, *Computer Methods and Programs in Biomedicine*, vol. 154, 2018, doi: 10.1016/j.cmpb.2017.11.007.

[7] C. Chu, C. Chen, L. Liu, and G. Zheng, “FACTS: Fully Automatic CT Segmentation of a Hip Joint”, *Annals of Biomedical Engineering*, vol. 43, no. 5, 2015, doi: 10.1007/s10439-014-1176-4.

[8] P. Xu, F. Moshfeghifar, T. Gholamalizadeh, M. B. Nielsen, K. Erleben, and S. Darkner, “Auto-segmentation of Hip Joints Using MultiPlanar UNet with Transfer Learning”, in *Medical Image Learning with Limited and Noisy Data*, in Lecture Notes in Computer Science. Cham: Springer Nature Switzerland, 2022, pp. 153-162. doi: 10.1007/978-3-031-16760-7_15.

[9] R. Zhao, H. Cai, H. Tian, and K. Zhang, “Morphological consistency of bilateral hip joints in adults based on the X-ray and CT data”, *Surgical and Radiologic Anatomy*, vol. 43, no. 7, 2021, doi: 10.1007/s00276-020-02676-4.

[10] Czech Republic, *Act No. 96/2004 Coll., on Conditions for Acquisition and Recognition of Competence to Practice Non-Medical Health Professions and to Perform Activities Related to the Provision of Health Care and on Amendments to Certain Related Acts (Act on Non-Medical Health Professions)*, Collection of Laws, 2004.

[11] F. Isensee, P. F. Jaeger, S. A. A. Kohl, J. Petersen, and K. H. Maier-Hein, “NnU-Net: a self-configuring method for deep learning-based biomedical image segmentation”, *Nature Methods*, vol. 18, no. 2, 2021, doi: 10.1038/s41592-020-01008-z.

Bloody Forecast: Daily Blood Demand Prediction Using Various Modeling Approaches

Martina Dankova
Dept. of Biomedical Engineering
FEEC, Brno University of Technology
Brno, Czechia
238521@vutbr.cz

Stanislava Koskova
Transfusion and Histic Treatment Dept.
University Hospital Brno
Brno, Czechia
koskova.stanislava@fnbrno.cz

Filip Plesinger
Supervisor
Dept. of Medical Signals
Institute of Scientific Instruments of the CAS
Brno, Czechia
fplesinger@isibrno.cz

***Abstract*—Sufficient blood supply is critical not only for scheduled surgeries, but also for emergency medical interventions. In our study, we focus on predicting the daily blood demand separately for two blood types: A+ and O-, based on data from the Transfusion and Tissue Department of University Hospital Brno. The dataset consisted of data on blood demand from 2021 to 2024 and was extended by data regarding non-working days, national and school holidays, seasons, and influenza epidemics. The performance of various prediction models was measured using the normalized Mean Absolute Error (nMAE), which reflects the average prediction error relative to the average daily blood demand. When tested on data from 2023, the best performance was achieved by linear regression models, with a nMAE of 26% for A+ and 50% for O-, indicating lower predictability for blood types with smaller populations. Interestingly, models for different blood types use different features, as the demand for individual blood types depends on different factors. Despite relatively high nMAE values, the models still outperformed a "qualified guess" approach based only on historical averages.**

***Index Terms*—Blood demand, computational modeling, machine learning, feature selection**

I. Introduction

Blood supply management is crucial for ensuring adequate blood supply for transfusion centers. Predicting blood demand is a challenging task, as it is influenced by a variety of factors such as patient needs, seasonal variations, public holidays, and more. Accurate forecasting of blood requirements is essential to ensuring that blood donations are efficiently managed.

This study applies several computational models to predict blood demand in a transfusion center. Among these models, linear regression was employed to analyze the relationship between the blood demand and various factors including holidays, seasons, influenza epidemic and other relevant predictors. The goal is to develop a model that can be directly applied by transfusion centers to predict future blood requirements and ensure optimal blood supply.

Predicting the amount of donated blood is a well-established research problem and has been addressed in several studies using various predictive models. Studies focus on forecasting the total amount of blood donations over time, especially weekly (e.g. [1], [2]). However, the prediction of blood demand by specific blood types remains a less frequently explored task. Notably, one study [3] predicted daily blood demand with great performance, but the prediction was made for larger volumes of blood and it did not separate data by blood type. This gap shows the need for more detailed models that can predict daily blood demand for individual blood types.

II. Method

All steps of the analysis — including data preprocessing, feature extraction, model training, and evaluation — were conducted in Python 3.10 [5]. The implementation relied on libraries including Pandas [4] and Numpy [6] for data handling, Scikit-learn [7] and Statmodels [8] for machine learning models, and Matplotlib [9] for visualization.

A. Dataset

For creation of the models, dataset describing blood demand in University Hospital Brno was used. The data were collected in course of whole 3 years (2021, 2022 and 2023) and first 9 months of 2024. Dataset contained information about daily blood demand for individual blood types.

B. Used features

All features used for training were created based on properties of given days and influenza epidemic status in the Czech Republic and in the South Moravian Region. The derived features are grouped into four thematic categories.

The first category focuses on working and non-working days. The isWeekend feature indicates whether a given day is a weekday or a weekend, while isHoliday marks Czech national holidays. The isFreeDay feature combines these two, distinguishing between working and non-working days. The SchoolHoliday feature captures information about school holidays, including autumn breaks, Christmas, spring breaks, end-of-semester breaks, Easter holidays, and summer vacations. Additionally, the freeInRow feature reflects the number of consecutive non-working days a given day belongs to. The last three features in this category — freedaysCurrentWeek, freedaysPreviousWeek, and freedaysNextWeek — indicate the number of non-working days in the current, previous, and upcoming week, respectively.

The second category is based on influenza data from the National Institute of Public Health [10]. These features capture the number of patients tested for influenza both across the Czech Republic (CR_test_3weeksago) and in the South Moravian Region (JMK_test_3weeksago), as well as the number of positive test results (CR_pos_3weeksago, JMK_pos_3weeksago). The feature JMK_function_3weeksago indicates whether influenza data for the South Moravian Region is available, as hospitals in Brno did not report data every week. Since the models are supposed to be used to predict blood demand two weeks ahead and National Institute of Public Health is publishing the statistics with a slight delay, the values of these features must be from three weeks before the prediction day.

The last two categories include features that provide information about the specific day of the week and the corresponding calendar month.

C. Features selection, model training and testing

After preparing the dataset, forward feature selection process was manually implemented. Model started with an empty feature list, and in each iteration, the feature that improved the model's performance the most was added. This process continued until performance began to deteriorate. Statmodels was used for training the models and calculating the p-values to assess the statistical significance of individual features. The models were trained using data from the full years of 2021 and 2022, as well as the first three quarters of 2024. They were then tested on data from the entire year of 2023. The performance of the models was evaluated using the normalized mean absolute error (nMAE), which compares the mean absolute error with the average daily demand.

D. Comparison with other modeling approaches

In addition to linear regression, more advanced machine learning methods were also implemented. The used forward neural network consisted of a single hidden layer with 8 and 10 neurons for A+ and O-, respectively, determined through manual hyperparameter optimization. Neural network was using the ReLU activation function and the ADAM optimizer. The implemented random forest algorithm had 50 estimators and unlimited maximal depth.

Furthermore, we prepared a Naive model to represent an informed estimate made without the use of any machine learning approach. Naive model simply averages the values from previous years (aligned by the days of the week).

III. Results and Discussion

A. Models' performance

Using the set of prepared features and a basic linear regression approach, blood demand can be estimated with normalized Mean Absolute Error of $26.2 \pm 22\%$ for the A+ blood type and $50.4 \pm 45\%$ for the O- blood type. The relatively high standard deviations indicate that the model's accuracy varies significantly between individual days. The naive model achieved $33.5 \pm 27\%$ nMAE for A+ and $61.5 \pm 60\%$ nMAE for O-, meaning that although the linear regression model has a relatively large error, especially for O-, it still outperforms 'qualified guess.' The comparison between the naive model and linear regression is shown in Fig. 1. This comparison also reveals that the blood type with higher average daily demand is more predictable, despite both datasets being the same size.

The results of all the models tested are displayed in Table I showing, that neither of these methods achieved better performance as linear regression. This could be caused by the limited dataset, with only 1,004 training samples, which may not have been sufficient for these more complex models.

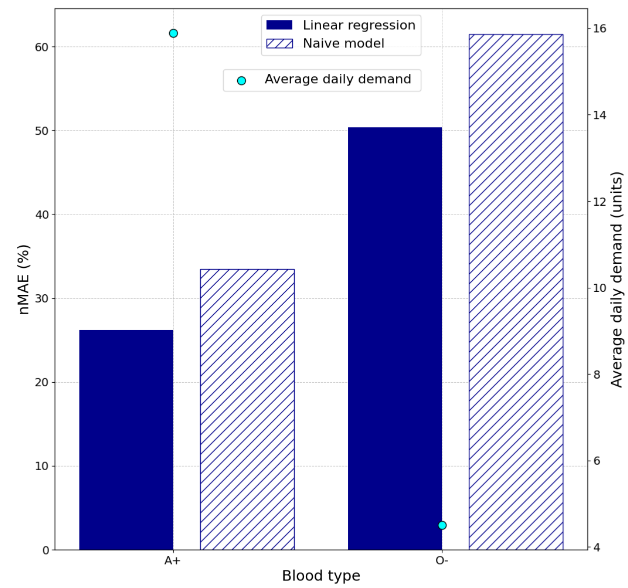

Fig. 1: Comparison of error of the naive model and linear regression model (bar chart). The figure also includes information on the average daily expenditure, represented by the dots.

TABLE I: Comparison of different models: normalized MAE and standard deviation for individual blood types

Model	Linear regression	Neural Network	Random Forest	Naive model
A+	$26 \pm 22\%$	$28 \pm 23\%$	$29 \pm 25\%$	$34 \pm 27\%$
O-	$50 \pm 45\%$	$53 \pm 45\%$	$57 \pm 47\%$	$62 \pm 60\%$

The prediction performance is also visualized over time, as shown in Fig. 2 and as a kernel density estimate (KDE) plot of predicted and real values in Fig. 3 and 4 .

B. Automatically selected features

The linear regression models for different blood types not only differ in performance but also in features they use. The overview of selected features is shown in table II. Both models selected several features from the category focused on non-working days, which corresponds with the fact that planned surgeries are not scheduled on weekends and national holidays. There is a significant decrease in December, probably due to the Christmas period. Higher numbers of positive influenza cases also lower blood demand presumably due to surgeries cancellation. Additionally, A+ demand appears to be lower

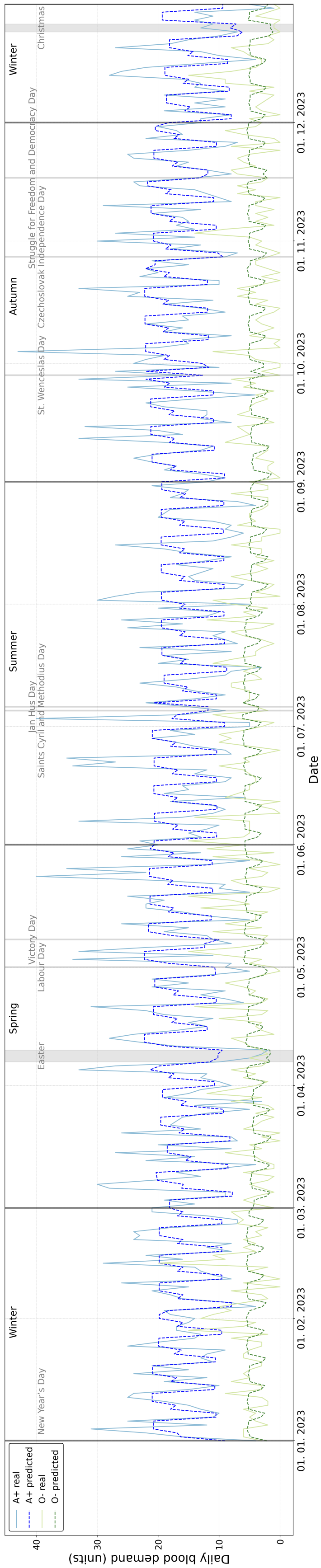

Fig. 2: Predicted and real values for both blood types over time

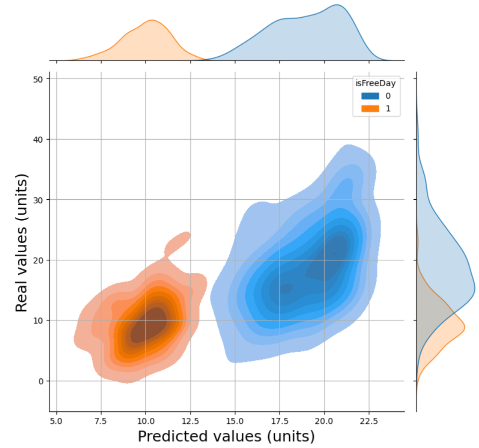

Fig. 3: A KDE plot comparing predicted and real values of blood demand for A+, with the values colored based on the classification of the day as either a working or non-working day.

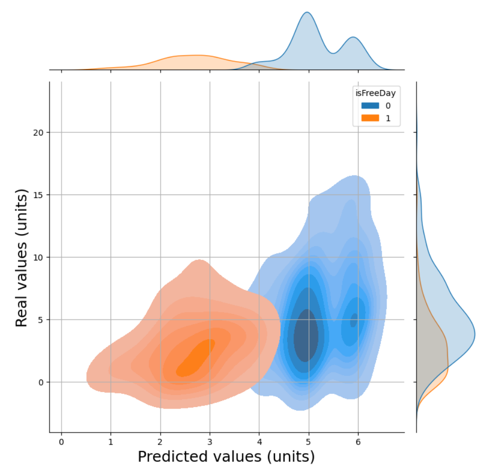

Fig. 4: A KDE plot comparing predicted and real values of blood demand for O-, with the values colored based on the classification of the day as either a working or non-working day.

on Mondays and Tuesdays, likely because patients are not admitted to the hospital over the weekend, and therefore surgeries are not performed on those days. In particular, all significant features for A+ have negative coefficients.

However, for O-, the coefficients for June and July are positive. According to the experience of Tissue and Histic Department, this could be related to a higher rate of car accidents or sports-related injuries during these months. O- is the universal donor type [11] and is commonly given to patients of all blood types in urgent cases with a risk of bleeding out.

C. Impact of COVID-19 pandemic on training data

A significant portion of the training dataset was collected during the COVID-19 pandemic. To find whether including 2021 in training is beneficial or not, some models were retrained on a dataset with 2021 data excluded. When tested on the 2023 dataset, the linear regression model for A+ and

TABLE II: Overview of selected features for individual models

Feature category	Feature	A+	O-
	Intercept	21.39	5.02
Days off	isWeekend	-2.2	
	isHoliday	-0.84	
	SchoolHoliday	-1.55	-0.33
	isFreeDay	-8.78	-1.92
	freeinRow	0.36	-0.38
	FreedaysCurrentWeek	0.31	0.07
	FreedaysPreviousWeek	-0.08	
	FreedaysNextWeek		
Influenza	JMK_pos_3weeksago	0.53	
	JMK_test_3weeksago		0.06
	CR_pos_3weeksago	-1.04	
	CR_test_3weeksago	0.44	
	JMK_function_3weeksago		-0.20
Day of the week	Monday	-3.00	
	Tuesday	-3.89	
	Wednesday		0.25
	Thursday		
	Friday		
	Saturday		0.61
	Sunday		
Calendar month	January		
	February		
	March	-1.71	-0.83
	April		
	May	0.64	0.46
	June		0.74
	July	0.02	0.91
	August		
	September		-0.56
	October	1.03	
	November		
	December	-2.17	-0.13

The number in each cell represents the linear regression coefficient for the corresponding feature, while the color of the cell indicates the p-value of the feature. Yellow means p-value under 0.05 representing statistically significant features. Gray means features that are not significant but still are improving model's performance. White-colored features were not selected during forward feature selection. The first row represents the intercept, which is the baseline value of the linear regression model.

O- achieved performances of 26.1% and 50.9%, respectively. In comparison to the results obtained using the full training dataset (26.2% for A+ and 50.4% for A-), it can be concluded that excluding COVID-affected data does not substantially alter the performance of the linear regression model. However, the performance of naive models deteriorated more significantly when the ”COVID years” were excluded. When the model was trained using data from 2022 and 2024, it resulted in a nMAE of 37% for A+ and 67% for O-. If the model relied solely on 2022 data, the performance was even worse: 40% for A+ and 75% for O-. This comparison suggests that, despite the distortion caused by the COVID-19 pandemic in the 2021 data, they still contribute to improving the models' performance.

IV. Conclusion

We developed predictive models to estimate the daily blood demand for two specific blood types, A+ and O-. The models trained using linear regression demonstrate how the demand for each blood type depends on different features, with varying performance for each blood type. Linear regression not only outperformed more sophisticated models, but is also the most practical choice for the given task. Its simple implementation and interpretability of results make it an ideal tool for use in the Transfusion and Tissue Department, where it can effectively serve to predict blood demand in practice.

Acknowledgment

This research was supported by the project RVO:68081731 by the Czech Academy of Sciences.

The data used in this study were provided by the Transfusion and Tissue Treatment Department, University Hospital Brno. We would like to express our sincere gratitude for their support and cooperation.

References

[1] PLESINGER, Filip, Stanislava KOSKOVA, Eniko VARGOVA, martina ADAMCOVA, Jan PAVLUS, Gabriela KOPECKOVA, Radovan SMISEK a Hana LEJDAROVA. Holiday Hemoglobin: How the Vacations Affect Blood Donations across Diverse Urban Sites [online]. In: . 2024, 2024-12-1, - [cit. 2025-03-11]. Available at: doi:10.22489/CinC.2024.075

[2] LI, Xiaofei, Xinyi DING, Helong GUO a Xiao ZHANG. Improved neural network for predicting blood donations based on two emergent factors. Transfusion Clinique et Biologique [online]. 2023, 30(2), 249-255 [cit. 2025-03-14]. ISSN 12467820. Available at: doi:10.1016/j.tracli.2023.01.006

[3] WANG, Yajie, Wei ZHANG, Quan RAO, Yiming MA, Xinyi DING, Xiao ZHANG a Xiaofei LI. Forecasting demands of blood components based on prediction models. Transfusion Clinique et Biologique [online]. 2024, 31(3), 141-148 [cit. 2025-03-14]. ISSN 12467820. Available at: doi:10.1016/j.tracli.2024.04.003

[4] W. McKinney, "Data Structures for Statistical Computing in Python," Proc. 9th Python Sci. Conf., pp.56–61, 2010.

[5] G. Van Rossum et al., "Python 3 Reference Manual," Nature, vol. 585, no. 7825, pp. 357–362, 2009.

[6] C. R. Harris et al., "Array programming with NumPy,"Nat. 2020 5857825, vol. 585, no. 7825, pp. 357–362, Sep. 2020.

[7] F. Pedregosa et al., "Scikit-learn: Machine learning in Python," J. Mach. Learn. Res., 2011.

[8] S. Seabold and J. Perktold, "Statsmodels: Econometric and Statistical Modeling with Python," in Proceedings of the 9th Python in Science Conference, 2010.

[9] J. D. Hunter, "Matplotlib: A 2D graphics environment," Comput. Sci. Eng., vol. 9, no. 3, pp. 90–95, 2007.

[10] STÁTNÍ ZDRAVOTNÍ ÚSTAV. Zprávy o chřipkové aktivitě, hlášení a výsledky laboratorních vyšetření [online]. [cit. 2025-03-14]. Available at: https://szu.gov.cz/temata-zdravi-a-bezpecnosti/a-z-infekce/ch/chripka/zprava-o-chripkove-aktivite-hlaseni-a-vysledky-laboratornich-vysetreni

[11] ČESKÝ ČERVENÝ KŘÍŽ. Jak darovat krev [online]. [cit. 2025-02-13]. Available at: https://web.archive.org/web/20090624015829/http://www.cckpraha1.cz/krev.htm

Analysis of Temporal Speech Impairments in Prodromal Dementia with Lewy Bodies

1st Anar Davaajargal
Department of Telecommunications
Brno University of Technology
Brno, Czech Republic
240146@vut.cz

2nd Krystof Novotny
Department of Telecommunications
Brno University of Technology
Brno, Czech Republic
ORCID: 0009-0005-7232-0841

***Abstract*—Dementia with Lewy bodies (DLB) is the second most common form of neurodegenerative dementia. The progressive deterioration of motor and cognitive functions, accompanied by behavioral changes, severely impacts the quality of life of affected individuals and those around them. Early diagnosis is therefore essential for timely intervention and appropriate treatment. Despite its possible clinical significance, research specifically addressing speech impairments in DLB remains limited. Acoustic analysis offers a cost-effective, non-invasive approach for paraclinical diagnosis, yet its potential in identifying DLB-specific speech patterns remains partially underexplored.**

This study investigates a key aspect of speech production—temporal parameters (related to speech tempo and pauses), with an extension into the linguistic domain. Statistical evaluation was conducted using the Mann-Whitney U test and descriptive analysis. Notable discriminatory power in differentiating the prodromal DLB group from healthy controls was observed for parameters such as *MWPM of Longer Words*, *Median Pause Length*, *Occurrence of Repeated Words*, and *Net Speech Rate*, particularly in the monologue task, which exhibited greater effectiveness compared to the text-reading task. This analysis underscores the potential utility of temporal speech parameters for the early detection of DLB while also introducing and evaluating novel custom metrics tailored for this purpose.

***Index Terms*—acoustic analysis, dementia with Lewy bodies, temporal speech parameters, digital speech biomarkers**

I. Introduction

Dementia with Lewy bodies (DLB) is recognized as the second most prevalent neurodegenerative dementia (estimated to affect up to 22.8% of individuals with dementia), following Alzheimer's disease (AD). It progresses faster and has a wider range of symptoms, resulting in lower quality of life and shorter life expectancy for patients. DLB uniquely manifests a combination of cognitive decline, characteristic of AD, and motor dysfunction, akin to Parkinson's disease (PD), leading to challenges in accurate diagnosis and treatment. This overlap often results in misdiagnosis, complicating patient management and delaying appropriate interventions [1].

Speech impairments have been reported as a notable symptom in DLB, encompassing reduced speech fluency, prolonged pauses, and slowed speech rate [2]–[5]. However, these speech characteristics remain underexplored as potential diagnostic markers. Moreover, since linguistic diagnostic tools are language-dependent, there is a knowledge gap concerning the temporal speech analysis of early DLB with respect to the Czech language. Given the non-invasive and cost-effective nature of acoustic analysis, investigating speech patterns offers a promising avenue for early detection of DLB. Identifying specific speech parameters associated with DLB could enhance diagnostic accuracy, facilitating timely and targeted therapeutic strategies.

This study aims to contribute to a deeper understanding of speech impairments in DLB through acoustic analysis of temporal aspects of speech (tempo and pauses), which may reflect difficulties in word retrieval, impaired semantic verbal fluency, and reduced grammatical flexibility.

A. State of the art

The number of studies examining the speech of DLB patients is relatively limited. Previous works have highlighted significant temporal speech impairments in DLB, particularly slowed speech rate and increased number of pauses. DLB patients often speak more slowly and spend considerably more time in silence compared to other groups [2]–[5]. For example, Ash et al. 2011 found that DLB patients have a significantly lower speech rate than Parkinson's disease (PD) patients or healthy controls (HC), with DLB speakers spending more than one-third of their speech time in silent pauses (far exceeding PD or HC levels) [2]. Such dysfluency has been repeatedly observed in DLB and is thought to reflect the combined impact of cognitive-linguistic deficits and parkinsonian motor slowing [1], [3]. In contrast, AD has been reported to show milder or mixed results in these prosodic measures (e.g., pause duration, speech rate) and instead exhibits relatively greater impairments in lexical and semantic content [3]. Direct comparative analyses presented by Yamada et al. 2022 confirm divergent profiles: DLB speech shows more severe prosodic/acoustic deviations (slower rates, longer silences, monotonous intonation), whereas AD speech is characterized by higher-level linguistic deficits [3].

Digital speech biomarkers have emerged as valuable tools for quantifying and monitoring these impairments. Machine-learning models using multi-dimensional speech features (rate, pause metrics, etc.) have been reported to reliably distinguish DLB from AD and healthy aging [3]. Automated analyses of speech have also revealed that the duration of pauses increases progressively from healthy controls to mild and moderate dementia [6]. Although this study does not focus directly on DLB, its findings may be beneficial to our research because the number of studies longitudinally addressing speech in DLB is minimal. As reported by Ash et al. 2016, longitudinal evidence in Lewy body disorders shows similar results. As cognitive decline advances, speech becomes significantly slower and less fluent over time [2]. These findings underscore the potential of objective speech analytics as a non-invasive means to monitor DLB-related decline and to differentiate DLB from other neurodegenerative diseases.

II. Methodology

A. Database

The study corpus consists of three distinct cohorts according to their respective diagnoses.

- preDLB – patients in the prodromal stage of DLB,
- NonHC – individuals without cognitive deficits but who have abnormal values on one of the scales examined, e.g., RBDSQ, UPDRS, etc. (also referable to as the ”grey zone”),
- HC – healthy controls.

Individuals with prodromal DLB were diagnosed based on the criteria published in [7]. The study participants were recorded in the Applied Neuroscience group of the Central European Institute of Technology as part of project no. LX22NPO5107 (MEYS): Financed by the European Union – Next Generation EU. All study participants signed an informed consent form and the study was approved by the local ethics committee.

Table I provides statistics on the age distribution of the groups, including sex. The Mann-Whitney U test showed an imbalance in the age distribution of the analysed cohorts (preDLB vs NonHC: $p = 0.0025$; preDLB vs HC: $p = 0.0185$). The preDLB group is significantly older than the other two groups. This disparity needs to be dealt with because age manifests itself in the human voice, so it would introduce a bias in the observed parameters. The Chi-squared test calculated over the sex distributions within the three cohorts showed no significant differences.

TABLE I
PARAMETERS WITH $p < 0.05$ (PREDLB VS. HC)

Group	*n*	$\bar{x}$	s	X_{min}	*Me*	X_{max}
preDLB	45	69.88	6.38	54.36	71.19	81.33
Males	22	71.78	5.09	59.82	71.49	81.33
Females	23	68.07	7.04	54.36	70.58	76.15
NonHC	41	65.49	7.09	50.54	65.78	79.51
Males	11	67.28	6.76	55.94	67.23	78.59
Females	30	64.84	7.20	50.54	65.65	79.51
HC	55	67.29	6.03	55.67	66.68	83.10
Males	24	67.18	5.18	58.79	66.35	75.62
Females	31	67.38	6.70	55.67	67.42	83.10

B. Speech recording

This study utilizes speech recordings from a dataset created using the CoBeN speech acquisition protocol [8]. The first and second tasks (TSK1 and TSK2) out of a total of 17 tasks were considered to be the most suitable for the calculation of temporal parameters.

TSK1 consists of a monologue that should last at least 90 s without physician intervention. The speakers are instructed to talk about their hobbies, family, occupation, current activities, etc. This task examines speakers' ability to produce a meaningful commentary, i.e. a real-time production of the content itself and its reproduction through speech is required here.

TSK2 requires the speaker to read a short text, which they have time to prepare before recording. This task is therefore more focused on multimodality, linking written text with speech production.

C. Speech parametrization

Based on various studies that examined impairments related to DLB [9]–[11], a set of relevant temporal parameters was selected:

- *Word Count* – total word count
- *Utterance Duration* – duration of the speech
- *WPM* – number of words per minute
- *MWPM* – WPM without the pauses
- *Net Speech Rate* – total syllable count divided by the duration of speech without the pauses
- *Speech Tempo* – number of syllables per second divided by the duration of the speech
- *Pause Duration* – total length of pauses
- *Pause Duration Rate* – total pause length divided by the duration of the speech
- *Pause Frequency* – number of pauses divided by the duration of the speech
- *Pause Occurrence* – number of pauses divided by the total syllable count
- *Average Pause Duration* – total pause length divided by the number of pauses
- *Median Pause Duration* – median length of pauses

In addition to the parameters derived from the aforementioned studies, a set of original parameters was developed for this study based on the hypotheses of expected speech disorder manifestations:

- *The Longest Pause Duration* – length of the longest pause
- *Occurrence of Repeated Words* – number of repeated words divided by total word count
- *MWPM of Longer Words* – MWPM of three or more syllabic words
- *Pause Duration Slope* – slope of the linear regression line tracing the evolution of pause lengths

Almost all of the proposed parameters are applicable to both investigated tasks; however, due to the nature of the task, measuring the *Word Count* and *MWPM* was not meaningful for TSK2. In total, 30 parameters are tested on each participant.

The detection of pauses was carried out using the *pyAudioAnalysis*[1] library. For pause analysis, a semi-supervised segmentation function was used to identify the silent parts. This function utilizes a support vector machine (SVM) model to distinguish between frames with high and low sound energy.

The *SpeechRecognition*[2] library was selected to analyze the parameters related to the word count calculations. From the supported models, Google Speech Recognition was utilized to obtain audio transcriptions.

The segmentation of text into syllables was performed using the sekacek.py[3] program, which was modified to ensure proper compatibility with the proposed codes. The program is designed to divide Czech text into syllables by applying rules for machine-based syllabification in the Czech language.

D. Statistical analysis

The raw data first had to be adjusted for covariates. The age distributions within the three investigated cohorts are significantly imbalanced. There is no significant bias due to sex, however, sex is still present in human speech, so mathematical removal of its influence helps the overall compactness of the analyzed data. The calculated metrics were therefore adjusted for covariates using linear regression. The next step involved computing descriptive statistics based on the adjusted data for each group.

To assess the discriminative power of the proposed parameters, the nonparametric Mann-Whitney U test was applied. The comparisons included all possible group pairings: HC vs. NonHC, preDLB vs. HC, and preDLB vs. NonHC. The first scenario was conducted to determine whether the HC and NonHC groups could be merged for comparison with the preDLB cohort. Numerous measurable parameters, primarily related to speech pauses, indicated a probable disruption in speech fluency within the NonHC cohort. Therefore, the HC and NonHC groups are not compatible and thus based on this finding, the prodromal DLB cohort was analysed separately compared to each of the groups.

III. Results

A. Mann-Whitney U test

In Tables II and III, the selected parameters are ranked in ascending order according to their p-values. The significance level was set at $\alpha = 0.05$. However, it should be noted that none of the parameters analyzed in any of the scenarios came out as significant after False Discovery Rate correction (Benjamini-Hochberg).

B. Descriptive statistics

Tables IV and V present specific results of the descriptive statistics parameters with $p < 0.05$ for both scenarios of the preDLB group. The medians are compared for the following discussion and conclusions.

[1]GitHub: https://github.com/tyiannak/pyAudioAnalysis
[2]GitHub: https://github.com/Uberi/speech_recognition
[3]GitHub: https://github.com/Gldkslfmsd/sekacek

TABLE II
Parameters with $p < 0.05$ (preDLB vs. HC)

Parameter	p-value
MWPM of Longer Words (TSK1)	0.0055
Occurrence of Repeated Words (TSK1)	0.0354
Net Speech Rate (TSK1)	0.0367
Average Pause Duration (TSK2)	0.0483
MWPM (TSK2)	0.0491
Net Speech Rate (TSK2)	0.0499

TABLE III
Parameters with $p < 0.05$ (preDLB vs. NonHC)

Parameter	p-value
MWPM of Longer Words (TSK1)	0.0098
Median Pause Duration (TSK1)	0.0178
Net Speech Rate (TSK1)	0.0493

TABLE IV
Results of descriptive statistics (preDLB vs. HC)

Parameter	preDLB	$\neq$	HC
MWPM of Longer Words (TSK1)	35.62	$<$	41.48
Occurrence of Repeated Words (TSK1)	0.00666	$>$	0.00661
Net Speech Rate (TSK1)	4.68	$<$	5.22
Average Pause Duration (TSK2)	0.484	$<$	0.527
MWPM (TSK2)	176.13	$<$	194.11
Net Speech Rate (TSK2)	5.18	$<$	5.70

TABLE V
Results of descriptive statistics (preDLB vs. NonHC)

Parameter	preDLB	$\neq$	NonHC
MWPM of Longer Words (TSK1)	35.62	$<$	42.59
Median Pause Duration (TSK1)	0.95	$>$	0.76
Net Speech Rate (TSK1)	4.68	$<$	5.33

IV. Discussion

A comprehensive analysis of both scenarios for the preDLB cohort reveals that the TSK1 parameters exhibit a higher discriminatory power. In the preDLB vs. HC scenario, all three parameters with the best results, achieving significant p-values, are measured in the monologue task. The same applies to the preDLB vs. NonHC scenario. This finding may indicate deficits in cognitive functions that contribute to greater impairments in grammar, executive functions, memory, semantics, and comprehension compared to both HC and other disorders within the Lewy body spectrum disorder (LBSD) family, as concluded by studies [9] and [12]. These types of deficits evidently make fluent speech significantly more challenging for the preDLB cohort, as they must generate content in real-time. To further investigate this phenomenon, it would be beneficial to utilize insights from a task that requires participants to retell a read story, similar to the approach used in the aforementioned study [9].

Regarding individual parameters, the parameter *MWPM of Longer Words (TSK1)*, which was introduced and developed in this study, achieved significant results. In both scenarios comparing the preDLB group, it yielded the best results, with values of $p < 0.01$, indicating exceptionally strong discriminatory power. The speech production of both HC and NonHC cohorts contains a significantly higher proportion of longer and more complex words during monologue, once again implying impaired cognitive abilities in preDLB. Another parameter with remarkable results in both scenarios is *Net Speech Rate* for TSK1. In the preDLB vs. HC scenario, this parameter is also among the significant ones for TSK2. A slower syllable production rate, objectively emphasized by the exclusion of pauses, probably indicates the contribution of motor impairments, which DLB shares with other disorders within the LBSD family. Furthermore, there appears to be a noticeable difference in pause durations. The parameter *Median Pause Duration* was higher for TSK1 in the preDLB group across both scenarios (although it did not reach the significance level in the preDLB vs. HC scenario, it achieved acceptable results in the Mann-Whitney *U* test, which were further confirmed by descriptive statistics). This suggests that during monologue tasks, hesitations or silences spent formulating content were longer.

Considering the parameters significant for each group individually, *Occurrence of Repeated Words*, a newly introduced parameter, shows substantial discriminatory power in the preDLB vs. HC comparison. The hypothesis was confirmed that patients with DLB would repeat words more often due to difficulties in naming objects and finding the correct terms, similar to AD [13]. The *Average Pause Duration* is another significant parameter. The preDLB group has shorter pauses than HC for TSK2. At first glance, this result might seem contrary to expectations; however, another statistically significant parameter, *MWPM*, from the same scenario and task helps provide a clearer understanding of the reading pattern. This means that the overall reading pace of HC, after excluding pauses, is significantly higher. The low average pause durations, combined with the lower *MWPM* in the preDLB group, may suggest an unnatural monotony in their reading (e.g., manifesting in a lack of dramatic pauses, etc.). *MWPM* (along with its variation) has proven to be an important parameter for this area of interest, as in the study [9].

Lastly, the preDLB vs. NonHC scenario highlights a certain significance of a newly tested parameter, *The Longest Pause Duration (TSK2)*, which is noticeably greater in the preDLB group during reading. Theoretically, this could be attributed to attention deficits, as mentioned in [13].

The study was primarily limited by the small database, as the parameters were tested on a sample of only 45 patients in the prodromal stage of DLB. Interesting results could potentially be achieved through the use of the automated analysis of the study [14], which considers different types of pauses and incorporates respiratory-related metrics. More precise results could also be obtained through an additional analysis of the discriminatory power of all metrics as a whole, using machine learning.

V. Conclusion

This study explored acoustic speech analysis for early-stage DLB detection on the Czech dataset. Key parameters, including *MWPM of Longer Words* and *Net Speech Rate*, showed strong discriminatory power. Newly introduced metrics, describing the temporal domain overlapping to the linguistic area, proved valuable. Despite a small sample size, results suggest that temporal speech analysis could aid early diagnosis. Future work should refine methods with larger datasets, implement more measures describing the linguistic sphere, and possibly test on the multilingual cohorts.

References

[1] M. Kobayashi, Y. Yamada, K. Shinkawa, M. Nemoto, M. Ota, K. Nemoto, and T. Arai, "Vocal expression of emotions discriminates dementia with lewy bodies from alzheimer's disease," *Alzheimer's dementia : diagnosis, assessment disease monitoring*, vol. 16, no. 2, pp. e12 594–n/a, 2024.

[2] S. Ash, C. McMillan, R. G. Gross, P. Cook, D. Gunawardena, B. Morgan, A. Boller, A. Siderowf, and M. Grossman, "Impairments of speech fluency in lewy body spectrum disorder," *Brain and language*, vol. 120, no. 3, pp. 290–302, 2012.

[3] Y. Yamada, K. Shinkawa, M. Nemoto, M. Ota, K. Nemoto, and T. Arai, "Speech and language characteristics differentiate alzheimer's disease and dementia with lewy bodies," *Alzheimer's dementia : diagnosis, assessment disease monitoring*, vol. 14, no. 1, pp. e12 364–n/a, 2022.

[4] S. Ash, C. McMillan, R. G. Gross, P. Cook, B. Morgan, A. Boller, M. Dreyfuss, A. Siderowf, and M. Grossman, "The organization of narrative discourse in lewy body spectrum disorder," *Brain and language*, vol. 119, no. 1, pp. 30–41, 2011.

[5] S. Shellikeri, S. Cho, M. Y. Liberman, E. Howard, Y. Balganorth, D. Weintraub, E. B. Lee, J. Q. Trojanowski, D. J. Irwin, M. Grossman, and N. Nevler, "Automatic analysis and validation of digitized speech markers in lewy body spectrum diseases with alzheimer's disease co-pathology," *Alzheimer's dementia*, vol. 17, no. S4, p. n/a, 2021.

[6] R. A. Sluis, D. Angus, J. Wiles, A. Back, T. A. Gibson, J. Liddle, P. Worthy, D. Copland, and A. J. Angwin, "An automated approach to examining pausing in the speech of people with dementia," *American journal of Alzheimer's disease and other dementias*, vol. 35, pp. 1 533 317 520 939 773–1 533 317 520 939 773, 2020.

[7] I. G. McKeith, T. J. Ferman, A. J. Thomas, F. Blanc, B. F. Boeve, H. Fujishiro, K. Kantarci, C. Muscio, J. T. O'Brien, R. B. Postuma *et al.*, "Research criteria for the diagnosis of prodromal dementia with lewy bodies," *Neurology*, vol. 94, no. 17, pp. 743–755, 2020.

[8] "Standardized protocol for language and acoustic assessment and analysis," 2018. [Online]. Available: https://coben.ceitec.cz/download/154

[9] S. Ash, C. McMillan, R. G. Gross, P. Cook, D. Gunawardena, B. Morgan, A. Boller, A. Siderowf, and M. Grossman, "Impairments of speech fluency in lewy body spectrum disorder," *Brain and language*, vol. 120, no. 3, pp. 290–302, 2012.

[10] G. Gosztolya, R. Balogh, N. Imre, J. V. Egas-Lopez, I. Hoffmann, V. Vincze, L. Tóth, D. P. Devanand, M. Pákáski, and J. Kálmán, "Cross-lingual detection of mild cognitive impairment based on temporal parameters of spontaneous speech," *Computer Speech & Language*, vol. 69, p. 101215, 2021.

[11] J. Rusz, J. Hlavnička, M. Novotnỳ, T. Tykalová, A. Pelletier, J. Montplaisir, J.-F. Gagnon, P. Dušek, A. Galbiati, S. Marelli *et al.*, "Speech biomarkers in rapid eye movement sleep behavior disorder and parkinson disease," *Annals of neurology*, vol. 90, no. 1, pp. 62–75, 2021.

[12] S. Ash, C. York, T. Bisbing, N. Min, O. Kofman, and M. Grossman, "Longitudinal decline in speech fluency in lewy body spectrum disorder (s35. 005)," 2016.

[13] B. Klimova and K. Kuca, "Speech and language impairments in dementia," *Journal of Applied Biomedicine*, vol. 14, no. 2, pp. 97–103, 2016.

[14] J. Hlavnička, R. Čmejla, T. Tykalová, K. Šonka, E. Ržička, and J. Rusz, "Automated analysis of connected speech reveals early biomarkers of parkinson's disease in patients with rapid eye movement sleep behaviour disorder," *Scientific reports*, vol. 7, no. 1, p. 12, 2017.

Wildlife Tracking System

1st Bc. Jakub Zdražil
Faculty of Electrical Engineering and Communication
Brno University of Technology
Brno, Czech Republic
230917@vut.cz

2nd Ing. Pavel Paluřík
Faculty of Electrical Engineering and Communication
Brno University of Technology
Brno, Czech Republic
xpalur01@vut.cz

***Abstract*—The aim of this work is to design a battery-powered IoT device to be placed on snap traps for wildlife trapping. The use of this device aims to simplify and streamline the work of the forest administration. The device, whose functions are controlled by an ESP32 microcontroller, is connected to the network using NB-IoT technology, specifically CatM-2 technology and the corresponding SIM card. This allows the device to operate seasonally and without the need to pay flat fees, as is the case with competing devices. The device also allows the recognition of captured animals based on their weight, which will reduce the number of incorrect trap triggers and thus allow the forest management to capture only a narrower range of animals. At the same time, however, unlike devices that take photographs or videos, the amount of data to be transmitted is reduced.**

***Index Terms*—Wildlife, snap trap, IoT, hardware design, LTE CatM, NB-IoT, ESP32**

I. Introduction

Hunting may seem uninteresting or unnecessary to many today, but the opposite is true. For generations, hunters have helped maintain the balance and safety of animal populations near human settlements. Part of this involves controlling so-called nuisance species-both native animals and species introduced by human activity. Especially the introduced ones can pose a threat, as they often lack natural predators and spread rapidly.

One method of control is culling, but this approach has its limits. It cannot be done near homes due to safety risks, and it may seem inhumane to some. It is also time-consuming, requiring hunters to spend hours waiting for animals.

A more efficient method is trapping, most often using snap traps - cages with mechanisms that close when an animal enters. The animal can then be relocated or humanely euthanized. This method is safer for people and saves hunters time. However, animals may still suffer stress if left in traps for long periods. Since hunters cannot constantly monitor traps and quiet surroundings are needed, they often check them only every few days.

The goal of this work is to develop a device that can be attached to the trap and notify the hunter via a suitable communication method when an animal is caught.

II. Commercially available devices

The first and quite logical option is the use of so-called trail cameras. These devices are very widespread and popular among hunters because their price has been relatively cheap in recent years, making them an affordable alternative. The disadvantage of these trail cameras is their short battery life per charge in a mode that sends photos from the location to the user. The second disadvantage is their higher data consumption and therefore increased operating costs in terms of data consumed, which in many cases also has to be paid when the device does not have to be in use for a longer period of time.

A total of three devices have been found that are very similar in function and focus to the concept of this device:

- **OcuTrap [1]** - This device, currently in pre-order status, offers a complete solution including trap and camera. While this makes the whole deployment process easier, the user is limited by the uniform size of the trap and the relatively high purchase price.
- **Remoti Systems [2]** - The device from US manufacturer Remoti Systems has the longest lifetime per charge of the three devices - up to five years, according to the manufacturer. It uses limit switches to detect animals inside the trap. However, there is not much information about its availability and price.
- **Skyhawk Kiwi [3]** - It is the most comprehensive product of all these devices with a range of accessories and variants. It uses a magnetic sensor and an accelerometer to detect the animal in the trap.

However, all devices have several disadvantages. The first one is the need to purchase a subscription, without which the device cannot be used, The subscription includes charges for the relevant SIM card. These subscriptions often have to be paid even when the device is not in active use. The second disadvantage is the inability of these devices to recognise a captured animal. Thus, conventional mechanical traps are often triggered unjustifiably by wind gusts or the movement of small animals such as rodents. The ability to detect the captured animal would minimize the number of such false captures.

III. System design

A. Hardware Design

As the device will be located away from any mains power, emphasis has been placed on its low power consumption and optimisation for battery power.

For power supply, a set of Li-ion batteries type 18650 with a capacity of 2500 mAh and with the appropriate charging and protection circuits was chosen. The reason for this is their easy availability - the user can simply purchase new batteries in case of reduced capacity. Another advantage is the ease of use and recharging. The device can be recharged via the USB-C port on the circuit board, but more often than not, the device is expected to be deployed on site longer than the battery capacity will last. In this case, it is more practical to replacethe batteries on-site than to carry the entire device. Replacing and recharging these batteries is also easy for the average user thanks to the widely available chargers. A dual 18650 battery design was chosen to achieve longer battery life per charge. Using a single battery with a higher capacity would make on-site replacement difficult.

The main microprocessor ESP WROOM 32E [4], which takes care of most of the functions in the device, is connected to the other peripherals of the device. One of its main advantages is that it has sufficient power to enable the device to communicate with all intended peripherals, especially the NB-IoT module. Another important feature of this microcontroller is its low power consumption in deep sleep, when it is in the order of tens of μA. The processor is clocked at up to 240 MHz. The ESP32 specification lists up to 34 GPIO (General Purpose Input Output) pins that can be configured in different ways depending on the application. However, for the ESP32-WROOM-32E module, 26 GPIO pins are output on the physical pins of the module, which corresponds to some GPIO pins being used internally (e.g., for SPI flash) and not available on the connectors.

The device is connected to the network using NB-IoT (Narrow Band - Internet of Things) technology. Using this technology, it sends data to a server, which the user then connects to using their own user terminal. This user terminal means a smartphone or computer. The connection to the network is provided by the BG77 module from Quectel [5]. The module supports both CatM1 and CatM2 technology. It also contains a GNSS module supporting GPS (Global Positioning System), GLONASS (Globalnya Navigacionaja Sputnikovaja Systema), Galileo, Beidou and QZSS (Quasi-Zenith Satellite System), which provides the device or user with information about the location of the trap. The user should also be able to communicate back to the device to change some of the setting parameters without the need for physical access.

The device is also connected to the HX711, a 24-bit ADC (Analog to Digital Converter). This has a higher noise immunity and higher accuracy compared to the dedicated ADC in the ESP32 module. Connected to this ADC are YZC-131 strain gauge sensors, which periodically measure the weight of the trap and are therefore able to detect the presence of an animal in the trap.

The SG90 servo motor is responsible for lowering the trap door, which ensures the release of the mechanism and trapping the animal inside the trap.

The DS18B20 temperature sensor monitors conditions in the immediate environment. This gives the user sufficient information to assess how long the animal is able to stay in the trap. This temperature sensor operates on 1-Wire technology, which allows data transmission over only one wire [6].

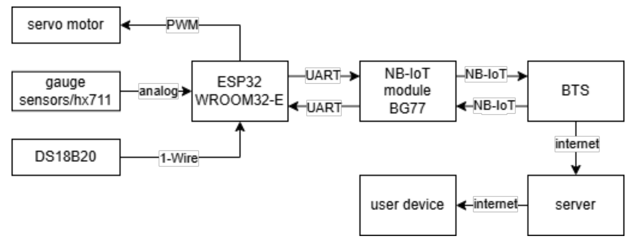

Fig. 1. A simplified diagram of the system's operation

B. PCB design [7]

A four-layer PCB (SIG, GND, PWR, SIG) was chosen for this project. The top and bottom layers serve for signal transmission, the other two layers serve as ground and power supply respectively.

As mentioned, a set of 18650 batteries will power the device. The batteries are protected against overvoltage by a MOSFET transistor. The battery can be charged by an external charger or by using the USB-C connector that is part of the PCB board, which also has additional features that will be explained below. The connector supplies USB standard signals such as VBUS, DP, DN and GND to the board. Charging and proper discharging of the battery is handled by the MCP73871-3CCI/ML integrated circuit. The circuit allows control of the battery charging and discharging current, and also includes battery protection and a temperature sensor that disconnects the battery when it overheats. The integrated circuit includes three outputs to monitor battery status and charging status.

For this particular application, the exact value of the battery status is also important. The MAX17048G+ module takes care of monitoring the exact battery status. This module transmits battery status information to the ESP32 microcontroller via the I2C serial bus.

The individual components of the device operate at a total of three different voltage levels:

- **5 V** - servo motor and gauge sensors
- **3.3 V** - ESP32
- **1.8 V** - BG77 and its peripheries - SIM (Subscriber Identity Module)

Conversion to 1.8V is handled by the MCP1802T-1802I/OT voltage regulator. In the case of 3.3 V and 5 V values, due to the voltage range allowed by the 18650 battery, it is necessary to use a buck-boost source with a corresponding output. This is achieved by using a pair of TPS63021DSJR buck-boost converters.

Unlike the ESP32 module, the BG77 module does not have integrated antennas. Their connection must therefore be made in the form of an external antenna, which is connected to the U.FL-R-SMT connector. The BG77 module allows several forms of communication. It contains a total of three separate UART (Universal asynchronous receiver-transmitter) outputs for the purposes of debug communication, sending GNSS data and main communication with the ESP32 module using AT commands. The GNSS data can be sent via the main UART with the correct sequence of AT commands, for debug and firmware update purposes the aforementioned USB-C connector and corresponding USB communication is used.

The ESP32 module connects all other peripherals to form a single functional unit. The UART and any external USB-UART converter are used for firmware upload.

The virtually generated PCB is visible in Fig.2

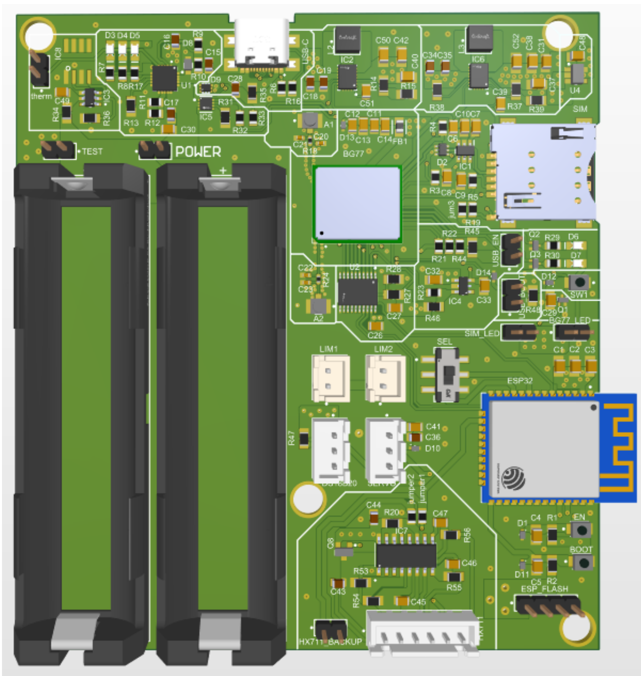

Fig. 2. Virtually generated PCB structure

C. Housing design

It is evident from the application that the equipment will be placed outdoors, thus exposed to all kinds of weather conditions, and the design of the housing must also correspond to this.

The initial proposal was for a process, which would make it impossible or at least difficult to damage or steal equipment. This would involve connecting peripherals (sevo motor, temperature and weight sensors) via an extended cable, which would then allow the device to be placed, for example, on a tree trunk at a height that would prevent easy access. However, this solution was rejected during the design of the initial device concept as such a solution is not offered in all situations. However, the addition of this solution is relatively simple.

The design of the housings will therefore be primarily concerned with placement on the trap body itself.

3D printing was chosen as the production process. Only basic protection is envisaged for the purpose of testing the device under ideal weather conditions. In the case of longer-term use, the 3D product can be coated accordingly to ensure sufficient resistance, especially against rain.

Another option is to use commercially available, waterproof boxes, but this solution is beyond the scope of this paper.

The individual weight sensors will be placed on a false floor that will be placed on the existing floor inside the trap. This is because the trap itself in some cases takes on a high weight, thus reducing the mechanical strength requirements of the whole structure. A total of four sensors will be used and placed in each corner.

D. Software design

In particular, the software should provide for the lowest possible energy consumption of the equipment, while at the same time allowing for easy operation of the equipment at the installation site to speed up the process of placing and commissioning the trap.

In the considered design of the device, it is assumed that the basic functions of the device are controlled by a switch with three positions:

- **off** - in this position the device will be switched off, no communication is taking place or activity on the device
- **settings** - in this position the WiFi module of the microcontroller will be activated in the AP (Access Point) mode. The user will thus be able to perform device settings at the destination directly on the device.
- **trap mode** - in this switch position, the device deactivates its access point for maximum power conservation and will be ready for full operation

The intended logic of the program is clear from Fig. 3 and Fig. 4.

The battery status is continuously monitored and the user is informed of this value at regular intervals. If the batteries are removed, the entire device is reset. The individual settings, both system and user, remain present in the ESP32 memory.

C was chosen as the programming language because it is supported by the chosen ESP32 microcontroller and provides sufficient support and a selection of suitable libraries.

E. Server design

The server is an important component in the whole system as it provides communication between the user and the device. The MQTT (MQ Telemetry Transport) protocol was chosen as the primary protocol for communication between the device and the server. This is a lightweight network protocol that allows a group of devices to connect to a specific server. By subscribing to a given message type (topic), devices then receive only the specific messages whose content is relevant to them. This can simplify the setup of devices if there are a large number of them in one location.

Home Assistant was then chosen as the test platform for the server itself. It is an open-source server platform based on the Linux operating system. Home Assistant is already supported by both of the most widely used mobile phone operating systems in the form of corresponding applications, and also offers a web browser version. A number of features are

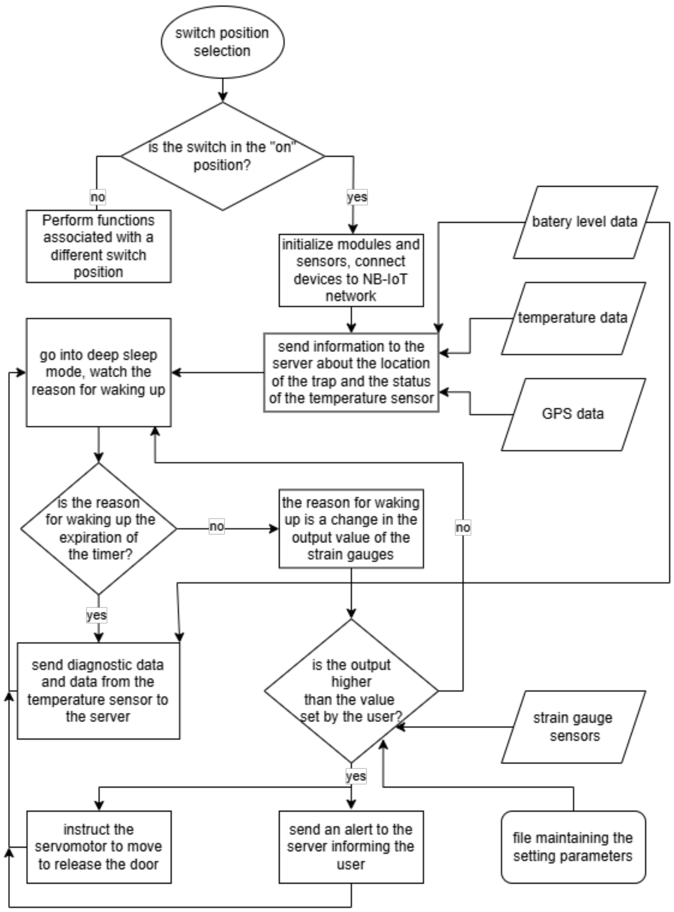

Fig. 3. Schematic of program logic in device operating mode

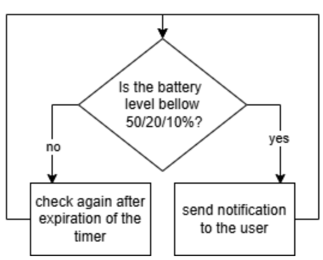

Fig. 4. Schematic of program logic responsible for battery management

available, such as the ability to send push notifications to the mobile device (Fig. 5). The InfluxDB database was chosen for data storage, while Grafana was chosen for displaying those stored data. Both of these platforms can be easily implemented in the Home Assistant system and allow them to work together. In the next phase of development, a custom server platform can be developed.

IV. Conclusion

This article discusses the development of an IoT device used to monitor wildlife traps. The article discusses the motivation and reasons for developing such a device. The device will enable better management of these traps by forest service

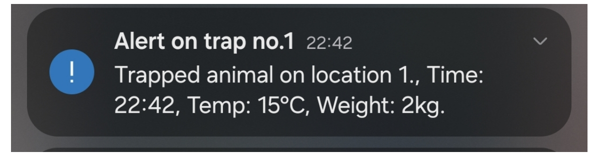

Fig. 5. Push notification on Android system

personnel and ordinary hunters. It will also help to reduce the time an animal is trapped to the shortest possible time. This avoids excessive suffering for the trapped animal.

Next, the article discusses the development of PCBs. A four-layer PCB board design with a pair of 18650 batteries was chosen. The individual components and their functions are described in chapter III-B.

Cat-M technology has been chosen as the main communication technology, which provides sufficient coverage for this application in the Czech Republic and offers a suitable communication form in terms of tariff price.

The C language was chosen for the software development as it provides sufficient support both in the form of available libraries and in the form of support from the perspective of the ESP32 microcontroller used.

To verify the capabilities of the server part of the system, the Home Assistant platform was chosen, which also allows connection with the InfluxDB database program and the Grafana graphic program.

V. Future Work

Further development of the project will be aimed at:

- software development and debugging
- server database with user UI
- PCB assembly
- creation of housing for complete equipment
- creating mounts for strain gauge sensors and servo motor

References

[1] OCUTRAP. *OcuTrap*. Online. Dostupné z: https://ocutrap.com/. [cit. 2024-10-08].

[2] REMOTISYSTEMS. *Remoti*. Online. Dostupné z: https://www.remotisystems.com/. [cit. 2024-10-08].

[3] TRAPMATE. *Skyhawk Trapmate*. Online. Dostupné z: https://trapmate.ai/. [cit. 2024-10-08].

[4] *ESP32-WROOM-32E: Datasheet Version 1.7*. Online. In: ESSPRESSIF. 2024. Dostupné z: https://www.espressif.com/sites/default/files/documentation/esp32-wroom-32e_esp32-wroom-32ue_datasheet_en.pdf. [cit. 2024-11-19].

[5] *Quectel BG77: Ultra-Compact LTE Cat M1/Cat NB2 Module*. Online. In: . 2020. Dostupné z: https://www.mouser.com/datasheet/2/1052/Quectel_BG77_LPWA_Specification_V1.2-1829934.pdf?srsltid=AfmBOoqHrdtJV09KMEoxeF5kgJNpvv_OBIUTxJcRD0araXdA5Z6HAxcu. [cit. 2024-11-19].

[6] *DS18B20: Programmable Resolution 1-Wire Digital Thermometer*. Online. In: Analog Devices. 2019. Dostupné z: https://www.analog.com/media/en/technical-documentation/data-sheets/DS18B20.pdf. [cit. 2024-11-19].

[7] ŠANDERA, Josef. *Návrh plošných spojů pro povrchovou montáž*. Praha: BEN - technická literatura, 2006. ISBN 80-730-0181-0.

Design of an inter-satellite communication and ranging payload for a rendezvous and proximity operations mission

Alexander Bekeč
Department of Radio Electronics
Brno University of Technology
Brno, Czech Republic
xbekec00@vut.cz

Jiří Veverka
Department of Radio Electronics
Brno University of Technology
Brno, Czech Republic
xvever12@vut.cz

Jan Gromeš
Department of Satellite Systems
VZLU AEROSPACE, a.s.
Brno, Czech Republic
gromes@vzlu.cz

***Abstract*—This paper presents the design of an inter-satellite communication and round-trip time-of-flight ranging payload for a rendezvous and proximity operations mission, based around the commercial off-the-shelf transceiver SX1280 by Semtech. The payload is designed to operate in the S-band *Space Operations* frequency band (from 2.20 to 2.29 GHz), with the ISM band (from 2.4 to 2.5 GHz) available for ground testing.**

***Index Terms*—inter-satellite communication, crosslink, ranging, round-trip time-of-flight, satellite payload, rendezvous and proximity operations**

I. Introduction

The use of low-power modulation techniques, especially LoRa, has been gaining on popularity in the field of satellite communications in recent years. In comparison to more traditional modulation techniques, it often provides much better link budget characteristics, better interference resilience [1] and better Doppler shift resilience (allowed frequency drift up to a quarter of the bandwidth [2]).

Several satellite missions have already implemented LoRa-based communications, primarily in the VHF (e.g. SWARM or STARLINK) and UHF bands (e.g. FOSSASAT, NORBY, TIANQI, V-R3X or PY4), for uplink and downlink, as well as satellite IoT services [3].

In addition to the UHF communication capabilities, Semtech's SX1280 transceivers were also integrated on-board V-R3X satellites [4], successfully operating in the non-nominal *Space Operations* band at the frequency of 2.2236 GHz [5]. They were also implemented in successive PY4 mission [6].

The SX1280 is a low power, half-duplex LoRa transceiver with ranging capability, operating nominally in the S-band ISM band (from 2.4 to 2.5 GHz), with a maximal output power of 12.5 dBm (17.8 mW). The transceiver provides an option to select from three modulations: GFSK, FLRC and LoRa, with LoRa modem including a built-in ranging engine [1]. Theoretically, the transceivers can achieve sub-metre accuracy of relative distance measurement [7].

II. System Architecture

The entire design process of the payload was driven by the set of requirements, based on provided mission requirements. This set most notably includes:

- external communication interfaces: CAN, I^2C and RS422,
- support of Cubesat Space Protocol (CSP),
- operational range (relative distance) between 10 metres and 10 kilometres,
- accuracy of relative distance measurement below 2 metres (in the operational range),
- power consumption of the payload below 1 W,
- range of operational temperatures between -20 and 50 °C,
- range of survival temperatures between -40 and 60 °C,
- form factor partially based on LibreCube PC/104 board specifications [8],
- minimal frequency range from 2.242 to 2.282 GHz.

The payload shall be powered by stabilised 3.3 V channel from satellite's electrical power system (EPS). The payload can be connected to the satellite platform via Samtec SSQ-126-04-G-D stack connector (power, CAN and I^2C) and/or Harwin G125-MH10605L1P connector (power and RS422). Each module is interfaced by two Samtec FSI-110-03-G-D-AD mezzanine connectors.

Ultimately, a three-board design of the payload was chosen, with a single motherboard (dock) and two daughterboards (modules), to provide a high level of modularity. This also allowed for the use of an off-the-shelf, flight-proven on-board computer to significantly reduce the risks associated with the development of a new payload computer.

The final high-level system architecture of the payload is shown in Fig. 1.

A. Link budget

The aforementioned SX1280 transceiver is used on both sides of the inter-satellite link, with a maximal output power of 12.5 dBm, maximal input power of 0 dBm, and sensitivity of -130 dBm (at spreading factor 12 and bandwidth 204 kHz) [1]. Inspiration for antenna parameters is taken from EXA SSA03 S-band truncated patch antenna [9], with a gain of 7.2 dBi at θ = 0° and -2.8 dBi at θ = 90°. Insertion losses at both sides are caused by filter insertion loss, splitter (3 dB) and its insertion loss. These values are based on the simulations

DOI 10.13164/eeict.2025.84

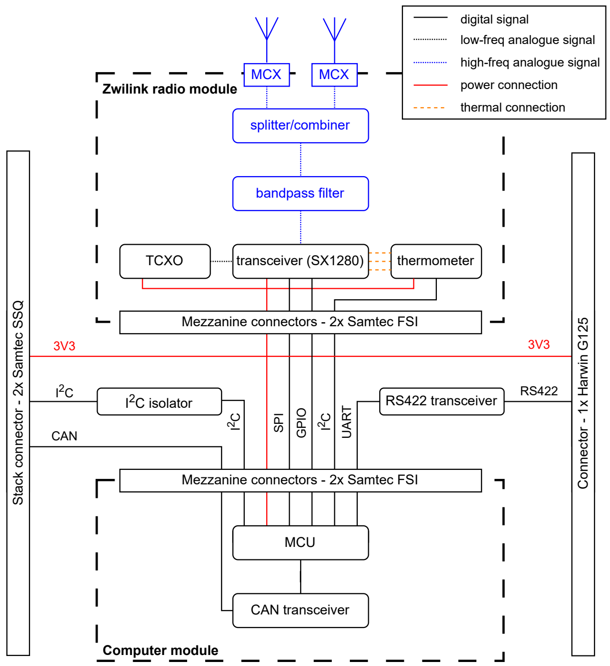

Fig. 1. Diagram of high-level system architecture of the payload.

conducted in Ansys Electronics Desktop. Rough estimation of RF cabling losses is also included in this figure.

Table I presents the best-case scenario, with both satellites pointing at each other. The optimal values of spreading factor and bandwidth for ranging are based on the application note by Semtech [7].

Table II presents the worst-case scenario, with first satellite pointing at the freely rotating second satellite (i.e. in case of attitude control system failure). As there are two antennas planned at the opposite sides of a satellite, maximal considered misalignment angle is 90°.

In the best-case scenario, the payload is capable of ranging (with positive link budget) to up to 29 kilometres (in optimal configuration, with a theoretical achievable accuracy below 0.5 metres), in the worst-case scenario it falls to 6 kilometres. Safe-mode communication (with a theoretical data rate of 0.595 kbps) in the best-case scenario is possible up to 180 kilometres, in the worst-case scenario up to 46 kilometres. For comparison, maximum data rate communication (with a theoretical data rate of 253.91 kbps) is possible up to 5 kilometres in the best-case scenario.

III. Hardware Design

As described in the section *System Architecture*, the payload consists of a single motherboard and two modules - the radio module and the payload computer module. Both the motherboard and the radio module have been designed in-house and use the same printed circuit board (PCB) six-layer stack-up

TABLE I
LINK BUDGET - BORESIGHT (BEST-CASE SCENARIO)

Variable	**Unit**	**Ranging** (in optimal mode)			**Communication** (in safe-mode)		
Bandwidth	kHz	1625			204		
Spread. factor	-	10			12		
Frequency	MHz	2262			2262		
Rel. distance	km	0.01	10	100	0.01	10	100
Transmitter							
Output power	dBm	12.5			12.5		
Insertion loss	dB	6			6		
Antenna gain	dBi	7.2			7.2		
Other losses							
Free-space path	dB	60	120	140	60	120	140
Polarisation	dB	0			0		
Misalignment	dB	0			0		
Receiver							
Antenna gain	dBi	7.2			7.2		
Insertion loss	dB	6			6		
Input power	dBm	-45	-105	-125	-45	-105	-125
Sensitivity	dBm	-114			-130		
Final Margin	**dB**	**69**	**9**	**-11**	**85**	**25**	**5**

TABLE II
LINK BUDGET - ONE SATELLITE FREELY ROTATING (WORST-CASE SCENARIO)

Variable	**Unit**	**Ranging** (optimal)			**Communication** (in safe mode)		
Bandwidth	kHz	1625			204		
Spread. factor	-	10			12		
Frequency	MHz	2262			2262		
Rel. distance	km	0.01	10	100	0.01	10	100
Transmitter							
Output power	dBm	12.5			12.5		
Insertion loss	dB	6			6		
Antenna gain	dBi	7.2			7.2		
Other losses							
Free-space path	dB	60	120	140	60	120	140
Polarisation	dB	3			3		
Misalignment	dB	10			10		
Receiver							
Antenna gain	dBi	7.2			7.2		
Insertion loss	dB	6			6		
Input power	dBm	-58	-118	-138	-58	-118	-138
Sensitivity	dBm	-114			-130		
Final Margin	**dB**	**56**	**-4**	**-24**	**72**	**12**	**-8**

to allow panelisation for cheaper manufacture. The selected PCB material is Isola PCL370HR, suitable for aerospace applications, with high glass transition temperature. To reduce the risk of outgassing, silkscreen layers were removed and only selective solder mask is present with the minimal amount required for the assembly purposes. All long traces were buried in inner layers and copper fills on top and bottom layers were limited to only necessary amount.

In terms of components, primarily automotive-grade components were used for the non-RF parts of the payload.

The hardware of the payload has already been manufactured in the first revision, and is currently being worked on and tested.

A. Motherboard / Dock

The motherboard, as the main board of the payload, is primarily responsible for the interconnection of individual modules and the platform, and for the mechanical support of the modules. The form factor of the board is partially based on LibreCube board specifications, as stated in the requirements. Renders of the motherboard are shown in Fig. 2.

Power is supplied by platform's EPS primarily through the stack connector, with an option to power the payload directly through the Harwin G125 connector. Selection of specific power and ground channels is possible with 0 Ω resistors. Ferrite beads and filtering capacitors are implemented in the power path (close to the mezzanine connectors) to suppress noise coming from the platform.

As there is no RS422 transceiver already implemented in the payload computer, it is implemented externally on the motherboard and communicates with the computer via the UART. The transceiver used is a THVD1424 by Texas Instruments. The RS422 is connected via the Harwin G125 connector.

To safely disconnect the payload from the main I^2C bus in case of payload failure, an I^2C isolator (PCA9507D by NXP) was added between the payload computer module and the stack connector.

Several testpoints were added for testing and debug purposes at accessible places of the motherboard. LED indicators were also added to provide power-on and busy status information.

B. Zwillink Radio Module

The radio module of the payload, called Zwillink, is a daughterboard serving as the transceiver and radio frequency (RF) front-end of the payload. At the heart of the module is an SX1280 transceiver, referenced by a 52 MHz clipped-sine temperature-compensated crystal oscillator (TCXO). The transceiver communicates with the payload computer via SPI, with GPIO used for status monitoring and interrupts.

The form factor of the module is inspired by the selected payload computer (NanoMind A3200 by GomSpace) to achieve interchangeability of the radio module and payload computer module on dock. This is also made possible by the same location of the mezzanine FSI connectors and compatible pinout. Renders of the radio module are shown in Fig. 3.

On the bottom side of the board, just directly across the transceiver, an I^2C thermometer (TMP275-Q1 by Texas Instruments) is placed to measure the temperature of the transceiver, primarily for temperature calibration of the ranging measurement. Thermally conductive vias are placed between the transceiver and the thermometer to allow heat transfer.

An aluminium cover will be placed on the radio module to provide electromagnetic interference (EMI) and mechanical shielding. It will also act as a heat sink for the transceiver.

The RF front-end is composed of 50 Ω coplanar waveguide, bandpass filter, splitter/combiner (SCN-2-27+ by Mini-Circuits with an external 100 Ω resistor) and two surface-mount MCX connectors (CONMCX002-SMD-T by TE Connectivity) for antenna connection. The filter is custom-designed 4^{th} order modified Chebyshev bandpass filter with 3dB bandwidth from 2.11 to 2.59 GHz and insertion loss (in peak) of 0.99 dB at 2.262 GHz. Simulated characteristics are shown in Fig. 4.

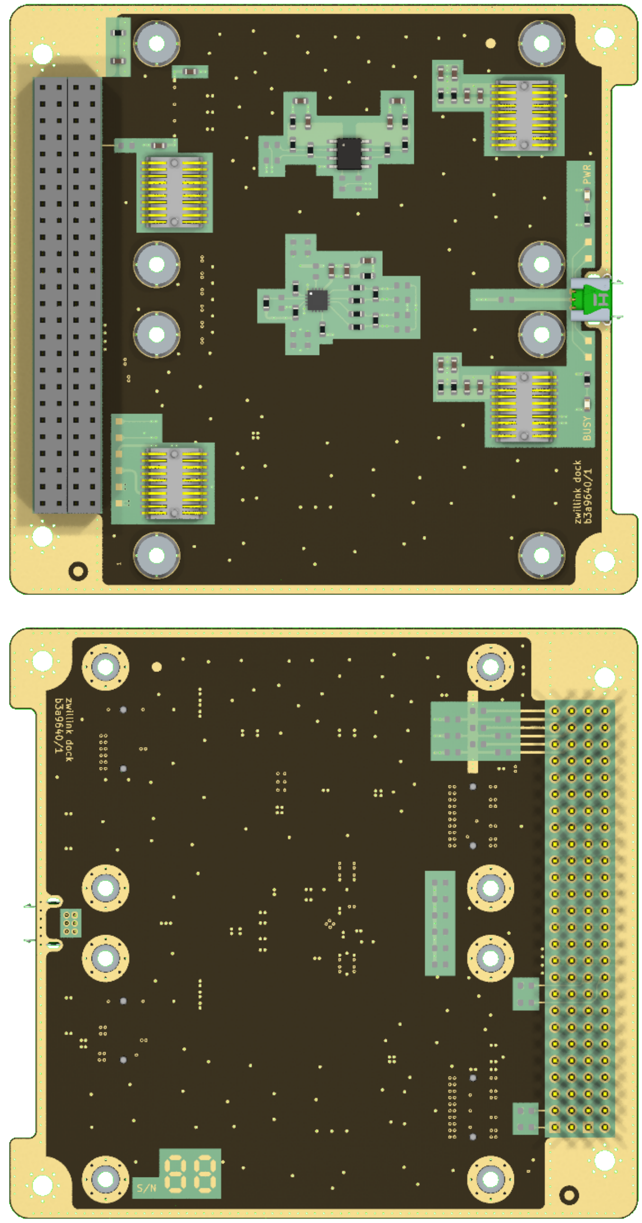

Fig. 2. Top and bottom view of the motherboard

For debug purposes, LED indicators were added to provide power-on and busy status information, located between the MCX connectors.

C. Computer Module

Off-the-shelf, flight-proven on-board computer NanoMind A3200 by GomSpace was selected for the payload computer. NanoMind is based on Atmel AT32UC3C microcontroller and

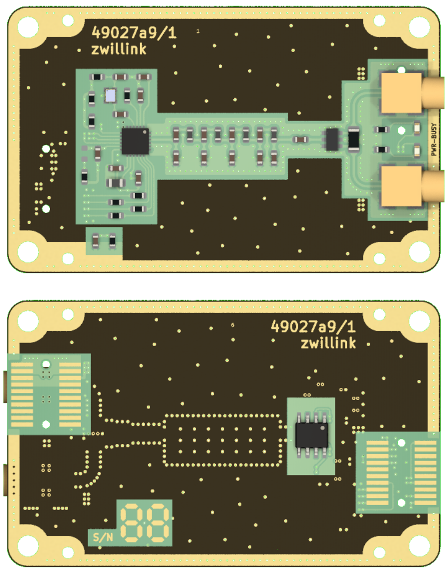

Fig. 3. Top and bottom view of the Zwillink radio module

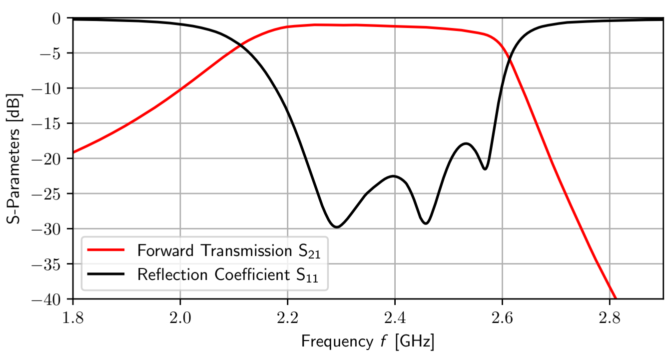

Fig. 4. Frequency characteristics of the designed filter

offer single CAN and SPI, two I^2C and UART, and multiple GPIO connections [10].

IV. Software Architecture

Application-specific software of the payload, which is responsible for handling of the communication and ranging, needs to be highly autonomous, as there is only limited contact with the ground segment during the orbit. Ranging will be based on a master-slave architecture, with one of the satellite acting as the master and handling all of the ranging between satellites. Automatic initiation of configuration changes (to achieve better range, data rate or ranging accuracy) will be based on either received signal strength indication (RSSI) or packet loss characteristics. Watchdog time-out will be used to put the communication into safe-mode with lower data rates, but with the better link budget and therefore range, in the case there was no established communication between the satellites for specified amount of time.

Many of the settings will be based on modifiable configuration table, including settings such as centre frequency, nominal spreading factor and bandwidth for safe-mode and ranging. In addition to this table, read-out table will provide some important information, like frequency error and RSSI of the last received packet, or time-of-flight of the last ranging exchange.

All of the application-specific software described above will be running on top of the software provided by computer manufacturer, that will handle the routing and processing of the CSP packet, and external communications of the payload with the subsystems of the platform.

V. Conclusion

In this paper, the design of an inter-satellite communication and ranging payload suitable for rendezvous and proximity operations CubeSat missions have been presented. The maximal theoretical relative distance between satellites, when they should still be able to communicate in safe-mode is 180 kilometres, according to the presented link budget. The hardware design of the motherboard and radio module was described, with the basic description of the system architecture and the proposed software architecture.

Acknowledgement

I want to thank the supervisor of my master's thesis Ing. Jiří Veverka and the consultant Ing. Jan Gromeš for their help during the writting of this paper, and master's thesis in general. I also want to thank my collegues Rémy Chatel and Tomáš Novotný from VZLU AEROSPACE for their help during the hardware design process and manufacturing preparation of the payload.

References

[1] Semtech, "SX1280/SX1281 Data Sheet", Rev 3.3, Online, September 2023. Available online at: https://www.semtech.com/products/wireless-rf/lora-connect/sx1280

[2] Semtech, "LoRa® Modem Doppler Immunity", Online, October 2023. Available online at: https://www.semtech.com/products/wireless-rf/lora-connect/sx1280

[3] TinyGS, "Satellites - TinyGS", Online, 2025. Available online at: https://tinygs.com/satellites

[4] M. Holliday, K. Tracy, Z. Manchester, and A. Nguyen, "The V-R3x Mission: Towards Autonomous Networking and Navigation for CubeSat Swarms," Vilamoura (Portugal): The 4S Symposium, May 2022. Available online at: https://rexlab.ri.cmu.edu/papers/vr3x.pdf

[5] A. Nguyen, "V-R3x Technology Demonstration Overview and Lessons Learned", Mountain View (United States of America): NASA Ames Research Center, November 2021. Available online at: https://www.nasa.gov/smallsat-institute/community-of-practice/v-r3x-technology-demonstration-overview-and-lessons-learned/

[6] M. Holliday, et. al., "The PY4 Mission: A Low-Cost Demonstration of CubeSat Formation-Flying Technologies," Logan (United States of America): 38th Annual Small Satellite Conference, August 2024. Available online at: https://digitalcommons.usu.edu/smallsat/2024/all2024/56/

[7] Semtech, "An Introduction to Ranging with the SX1280 Transceiver (AN1200.29)", Online, March 2017. Available online at: https://www.semtech.com/products/wireless-rf/lora-connect/sx1280

[8] LibreCube, "LibreCube Board Specification", Online. Available online at: https://librecube.gitlab.io/standards/board_specification/

[9] Ecuadorian Space Agency, "SSA03 - Compact high gain S-band patch antenna", Online. Available online at: https://www.cubesat.market/_files/ugd/696de6_11a70a540c8b43989db954ba7eca21cb.pdf

[10] GomSpace, "NanoMind A3200 Datasheet", Online, 2021. Available online at: https://gomspace.com/UserFiles/Subsystems/datasheet/gs-ds-nanomind-a3200_1006901-117.pdf


There is no better time than now to be an **intelligent power management company.**

Tool for Analysis of Domain Records Collected from Open Sources

1st Ondrej Dohnal
Department of Telecommunications
Brno University of Technology
Brno, Czech Republic
ORCID: 0000-0003-4301-9708

2nd Jan Jerabek
Department of Telecommunications
Brno University of Technology
Brno, Czech Republic
ORCID: 0000-0001-9487-5024

***Abstract*—The Domain Name System (DNS) enables access to online resources via human-readable domain names, but retrieving subdomain information requires open-source intelligence (OSINT) platforms like VirusTotal or CRT.sh, which differ in data formats and retrieval methods. This paper introduces a tool that automates the collection, processing, and analysis of DNS records from multiple OSINT sources, handling key records, removing duplicates, and supporting standardized output formats (YAML, JSON). With a modular and extensible design, the tool ensures efficiency, accuracy, and reliability through asynchronous data fetching and rigorous validation, benefiting security researchers, network administrators, and forensic analysts. Future improvements may expand OSINT sources and enhance analytical capabilities for better domain intelligence.**

***Index Terms*—Cybersecurity, Data Processing, DNS, Domain Name System, Domain Records, OSINT**

I. Introduction

The Domain Name System (DNS) is a fundamental component of the Internet, enabling users to access resources through human-readable domain names instead of numerical IP addresses. Despite its efficiency, DNS has inherent limitations, particularly in retrieving information about subdomains. To address this gap, various open-source intelligence (OSINT) platforms such as *VirusTotal*, *CRT.sh*, and *Shodan.io* have emerged, collecting and providing access to domain records. However, the inconsistency in data formats and retrieval methods among these platforms presents challenges for users who need to analyze domain information efficiently.

This paper introduces a tool designed to automate the retrieval, processing, and analysis of DNS data from multiple OSINT sources. By leveraging asynchronous data fetching, deduplication techniques, and standardized output formats (YAML, JSON), the tool simplifies the process of domain record examination. Additionally, it enables users to track the historical evolution of DNS records, which is crucial for security research, infrastructure monitoring, and forensic investigations. The tool's modular architecture ensures flexibility and expandability, allowing for future integrations with additional data sources.

This work is supported by Technology Agency of the Czech Republic under Grant FW11020057.

II. Background and Preliminaries

DNS enables users to simplify the usage of the Internet network. One of its main purposes is translating between domain names, which are easily memorable by end users, and IP addresses [1].

A. OSINT

OSINT refers to the process of collecting, analyzing, and utilizing publicly available information from diverse sources, including websites, social media, government records, and cybersecurity platforms. OSINT tools and techniques enable security researchers and analysts to gather intelligence on domain records, network infrastructure, and potential vulnerabilities without direct access to target systems [2].

B. Subdomain enumeration

Subdomain enumeration is a crucial aspect of OSINT that involves identifying all the subdomains associated with a domain. This is especially valuable for security assessments, where understanding the structure of a target's domain can reveal potential vulnerabilities or forgotten assets [3].

Collected information about domains and subdomains can be used as a potential source of targets for penetration testing.

C. Related work

Another approach to subdomain enumeration and domain intelligence gathering is the use of specialized tools such as *OWASP Amass* [4], an open-source framework designed for network mapping and attack surface discovery. Amass integrates multiple OSINT sources and performs active and passive reconnaissance to enumerate subdomains and associated infrastructure. While Amass is highly effective for security assessments and external asset discovery, its focus is on broad reconnaissance rather than structured DNS record processing. In contrast, the proposed tool is specifically designed for automated retrieval, validation, and analysis of DNS data from OSINT sources, emphasizing structured output formats such as JSON and YAML, as well as deduplication and historical tracking.

OSINT has been shown to enhance cyber threat intelligence, particularly in detecting botnet activities that exploit DNS-based domain generation algorithms (DGA), highlighting the importance of DNS analysis in cybersecurity [5].

III. Proposed Methodology

The objective of the proposed tool is to facilitate the automated retrieval and analysis of DNS data, especially subdomain enumeration, from various open sources (OSINT). This tool enables the examination of both current and historical DNS records for a given domain and its subdomains. Additionally, it provides data processing capabilities, duplicate removal, and output generation in standardized formats (YAML, JSON), with options for visualizing the temporal evolution of DNS record changes.

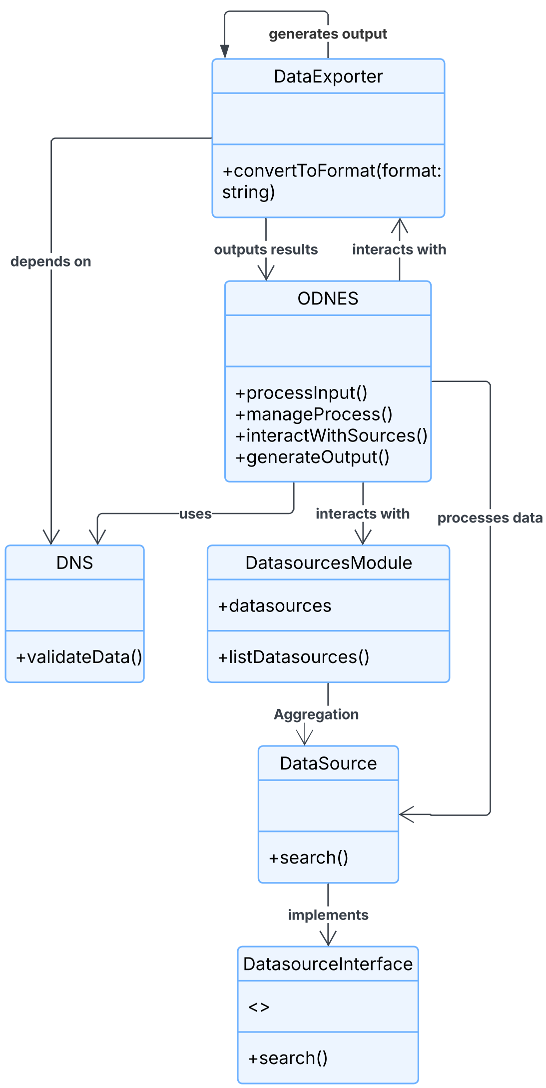

Fig. 1. Architectural diagram of designed ODNES application

A. Tool design

The tool is designed to retrieve DNS data by processing common DNS record types such as A, AAAA, MX, CNAME, NS, TXT, and SOA. Known subdomains of each queried domain are also processed. Data from different sources is fetched asynchronously to optimize performance and reduce latency. The system also incorporates historical data when available, which is crucial for analyzing infrastructure changes, detecting anomalies, and understanding the evolution of domain configurations. After collecting data from multiple sources, a deduplication process ensures consistency and clarity in the final results. The processed data is then exported in human-readable and machine-readable formats to facilitate both manual and automated analysis.

B. Architecture

The tool follows a modular architecture, as seen in figure 1, allowing easy expansion with additional data sources. Each data source is implemented as a separate module that communicates with the core system through a standardized interface. The main module, ODNES, manages the entire process, from data acquisition to output generation. It interacts with the Datasources and Data Exporter modules, using a defined API, to retrieve, process, and format the data. The Datasources module handles communication with external data sources, each implemented as an independent module for easy extensibility. The DNS module ensures the validity of retrieved data before further processing, and the Data Exporter module converts processed data into the desired format. If no format is specified, results are displayed in the standard output in a human-readable format. The application also supports saving results to a file if required by the user.

C. Implementation

Python is used for implementation due to its extensive support for relevant libraries, such as `aiohttp` [6] for API communication and `aiopg` [7] for PostgreSQL communication. The internal workflow of the tool begins with user input, where a domain is specified for analysis. The user may also define the output format or specify a target file for storing results. The Datasources module then retrieves data asynchronously from external sources such as *VirusTotal* or *CRT.sh*. Once data is collected, the DNS module verifies its actuality and consistency, ensuring it adheres to the required format and is free from errors. A deduplication process removes redundant entries before storing them in an internal data structure. The Data Exporter module then generates the final output in the specified format. If an output file is provided, data is saved accordingly; otherwise, it is displayed on the standard output.

D. Data Validation

Verifying the validity of retrieved data is a crucial step in processing information from various external sources. Data acquired via APIs from services such as *VirusTotal* or *CRT.sh* may contain incorrect, incomplete, or outdated information. The DNS module ensures that all data meets predefined format, consistency, and timeliness requirements before further processing. This validation process includes format verification, ensuring that each record contains key attributes such as DNS record type, domain name, and record value. Any missing attributes result in the record being marked as invalid unless a specific option is provided, and it is excluded from further processing.

By implementing rigorous validation mechanisms, the tool ensures the reliability and accuracy of the processed DNS data, making it a robust solution for domain intelligence and security analysis.

IV. Results

Based on the general design described in the previous section, a functional prototype was implemented.

A. Development

For development and package management, `Poetry` was used, a tool that simplifies dependency management and allows for seamless installation, updates, and distribution of Python packages. This ensured consistency across different development and production environments. The core functionality of the application relies on several key dependencies, including `aiohttp` for asynchronous HTTP requests to external APIs like *VirusTotal*, `aiodns` for asynchronous DNS resolution to improve data retrieval efficiency, and `aiopg` for communication with the *CRT.sh* PostgreSQL database.

B. Data acquisition

One of the key functionalities of the tool is data retrieval from external sources, with *VirusTotal* API being one of the primary sources. A dedicated `VirusTotal` Datasource module was implemented to facilitate API communication, providing a search method for retrieving domain-related information. The module uses an API key for authentication and constructs dynamic URLs using placeholders for domain and resource types. For example, querying the DNS record of 'example.com' results in a structured API request URL. HTTP headers are included to specify the response format and API authentication for requests. A session is used for efficient repeated queries, minimizing overhead. Responses are processed into Python lists for easy analysis.

Listing 1. CRT.sh PostgreSQL query

```
SELECT DISTINCT sub.NAME_VALUE
FROM (
 SELECT cai.*
 FROM certificate_and_identities cai
 WHERE plainto_tsquery('certwatch', %s)
 @@ identities(cai.CERTIFICATE)
 AND cai.NAME_VALUE ILIKE %s
 LIMIT 10000
) sub;
```

Secondary implemented external source *CRT.sh* uses a publicly available PostgreSQL database. A dedicated `CRT.sh` Datasource module was implemented to abstract over the database and provide the needed data. A simple SQL query, as seen in listing 1, was written to extract the data from the database.

Datasource module supports automatic loading of all installed individual scope-specific datasource submodules. Loading mechanism can be seen in listing 2.

Listing 2. Automatic datasource loading

```
modules=glob.glob(join(dirname(__file__),
        "*.py"))
__all__=[basename(f)[:-3]
     for f in modules
     if isfile(f)
     and not f.endswith('__init__.py')]
from odnes.datasources import *
subclasses=Datasource.__subclasses__()
datasources=[cls() for cls in subclasses]
names=[cls.__name__ for cls in subclasses]
```

C. Output formatting

The tool provides various output options, including YAML (as seen in figure 2) and JSON (as seen in figure 3) formats, ensuring compatibility with both manual and automated analysis workflows. During testing, different domain queries and data sources were verified to ensure correct API communication and data retrieval. The tool's ability to process DNS records, subdomain data, and other DNS-related information was tested extensively. The configuration file parameter allowed for testing different API keys, ensuring flexibility in deployment.

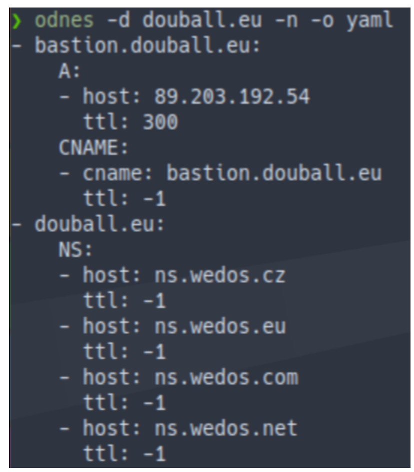

Fig. 2. Shortened example of YAML output for domain 'douball.eu'

D. Configuration

The application uses a configuration file, config.ini, which currently stores the VirusTotal API key. The file is placed alongside the main module and serves as a template for user-specific configurations. The ConfigParser library is utilized to load configuration sections into a dictionary for further processing. Additionally, the ArgumentParser library is used to handle user-provided parameters, such as domain queries and output format selection. The modular design allows users to specify their API keys without manually entering them for each request.

V. Evaluation

Testing was performed through the command line, evaluating different parameters and functionalities. The primary focus was validating the -d parameter, which specifies the domain

Fig. 3. Shortened example of JSON output for domain ‘douball.eu‘

for analysis. The tool was tested with various domain inputs to confirm proper API communication and data retrieval.

Each source requires specific query structures and response handling, and tests verified correct processing of VirusTotal API responses and CRT.sh database queries. Additionally, the -c option allowed testing with different configuration files, enabling assessment under varied API credentials. Overall, testing ensured both fundamental functionality and robustness across different scenarios, verifying the tool’s reliability for domain intelligence tasks.

Data validity was checked against utility `dig`, which provides actual DNS records. Outputs from the `odnes` tool were checked against actual data provided by `dig` to prove the correctness of the obtained information. If a nonexistent domain is presented to the tool, the default behavior is to inform the user that the specified domain was not found, as seen in figure 4. This is also verifiable using the `dig` utility. Figure 5 shows an example of an ‘A‘ DNS record. When the found subdomain was queried in `dig` as seen in figure 6. After comparing the result from `odnes` and `dig`, it is evident that the results match.

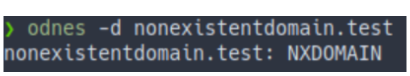

Fig. 4. Example of nonexistent domain, resulting in NXDOMAIN

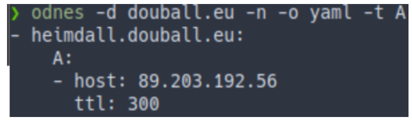

Fig. 5. Shortened example of ‘A‘ records filtered results

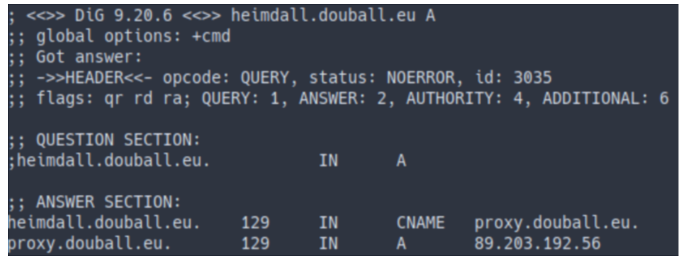

Fig. 6. Actual DNS record provided by dig for domain ‘heimdall.douball.eu‘

VI. Conclusion

The proposed tool provides an effective solution for automated domain record retrieval and analysis using OSINT sources. By integrating multiple data sources, performing data validation, and offering standardized output formats, it enhances the efficiency and accuracy of DNS intelligence gathering. The implementation of asynchronous data fetching significantly reduces latency, while the modular architecture ensures adaptability for future extensions.

Through rigorous testing and validation, the tool has demonstrated its reliability in handling various domain-related queries. It supports security researchers, network administrators, and forensic analysts in monitoring domain changes, detecting anomalies, and gaining deeper insights into domain infrastructure. Future improvements may include the incorporation of additional OSINT platforms, enhanced visualization capabilities, and improved data correlation techniques to further refine domain intelligence analysis.

References

[1] C. Liu and P. Albitz, *DNS and BIND*, 5th ed. Sebastopol: O’Reilly, c2006.
[2] A. S. Ram, A. Thalakkat, D. Udayan, A. A. Khader, H. K, and V. George, “Exploring OSINT for Modern Day Reconnaissance,” in *2023 Annual International Conference on Emerging Research Areas: International Conference on Intelligent Systems (AICERA/ICIS)*, 2023, pp. 1–6.
[3] G. J. Kathrine, R. T. Baby, and V. Ebenzer, “Comparative analysis of subdomain enumeration tools and static code analysis,” *ISSN (Online)*, pp. 2454–7190, 2020.
[4] “Owasp amass,” 2024. [Online]. Available: https://owasp.org/www-project-amass/
[5] H. Suryotrisongko, Y. Musashi, A. Tsuneda, and K. Sugitani, “Robust Botnet DGA Detection: Blending XAI and OSINT for Cyber Threat Intelligence Sharing,” *IEEE Access*, vol. 10, pp. 34 613–34 624, 2022.
[6] “Welcome to AIOHTTP,” 2025. [Online]. Available: https://docs.aiohttp. org/en/stable/
[7] “Welcome to AIOPG,” 2025. [Online]. Available: https://aiopg. readthedocs.io/en/stable/

Platform for detection and monitoring of the devices connected to the power grid

1st Radim Macho
FEEC, Brno University of Technology
Brno, Czech Republic
221666@vut.cz

2nd Petr Musil
Department of Telecommunications
FEEC, Brno University of Technology
Brno, Czech Republic
musilp@vut.cz

***Abstract*—This paper summarizes the creation of a platform for detection and monitoring devices connected to the power grid. The platform will provide monitoring of the power grid, for the purpose of detecting connected devices, with regard, to their potential threat to the operation of critical systems. The monitoring and detection will be performed using data provided by power-line communication modems connected to the monitored power grid. Data provided by power-line communication modems are in the form of the frequency spectrum of the noise. The the frequency spectrum of the noise will be statistically described, and this statistical description of the data will be used for training the machine learning model and subsequent detection of connected devices based on machine learning model prediction. All calculations of the statistical description of data, creation of machine learning model and subsequent detection and monitoring will be processed locally on a microcomputer using custom-developed code.**

***Index Terms*—electrical network, frequency spectrum of the noise, power-line communication, machine learning**

I. Introduction

Every device connected to the power grid influences this network in a certain way. This influence on the power grid can disrupt the operation of devices performing the functionality of critical systems.

This is one of the reasons why it is necessary to protect critical systems from a hardware perspective. The platform described in this paper will provide the ability to monitor the electrical network and detect connected devices in order to protect critical systems by identifying foreign devices that could have a negative impact on the operation of critical systems.

A. Power-line communication

Power-line communication, hereinafter referred to as PLC, is a technology that enables data transmission over the power grid, while maintaining the functionality of the power grid.

The PLC always utilizes at least 2 modems for establishing communication network on top of the power grid. One modem operates as a transmitter while the other functions as a receiver. Modems can interchange their roles or function as both a transmitter and a receiver simultaneously as needed.

The transmitting modem modulates a high-frequency signal, representing data for transfer, onto a signal present in the power grid. For Europe inside the building power grid the signal is 230 V, 50 Hz sine wave.

The receiver listens to these modulated high-frequency signals, demodulates them, and thereby obtains the transmitted data [4].

B. Machine Learning

Machine learning is a general term for algorithms that allow a program to learn. The term learning of a program means the ability of a program to change its internal properties and parameters. This change of parameters is in order to achieve better results of the program.

Programs utilizing machine learning mechanisms employ two fundamental steps. The first step is training, sometimes referred to as the learning step. In this step, data is provided to the program, based on which the program creates a machine learning model.

The model of machine learning is a term for the representation of all system parameters adjusted in the training step.

The prediction is the second step in which data is provided to the model, and the model subsequently delivers the corresponding result based on provided data [5].

There is a large number of methods and types of machine learning, which can be divided into three basic categories:

- Supervised learning: The model is provided with the labeled data, and it is trained to accurately predict outcomes based on the input data, an example is data classification
- Unsupervised learning: The model is trained on unlabeled data, it is taught to look for hidden patterns and connections, an example is the search for connections in statistics.
- Reinforcement learning: The model is not taught once, but learns repeatedly through feedback, where the model makes a step and is then either rewarded or punished based on of an external evaluation of the step, an example are automated robots or marketing and advertising algorithms. [5]

A large number of methods used for creating machine learning models fall into the categories mentioned above. Among the most commonly used methods are:

- Neural Network: method inspired by biological neurons that connect together in layers, utilized in tasks such as image or speech recognition.

- Decision trees: A decision-making method based on conditions into individual branches, with the prediction result at the end of the branch, a simple method.
- Random forest: method based on the use of a larger number of decision trees, the result is the average of all trees, a robust method with resistance to overfitting.
- Support vector machines: The method searches for data group boundaries, which it divides into categories with the maximum possible distance.
- Naive Bayes: The method is based on Bayes theorem with the assumption of input independence, simple and effective for basic text classifications. [5]

A standard example of machine learning is computer vision, which involves the recognition of the content of a visual image by a computer. Another example could be, for instance, the prediction of data trends, such as weather forecasting, or perhaps the autonomous movement of a robot maintaining stability [5].

II. Platform design

The platform utilizes a network of PLC modems that operate independently. These PLC modems are capable of measuring the frequency spectrum of the noise and sending the measured values to the platform.

The platform operates on this existing network of PLC modems from which the frequency spectrum of the noise is obtained.

Custom-written code is utilized for platform operation. Using this custom-written code, platform process the values of the frequency spectrum of the noise. These processed values are used together with machine learning algorithms to create its own machine learning model.

The created machine learning model is subsequently used for monitoring and detecting connected devices connected to the power grid by their influence on the the frequency spectrum of the noise. The results of monitoring and detection are displayed to the user in a legible form in real time.

Detection and monitoring operate fully automatically after the machine learning model has been created, and the users are presented only with the results.

The custom-written code ensures all control of the platform, the creation and modification of the machine learning model, processing of the frequency spectrum of the noise data, and automated functioning of detection and monitoring with the display of results to the users.

A. Platform requirements

The platform as an extension to the existing network of PLC modems should be compact, low-maintenance, yet still possess sufficient performance.

This was the reason for choosing suitable and available microcomputer and accessories. The price of individual components is taken into account.

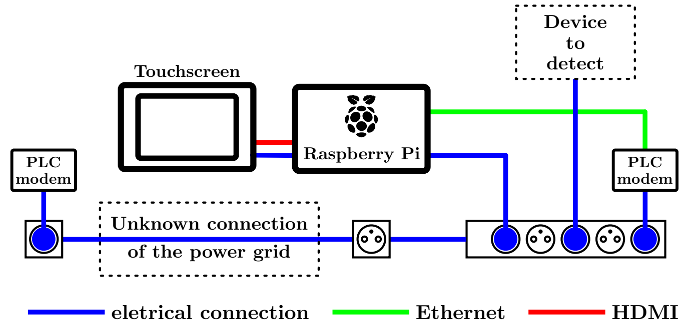

Fig. 1. Topology of the platform regarding to PLC modems and device to detect.

B. Hardware selection

The microcomputer chosen for the creation of the platform is the Raspberry Pi 5 (hereinafter referred to as RPi5) in the variant with 8 GB of RAM. This is the optimal solution from the available microcomputer variants. It disposes sufficient computing power for the platform, small size and an acceptable price.

The RPi5 itself does not contain cooling of any type. For this reason, the ICE Tower Plus cooling fan has been added to the RPi5, providing constant passive cooling. If the processor temperature exceeds the threshold of $60\,^{\circ}$, additional active cooling is provided by a fan.

To enable the independent operation of the platform, a 7” touchscreen display with OLED technology has been added to the RPi5 for lower power consumption while still providing high-quality display output. This touchscreen display will be used as both an input and output interface.

C. Platform topology

The complete topology of the platform, PLC modems and device to detect is shown on Fig. 1.

The two PLC modems are connected to the power grid using standard electrical wall socket. The specific scheme of the power grid between the PLC modems is unknown. To this same power grid is connected device to be detected by the platform. The RPi5 is also connected to this network, but only for the purpose of providing the power supply to the RPi5.

PLC modem connected closer to the device to be detected, is connected to the RPi5 using Ethernet cable through which the measured data is transmitted.

The touchscreen display is connected to the RPi5 by 2 cables. One for power supply and one for displaying information.

The platform can be connected to the internet using wireless connectivity of the RPi5, or it can be wired using the PLC modems themselves.

D. Data measurement with PLC modems

The selected PLC modems allow measurements of the frequency spectrum of the noise using a proprietary program. Unfortunately, this proprietary software is not compatible with the selected hardware and software. For this reason, the need arose to replace the functionality of the proprietary program with our own code.

1) Communication with PLC modems: Network communication between the computer and the PLC modem was observed while using the proprietary program. The analysis of the captured communication revealed several facts.

The PLC modems communicate using the UDP (User Datagram Protocol), based on a request-response communication principle.

2) Request for data measurement: The request for measured data from the connected device is in the form of a single UDP packet. This UDP packet is sent to the correct, predefined port.

The data part of the packet contains encoded information about the type of measurement, the number of channels, and other specifications provided by the PLC modems.

3) Response with measured data: The PLC modem responds to the request with measured data contained within five UDP packets sent back to the connected device. The payload of these five packets contains the header and measurement values in encoded form.

4) Measured data decoding: The method of encoding the transmitted measured data in UDP packets was unknown. For this reason, several methods of value decryption have been tested.

The final and only successful method was reverse engineering method, where the proprietary program for PLC modems was decompiled using a decompiler. Subsequently, the decompiled files were manually reviewed in order to locate the internal decoding function which provides conversion of all sended characters into measured values of the frequency spectrum of the noise.

E. Data processing

The measured data provided by PLC modems in the form of the frequency spectrum of the noise are in the form of 6400 values. 3200 values are for each of the two measured channels. In the context of optimization, the data are statistically processed.

Statistical processing is carried out by dividing the entire data sample into equally sized intervals. Each interval is statistically defined by the following parameters: average value, minimum value, maximum value, most frequently occurring value (mode), middle value (median), standard deviation.

The statistically described data are subsequently used for the creation of a machine learning model and subsequent detection of devices connected to the power grid.

F. Device detection

The detection of the devices connected to the power grid is based on their influence on the frequency spectrum of the noise. These values are not used directly, but are statistically processed as mentioned in the chapter II-E.

A dataset of devices is created, containing statistically processed data of the frequency spectrum of the noise. The dataset contains measured statistical data for the empty grid and for each device intended for detection in the same quantity measured on the monitored power grid.

Fig. 2. The physical form of the platform.

To create a machine learning model, two-thirds of the dataset are used as training data, while the remaining third is used as validation data. The machine learning model created in this way is subsequently used for the detection of connected devices.

The detection of the connected device is based on the prediction of a machine learning model that is provided with statistically processed current measured value of the frequency spectrum of the noise. The machine learning model will return a list of probabilities. Each probability value in the list corresponds to the likelihood that the given device is currently connected to the power grid.

This list serves as the result of the detection of the connected device, and its outcomes are presented to the user.

III. Final platform functionality

The hardware appearance of the platform is displayed in the Fig. 2. The Fig. 2 captures the RPi5 providing computing power and a touchscreen functioning as an input-output peripheral for controlling the platform and displaying detection and monitoring results.

A. Implemented functions

The platform is designed to automatically measure multiple times the device to create the data dataset necessary for creating a machine learning model.

The platform is capable of creating, storing, and re-loading this machine learning model from internal memory.

The platform is capable of displaying monitoring results and device detection in real-time in a user-readable format. Monitoring is carried out in the form of displaying color-coded text OK for the network without foreign devices, otherwise, DETECTED is displayed. Device detection is performed by displaying the top 5 devices with the highest probability of current connection to the power grid.

The platform also provides two additional functions. The first function, shown in Fig. 3, is a basic spectral analyzer that displays the current frequency spectrum of the noise for both channels, ranging from 2 MHz to 80 MHz.

The second function, shown in Fig. 4, provides a time analysis of the frequency spectrum of the noise. This function measure and save in background the current frequency

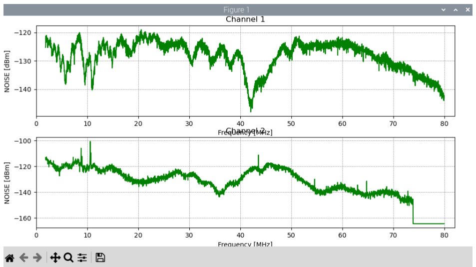

Fig. 3. Spectrum analyzer charts function window.

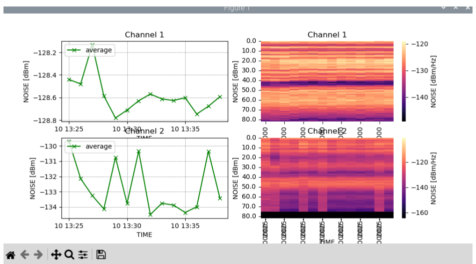

Fig. 4. Time analysis charts function window.

spectrum of the noise every hour and displays 4 charts when called. The graphs contain the average value and heatmap of the frequency spectrum of the noise values for each channel.

B. Functioning in practice

1) Platform setup: After the launch of the platform, we created a new power grid for monitoring. The platform automatically measured the frequency spectrum of the noise 500 times for the zero point of the power grid.

Subsequently, the devices were measured upon connection to the power grid to be detected. It was a power brick, computer monitor and a table lamp in the switched on and switched off state. Each device was measured 500 times with a one-second interval between measurements.

These measurements create a dataset for the creation of a machine learning model, that was created using them. Subsequently, the detection and monitoring of the power grid were initiated using this created machine learning model.

2) Detection and monitoring accuracy: Power grid monitoring is mostly reliable, thus the platform is capable of recognizing whether the power grid is in its basic configuration or if a foreign device has been connected to it.

The detection of connected devices was mostly reliable for recognizing different devices. However, single-sample detection errors occurred that may be caused by a sudden change in the frequency spectrum of the noise, such as an internal change in an already connected device.

The highest error rate in detection occurred when detecting multiple different states of the same device, namely the table lamp in both the on and off positions. The confusion of the states was up to 50 %. However, a one of the table lamp states was always been at the top of the top 5 devices list.

Overall, both detection and monitoring can be considered quite reliable if the detection of the specific state of individual devices is not required.

IV. Conclusion

A platform was created to monitor the power grid and detect the devices connected to the power grid.

The platform is based on custom-written Python code running on Raspberry Pi 5. Python code uses machine learning for detection and monitoring. Detection is based on values of the frequency spectrum of the noise provided by the PLC modems.

By using the reverse engineering was discovered how PLC modems communicate with the connected device and how they transmit measured data. The found principles are emulated by the custom-written Python code.

The platform is usable as a tool responding to user requests. The user is able to create different models, add devices, save and upload models, and perform power gird monitoring and device detection.

The power grid monitoring is reliable. The detection of individual devices is reliable in recognizing individual devices. If devices are recorded in multiple states or if there are multiple very similar devices, confusions arise, but the type of device is recognized.

The platform includes two additional functions. The first function displays the current frequency spectrum of the noise of both measured channels, which is refreshed every second. This function serves as a basic spectral analyzer.

The second added feature provides a time analysis of the frequency spectrum of the noise. This function displays the average noise value and heatmap of both channels over the entire duration of using the currently selected model.

References

[1] FOROUZAN, Behrouz A. *TCP/IP protocol suite.* 4th ed. McGraw-Hill Forouzan networking series. Boston, Mass.: McGraw-Hill, 2010. ISBN 978-0-07-337604-2.

[2] ALCOCK, Shane; MÖLLER, Jean-Pierre a NELSON, Richard. *Sneaking Past the Firewall.* Online. In: Proceedings of the 2016 Internet Measurement Conference. New York, NY, USA: ACM, 2016, s. 231-237. ISBN 9781450345262. Dostupné z: https://doi.org/10.1145/2987443.2987447. [cit. 2024-10-30].

[3] KUMAR, Santosh a RAI, Sonam. *Survey on Transport Layer Protocols: TCP & UDP.* Online. Foundation of Computer Science (FCS), NY, USA: International Journal of Computer Applications, 2012. Dostupné z: https://doi.org/10.5120/6920-9285. [cit. 2024-10-22].

[4] MAJUMDER, A. a CAFFERY, J. *Power line communications: an overview.* Online. IEEE Potentials. 2004, roč. 23, č. 4, s. 4-13. ISSN 0278-6648. Dostupné z: https://doi.org/10.1109/MP.2004.1343222. [cit. 2024-12-03].

[5] MAHESH, Batta. *Machine Learning Algorithms.* 9th. Gujarat: International Journal of Science and Research, 2018. ISSN 2319-7064.

Evaluation of Energy Consumption in Different LoRaWAN End Device Classes

Filip Stryk
Department of Radio Electronics
FEEC, Brno University of Techonology
Brno, Czech Republic
xstryk01@vutbr.cz

Aleš Povalač
Department of Radio Electronics
FEEC, Brno University of Techonology
Brno, Czech Republic
povalac@vutbr.cz

***Abstract*—This paper presents a comparison of the power consumption of different LoRaWAN classes (A, B, and C). It also describes the design and implementation of a LoRaWAN GNSS tracker based on the STM32WLE5 microcontroller (in the form of the Seeed Studio Wio-E5 module), which integrates the LoRa transceiver and offers convenient approach instead of the usual need for separate microcontroller and transceiver. The tracker also serves as a platform for the power consumption measurements and analysis.**

***Index Terms*—LoRaWAN, IoT, GNSS, STM32, tracking, power consumption**

I. Introduction

LoRaWAN is a widely used Low-Power Wide-Area Network (LPWAN) protocol designed for energy-efficient, long-range communication [1], making it ideal for battery-powered IoT devices. One of the key challenges in the design of such devices is minimizing power consumption to extend battery life, especially in applications where frequent maintenance is impractical. LoRaWAN defines multiple device classes (A, B, and C), each with different trade-offs between power consumption and communication latency. This paper focuses on comparing the power consumption across these classes, using a custom-designed GNSS tracker based on the STM32WLE5 microcontroller as a test platform. In addition to the comparison, the paper explores various low-power modes and optimization techniques to reduce overall energy usage, providing insights into how design choices affect the performance and longevity of LoRaWAN-enabled devices.

II. LoRaWAN

LoRaWAN specifies three classes for end devices – Class A, B, and C [1, 2]. Individual classes differ in downlink communication capabilities, which also affects the power consumption of the end device.

Class A devices open two receive windows following the data transmission in the uplink direction. The first window opens one second after the end of the transmission, while the second window opens after two seconds [3]. First receive window uses the same frequency and data rate as the preceding uplink. The second window uses a fixed frequency and data rate.

Class B introduces additional receive windows (ping-slots), that open at predetermined intervals. The period of the ping-slots depends on the network and can be set in the range from 1 to 128 seconds, following powers of two. To maintain synchronization across the network, end devices must also receive periodic beacons, which are broadcast by gateways every 128 seconds.

Class C devices listen continuously when they are not transmitting or opening receive windows by the definition of class A.

III. LoRaWAN GNSS Position Tracker

A. Design

The block diagram of the designed tracker is presented in Fig. 1. Its core components include a microcontroller, a radio, and a Global Navigation Satellite System (GNSS) module.

The device is powered by a single Li-Ion cell that can be charged via USB. A Switched-mode Power Supply (SMPS), based on TPS63001 generates the required 3.3 V supply voltage. The input voltage for the SMPS can be either battery or USB. The selection of the power source is managed by the Power Management Integrated Circuit (PMIC) MCP73871, which also handles battery charging. When both USB and battery are connected, the device is powered by USB while the battery charges, ensuring that the device's current consumption does not affect the charging process.

The tracker is built around the Seeed Studio Wio-E5 module, which features the STM32WLE5JC microcontroller. The STM32WLE5JC integrates 32-bit ARM Cortex-M4 CPU and Sub-GHz radio [4]. These include LoRa modulation and the EU868 band required for this device. This offers a convenient solution by integrating a high-performance CPU and a LoRa

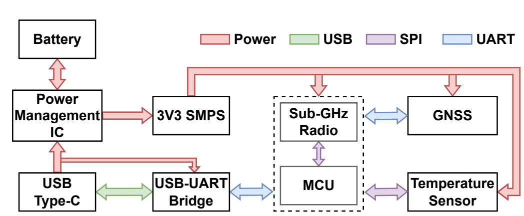

Fig. 1: Block diagram of the designed tracker.

transceiver into a single compact device instead of the usual need for a separate tranceiver.

For GNSS functionality, the tracker utilizes the Quectel L76-L receiver. It outputs data in the form of NMEA0183 messages via the UART interface, which is connected to the microcontroller. The TMP126 temperature sensor, which is connected to the microcontroller via SPI interface, is used to measure the environment temperature. USB to UART bridge enables logging and configuration of the device via serial terminal.

A visualization of the designed Printed Circuit Board (PCB) is shown in Fig. 2. The EU868 band antenna is connected via SMA connector, while the GPS antenna connects via u.fl connector. Additionally, the board features three jumpers that allow current measurement for the entire device or individually for the GNSS and Wio-E5 modules.

B. Firmware

The device firmware is developed using STM32 Hardware Abstraction Layer (HAL) libraries, with project configuration facilitated by the STM32CubeMX tool. STM32CubeWL package is utilized to manage the integrated sub-GHz radio and handle all LoRaWAN communication. The lwGPS [5] library is employed to parse and process NMEA messages received from the GNSS module.

Upon power-on, the firmware initializes essential peripherals including GNSS module, swich is configured to periodically alternate between power-save and run mode, during which it transmits NMEA messages containing the current position to the microcontroller.

The most recent GNSS position is periodically transmitted over the LoRaWAN network, along with the corresponding acquisition time, temperature, and battery voltage. To minimize payload size, the data is sent in a compact raw byte format as follows:

- **Latitude** (4 bytes) in millionths of a degree, i.e. value in the range of ±90 000 000,
- **Longitude** (4 bytes) in millionths of a degree, i.e. value in the range of ±180 000 000,

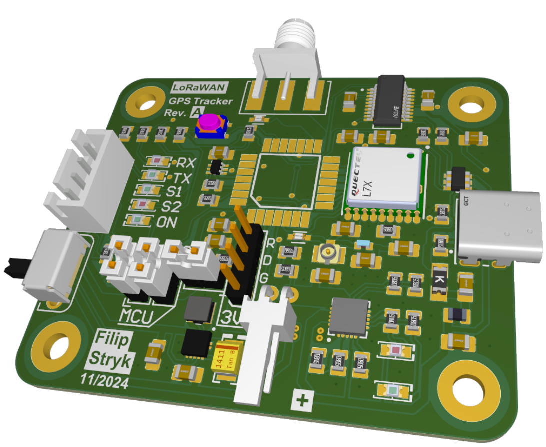

Fig. 2: Tracker

- **Altitude** (2 bytes) in meters,
- **Timestamp** (4 bytes) of the last known position fix as a UNIX timestamp in seconds,
- **Temperature** (1 byte) reading from the TMP126 sensor in degrees Celsius,
- **Battery voltage** (2 bytes) in tens of millivolts.

IV. Energy Consumption

A common requirement for LoRaWAN devices is long battery life, which requires a focus on low power consumption. This paper explores various power reduction methods and analyzes their impact across different LoRaWAN classes.

Due to variations in power consumption and differences in low-power mode behavior among available GNSS modules, the GNSS module was excluded from the analysis. This ensures an objective comparison of energy consumption between LoRaWAN classes and available low-power modes of the STM32WLE5.

A. Optimization

STM32WLE offers various low-power modes to reduce energy consumption [6]. Individual modes differ in terms of which peripherals remain active, which clock signals continue running, and how the voltage domains are powered.

By default, the microcontroller starts in Run mode after power-up. From there, it can transition into several low-power modes. The first, Sleep mode, has the highest power consumption among them; in this state, only the CPU clock is disabled while all peripherals can remain active and can wake up the CPU. Beyond Sleep mode, the STM32WLE5 offers three Stop modes (Stop 0 to Stop 2) with progressively lower power consumption. These modes primarily differ in terms of available peripherals and the active internal voltage regulator. In Stop modes, SRAM content is preserved, and all clocks are disabled except for LSI and LSE [7]. Overview of the low-power modes is available in the Tab. I together with their current consumption according to the datasheet [6].

In addition to low-power modes, other techniques can further reduce power consumption. One such method is configuring unused pins as analog inputs. This disables the default-enabled Schmitt trigger, which can otherwise randomly toggle when left floating, thereby reducing unnecessary power consumption [8]. Another approach to reducing energy consumption is disabling peripherals that are only needed intermittently. By dynamically enabling and disabling them based on operational requirements, the system ensures peripherals are active only when necessary, optimizing energy efficiency.

Several strategies can be employed to reduce power consumption from a LoRaWAN communication perspective. Energy consumption during transmission is highly dependent on the transmit power and data rate. These parameters can be optimized using ADR, which enables the LoRaWAN network server to dynamically adjust transmission settings for each device based on connection quality [2]. Power consumption is also influenced by transmission duration, making it essential to use the most efficient data format possible to minimize transmission time.

TABLE I: Overview of low-power modes of STM32WLE5 [6].

State	I_{DD} (μA)	Description
Run	1 100.0	Active state of the MCU in which the processor executes code and peripherals operate normally.
Sleep	570.0	CPU clock turned off, all peripherals can run.
STOP0	390.0	All clocks in V_{CORE} domain stopped, PLL, MSI, HSI16 and HSE32 stopped; fastest wakeup time.
STOP1	4.150	Lower number of available peripherals, higher wakeup time.
STOP2	0.885	Only CPU, SRAM and some peripherals preserve contents; LSI and LSE can run and RTC can remain active.

B. Analysis

To compare power consumption across different classes of LoRaWAN end device and low-power modes, multiple measurements of the Wio-E5 module's power consumption were conducted on the designed tracker. Measurements were conducted for all LoRaWAN classes and selected power-saving modes. Each measurement was taken in two scenarios – best-case and worst-case, with ADR disabled. The best-case scenario corresponds to the minimum transmit power and maximum data rate, while the worst-case scenario involves the maximum transmit power and minimum data rate. Specifically, the best-case measurements were taken at a transmit power of 0 dBm (the minimum value allowed by the LoRaWAN middleware) and a data rate DR5 (SF7BW125). For the worst-case scenario, the transmit power was set to 16 dBm (maximum allowed in the EU868 band) and the data rate to DR0 (SF12BW125).

For each case, the current consumption profile was measured using the Nordic Semicondutor Power Profiler Kit II. The example of measured waveforms for all classes in STOP2 mode and the best-case scenario are shown in Fig. 3 (ping-slot periodicity is set to four seconds for demonstration purposes in Fig. 3b). The waveforms clearly show increased consumption when the device is transmitting or opening receive windows. Fig. 3c illustrates the increased consumption over the measurement period, resulting from the continuously open receive window in Class C.

The average current for each state (TX, RX1, RX2, RXBC, and RXP – refer to Tab. II for explanation) was measured from the current profiles, along with the duration of each state and current in IDLE state. The measurements can be seen in Tab. II and Tab. III. For each state, the power consumed was also calculated. The measured transmission durations closely match theoretical values of airtime. For example, the theoretical airtime for a 17-byte payload at DR5 is 71.9 ms [9] while the measured value is 72 ms (see Tab. II). The transmit and receive current values are the same for all low-power modes, which only affect idle energy consumption (see Tab. III). Also the measured IDLE consumption values are in the same range as those provided in the datasheet (see Tab. I). The differences arise because the datasheet values assume all peripherals are disabled.

Based on the measured values, the energy consumption over a 24-hour period was calculated for the device operating under the test scenario, where a 17-byte packet is transmitted every 5 minutes and the beacon and ping-slot period for Class B is set to 128 seconds. The calculated results are used to compare the impact of power-saving modes in combination with different LoRaWAN classes on overall consumption of the device. These results are shown in Tab. IV.

The values in the table clearly show that Class C consumes significantly more power than Class A and Class B. This observation aligns with the assumption presented in Fig. 3 of [10], which indicates that Class C's consumption is 333 times higher than that of Class B. In comparison, the measured values in the most energy-efficient mode, STOP2, show that Class C consumes approximately 260 times more. The discrepancy can be caused by variations in data payload length as well as differences in transmission and reception periods. The data also reveals that without proper power optimization or the use of low-power modes, Class A loses its advantage in achieving the lowest power consumption, with its efficiency compared to Class B differing by only a fraction of a percent. However, when optimized effectively, the consumption of Class A is reduced by approximately 85 % compared to Class B. Compared to Class C, the reduction is even more significant, reaching several thousand percent.

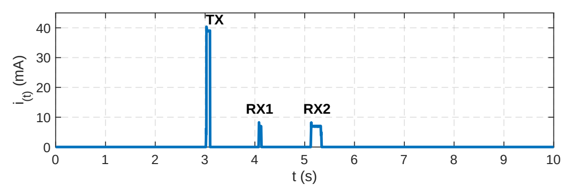

(a) Class A

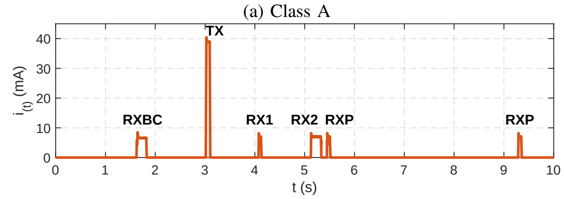

(b) Class B

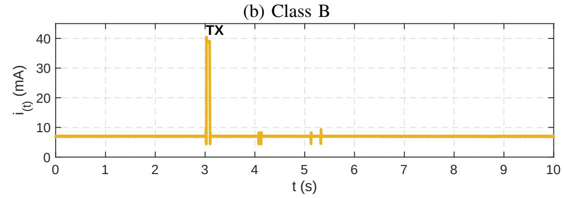

(c) Class C

Fig. 3: Current consumption profiles.

TABLE II: Consumption of the Wio-E5 for transmission and receive windows.

State		P_{TX} = 16 dBm, DR0			P_{TX} = 0 dBm, DR5		
		t (ms)	I_{AVG} (mA)	E (mWs)	t (ms)	I_{AVG} (mA)	E (mWs)
TX	Uplink transmission	1 674	83.0	458.9	72	42.9	10.2
RX1	Receive window 1	195	9.5	6.1	45	9.5	1.4
RX2	Receive window 2	195	9.5	6.1	195	9.5	6.1
RXP	Class-B ping-slot	57	9.5	1.8	57	9.5	1.8
RXBC	Class-B beacon reception	176	9.1	5.3	176	9.1	5.3

TABLE III: Consumption in IDLE for different conditions.

Class	Mode	I_{AVG} (μA)
A, B	RUN	5500
A, B	STOP1	16.4
A, B	STOP2	1.48
C		9500

TABLE IV: Comparison of consumption over 24 hours for the test scenario

Mode	Class	P_{TX} = 16 dBm, DR0 E (mWh)		P_{TX} = 0 dBm, DR5 E (mWh)	
RUN	A	470		437	
	B	471	+0.2 %	438	+0.2 %
	C	785	+67 %	753	+72 %
STOP1	A	38.9		2.70	
	B	40.3	+3.6 %	4.02	+49 %
	C	785	+1 917 %	753	+27 789 %
STOP2	A	37.8		1.54	
	B	39.1	+3.4 %	2.86	+85 %
	C	785	+1 977 %	753	+48 796 %

V. Conclusion

The goal of this work was to compare the impact of different LoRaWAN classes combined with power-saving strategies on device power consumption. The custom-designed GNSS tracker was used as the measurement platform. In addition, this work provides an overview of the STM32WLE5 microcontroller's low-power modes and outlines other techniques for reducing energy consumption. The measured results demonstrate that the power consumption differences between LoRaWAN classes are strongly affected by the level of power optimization applied and the device's current consumption during idle periods.

Acknowledgment

During writing of this paper, authors used the AI tools (DeepL, Writefull) for translations, text refinement. The text was subsequently reviewed and edited as needed. Authors take full responsibility for the content of this work.

Research described in this paper was supported by the Internal Grant Agency of the Brno University of Technology under project no. FEKT-S-23-8191.

References

[1] *LoRa and LoRaWAN*. Application note AN1200.86. Semtech Corporation, 2024. URL: https://www.semtech.com/uploads/technology/LoRa/lora-and-lorawan.pdf (accessed on 14 Mar. 2025).

[2] *TS001-1.0.4 LoRaWAN L2 1.0.4 Specification*. Technical specification. LoRa Alliance, 2020. URL: https://resources.lora-alliance.org/technical-specifications/ts001-1-0-4-lorawan-l2-1-0-4-specification (accessed on 14 Mar. 2025).

[3] *LoRaWAN Regional Parameters RP002-1.0.4*. Technical specification. LoRa Alliance, 2020. URL: https://resources.lora-alliance.org/technical-specifications/rp002-1-0-4-regional-parameters (accessed on 14 Mar. 2025).

[4] *STM32WLEx – Wireless MCUs with LoRa Support*. STMicroelectronics. URL: https://www.st.com/en/microcontrollers-microprocessors/stm32wlex.html (accessed on 14 Mar. 2025).

[5] Tilen Majerle. *Lightweight GPS NMEA parser for embedded systems*. 2025. URL: https://github.com/MaJerle/lwgps (accessed on 14 Mar. 2025).

[6] *Multiprotocol LPWAN 32-bit Arm Cortex-M4 MCUs, LoRa, (G)FSK, (G)MSK, BPSK, up to 256KB Flash, 64KB SRAM*. Datasheet DS13105. Rev. 4. Feb. 2020. URL: https://www.st.com/resource/en/datasheet/stm32wle5jc.pdf.

[7] *STM32WLEx advanced Arm-based 32-bit MCUs with sub-GHz radio solution*. Reference manual RM0461. Rev. 9. Apr. 2024. URL: https://www.st.com/resource/en/reference_manual/rm0461-stm32wlex-advanced-armbased-32bit-mcus-with-subghz-radio-solution-stmicroelectronics.pdf.

[8] *STM32 microcontroller GPIO hardware settings and low-power consumption*. Application note AN4899. Rev. 3. Mar. 2022. URL: https://www.st.com/resource/en/application_note/an4899-stm32-microcontroller-gpio-hardware-settings-and-lowpower-consumption-stmicroelectronics.pdf.

[9] *Airtime calculator for LoRaWAN*. 2021. URL: https://avbentem.github.io/airtime-calculator/ttn/eu868/17 (accessed on 14 Mar. 2025).

[10] *LoRaWAN Device Classes*. Application note AN1200.87. Semtech Corporation, 2024. URL: https://www.semtech.com/uploads/technology/LoRa/lorawan-device-classes.pdf (accessed on 15 Mar. 2025).

Experiments with the 5G beam search in millimeter waves - raytracing and practical indoor measurements

Marek Černý
Department of Radio Electronics
FEEC, Brno University of Technology
Brno, Czech Republic
xcerny76@vut.cz

Roman Maršálek
Department of Radio Electronics
FEEC, Brno University of Technology
Brno, Czech Republic
marsaler@vut.cz

Radek Závorka
Department of Radio Electronics
FEEC, Brno University of Technology
Brno, Czech Republic
xzavor03@vut.cz

***Abstract*—This paper investigates the transmission characteristics of 5G signals in the millimeter-wave frequency band, focusing on indoor environments. The objective is to simulate the propagation behavior using a ray tracing approach and validate the results through experimental measurements. Simulations are conducted in Python utilizing the Sionna library, with an emphasis on channel impulse response analysis and bit error rate (BER) performance under various conditions.**

***Index Terms*—5G, millimeter-wave, Synchronization Signal Block, Sionna, ray tracing, channel impulse response, bit error rate**

I. Introduction

The advent of fifth-generation (5G) wireless communications has ushered in a new era of connectivity, promising unprecedented data speeds, ultra-reliable, low-latency communications, and massive device connectivity. To meet the stringent requirements of 5G, novel technologies have been introduced, including massive Multiple Input Multiple Output (MIMO), millimeter-wave (mmWave) frequencies, advanced beamforming techniques and refreshed physical layer compared to the previous 4th generation (4G) Long-Term Evolution (LTE) standard [1] [2].

As the evolution of the 4G LTE standard, the 5G NR (New Radio) has introduced a critical component called the synchronization signal block (SSB). This new structure includes the primary synchronization signal (PSS), the secondary synchronization signal (SSS), and the physical broadcast channel (PBCH), along with its associated demodulation reference signal (DMRS) [3]. The synchronization signal block is periodically transmitted on the downlink by each 5G NR cell to allow the user equipments to perform the synchronization procedure [4]. This structure consists of 960 resource elements in the OFDM grid. These resource elements are divided into 4 OFDM symbols in the time domain and 240 subcarrier frequencies in the frequency domain [3].

This paper presents our experiments with cell search at mmwave frequencies in the indoor environment. It compares the measurements with Sivers EVK06002/EVK06003 evaluation kits and Xilinx ZCU111 as the baseband solution, with the raytracing simulation in Sionna environment. For the LOS scenario, the transmission of 5G payload is also simulated for various modulation and coding schemes and different subcarrier spacings.

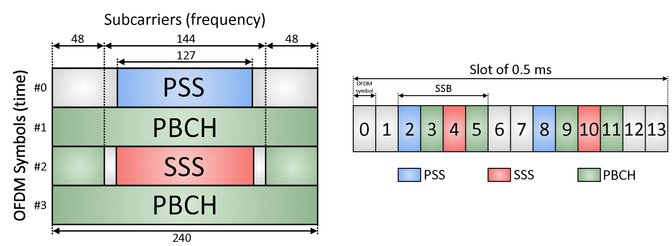

(a) SS/PBCH block structure (b) Subframe organization

Fig. 1: SSB structure [3]

II. Ray tracing and channel impulse responses

Due to the characteristics of the used evaluation kits, an indoor scenario was considered. An open-source python library Sionna from Nvidia was used for simulations. The 3D model of the student workshop at the Department of Radio electronic was created in Blender. Scene objects had to be simplified due to the sizes of the exported files. Most assigned materials were taken from Sionna, defined according to International Telecommunication Union. The custom materials and their properties are summarized in Tab. I.

TABLE I: Parameters of custom materials

Material name	Relative permitivity	Conductivity [S/m]
polycarbonate	3	0.001
cardboard	2.3	0.001
plastic	2.8	0.0001
ceramic	6	0.0001

A. Line-of-Sight scenario

Line-of-Sight scenario was simulated for a transmitter and receiver located at opposite corners of the station, as shown in Fig. 2. A channel impulse response shown in Fig. 3 contains

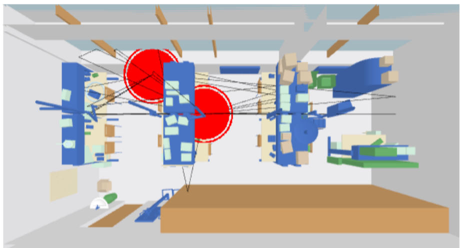

Fig. 2: Line-of-Sight (LOS) scenario

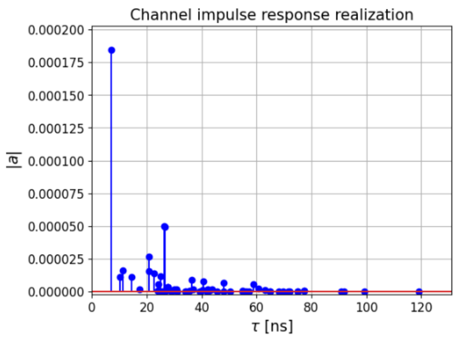

Fig. 3: Channel impulse response in delay domain for LOS scenario

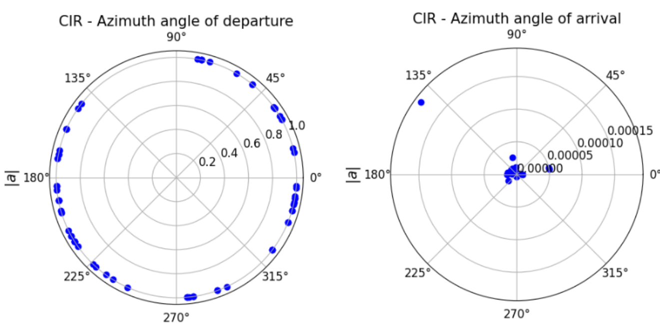

(a) Angles of departure (b) Angles of arrival

Fig. 4: Channel impulse response in angular domain for LOS scenario

all paths for up to five reflections. The line-of-sight path arrived at the receiver with a delay of 7 ns and with the highest passband channel coefficient. Furthermore, there were two other significant single-reflection paths, which had delays of 20 ns and 26 ns. Both the transmitter and receiver had an omnidirectional antenna set up as can be seen in the Fig. 4a. Fig. 4b shows the directional characteristic of the received signal. The direct path was received from 143 degrees. The path reflected from the side of the station was received from 109 degrees, and the path reflected from an obstacle behind the receiver was received from the angle of 12 degrees.

B. Non-Line-of-Sight scenario

Non-Line-of-Sight scenario was simulated for a transmitter and receiver located at student stations/workplaces across with obstacle between them as shown in Fig. 5, the corresponding channel impulse response is shown in Fig. 6. Since there is no direct line of sight between the transmitter and receiver, the maximum value of the passband channel coefficient does not differ significantly from the coefficients of the other paths. The differences in coefficient values were determined by the distance of the path, the number of reflections, and the material of the objects from which the beam was reflected. Fig. 7a shows that beams were received from a larger number of directions. Paths received from 0 degrees were reflected from the ground and ceiling. Reflections from the cabinet were received at around 300 degrees. Other significant paths were reflected from the window and received at angles of around 60 degrees. The last paths were reflected from the station at an angle of 120 degrees.

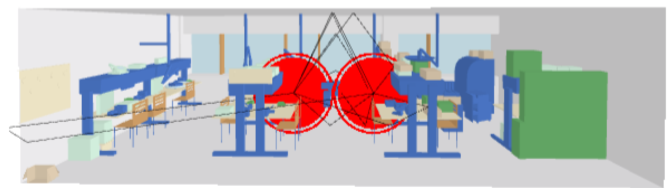

Fig. 5: Non-Line-of-Sight (NLOS) scenario

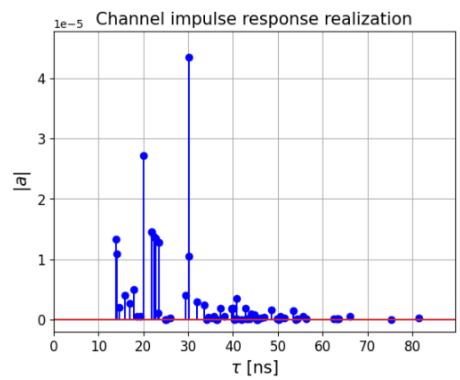

Fig. 6: Channel impulse response in delay domain for NLOS scenario

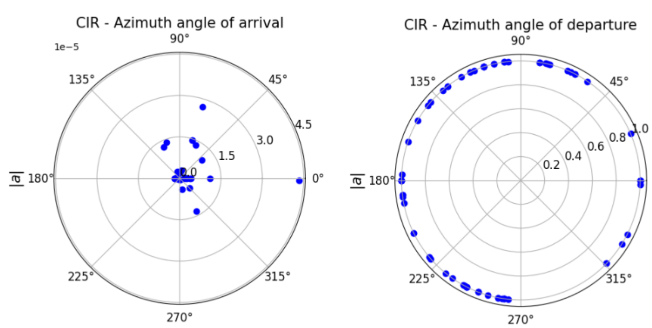

(a) Angles of arrival (b) Angles of departure

Fig. 7: Channel impulse response in angular domain for NLOS scenario

III. Bit Error Rates

Bit error rates were simulated for the LOS scenario. Basic parameters have been set to 16 QAM modulation, LDPC coding with 378/1024 code rate and 120 kHz subcarrier spacing. Subsequently, their individual values were changed. Ideal BER curves were simulated in an AWGN channel.

The bit error rates for the available modulations are shown in Fig. 8a. Modulations with a higher number of bits per symbol needed a greater margin from noise. This is due to the fact that higher number of bits is reflected in the constellation diagram by a larger number of symbols, which have smaller distances between them. This increases the probability of misinterpreting a symbol in the presence of noise. The advantage of higher order modulations is higher data rate for transmission.

Fig. 8b shows bit error rate curves for different code rates. As expected, the best noise immunity was achieved at the lowest code rate, while the worst BER results were achieved at the highest code rate. This is because a lower code rate adds more redundant bits, allowing for the correction of a greater number of errors caused by noise, interference, or distortion. Its disadvantage is a reduction in the effective data rate, because a larger part of the link capacity is used for redundant data.

The influence of subcarrier spacings on bit error rates are shown in Fig. 8c. Smaller subcarrier spacing values were more resistant to noise. Larger subcarrier spacings were not as robust to noise, but their advantage is better resistance to Doppler shift and they are also more susceptible to inter-symbol interference (ISI) but need more bandwidth. In this case, the theoretical curves differ the most from the simulated ones. Subcarrier spacing had almost no effect on the theoretical curves. This was probably caused by the fact that they were not exposed to ISI, unlike the simulated ones.

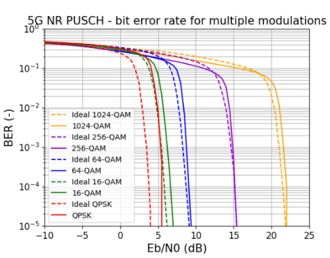

(a) BER curves for different modulations

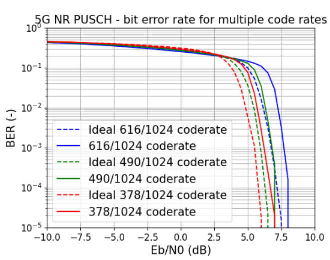

(b) BER curves for different code rates

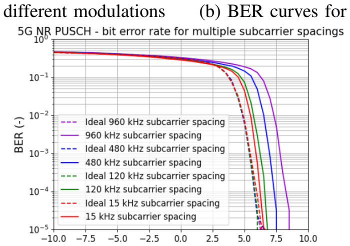

(c) BER curves for different subcarrier spacings

Fig. 8: Bit error rate curves for LOS scenario

IV. Measurements

A. Beam steering evaluation kits

Measurements were performed on the evaluation kits EVK06002/EVK06003 from Sivers semiconductors, connected to Xilinx ZCU111 RFSoC development board serving as the baseband signal generation and acquisition device. This beam steering kit covers frequencies from 57 to 71 GHz, supports (according to the datasheet) modulations up to 64 QAM and has integrated beam book for steering settings. The transmitter can be steered only in azimuth within the range of ±45 degrees. The receiver can be steered in azimuth within the range of ±45 degrees and elevation ±18 degrees.

B. Transmitted and received signals

The transmitted signal consisted of several Synchronization Signal Blocks in a row. Data was transmitted only in the Primary Synchronization Signal and Secondary Synchronization Signal parts. To detect the direction of data transmission, a certain quadruple of subcarriers was zeroed, deviating our setup from the 5G NR standard, but relaxing the data processing.

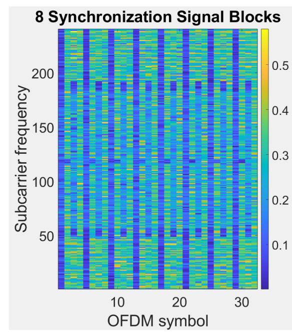

(a) Detected path

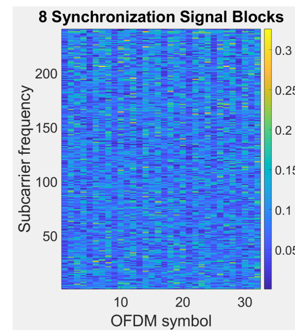

(b) Noise

Fig. 9: Reference Signal received power in time-frequency domain

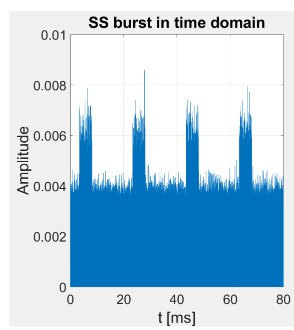

(a) Detected path

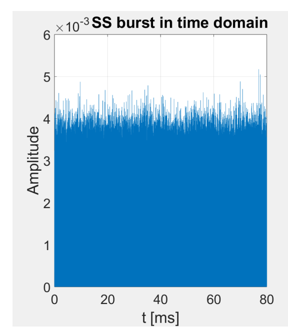

(b) Noise

Fig. 10: Synchronization Signal burst in time domain

An example of the resource grid of the captured signal is shown in the Fig. 9a. In this case, subcarrier frequencies 116 to 120 were not transmitted, which corresponds to a transmission angle of -2.9 degrees. Fig. 9b shows a resource grid where the transmission angle cannot be recognized due to receiving a signal with a value lower than the noise. The difference in correctly received signal and noise, i.e., signal with not received SSB, levels is evident from the Fig. 10.

C. Line-of-Sight measurement

The transmitter and receiver were deployed according to the simulation. The measurement results are shown in a Fig. 11

representing the angle of transmitted beam and the received signal strength. The line-of-sight path was almost the same as in the simulation. The simulated path transmitted at 350 degrees was shifted to 337 degrees due to the simplified model. The other paths were lost below the noise level. Note that the results shown here are results of our first measurements and some of the parameters were probably not setup in an optimal way, such as gains at the transmitter and receiver, or transmitted power. Moreover, the development kit used is not able to span the whole 360 degree range, so only part of the angular information is shown. The same applies also to NLOS case shown below.

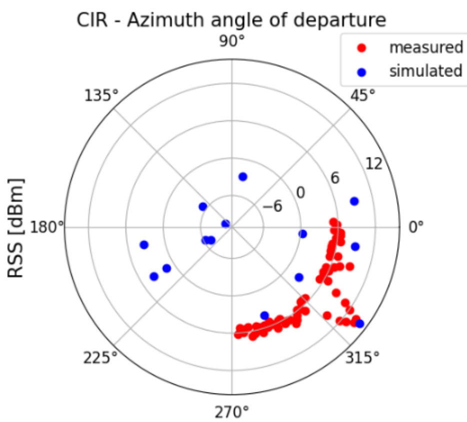

Fig. 11: Channel impulse response in angular domain for LOS scenario - comparison between measurements and raytracing simulations

D. Non-Line-of-Sight measurement

For Non-Line-of-Sight transmission, reflections from the cabinet were measured. Fig. 12 shows the measured values. It is evident that the main reflection from the cabinet was almost identical to the simulation. Due to the simplification of the model, some paths in the simulation disappeared. These paths could have been reflected from transitions and irregularities in the cabinet, however, their values approximately corresponded to the other reflections.

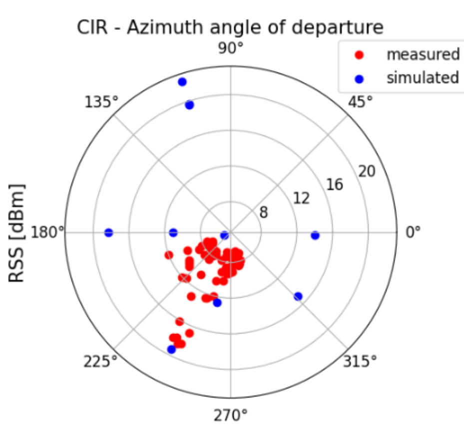

Fig. 12: Channel impulse response in angular domain for NLOS scenario - comparison between measurements and raytracing simulations

Conclusion

In this paper, we have presented our experiments with cell search at mm-wave frequencies in the indoor environment.

The raytracing and Channel impulse responses were simulated using the Sionna library. Channel impulse responses were simulated for both Line-of-Sight and Non-Line-of-Sight scenario in delay and angular domain. For the Line-of-Sight scenario, bit error rates were calculated in terms of modulations, code rate and subcarrier spacings.

Furthermore, the real signal transmissions were measured for simulated scenarios with the use of Sivers EVK06002/EVK06003 evaluation kits and Xilinx ZCU111 as the baseband solution. In the case of Line-of-Sight scenario, the impulse response was almost the same as in the simulated case, only one path was angularly shifted. For Non-Line-of-Sight scenario, the main reflection from the cabinet was similar with the simulation. New paths emerged in the measurements that were not present in the simulations because the model was simplified. Moreover the used kits were not able to cover the whole 360 degree span of angles. Further improvement may also be expected from the optimization of RF signal parameters.

All simulation and evaluation scripts including measured data are available from github repository https://github.com/marekcrn/Masters-thesis.

Acknowledgment

I would like to express my sincere gratitude to my supervisor, prof. Ing. Roman Maršálek, Ph.D, for his invaluable help, advise, and guidance throughout this project. I would also like to express my sincere gratitude to Ing. Radek Závorka for assistance with measurements and data processing.

References

[1] Akarsh Saxena, Stuti Bharadwaj, “5G Network Technology and Its Implications, Impact on Applications”, Mathura, India, 2023, ISSN: 2456-3315

[2] Navid Fazle Rabbi, “Introduction to 5G,” Islamic University of Technology, January 2020, DOI:10.13140/RG.2.2.14027.00804

[3] Tuninato, R., Riviello, D.G., Garello, R. et al. “A comprehensive study on the synchronization procedure in 5G NR with 3GPP-compliant link-level simulator,” J Wireless Com Network 2023, 111 (2023).

[4] E. Dahlman, S. Parkvall, J. Sköld, “5G NR: the next generation wireless access technology,” pp. 311–334. Academic Press, London (2018).

Methods for securing Linux-based embedded systems

1st Tomáš Nagy
Department of Telecommunication
Brno University of Technology
Brno, Czech Republic
xnagyt01@vutbr.cz

2nd Pavel Paluřík
Department of Telecommunication
Brno University of Technology
Brno, Czech Republic
xpalur01@vutbr.cz

3rd Lukáš Jablončík
Department of Electrical and Electronic Technology
Brno University of Technology
Brno, Czech Republic
xjablo02@vutbr.cz

***Abstract*—This paper focuses on the design and implementation of a secure Linux-based system for Compulab embedded devices serving as communication gateways in smart buildings. The primary goal is to protect the gateway against potential cyber threats while ensuring automated device management and secure and uninterrupted system operation with minimal downtime. We will briefly analyze three existing IoT security reference models and IoT vulnerabilities while proposing a resilient architecture with robust protection mechanisms. The final system is designed for efficient operation, minimal downtime, and compliance with stringent security requirements. Real-world testing will be conducted to verify its effectiveness, ensuring reliability and adaptability in modern smart building environments.**

***Index Terms*—Embedded system, Linux, Gateway, IoT, Security, Compulab**

I. Introduction

The Internet of Things (IoT) represents a transformative paradigm where physical objects, such as sensors, appliances, and communication gateways, are interconnected through advanced communication networks. It enables seamless connectivity, facilitating real-time data exchange and automation across industries like smart homes, healthcare, and industrial automation. The rapid expansion of IoT has been driven by advancements in embedded systems, wireless communication protocols, and cost-effective computing components, leading to smart environments that enhance efficiency, sustainability, and user experience [1].

However, IoT's widespread adoption also introduces significant security challenges. Many IoT devices operate with limited computational resources, making them vulnerable to cyberattacks, unauthorized access, and data breaches [2]. Traditional security models are often inadequate, necessitating new approaches tailored to IoT's constraints. This includes implementing effective authentication mechanisms and employing cryptography to ensure data integrity and confidentiality. Furthermore, monitoring and logging play a critical role in securing IoT ecosystems. Centralized log management allows organizations to collect and analyze logs from IoT devices in real-time to detect anomalies, track device performance, and identify potential security breaches early on [3].

Additionally, automated and secure software updates play a crucial role in maintaining IoT security, ensuring devices receive necessary patches and improvements without manual intervention. Combined with effective monitoring practices, these measures enhance operational resilience. To secure IoT ecosystems in the long term, regulatory frameworks and industry standards must continuously evolve to address emerging cybersecurity and privacy challenges, ensuring the reliability and protection of interconnected systems [4].

II. IoT Reference models

There are three main IoT reference models commonly discussed in both academic and industry literature [5]:

- **3-level model:** The earliest framework views IoT as an extension of wireless sensor networks (WSNs), pairing them with cloud servers to deliver user services. Think of it as "$sensors + cloud = basic\ IoT$."
- **5-level model:** Designed to streamline collaboration in enterprises, this splits complex systems into manageable layers.
- **Cisco 7-level model:** Proposed in 2014, this comprehensive framework adds granularity by separating tasks like data processing, analytics, and user interfaces. Unlike the simpler models, it supports two-way data flow: Top-down and Bottom-up.

Since a full discussion of all three models is beyond the scope of this paper, we will focus on the CISCO model to analyze IoT security threats and countermeasures at each level.

A. Cisco 7-level model

The next section provides a brief overview of its structure in a bottom-up hierarchical progression [5].

1) **Edge devices:** The initial level of this reference model includes various computing nodes such as sensors, RFID readers, and different types of RFID tags. At this stage, it is crucial to ensure data confidentiality and integrity as we move up through the levels.
2) **Communication:** This level encompasses all the elements that facilitate the transfer of information or commands. It includes: communication among devices at the first level, interactions between components within the second level, and the exchange of data between the first level and the third level.
3) **Edge computing:** Also known as fog computing, involves basic data processing closer to the network's

edge. Real-time applications rely on this for quick computations. The extent of processing depends on the power of the service providers, servers, and nodes, typically using simple signal processing and learning algorithms.
4) **Data accumulation:** Involves storing data for future analysis or sharing with higher-level servers, as not all applications require immediate processing. This level also fuses on determining data relevance to higher levels.
5) **Data abstraction:** Simplifies and optimizes data for easier or more efficient processing. Key tasks include normalizing, de-normalizing, indexing, consolidating data, and enabling access to multiple data sources.
6) **Applications** Interpretation of data, where software interacts with the data accumulation and abstraction levels.
7) **User space:** The primary objective is to deliver accurate and timely information to users.

III. IoT security risks

This section represents an analysis of potential attacks and vulnerabilities at each layer of the reference model. Figure 1 outlines all of the most common attack scenarios. The following text will only provide a description of a select few types.

Based on existing attack taxonomies and real-world attacks, five key dimensions for classifying attacks on embedded systems are identified [6]:

- Prerequisite – The conditions that must be met for an attacker to execute an attack.
- Attack type – The techniques exploiting vulnerabilities.
- Vulnerability – The weaknesses that an attacker can exploit.
- Target – The specific part of the system being attacked, whether a particular layer of the architecture or the entire embedded device.
- Final effect – The potential impact of a successful attack.

A. Prerequisites

Local or Remote access - To target an IoT device, attackers typically need some level of access, either physically on-site or remotely. This access often doesn't require high-level administrator privileges; standard user access is usually sufficient.

Internet facing - Internet connectivity exposes IoT devices to remote vulnerabilities. Attackers can exploit these vulnerabilities without needing access privileges, simply by discovering and communicating with the device over the network.

Direct physical access - This type of access means the attacker must physically reach the device. However, they may not need any special permissions to utilize the device's services.

B. Attack type

Injection - Embedded devices are vulnerable to attacks involving the injection of crafted network packets or the manipulation of program inputs. These methods take advantage of parsing errors in protocol implementations and software.

Hijacking - A hijacking attack is when an attacker takes unauthorized control over a system, session, or communication channel. This type of attack can exploit vulnerabilities in authentication, session management, or unsecured communication protocols.

Sniffing - Involves intercepting network communication to extract sensitive data, such as credentials or device configurations. Unencrypted information enables attackers to conduct advanced attacks, like injecting malware by adding rogue nodes to authorized lists.

C. Vulnerability

Weak access control and authentication - Many devices rely on default, weak, or even hard-coded passwords. Attackers who discover these credentials can easily bypass access controls with minimal effort, gaining unauthorized access to the system.

Programming vulnerabilities - Many vulnerabilities result from programming errors. These issues can lead to control flow attacks, such as input parsing flaws that cause buffer overflows or memory management mistakes, like using pointers that reference freed memory.

Improper use of cryptography - Incorrect implementation leads to serious security flaws, such as the use of poor random number generation for keys and vulnerabilities in cryptographic protocols.

D. Effect

Denial of Service - Cyberattack aimed at disrupting or completely halting access to computer systems or services. This is typically achieved by overwhelming the target with a massive volume of requests, exhausting its resources and rendering it unusable.

Unauthorized access - This technique involves bypassing security measures to infiltrate a system or escalating existing privileges to gain higher-level control, allowing deeper access to sensitive functions and data.

Information misuse - Cybercriminals frequently disseminate information obtained through successful cyberattacks.

IV. Secure IoT System Architecture Design

The following chapter focuses on the practical design of a secure IoT system. This design encompasses not only technical aspects but also conceptual and organizational approaches essential for ensuring system security in real-world deployment. Emphasis is placed on identifying appropriate security measures and mitigating potential threats.

A. Secure Boot

Compulab utilizes the robust security features of NXP's i.MX8M Mini System-on-Chips by integrating the High Assurance Boot (HAB) module to ensure a secure and trusted boot process. The HAB module employs a combination of public-key cryptography, secure keys, and signature verification techniques. The boot process follows a multi-stage (chain-of-trust) boot sequence with trusted code execution.

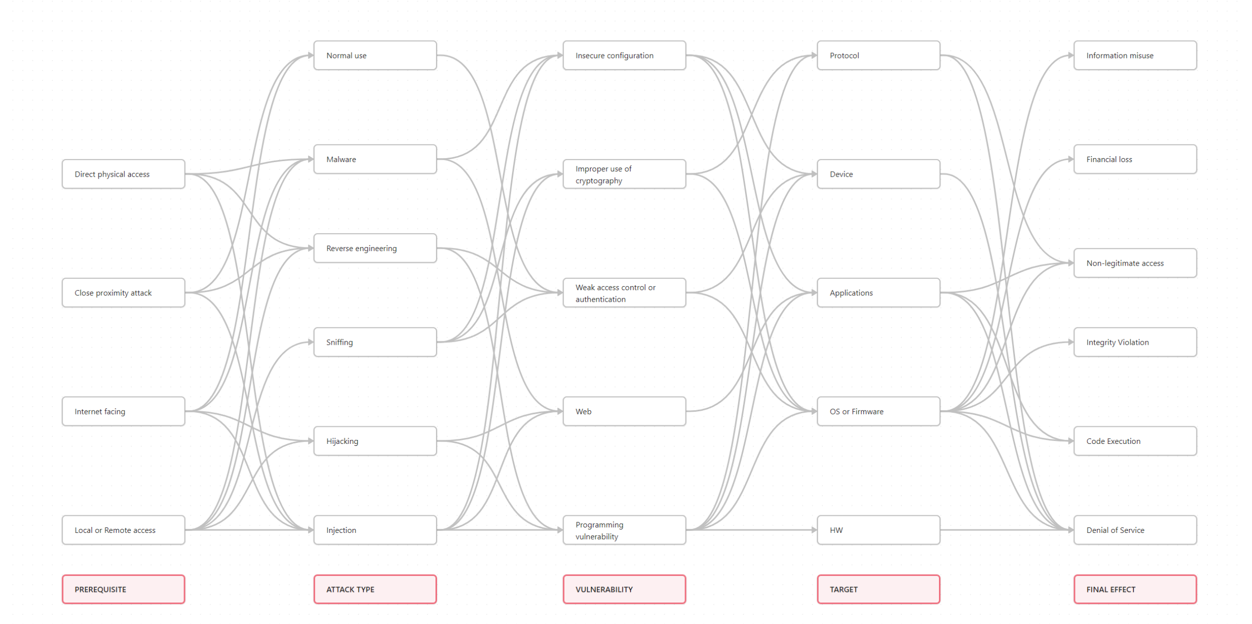

Fig. 1. Frequent IoT attack scenarios

A simplified version of the boot process is illustrated in Figure 2. Here is the explanation of the boot process:

1) BootROM execution - performs basic hardware initialization. If HABv4 is enabled BootROM verifies the digital signature against public keys fused into the SoC. Validates the IVT (Image Vector Table) and CSF (Command Sequence File).
2) First-Stage Bootloader (SPL) - initializes DDR firmware, loads the FIT image (`flash.bin`), containing U-Boot with HABv4 support.
3) Second-Stage Bootloader (U-Boot) - initializes more complex hardware, loads the Linux kernel and the device tree, boots into the OS. The U-Boot binary must be signed. HABv4 verifies its signature before execution. U-boot also verifies whether the kernel is signed.
4) Linux Kernel Execution - mounts root filesystem and launches user-space applications.

B. Disk encryption with CAAM hardware

The Cryptographic Acceleration and Assurance Module (CAAM) provides hardware-backed security for cryptographic operations, including secure key management. Tagged keys (specifically black keys) are a core feature designed to protect encryption keys from exposure. Table I presents an overview of the key features of the CAAM module. Here is a brief demonstration on how to create and use cryptographic keys with CAAM for encrypting and decrypting data on an embedded device.

- Verify that cryptographic transformations are registered in the kernel.
- Generate a 16-byte black key encrypted with CBC mode from a given plain text.

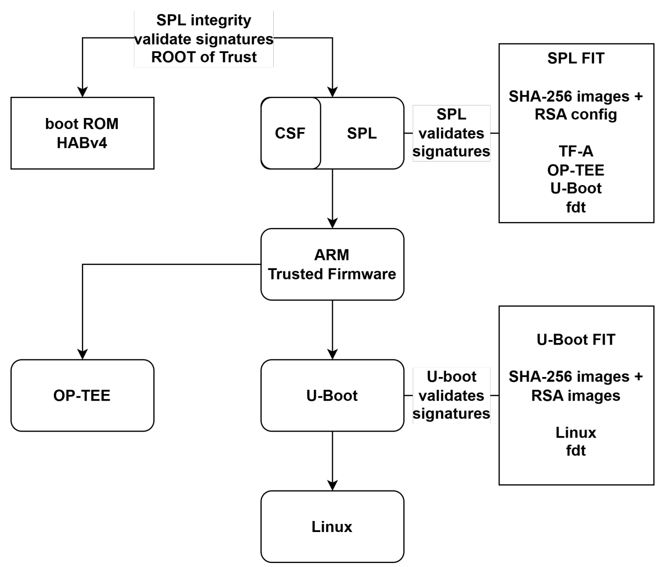

Fig. 2. Generic Boot Flow using HABv4

- Add the key in a key retention service with `keyctl`.
- Create a secure volume or mount an existing one that needs to be encrypted.
- Create a device-mapper and specify the mapping table with `dmsetup`.
- For the new volume specify the filesystem and set up a mount point.
- Verify the process after rebooting the device.

TABLE I
CAAM BLACK KEY OVERVIEW

Properties	Description
Definition	Hardware-encrypted keys protected by CAAM's OTPMK.
Key Length	128/192/256-bit AES keys encrypted using AES-ECB or AES-CCM.
Encryption Modes	AES-ECB (fast) and AES-CCM (with 12-byte MAC for integrity checks).
Security Features	Device-specific, tamper-resistant, and never exposed in clear text.
Use Cases	Encrypted storage, secure boot, and TLS key protection.
Storage	Stored as cryptographic blobs with MAC tags (CCM mode).
Kernel Support	Integrated with Linux key retention service and dm-crypt.
Limitations	Irreversible OTPMK dependency and increased blob size with CCM.

C. *Embedded system secure updates*

Embedded devices have unique software update requirements due to limited hardware resources, specialized functions, and deployment in critical applications. Key requirements include: atomicity, recovery, remote updates, security, efficiency. Therefore, this paper focuses on containerized updates, which satisfy the preceding requirements as well as achieve minimal system downtime. Enhanced security for containerized updates is achieved through the digital signing of container images and firmware, leveraging hardware-backed keys, such as the CAAM black keys. Alternatively, deploying a secure TLS Watchtower application, which automates the monitoring of container image repositories and facilitates the immediate retrieval and deployment of new images to the system upon their availability.

D. *Secure remote access*

Remote access to embedded systems is essential for monitoring, maintenance, and updates, but it also introduces security risks. Due to the risks associated with the device's deployment environment, remote headless management is mandated, eliminating the need for on-site physical interaction. Secure remote access strategies include:

- SSH hardening - disabling root login, using SSH key authentication (require users to authenticate exclusively via certificate-based methods), restriction of IP addresses, changing the default SSH port, enabling fail2ban feature, restricting access to a specific group of users, implementing logging and monitoring.
- VPN technologies - establishing WireGuard tunnel for encrypted connection to remote servers, implementing multi-factor authentication for an extra layer of security.
- Disable local user and enforce headless operation.

E. *Advanced Whitelisting Strategies*

Application whitelisting is a proactive security measure that allows only pre-approved applications to execute on a system. How to achieve:

- Identify essential business applications.
- Define rules specifying which applications are permitted.
- Enforce and maintain the policies.

There are various types of application whitelisting; however, the most suitable for our IoT deployment is the certificate-based, since we can leverage the CAAM module. This method ensures that only applications signed with trusted certificates can execute. These applications need to be signed manually by our administrator with a specific key.

V. CONCLUSION

This paper explored methods for securing Linux-based embedded systems, focusing on application whitelisting, secure boot, and remote management. We proposed strategies including hardware-backed signing, containerized updates, and centralized logging. While the model outlines a robust security framework, its effectiveness in real-world scenarios remains to be validated through practical implementation and testing. This theoretical study indicates that unexpected anomalies and evolving intrusion techniques may pose challenges, reinforcing the importance of ongoing research into dynamic and adaptable security strategies.

ACKNOWLEDGMENT

The research presented in this paper was conducted as part of my master's thesis. I would like to express my sincere gratitude to Pavel Paluřík, my thesis supervisor, for his invaluable professional guidance, expertise, and unwavering support throughout this process. I would also like to extend my heartfelt thanks to Lukáš Jablončík for generously providing the Compulab device, which played a crucial role in the implementation and testing phases of this project.

REFERENCES

[1] KENTON, Will. What Is the Internet of Things (IoT)? How It Works and Benefits. Online. Investopedia. 2022, 2022-12-27. Available at: https://www.investopedia.com/terms/i/internet-things.asp.

[2] YASAR, Kinza a S. GILLIS, Alexander. Internet of things (IoT). Online. TechTarget. 2024, 2024-06. Available at: https://www.techtarget.com/iotagenda/definition/Internet-of-Things-IoT.

[3] GREENGARD, Samuel. Internet of Things. Online. Britannica. 2022, 2025-02-13. Available at: https://www.britannica.com/science/Internet-of-Things.

[4] PRAKASH, Prateek. Configure logging and monitoring for security events in your AWS IoT environment. Online. AWS. 2025, 2025-03-08. Available at: https://docs.aws.amazon.com/prescriptive-guidance/latest/patterns/configure-logging-and-monitoring-for-security-events-in-your-aws-iot-/environment.html.

[5] NIA, Arsalan & JHA, N.K.. (2016). A Comprehensive Study of Security of Internet-of-Things. IEEE Transactions on Emerging Topics in Computing. PP. 1-1. 10.1109/TETC.2016.2606384.

[6] PAPP, Dorottya & MA, Zhendong & BUTTYAN, Levente. (2015). Embedded systems security: Threats, vulnerabilities, and attack taxonomy. 145-152. 10.1109/PST.2015.7232966.

Aggregation and Evaluation of Vulnerabilities from CVE Databases for Effective Security Assessment

1st Adam Tucek
Department of Telecommunications
FEEC, Brno University of Technology
Brno, Czechia
xtucek08@vut.cz

2nd Willi Lazarov
Department of Telecommunications
FEEC, Brno University of Technology
Brno, Czechia
lazarov@vut.cz

***Abstract*—As digital technologies evolve, cyber threats continue to increase, often due to vulnerabilities in modern systems. This situation has led to the establishment of open databases and standardized methods for classifying, categorizing, and assessing software vulnerabilities. This paper addresses the domain of Common Vulnerabilities and Exposures (CVE) and introduces an innovative solution for aggregating CVE records to support security assessment and reporting.**

***Index Terms*—CVE, CWE, CVSS, CPE, vulnerabilities**

I. Introduction

Rapid advancement of information technology is closely related to the growing volume of software and its increasing integration with other technologies. Companies prioritize maximum automation while minimizing human intervention. However, this trend also leads to greater complexity and a rising number of software vulnerabilities. For example, the National Vulnerability Database (NVD) currently lists nearly 270,000 vulnerabilities, with more than 34,000 reported in 2024 in contrast to 2016, when only 6,000 vulnerabilities were recorded [1], [2]. Furthermore, organizations can rely only on a single source, such as NVD, to track potential vulnerabilities within their systems. However, these databases may not always provide all the information needed to accurately identify and mitigate security risks. Since different databases offer varying details, they can influence user's understanding of a given vulnerability, pointing the need to aggregate and analyze information from more sources.

This paper presents an innovative tool that enables developers to efficiently analyze their software and search for existing Common Vulnerabilities and Exposures (CVE). The tool aggregates data from available sources to provide comprehensive information about CVEs, supplemented by additional details such as severity, vulnerability category, and exploits. To achieve this, the tool uses open standards, including Common Platform Enumeration (CPE), the Common Vulnerability Scoring System (CVSS), and Common Weakness Enumeration (CWE). This solution supports software developers and penetration testers in identifying known vulnerabilities that can be addressed and properly eliminated.

The research described in this paper was financially supported by the Technology Agency of the Czech Republic, project No. FW11020057.

II. Background and Related Work

One of the key aspects of preventing vulnerabilities in computer systems is the development and use of common standards that enable a clear description and communication of information about known vulnerabilities. To address this need, the CVE system was developed with the primary objective of providing a standardized method to name vulnerabilities. The CVE system works alongside other security standards, such as CWE and CPE, to help users better understand vulnerabilities within their information systems.

A. Classification and Identification of Vulnerabilities

The CVE program provides a system of common unique identifiers for computer security vulnerabilities in the form of a short string that consists of a prefix, current year, and a random unique number. For example, CVE-2023-23397 represents a vulnerability in Microsoft Outlook that allows an attacker to obtain the victim's Net-NTLMv2 hash, which can then be used for lateral movement within the compromised organization's network [3]. These identifiers are assigned by the CVE Numbering Authority (CNA), usually large tech companies like Google, Red Hat, or CERT teams. Although the CVE itself does not provide any technical information about the vulnerability, it allows for easier identification of vulnerabilities in existing systems and enables better tracking in online databases, which can provide detailed information to software developers [4], [5].

Following CVE, the CWE program works on a similar principle. It provides unique identifiers for weaknesses, faults that in certain conditions might lead to the system becoming vulnerable to attacks. The identifier itself consists of a prefix, unique random number, and the CWE name, which describes the weakness itself. CWE uses the principles of inheritance when assigning unique identifiers. In addition, the CWE records also contain references to other weaknesses (*Nature*). Using parent-child relations, a tree structure is created, starting from generic records (e.g., *CWE-707: Improper Neutralization*), which describes basic concepts, to child CWEs that detail specific weaknesses (e.g., *CWE-94: Improper Control of Generation of Code*). These CWEs can be connected to one or more CVE records [6].

The severity of CVE is assessed using the CVSS standard based on the scores calculated (in version 4.0) from the base metric group, threat metric group, and environmental metric group. The severity score of each group is influenced by the metric variables and the impact on confidentiality, integrity, and availability. The final evaluation results in a CVSS score (on a scale of 0–10) and a CVSS vector, which contains all variables and values of the metrics groups [7].

To provide a technology specification and improve the accuracy of vulnerability searches, CPE can be used as input for searching CVE records. CPE is a standardized machine-readable format for clear identification of IT products and platforms. In practice, it is a string that consists of several parts, each of them describing a specific part of a product. For example the CPE *cpe:2.3:a:redhat:wildfly:8.0.0:beta1:*:*:*:*:*:** represents version (2.3) of the CPE standard, the described product being a software (*a*), vendor that provides the software (*redhat*), name of the product itself (*wildfly*), exact version of the product (*8.0.0*), and additional information related to the version (*beta1*). The CPE can also contain other more specific information, such as language, edition, target software, and target hardware. In case this information is unknown or not relevant, it is replaced by the "*" sign [8].

B. Comparison of CVE Databases

To select appropriate open sources for the implementation of the proposed solution, we analyzed the available CVE databases. The comparison of open CVE databases is listed in Table I and includes the following parameters:

- Search for CVE without authorization.
- Application programming interface (API).
- Filtering results using API endpoints.
- Presence of CVSS vulnerability assessment.
- Reference to one or more CWE records.
- Ability to search for CVEs using CPE.

TABLE I
COMPARISON OF CVE AND EXPLOIT DATABASES

Database	Public	API	Filters	CVSS	CWE	CPE
NVD [2]	✓	✓	✓	✓	✓	✓
CVE Details [9]	✗	✓	✓	✓	✓	✓
CVE List [10]	✓	✓	✓	✓	✓	✓
Exploit DB [11]	✓	✓	✓	✗	✗	✗
Snyk [12]	✗	✓	✓	✓	✗	✗
VulnDB [13]	✗	✓	✓	✓	✓	✓
OSV [14]	✓	✓	✓	✓	✗	✗
Vulners [15]	✗	✓	✓	✓	✓	✓

The comparison shows that the NVD and CVE List databases are the most suitable for custom integration, as they contain the largest amount of information and allow easy access without prior authorization. While the VulnDB, Vulners, CVE Details, and Snyk databases provide some important information, access is restricted to paid accounts only. Although the OSV database offers public access, it does not support searches using CPE. In addition, we included Exploit DB, which does not contain CVE records but can be used for searching exploits based on the linked CVE references.

III. System for Aggregation and Analysis of CVE from Open Sources

As mentioned in Section I, one of the challenges related to the search for vulnerabilities is fragmentation of the available information. To address this challenge, this paper proposes an innovative solution that allows users to efficiently collect, aggregate, analyze, and evaluate data from multiple open sources, producing a readable report with all the necessary information on possible vulnerabilities within the system. The architecture of the proposed solution is shown in Figure 1 and each phase is described in the following sections.

A. Input and Parsing

The first phase is parameterization, which is done in the *Input and parsing module*. This module serves as an interface between the user and the tool itself. It ensures appropriate acceptance of input data from the user (single CPE string or file containing multiple CPEs) and other tool settings, which are then passed to other modules. It also provides a basic user guide on how to use the proposed tool.

B. Data Aggregation

The next and main phase of the search for existing vulnerabilities is information gathering. This is done in the search module using user input provided from the previous phase. The module constructs queries to different available database APIs, which typically return data in JSON format, making it easy for further processing. The module also uses assistance queries, such as retrieving lists of CVEs for a specific CPE. Based on the comparison in Table I, the module implements the following public databases, which are used in the collection process as default open sources:

- **NVD** and **CVE List** – public databases containing CVE records, including their description, CVSS vector, base score, affected products and other references.
- **CWE (MITRE)** – CWE details that can be referenced in the CVE records found in the initial search.
- **ExploitDB** – available exploits linked to CVEs.

While these databases serve as the base data source, one of the key function of the proposed tool is extensibility. Therefore, if the user has access (e.g., API token) to other databases with restricted access, it is possible to include them as an additional source of information for aggregation.

C. Data Normalization

Since different databases return structured data in various formats, additional processing is required to ensure a consistent structure for data analysis and evaluation. As the primary goal is not to provide complex data objects, only the most common and critical vulnerability information is selected. This includes the CVE ID, publication date, brief description, linked CWEs, and reference to the relevant exploit (if available). The tool standardizes these data into uniform objects for each database and forwards them to the next module.

D. Analysis, Evaluation, and Unification

Once all data from open sources have been collected and transformed into a common format, they can be processed by the next module, which consists of three phases:

1) **Analysis** – First, the received data are analyzed. During this stage, the module examines each individual field to determine whether all necessary information has been provided. If any data are missing, the corresponding fields are marked. Furthermore, the analytical module extracts additional information, such as the description length and the number of sources used.
2) **Evaluation** – After the analysis phase is complete, the data can be evaluated to determine which records will be part of the final report, using the information collected in the aggregation phase. By default, the tool uses basic metrics (description length) to determine which information will be used. If information is provided from multiple sources, it will be marked as verified.
3) **Unification** – In the last phase, the module runs unification, during which all previously analyzed and evaluated data are transformed into CVE objects that contain information about the identified vulnerability. This phase also includes removing duplicates of the same records.

Once the data have been fully processed and unified, they are forwarded to the reporting module.

E. Output and Report

The last module of the proposed tool generates the output and report, providing a proper communication of the results to the user. The tool offers multiple ways of providing this information, including basic output in the terminal, exports in JSON format, and structured reports using generated HTML files or PDF for a more readable output. The output contains the original CPE (input), followed by the relevant CVEs with detailed information. These outputs can also be integrated with third-party software, such as Cyber Threat Intelligence (CTI) platforms, to analyze threats on a larger scale.

Furthermore, another advantage of the proposed tool is the ability to use existing reports as input. In this case, instead of performing the CPE-based search, which results in a complete report of possible CVEs, the tool will only show the difference, such as new CVE records for a CPE or changes in vulnerability scoring since the last report was generated. This feature is particularly useful for regular vulnerability scanning to get a point-in-time snapshot of the security status.

IV. Experimental Testing

Based on user input, either a single CPE or a text file containing multiple CPEs, the tool is capable of querying multiple databases (NVD, CVE List, CWE, and ExploitDB) to provide common vulnerability information to the user. The time this process takes is heavily dependent on the number of CPEs, with the most time-consuming part of a regular run of the tool being waiting for a response from different databases and processing collected results.

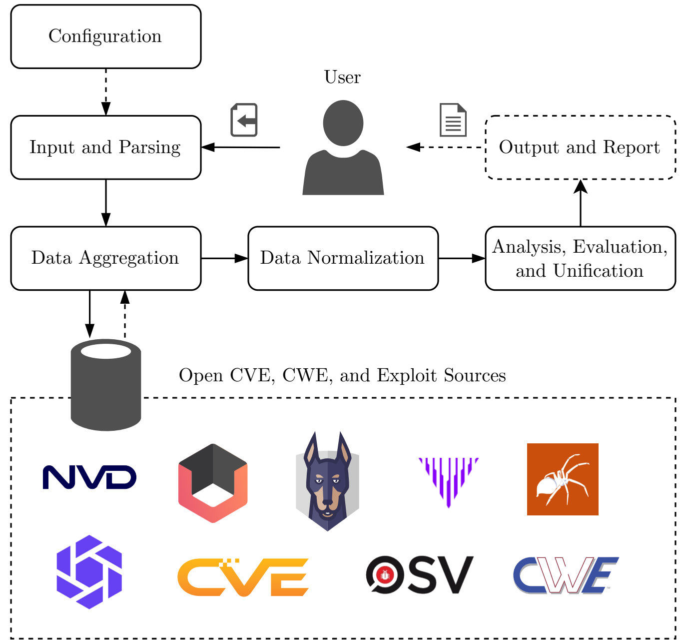

Fig. 1. Workflow of the proposed tool

During experimental testing, the NVD database generally provides responses faster than the CVE List. For instance, a CPE with a single related CVE takes less than a second to process, increasing to up to 3 seconds while querying the NVD and up to 20 seconds when querying the CVE List for a CPE with a higher number of CVE records (tested with 80 CVE records). However, the database may sometimes delay its response for several seconds when API usage is high. The module outputs from the experimental testing are listed in Appendix A, which contains examples of data objects obtained from the NVD, CVE List, and CWE (MITRE).

V. Conclusions and Future Work

In this paper, we analyzed open databases and other sources to collect valuable information on vulnerabilities searched by CPE. To support the manual process of security assessment, we designed and developed a tool for aggregating information about common vulnerabilities and exploits. The implemented solution uses public databases and open standards, focusing on modularity and further extensibility with additional open sources for data collection. The main contribution of this work lies in automating the search for vulnerabilities from multiple sources while increasing the credibility by cross-referencing the collected information. However, as presented in this paper, our solution is experimental. Therefore, we aim to extend the implemented modules in the future. Specifically, we will focus on adding more open sources and integrating this tool with third-party software, such as CTI platforms.

Acknowledgements

We express our gratitude to cybersecurity experts from Škoda Auto for their feedback on the proposed solution and its functions presented in this paper.

References

[1] H. Hanif, M. H. N. M. Nasir, Ab Razak, M. F., A. Firdaus, and N. B. Anuar. “The rise of software vulnerability: Taxonomy of software vulnerabilities detection and machine learning approaches“ *Journal of Network and Computer Applications*, vol. 179, p. 103009, Apr. 2021.

[2] “NVD Dashboard,“ NIST. https://nvd.nist.gov/general/nvd-dashboard (accessed Feb. 10, 2025).

[3] “CVE-2023-23397“ NIST. https://nvd.nist.gov/vuln/detail/cve-2023-23397 (accessed Feb. 10, 2025).

[4] “About the CVE program,“ CVE. https://www.cve.org/About/Overview/ (accessed Feb. 28, 2025).

[5] “What is a CVE?,“ Red Hat. https://www.redhat.com/en/topics/security/what-is-cve (accessed Feb. 28, 2025).

[6] “About CWE,“ MITRE CORPORATION. https://cwe.mitre.org/about/index.html (accessed Feb. 28, 2025).

[7] “Common Vulnerability Scoring System SIG,“ FIRST. https://www.first.org/cvss/ (accessed Feb. 28, 2025).

[8] “Official Common Platform Enumeration (CPE) Dictionary,“ NIST. https://nvd.nist.gov/products/cpe (accessed Feb. 28, 2025).

[9] “CVEdetails,“ SecurityScorecard Inc. https://www.cvedetails.com/ (accessed Feb. 10, 2025).

[10] “CVE Services API,“ MITRE CORPORATION. https://cveawg.mitre.org/api-docs/ (accessed Feb. 10, 2025).

[11] “Exploit Database,“ OffSec Services Ltd. https://www.exploit-db.com/ (accessed Feb. 10, 2025).

[12] “Snyk Vulnerability Database,“ Snyk Ltd. https://security.snyk.io/ (accessed Feb. 10, 2025).

[13] Risk Based Security. “VulnDB,“ pyxyp inc. https://vuldb.com/ (accessed Feb. 10, 2025).

[14] “A distributed vulnerability database for Open Source,“ OSV. https://osv.dev/ (accessed Feb. 10, 2025).

[15] “All-in-one vulnerability intelligence,“ Vulners Inc. https://vulners.com/ (accessed Feb. 10, 2025).

Appendix

We list examples of normalized data objects in Listing 1, where the dots symbol (...) indicates that the value has been truncated for presentation purposes. The demonstration of the final report containing one of the CVE records related to *cpe:2.3:a:oracle:access_manager:12.2.1.4.0:*:*:*:*:*:*:** is shown in Figure 2.

Listing 1. Normalized CVE records

```
[
  {
    "id": "CVE-2020-35452",
    "cwe": ["CWE-787"],
    "date_published": "2021-06-10T07:10:21",
    "description": "Apache HTTP Server versions 2.4.0 to
        2.4.46 A specially crafted Digest nonce can cause a
         stack overflow in mod_auth_digest...",
    "cvss_vector": "CVSS:3.1/AV:N/AC:L/PR:N/UI:N/S:U/C:L/I:
        L/A:L",
    "cvss_score": "7.3",
    "source": "NVD"
  },
  {
    "id": "CVE-2021-26690",
    "cwe": ["CWE-476"],
    "date_published": "2021-06-10T07:10:22",
    "description": "Apache HTTP Server versions 2.4.0 to
        2.4.46 A specially crafted Cookie header handled by
         mod_session can cause a NULL pointer...",
    "cvss_vector": "CVSS:3.1/AV:N/AC:L/PR:N/UI:N/S:U/C:N/I:
        N/A:H",
    "cvss_score": "7.5",
    "source": "NVD"
  },
  {
    "id": "CVE-2020-13938",
    "cwe": ["CWE-862"],
    "date_published": "2021-06-10T07:10:21",
    "description": "Apache HTTP Server versions 2.4.0 to
        2.4.46 Unprivileged local users can stop httpd...",
    "cvss_vector": "CVSS:3.1/AV:L/AC:L/PR:L/UI:N/S:U/C:N/I:
        N/A:H",
    "cvss_score": "5.5",
    "source": "NVD"
  },
  {
    "id": "CVE-2021-26691",
    "cwe": ["CWE-787", "CWE-122"],
    "date_published": "2021-06-10T07:10:21",
    "description": "In Apache HTTP Server versions 2.4.0 to
         2.4.46 a specially crafted SessionHeader...",
    "cvss_vector": "CVSS:3.1/AV:N/AC:L/PR:N/UI:N/S:U/C:H/I:
        H/A:H",
    "cvss_score": "9.8",
    "source": "NVD"
  }
]
```

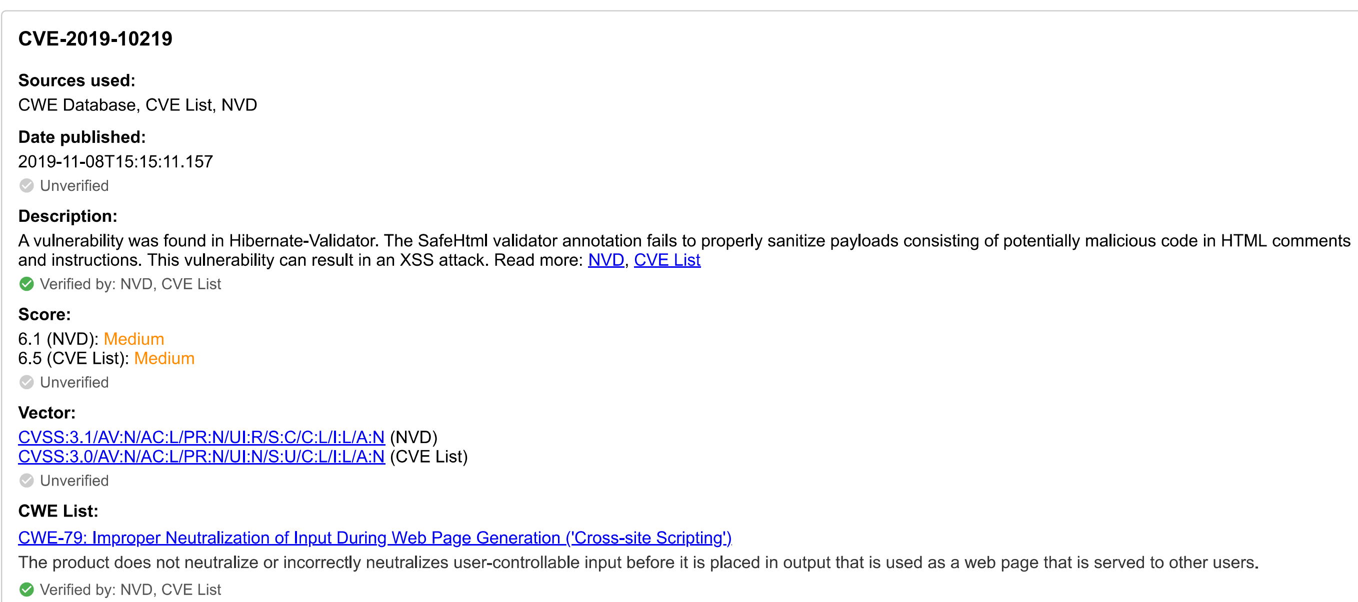

CVE-2019-10219

Sources used:
CWE Database, CVE List, NVD

Date published:
2019-11-08T15:15:11.157
Unverified

Description:
A vulnerability was found in Hibernate-Validator. The SafeHtml validator annotation fails to properly sanitize payloads consisting of potentially malicious code in HTML comments and instructions. This vulnerability can result in an XSS attack. Read more: NVD, CVE List
Verified by: NVD, CVE List

Score:
6.1 (NVD): Medium
6.5 (CVE List): Medium
Unverified

Vector:
CVSS:3.1/AV:N/AC:L/PR:N/UI:R/S:C/C:L/I:L/A:N (NVD)
CVSS:3.0/AV:N/AC:L/PR:N/UI:N/S:U/C:L/I:L/A:N (CVE List)
Unverified

CWE List:
CWE-79: Improper Neutralization of Input During Web Page Generation ('Cross-site Scripting')
The product does not neutralize or incorrectly neutralizes user-controllable input before it is placed in output that is used as a web page that is served to other users.
Verified by: NVD, CVE List

Fig. 2. CVE record included in the final report

Strategic Threat Intelligence in Cyberspace

1st Martina Molnarova
Department of Telecommunications
FEEC, Brno University of Technology
Brno, Czechia
xmolna07@vut.cz

2nd Willi Lazarov
Department of Telecommunications
FEEC, Brno University of Technology
Brno, Czechia
lazarov@vut.cz

***Abstract*—This paper underscores the critical role of Cyber Threat Intelligence in modernised societies, particularly in addressing hybrid threats. Firstly, it outlines a theoretical attack profile utilised by adversaries in hybrid and cyber operations. Subsequently, it presents a methodology to counter these threats, incorporating an iterative defence cycle for ongoing refinement. Lastly, the paper demonstrates an implementation of this methodology as a web application to support strategic intelligence.**

***Index Terms*—cyber threat intelligence, hybrid threats, hybrid warfare, cyberspace, cyberattacks, methodology**

I. Introduction

In today's rapidly evolving digital landscape and cyberspace domain, the need for effective Cyber Threat Intelligence (CTI) is steadily increasing. The growing complexity of cyber threats, which are becoming increasingly intertwined with broader societal and geopolitical dynamics, demands a more structured and intelligence driven approach to cybersecurity. Hybrid threats, in particular, represent a multifaceted challenge, as they encompass not only traditional cyberattacks, but also incorporate tactics aimed at destabilising societies through traditional forms of warfare, disinformation campaigns, and economic or diplomatic coercion.

By analysing current cybersecurity challenges, hybrid threats, existing defence strategies, and prevailing methodologies in the field, this paper seeks to propose a structured methodology for strategic threat intelligence that enhances the defensive capabilities of the targeted entities. The proposed methodology provides a comprehensive approach to current and new cyber threats with a specific focus on mitigating the risks associated with hybrid threats.

II. Background and Related Work

CTI is regarded as subset of the broader field of Threat Intelligence (TI) [1], which encompasses the analysis and evaluation of various types of threats beyond cyberspace. TI considers a wide range of threats, such as terrorism, economic instability, and geopolitical risk [4]. However, CTI specifically focuses on cyber threats that have the potential to compromise the security of individuals, organisations, or entire nations. In general, CTI can be characterised as a systematic approach that facilitates the collection and analysis of substantial amounts of data, which can then be used to improve defensive measures and proactively mitigate cyber threats [1].

The research described in this paper was financially supported by the Technology Agency of the Czech Republic, project No. FW11020057.

A. Hybrid Threats

Hybrid threat can be broadly defined as a method of confrontation between two opposing sides, usually involving an aggressor operating covertly and a defending state that is the target of the attack [5], [6]. Hybrid conflicts are characterised by their complexity, as they deploy a combination of adaptive strategies designed to counter defensive measures. As a result, hybrid threats are considered a fusion of various techniques aimed primarily at undermining the stability and integrity of the target state. They also involve the continuous adaptation of strategies to prevent detection of the attack [6].

These threats are also reflected in the information and cyber environment and their hybrid nature incorporates both conventional and non-conventional forms of warfare [6]. These may include explicit threats of open conflict, as well as political or diplomatic coercion. In addition, hybrid strategies frequently involve tactics designed to destabilise societies by fostering an environment in which the general public becomes increasingly susceptible to disinformation by utilising conventional tools such as social networks, online news, or fake accounts to spread the desired narrative [6]. This, in turn, can erode trust in governmental institutions and diminish the public's ability to distinguish between factual information and false narratives, ultimately contributing to societal instability [6].

B. Cyber Threat Intelligence

As outlined above, CTI is implemented using various established methodologies currently in use [1]. Here, a methodology refers to a structured process that, when applied systematically, enables the utilisation of specific techniques and tools to enhance data collection, advanced analysis and pattern identification within the realm of cyber threats and ongoing cyberattacks [4]. Consequently, several methodologies have been developed to support both proactive and reactive cyber defence [4]. However, many of these approaches have not been explicitly adapted to address hybrid threats, although certain methodologies, particularly those of the defence industry, can be modified for this purpose.

For the purposes of the presented research, several methodologies were examined in relation to both hybrid threats and CTI. In the presented analysis, the following methodologies were selected: Cyber Kill Chain (CKC) [7], MITRE ATT&CK [8], Diamond Model of Intrusion Analysis [9], F3EAD [10], OODA loop [11], and CARVER matrix [12].

Each of these methodologies possesses distinct characteristics in terms of focus, objectivity, flexibility, and reactivity, as summarised in Table I. CKC focuses primarily on structuring cyberattacks, offering a semi-objective approach with low flexibility and a predominantly reactive stance. Similarly, the Diamond Model of Intrusion Analysis emphasises attacker behaviour, also employing a semi-objective approach with limited adaptability. In contrast, MITRE ATT&CK provides a high level of objectivity and flexibility. Methodologies such as F3EAD and the Carver Matrix offer more flexible frameworks, although their effectiveness depends on implementation. The OODA loop, designed for rapid decision-making, provides high flexibility but operates with lower objectivity.

Through extensive research and analysis, we determined that while certain methodologies could be adapted to function within specific areas of strategic threat intelligence, they require careful modification to align with proactive demands of hybrid threats. The predominance of reactive approaches of these methodologies presents a key limitation, as hybrid threats require proactive intelligence gathering and response mechanisms. Therefore, we propose a new methodology for strategic threat intelligence to address these gaps.

III. Proposal of a Hybrid Methodology

Based on the findings of this research, this paper proposes a novel methodology designed to allow an effective response to both potential and existing threats in the context of hybrid warfare and cyber threats. To develop this methodology, we first outline a theoretical step-by-step approach used by an attacker. Subsequently, we introduce a methodology designed to counter these identified steps, ensuring a comprehensive and systematic approach to attack threat mitigation using both cyberattacks and hybrid strategies.

A. Attack Flow Profiling

As described in the previous section, the development of an effective methodology requires a clear understanding of the adversary's approach. To achieve this, a generic theoretical attack profile has been formulated, outlining the steps an attacker may follow when conducting hybrid and cyber-based operations. This structured framework works as the foundation for subsequent counter-methodology proposed in this paper. The theoretical attack profile is defined as follows:

1) Reconnaissance of the target: In the initial phase of the attack, the adversary collects intelligence relevant to the target entity. Through systematic data analysis, the attacker identifies potential vulnerabilities that can be exploited to infiltrate key individuals, organisations, or targeted systems. In this phase of the hybrid attack, information regarding the target's ability to actively defend itself is also obtained.

2) Analysis of weaknesses and vulnerabilities of the target: This phase involves a thorough assessment of the identified vulnerabilities, determining which are most exploitable. Particular emphasis is placed on weaknesses that could cause the greatest operational, infrastructural, or social disruption.

3) Formulation of Strategy using DIMEFIL: At this stage, the attacker defines the most effective initial attack vector by strategically combining the elements of the Diplomatic, Information, Military, Economy, Finance, Intelligence, and Law (DIMEFIL) tools. The objective is to maximise pressure on the target entity through coordinated approach.

4) Optimisation of the attack direction: Based on previous behavioral analysis, political dynamics, and societal context within the target state, the attacker refines the attack strategy to align with evolving objectives. The strategy remains adaptable, allowing modifications in response to target's defence or external circumstances.

5) Infiltration of key subjects: This phase involves active infiltration of critical individuals, organizations, or systems that are essential to the success of the attack. This may include direct cyberattacks, social engineering tactics, or even physical infiltration of governmental or institutional structures.

6) Initiation of active attack: The attack transitions from passive to active state. At this stage, the attacker executes direct offensive actions, which may include large-scale cyberattacks targeting national infrastructure, critical services, or key government sectors. Additionally, disinformation campaigns and psychological operations may be escalated to induce societal panic and instability.

7) Concealment of presence: While concealment is often a continuous process throughout the attack, it becomes particularly crucial once active operations are underway. Within cyberspace, attackers employ conventional obfuscation techniques, while in broader narrative, they may manipulate public perception through disinformation, false attribution, or controlled leaks to shape responses in their favour.

8) Escalation: This phase depends on whether previous actions have yielded the desired outcomes. If necessary, the attacker may intensify operations, further destabilising political and societal landscape. In extreme cases, escalation may contribute to civil unrest, national or international conflicts, or even regime change.

9) Active coercion: If attacker has gained significant control over key systems, political structures, or public disclosure, they may begin exerting direct pressure on the target state. This coercion may manifest through economic manipulation, political demands, or widespread societal influence aimed at achieving target objectives.

10) Termination of the attack: The conclusion of the attack may occur in two distinct ways. The first is abrupt withdrawal, where the attacker ceases operations suddenly, and often occurs when the objective is to create confusion, fear, or instability. The second is gradual disengagement, in which the attacker's presence slowly diminishes, particularly in cases where the main objective was to influence long-term political, diplomatic, or strategic decisions.

11) Final assessment and benefits: The final phase consists of evaluating the overall effectiveness of the attack. This includes analysing the strategies employed, assessing whether the predetermined objectives were met, and extracting insights to refine future operations.

TABLE I
COMPARISON OF EXISTING METHODOLOGIES

Methodology	Main focus	Objectivity	Flexibility	Reactivity
Cyber Kill Chain	Attack structure	Semi-objective	Low	Reactive
MITRE ATT&CK	Tactics, techniques, and procedures	High-objective	High	Reactive and proactive
Diamond Model of Intrusion Analysis	Attacker's behaviour	Semi-objective	Low	Reactive
F3EAD	Strategic and tactical information	Implementation dependent	Flexible	Reactive
OODA loop	Fast decision-making	Low-objective	High	Reactive
CARVER Matrix	Evaluation based on vulnerabilities	High-objective	Flexible	Reactive

B. *Strategic Threat Intelligence*

By understanding the structured progression of the defined attack profile, it becomes possible to design a strategic methodology that directly counteracts each phase. The following steps outline a proposed framework for detecting, mitigating, and responding to hybrid and cyberattacks, particularly when conducted together as a part of hybrid warfare. The methodology is visualised in Figure 1 and includes:

1) Monitoring and reconnaissance detection: In the initial phase, continuous monitoring is established to detect early indicators of adversarial reconnaissance. This includes analysing network traffic, system logs and Open Source Intelligence (OSINT) alongside monitoring broader geopolitical developments. The main goal of this phase is to identify suspicious activities that suggest the impending attack, enabling a proactive analysis of potential attack profiles and forecasting adversary's likely course of action.

2) Vulnerability identification and assessment: Once mechanisms for detecting early signs of an attack are in place, the focus shifts to systematically identifying vulnerabilities within critical systems and trusted communication channels. This phase employs both automated tools and manual assessments to evaluate the severity of those vulnerabilities. A structured prioritisation process is then used to determine which weaknesses, if exploited, could result in greatest operational, infrastructural, or societal disruption, thereby guiding immediate mitigation efforts of said vulnerabilities.

3) Threat scenarios modelling: Building on identified vulnerabilities, this phase involves simulating potential threat scenarios to anticipate adversary's strategic moves. By analysing how elements of the DIMEFIL framework may be exploited, defender can predict likely targets and the methods an attacker may employ. This analysis informs the development of tailored response strategies designed to neutralise specific adversarial tactics and procedures. The outputs of this phase are then used to detect and counter identified infiltration threats.

4) Detection and counter threat infiltration: This phase acts as a bridge between proactive preparation and active response. It entails real time surveillance across both cyber and physical domains to actively detect any signs of infiltration. Effective countermeasures include monitoring for unauthorised access or anomalous behaviour, as well as establishing robust information-sharing protocols among key state and private-sector entities. Such measures ensure that any attempt to breach critical infrastructures or compromise critical individuals is swiftly identified and suppressed.

5) Identification of initial threat indicators: Transitioning into active defence, this phase focuses on detecting the first clear signs of the attack. Early warning systems, specially designed for hybrid threats, monitor state-controlled media, primary news outlets, flagged social media accounts, and behavioural changes in critical personnel or organisations. Rapid identification of these indicators is vital to trigger an immediate and coordinated defensive response.

6) Detection of adversarial masking techniques: Recognising that adversaries may employ obfuscation strategies to hide their presence, this phase concentrates on uncovering such concealment efforts. Defensive analysis involves detecting patterns in digital communications and monitoring shifts in public narratives that could indicate covert operations. Additionally, evaluating changes in the geopolitical landscape helps identify indirect signs of adversarial masking techniques that may indicate an incipient hybrid attack.

7) Reaction planning to possible escalation: When early indicators suggest an escalation in adversary's operations, predetermined response strategies are activated. This phase emphasises adaptive measures such as deploying rapid-response teams, initiating cyber defence protocols, and executing de-escalation techniques to stabilise public sentiment in a positive direction. These actions are designed to contain the threat and prevent further intensification of the attack.

8) Mitigation of cyber and influential operations: In cases where disinformation and psychological operations are deployed to incite panic or create negative public sentiment towards a targeted organisation, this phase focuses on mitigating their impact. It involves proactive narrative control and strategic communication efforts to restore public trust in the institutions targeted by hybrid attack. Pre-established emergency communication channels are utilised to disseminate accurate, calming information, ensuring that the state maintains order even during heightened crisis conditions.

9) Forensics, retrospective investigation and assessment: After the attack, a comprehensive forensic analysis is conducted to evaluate the effectiveness of the response. This phase includes a retrospective investigation of the attack timeline, as assessment of each defensive action taken, and the identification of learned lessons. If an attack does not occur, this phase is used to evaluate prepared plans to ensure their future effectiveness. The insights gained are integrated into an iterative defence cycle, presented as this methodology and shown in Figure 1, ensuring continuous improvement of mitigation plans derived from this approach for future attacks.

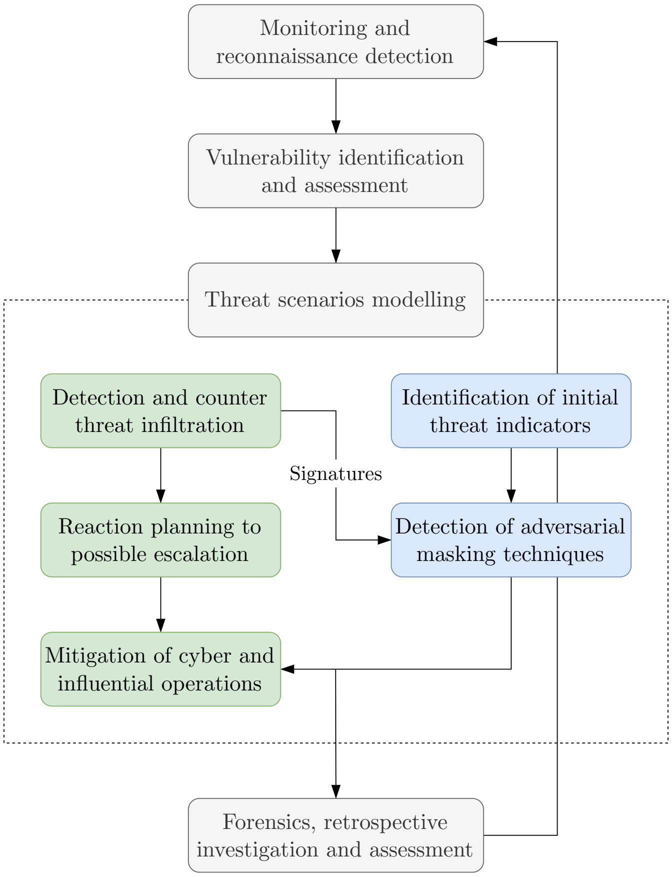

Fig. 1. Phases of the proposed strategic methodology

C. Implementation and Application

Due to the necessity of functionally testing the proposed methodology, we developed a web application (see Figure 2). The application is designed to generate reports based on the proposed methodology and incorporates visualisation tools to enhance data interpretation. The backend of the application is implemented in JavaScript, with an integrated PostgresSQL database, while the frontend uses TypeScript in conjunction with the Vue.js framework, ensuring a user-friendly and intuitive control over the functions of the application.

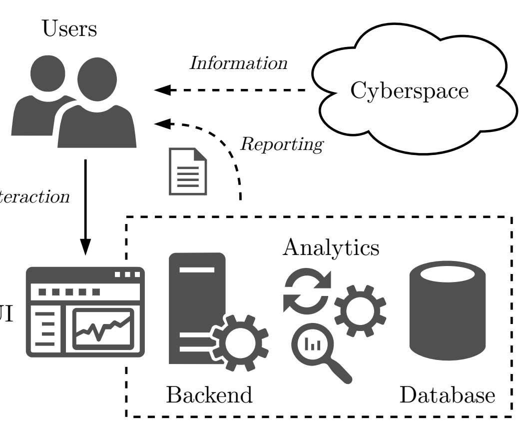

Fig. 2. Interactive application for strategic intelligence

The application enables users to create CTI reports based on the information gathered and pre-established template, that reflects the defined methodology and the principles derived from its steps. The CTI template serves as the foundation for structuring and standardising the reporting process, ensuring consistency and rigour in the presentation of data. In addition, the system allows users to create, organise, and visualise the information and data gathered, which are structured within the report template. In addition to facilitating the creation and analysis of reports, the application integrates statistical tools that support the visualisation of attack patterns and historical trends, providing a comprehensive framework for both retrospective analysis and proactive threat assessment.

IV. Conclusions and Future Work

This paper reaffirms that robust Cyber Threat Intelligence is indispensable in countering the multifaceted challenges posed by hybrid threats with the incorporation of cyber threats in modernised societies. By first formulating a theoretical attack profile and subsequently proposing an iterative systematic defence methodology, as demonstrated through a practical web application, this paper contributes a comprehensive framework for both proactive and reactive defence in cyberspace. In future research, we will focus on extending the methodology and its application to further support strategic intelligence.

Acknowledgements

We express our gratitude to the Cyber and Information Warfare Command of the Czech Army for feedback on the proposed methodology and application.

References

[1] V. Mavroeidis and S. Bromander. “Cyber threat intelligence model: an evaluation of taxonomies, sharing standards, and ontologies within cyber threat intelligence,“ in *2017 European Intelligence and Security Informatics Conference (EISIC)*, 2017, p. 91-98.
[2] M. Lee. *Cyber Threat Intelligence*, Canada: John Wiley and Sons, 2023.
[3] N. Sun, M. Ding, J. Jiang, W. Xu, X. Mo, Y. Tai, and J. Zhang. “Cyber Threat Intelligence Mining for Proactive Cybersecurity Defense: A Survey and New Perspectives,“ *IEEE Communications Surveys & Tutorials*, vol. 25, no. 3, pp. 1748-1774, May 2023.
[4] J. Pirc, D. DeSanto, I. Davison, and W. Gragido. *Threat Forecasting: Leveraging Big Data for Predictive Analysis*, USA: Elsevier, 2015.
[5] G. F. Treverton, A. Thvedt, A. R. Chen, K. Lee, and M. McCue. *Addressing Hybrid Threats*, Sweden: Bromma, 2018.
[6] W. A. Qureshi. “The Rise of Hybrid Warfare,“ *Notre Dame Journal of International & Comparative Law*, vol. 10, no. 2, June 2020.
[7] M. Lockheed. “Gaining the Advantage - Applying Cyber Kill Chain (Methodology to Network Defense),“ lockheedmartin.com. https://www.lockheedmartin.com/content/dam/lockheed-martin/rms/documents/cyber/Gaining_the_Advantage_Cyber_Kill_Chain.pdf (accessed Feb. 26, 2025).
[8] B. E. Strom, A. Applebaum, D. P. Miller, K. C. Nickels, A. G. Pennington, and C. B. Thomas. “MITRE ATT&CK: Design and Philosophy,“ attack.mitre.org. https://attack.mitre.org/docs/ATTACK_Design_and_Philosophy_March_2020.pdf (accessed Feb. 26, 2025).
[9] S. Caltagirone, A. Pendergast, and C. Betz. “The Diamond Model of Intrusion Analysis,“ *Threat Connect*, vol. 298, no. 0704, pp. 1-61, 2013.
[10] J. A. Gomez. “The Targeting Process: D3A and F3EAD,“ *Small Wars Journal*, vol. 1, pp. 1-17, July 2011.
[11] C. Richards. “Boyd’s OODA Loop,“ *Sjøkrigsskolen Journal*, vol. 5, no. 1, pp. 142-165, 2020.
[12] “Special Operation Forces Intelligence and Electronic Warfare Operations – Appendix D,“ irp.fas.org. https://irp.fas.org/doddir/army/fm34-36/appd.htm (accessed Feb. 27, 2025).

Digital Twin of a Lithium-ion Battery

Vojtěch Šibor
Department of Electrical and Electronic Technology, FEEC
Brno University of Technology
Brno, Czech Republic
xsibor00@vut.cz

Petr Vyroubal
Department of Electrical and Electronic Technology, FEEC
Brno University of Technology
Brno, Czech Republic
vyroubal@vut.cz

***Abstract*—This paper aims to explain the concept of a digital twin, its capabilities for monitoring lithium-ion batteries and the individual steps necessary for its creation and operation. These steps include data analysis, process of making an equivalent circuit model of the battery system and fundamental model of the digital twin. All these steps are accordingly described in further detail. The advantage of a digital twin lies in its predictive capability regarding the battery's condition and lifespan.**

***Keywords*—digital twin, lithium-ion battery, battery systems, Ansys Twin Builder**

I. Introduction

Nowadays, companies strive to get a competitive advantage to reach a wider range of customers. This advantage can be ensured by a better quality of the products, use of innovative processes in manufacturing, reduction of production time and by implementation of Industry 4.0. This concept is a process of digitalization that involves remote control of the production by smart applications such as: IIoT, cloud computing, big data, virtual documentation and digital twins. A digital twin is a virtual representation of a physical object or system. The system is equipped with sensors that monitor its vital parts. Additionally, data are collected in real time and enable physical and digital counterparts of the digital twin to update and interact with each other. Data are primarily stored and processed on cloud platforms. Digital twins are a way to optimize performance, predict failures and stress factors of the physical system. In the industrial sector, digital twins are used for oil platforms, electric vehicles and renewable energy. Due to the ecological international movement, there are major investments in renewable energy [1], consequently, there is going to be a need for energy storage. Hence, this paper focuses on the use of digital twins in battery storage.

II. Digital Twin of a Lithium-ion Battery

This paper was approached using Ansys Twin Builder to create a digital twin. In this software, the digital twin is a combination of electrical and thermal models. The basis of the electrical model is a physical lithium-ion (Li-ion) battery upon which are measured changes of voltage and temperature over time, in response to unit steps and rest periods. Values of voltage are then fitted in Twin Builder and a black box for electrical model is created. Whereas the temperature model is based on a 3D geometry of the Li-ion cell. In this paper are used Li-ion 18650 cells. The 3D model is further used for the finite element method in Ansys Fluent. This physical model is used to calculate training data for Twin Builder, facilitating the creation the temperature model. Both models are then combined into a digital twin that is connected to its real-world counterpart afterwards.

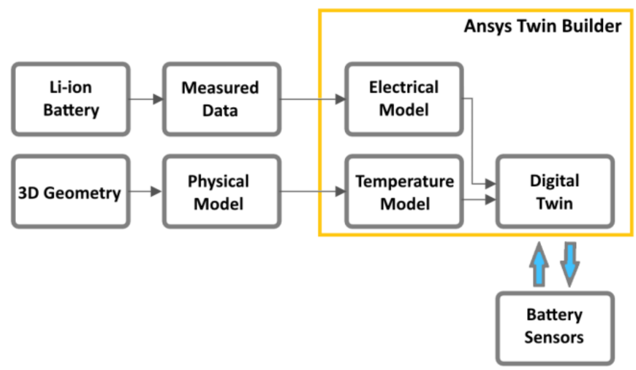

Fig. 1. Flowchart for digital twin creation.

III. Electrical Model

A. Measuring Profile

Data from the electrical model are measured by a potentiostat on the Li-ion battery, this method was chosen due to its simplicity and feasibility in laboratories. The profile is shown in Fig. 2 and consists of three phases. In the first phase, the battery is charged from an unknown voltage to full capacity.

The second phase involves a measurement of static capacity which consists of a full discharge and full charge of the cell by Constant Current Constant Voltage (CCCV). It is a specific method of discharging (or charging). The battery is initially discharged at a constant current until it reaches the cut-off voltage, after which there is a transition to constant voltage discharge, where the current gradually decreases until it reaches its minimum value.

Whereupon follows the third phase, the Hybrid Pulse Power Characterization (HPPC) test, which is a series of unit steps in multiple states of charge of the battery. The third phase is designed as recommended by Ansys [2], as depicted in Fig. 2. To explain the measuring profile, it is necessary to explain two terms. First is Charge Rate (C), the base load is defined as 1C, meaning the battery will be fully discharged in one hour. For example, if the nominal capacity of the battery is 2600 mAh, then a 1C discharge current corresponds to 2.6 A. At 0.5C, the discharge current would be half of that, namely, 1.3 A. The second term is State of Charge (SoC), indicating the relative amount of charge stored compared to the total battery capacity as a percentage. It can be expressed by the formula:

$$SoC = \frac{Q}{Q_n} \cdot 100 \tag{1}$$

Where Q is charge stored in the battery and Q_n is nominal capacity.

Then it is possible to define individual steps as:

- Resting period for 60 minutes
- Discharge pulse: 1C for 10 seconds
- Rest for 10 minutes (relaxation)
- Charging pulse: 1C for 10 seconds
- Rest for 10 minutes (relaxation)
- Discharge by 0.2C until capacity drops by 10 % SoC
- The process is repeated until the battery is fully discharged
- Subsequently, a similar process is then repeated for charging [2]

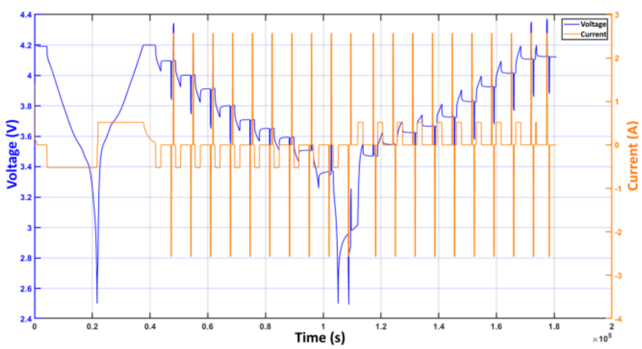

Fig. 2. Measuring profile.

This profile was measured at an ambient temperature of 25 °C, while two additional analogous profiles were measured at -5 and 45 °C to enhance performance under potential changes in temperature in the surrounding environment.

B. Measured Data

The measurement output is an Excel file containing columns of values for time, voltage, current, capacity and temperature. The complete file contains over 300,000 lines. The measurement set was designed with pulse-to-pulse responses, which is convenient not only because the battery reaches a steady state, but at the same time the individual measured parts are separated by a series of zeros, which is essential for data processing in the next step.

C. Data Processing

Since the fitting function in Twin Builder requires only discharge pulses and their voltage responses, extracting such discharge curves from the Excel file is necessary. As demonstrated in Fig. 3 that shows a voltage drop due to pulse discharge in time interval from T_0 to T_1, which continues with a voltage response during relaxation period until the time T_2. Resemblant pulses have to be acquired for all states of charge.

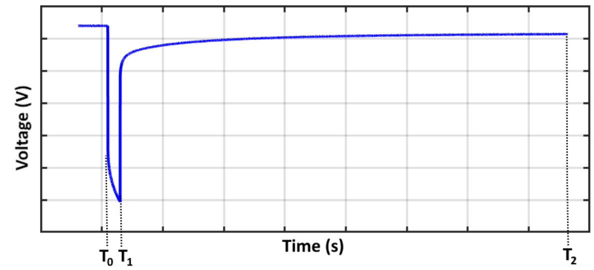

Fig. 3. Example of a discharge pulse and voltage response. [3]

This process of data extraction was performed by a code in MATLAB. The code is based on searching for zeros and non-zero values of electrical current throughout the measured data and its flow chart is depicted in Fig. 4.

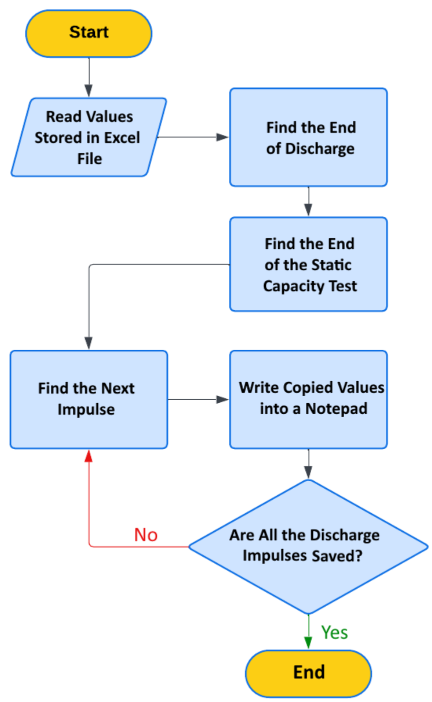

Fig. 4. Flowchart of the code in MATLAB.

As it was mentioned previously, between each charge and discharge period is a sequence of zeros, this helps to differentiate between measurement profile phases and different states of charge. At this moment, the initial charge and test of static capacity are irrelevant, therefore this part is passed without further processing to get to the important segment of the Excel file, the HPPC. Rows of the following SoC are then gone through. When the code allocates a discharge pulse, its voltage response and time are stored and written into a notepad. To obtain one text file for each voltage response, the previous steps are looped 11 times in a for-loop, which proved more convenient than using correlation methods due to the periodic nature of the pulses and relaxations. Every notepad must have a defined structure starting with the temperature and SoC. To improve the quality of the model further, data could be expended by more profiles that have various discharge currents.

D. Equivalent Circuit Model and Parameter Fitting

Equivalent circuit model (ECM) is an essential part of the electrical model and its schematic diagram is shown in Fig. 5.

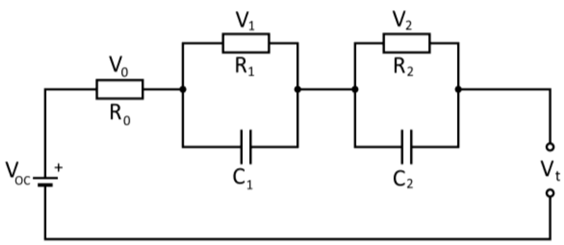

Fig. 5. Equivalent circuit model of a battery.

Where V_{OC} denotes open-circuit voltage, R_0 is internal resistance and V_t is voltage between the terminals of the battery. The first RC branch represents the fast phenomena and the second RC branch represents the slow phenomena in the battery.

All the following steps are carried out in the Twin Builder interface. Firstly, the parameters of electronic components in the ECM have to be determined. Therefore, a fitting function is used. This function operates based on the Jiang-Hu algorithm which is discussed in greater detail in literature [3] and [4]. Secondly, after completing the fitting process, the ECM is viewed as a black box and it is accessible as a functional block. Thirdly, the block is connected into a virtual circuit with a current source, voltmeter and block with temperature data. Finally, the electrical model is ready to be used.

E. Validation

In the last step, the accuracy of the model has to be verified. For validation was used the same profile as for the data acquisition in the first step. However, it can not be used exactly as it is. A notepad with time and current values is needed for the current source. Additionally, Twin Builder reads positive values of current as discharge current, hence the values have to be inverted. After a simulation are obtained verification data that can be compared to the physically measured data by potentiostat. The comparison is depicted in Fig. 6, where the red curve represents the measured data at 25 °C and the blue curve represents the simulated data. A small deviation around the time of $12 \cdot 10^4$ seconds is caused by the limitation of the potentiostat, which automatically lowers the discharge current to prevent the battery from damage. Nonetheless, the deviation is negligible since batteries are not used below the limit values.

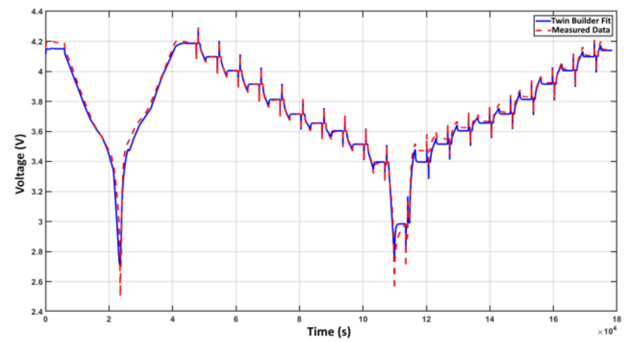

Fig. 6. Comparison of measured data (red) and data from simulation (blue).

Although the initial validation has been completed, further verification is required. To ensure the robustness of the electrical model, another profile will be measured. This profile is designed to reflect the behavior of a commercially used battery in an electric vehicle and to represent a 50-hour operation under temperature conditions different from those previously used. The profile is illustrated in Fig. 7. The same load profile will be applied to the electrical model, and the resulting data will be compared to the measured values again.

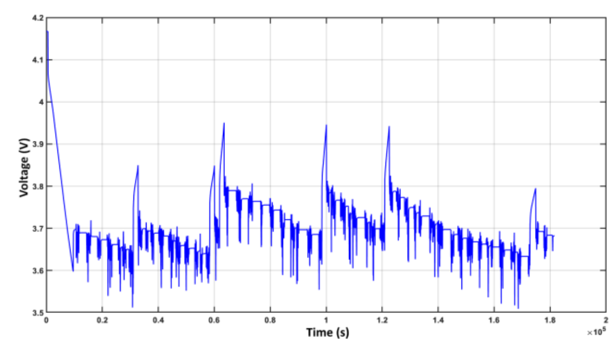

Fig. 7. Voltage profile of a commercially used battery.

F. Evaluation

Root Mean Square Error (RMSE) was adopted as the metric for evaluating the quality of the model. It is used to compare two vectors of voltage values.

$$RMSE = \sqrt{\frac{1}{n}\sum_{i=1}^{n}(y_i - \hat{y}_i)^2} \tag{2}$$

Where n denotes the number of values, y_i is the actual value and $\hat{y}_i$ is the predicted value. The RMSE was calculated by MATLAB and it was determined to be $4.404 \cdot 10^{-2}$ V.

IV. Conclusion

To summarize, the creation of a digital twin for a Li-ion battery was described. The profile used for data acquisition was presented and it was explained how the data were subsequently processed in MATLAB. An electrical model was developed using a fitting method in Twin Builder. Then, it was validated that the electrical model could perform simulations of the real-world Li-ion battery.

This paper will be further extended by incorporating a thermal model. A Multi-Scale Multi-Domain (MSMD) battery model will be created in Ansys Fluent to determine the development of temperature within the battery. Experimental validation will be carried out using surface temperature data obtained from measurements of a real battery, with ambient conditions stabilized by a climatic chamber. The verified data will then serve as training data for the development of a reduced-order thermal model in Ansys Twin Builder. Electrical and thermal models will be connected to its real-world counterpart, forming a complete digital twin. Digital twins are particularly useful for predicting battery lifespan, and the use of reduced-order models enables fast, real-time computations within seconds. In addition, there are numerous possibilities for employing digital twins in battery systems, including cooling regulation, what-if analyses or current adjustments.

References

[1] W. Liu, Y. Shen, and A. Razzaq, "How renewable energy investment, environmental regulations, and financial development derive renewable energy transition: Evidence from G7 countries," *Renewable Energy*, vol. 206, Feb. 2023, doi: https://doi.org/10.1016/j.renene.2023.02.017.

[2] T. Duncan, "Building Better Batteries: Characterize Battery Parameters for Simulation," *ansys.com*, Apr. 13, 2021. https://www.ansys.com/blog/building-better-batteries.

[3] S. Jiang, "A Parameter Identification Method for a Battery Equivalent Circuit Model," *SAE Technical Paper Series*, Apr. 2011, doi: https://doi.org/10.4271/2011-01-1367.

[4] X. Hu, L. Collins, S. Stanton, and S. Jiang, "A Model Parameter Identification Method for Battery Applications," *SAE Technical Paper Series*, Apr. 2013, doi: https://doi.org/10.4271/2013-01-1529.

Evaluation of Eddy Effects in Winding of High-Speed Synchronous machines for EV Systems

1st Jakub Rosendorf
Dep. of Power Electrical and Electronic Engineering
Brno University of Technology, FEEC
Brno, Czech Republic
230416@vut.cz

2nd Petr Chmelíček
Garrett Motion Czech Republic s.r.o.
Brno, Czech Republic
petr.chmelicek@garrettmotion.com

3rd Jan Bárta
Dep. of Power Electrical and Electronic Engineering
Brno University of Technology, FEEC
Brno, Czech Republic
0000-0001-6575-8320

***Abstract*—This paper introduces and examines the effects of AC losses in the stator winding of high-speed interior permanent magnet synchronous machines. With a particular focus on usage in electrical vehicles. Using the finite element method. This paper describes how eddy effects influence conductors on the basis of their material and position in the stator slot. For the purpose of optimization of EV drives.**

***Index Terms*—Motor; PMSM; IPMSM; high-speed; aluminum; copper; winding; hairpin; eddy effects; EV; AC losses**

I. Introduction

In recent years, the automotive industry has shown significant growth. This rapid development put in increasing demands for many parameters of electrical motors, especially in terms of efficiency, cost, and power density. In general, the cheapest option is often an induction motor; however, it is prone to lack efficiency and power density compared to synchronous motors. Especially when we talk about synchronous motors with permanent magnets (PMSM), which generally show the highest power density of all variants, as shown in [1]. Over the years, Permanent Magnet Synchronous Motors (PMSMs) have been continuously optimized for this reason, and many modern PMSM design concepts are based on a V-shape arrangement of permanent magnets [2], utilizing both torque from magnetic flux from the PM and additional torque from differing reluctance between the d- and q- axes.

In pursuit of further increasing power density, it might be advantageous to move toward higher operating speeds for motors to be used as the main drive of EVs since the increased speed can reduce volume for the same output power, as shown in [3].

With the use of high-speed motors, many new challenges have arisen. High-speed motors often differ from motors intended for medium- and low-speed applications. These differences are mainly due to the varying distribution of losses caused by an increasing share of mechanical losses and significant parasitic effects from the magnetic field interacting with conductive materials. High-speed machines also face increased mechanical challenges due to greater centrifugal and friction forces, as described in [4].

The high-frequency magnetic field can induce a significant voltage in the volumes of all conductive materials penetrated by this magnetic flux. This effect significantly alters what would usually be considered as the optimal solution for stator winding design.

When designing motors for electric vehicle (EV) applications, it is often considered advantageous to use hairpin conductors, as they offer higher fill factors compared to round conductors and also allow for easier automation of manufacturing for large-scale production, as presented in [5]. However, because of the increased solid cross section, hairpin conductors are strongly affected by the additional AC losses created in their volume. The impact of eddy currents introduces the question of when the use of hairpin conductors is no longer advantageous and at what point the benefits of using classic rounded conductors outweigh those of hairpin conductors. The publication [6] shows that for current frequencies below 1000 Hz, hairpin conductors are often more advantageous. However, as shown in [7], with increasing frequency, higher segmentation becomes more beneficial.

This paper presents alternative solutions for the use of different conductor materials. Since the effect of the eddy current depends on the conductivity of the material as described in [8], it may be advantageous to use materials other than traditional copper for conductors. These have already been researched to some extent in the publication [9], but the range of speeds evaluated considered by the authors ended at 25,000 rpm. This paper examines the influence of different material combinations at speeds up to 30,000 rpm. Furthermore, this paper presents more detailed insight into the loss distribution between individual conductors and compares the susceptibility to the eddy effect for different material variations.

II. Electrical machine under study and analysis of AC Winding losses

For the analysis conducted in this study, a typical topology of the Interior Permanent Magnet Synchronous Motor (IPMSM) used in EV applications was selected, as shown

This research work has been carried out in the Centre for Research and Utilization of Renewable Energy (CVVOZE). Authors gratefully acknowledge financial support from the Ministry of Education, Youth and Sports under institutional support and BUT specific research programme (project No. FEKT-S-23-8430).

in Fig. 1. A similar motor configuration is employed, for example, in the Chevy Bolt [10].The key parameters of the studied machine are provided in Table I.

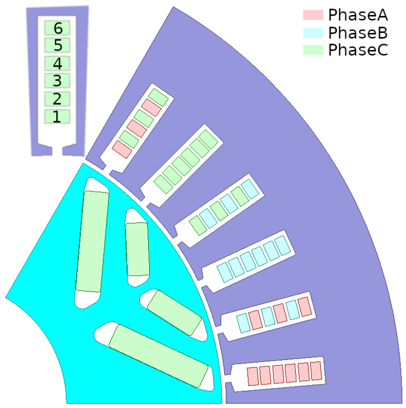

Fig. 1. IPMSM in Ansys Maxwell, with detail of single stator slot, labeled with the number of layers.

TABLE I
KEY MACHINE PARAMETERS

Max torque	150 Nm	Max speed	30000 rpm
Nominal power	130 kW	Nominal torque	42 Nm
Pole pairs	3	Max Temp.	180 °C

The winding of the selected machine is a multilayer hairpin with six conductors (3 parallel pairs in series) per slot. Coils have a shortened winding pitch by ± 30°. Three variants of the studied model were chosen. First, with all copper conductors, second with aluminum conductors, and third, a hybrid variant where conductors 1 and 2 were made of aluminum and 3, 4, 5, and 6 were made of copper. All conductors were considered at a constant temperature of 180 °C. The machine uses a rotor with four embedded permanent magnets in the V shape per pole.

The studied electrical machine was analyzed for selected variants, Cu, Al, and AlCu, with a focus on winding performance, especially with regard to losses created in winding conductors. These losses can be divided into two main components, AC and DC. DC losses are losses present as a result of the desired current flowing through the conductors as if it were a DC current of equivalent amplitude. AC losses are a portion of losses that are caused by current formed by eddy effects and do not create torque. All other losses were equal for all models.

III. RESULTS AND DISCUSSION

A. Efficiency comparison

The Cu variant was expected to have the highest efficiency for lower speeds due to copper's lowest DC resistance. From the efficiency map in Fig.2 can be seen that the efficiency of the Cu variant peaks around 16 000 rpm. The Al variant efficiency, calculated in Fig.3, does peak around 28 000 rpm. When compared with the Cu variant, it can be seen that overall efficiency is lower across the evaluated speed range; however, the peak is shifted, as expected, towards higher speeds. The hybrid AlCu variant's efficiency peaked around 26 000 rpm, falling in between the Al and Cu variants. Although having a larger overall efficiency than that of the Al variant, it still falls short of that of the Cu variant in most of the evaluated range.

B. Sensitivity to eddy effects

These findings can be attributed to the conductors' sensitivity to eddy current effects. As shown in Fig.2, the overall losses increased significantly with speed due to eddy currents introducing additional losses in the conductors. In the case of the Cu variant, the additional losses increased by 44% under the worst conditions. When the Al variant is evaluated, it becomes evident that the increased baseline resistance results in a lower effect of eddy currents. As shown in Fig.6 additional losses increased under the worst conditions by 22%, that is, 22 percentage points lower in comparison to the Cu variant. The AlCu variant showed significantly better performance in terms of resistance to the effects of eddy current. As shown in Fig.7 the additional losses increased by 29% under the worst conditions, which is 15 percentage points lower than the Cu variant. This further demonstrates that conductors are not affected uniformly, as the AlCu variant shows only 9 percentage points higher additional losses than the Al variant, despite having 4 out of 6 conductors made of copper.

To better understand the winding sensitivity to eddy effects, the equivalent resistance was calculated. The equivalent winding resistance (R_{equiv}) is defined as the resistance that the winding would have to have in order for the same losses to be present without the eddy effect and is thus equivalent to the ohmic losses in the whole winding. In this case, R_{equiv} represents losses of a single phase, while R_{DC} represents the baseline resistance that would be measured by DC current. For the Cu variant, R_{equiv} and R_{DC} are shown in Fig.8. From this figure, it is possible to determine that the winding losses grow with the square of the speed. It is also possible to see that the winding losses increased by 67% due to eddy effects under the worst conditions. For the Al variant, it can be seen from Fig.9 that the DC resistance is larger by 53% in comparison with the Cu variant; however, the R_{equiv} does grow slower, only increasing from the baseline by 30% under the worst conditions. As the previous result showed, the AlCu variant falls in between the two others, showing larger R_{DC} than the Cu variant, while R_{equiv} grows faster than for the Al variant. The AlCu variant increased its R_{equiv} by 45% from R_{DC} under the worst conditions.

C. Loss distribution in the stator slot

This difference between the first two and the AlCu variant is possible to explain by loss distribution between the individual conductors in a single slot for the rated point with worst-case overall losses. Loss distributions are shown for the first slot occupied by a single phase. The slots shared by two phases showed similar results with a difference less than 1 percentage

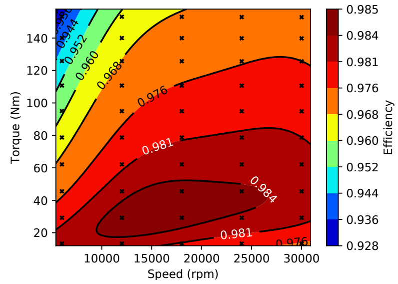

Fig. 2. Efficiency map for Cu winding.

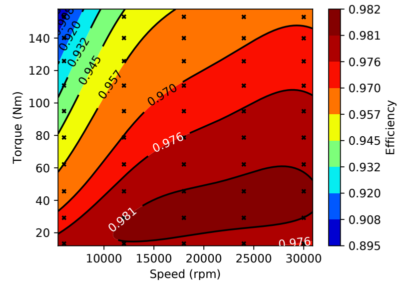

Fig. 3. Efficiency map for Al winding.

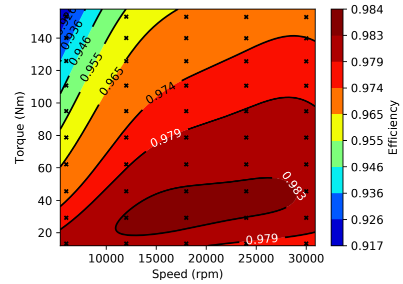

Fig. 4. Efficiency map for Al-Cu winding.

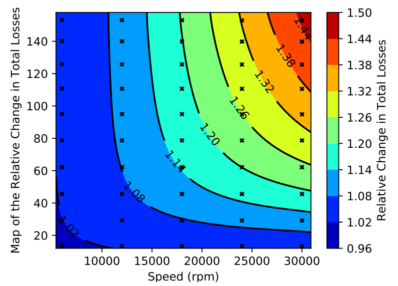

Fig. 5. Map of loss increase due to eddy effects on Cu winding.

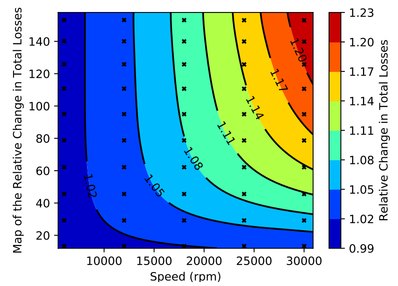

Fig. 6. Map of loss increase due to eddy effects on Al winding.

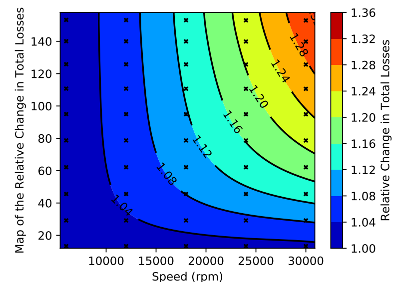

Fig. 7. Map of loss increase due to eddy effects on Al-Cu winding.

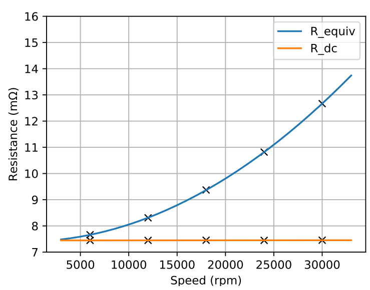

Fig. 8. Phase resistance for Cu winding

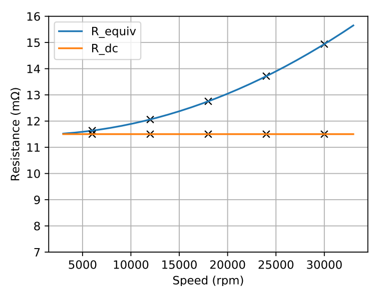

Fig. 9. Phase resistance for Al winding

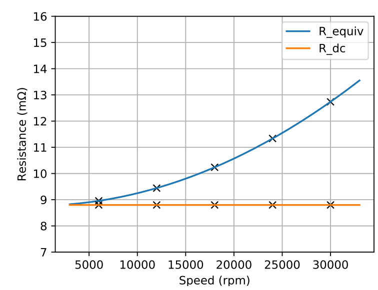

Fig. 10. Phase resistance for Al-Cu winding

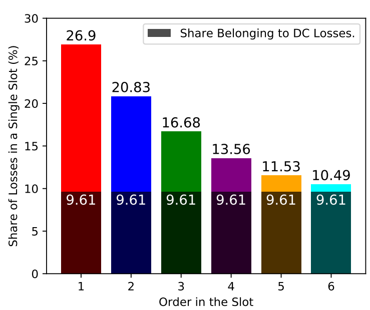

Fig. 11. Distribution of losses in Cu winding

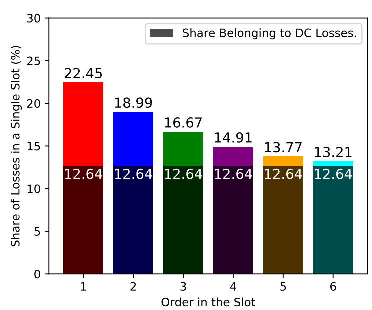

Fig. 12. Distribution of losses in Al winding

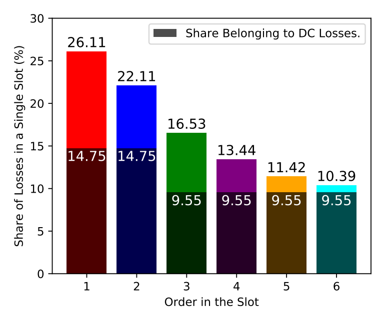

Fig. 13. Distribution of losses in Al-Cu winding

point. From Fig.11 can be seen that the loss distribution for the Cu variant is significantly dominated by the first two conductors, responsible for 47.7% of all losses. It can also be seen that AC losses take the majority share for the same first two conductors, showing that the susceptibility to the eddy effects is mostly created by the conductors closest to the slot opening. When the Al variant is considered, it can be seen from Fig.12 that the loss distribution is more even compared to the Cu variant. The Al variant also shows low susceptibility to the eddy effects, since no conductor has the majority share of the AC losses, and the DC losses take a larger share than for the Cu variant. This uneven loss distribution is the main reason for the creation of the hybrid AlCu variant. Its loss distribution is shown in Fig.13. Similarly to the Cu variant, the loss distribution for the AlCu is mainly concentrated in the first two conductors; however, here it can be seen that the main share consists of DC losses. The previous results of the comparison of susceptibility to the eddy effects of the Cu and AlCu variants can therefore be explained by this distribution.

D. Performance comparison

When all of the results presented are considered, it is clear that the Cu variant is the most advantageous for this winding topology and the operation speed range. From Fig.14 it can be seen that the Al variant does not improve in terms of overall losses across the evaluated speed and torque range; it is, however, expected based on the visible trend that for speeds significantly higher, Al winding might become desirable, specially when additional considerations are taken such as its lower mass in comparison to copper. The AlCu variant compared in Fig.15 matches the Cu variant in terms of overall losses for speeds around the top speed range of 30000 rpm. It is expected that the AlCu variant will become advantageous sooner than the Al variant while the Al will probably outcompete both for significant speeds; however, for such high speed, a different topology altogether should be chosen.

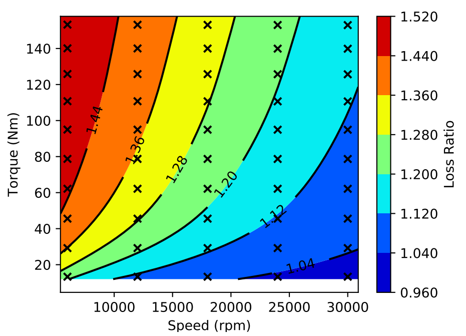

Fig. 14. Map of loss comparason between Al and Cu windings

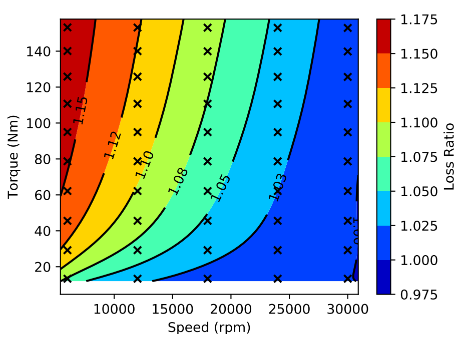

Fig. 15. Map of loss comparason between Al-Cu and Cu windings

IV. Conclusion

In this paper, an analysis of the influence of the material choice for the conductors on the stator winding was performed for the IPMSM model. The use of aluminum conductors was shown to significantly reduce the eddy effects present at higher speeds compared to copper conductors, as can be seen in Figs.8 and 9. Since Al has a higher baseline resistance, it performed worst of the three variants for slower speeds. It was shown that eddy effects do not affect all conductors uniformly. It was shown in Fig.11 that the first conductor is responsible for the highest share of losses in the star slot.

This creates a possibility of reducing the eddy effects while preserving the low DC resistance by using hybrid AlCu winding, where the first two conductors were replaced with Al. This hybrid variant showed an improvement in the increase in the equivalent resistance over copper while also being better in overall efficiency compared to the Al variant. The results show that for this specific winding topology and speeds, copper winding was overall most advantageous, while the hybrid variant matches the Cu variant for speeds around 30 000 rpm. Based on the R_{equiv} trend, it can be expected that for speeds higher than 30 000 rpm, the AlCu variant will be more advantageous while the Al variant will surpass both in efficiency for speeds significantly higher.

In conclusion, while the Cu variant is the most commonly used, the hybrid winding can offer advantages for automotive applications, particularly with increasing motor operating speeds. Aluminum winding may offer advantages for high-speed motors, where lower mass and higher efficiency at very high speeds are critical.

This study contributed to the optimization of PMSM designs by providing insight into the selection of materials for conductors and their impact on efficiency and loss distribution at varying operating speeds.

References

[1] A. Chinthala and S. Vuddanti, "Performance Analysis of Induction Motor and PMSM for Electrical Vehicle Traction Application," 2022 IEEE International Conference on Distributed Computing and Electrical Circuits and Electronics (ICDCECE), Ballari, India, 2022, pp. 1-6, doi: 10.1109/ICDCECE53908.2022.9793305.

[2] N. Murali, S. Ushakumari and M. V. P, "Performance comparison between different rotor configurations of PMSM for EV application," 2020 IEEE REGION 10 CONFERENCE (TENCON), Osaka, Japan, 2020, pp. 1334-1339, doi: 10.1109/TENCON50793.2020.9293844.

[3] Aiso, Kohei, and Kan Akatsu. 2022. "Performance Comparison of High-Speed Motors for Electric Vehicle" World Electric Vehicle Journal 13, no. 4: 57. https://doi.org/10.3390/wevj13040057

[4] X. -F. Qin and J. -X. Shen, "Multi-Physics Design of High-Speed Large-Power Permanent Magnet Synchronous Motor," 2020 Fifteenth International Conference on Ecological Vehicles and Renewable Energies (EVER), Monte-Carlo, Monaco, 2020, pp. 1-5, doi: 10.1109/EVER48776.2020.9243113.

[5] G. Berardi, S. Nategh, N. Bianchi and Y. Thioliere, "A Comparison Between Random and Hairpin Winding in E-mobility Applications," IECON 2020 The 46th Annual Conference of the IEEE Industrial Electronics Society, Singapore, 2020, pp. 815-820, doi: 10.1109/IECON43393.2020.9255269.

[6] J. Jiang et al., "Design of Hairpin Winding and Random Winding Stators for High Speed Heavy-Duty Traction Motor," 2023 IEEE Vehicle Power and Propulsion Conference (VPPC), Milan, Italy, 2023, pp. 1-6, doi: 10.1109/VPPC60535.2023.10403273.

[7] E. Preci et al., "Segmented Hairpin Topology for Reduced Losses at High-Frequency Operations," in IEEE Transactions on Transportation Electrification, vol. 8, no. 1, pp. 688-698, March 2022, doi: 10.1109/TTE.2021.3103821.

[8] PYRHÖNEN Juha, Tapani JOKINEN, and Valéria. HRABOVCOVÁ. Design of rotating electrical machines. 2nd edition. Chichester: Wiley, 2014.

[9] G. Cutuli, S. Nuzzo, T. Zou, G. Franceschini, C. Gerada and D. Barater, "Multi-objective Optimizations of Copper and Aluminum Hairpin Windings: a Comparison," 2023 IEEE Energy Conversion Congress and Exposition (ECCE), Nashville, TN, USA, 2023, pp. 3796-3801, doi: 10.1109/ECCE53617.2023.10362293.

[10] F. Momen, K. Rahman and Y. Son, "Electrical Propulsion System Design of Chevrolet Bolt Battery Electric Vehicle," in IEEE Transactions on Industry Applications, vol. 55, no. 1, pp. 376-384, Jan.-Feb. 2019, doi: 10.1109/TIA.2018.2868280.

Availability of Railway Frequency Converter to Provide Ancillary Services

Tomáš Fryšták
Faculty of Electrical Engineering and Communication
Brno University of Technology
Brno
xfryst02@vutbr.cz

***Abstract*— This article deals with the utilization of traction inverters for providing non-frequency ancillary services. A key element is the active front-end (AFE), which enables bidirectional power flow and the control of both active and reactive power, thereby contributing to grid voltage quality regulation, the elimination of harmonic distortion, and ensuring symmetrical grid loading. To determine the availability of reactive power, a simulation model was created using the PSCAD environment, which includes the power grid, transformer equipment, and the inverter itself. The model uses real-time data on line loading based on actual train operation schedules and considers operational constraints such as voltage and current limits. For different levels of line loading (low, medium, and high), the availability of inductive and capacitive reactive power was analyzed.**

***Keywords*— Inverter, availability, reactive power**

I. Introduction

The Strategic Plan for Transport of the Czech Republic plans to electrify non-electrified lines as one of the ways to more efficient and more environmentally friendly transport and to convert the currently electrified lines powered by a 3kV DC system (currently 1795 km) to a single AC power supply system of 25 kV 50 Hz (currently 1382 km), thus unifying the traction system in the Czech Republic. In total, 3,177 km of lines out of 9,459 km have been electrified [1]. The preference for AC traction is due to its advantages over DC traction. Until now, AC traction has been powered by transformers connected to the distribution network. However, as part of the conversion of part of line 330, solid-state power converters were used to supply power. These converters have certain advantages over the transformers used. For example, symmetrical loading of the power supply network, separation of the traction system from the power supply system, no harmonic disturbances are transmitted, the possibility of operating the traction system without the need to divide it into individual sections and reactive power regulation [2]. One possible use of the inverter is to support the distribution system. Due to the increasing power of traction vehicles, the increasing volume of traffic, the DC power system with a voltage of 3 kV is no longer sufficient and it is desirable to replace it with an AC traction system with parameters of 25 kV 50 Hz and thus unify the traction system in the Czech Republic. The transition to a unified traction system will bring more efficient power supply with lower losses, compatibility with high-speed lines and cheaper electrification of other non-electrified lines. This move is also advantageous in terms of the needs of haulers, who will not have to have vehicles capable of operating on multiple power systems [3].

At the same time, AC traction in the Czech Republic is mainly powered by traction transformers. Since the 25 kV 50 Hz traction system is single-phase, its energy consumption from the three-phase network leads to asymmetrical loading of the individual phases. This causes voltage asymmetry due to asymmetrical voltage drop in distribution system lines. The power system is not optimally loaded, which can lead to reduced efficiency and increased losses. The power electronics of the locomotive converters produce higher harmonic frequencies which are transmitted to the grid due to the coupling of the transformers. This may lead to higher overall network static frequency converter (SFC) interference. In addition, the power supply to the transformers also affects the operation of the railway itself. To reduce the effect of single-phase load asymmetry, the transformers are always connected between two different phases of the power system. It follows that if we were to operate the traction system interconnected with all the traction substations, inter-phase short circuits would occur. There before, it is necessary to operate part of the system separately. Each transformer feeds only one part of the overhead line section. A neutral field must be established between the sections, which the dependent traction vehicle must pass with the collector withdrawn to avoid short-circuiting the individual sections SFC eliminates these disadvantages. This of course has an impact on the operation and organization of rail traffic.

II. SFC Feeder

The converter consists of an three-phase active front-end (AFE) that allows bidirectional power flow and control of both active and reactive power. This is particularly important in applications where there is a need to improve the quality of the grid voltage, regulate the voltage at point of connection by supplying or drawing reactive power, eliminate harmonic distortion, provide symmetrical power draw, or provide ancillary services. AFE inverters thus contribute to higher stability of the power system and enable efficient power flow control in distribution and transmission networks. A single-phase inverter is connected to the AFE via a DC link to ensure the flow of power to and from the traction system and the provision of its parameters. In terms of reactive power, both converters can operate independently of each other. Overall, running the inverter in place of the traction transformer brings several advantages. It can load the power grid symmetrically. Interference caused by the operation of traction-dependent rail vehicles is not transmitted to the power grid. The inverter is not always fully utilized and the currently unused capacity of the inverter to provide traction power can be used to provide ancillary services to the electricity network. However, the availability of the inverter for providing reactive power should be determined, as the AFE must primarily transfer the active power for feeding the catenary system. [4].

III. Ancillary Services

The rules for the provision of ancillary services are summarized in Annex 7 of the Distribution System Operating (DSO) Rules [5]. Frequency and non-frequency ancillary services are defined. Annex 7 to the DSO Rules specifies the rules applicable to ancillary services, the principles of their measurement, certification and evaluation for providers of frequency ancillary services and non-frequency ancillary services. The requirements set out apply both to newly connected equipment and to existing equipment operating in parallel with the distribution system. Non-frequency ancillary services are used for local voltage stabilization and reactive power control, thereby contributing to voltage stability. Generating plants connected to the system of non-frequency ancillary services are obliged to participate in voltage control by supplying or withdrawing reactive power according to the requirements of the distribution system operator; the obligatory control zone of generating plants is specified in Annex 4 of the Distribution System Operation Rules [6]. The control of reactive power might be either autonomous or controlled centrally by DSO. The active participation of generating plants in the stabilization of the network is technically, organizationally and economically assessed by the DSO. Generating plants must pass certification tests and their participation in the system is contractually agreed. Similar procedure is expected in certification process of the SFC.

IV. Simulation of SFC in PSCAD

A certain percentage of the installed power is used to supply traction for a certain period of time; the inverter is not used 100% of the time. This leads to the idea of how to use this unused power. One option is to use this available power to provide ancillary services. Such an application is pioneering; nowhere in Europe are inverters operated in this way in a similar application. However, the actual availability of the inverter is unknown. Several factors affect the availability of the inverter. First of all, the independent loading of the inverter with traction load. To determine the availability of the inverter to provide non-frequency support services, simulation in the PSCAD simulation environment is used. The model created consists of the grid feeder, line model, transformers and the inverter itself. The simulations need to process a large volume of data, so the design of the model was based on the requirement to keep the model as simple as possible while representing the inverter. Therefore, the model is simulated using current sources. The current sources are controlled based on the requirement to supply or draw reactive and active power. The active power time profile was simulated using OpenTrack and Open Power Net, according to the actual train traffic schedule for three levels of line traffic load (light, medium and heavy traffic). In order to compare the performance differences according to the individual line traffic load, the active power waveforms for each scenario are shown in Fig. 1. Because the calculated active power profiles leads to large datasets, a simplification method has been selected in order to accelerate the simulation. Out of the total hourly waveforms, a window of 8.3 minutes was simulated. Every tenth value was selected from the second values of the active power waveform. Fig. 4 shows the already created P and Q profile for the PSCAD simulation program. The active power value taken from the simulated waveform is kept constant for 6.5 seconds. Subsequently, a reactive power ramp is added in 0.5 Mvar increments, the values are gradually changed in 0.1 second increments from -16 Mvar to 16 Mvar. Thus, the limiting values of reactive power in the given interval are found. The active and reactive power waveforms are entered into the simulation using generated text files containing the power values attributed to a particular simulation time. Several limiting factors are introduced. First and foremost is the inverter current load. The installed capacity of the inverter used for the simulation is 16 MVA. This implies a current limitation for this particular type of 2800 A. Another limiting factor is the voltage of the power grid from which the inverter is supplied. In this particular case, the grid is rated at 110 kV, The prescribed operating limits must not exceed ± 10%. The voltages in Fig. 6 are given in proportional units. In the same graph, the current curve of the inverter is plotted, note the intervention of the current limiter in a current limit state close to the abovementioned value of 2800 A. The simulation results observed are mainly the maximum reactive power supply and demand at a certain operating load of the inverter, which could be used to provide non-frequency support services, and which does not exceed the mentioned limiting criteria of the simulation. For the simulation, the grid voltage was set to 110 kV, and the frequency was set to 50 Hz. The value of the short circuit power of the network was set to 4500 MVA (relatively hard network).

V. The Results

Simulation of medium loaded track was chosen to present the performance results in Fig. 5, as the progression of the active, reactive and apparent power during the simulation is shown. The active power is represented by red line, it is always constant in the test window, the curvature of the curve is only caused by the actual elements inserted in the circuit, such as the transformers and the filter. The reactive power test ramp is shown in blue. One ramp for one sample of active power. The resulting triangular shape is due to the simulation setup. It is desirable that the data in the dynamic simulation changes smoothly. The apparent power is shown in green. In the graph, it can be noticed that the upper peaks of reactive and apparent power are constrained when reactive power is supplied to the grid. In this case, it is a current limitation, where the current values for a given load in the simulation got above the specified maximum inverter current load of 2800 A. Fig. 6 shows a development of voltage and current during simulation. When the voltage or current have exceeded the allowable limits, the set reactive power is considered as maximal available in the moment. The histograms determined the availability for all three track loading scenarios. The 95-quantile is similar for all loads - they are the same SFC and for all runs there are states where the active power is low and therefore the maximum available reactive power is close to the nominal power of the SFC. On the other hand, the installed power values are not reached. This is because the active power of the waveforms input to the simulation is zero only in a few states. The achievable capacitive power is higher because the supply of reactive power raises the voltage and the SFC is a current source. On the other hand, the 5-quantiles are different among the scenarios. The 5-quantiles express the minimum available reactive power that will be available at 95% (5% excludes extremes in selected waveform intervals) and thus represents a value that is suitable for contractual arrangements for non-frequency grid support. In the case of inductive reactive power Fig. 2, the Q values are as follows. 14.39 - 14.67 Mvar for the low frequented line (LFL), 11.97 - 14.64 Mvar for the medium frequented line (MFL) and 7.10 - 14.65 Mvar for the high frequented line (HFL). In the case of the reactive power capacity Fig. 3, the values for the low frequented line (LFL) are 14,96 - 15,25 Mvar, for the medium frequented line (MFL) 14,89 - 15,25 Mvar and for the high frequented line (HFL) 9,60 - 15,25 Mvar. All values are taken from measurement point 1 (PoM 1).

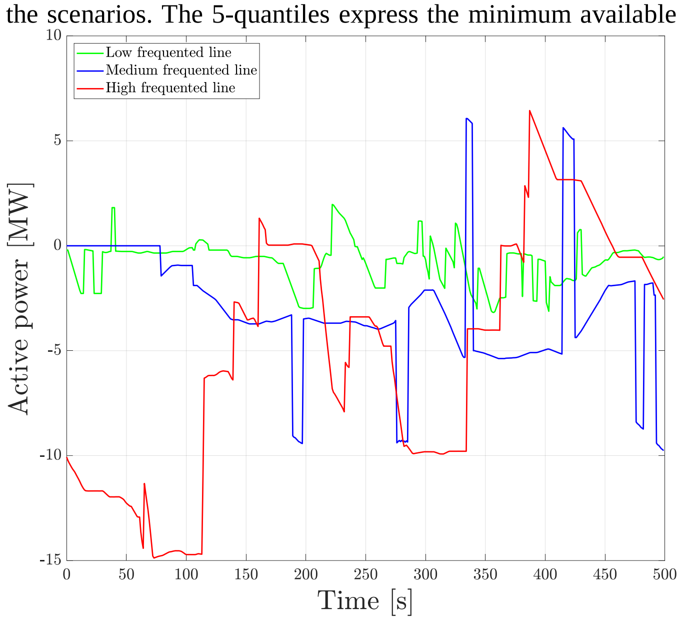

Fig. 1 Active power before sampling.

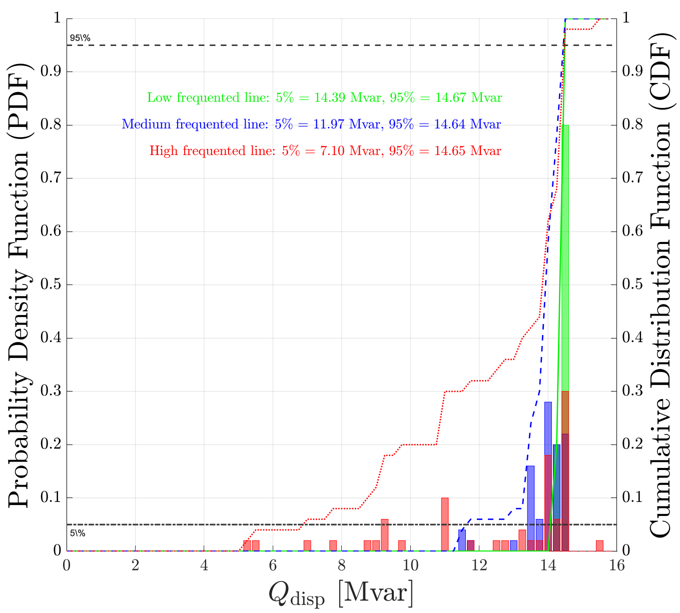

Fig. 2 Inductive reactive power.

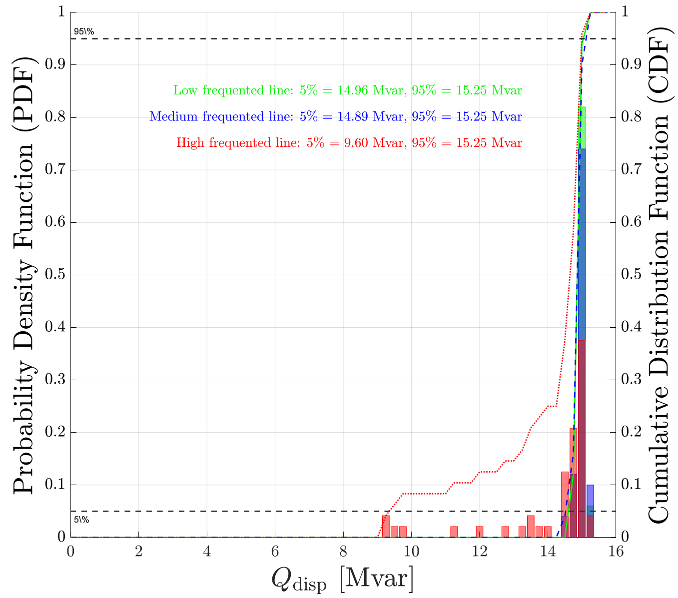

Fig. 3 Capacitive reactive power.

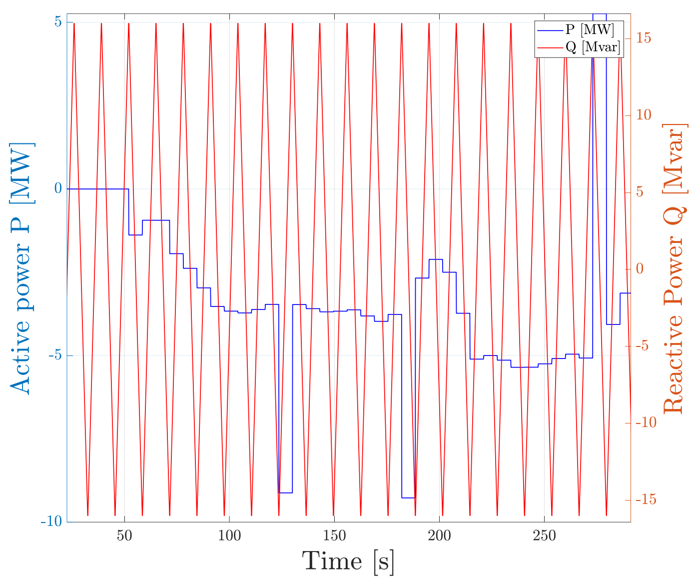

Fig. 4 Profiles of active (blue) and reactive (red) power for simulation scenario.

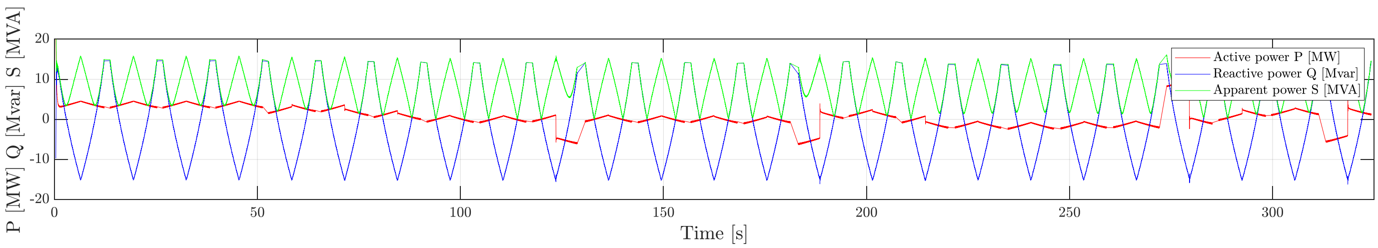

Fig. 5 Active, reactive and apparent power at PoM_1 during the simulation.

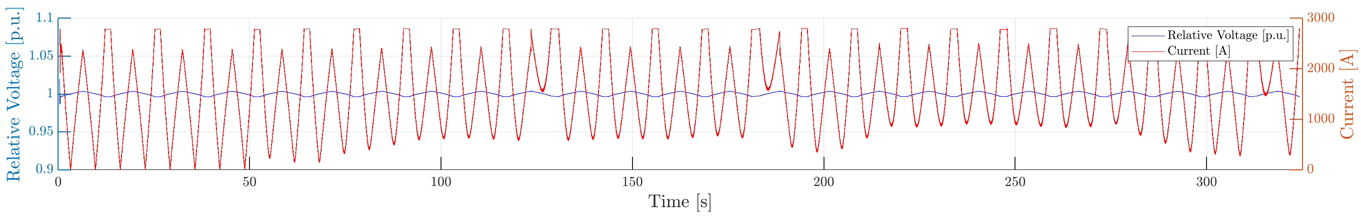

Fig. 6 Voltage and current during the simulation.

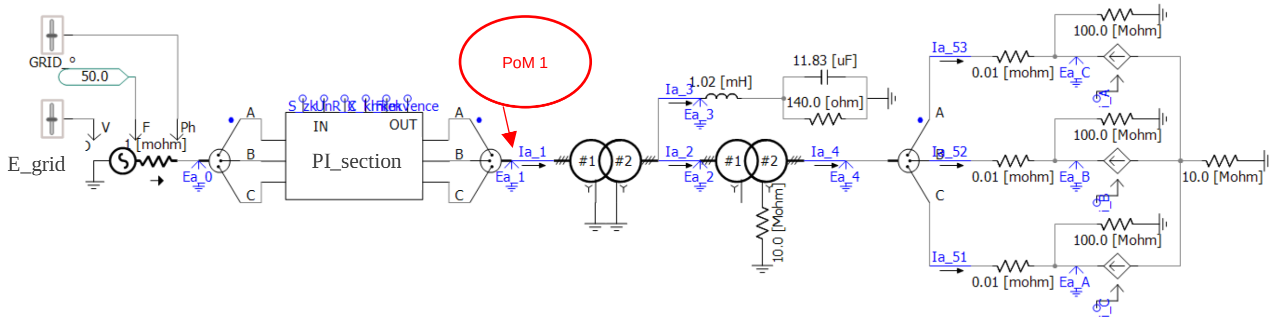

Fig. 7 SFC network diagram and its connection in the PSCAD simulation program.

VI. CONCLUSIONS

The presented approach to determine the availability of SFC to provide reactive power realistically, while the operating conditions of the railway system, including the actual impedance of the distribution network and the SFC inverter connection parameters, input transformers and filters. As a result, the availability of the inverter to provide non-frequency support services can be determined relatively accurately at the design stage, allowing a prediction of economic performance. In the presented example, the simulation results showed that the potentially available reactive power for providing support services is different among loading scenarios. For the inductive reactive power, the availability ranges are: 14.39-14.67 Mvar for LFL, 11.97-14.64 Mvar for MFL and 7.10-14.65 for HFL. For the capacitive reactive power, the availability ranges are: 14.96-15.25 Mvar for LFL, 14.89-15.25 Mvar for MFL and 9.60-15.25 for HFL. However, the results are based on a relatively short 8.3 minute segment and availability should be more accurately determined by selecting and simulating longer input active power data set for a given line load. These results present the potential of traction inverters to actively participate in the stabilization of the distribution grid through non-frequency ancillary services. The next step is to derive analytical mathematical model of the system to be used in software for traction system designers.

REFERENCES

[1] Declaration on national and regional railways. Online. 2022. Available: https://www.spravazeleznic.cz/dopravci/prohlaseni-o-draze-2024. [cit. 2025-03-15].

[2] Hu, H., Liu, Y., Li, Y. et al. Traction power systems for electrified railways: evolution, state of the art, and future trends. Rail. Eng. Science 32, 1–19 (2024). https://doi.org/10.1007/s40534-023-00320-6

[3] “KONCEPCE ROZVOJE ELEKTRICKÉ TRAKCE V ČESKÉ REPUBLICE” [CONCEPT OF DEVELOPMENT OF ELECTRIC TRACTION IN THE CZECH REPUBLIC] (in Czech). Online. In: Ministry of Transport. 2023. Available: https://md.gov.cz/getattachment/Dokumenty/Drazni-doprava/Zeleznicni-infrastruktura/Koncepce-rozvoje-elektricke-trakce-2023.pdf.aspx?lang=cs-CZ. [cit. 2025-03-27].

[4] P. Sacco, P. Ladoux, S. Sanchez, B. Sonier and M. Hassan, "The Static Phase Converter. A Solution to Reinforce the Power Supply of 25 kV/ 50Hz Railway Lines," 2024 IEEE International Conference on Electrical Systems for Aircraft, Railway, Ship Propulsion and Road Vehicles & International Transportation Electrification Conference (ESARS-ITEC), Naples, Italy, 2024, pp. 1-6, doi: https://doi.org/10.1109/ESARS-ITEC60450.2024.10819849.

[5] Grid Code – Annex 7. Online. CEZ Distribution. 2024. Available: https://www.cezdistribuce.cz/file/edee/distribuce/ppds/ppds-2021_priloha-7.pdf. [cit. 2025-03-15].

[6] Grid Code – Annex 4. Online. CEZ Distribution. 2024. Available: https://www.cezdistribuce.cz/file/edee/distribuce/ppds/ppds-2022_priloha-4.pdf. [cit. 2025-03-15]

Vision-Based Autonomous UAV Tracking and Control

1st Josef Bartoněk
Department of Control and Instrumentation
Brno University of Technology
Brno, Czech Republic
xbarto0f@vutbr.cz

2nd Jiří Janoušek
Department of Theoretical and Experimental Electrical Engineering
Brno University of Technology
Brno, Czech Republic
jiri.janousek@vut.cz

***Abstract*—This paper presents a vision-based control approach for unmanned aerial vehicles (UAVs), focusing on the detection and tracking of airborne objects. The proposed system integrates deep-learning-based object detection using YOLO models with computationally efficient tracking algorithms to ensure real-time performance. The control methodology involves extracting positional information from visual data and generating attitude commands to regulate UAV movement via MAVLink communication. The implementation is optimized for deployment on a Raspberry Pi 5, leveraging OpenCV and NCNN frameworks. Experimental results demonstrate the system's capability to detect and track small UAVs while maintaining high frame rates, enabling reliable feedback-based flight adjustments.**

***Index Terms*—UAV, drone, detection, tracking**

I. Introduction

Unmanned Aerial Vehicles (UAVs) have become a key technology with a wide range of applications, from industrial use and search-and-rescue operations to counter-UAV defense. Their ability to operate autonomously and adapt to dynamic environments makes them ideal for surveillance, delivery, and reconnaissance missions. A crucial aspect of UAV success lies in the integration of advanced object detection and tracking algorithms, enabling efficient navigation and interaction with their surroundings.

This work aims to develop a comprehensive software solution that allows a UAV to detect airborne objects and adjust its flight path based on visual data from an onboard camera system. The primary objective is to enable real-time tracking of flying objects and integrate this capability into the UAV's control system. The work involves researching existing object detection and tracking methods, implementing and testing suitable algorithms, and designing a robust feedback control system for flight regulation.

The focus will be on optimizing the software for onboard deployment, ensuring real-time performance in dynamic conditions, such as rapid object maneuvers. Finally, the developed system will be integrated into a real UAV and tested in various scenarios. The results will provide valuable insights for UAV applications in real-world conditions, contributing to advancements in autonomous aerial tracking and navigation.

II. Image processing

For this work, a comprehensive software solution was designed, developed, implemented, and tested to detect and track flying objects and control the UAV based on visual data.

The entire program is written in C++ and is compatible with the Bookworm operating system running on Raspberry Pi 5.

The core principle of the software is as follows: First, object detection is performed on the latest captured frame. If detection is successful, object tracking is initiated. After each subsequent frame is captured, tracking continues, and based on this tracking, the UAV's movement is adjusted accordingly.

Each of these steps will be addressed in its respective chapter.

A. Detection Methods for Low-Altitude UAVs

Detection of low-altitude drones involves multiple approaches, including frequency spectrum analysis, acoustic characteristics, microwave signal reflection, and optical analysis. Frequency spectrum-based detection allows rapid identification of UAV presence; however, technologies like Frequency Hopping Spread Spectrum (FHSS), which rapidly switches communication channels, significantly hinder signal localization. Acoustic analysis, detecting drones based on their sound, is effective for larger and noisier UAVs but less suitable for smaller, low-noise models. Microwave signal reflection, used in radar systems, efficiently detects larger UAVs but becomes less effective as drone size decreases. Optical analysis, based on image processing, is highly dependent on lighting conditions, which can introduce significant distortions, especially in low-light environments. [1]

Deep learning-based object detection is rapidly evolving and is widely used in pedestrian detection and facial recognition. [1] In recent years, deep learning has gained significant attention in research due to its success in pattern recognition and computer vision. Convolutional Neural Network (CNN)-based methods have revolutionized object detection by extracting deep, high-level features for class and bounding box predictions. [2]

Object detectors fall into two categories: two-stage and single-stage. Two-stage methods, such as Region-Based CNN (R-CNN), first generate region proposals and then classify them using CNN-based feature extraction, refining bounding boxes. While accurate, these methods are relatively slow. [2]

Single-stage detectors, such as You Only Look Once (YOLO) and Single Shot Multibox Detector (SSD), perform classification and localization in a single step. This unified training and inference approach enables direct optimization for detection performance. Among them, YOLO stands out for its balance between accuracy and speed. [2]

B. YOLO: A Real-Time Object Detection Algorithm

YOLO is a fast and efficient object detection algorithm that introduces a revolutionary approach by simplifying the entire identification and localization process into a single pass through a neural network. Unlike traditional methods such as R-CNN or SSD, which rely on complex pipelines with region proposals and classification, YOLO processes the entire image at once. This unified approach allows the prediction of bounding box coordinates and class probabilities directly from image pixels, enabling real-time detection with low latency. [3]

YOLO formulates object detection as a regression problem. The image is first divided into a grid, and each grid cell predicts bounding boxes along with their confidence scores and class probabilities. [3]

However, a notable challenge remains the accurate localization of smaller objects. [3]

C. Image Acquisition Using LCCV and OpenCV

For efficient acquisition and processing of image data on the Raspberry Pi platform, a combination of the libcamera and OpenCV (Open Source Computer Vision Library) libraries can be used, with LCCV (libcamera bindings for OpenCV) providing a practical bridge between these technologies. Since the transition to the libcamera library in the Raspbian Bullseye system, camera management has undergone significant changes, enabling broader support for modern hardware while breaking compatibility with older tools. LCCV facilitates the integration of the camera into C++ applications by capturing images directly into the ‘cv::Mat‘ format, allowing for seamless processing, including object detection, filtering, and image transformations. [7]

D. Implementation of YOLO on Raspberry Pi using NCNN

First, the YOLOv3-Tiny model was implemented and tested using OpenCV’s Deep Neural Network (cv::dnn) module. Unfortunately, it demonstrated limited capability in detecting smaller drones. However, it performed better when detecting planes, as shown in Fig. 1, although the aircraft needed to be relatively close for successful detection.

Due to these limitations, the YOLOv8 model was implemented using the NCNN framework. Detections were filtered to include only the ”airplane” category. During testing against a clear or slightly cloudy sky, the model demonstrated a strong ability to detect small UAVs (drones), identifying objects as small as 30×30 pixels, as shown in Fig. 2.

Although this would theoretically be sufficient for object localization and could be used for control based on visual

Fig. 1. Detection of a model aircraft using YOLOv3-Tiny.

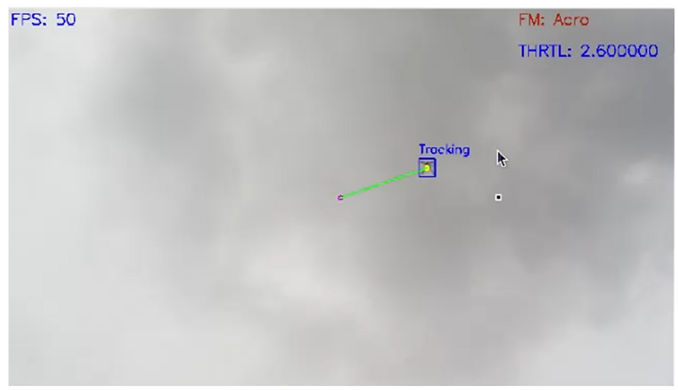

Fig. 2. Detection of a small drone using YOLOv8.

information, the low frame rate of only 5 FPS makes this impractical. Therefore, we propose using the YOLO model solely for the initial detection phase and then initializing a tracker based on this detection, which requires significantly less computational power.

E. Object Tracking

After successfully detecting an object, it is crucial to track it in subsequent frames to determine its trajectory and movement dynamics. Object tracking enables the UAV to continuously respond to changes in the target’s position without requiring repeated detections, which can be computationally expensive. For the implementation of the tracking system, OpenCV was chosen due to its extensive collection of optimized tracking algorithms, ease of integration, and support for real-time processing on embedded platforms.

OpenCV is an open-source library for computer vision, machine learning, and video analysis, originally introduced by Intel at the turn of the millennium. [4] [6]

Today, OpenCV includes over 2,500 optimized algorithms for tasks such as face detection and recognition, object identification, motion tracking, and 3D object modeling. It provides interfaces for C++, Python, and MATLAB and supports Windows, Linux, Android, and macOS. The estimated number of OpenCV downloads exceeds 18 million. [4] [6]

Tracking algorithms implemented in OpenCV consist of three main components:

TrackerFeatureSet – A model representing the visual appearance of the target object. OpenCV allows feature extraction using methods such as HAAR, HOG, LBP, and Feature2D. [5]

TrackerSamplerAlgorithm – A mechanism for assigning model parts to image regions in each frame, computing image patches based on the last known target position. [5]

TrackerModel – A mechanism for continuous learning and updating of target models as their appearance changes over time. It maintains all possible state candidates and calculates the trajectory. [5]

The implementation allows for easy selection of the tracking algorithm, such as MOSSE or KCF, by simply modifying a build-time parameter in CMake. During testing, MOSSE was chosen due to its ability to achieve the highest FPS, as benchmarked in [5]. On the Raspberry Pi 5, this implementation achieved an average of 45–50 FPS using MOSSE.

III. Flight Control System

The core of every drone (multicopter) is the flight control unit, which serves as the central interface for all hardware components, including Electronic Speed Controllers (ESCs), GPS, compass, and RC receiver. It integrates sensor inputs and ensures stable and smooth flight. [8]

However, a flight control unit cannot operate without firmware—a software component that governs its functionality. While the flight controller is a physical device, the firmware is the digital code that controls it. Commonly used firmware includes ArduPilot, PX4, and BetaFlight. [8]

Flight controllers provide essential functionalities such as automatic leveling, position hold, autonomous mission execution, and return-to-home features. However, they also have limitations—autonomous missions, for instance, must be preplanned and static. [8]

For the development of advanced applications, flight controllers alone are insufficient due to constraints in memory and processing power. [9] [8]

For this work, the ArduPilot software was chosen, specifically the Guided NoGPS mode.

A. Communication with the Flight Controller

The onboard computer, in this case, a Raspberry Pi 5, can be easily connected to the flight controller via a serial link. Using the MAVLink (Micro Air Vehicle Communication Protocol), the onboard computer can communicate with the flight controller, enabling seamless data exchange and command execution. [9]

MAVLink is a communication protocol for drones and their components. It uses a hybrid architecture combining publish-subscribe and point-to-point communication. Telemetry data is sent as topics, while configurations like mission and parameter protocols use point-to-point messaging. [10] [11]

IV. Vision-Based UAV Control

To control the UAV's attitude, the MAVLink command `SET_ATTITUDE_TARGET` is used. This command allows setting the vehicle's target attitude and climb rate or thrust. The core of this command is the attitude quaternion, which is a four-element vector representing the vehicle's orientation in three-dimensional space.

The command parameters include attitude quaternion, which determines the desired orientation of the UAV, and thrust from 0 to 1, controlling the UAV's climb or descent rate. The target throttle is based on the hover throttle value obtained from the flight controller.

In this system, after obtaining the current attitude of the drone, the error from visual tracking is computed. Based on this error, a new quaternion is calculated and sent via `SET_ATTITUDE_TARGET` to adjust the UAV's orientation.

A. Error Computation from Image Data

To get the error, we first compute the pixel displacement of the detected object from the center of the image frame:

$$\Delta x = x_{\text{target}} - \frac{W}{2} \tag{1}$$

$$\Delta y = y_{\text{target}} - \frac{H}{2} \tag{2}$$

where $x_{\text{target}}, y_{\text{target}}$ represent the target object's center coordinates in pixels, and W, H denote the image frame width and height, respectively.

Next, we convert this pixel displacement into an angular error by considering the camera's field of view (FoV):

$$\theta_x = \Delta x \cdot \frac{\text{FoV}_x}{W} \tag{3}$$

$$\theta_y = \Delta y \cdot \frac{\text{FoV}_y}{H} \tag{4}$$

where $\text{FoV}_x, \text{FoV}_y$ are the horizontal and vertical fields of view of the camera in degrees.

Conclusion

This work presented a vision-based control system for UAVs, integrating object detection, tracking, and attitude regulation into a single pipeline. By leveraging deep learning for initial detection and efficient tracking algorithms for continuous object monitoring, the system achieves a balance between accuracy and computational efficiency. The implementation on a Raspberry Pi 5 demonstrates that real-time tracking can be achieved, with MOSSE-based tracking maintaining an average of 45–50 FPS. The integration with ArduPilot allows precise UAV control based on visual input, showcasing the feasibility of autonomous flight adjustments without GPS. While the current system achieves reliable performance under clear sky conditions, future improvements could focus on enhancing robustness in complex environments, improving detection under varying lighting conditions, and integrating predictive control models for smoother flight trajectory adjustments.

References

[1] X. Yuan, J. Xia, J. Wu, J. Shi, and L. Deng, “Low Altitude Small UAV Detection Based on YOLO model,” 2020.

[2] Y. Hu, X. Wu, G. Zheng, and X. Liu, “Object Detection of UAV for Anti-UAV Based on Improved YOLO v3,” 2019.

[3] J. Redmon, S. Divvala, R. Girshick, and A. Farhadi, “You Only Look Once: Unified, Real-Time Object Detection,” 2016. [Accessed: Oct. 29, 2024].

[4] I. Culjak, D. Abram, T. Pribanic, H. Dzapo, and M. Cifrek, “A brief introduction to OpenCV,” 2012.

[5] A. Brdjanin, N. Dardagan, D. Dzigal, and A. Akagic, “Single Object Trackers in OpenCV: A Benchmark,” 2020.

[6] OpenCV “About.” 2024.

[7] LCCV, “Readme”. 2024.

[8] C. Bergquist, “What Is A Flight Controller?”. Drone Dojo, 2022.

[9] Ardupilot, “Communicating with Raspberry Pi via MAVLink”. 2024.

[10] MAVLink, “Introduction”. 2024.

[11] MAVLink, “Protocol Overview”. 2024.

Surface Engineering of Piezoelectric Semi-Crystalline Polymer Scaffolds via Plasma Treatment for Improved Adhesion and Integration of Osteoblasts

Bc. Tereza Havlíková
Department of Physics, Faculty of Electrical Engineering and Communication
Brno University of Technology
Technická 2848/8, 61600 Brno, the Czech Republic
Tereza.Havlikova1@vut.cz

***Abstract*—The surface properties of tissue scaffolds are of critical importance in the field of bone tissue engineering as they primarily influence cell adhesion. Piezoelectric semicrystalline synthetic polymers such as polyvinylidene fluoride have attracted considerable attention as biomaterials because of their ability to mimic the electrical environment of the native bone extracellular matrix. However, their osteointegration potential remains limited by their inherently low surface energy and suboptimal cell attachment properties. This study investigated the effect of plasma treatment on the surface properties of PVDF nanofiber scaffolds and the subsequent effects on cell adhesion. The plasma treatment process affects the surface morphology and wettability in relation to the gas used during the modification, thereby enhancing its interaction with the biological environment. Preliminary characterization of these surface modifications was conducted using scanning electron microscopy and water contact angle measurements, while the influence on cell adhesion and infiltration was investigated using confocal laser scanning microscopy.**

Keywords—cell adhesion, electrospinning, nanofibers, osteoblasts, piezoelectricity, plasma treatment, PVDF, scaffold

I. Introduction

A promising alternative to traditional methods of treating bone diseases is the development in the field of bone tissue engineering (BTE). It represents a range of natural and synthetic biocompatible materials for the production of artificial 3D frameworks mimicking the natural architecture and function of bone tissue extracellular matrix (ECM). In combination with suitable colony of healthy cells extracted ideally from the patient, the scaffold has the potential to replace whole tissue grafts from donors used in current treatment methods. The use of artificial scaffolds holds great promise for preservation, restoration, and enhancement of function in damaged tissues while concurrently reducing the risks to the patient [1, 2].

Substitutes for natural bone grafts must be biocompatible and exhibit a porous, flexible, and stable microarchitecture with respect to the target tissue to ensure proper mechanical support, nutrient supply, and waste transport. In addition, they should facilitate cell adhesion and infiltration, neovascularization, stimulate growth and act as a reservoir for biomolecules [3].

A wide variety of biocompatible materials can be used for BTE, including metals, bioceramics, natural or synthetic polymers, and their composites. The utilization of synthetic nanomaterials offers several distinct advantages, particularly the use of nanofibers. Primarily, their chemical, physical, and morphological properties can be meticulously tailored during the manufacturing process for adequate replication of the target tissue [2]. The diameter of the fabricated nanofibers closely corresponds to that of the fibers in the ECM, and their relatively large surface area facilitates proper cell adhesion. Furthermore, if required, these nanomaterials can be subjected to functional modifications to enhance their performance without compromising their integrity [4].

In the process of healing, the stimulation of bone tissue to undergo osteogenesis and osteoinduction can be achieved through the induction of specific signaling pathways, ion exchange, growth factors, and electric stimulation. It has been established that the piezoelectric properties of certain materials are associated with these processes, as such materials generate electrical impulses when mechanically stressed, which can result in the stimulation of cells [5].

Polyvinylidene fluoride (PVDF), a synthetic semi-crystalline polymer, has been shown to possess piezoelectric properties, exhibit high biocompatibility, demonstrate favorable mechanical parameters, and, through specific production techniques (e.g., electrospinning), can be utilized to create a fine nanofiber tissue scaffold that is both highly porous, flexible, and piezoelectric [6]. PVDF exhibits three distinct crystalline phases, α (alpha), β (beta), and γ (gamma). The polar β-phase is of particular significance in PVDF because it exhibits the most potent piezoelectric properties [7].

Plasma treatment is a commonly employed technique for altering the surface characteristics of polymers, such as PVDF, as it generates a highly reactive chemical environment capable of modifying and functionalizing a wide variety of materials. This approach is particularly effective for increasing the surface energy, improving wettability and adhesion, and for surface cleaning or etching through irreversible chemical reactions. By carefully adjusting parameters such as the ionization source, gas type, and exposure duration, surfaces with precisely tailored properties can be fabricated for specific applications. It has been demonstrated that oxygen and/or argon plasma treatment can alter PVDF surfaces without compromising the β-phase content, may even increase its share, leading to improved cell adhesion and infiltration compared to untreated surfaces. The primary distinction between these two gases pertains to their respective surface-activation mechanisms. Specifically, the utilization of Ar plasma predominantly leads to physical etching, whereas O_2 plasma enhances surface energy also through surface chemical reactions – oxygenation and defluorination [6, 8, 9].

This work draws from previous comprehensive research and its results [10], which provided an overall assessment of the adaptability of PVDF nanofibers for bone tissue engineering. The paper focuses on a specific aspect of surface modification of nanofibers by oxygen and/or argon plasma and summarizes its effect on scaffold morphology and cellular integration. The plasma treatment working parameters were derived from studies conducted by Kitsara et al. [8] and Correia et al. [9]. The resulting 7 sets of samples consisting of modified and unmodified nanofibers were then compared considering variations in the gas type, power, and treatment time.

II. Materials and Methods

A. Fabrication of the Tissue Scaffold

The nanofiber samples (1 × 1 cm) investigated in this study were produced using a 4SPIN electrospinning device, with a single needle acting as the emitter and a cylindrical collector (Contipro, Dolní Dobrouč, the Czech Republic) at room temperature. The prepared polymer solution was dispensed through the emitter at a flow rate of 35 μL/min, as the collector was rotated at 2000 rpm under an applied voltage of 50 kV.

The material used consisted of a 20% PVDF polymer solution with a molecular weight of 275.000 g/mol, which was dissolved in a solvent of dimethyl sulfoxide and acetone prepared in 7:3 ratio. The mixture was continuously heated and stirred at 80 °C and 200 rpm for 24 h to ensure homogeneity prior to electrospinning.

B. Surface Modification and Sample Preparation

A NANO Plasma Cleaner (Diener electronic, Ebhausen, Germany) was selected for cleaning and modifying the sample surfaces by O_2 plasma, Ar plasma, or O_2+Ar plasma for 2 min at 200 W or 10 min at 300 W.

To prevent charge accumulation on the sample surface and to secure the nanofibers during SEM to ensure unobstructed observation, a carbon coating was applied using a Coater EM ACE600 instrument (Leica Microsystems, Germany).

C. Cell Cultivation and Staining

The human osteosarcoma cell line Saos-2 (HTB-85; ATCC, Manassas, VA, USA) is widely regarded as the most representative cell model utilized in BTE, exhibiting activity very similar to that of osteoblasts. A key benefit of this model is its ability to facilitate rapid and simplistic cultivation process.

Saos-2 cells were maintained in Dulbecco's Modified Eagle's Medium supplemented with 10% fetal bovine serum and 5% penicillin/streptomycin (50 IU mL^{-1} and 50 μg mL^{-1}). Cells were cultured at 37 °C in a humidified incubator with 5% CO_2. For cell extraction, 0.25% trypsin-EDTA solution was used, followed by cell seeding at a density of 1×10^3 cells/mL onto separate sterile prehydrated PVDF samples. Cells fixed with paraformaldehyde were permeabilized using a 0.5% Triton-X 100 solution and a 2% bovine serum albumin solution to facilitate dye penetration. After thorough washing with deionized water, the cells were stained with DAPI to label nuclei and FITC to highlight the cell membrane. All chemicals were obtained from Sigma Aldrich (St. Louis, MO, USA).

D. Methods for Characterization of Surface Plasma Modifications of Scaffolds and Cell Viability

1) Scanning Electron Microscopy (SEM): Surface morphology of manufactured polymer scaffolds and the behavior between the nanofibers and Saos-2 cells regarding plasma treatment were observed by SEM using LYRA3 microscope (Tescan, Brno, Czech Republic). The following parameters were set for all observations: detector SE, voltage 5kV, working distance 9 mm, and given magnification and field of view.

2) Water Contact Angle Measurement: The water contact angle was measured according to Young's equation using a System E instrument (Advex Instruments, Brno, Czech Republic) for the experimental procedure, while See 7.0 software was used to analyze the contact angles based on the captured images. To ensure consistency, 10 individual 3 μL droplets of distilled water were applied sequentially to the surface of the samples using a micropipette. Measurements were taken at t = 4s after droplet deposition and an image was captured for analysis. The final contact angle for each sample was calculated as the mean of ten independent measurements to ensure reliability.

3) Confocal Laser Scanning Microscopy (CLSM): The interaction between fluorescently labelled cells and PVDF nanofibers was analyzed by immunofluorescence microscopy using a Zeiss LSM 880 confocal microscope (Carl Zeiss AG, Jena, Germany) equipped with C-Apochromat 40× and Plan-Apochromat 20× objectives. Excitation wavelengths of 488 nm and 405 nm were used for FITC and DAPI staining, respectively, to highlight the cell membrane and nuclei. Post-processing and quantitative analysis of the acquired images were performed using Zeiss ZEN 3.10 LITE software.

III. Results

A. Surface Morphology Analysis

Plasma-treated and reference samples, prepared for analysis and labelled as shown in Table I., were examined and visualized by SEM at view field of 48 μm with magnification of 11.5k×.

TABLE I. OVERVIEW OF SAMPLES

Sample	Modification	Gas Type	Time/min	Power/W
S1	No	–	–	–
S2	Yes	O_2	2	200
S3	Yes	Ar	2	200
S4	Yes	O_2+Ar	2	200
S5	Yes	O_2	10	300
S6	Yes	Ar	10	300
S7	Yes	O_2+Ar	10	300

The reference sample labelled S1 as seen in Fig.1 a) exhibits thin and smooth nanofibers forming a stable directed structure with relatively large pores. Sample S3, shown in Fig.1 d), treated with Ar at low treatment time and power (2 min, 200 W) also shows no noticeable change in the nanofiber structure or its surface. In contrast, sample S4 in Fig. 1 c), treated with O_2+Ar at the same low plasma settings, shows nanofibers whose entire homogeneous structure has been disrupted by etching, becoming warped and coalescing. The strongest effect of etching at given low setting can be observed on sample S2 in Fig.1 b) treated with O_2 alone, where the fibers are already so twisted and coupled that they significantly reduce the average pore size creating a mushroom-like structure. After examining the samples S5 and S7, it can be concluded that due to intensive O_2 and O_2+Ar plasma treatment (10 min, 300 W), they no longer meet the requirements for a porous nanofibrous scaffold. The resulting structure due to high plasma power resembles a cohesive mixture of differently sized clumps rather than thin nanofibers, which would make cell infiltration impossible. On the contrary, nanofibers in S6 do not show any visible effects of the Ar plasma treatment on higher settings.

As mentioned above, the O_2 plasma has not only physical effects (e.g. cleaning, roughening) but also chemical effects on the modified material, breaking the C–F and C–H bonds in various ways and introducing polar groups, increasing the surface energy overall but not uniformly. Mechanical deformation such as torsion can occur due to local differences in surface energy. Surface chemical reactions and physical etching can explain also the partial disruption of the nanofiber structure and subsequent cross-linking [9]. The degree of energy change can be verified by measurement of surface wettability.

B. *Wettability Assay*

The values within the hydrophobicity interval are indicative of a surface's tendency to resist penetration by water or other polar substances, with a range set between 90° and 150° for the contact angle of water on a solid surface. The hydrophilicity interval, defined as the surface's capacity for positive interaction with water, ranges from 0° to 90°. Surfaces with high surface energy relative to the surface tension of the liquid possess strong, attractive forces between their molecules, thereby facilitating liquid wetting of the surface. In principle, plasma treatment should through process of physical and chemical etching augment the surface energy of the material, which should result in enhanced adhesion properties [1].

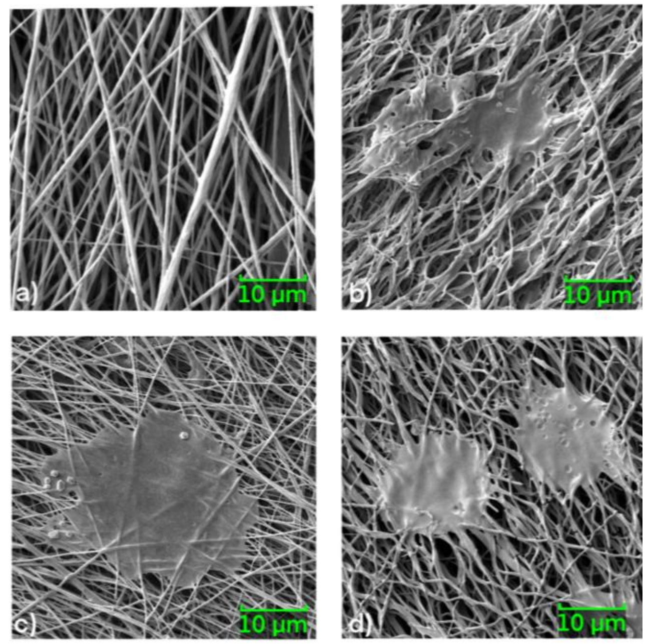

Fig.1. Surface morphology changes after plasma treatment and interactions with cells were visualized through SEM – image a) displays reference sample S1 of unmodified nanofibers, b) shows O_2 plasma treated sample S2, c) shows sample S3 treated with Ar plasma and image d) displays O_2+Ar plasma treated S4.

The water contact angle measurements confirmed that the reference PVDF nanofibers in sample S1 exhibited inherent hydrophobicity, with an average contact angle of 124.6°. Similar results were achieved by Černohorský et al. [7]. A brief exposure to Ar plasma in sample S3 (2 min, 200 W) led to a minor reduction in the contact angle to 122.2°, thus maintaining the material's hydrophobic nature. Conversely, the treatment of sample S2 with O_2 plasma under identical conditions resulted in a substantial alteration of the surface energy, leading to a significant reduction in the contact angle to 22.8°, rendering the material hydrophilic. A comparable effect was observed for sample S4, where a combination of O_2+Ar plasma treatment resulted in a contact angle of 32.5°, also within the hydrophilic range. It is noteworthy that all the deposited droplets exhibited stability in $t = 600s$ in every measurement previously mentioned. For sample S6 treated with Ar plasma for 10 min at 300 W, the deposited droplets were immediately absorbed, resulting in a contact angle value equal to 0° (hydrophilic). The positive effects of O_2 plasma on β-phase content were confirmed by Havlíková et al. [10]. The results from the wettability assay are summarized in Table II.

TABLE II. WATTER CONTACT ANGLE MEASUREMENTS

Sample	Contact Angle [°]	Wetting Character
S1	124.6	Hydrophobic
S2	22.8	Hydrophilic
S3	122.2	Hydrophobic
S4	32.5	Hydrophilic
S6	0	Hydrophilic

C. *Cell Adhesion, Spreading and Scaffold Infiltration*

The shape of individual cells and the character of adhesion and infiltration of the nanofiber scaffold in relation to surface modification by plasma were evaluated using SEM and CLSM.

The analysis has confirmed that nanofibers provide cells with a sufficiently strong and stable structure on which they can attach and grow. The cells naturally take on a spherical shape, but as they grow on the nanofibers, they become slightly elongated in the direction of the fiber orientation. This mimics the arrangement in natural bone tissue and aids the cells in communication and increases overall viability. A significant proportion of cells adhered to untreated nanofibers in the reference sample; however, the excessively large pores and highly hydrophobic surface of these nanofibers provided insufficient support and suboptimal adhesion capabilities, thereby hindering the formation of larger structures.

The findings demonstrated that samples which underwent treatment with Ar plasma at both lower and higher settings did not demonstrate enhanced compatibility with Saos-2 cells in comparison to the reference sample. Conversely, the treatment of samples with O_2 plasma and O_2+Ar plasma resulted in improved results attributable to increased hydrophilicity and bioactivity due to surface functionalization by oxygen. Furthermore, see Fig.2 b), CLSM provided more reliable insights into the manner in which cells infiltrated deeper layers of the tissue scaffold, forming both surface and spatially distributed clusters on these hydrophilic samples. In contrast, on hydrophobic samples, the cells remained predominantly on the surface and did not form tissue-like clusters as seen in Fig.2 a). As illustrated in Fig.2 b), blue-stained regions representing nuclei were often overridden by signal from green-stained cell cytoplasm.

IV. Conclusion

The electrospun PVDF nanofibers, fabricated under the specified fabrication parameters and treated with O_2 or O_2 +Ar plasma at treatment time of 2 min and power of 200 W, meet the basic requirements for a nanoporous tissue scaffold while

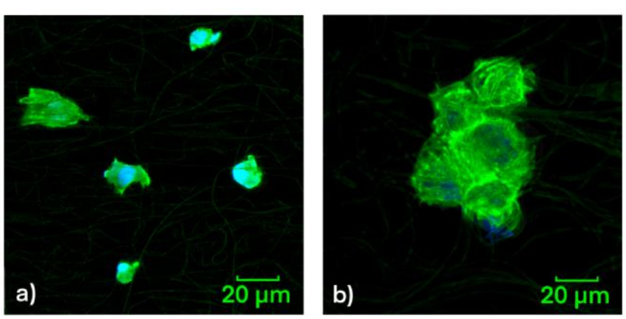

Fig. 2. Saos-2 cell attachment visualized through immunofluorescence and CLSM, where image a) displays individual cells in Ar treated sample S3, and image b) shows cell cluster in O_2 treated nanofiber sample S2.

providing hydrophilic conditions. It was found that slightly reducing the pore size of the scaffold and providing a denser support framework, in addition to increasing the surface energy, was beneficial for the adhesion and expansion of Saos-2 cells. The incorporation of oxygen into the surface bonds is likely to enhance the overall bioactivity of the carrier, and the plasma treatment process itself should contribute to the increase in piezoelectric β-phase content through mechanical stress and electrical polling, as can be further demonstrated by Fourier transform infrared spectroscopy. Further experiments with extended culture periods would provide valuable insights into the long-term biocompatibility and cellular colonization of the tissue scaffold.

Acknowledgment

I would like to express my gratitude to my supervisor Ing. Nikola Papež Ph.D. for his guidance, continuous support, and insightful suggestions throughout this research. I also extend my appreciation to doc. Mgr. Zdenka Fohlerová Ph.D. and collaborators at the BUT´s Department of Physics for their assistance and shared knowledge.

References

[1] SHARMA, P., KUMAR, P., SHARMA, R. and BHAT, V. D. Tissue Engineering; Current Status & Futuristic Scope. *Journal of Medicine and Life* [online]. 2019, 12(3). DOI: 10.25122/jml-2019-0032.

[2] CHOCHOLATA, P., KULDA, V. and BABUSKA, V. Fabrication of Scaffolds for Bone-Tissue Regeneration. *Materials* [online]. 2019, 12. DOI: 10.3390/ma12040568.

[3] BOSE, S., ROY, M. and BANDYOPADHYAY, A. Recent advances in bone tissue engineering scaffolds. *Trends in Biotechnology* [online]. 2012, 30(10), 546–554. DOI: 10.1016/j.tibtech.2012.07.005.

[4] DAHLIN, R. L., KASPER, F. K. and MIKOS, A. G. Polymeric Nanofibers in Tissue Engineering. *Tissue Engineering Part B: Reviews* [online]. 2011, 17(5). DOI: 10.1089/ten.TEB.2011.0238.

[5] YANG, C., JI, J., LV, Y., LI, Z. and LUO, D. Application of Piezoelectric Material and Devices in Bone Regeneration. *Nanomaterials* [online]. 2022, 12(24). DOI: 10.3390/nano12244386.

[6] DUMITRESCU, L. N., NEACSU, P., et al. Induced Hydrophilicity and In Vitro Preliminary Osteoblast Response of Polyvinylidene Fluoride (PVDF) Coatings Obtained via MAPLE Deposition and Subsequent Thermal Treatment. *Molecules* [online]. 2020, 25(3). DOI: 10.3390/molecules25030582.

[7] ČERNOHORSKÝ, P., et al. Structure Tuning and Electrical Properties of Mixed PVDF and Nylon Nanofibers. *Materials* [online]. 2021, 14(20), 6096. DOI: 10.3390/ma14206096.

[8] KITSARA, M., et al. Permanently hydrophilic, piezoelectric PVDF nanofibrous scaffolds promoting unaided electromechanical stimulation on osteoblasts. *Nanoscale* [online]. 2019, 11. The Royal Society of Chemistry.

[9] CORREIA, D., et al. Influence of oxygen plasma treatment parameters on poly(vinylidene fluoride) electrospun fiber mats wettability. *Progress in Organic Coatings* [online]. 2015, 85, 151–158.

[10] HAVLÍKOVÁ, T., PAPEŽ, N., FOHLEROVÁ, Z., KASPAR, P., DALLAEV, R., ČÁSTKOVÁ, K. and ŢĂLU, S. Adaptability of Electrospun PVDF Nanofibers in Bone Tissue Engineering. *Polymers* [online]. 2025, 17, 330. DOI: 10.3390/polym17030330.

Machine Learning-Driven Detection of Repetitive Manufacturing Processes Using Radar Sensor

Bc. Tomáš Martiník
Department of Control and Instrumentation
Brno University of Technology
Brno, Czech Republic
xmarti95@vutbr.cz

***Abstract*—This paper presents a non-invasive system for detecting repetitive manufacturing cycles using pulse-coherent radar and machine learning. The Acconeer A111 radar sensor, combined with an Arducam USB camera, is integrated within a ROS2-based data acquisition framework. The system operates in Envelope and Sparse radar modes, optimized for tracking static and dynamic motion. A YOLO-based model analyzes radar heatmaps to detect repetitive cycles automatically.**

The approach was validated through controlled experiments and in an industrial setting. Results demonstrate the system's potential to accurately detect production cycles without modifying existing machinery, highlighting its potential for real-time process monitoring and optimization.

***Index Terms*—Radar sensing, ROS2, data collection, machine learning, production monitoring.**

I. Introduction

The rapid development of Industry 4.0 has highlighted the importance of data-driven manufacturing, where precise monitoring of production processes is essential for optimizing performance and ensuring efficiency. Traditional approaches to production cycle tracking often rely on direct machine integration, requiring physical modifications and additional sensor installations. These solutions are not only costly but can also lead to disruptions in manufacturing operations, requiring re-certification of production lines.

To address these challenges, this paper presents a non-invasive system for monitoring production cycles using a combination of a pulse-coherent radar sensor and a camera. Unlike conventional methods, the proposed approach does not require any modifications to existing machinery, making it highly scalable and adaptable to different manufacturing setups. The primary objective is to develop an automated system capable of detecting repetitive cycles in real-time using radar data, thus providing valuable insights into production efficiency without interfering with industrial workflows.

II. Pulse-Coherent Radar Overview

Pulse-coherent radar enables precise motion and distance measurements by analyzing phase and amplitude variations in reflected electromagnetic waves. This paper utilizes the Acconeer A111 radar sensor, which supports multiple acquisition modes.

A. Principle of Operation

The Acconeer A111 emits electromagnetic pulses, which reflect off objects and return to the sensor. By measuring the time delay and phase shift, the radar determines distance and motion. Coherent processing enables detection of small displacements, making it effective for cycle tracking.

B. Radar Data Acquisition Modes

The radar supports several modes, each optimized for different applications:

- **Envelope Mode** – High-precision distance measurement, ideal for detecting static and slow-moving objects.
- **Sparse Mode** – Captures motion with high temporal resolution, allowing velocity estimation.
- **IQ Mode** – Provides complex in-phase (I) and quadrature (Q) data, suitable for Doppler-based motion analysis.
- **Power bins** – Provides basic object presence information.

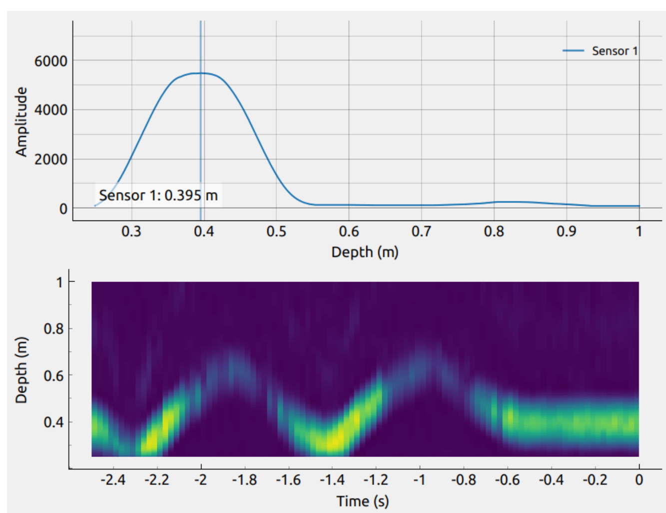

Fig. 1. Example of Envelope mode output.

After evaluation, **Envelope** and **Sparse** modes were selected as the most effective for detecting production cycles.

1) Envelope Mode: Envelope mode captures reflection amplitude across the detection range, providing high spatial resolution. Initial testing at **10 Hz** sampling was insufficient for tracking cycles, leading to an optimized **40 Hz** rate, ensuring consistent detection of moderate-speed objects.

2) Sparse Mode: Sparse mode provides reduced data density but higher temporal resolution, making it suitable for tracking rapid motion. Two configurations were tested: **16 sweeps per frame** at **90 Hz**, prioritizing higher frequency, and **32 sweeps per frame** at **50 Hz**, capturing finer motion details. Sparse mode measures at 6 cm intervals but accumulates multiple sweeps per frame, enabling high-speed motion tracking. The 32-sweep configuration provided the best trade-off between resolution and update rate [1].

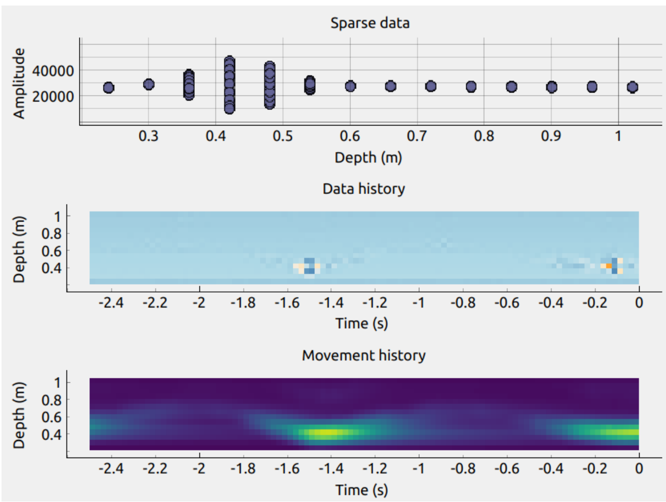

Fig. 2. Example of Sparse mode output.

C. Final Radar Configuration for Cycle Detection

The following radar configurations were used:

- **Envelope Mode** (40 Hz) – Optimized for detecting static or slow-moving components.
- **Sparse Mode** (50 Hz, 32 sweeps per frame) – Captures rapid motion changes and velocity estimation .

III. Design and Fabrication of a Sensor Holder

A custom 3D-printed holder was designed to ensure precise alignment and stable mounting of the radar sensor and camera. Developed in Fusion 360, the holder was optimized for robustness, ease of assembly, and tripod compatibility.

A. Design Requirements

The holder was designed to meet the following key requirements:

- **Parallel alignment:** Ensuring synchronized radar and camera data capture.
- **Stable mounting:** Secure attachment to a tripod with minimal vibrations.
- **Cable management:** Openings for organized routing of power and data cables.
- **Modularity:** Easy assembly, disassembly, and modification if needed.

B. CAD Modeling and 3D Printing

The radar sensor and camera were positioned as close as possible while maintaining accessibility for mounting screws. The optimal device spacing was determined to be **42.6 mm**. Key features of the 3D model include:

- Snap-fit slot for the Acconeer A111 radar sensor.
- Recessed compartment for the PCB and connectors.
- 1/4”-20 UNC threaded hole for tripod mounting.

To ensure durability, the back wall thickness was set to **4 mm**. Fig. 3 shows the final 3D model.

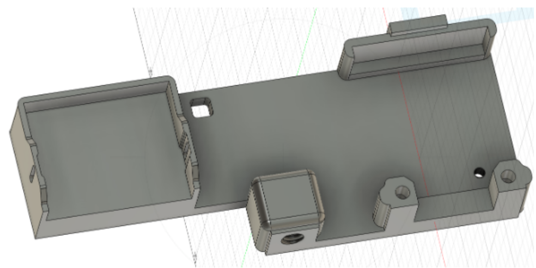

Fig. 3. 3D model of the sensor holder, designed in Fusion 360.

C. 3D Printing and Assembly

The holder was printed on an **Original Prusa i3 MK3S+** using **black PETG filament**, selected for its durability and slight flexibility. The key print parameters were:

- **Layer height:** 0.20 mm (optimized for a balance between precision and print speed).
- **Infill density:** 15% (ensuring structural integrity while minimizing material usage).
- **Supports:** Not required due to an optimized design.

The printing process was completed in approximately **3 hours**, followed by minor post-processing, including refining the tripod thread.

During assembly, the Acconeer A111 radar module was securely snapped into its designated slot. The PCB was mounted using M2 screws and 6 mm standoffs to ensure a stable fit. The Arducam USB camera was carefully positioned and fixed in place with M3 screws. To maintain a clean and organized setup, all cables were routed through dedicated openings. Finally, the entire assembly was mounted onto a standard tripod, ensuring a stable platform for data collection.

D. Evaluation and Refinements

Initial testing confirmed proper alignment and stable operation. Several minor design improvements were implemented:

- Increased back wall thickness to **4 mm** for improved stability.
- Adjusted the snap-fit mechanism to simplify sensor insertion and removal.
- Added an indentation for easier access to camera screws.

These refinements resulted in a durable and practical sensor mount, suitable for long-term industrial monitoring applications.

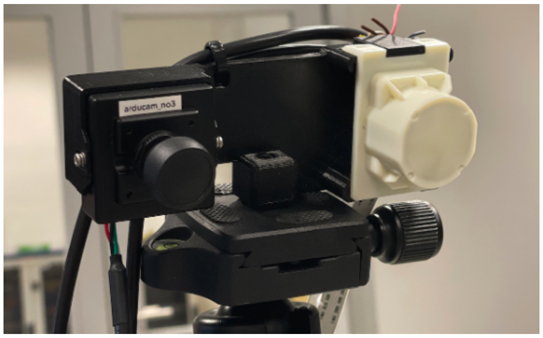

Fig. 4. Final assembled holder with radar sensor and camera.

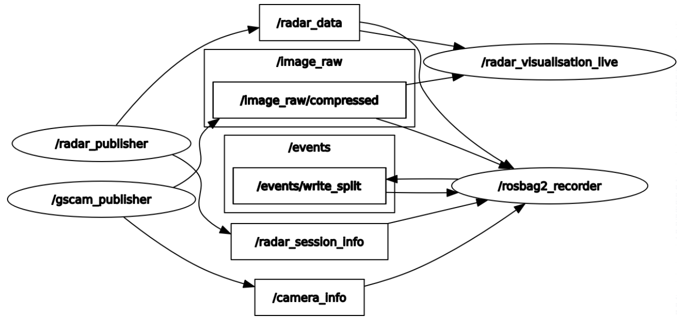

Fig. 5. System architecture of radar and camera data acquisition in ROS2.

IV. ROS2-Based Data Collection System

To ensure efficient and modular data acquisition, the system was implemented within the ROS2 framework. This architecture enables seamless synchronization between radar and camera data while facilitating real-time processing and storage. The data collection system runs in a custom Docker container and consists of two primary ROS2 nodes.

A. Docker-Based ROS2 Environment

To create a reproducible and portable development environment, a dedicated Docker container was designed for running ROS2-based data acquisition. The container includes:

- **ROS2 Jazzy** – the latest ROS2 distribution.
- **GStreamer and OpenCV** – for handling video streams.
- **Acconeer Exploration Tool** – for direct radar communication.
- **Custom Python environment** – with dependencies for radar data processing and visualization.

The Docker container ensures consistency across different machines and allows deployment on embedded hardware platforms without manual installation of dependencies.

B. Data Collection Nodes

The system consists of two primary ROS2 nodes responsible for data acquisition and publishing:

- **GSCam2 node:** This node captures and publishes image data from the Arducam USB camera. The camera is set to operate at 10 FPS and 1920×1080 resolution, and the video stream is compressed to 640×360 resolution using H.264 encoding for efficient transmission. The node is configured to output images in JPEG format, making it suitable for real-time processing and storage [2].
- **Radar Reader Node:** A custom ROS2 node developed in Python using Acconeer's SDK. It collects radar data in real time and publishes it to a ROS2 topic. The node supports both Envelope and Sparse mode.

Both nodes publish synchronized data streams, which are recorded into ROS2 bag files for offline analysis.

C. Automated System Launch

To streamline data collection, an XML-based launch file was created to automatically start both ROS2 nodes with predefined parameters. This configuration ensures proper synchronization and allows rapid switching between different radar modes.

The launch file includes:

- **Camera parameters** (device ID, resolution, encoding format).
- **Radar configuration** (serial port, range interval, update rate, service mode).
- **QoS settings** to ensure reliable data transmission in real-time applications.

The system's modularity allows easy extension with additional sensors or data processing pipelines, making it adaptable for various industrial monitoring applications [3], [4].

V. Experimental Setup and Initial Measurements

To validate the proposed system and optimize radar parameters, a series of controlled experiments were conducted to assess its ability to detect repetitive motion patterns. The experiments included:

- **Hand movement:** Initial data acquisition testing.
- **Pendulum motion:** Cyclic motion for machine learning-based cycle detection.
- **Robotic arm:** Industrial motion tracking with structured and unstructured cycles.
- **Industrial deployment:** Real-world cycle measurement in a manufacturing environment.

All experiments were conducted using both Envelope and Sparse radar modes, with optimized sampling frequencies based on preliminary findings.

A. Hand Movement and Pendulum Tests

The first tests involved simple hand movements over the radar sensor to validate live data visualization and logging. A real-time tool displayed radar responses, allowing immediate assessment of signal quality.

Subsequently, a pendulum was introduced to generate periodic motion patterns. Data from 32 recorded cycles were annotated and used to train a YOLOv8 model for cycle detection. The model successfully identified all cycles, confirming the radar's capability to detect repetitive motion [5].

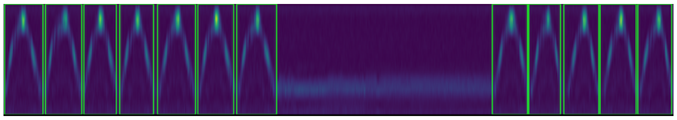

Fig. 6. Example of YOLO-based cycle detection on radar heatmap.

B. Robotic Arm Motion Analysis

To further validate the system, a robotic arm was programmed to execute both repetitive and irregular motions.

- **Cyclic movements:** The system reliably detected repetitive robotic arm actions.
- **Irregular sequences:** More complex radar responses were observed, requiring additional filtering to distinguish structured patterns from noise.

C. Industrial Deployment

The system was tested in a real manufacturing setting across three use cases:

- **Simple container movement:** Monitoring repeated box movements.
- **Drilling station:** Detecting operator-initiated cycles with variable timing.
- **6-Axis robot workstation:** Observing automated pick-and-place operations.

Radar-based cycle detection successfully identified structured movements, demonstrating its potential for non-invasive monitoring in industrial environments.

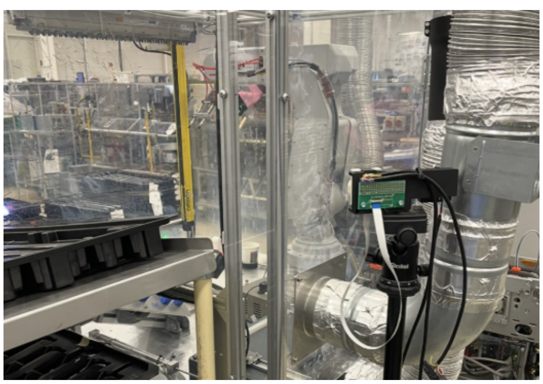

Fig. 7. Setup of industrial deployment experiment.

VI. Detection of Unknown Patterns using Matrix Profile

To improve the flexibility of repetitive cycle detection, the Matrix Profile method was explored. This technique, based on the Mueen-Keogh (MK) algorithm, enables unsupervised discovery of repeated motifs in time series without prior knowledge, making it ideal for industrial scenarios with varying cycle lengths.

A. Radar Signal Transformation and Motif Extraction

Radar data in the form of 2D heatmaps was first converted into a 1D signal by averaging column-wise pixel intensities. Using the Python *STUMPY* library, the Matrix Profile was computed over this signal with an adaptive window length. Motifs were identified as the most similar subsequences, revealing repeated cycle patterns.

These patterns serve as additional inputs for subsequent classification models, complementing visual detection approaches and improving robustness in noisy environments [6], [7].

VII. Conclusion and Future Work

This paper introduced a modular system for non-invasive detection of repetitive manufacturing cycles using radar sensing and ROS2-based data acquisition. Combined with YOLO-based cycle detection on radar heatmaps, the system demonstrated accurate performance in both lab and industrial settings.

A second, unsupervised approach was explored using Matrix Profile to identify repeating motifs from radar time series. This opens the door for hybrid detection pipelines, combining deep learning with pattern discovery.

Future development will focus on deploying the detection logic as a ROS2 node with real-time processing and CNN-based classification of motifs. Emphasis will also be placed on optimizing models for embedded platforms and extending adaptability across different manufacturing lines.

Acknowledgment

This work was conducted as a master's thesis under the supervision of Ing. Karel Horák, Ph.D., at the Department of Control and Instrumentation, Brno University of Technology. The experimental measurements were carried out at ALPS Electric Czech, s.r.o., where they were assigned and overseen by Ing. Josef Nevrlý. The author acknowledges the use of OpenAI's ChatGPT as a support tool for translation and language refinement.

References

[1] Acconeer AB. *Acconeer Documentation*. Online. Available at: https://docs.acconeer.com/. [accessed 2025-01-27].

[2] Arducam. *Arducam 1080p Low Light WDR USB Camera Module – Datasheet*. Online. Available at: https://www.uctronics.com/download/Amazon/B020101.pdf)[accessed 2025-03-12].

[3] Open Robotics. *ROS 2 Documentation Jazzy*. Online. Available at: https://docs.ros.org/en/jazzy/index.html. [accessed 2025-03-12].

[4] C. McQueen. *GSCam2 - ROS 2 Camera Streaming Package*. Online. Available at: https://github.com/clydemcqueen/gscam2. [accessed 2025-03-12].

[5] Ultralytics. *Ultralytics Documentation*. Online. Available at: https://docs.ultralytics.com/. [accessed 2025-03-12].

[6] A. Mueen, E. Keogh, Q. Zhu, S. Cash, B. Westover. *Exact Discovery of Time Series Motifs*. Available at: http://alumni.cs.ucr.edu/~mueen/pdf/EM.pdf [accessed 2025-04-07].

[7] STUMPY Developers. *STUMPY Documentation*. Online. Available at: https://stumpy.readthedocs.io/. [accessed 2025-04-07].

Expression profiles of sRNA genes in *Caldimonas thermodepolymerans*

Kristýna Heřmánková
Department of Biomedical Engineering, Faculty of Electrical Engineering and Communication
Brno University of Technology
Brno, Czech Republic
ORCID: 0009-0002-6720-0499

Katarína Šlosárová
Institute of Food Science and Biotechnology, Faculty of Chemistry
Brno University of Technology
Brno, Czech Republic
ORCID: 0009-0004-3216-3514

Stanislav Obruča
Institute of Food Science and Biotechnology, Faculty of Chemistry
Brno University of Technology
Brno, Czech Republic
ORCID: 0000-0002-9270-195X

Karel Sedlář
Department of Biomedical Engineering, Faculty of Electrical Engineering and Communication
Brno University of Technology
Brno, Czech Republic
ORCID: 0000-0002-8269-4020

***Abstract* — Regulation of gene expression represents a complex process that monitors the requirements of cells for specific gene products and adjusts their production accordingly. Each stage of gene expression employs different regulatory mechanisms. Here, we pay attention to post-transcriptional regulation by non-coding genomic elements - small RNAs (sRNAs). The aim is to address the problem of missing structural annotations of sRNA genes that play a key role in the rapid response of bacterial cells to stress conditions. For these purposes, we analyse the transcriptomic data of *Caldimonas thermodepolymerans* DSM 15344^T, a promising adept for industrial biotechnology applications, especially for producing polyhydroxyalkanoates (PHA). Analysis of the RNA-Seq data results in a list of predicted sRNAs. Furthermore, the association of these regulatory elements with specific genes is indicated using loci information and sRNA gene co-expression analysis. Finally, sRNA expression analysis was performed to reveal the relationship of sRNA regulation to genes involved in PHA metabolism.**

Keywords — polyhydroxyalkanoates, RNA-Seq, Caldimonas thermodepolymerans, expression analysis, small RNA

I. Introduction

Bacterial small RNAs (sRNAs) are non-coding (in most cases) regulators of gene expression, specifically post-transcriptional regulators. The RNA-RNA interaction between sRNAs and mRNA molecules, i.e., their targets, is affecting the subsequent translation process of these mRNAs into proteins. There are multiple regulatory mechanisms employed by sRNAs, such as transcription attenuation, transcription interference, direct binding to RBS (Ribosome Binding Site), and/or enhancement of translation by making RBS accessible [1]. Generally, sRNAs can be distinguished into two classes, activators and/or repressors of translation. Activating sRNAs, upon interaction with the target mRNA, promote the translation process, while repressing sRNAs (more common) inhibit the translation of the target mRNA into a protein.

The post-transcriptional regulation by sRNAs helps an organism quickly adapt its metabolism according to environment and/or stress conditions [2]. Thus, the regulation of small RNAs represents one of many layers of bacterial regulatory processes, and its study can further deepen one's understanding of how bacteria respond to specific conditions.

Small RNAs can be of two types depending on their locus relative to the target molecule, affecting the RNA-RNA interaction. *Cis*-encoded sRNAs are transcribed from the opposite strand as their target, so their sequences partially overlap. Therefore, this shared sequence of the *cis*-encoded sRNA and its target act as their binding site, which is perfectly complementary.

Trans-encoded sRNAs are expressed from complete intergenic regions (IGRs), so unlike *cis*-encoded sRNAs, they do not overlap any genomic element on the opposite strand. This results in imperfect complementarity between *trans*-sRNA and its target. Furthermore, the imperfect base pairing allows *trans* sRNA to regulate several targets. However, due to the limited base pairing between *trans* sRNA and its target, the RNA-RNA interaction requires the assistance of RNA-binding proteins, such as Hfq or ProQ [3].

The latest research shows that sRNAs can be predicted from RNA sequencing (RNA-Seq) [4]. RNA-Seq [5] is a technology to study genome-wide gene expression, i.e., the whole transcriptome of an organism. This set of all expressed genes, i.e., transcripts, includes coding genes whose product is a protein and non-coding genes whose final product is a functional RNA, e.g., tRNA, rRNA. In addition to the information about which genes are transcribed, RNA-Seq also provides a transcription quantification of expressed genes. Thanks to this, one can observe how the gene expression of an organism changes under different conditions and/or over time and thus understand changes in the transcriptome compared to the behavior of an organism (phenotype).

While the annotation of bacterial coding genes and even some types of non-coding genes (tRNAs and rRNAs) are available in high quality, the annotation of sRNAs is still lagging and is rarely included in automatic annotation pipelines. The limitation lies in unknown orthologues for many sRNAs, causing our inability to predict them directly from the genome

This work has been supported by grant project FCH/FEKT-J-25-8798.

sequence. Since the expected number of sRNA genes in bacteria is in the hundreds per genome [2], the genome-wide technique, RNA-Seq, accompanied by subsequent computational analyses represents an appropriate procedure for their prediction.

Current environmental issues include pollution with plastics. Their versatile properties make them an essential part of our daily lives, and the inexpensive production process causes them to be overproduced compared to other greener alternatives. This issue cannot be solved by recycling as most plastics are made of composites and, therefore, are inappropriate for recycling. Most physical and chemical recycling scenarios reduce the quality and safety of the recycled materials [6].

Polyhydroxyalkanoates (PHAs) are biodegradable, biocompatible, and, above all, renewable materials that have the potential for use in many industries. They are naturally produced and accumulated by microorganisms as a storage of carbon and energy. Due to their properties, PHAs are promising polymers for the replacement of fossil fuel-based plastics. The main problem is the high production cost, which makes them uncompetitive with petroleum-based plastics [7]. While biopolymers alone may not completely solve global plastic pollution by replacing synthetic polymers in all applications, they can be strategically applied in areas such as biomedicine or in specific single-use products like PHA. To address these economic challenges, the NGIB – Next Generation Industrial Biotechnology concept [8][9] brings the idea of using waste substrates and/or using extremophilic microorganisms for the production of PHA.

An interesting adept is *Caldimonas thermodepolymerans*, formerly known as *Schlegelella thermodepolymerans* is a moderately thermophilic bacterium isolated in 2003 [10]. It can accumulate a significant amount of the most abundant PHA, poly3-hydroxybutyrate P(3HB), up to 87% w/w of CDM [11]. Moreover, the preferable sugar for *C. thermodepolymerans* is xylose over other sugars which is advantageous for the industrial production of PHA from different lignocellulose-based resources [11]. *C. thermodepolymerans* is a non-sporulating gram-negative bacterium which is also a benefit for biotechnological processes.

II. Materials and Methods

A. Cultivation

The bacterium was cultivated in two steps. In the first part of the cultivation, a nutritionally rich medium (Nutrient broth) was used (100 mL Erlenmeyer flasks, filling 50%). This phase entailed 20 h at 50 °C and constantly shaking at 180 rpm. Subsequently, for the production phase, mineral medium was used (9.0 g/L $Na_2HPO_4 \cdot 12 H_2O$, 1.5 g/L KH_2PO_4, 1.0 g/L NH_4Cl, 0.2 g/L $MgSO_4 \cdot 7 H_2O$, 0.02 g/L $CaCl_2 \cdot 2 H_2O$, 0.0012 g/L Fe(III)NH4citrate, 0.5 g/L yeast extract) with 20 g/L carbon sources (cellobiose, glucose, xylose) and trace element solution (50.0 g/L EDTA, 13.8 g/L $FeCl_3 \cdot 6 H_2O$, 0.84 g/L $ZnCl_2$, 0.13 g/L $CuCl_2 \cdot 2 H_2O$, 0.1 g/L $CoCl_2 \cdot 6 H_2O$, 0.016 g/L $MnCl_2 \cdot 6 H_2O$, 0.1 g/L H_3BO_3, dissolved in distilled water) and 5% v/v of culture from complex medium (250 mL Erlenmeyer flasks, filling 40%). This part of the cultivation took 72 h, also at 50 °C and constantly shaking at 180 rpm.

Triplicates of biomass samples (3 × 10 mL) were determined gravimetrically (dried at 80 °C until constant weight was obtained). The biomass was centrifuged (6 000 × g, 5 min), then washed with 10 mL distilled water, and centrifuged again. The supernatant was discarded, and the pellet of biomass was dried to constant weight. PHA content in dry biomass was determined by gas chromatography with a flame ionization detector.

The graph in Fig. 1 shows the growth and production of PHB by the bacterium during cultivation, with error bars representing the standard deviation from three biological replicates.

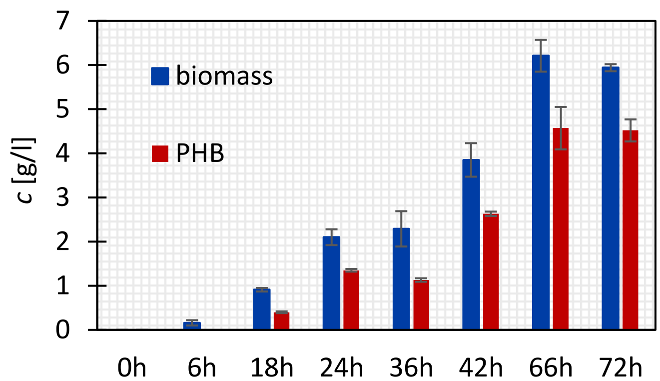

Fig. 1. Growth and PHB production of *C. thermodepolymerans* DSM 15344^T.

B. RNA extraction and sequencing

RNA isolation followed an optimized extraction protocol consisting of a combination of procedures focused on RNA isolation, where the crucial point was addition of 1 mL of TRIzol per 40 mg of wet biomass followed by incubation for 5 min to permit complete dissociation of the nucleoproteins complex. Then, 0.1 mL of 1-bromo-3-chloropropane per 1 mL of TRIzol™ Reagent used for cell lysis was added, and the tube was securely capped and incubated for 2–3 min at room temperature. Afterwards, the samples were centrifuged at 11,000 × g at 4 °C for 15 min. Subsequently, the supernatant containing the RNA was transferred to a new tube where 70 v/v % EtOH was added at a ratio 1:1. Then, the samples were transferred to spin columns and the procedure continued according to the manual of the NucleoSpin RNA Plus isolation kit (Macherey-Nagel) with washing and drying steps of silica membrane and elution of RNA that were stored at −80 °C till the sequencing. Ribodepletion was performed with RiboCop rRNA Depletion Kit for Bacteria Mixed bacterial samples (Lexogen, AT). Strand-specific sequencing libraries were prepared with NEBNext Ultra II Directional RNA Library Prep Kit (New England Biolabs, USA) and sequenced with Illumina NextSeq550 to produce reversely stranded reads. Unique Molecular Identifiers (UMIs) were added using xGen Duplex Seq Adapters (IDT, USA). The transcriptomic dataset thus consists of 8 samples corresponding to 8 time points during the cultivation of *Caldimonas thermodepolymerans* DSM 15344^T on xylose. Each of the time points was measured in three biological replicates resulting in 24 samples. Sample names of relevant time points are summarized in Table I.

TABLE I. RNA-SEQ SAMPLES

Sample name	1-3	4-6	7-9	10-12	13-15	16-18	19-21	22-24
Time	0h	6h	18h	24h	36h	42h	66h	72h

C. *Small RNAs prediction*

RNA-Seq reads were mapped to the complete reference genome of *C. thermodepolymerans* DSM 15344^T [12], followed by sequencing depth analysis. The sRNA prediction was done using baerhunter tool [13]. The mean of normalized gene sequencing depth using the *sizeFactors* function of the DESeq2 package [14] was used as the *high_cut_off* threshold with value of 31. Other thresholds remained set to default. Further, a count table containing quantity of reads that mapped to each gene, including newly predicted sRNAs, was generated with baerhunter along with *featureCounts*, R Subreads [15] package.

D. *PHA-related small RNAs selection*

From the list of predicted sRNAs, relation to PHA metabolism was inferred using either loci information or co-expression analysis. Considered PHA-related genes are summarized in Table II according to [16]. Predicted sRNA sequences that overlapped in some way with any of the listed genes were considered PHA-related *cis*-encoded sRNAs.

Similarities in expression profiles were used to search for *trans*-encoded sRNAs related to PHA metabolism. The co-expression analysis was performed using the WGCNA (weighted gene co-expression network analysis) package [17]. Significant correlations (positive or negative – *unsigned* network type) between expression profiles of genomic elements clustered genes of PHA metabolism and predicted sRNA genes into different groups. These *trans*-encoded sRNAs that were classified in the same group as the above-mentioned PHA-related genes are further proposed to regulate this PHA metabolism.

TABLE II. GENES INVOLVED IN PHA METABOLISM OF *C. THERMODEPOLYMERANS* 15344^T.

Gene name	**Locus tag**	**Start**	**End**	**Strand**
phaZi	IS481_07130	1 487 934	1 489 175	-
phaP	IS481_07490	1 592 081	1 592 638	-
phaR	IS481_08360	1 778 868	1 779 455	+
phaC	IS481_08630	1 827 923	1 829 620	+
phaA	IS481_08635	1 829 672	1 830 850	+
phbB	IS481_08640	1 830 969	1 831 706	+
phaZe	IS481_15185	3 219 150	3 220 631	-

E. *Analysis of expression profiles*

Changes in expression profiles of PHA-related genes and sRNA genes were obtained with expression analysis performed with the DESeq2 package [14]. Heatmaps were generated using the pheatmap package [18].

III. RESULTS AND DISCUSSION

A. *Putative small RNAs*

Overall, 736 sRNA sequences were predicted from intergenic regions (IGRs) in the genome of *C. thermodepolymerans*. Predictions that overlapped any annotated element on the opposite strand were marked as *cis*-encoded sRNA, and out of 736, this bacterial genome possesses 731 sRNAs of this type. The remaining five predictions were assigned to *trans*-encoded sRNAs located in complete IGR.

The heatmap from expression analysis of all predicted sRNA genes is shown in Fig. 2. Rows represent the expression profile of each sRNA through all time points shown in columns. A relative expression of sRNA genes across samples is encoded by

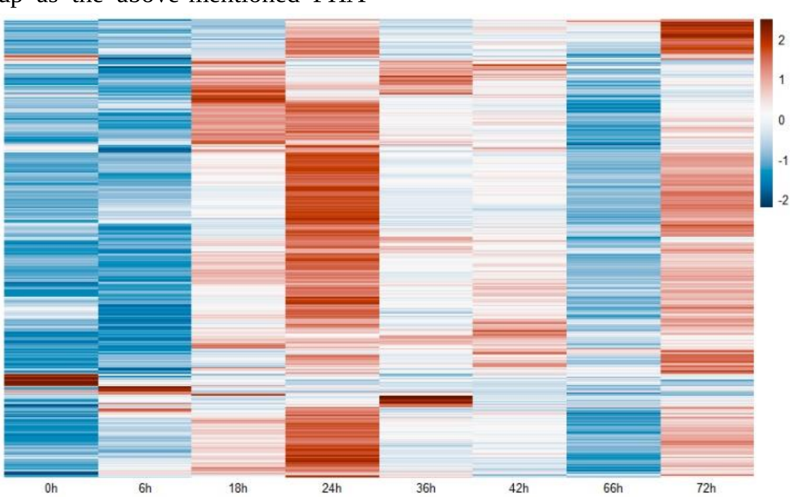

Fig. 2. Expression profiles of sRNA genes in *C. thermodepolymerans*.

Z-score visualized by a colour scale. Shades of red represent above-average expression of sRNA in a particular sample (time point) relative to its expression across all samples. Contrarily, shades of blue mean below-average expression compared to other samples. The white colour then represents the average expression at a given time. The dark red or dark blue colour suggests differentially expressed (but were not statistically tested) sRNA genes compared to other conditions.

Hierarchical clustering on sRNA genes (rows) was performed, and thus clusters of similar expression profiles are visible. The vast majority of sRNAs are less expressed at the beginning of the culture time (0h and 6h). Further, their expression grows and peaks above average at the 24-hour time point, and from now the expression tends to average again during the following 2-time points. At the time of 66h, the expression below average again prevails. Finally, at the end of culture, the expression of sRNAs rises again above average, in some cases even reaching the maximum value.

Small clusters of sRNA genes show strong expressions (dark red) at different stages of cultivation, specifically 0h, 6h, 36h, and 72h. These suggest activations of stress response pathways specific to the stage of cultivation. Further analyses will reveal which pathways were activated and thus reveal the functions of these sRNAs.

B. *Small RNAs involved in PHA metabolism*

Due to the great industrial potential of *C. thermodepolymerans*, primarily PHA production, attention was paid to PHA metabolism. Predicted sRNAs that were either directly or indirectly assigned to genes involved in PHA metabolism are summarized in Table III.

Similar to the previous section, a heat map of expression profiles is shown in Figure 3, but this time it includes only genes related to PHA metabolism and the associated sRNAs from Table III.

TABLE III. PHA-RELATED SMALL RNA GENES.

Gene name	Start	End	Strand	sRNA type
putative_sRNA:76	414827	415113	-	*trans*
putative_sRNA:218	1184282	1184560	-	*trans*
putative_sRNA:291	1581882	1582055	+	*trans*
putative_sRNA:347	1830521	1831114	-	*cis*
putative_sRNA:599	3219814	3220466	+	*cis*
putative_sRNA:637	3383652	3384012	-	*trans*

Two sRNAs were found to overlap two resp., three genes from Table II, therefore, are listed and assigned to the *cis*-encoded type. *Putative_sRNA:347* overlaps *phaCAB* [11] operon, more specifically with the *phaA* and *phbB* gene, and thus appears to regulate the expression of the entire operon, including the gene for PHA synthase, *phaC*. The second *cis*-encoded sRNA, *putative_sRNA:599*, overlaps and thus might regulate the *phaZe* gene encoding for extracellular depolymerase.

The *trans*-encoded sRNAs are assigned as PHA-related genes thanks to the similarities in expression profiles. Expression profiles in Fig. 3 show that *putative sRNA:76* was assigned to possibly regulate the *phaZe* gene but also tends to cluster together with the *phaP* and *phaZi* genes. The only time point where *putative sRNA:76* and *phaZe* show more significant differences is 42h, where sRNA is expressed above average and at the same time, the *phaZe* gene is expressed less than in other samples. This might conclude that this sRNA acts as a post-

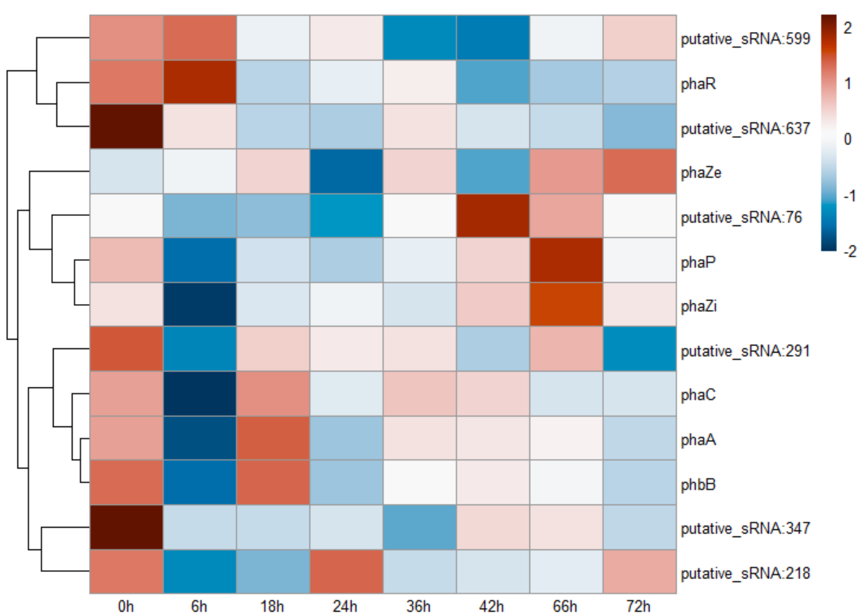

Fig. 3. Expression profiles of genes involved in PHA metabolism along with assigned sRNA genes.

transcriptional repressor of *phaZe* and at the time of 42h is repressing the production of extracellular depolymerase.

The *putative_sRNA:218* was assigned again to *phaZe*, but this time seems to regulate the extracellular depolymerase in earlier stages of cultivation, specifically 0-24h. This might also be a post-transcriptional repression.

The last sRNA that was marked as related to *phaZe is putative_sRNA:291*. The most significant expressions of both genes are related to the last time point representing the stationary phase, and their expressions are opposite. The conclusion is similar to previous ones, but in this case, we can only guess whether increased expression of sRNA would cause a decrease in the expression of *phaZe*.

The only *trans*-encoded sRNA related to phaCAB operon is *putative_sRNA:637*. Its expression peaks at the start of the cultivation and might enhance the expression of the *phaCAB* operon at the inoculum phase.

IV. Conclusions a further perspectives

The transcription in IGRs revealed a high abundance of non-coding regulatory elements that remained hidden due to the lack of annotations and even awareness of their existence. The analysis of predicted sRNA genes was mainly devoted to PHA metabolism in *Caldimonas thermodepolymerans* DSM 15344^{T}. Out of 736 predicted sRNAs, six candidates were suggested as PHA-related, either *trans*-encoded or *cis*-encoded. Their expression profiles were compared with expression profiles of genes involved in PHA metabolism, and the regulation type was proposed. Further steps will include the statistical testing for differential expression of genes/sRNA genes followed by the GO enrichment analysis to understand the events at each time point and/or assign a function to predicted sRNAs. In the follow-up research, the PHA-related sRNAs will be analysed in a wet laboratory to experimentally verify the *in silico* approach. Successfully validated sRNA genes will be subjected to genetic engineering tools to increase the production of PHA bacteria and thereby enhance its biotechnological potential.

Acknowledgment

This work has been supported by grant project FCH/FEKT-J-25-8798. The authors would like to thank Ing. Xenie Kouřilová, PhD. for her expert work in cultivating the samples used in this study.

References

[1] BERVOETS I., CHARLIER D., 2019. Diversity, versatility and complexity of bacterial gene regulation mechanisms: opportunities and drawbacks for applications in synthetic biology. *FEMS Microbiology Reviews*, Volume 43, Issue 3, pages 304–339. Doi: 10.1093/femsre/fuz001.

[2] GOTTESMAN, S. and STORZ, G., 2011. Bacterial Small RNA Regulators: Versatile Roles and Rapidly Evolving Variations. *Cold Spring Harbor Perspectives in Biology*. 2011-12-01, roč. 3, č. 12, pp. a003798-a003798. ISSN 1943-0264. Doi: 10.1101/cshperspect.a003798.

[3] SMIRNOV A., FÖRSTNER K.U., HOLMQVIST E., OTTO A., GÜNSTER R, BECHER D., REINHARDT R., & VOGEL J., 2016. Grad-seq guides the discovery of ProQ as a major small RNA-binding protein, *Proc. Natl. Acad. Sci. U.S.A*. 113 (41) 11591-11596. Doi: 10.1073/pnas.1609981113.

[4] SEDLAR, K. and ZIMMER, R., 2022. Comparison of Stranded and Non-stranded RNA-Seq in Predicting Small RNAs in a Non-model Bacterium. *Bioinformatics and Biomedical Engineering*. *Lecture Notes in Computer Science. Cham: Springer International Publishing*, p. 45-56. ISBN 978-3-031-07801-9. Doi: 10.1007/978-3-031-07802-6_4.

[5] WANG, Z.; GERSTEIN, M. and SNYDER, M., 2009. RNA-Seq: a revolutionary tool for transcriptomics. *Nature Reviews Genetics*. Roč. 10, č. 1, pp. 57-63. ISSN 1471-0056. Doi: 10.1038/nrg2484.

[6] WILLIAMS, A. T. and RANGEL-BUITRAGO, N., 2022. The past, present, and future of plastic pollution. *Marine Pollution Bulletin*. Roč. 176. ISSN 0025326X. Doi: 10.1016/j.marpolbul.2022.113429.

[7] RAZA, Z. A.; ABID, S. and BANAT, I. M., 2018. Polyhydroxyalkanoates: Characteristics, production, recent developments and applications. *International Biodeterioration & Biodegradation*. Roč. 126, pp. 45-56. ISSN 09648305. Doi: 10.1016/j.ibiod.2017.10.001.

[8] CHEN, G. and JIANG, X., 2018. Next generation industrial biotechnology based on extremophilic bacteria. *Current Opinion in Biotechnology*. Roč. 50, pp. 94-100. ISSN 09581669. Doi: 10.1016/j.copbio.2017.11.016.

[9] YU, Lin-Ping; WU, Fu-Qing and CHEN, Guo-Qiang, 2019. Next-Generation Industrial Biotechnology-Transforming the Current Industrial Biotechnology into Competitive Processes. *Biotechnology Journal*. Roč. 14, č. 9. ISSN 1860-6768. Doi: 10.1002/biot.201800437.

[10] ELBANNA, K.; LÜTKE-EVERSLOH, T.; VAN TRAPPEN, S.; MERGAERT, J.; SWINGS, J. et al., 2003. Schlegelella thermodepolymerans gen. nov., sp. nov., a novel thermophilic bacterium that degrades poly(3-hydroxybutyrate-co-3-mercaptopropionate). *International Journal of Systematic and Evolutionary Microbiology*. 2003-07-01, roč. 53, č. 4, pp. 1165-1168. ISSN 1466-5026. Doi: 10.1099/ijs.0.02562-0.

[11] KOURILOVA, X.; PERNICOVA, I.; SEDLAR, K.; MUSILOVA, J.; SEDLACEK, P. et al., 2020. Production of polyhydroxyalkanoates (PHA) by a thermophilic strain of Schlegelella thermodepolymerans from xylose rich substrates. *Bioresource Technology*. Roč. 315. ISSN 09608524. Doi: 10.1016/j.biortech.2020.123885.

[12] MUSILOVA, J.; KOURILOVA, X.; BEZDICEK, M.; LENGEROVA, M.; OBRUCA, S. et al., 2021. First Complete Genome of the Thermophilic Polyhydroxyalkanoates-Producing Bacterium Schlegelella thermodepolymerans DSM 15344. *Genome Biology and Evolution*. 2021-04-01, roč. 13, č. 4. ISSN 1759-6653. Doi: 10.1093/gbe/evab007.

[13] OZUNA, A; LIBERTO, D; JOYCE, R M; ARNVIG, K B; NOBELI, I et al., 2020. Baerhunter: an R package for the discovery and analysis of expressed non-coding regions in bacterial RNA-seq data. *Bioinformatics*. 2020-02-01, roč. 36, č. 3, pp. 966-969. ISSN 1367-4803. Doi: 10.1093/bioinformatics/btz643.

[14] LOVE, M. I., HUBER, W., & ANDERS, S., 2014. Moderated estimation of fold change and dispersion for RNA-seq data with DESeq2. *Genome Biology*, *15*(12), 1–21. Doi: 10.1186/S13059-014-0550-8/FIGURES/9.

[15] LIAO, Y., SMYTH, G. K., & SHI, W., 2014. featureCounts: an efficient general purpose program for assigning sequence reads to genomic features. *Bioinformatics*, *30*(7), 923–930. Doi: 10.1093/BIOINFORMATICS/BTT656.

[16] MUSILOVA, J.; KOURILOVA, X.; HERMANKOVA, K.; BEZDICEK, M.; IEREMENKO, A. et al., 2023. Genomic and phenotypic comparison of polyhydroxyalkanoates producing strains of genus Caldimonas/Schlegelella. *Computational and Structural Biotechnology Journal*. Roč. 21, pp. 5372-5381. ISSN 20010370. Doi: 10.1016/j.csbj.2023.10.051.

[17] LANGFELDER, P., & HORVATH, S., 2008. WGCNA: An R package for weighted correlation network analysis. *BMC Bioinformatics*, *9*(1), 1–13. Doi: 10.1186/1471-2105-9-559/FIGURES/4.

[18] KOLDE R., 2018. pheatmap: Pretty Heatmaps. R package version 1.0.12, https://github.com/raivokolde/pheatmap.

Audio Declipping with Unfolded Douglas–Rachford Algorithm

Michal Švento
Dept. of Telecommunications, FEEC
Brno University of Technology
Brno, Czech Republic
michal.svento@vut.cz

***Abstract*—This paper addresses the problem of audio declipping, which occurs when audio signals exceed a certain level, causing distortion and loss of information. To enhance existing methods, we propose a novel solution combining deep unfolding with the Douglas–Rachford algorithm (DRA) within an optimization framework, offering a blend of deep learning and optimization. The declipping problem is formulated as an optimization task that aims to recover the original signal by minimizing sparsity in the time-frequency domain. Our approach transforms each iteration of DRA into a layer of a neural network, optimizing parameters based on training data. Experimental results demonstrate that the unrolled DRA (uDRA) achieves short inference time compared to classical declipping methods, although it does not yet match them in terms of restoration quality. This work highlights the potential of deep unfolding for efficient audio declipping, with future improvements needed to capture the complexities of audio distortion more effectively.**

***Index Terms*—audio inverse problems, deep unfolding, unrolling, declipping**

I. Introduction

Saturation is a common type of nonlinear audio degradation where the signal amplitude above a certain threshold is truncated. This results in harsh artifacts and a reduction of the dynamic range. Even when the distortion is intentional, such as in guitar effects, we usually seek to recover the lost signal information. The process of restoring a signal from its clipped observation is known as declipping.

The first approaches to solving such a task were model-based, assuming and forcing certain physical properties of the signal in the related inverse problem. The sparsity of audio signals in the time-frequency domain of the discrete Gabor transform (DGT) has achieved the state-of-the-art performance [1]–[6]. Despite their good performance, the major drawback of model-based algorithms is their very slow inference and still not plausible results for high distortion [7].

The era of data-based processing introduced many new, successful algorithms for solving audio inverse problems. Their strength is largely due to the availability of extensive training data and shorter inference times compared to traditional digital signal processing (DSP) techniques. However, neural networks lack higher interpretability, operate as black box mappers from distorted to clean signals, and often fail on unseen data.

Generative probabilistic models solve the inverse problem from the Bayesian perspective and have very good perceptual results [8]–[10], since they want to restore the signal to be in high density regions based on distorted observation. Despite the good perceptual results, the high-end GPU is needed for the comparable inference time with traditional DSP methods [9], which makes them also relatively slow.

The deep unfolding (DU), also known as algorithm unrolling, bridges model-based and data-driven approaches by transforming classical iterative optimization algorithms into structured neural networks with learnable parameters [7], [11]. This framework not only enhances computational efficiency but also enables data-driven adaptation while maintaining interpretability. A conceptually similar approach is found in Plug-and-Play (PnP) methods, which incorporate advanced denoising priors within iterative optimization schemes to solve inverse problems [12]–[14]. Both DU and PnP exploit the iterative nature of optimization, demonstrating how classical techniques can be enhanced by modern learning-based components.

Despite relatively large research regarding DU in image processing [15]–[17], to the best knowledge of the author, the DU is underexplored in the audio inverse problems [18]–[20], especially for nonlinear problems. In this paper the Douglas–Rachford algorithm (DRA) will be unrolled for the audio declipping task, where we expect that trainable parameters of DRA will enhance the success of the algorithm.

The rest of the paper is organized as follows. Section II formulates the problem and DU for the minimization problem. In Section III training and evaluation of the unrolled network are described. In the Section IV the performance of the modified algorithm and future improvements for the unfolding framework are discussed.

II. Method

A. Problem Formulation

Let $\mathbf{x}$ be an undistorted audio signal of length N, and consider a nonlinear distortion known as *hard clipping* with a threshold $\theta \in [0, 1]$. The hard clipping operation can be

The work was supported by the Czech Science Foundation (GAČR) Project No. 23-07294S. The author is grateful to NVIDIA for donation of the Titan XP graphic card, which has been used in this research. PhD study of Michal Švento is supervised by Pavel Rajmic. The author thanks for valuable comments and improvements from Pavel Rajmic, Ondřej Mokrý and Eloi Moliner.

expressed as the following element-wise mapping function $f_\theta(\mathbf{x}) \mapsto \mathbf{y}$:

$$y_n = \begin{cases} x_n & \text{if } |x_n| \le \theta \\ \theta \cdot \operatorname{sgn}(x_n) & \text{if } |x_n| > \theta. \end{cases} \tag{1}$$

To formalize the declipping problem, we define three disjoint index sets: R (reliable samples) corresponding to values that remain unchanged after clipping, H (high-clipped samples) corresponding to values that were clipped to $+\theta$, L (low-clipped samples) corresponding to values that were clipped to $-\theta$.

Using these sets, we may define the convex set $\Gamma \subset \mathbb{C}^P$ of feasible solutions in the time-frequency domain as

$$\Gamma = \{\mathbf{c} \mid (D\mathbf{c})(R) = \mathbf{y}(R), (D\mathbf{c})(H) \ge \theta, (D\mathbf{c})(L) \le -\theta\}, \tag{2}$$

The operator D is a synthesis operator, specifically the inverse discrete Gabor transform (DGT). As the analysis operator, D^*, the forward DGT is used such that these two operators satisfy the Parseval tight frame condition, $\mathbf{c} = D^* D\mathbf{c}$, where $\mathbf{c}$ are time-frequency coefficients.

The declipping problem is then formulated as the following optimization problem:

$$\arg\min_{\mathbf{c}} \|\mathbf{w} \odot \mathbf{c}\|_1 + \iota_\Gamma(\mathbf{c}), \tag{3}$$

where the first term promotes sparsity in the transform domain using a weighted ℓ_1-norm on the DGT coefficients $\mathbf{c}$, and $\iota_\Gamma(\mathbf{c})$ is the indicator function of the feasible set Γ, enforcing consistency with the observed clipped signal. This formulation is based on the assumption that the ℓ_1-norm of the DGT coefficients of the clean signal $\hat{\mathbf{x}}$ is sparser than that of the clipped signal $\mathbf{y}$, making sparsity minimization a useful constraint to recover the original signal.

B. Algorithmic solution

A well-known approach for solving problem (3) is the DRA [21]. In this work, we consider a version of DRA tailored to audio declipping, as proposed in [2].

Algorithm 1 Unfolded DRA

Require: initialaze $\mathbf{c}^{(1)} \in \mathbb{C}^P$, weights $\mathbf{w} \in \mathbb{R}^P$.
L layers (iterations), $\lambda = 1$, $\gamma > 0$

1: **for** $l = 1, 2, \ldots, L$ **do**
2: $\quad \hat{\mathbf{c}}^{(l)} = \operatorname{proj}_\Gamma \mathbf{c}^{(l)}$
3: $\quad \mathbf{c}^{(l+1)} = \mathbf{c}^{(l)} + \lambda(\operatorname{soft}_{\gamma\mathbf{w}}(2\hat{\mathbf{c}}^{(l)} - \mathbf{c}^{(l)}) - \hat{\mathbf{c}}^{(i)})$

return $\hat{\mathbf{x}} = D\hat{\mathbf{c}}^{(l)}$

The **projection step** (line 2) ensures that the iterates remain within the set of feasible solutions Γ. It can be expressed as

$$\operatorname{proj}_\Gamma \mathbf{c}^{(l)} = \mathbf{c}^{(l)} - D^*(D\mathbf{c}^{(l)} - \operatorname{proj}_{\text{time}}(D\mathbf{c}^{(l)})), \tag{4}$$

where $\operatorname{proj}_{\text{time}}$ is the projection operator in time domain defined element-wise as

$$(\operatorname{proj}_{\text{time}}(\mathbf{x}))_n = \begin{cases} y_n, & \text{for } n \in R, \\ \max(\theta, x_n), & \text{for } n \in H, \\ \min(-\theta, x_n), & \text{for } n \in L. \end{cases} \tag{5}$$

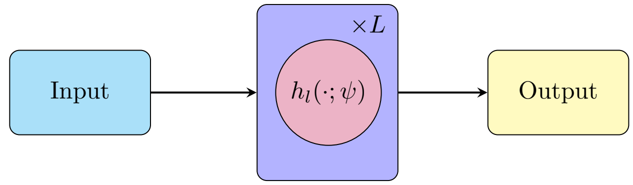

Fig. 1. DRA scheme for nonlearned variant and for tied unfolded algorithm, where ψ are shared between the layers.

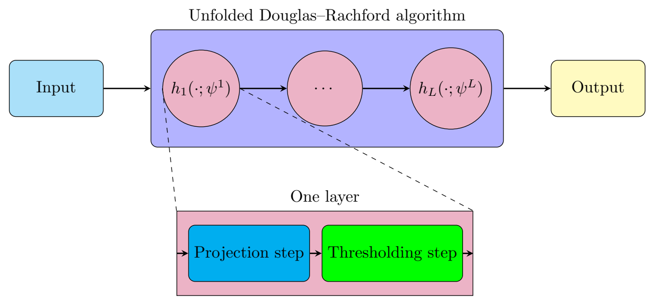

Fig. 2. Unfolded untied DRA with the detail of the first layer/iteration. The projection and thresholding step corresponds to lines 2 and 3 in Alg. 1.

The **thresholding step** (line 3) applies a soft-thresholding operator to promote sparsity in the DGT coefficients:

$$\operatorname{soft}_{\gamma\mathbf{w}}(\mathbf{c}) = \operatorname{sgn}(\mathbf{c}) \odot \max(|\mathbf{c}| - \gamma\mathbf{w}, 0), \tag{6}$$

where $\odot$ is the Hadamard product. We can then write one iteration as $\mathbf{c}^{(l+1)} = h_l(\mathbf{c}^{(l)}, \psi)$, where ψ is the full set of adjustable parameters $(\gamma, \mathbf{w})$ shared across the layers. This is shown in Fig. 1.

C. Deep Unfolding

Despite the good objective results of the DRA, it has two major drawbacks. It is quite difficult to set parameters ψ to achieve a good quality restoration, and a relatively high number of iterations are needed to converge. The deep unfolding aims to solve these two problems. It simplifies the user's choice by optimizing these parameters based on the training data. It is reached by transforming each iteration into a single neural network layer. Formally, we can see unfolding as a composition of functions

$$\mathbf{c}^{(L+1)} = h_L \circ h_{L-1} \circ \cdots \circ h_1(\mathbf{c}^{(1)}), \tag{7a}$$
$$\hat{\mathbf{x}} = D\hat{\mathbf{c}}^{(L+1)} = D(\operatorname{proj}_\Gamma \mathbf{c}^{(L+1)}). \tag{7b}$$

The parameters that are optimized are highlighted in red in Alg. 1. Based on the design choice, we distinguish between *tied* unrolling, with shared parameters along layers shown in Fig. 1, and *untied* unrolling, where the parameters of each layer are optimized separately, illustrated in Fig. 2 [18]. These design choices are explained more in Sec. III

III. Experiments and Evaluation

A. Network architecture

We selected a limited number of layers to guarantee fast inference, which is the main strength of the DU algorithm. Based on the survey paper [7], $L = 15$ layers were chosen. The setting of DGT and iDGT is the same as in [2]: FFT length, $n_{\text{fft}} = 8192$, hop size $a = 2048$, Hann window with size $m = 8192$, and $\mathbf{c}^{(1)}$ is always initialized with zeros.

B. Ablation study of learnable parameters

Firstly, the selection of learnable parameters was examined before training on a larger dataset. A mono segment, approximately 6 seconds in length at 44.1 kHz, was chosen from the MusicNet dataset train set [22]. This dataset consists of various classical music ensembles. The value of ΔSDR (defined in Sec. III-D) was examined, and the variant of weights with the highest value was selected.

The parameter λ was fixed to 1 for all experiments to ensure algorithm stability. The parameters γ and $\mathbf{w}$ in (6) were examined, with the best initialization or system for computing weights being tested. If γ is optimized, then $\mathbf{w}$ is fixed, and vice versa. For all experiments the untied version of DU was used [7].

In the first set of experiments, γ was optimized with a fixed weighting vector $\mathbf{w}$. The vector $\mathbf{w}$ was initially set to all-ones and a parabola-based approach from [2] was applied. However, these experiments did not lead to a significant improvement against the baseline because optimizing only γ is not expressive enough.

With $\gamma = 1$ fixed, the frequency weights $\mathbf{w}$ of coefficients were optimized. Following the symmetry of the FFT, only $n_{\text{fft}}/2+1$ weights were optimized in one layer, then replicated across the other half of the spectrum. This approach, however, did not produce good results, as it was highly sensitive to each frequency bin based on the training data.

To address this, the number of weighting bins was reduced using critical bands, as introduced by Zwicker [23]. With the simplified formulation [24], linearly spaced FFT bins are mapped to 26 bins:

$$\text{Bark}(f) = \left\lfloor \frac{26.81f}{1960+f} - 0.53 \right\rfloor. \tag{8}$$

This mapping implies that each Bark bin influences multiple FFT bins based on the human auditory system. The optimized Bark weights are then mapped back to the FFT bins. This approach resulted in the highest ΔSDR value in this single-signal study and was used in the proposed trained network.

C. Training

The 15-layer network was trained on the entire training set of MusicNet with a batch size of 4 and a segment length of 6 seconds for 50,000 iterations. The input signal-to-distortion ratio (SDR) for signal distortion was randomly drawn from 1, 3, 5, 7, and 10 dB for each batch. The network was optimized using Adam [25] with a learning rate of $2 \cdot 10^{-4}$. The selected loss function was error-to-signal ratio (ESR) with high-pass pre-emphasis filter as proposed in [26], to assign higher weight to high-frequency content. The trained weights are shown in Fig. 3. As seen in the figure, the mean of the weights for each bin resembles a parabola shape, which was also shown to be successful in [2]. The low values in the last critical bands (high frequencies) do not follow the parabolic shape, likely because these bands typically contain little signal content. As a result, the optimizer may assign smaller weights to these regions, as they have less perceptual impact on the overall signal.

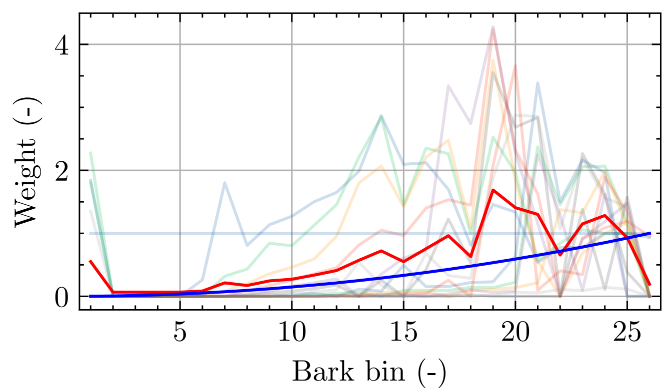

Fig. 3. Learned weights of uDRA in critical bands. The thick red line represents the mean of all layers at a given bin.

D. Comparison with baselines

We compare our learned algorithm uDRA with unweighted DRA and parabola-weighted DRA [2]. To compare the performance, nonlearned algorithms were run with 1000 iterations, as a region where the algorithm should converge and with 20 iterations to compare performance with similar processing time as the learned algorithm.

For evaluation, 10 segments were chosen from the test set of MusicNet. Objective metric ΔSDR is used.

The ΔSDR defines an improvement of SDR between restored signal $\hat{\mathbf{x}}$ and distorted signal $\mathbf{y}$. The SDR for two signals is defined $\text{SDR}(\mathbf{u}, \mathbf{v}) = 10 \log_{10} \frac{\|\mathbf{u}\|_2^2}{\|\mathbf{u}-\mathbf{v}\|_2^2}$, then $\Delta\text{SDR} = \text{SDR}(\mathbf{x}, \hat{\mathbf{x}}) - \text{SDR}(\mathbf{x}, \mathbf{y})$, where $\mathbf{x}$ is true target, $\hat{\mathbf{x}}$ is reconstructed and $\mathbf{y}$ is clipped signal [2]. The results are presented in 4. We can see that our algorithm outperforms classical algorithms if the number of iterations is similar, but it does not outperform the algorithm if the number of iterations reach the region of convergence.

E. Computational demands

The processing time of the algorithm is one of the strengths of uDRA. Table I shows the mean and variance of processing times for the algorithms computed on an Nvidia Geforce 4090 GPU and an i7-12700k CPU. The evaluation was performed on the same set of 60 signals used for the objective evaluation. As seen in the table, the inference times for 20 iterations of non-learned DRA and the 15-layer uDRA are quite similar for both the GPU and CPU, but objective results are better for the learned uDRA as presented in III-D.

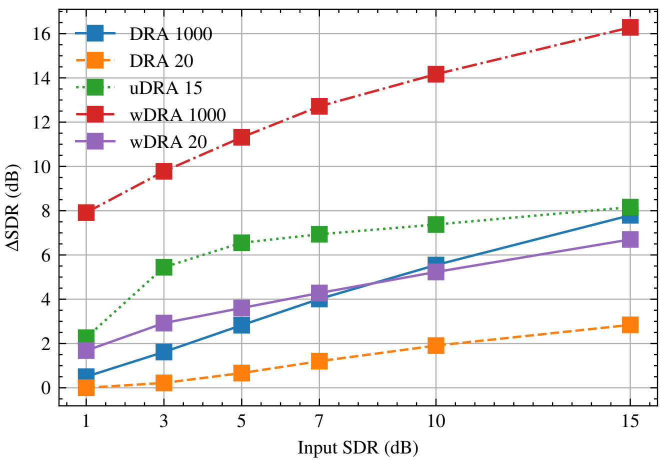

Fig. 4. The mean values of $\Delta\mathrm{SDR}$ for tested algorithms on 10 signal segments

TABLE I
PROCESSING TIME OF THE ALGORITHMS IN SECONDS

Method	GPU	CPU
DRA 1000	2.41 ± 0.03	252.13 ± 56.58
wDRA 1000	2.44 ± 0.02	251.52 ± 67.83
DRA 20	0.10 ± 0.02	5.05 ± 0.06
wDRA 20	0.04 ± 0.01	5.09 ± 0.04
uDRA 15	0.12 ± 0.03	3.85 ± 0.03

F. Discussion

While the 15-layer uDRA network shows promising results, the current configuration with only 390 parameters may not be sufficient to fully capture the complexity of signal distortion. Although the model performs well compared to classical algorithms, increasing the parameter space could offer more control over behavior of the system.

IV. Conclusion

In this article the deep unfolding of Douglas–Rachford algorithm was applied for audio declipping. The method has shown good performance in terms of objective metric. It beats the classical algorithms in a comparable number of iterations but it has not reached the perceptual quality of the parabola-weighted DRA with the guaranteed number of steps for convergence. However, we hope that a more complex neural network which would replace the one of the steps will solve this problem.

References

[1] P. Záviška, P. Rajmic, A. Ozerov, and L. Rencker, "A survey and an extensive evaluation of popular audio declipping methods," *IEEE Journal of Selected Topics in Signal Processing*, vol. 15, no. 1, pp. 5–24, 2021.

[2] P. Záviška, P. Rajmic, and J. Schimmel, "Psychoacoustically motivated audio declipping based on weighted l1 minimization," in *2019 42nd International Conference on Telecommunications and Signal Processing (TSP)*, (Budapest, Hungary), pp. 338–342, July 2019.

[3] B. Li, L. Rencker, J. Dong, Y. Luo, M. D. Plumbley, and W. Wang, "Sparse analysis model based dictionary learning for signal declipping," *IEEE Journal of Selected Topics in Signal Processing*, vol. 15, no. 1, pp. 25–36, 2021.

[4] S. Kitić, L. Jacques, N. Madhu, M. Hopwood, A. Spriet, and C. De Vleeschouwer, "Consistent iterative hard thresholding for signal declipping," in *Acoustics, Speech and Signal Processing (ICASSP), 2013 IEEE International Conference on*, pp. 5939–5943, May 2013.

[5] P. Záviška, P. Rajmic, O. Mokrý, and Z. Průša, "A proper version of synthesis-based sparse audio declipper," in *2019 IEEE International Conference on Acoustics, Speech and Signal Processing (ICASSP)*, (Brighton, United Kingdom), pp. 591–595, May 2019.

[6] K. Siedenburg, M. Kowalski, and M. Dörfler, "Audio declipping with social sparsity," in *2014 IEEE International Conference on Acoustics, Speech and Signal Processing (ICASSP)*, pp. 1577–1581, IEEE, 2014.

[7] E. Chen, X. Chen, A. Maleki, and S. Jalali, "Comprehensive examination of unrolled networks for solving linear inverse problems," 2025.

[8] E. Moliner, J. Lehtinen, and V. Välimäki, "Solving audio inverse problems with a diffusion model," in *2023 IEEE International Conference on Acoustics, Speech and Signal Processing (ICASSP)*, IEEE, jun 2023.

[9] J.-M. Lemercier, J. Richter, S. Welker, E. Moliner, V. Välimäki, and T. Gerkmann, "Diffusion models for audio restoration: A review," *IEEE Signal Processing Magazine*, vol. 41, no. 6, pp. 72–84, 2024.

[10] M. Švento, E. Moliner, L. Juvela, A. Wright, and V. Välimäki, "Estimation and restoration of unknown nonlinear distortion using diffusion," 2025.

[11] V. Monga, Y. Li, and Y. C. Eldar, "Algorithm unrolling: Interpretable, efficient deep learning for signal and image processing," *IEEE Signal Processing Magazine*, vol. 38, no. 2, pp. 18–44, 2021.

[12] Y. Romano, M. Elad, and P. Milanfar, "The little engine that could: Regularization by denoising (red)," *SIAM Journal on Imaging Sciences*, vol. 10, no. 4, pp. 1804–1844, 2017.

[13] T. Tanaka, K. Yatabe, M. Yasuda, and Y. Oikawa, "APPLADE: Adjustable plug-and-play audio declipper combining DNN with sparse optimization," in *2022 IEEE International Conference on Acoustics, Speech and Signal Processing (ICASSP)*, IEEE, may 2022.

[14] X. Wang and S. H. Chan, "Parameter-free plug-and-play ADMM for image restoration," in *2017 IEEE International Conference on Acoustics, Speech and Signal Processing (ICASSP)*, IEEE, Mar. 2017.

[15] K. Zhang, L. Van Gool, and R. Timofte, "Deep unfolding network for image super-resolution," in *IEEE Conference on Computer Vision and Pattern Recognition*, pp. 3217–3226, 2020.

[16] X. Wei, H. van Gorp, L. Gonzalez-Carabarin, D. Freedman, Y. C. Eldar, and R. J. G. van Sloun, "Deep unfolding with normalizing flow priors for inverse problems," *IEEE Transactions on Signal Processing*, vol. 70, pp. 2962–2971, 2022.

[17] Z.-X. Cui, Q. Zhu, J. Cheng, B. Zhang, and D. Liang, "Deep unfolding as iterative regularization for imaging inverse problems," *Inverse Problems*, vol. 40, p. 025011, jan 2024.

[18] P.-H. Vial, P. Magron, T. Oberlin, and C. Fevotte, "Learning the proximity operator in unfolded ADMM for phase retrieval," *IEEE Signal Processing Letters*, vol. 29, pp. 1619–1623, 2022.

[19] S. Wisdom, J. Hershey, J. Le Roux, and S. Watanabe, "Deep unfolding for multichannel source separation," in *2016 IEEE International Conference on Acoustics, Speech and Signal Processing (ICASSP)*, pp. 121–125, 2016.

[20] W. Yuan, S. Wang, J. Wang, M. Unoki, and W. Wang, "Unsupervised deep unfolded representation learning for singing voice separation," *IEEE/ACM Transactions on Audio, Speech, and Language Processing*, vol. 31, pp. 3206–3220, 2023.

[21] P. Combettes and J. Pesquet, "A Douglas–Rachford splitting approach to nonsmooth convex variational signal recovery," *IEEE Journal of Selected Topics in Signal Processing*, vol. 1, no. 4, pp. 564–574, 2007.

[22] J. Thickstun, Z. Harchaoui, and S. M. Kakade, "Learning features of music from scratch," in *International Conference on Learning Representations (ICLR)*, 2017.

[23] E. Zwicker, "Subdivision of audible frequency range into critical bands (frequenzgruppen)," *JOURNAL OF THE ACOUSTICAL SOCIETY OF AMERICA*, vol. 33, no. 2, pp. 248–&, 1961.

[24] H. Traunmüller, "Analytical expressions for the tonotopic sensory scale," *The Journal of the Acoustical Society of America*, vol. 88, p. 97–100, July 1990.

[25] D. P. Kingma and J. Ba, "Adam: A method for stochastic optimization," 2014.

[26] E.-P. Damskägg, L. Juvela, E. Thuillier, and V. Välimäki, "Deep learning for tube amplifier emulation," in *ICASSP 2019 - 2019 IEEE International Conference on Acoustics, Speech and Signal Processing (ICASSP)*, pp. 471–475, 2019.

Multipurpose Digital Audio Effect: Combining Different Techniques Within a Single Device

David Leitgeb
Department of Telecommunications
Brno University of Technology, Technicka 12
616 00 Brno, Czech Republic
david.leitgeb@vut.cz

***Abstract*—This paper introduces an audio effect (FX) plug-in module capable of processing the input signal with several common types of audio manipulation within up to 30 individual bands. The advantage of the proposed implementation lies mostly in its versatility, with potential applications ranging from simple delay up to spatial simulations, such as reverb. Unlike the existing commercial solutions that typically split the input signal into a fixed set of frequency bands, the proposed FX processes the input signal in parallel across all bands, with each band applying optional filtering and other processing independently. The proposed FX was implemented using the C++ programming language and the JUCE framework.**

***Index Terms*—digital audio effect, filter, delay line, low-frequency oscillator, sample interpolation, C++, JUCE**

I. Introduction

For nearly three decades, digital audio effects have served as powerful alternatives to analog and digital hardware-based solutions. The primary objective of such devices is to enable users to process audio signals in the desired manner with a minimal effort, including the audio effect (FX) proposed in this paper. They usually represent a more affordable way to process audio, while maintaining high-quality results. In general, FXs can be categorised by the resulting effect they have on the input signal, such as:

- time-based effects (delay, chorus, flanger),
- dynamic effects (compressor, limiter, expander),
- modulation effects (tremolo, vibrato),
- distortion effects (overdrive, distortion, fuzz) [1].

The proposed FX plug-in implementation represents a combination of multiple categories mentioned above.

There are several commercial products similar to the proposed FX plug-in. The most notable one is Spektral Delay[1] (Native Instruments) released in 2001, which also served as the initial inspiration for the proposed FX. Another notable FX plug-in is Sage | Spectral Delay (Puremagnetik) [2], which, according to the developers, was also inspired by Spektral Delay[2]. Other alternatives include MXXX (MeldaProduction) [3], SpecOps (Unfiltered Audio) [4], and Multipass (Kilo-Hearts) [5]. All of these products represent possible solutions for users who want to process audio with a more creative approach. Although these products offer similar functionality, the choice ultimately depends on the user's specific needs, including complexity, workflow, and other factors. For that reason, it is not possible to define one of the choices as state-of-the-art. The price range of these FX plug-ins is €35–€999 at the time of writing of this paper.

It is important to note that there are distinct differences between the devices mentioned and the FX plug-in proposed in this paper. The key difference lies in the principle of the input signal distribution between the individual bands. Similar FX plug-ins typically use the Fast Fourier Transform (FFT) algorithm to divide the input signal into individual frequency bands. In contrast, the implementation proposed in this paper uses an infinite impulse response (IIR) filter inside each of the individual bands' processing chains. As a result, this means that depending on the filter settings in each individual band, their output signal can overlap in the frequency domain. The outcome of this decision is that processing audio with the proposed FX plug-in will yield results with a different timbre. The aim was to provide a creative tool for spectral sound shaping that differs from existing solutions.

The purpose of this paper is to propose a powerful FX plug-in capable of creating complex sound timbres while maintaining ease of use. The plug-in is implemented using the C++ programming language and the JUCE framework [6], which is commonly used in the field of audio software development. The core of the algorithms were implemented mainly according to [1] and [7]. The source code for the plug-in, as well as the compiled version in the VST3 format, which is supported by most digital audio workstations (DAW), can be found in the following GitHub repository.[3].

This paper is organized as follows. Section II presents the methodology and key components of the implementation. Section III discusses a series of experiments conducted using the proposed FX plug-in, highlighting the most representative examples of the various effects achievable with the proposed implementation. Additional examples, including audio files, can be found in the dedicated GitHub repository. Section IV evaluates the proposed FX plug-in and concludes the paper. This paper is a continuation of the previous work presented

[1]Spektral Delay has been discontinued, and its description is no longer available on the Native Instruments website. However, some information about this product can still be found in internet archives.

[2]Sage | Spectral Delay was released after the implementation presented in this paper was finished.

[3]https://github.com/David-Leitgeb/multipurpose-dfx

in [8], which introduced a Matlab prototype of the proposed FX plug-in, later reimplemented in C++ and further extended into the form presented in this paper.

II. Methods

The following section contains a brief overview of the approaches used during the implementation process of the proposed FX plug-in. The complete source code with comments and the VST3 build of the FX plug-in can be found in the GitHub repository.

A. FX structure

Fig. 1 provides an overview of all the components included in the plug-in and their routing. The proposed FX plug-in incorporates the following signal processing methods:

- gain adjustment,
- frequency filtering,
- delay line with sample interpolation,
- panorama,
- low-frequency oscillator,
- feed-forward signal path,
- mix control.

The proposed FX plug-in consists of 30 individual bands, each with a set of user-adjustable parameters. Every band contains the components listed above. The routing details between these components are illustrated in Fig 1. It is important to mention once again that all the bands use the same signal as its input.

B. Filter

The first stage of signal processing applied to each individual band is filtering. Such systems can be implemented using various approaches, each with its own advantages and disadvantages. Two notable examples are infinite impulse response (IIR) and finite impulse response (FIR) filters. Digital signal processing (DSP) frameworks, such as JUCE, often provide this functionality by default. However, the proposed FX plug-in utilizes an IIR filter due to its lower computational requirements compared to FIR filters. Its implementation follows the approach described in [1].

This method uses the canonical second-order filter structure shown in Fig. 2. It was chosen for its simplicity, as the filter configuration is determined by calculating a set of coefficients. This filter structure is defined by the following difference equations [1]:

$$x_h(n) = x(n) - a_1 x_h(n-1) - a_2 x_h(n-2), \tag{1}$$

$$y(n) = b_0 x_h(n) + b_1 x_h(n-1) + b_2 x_h(n-2). \tag{2}$$

In these equations, b_0, b_1, b_2, a_1, a_2 are the calculated filter coefficients. Solving these equations results in the following transfer function:

$$H(z) = \frac{b_0 + b_1 z^{-1} + b_2 z^{-2}}{1 + a_1 z^{-1} + a_2 z^{-2}}. \tag{3}$$

In summary, the coefficients are calculated based on the parameters set by the user and subsequently applied in the transfer function.

The resulting type of filter depends on the equations used to calculate the coefficients. Seven types of filters can be achieved:

- HP – Highpass,
- LS – Low-shelving,
- BP – Bandpass,
- BR – Bandreject,
- P – Peak,
- HS – High-shelving,
- LP – Lowpass.

These filters are implemented as second-order filters. However, the lowpass and highpass types can also be switched to their first-order versions. In this case, the coefficients a_2, b_2 are simply set to zero.

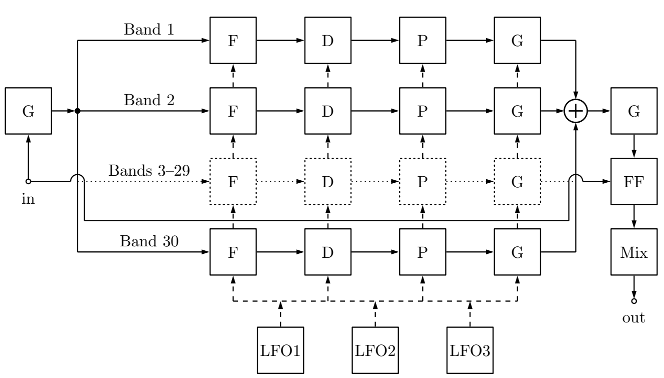

Fig. 1. Signal flow of the proposed FX plug-in, where G is the gain, F is the filter, D is the delay line, P is the panorama, and LFO1–LFO3 are the low-frequency oscillators.

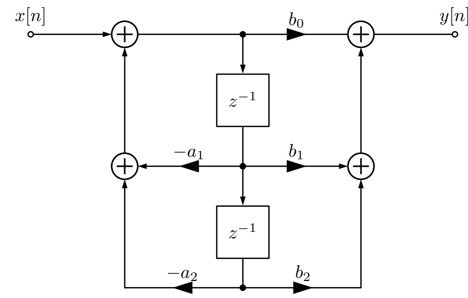

Fig. 2. Structure of a direct-form II second-order filter [1].

C. Delay line

After modifying the input signal using the chosen frequency filter, a delay is applied. The structure of the implemented delay line is shown in Fig 3. This implementation was selected for its versatility and was implemented according to [1]. As shown in the figure, this structure uses three routes: feedforward, blend, and feedback. The advantage of this structure lies in the variety of timbres that can be achieved depending on the settings of the individual parameters. Digital delay implementations use a technique called the circular buffer, which is longer than a regular processing buffer (the length of the circular buffer depends on the maximum achievable delay time). Both writing to and reading from this buffer occur simultaneously.

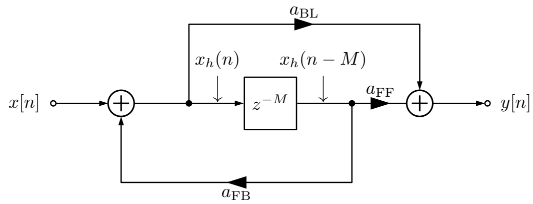

Fig. 3. Structure of the implemented delay line [1].

Since the FX plug-in features delay time modulation, it is crucial to implement some form of sample interpolation. A digital audio signal is stored as a set of discrete samples. With specific delay times and their modulation, a value between two consecutive samples is needed. If the delay time were static, it would be possible to use the nearest existing sample. However, with modulation, this approach would introduce audible artifacts. For this reason, sample interpolation must be used. Several types of sample interpolation exist, such as linear, second-order polynomial, and cubic. The delay line in the proposed FX plug-in utilizes second-order polynomial sample interpolation. This type of interpolation works by fitting a second-order polynomial to three consecutive samples. The process, implemented according to [7], works as follows: the three consecutive samples $x[n-1]$, $x[n]$ and $x[n+1]$ are known. The objective is to determine x within the region of the middle sample. Assuming that all three samples lie on a second-order polynomial, the interpolation can be expressed as follows:

$$\begin{aligned} y[-1] &= c_2(0-1)^2 + c_1(0-1) + c_0, \\ y[0] &= c_2 0^2 + c_1 0 + c_0, \\ y[1] &= c_2(0+1)^2 + c_1(0+1) + c_0. \end{aligned} \tag{4}$$

The values $y[-1]$, $y[0]$, and $y[1]$ correspond to the input samples $x[n-1]$, $x[n]$, and $x[n+1]$. The coefficients c_0, c_1, and c_2 are calculated as follows:

$$\begin{aligned} c_0 &= y[0], \\ c_1 &= (y[1] - y[-1])/2, \\ c_2 &= (y[1] - 2y[0] + y[-1])/2. \end{aligned} \tag{5}$$

The resulting interpolated value of the given sample can be calculated as:

$$x(t) = y(\tau) = c_2\tau^2 + c_1\tau + c_0, \tag{6}$$

where $\tau = t - n$ corresponds to the position of the given sample.

D. Low-frequency oscillator

Another essential component of the proposed FX plug-in is the low-frequency oscillator (LFO). This type of oscillator typically generates a signal with a frequency up to 20 Hz. The output signal is then used to modulate the values of the selected parameters. The proposed FX plug-in provides the user with three LFOs, each capable of generating a signal within the specified frequency range and with the following waveforms: sine, triangle, square, saw and sample&hold. The frequency of the LFO signal is commonly referred to as the rate parameter. In the proposed FX plug-in, it can be specified either in Hz or in note lengths. The LFO signal can be used to modulate the following parameters:

- filter cutoff frequency,
- delay length,
- panorama,
- gain.

During the implementation process, an issue had to be addressed: digitally generated signals can exhibit infinitely short transitions between individual values, resulting in significant amplitudes of higher harmonics at very high frequencies, which can cause aliasing. Using such signals would introduce audible artifacts. Because of this, a lowpass filter was applied to the LFO output. Several cutoff frequencies were tested (see Fig. 4) to find the right balance between reducing sudden changes in the signal and still resembling the original waveform. A cutoff frequency of 500 Hz was chosen, allowing the preservation of nearly 20 harmonics of the output signal for the highest LFO frequency.

Another issue that had to be addressed during the implementation process was time alignment with the DAW. As mentioned previously, the delay time can be specified in note lengths. The beats per minute (BPM) value is retrieved from the DAW, which means that calculating the correct delay time was not a problem. However, the challenge was to ensure proper time alignment with other tracks in the DAW. This issue was resolved by retrieving the song position pointer (SPP) and checking whether playback is active. The LFO phase is then adjusted accordingly.

E. Performance optimization

During the implementation process, several performance issues were addressed, as they had an impact on the overall performance of the FX plug-in. The simplest optimization was to ensure that no processing was performed for inactive bands. Another optimization method involved using the `juce::dsp::AudioBlock` class, which significantly reduced the number of times data are copied in the memory. Instead of duplicating the data, a reference to the buffer stored in memory is passed and rewritten. This approach was applied wherever possible. Additionally, a modulation

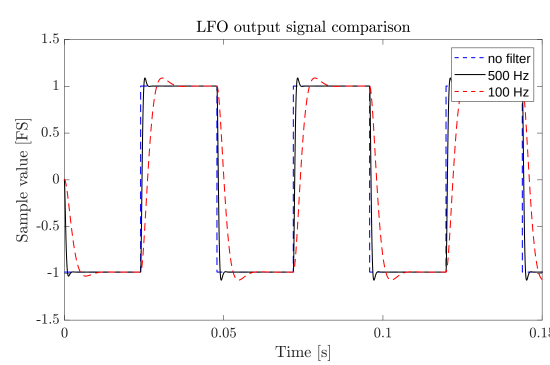

Fig. 4. Comparison of three LFO output signals.

update control was added. The value of this parameter can be adjusted by the user in the graphical user interface (GUI), depending on the scenario. This parameter defines the number of samples after which the modulation is updated. Rather than calculating the modulations on a sample-by-sample basis, the update interval can be extended to reduce the number of calculations. In practice, this means that the parameter can be set to a higher value, which may potentially introduce some artifacts. However, during export, this value can be set to one to ensure the highest possible quality of the output signal.

F. Presets

The final component implemented in the proposed FX plug-in was preset management. The implementation was done according to [9]. This system enhanced the workflow by providing an organized way to manage presets, making it easier to work with the plug-in and perform tests. Each experiment presented in the following section has its own preset file, which can be downloaded from the GitHub repository.

III. Experiments

This section presents a selection of experiments prepared using the proposed FX plug-in. The following text provides only essential information, while the complete parameter values used in these examples can be found alongside the full collection of experiments on the dedicated GitHub page.[4] The examples are available as corresponding sets of `.pdf`, `.wav`, and `.preset` files, which can also be downloaded from the GitHub repository.

A. Filter

The first example included in this paper focuses on the implementation of frequency filters. The frequency response of a bandreject filter with a center frequency of 1 kHz and a Q factor of 0.5 is shown in Fig. 5.

B. Delay line

The next two experiments explore the capabilities of the implemented delay line. The first example demonstrates the vibrato effect. Here, a 1 kHz sine wave is used as the input signal, with the delay time modulated by a sine wave LFO. This modulation results in a pitch oscillation, which is visible in the included spectrogram (see Fig. 6).

The second example illustrates the formation of a comb filter, achieved by slightly delaying a signal and summing it with the original input. The structure of the implemented delay line allows for the creation of both IIR and FIR comb filters. The frequency response of the FIR type is shown in Fig. 7, while both types are available as examples on the GitHub page and in the repository.

C. Low-frequency oscillator

The next example demonstrates a possible use of the LFO. In this case, a saw wave LFO signal modulates the center frequency of a bandpass filter. White noise is used as the input signal, and the resulting spectrogram is shown in Fig. 8.

[4]https://david-leitgeb.github.io/multipurpose-dfx/

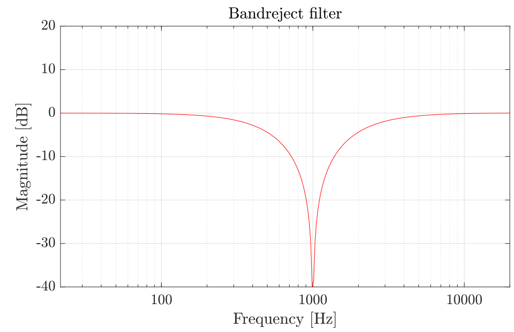

Fig. 5. Frequency response of the bandreject filter.

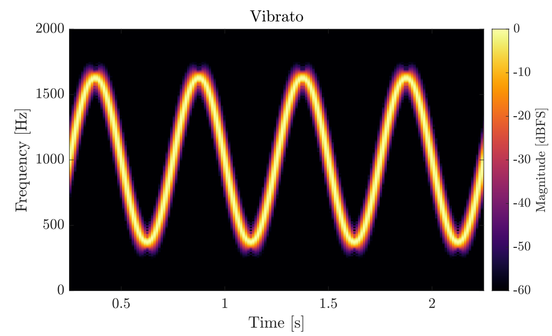

Fig. 6. Spectrogram of the vibrato effect.

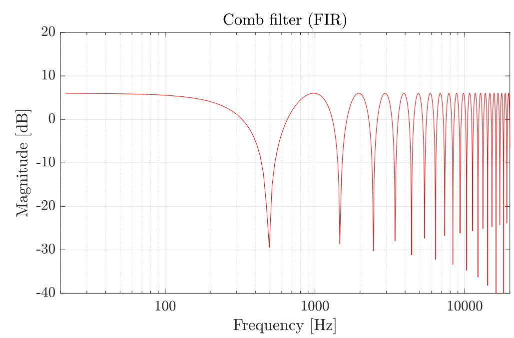

Fig. 7. Frequency response of the comb filter.

D. Sample interpolation

This example highlights the importance of the sample interpolation implemented in the proposed FX plug-in. Fig. 9 shows the waveform of the output signal both with and without second-order polynomial interpolation. For this experiment, a 1 kHz sine wave is used as the input signal. As shown in the figure, second-order polynomial interpolation eliminates abrupt changes in the waveform, which significantly reduces artifacts.

E. Panorama

The following example illustrates the functionality of the panorama parameter, which is modulated by a sine wave

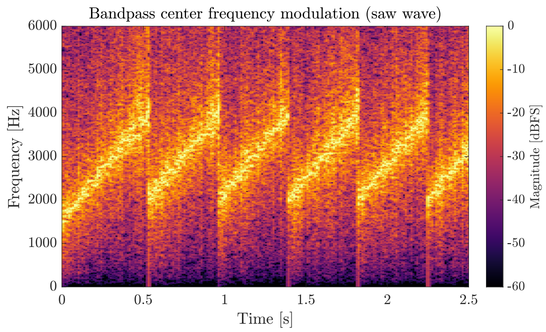

Fig. 8. Spectrogram of the bandpass filter modulated by the LFO.

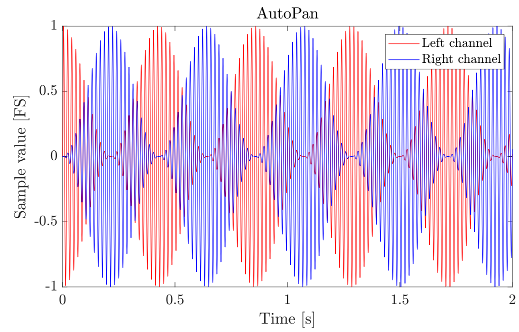

Fig. 10. Output signal of the Auto-Pan effect.

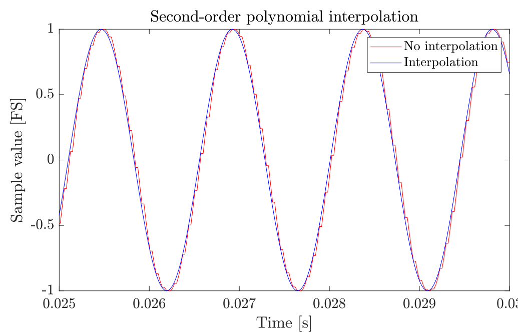

Fig. 9. Comparison of the output signal with and without second-order polynomial interpolation.

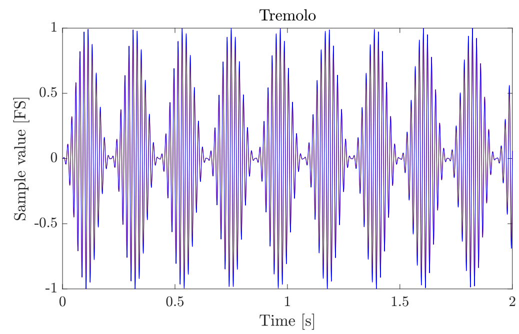

Fig. 11. Output signal of the tremolo effect.

LFO signal, creating an effect often referred to as Auto-Pan. A 55 Hz sine wave is used as the input signal, and the waveform of both the left and right channels of the output is shown in Fig. 10.

F. Tremolo

The final experiment focuses on the tremolo effect (see Fig. 11). This effect is created by modulating the gain of the input signal by an LFO, with a sine wave signal in this case. It is commonly used as a pedal effect for electric guitars. As in the previous example, a 55 Hz sine wave is used as the input signal.

IV. Conclusion

The result of this paper is a fully functional FX plug-in compatible with any DAW that supports the VST3 format. It features 30 individual bands, each offering multiple types of digital signal processing. The plug-in can be used for various purposes, ranging from simple delay effects to reverb simulation. A built-in preset manager enhances the workflow and improves the practical usability of the device. In addition, the plug-in has a fully scalable GUI, ensuring a sharp and consistent display across different screen resolutions.

Possible improvements for future work include extended delay time options, more complex band routing for greater flexibility, and a more advanced modulation system to expand creative possibilities of the FX plug-in.

All of the experiments presented in this paper, along with additional ones, can be viewed on the dedicated GitHub page. The source code for the proposed FX plug-in is available for download from the GitHub repository.

Acknowledgment

I would like to thank my supervisor doc. Ing. Jiří Schimmel, Ph.D. for guidance during the preparation of this paper.

References

[1] U. Zölzer, Ed., *DAFX: digital audio effects*, 2nd ed. Chichester: Wiley, 2011.

[2] Puremagnetik. "Sage | Spectral Delay" Puremagnetik. Accessed: Jan. 15, 2025. [Online.] Available: https://puremagnetik.com/products/sage-spectral-delay

[3] MeldaProduction. "MXXX" MeldaProduction. Acessed: Jan. 15, 2025. [Online.] Available: https://www.meldaproduction.com/MXXX

[4] Unfiltered Audio. "SpecOps" Unfiltered Audio. Accessed: Jan. 15, 2025 [Online.] Available: https://www.unfilteredaudio.com/products/specops

[5] Kilohearts AB. "Multipass" Kilohearts. Accessed: Jan. 15, 2025 [Online.] Available: https://kilohearts.com/products/multipass

[6] Raw Material Software Limited. "Home - JUCE" JUCE. Accessed: Jan. 15, 2025 [Online.] Available: https://juce.com/

[7] J. D. Reiss and A. P. McPherson, *Audio effects: theory, implementation and application*. Boca Raton: CRC Press, 2014.

[8] D. Leitgeb, "Experimental audio effect based on dynamic signal filtering," in Proc. I of the 30th Conf. STUDENT EEICT 2024, Brno, Apr. 23, 2024, pp. 163–166. [Online]. Available: https://www.eeict.cz/eeict_download/archiv/sborniky/EEICT_2024_sbornik_1.pdf

[9] The Audio Programmer, A. Murthy. Preset Manager in JUCE || Akash Murthy (Jun. 23, 2022). Accessed: Mar. 3, 2025. [Online Video]. Available: https://www.youtube.com/watch?v=YwAtWuGA4Cg

Optimized 5G-IoT Probe: Hardware Innovations and Practical Deployment

1st Pavel Palurik
Department of Telecommunications
Brno University of Technology
Brno, Czech Republic
pavel.palurik@vut.cz

2nd Radim Dvorak
Department of Telecommunications
Brno University of Technology
Brno, Czech Republic
xdvora2g@vutbr.cz

2nd Pavel Masek
Department of Telecommunications
Brno University of Technology
Brno, Czech Republic
masekpavel@vut.cz

***Abstract*—The efficient deployment of 5G-IoT networks relies on accurate field measurements to evaluate network performance in diverse environments. This study introduces a newly optimized 5G-IoT tester, developed to enhance the accuracy and efficiency of LTE-M and NB-IoT coverage assessment. The redesigned hardware and software architecture provide improved power efficiency, enhanced configurability, and intuitive user controls, making it a robust tool for industrial applications and network planning. Initial field measurements were conducted as part of a large-scale data collection effort, covering a subset of predefined 1,000 test locations. The recorded data were analyzed through heatmap visualizations, revealing coverage disparities, particularly in peripheral regions, and emphasizing the need for targeted network optimizations. Future work aims to expand the dataset, enabling more comprehensive coverage analysis and validation of predictive models for IoT deployment.**

***Index Terms*—5G-IoT, LTE-M, NB-IoT, signal analysis, network performance, field measurements, IoT connectivity**

I. Introduction

With increasing demands on the reliability and availability of fifth generation (5G) networks in the Internet of Things (IoT) world, there is a growing need for accurate and efficient methods to verify their parameters in real-world environments. LTE Cat-M and NB-IoT technologies, which are part of the 5G ecosystem, are becoming key elements of modern IoT solutions, especially in smart metering, industrial monitoring and sensor networks. While these technologies promise better coverage, lower power consumption and wider deployment options, real-world conditions in the field can significantly impact their effectiveness [1].

In previous research, a modular 5G-IoT tester was developed and tested to enable autonomous measurement of key parameters of LTE Cat-M and NB-IoT networks. This tester, already in its basic version, allowed the analysis of signal conditions, link quality and transmission characteristics in different environments. The first version of the device proved to be beneficial not only for research purposes, but also for practical applications in industry and IoT deployment planning [2].

Despite the positive results of the initial testing and experience gained from the initial deployment of the tester, including user feedback, a number of key areas for further improvement have been identified, particularly in the areas of hardware architecture, enhanced configuration options and more user-friendly controls.

In addition to the technological improvements, the new generation of testers offer a wider range of possibilities for practical use in real industrial applications with the industrial partners and companies involved. For example, it can be used for planning the deployment of IoT sensor networks, monitoring coverage quality in large buildings or testing signals in remote locations when deploying smart meters. By evaluating network parameters in detail, companies can better optimise the deployment of IoT devices, leading to reduced operational costs and increased communication reliability.

In the following sections of this article, the hardware enhancements to the tester, specific case studies of its use in practice with field measurements, and measurement results are described in detail. These results were analyzed and visualized in the form of a heatmap showing the signal strength and other parameters in the measured area. First, the new hardware design and key changes compared to the previous version are presented. Then, the application of the tester in mapping the NB-IoT network coverage in a real environment and how to visualize the results are described. The paper concludes with a discussion of the benefits of the improved tester and possible further development of this measurement tool.

II. Update Design Process

The first generation of the 5G-IoT testing instrument was a versatile and modular platform for evaluating network parameters within the scope of LTE Cat-M and NB-IoT environments. The device has proven its usefulness in experimental deployments where it enabled detailed analysis of signal quality and other key metrics. Although the tester was found to be an effective tool for basic coverage and network parameter assessment, the practical experience revealed several areas where significant improvements could be made. A key challenge was optimizing computing power for advanced network analysis, as the first-generation tester had limited efficiency. The optimized tester was designed for field operation, where ensuring a prolonged battery life without frequent charging is imperative. While the original solution offered basic power management, testing in real-world conditions revealed that enhancing the power supply circuitry and introducing more advanced power management modes could significantly extend the device's lifespan. Consequently, the subsequent iteration of the tester has been meticulously engineered to optimize the power architecture and implement an advanced power management mode facilitated by the ESP32 processor.

Modularity and expandability have also proven to be key factors in ensuring the long-term usability of the equipment. The first prototype was already capable of working with expandable modules. The new version of the tester takes this concept further through easy exchange of communication modules and support for new upcoming technologies such as 5G RedCap (Reduced Capability 5G) or full 5G. This flexibility allows not only compatibility with current standards, but also the adaptation of the device to new requirements without the need for major hardware modifications.

In addition to hardware changes, it was necessary to expand the ability to visualize the measured data. This first generation of the tester permitted rudimentary data acquisition and the subsequent presentation of findings on the screen. However, the interpretation of the data in the context of the specific site being measured was limited. To address these limitations, a new preview menu was integrated into the subsequent iteration of the tester, aiming to enhance device control and facilitate network coverage assessment. This enhancement has resulted in a user interface that is characterized by its enhanced intuitiveness, which, in turn, has led to a number of benefits. These include more effective measurement configuration options and enhanced visual feedback, which is now provided directly on the tester display. The redesign emphasizes the ability to easily set measurement parameters and a clearer display of key values. These changes allow for more efficient operation of the tester in the field.

This section provides an in-depth examination of individual innovations. First, specific hardware changes will be presented, followed by a marginal focus on software improvements that bring a higher level of interpretation of measurement results.

A. Motherboard PCB

As in the first prototype, the core design was preserved in the new version, with the main PCB remaining the central component of the tester. While most of the original features were retained, as depicted in Fig. 1, practical deployment and user feedback identified key areas for improvement, leading to significant enhancements in power management, energy efficiency, and additional peripheral modules.

One of the primary innovations in the power subsystem was the addition of a MAX17048G+ battery fuel gauge to the existing MAX77751 IC charging circuit (see Fig. 1). This integrated circuit allows for precise monitoring of the battery's State-of-Charge (SOC) using the advanced ModelGauge algorithm while maintaining an ultra-low quiescent current, minimizing its impact on usable battery capacity. The circuit communicates with the ESP32 via the I2C bus and provides continuous monitoring of charging and discharging under varying load conditions. Additionally, it offers programmable

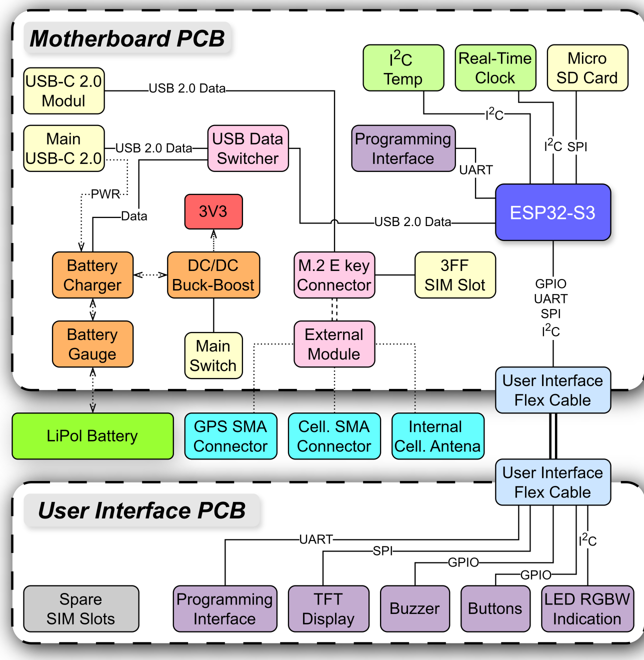

Fig. 1. LTE Cat-M Tester block diagram.

alerts for low SOC, overvoltage, or undervoltage, increasing the reliability of the tester in real-world conditions [3].

To ensure stable communication between the ESP32 and the battery charging circuit, a Schmitt trigger SN74LVC1G17DCK3 was implemented to eliminate sporadic signal errors that could lead to misinterpretation by the microcontroller.

Another significant enhancement involved upgrading the battery capacity. The original version used batteries with a capacity between 2500–3500 mAh, whereas the new version features a 4500 mAh battery. The selection was constrained by the physical dimensions of the device, requiring careful consideration of both width and thickness.

Further improvements to power management included replacing the voltage regulation circuit. After extensive testing of switched DC/DC converters, the Richtek RT6154AGQW buck-boost converter was selected. This converter ensures high conversion efficiency exceeding 90% and supports a wide input voltage range of 1,8–5,5 V, making it ideal for the device's lithium battery. In contrast, traditional buck converters would be limited by a lower operational voltage threshold of approximately 3,5 V. The RT6154AGQW requires minimal external components and is compatible with various battery types, including Li-Ion, group of alkaline, and Ni-MH, providing greater flexibility for future development [4].

One notable limitation of the previous design was the absence of a power switch for the device. This issue was addressed by utilizing the enable (EN) pin of the voltage converter, allowing the tester to be switched on and off efficiently without requiring a high-current power switch(see Fig. 2 for the updated PCB layout). The chosen low-voltage

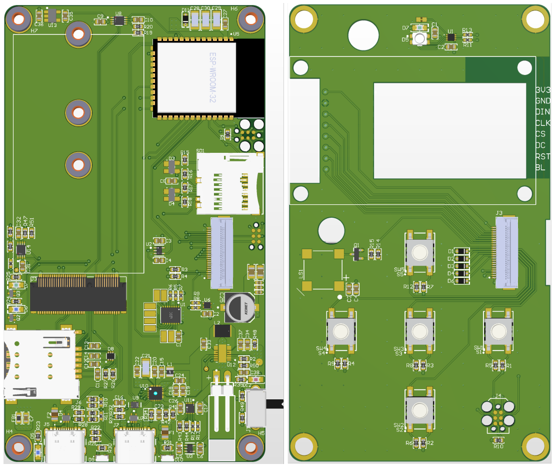

Fig. 2. 3D render of Tester PCBs.

switch OS102011MA1QN1 supports up to 12 V at 100 mA, making it well-suited for logic-level switching within the device's power constraints.

To expand the tester's capabilities, additional peripheral components were integrated into the main PCB. A Sensirion STS4X temperature sensor was added, providing highly accurate temperature measurements with a typical deviation of ±0.4 °C in common environmental conditions. This fully digital sensor communicates via the I2C bus and operates with an ultra-low power budget, minimizing its impact on overall energy consumption.

Another key addition was the high-accuracy RTC chip PCF2131, which includes an integrated temperature-compensated crystal oscillator. This circuit ensures precise timekeeping and offers a range of advanced functions, such as programmable alarms, automatic switch-over to a backup battery, and interrupt outputs. The RTC is powered directly from the main device battery through an LDO regulator MIC5365-3.0YC5-TR, selected to handle the fluctuating voltage levels of the lithium battery. Due to the extremely low power consumption of both the LDO and RTC, the timekeeping function can be maintained for several months even when the main switch is turned off [5].

The final major enhancement involved improving the connection between the motherboard and the user interface PCB, which includes the display and control buttons. To accommodate the increased number of signal lines—now totaling 24—a flex cable with a 0.5 mm pitch was introduced, ensuring a more reliable and efficient signal transmission between the boards.

B. User Interface PCB

The user interface board has also undergone modifications, enhancing both the device's usability and mechanical design. One of the key improvements was the replacement of standard buttons with low-profile switches, improving ergonomics and contributing to a more compact overall design. Another major enhancement involved reengineering the mounting and connection system of the display, making it not only mechanically replaceable but also reducing the total height of the enclosure. This modification significantly improved the portability of the device and its practicality for field applications.

Additional peripheral components were integrated into the user interface board to enhance user interaction. The first addition is an acoustic signaling system, implemented using the AD-85D3CR buzzer, which, with its 83 dBA sound level, provides an audible indication of measurement start and completion. The second enhancement is RGBW LED indication, which visually communicates the operational status of the tester. The KTD2027EWE-TR four-channel LED driver, which operates via the I2C bus, was chosen to control the LED signals, allowing for efficient and customizable color-coded status feedback.

C. Updated Enclosure

The enclosure of the device was redesigned to enhance its durability, ergonomics, and functionality while maintaining its 3D-printable nature. The new iteration introduces several structural improvements, optimizing both mechanical resilience and user experience (as depicted in Fig. 3, illustrating the tester enclosure).

One of the primary modifications focuses on the button integration, where refinements were made to minimize gaps around the buttons, ensuring improved tactile feedback while reducing potential points of ingress for dust and debris. Additionally, the overall thickness of the enclosure was reduced, making the device more compact and ergonomically suited for handheld operation. To improve durability, the corners of the enclosure are reinforced with TPU bumpers made from 85A Shore hardness material. During durability testing, the enclosure withstood a 1-meter drop onto a concrete surface without sustaining damage, effectively protecting the internal components of the tester.

A crucial improvement was the reinforcement of SMA connector mounts. The upper section of the enclosure now features internal plastic extrusions that prevent SMA connectors from rotating when tightened, ensuring a secure and stable connection over repeated use. Additionally, the enclosure now houses an integrated cellular IoT antenna, further optimizing the compact design and eliminating the need for an external mounting solution. On the rear side of the enclosure, several identification and instructional elements were incorporated. In addition to the university logo, each unit is now labeled with a unique serial number, derived from a portion of the ESP32 MAC address combined with a device series number, allowing precise tracking of individual testers. Furthermore, clear markings indicate which SMA connector corresponds to the cellular and GPS antenna, aiding users in quick and correct installation.

The enclosure remains fully disassemblable, secured with hex screws, allowing for easy maintenance, upgrades, or repairs while ensuring a robust structural integrity.

III. Measurement

Effective deployment of mobile IoT networks requires a detailed analysis of their coverage, signal quality, and avail-

Fig. 3. Design of a tester enclosure.

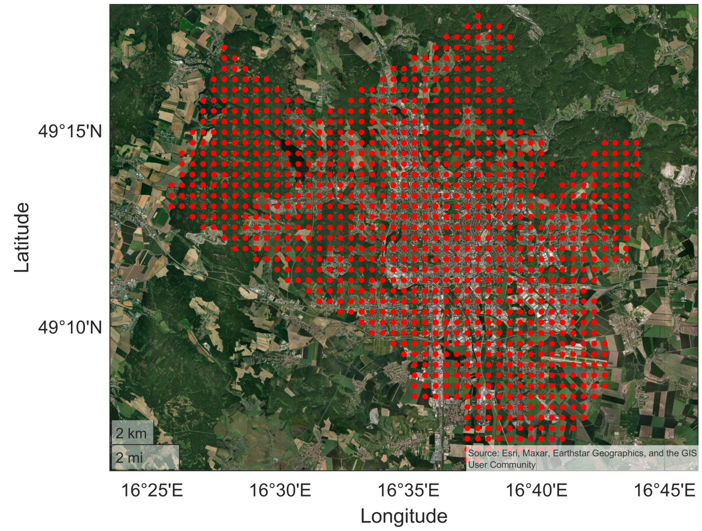

Fig. 4. Planned measurement points across the surveyed area.

ability across diverse environments. Existing studies have predominantly focused on densely urbanized areas, where mobile network infrastructure is well-optimized [6]. This research extends the analysis to a broader geographic scope, encompassing both high-density city centers and suburban and peripheral regions, where IoT communication conditions may differ significantly.

To ensure systematic and representative data collection, over 1,000 test points were defined based on a uniform 500-meter spatial grid, covering both urban and suburban areas of Brno (Fig. 4 illustrates the planned measurement points). The selection of measurement locations accounted for a variety of environmental conditions, including dense urban infrastructure, transportation corridors, industrial zones, and rural landscapes, enabling a comparative analysis of how different geographic and infrastructural factors influence network performance. The measurements presented in this study represent a partial dataset[dopnit highlight], which will be progressively expanded to construct a comprehensive geospatial representation of NB-IoT and LTE-M coverage.

The collected dataset not only provides an overview of real-world network conditions but also serves as a foundation for predictive coverage modeling, identification of weak-signal areas, and strategic planning of IoT device deployments. Moreover, these data offer a benchmark for validating theoretical coverage models, supporting network operators and infrastructure managers in refining deployment strategies in complex urban settings.

A. *Testing scenarios*

The field measurements were conducted under standardized conditions to ensure methodological consistency and minimize external interference.Each test site was defined by GPS coordinates, and if access was restricted, measurements were taken at the nearest feasible point without compromising data integrity.

At each measurement site, two sets of recordings were performed, corresponding to the two cellular IoT technologies deployed by Vodafone. The first set focused on NB-IoT operating in Band 20, while the second assessed LTE-M in Band 8. The primary parameters recorded were Reference Signal Received Power (RSRP), providing insight into signal strength, and Signal-to-Interference-plus-Noise Ratio (SINR), which quantifies the overall reception quality by comparing signal power to interference and noise. In addition, the Enhanced Coverage Level (ECL) was documented to categorize coverage conditions at each site.

To further characterize network performance and structure, additional parameters were recorded, including Cell ID and Physical Cell Identity (PCI) to identify the serving base station, Tracking Area Code (TAC) for tracking area assignment, and E-UTRA Absolute Radio Frequency Channel Number (EARFCN) to specify the operating frequency. The Timing Advance (TA) parameter was also measured to estimate the approximate distance between the device and the connected base station, offering insights into signal propagation and coverage range.

To further characterize network performance, additional parameters were recorded, including Cell ID and Physical Cell Identity (PCI) to identify the serving base station, Tracking Area Code (TAC) for network tracking area assignment, and E-UTRA Absolute Radio Frequency Channel Number (EARFCN) to specify the operating frequency. The Timing Advance (TA) parameter was also measured to estimate the device's approximate distance from the connected base station, providing insights into signal propagation and coverage range.

B. *Evaluation of measurements results*

To facilitate the interpretation of measurement results, geospatial heatmaps were employed, with RSRP values serving as the primary visualization metric (see Fig. 5 and Fig. 6 for LTE-M and NB-IoT heatmaps, respectively). These heatmaps provide a spatial representation of signal distribution

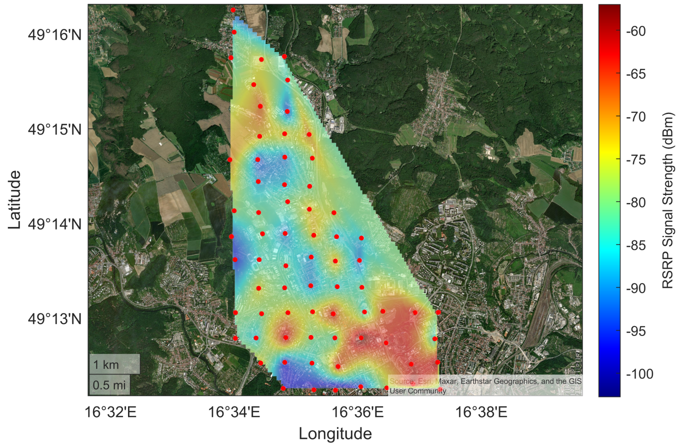

Fig. 5. Geographical distribution of RSRP for LTE-M (Band 8).

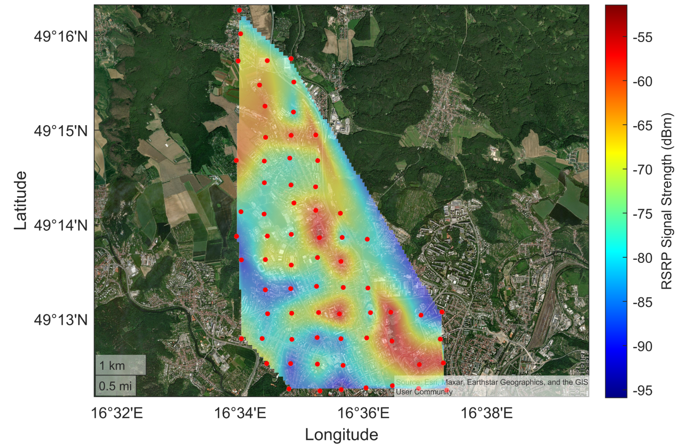

Fig. 6. Geographical distribution of RSRP for NB-IoT (Band 20).

across the surveyed region, highlighting areas with strong, moderate, and weak signal strength.

Analysis of the generated heatmaps reveals notable variations in signal strength, reflecting the heterogeneity of network performance across different environments. Densely populated urban areas exhibit stronger and more uniform signal coverage, attributed to a high density of base stations and optimized network infrastructure. In contrast, peripheral and industrial zones display greater signal fluctuations, with certain areas experiencing weaker coverage due to increased physical obstructions, interference, or a lower density of network infrastructure.

The observed distribution of RSRP values underscores the importance of geospatial signal analysis for optimizing IoT network deployments. Identified weak-signal areas may indicate potential coverage gaps, necessitating network enhancements, such as additional base stations or parameter adjustments to improve reliability. Furthermore, these findings can be leveraged to validate predictive network models, allowing for improved planning of future IoT deployments in diverse urban environments.

Beyond coverage evaluation, the insights derived from this dataset can support strategic IoT device placement, ensuring that critical infrastructure—such as smart meters, environmental sensors, and industrial monitoring systems—is deployed in locations with adequate connectivity. Additionally, this research provides a benchmark for future expansions, enabling a longitudinal assessment of how network improvements impact IoT accessibility over time.

IV. Conclusion

This study validates an optimized 5G-IoT tester for LTE-M and NB-IoT assessments This study presents the development and application of an optimized 5G IoT tester, designed to enhance the efficiency and accuracy of network measurement campaigns. The improved hardware and software architecture of the device enables precise, reliable, and scalable data collection, making it a valuable tool for evaluating real-world LTE-M and NB-IoT network performance. The measurements conducted with the optimized tester provide detailed geospatial insights into signal strength distribution, highlighting the impact of network infrastructure, environmental conditions, and urban planning on IoT connectivity.

The heatmap visualizations derived from the collected dataset effectively illustrate the variability in signal reception across the surveyed area, identifying both well-covered regions and zones with weaker connectivity. These findings contribute to network optimization efforts, enabling strategic IoT deployment and predictive modeling for improved coverage planning. Furthermore, the validated methodology ensures that future measurement campaigns maintain high reliability and consistency.

As part of ongoing research, the dataset will be expanded to additional regions, allowing for a more comprehensive assessment of network conditions across diverse environments. The extended dataset will further refine coverage predictions and support long-term optimization strategies for mobile IoT networks. By continuously improving measurement capabilities and expanding the scope of analysis, this work lays a foundation for more efficient and data-driven IoT deployments in both urban and rural settings.

References

[1] Y. M. Rind, M. H. Raza, M. Zubair, M. Q. Mehmood, and Y. Massoud, "Smart energy meters for smart grids, an internet of things perspective," *Energies*, vol. 16, no. 4, 2023. [Online]. Available: https://www.mdpi.com/1996-1073/16/4/1974

[2] P. Palurík and R. Dvořák, "Hardware design of mobile probe for validating 5g-iot technologies," in *Proceedings II of the 30th Conference STUDENT EEICT 2024: Selected papers*, ser. 1. Brno University of Technology, Faculty of Electrical Engineering and Communication, 2024, pp. 161–165.

[3] M. I. Products, *MAX17048/MAX17049 - 3µA 1-Cell/2-Cell Fuel Gauge*, 2016.

[4] R. T. Corporation, *RT6154A/B High Efficiency Single Inductor Buck-Boost Converter*, 2024.

[5] N. Semiconductors, *PCF2131: Nano-Power Highly Accurate RTC with Integrated Quartz Crystal*, 2025.

[6] C.-W. Yau, S. Jewsakul, M.-H. Luk, A. P. Y. Lee, Y.-H. Chan, E. C. H. Ngai, P. W. T. Pong, K.-S. Lui, and J. Liu, "Nb-iot coverage and sensor node connectivity in dense urban environments: An empirical study," *ACM Trans. Sen. Netw.*, vol. 18, no. 3, Sep. 2022. [Online]. Available: https://doi.org/10.1145/3536424

Smart Meter Emulator

David Kohout
Department of Telecommunications
Brno University of Technology
Brno, Czechia
kohout@vut.cz

Tomas Lieskovan
Department of Telecommunications
Brno University of Technology
Brno, Czechia
lieskovan@vut.cz

Petr Mlynek
Department of Telecommunications
Brno University of Technology
Brno, Czechia
mlynek@vut.cz

***Abstract*—This paper presents the design and development of a smart meter emulator based on the DLMS standard, specifically designed for performance, security, and processing testing of new Head-End Systems (HES) as part of Automated Meter Management. A HES systems are used by utility companies to periodically read data from large numbers of smart electricity meters. The emulator supports the simulation of hundreds of thousands of meters, enabling comprehensive evaluation of the HES's ability to handle high volumes of data, assess security vulnerabilities, and ensure overall system performance. Additionally, the emulator can be employed for training purposes, providing an effective tool for both system testing and personnel education in utility and educational environments.**

***Index Terms*—AMM, DLMS, Emulator, Performance Test, Smart Meter, Virtualization**

I. Introduction

The massive digitalization of industry and energy has introduced new challenges that must be addressed. Both existing and emerging systems face cybersecurity concerns and various threats, where an unsecured low-level element creates vulnerabilities compromising higher levels of the entire system. In this context, the energy sector is classified as critical infrastructure both within the European Union and the Czech Republic.

Due to these factors, in a live energy infrastructure, testing new security or communication solutions, integrating new components into the existing energy infrastructure, or evaluating firmware updates, data center functionalities, emergency response plans, and cybersecurity threats is not feasible under normal operating conditions. This constraint is primarily due to the fundamental requirement for high system availability in both the energy and data layers, as mandated by energy regulations and the necessity for real-time remote control.

The smart meter emulator was developed to address these challenges. This emulator can simulate hundreds of thousands of smart meters, enabling their use in a controlled test environment for evaluating new data collection systems (Head-End Systems, HES), developing and testing new functional processes, deploying advanced security algorithms, and assessing the overall cybersecurity of the entire infrastructure.

The proposed solution is designed for deployment within the infrastructure of an electricity distributor (utility), where it facilitates comprehensive testing in a secure and controlled environment. The emulator is implemented as a pre-configured virtual machine (VM), requiring only deployment within the target infrastructure.

II. Background

A. Related Work

Smart meter emulation plays a crucial role in testing and optimizing utility reading systems. A handful of commercial solutions are widely available for various testing purposes:

- Kalkitech DLMS Million Meter Simulator [1] – Simulates up to a million DLMS meters for large-scale performance testing. However, it lacks DLMS security features and is only available as a cloud solution, which may pose security concerns for utilities.
- Gurux DLMS Simulator [2] – Demonstrates the use of an open-source library to create a virtual smart meter but requires significant development.
- Grid eXchange Fabric DLMS Simulator [3] – An open-source IoT platform that can function as a virtual smart meter. However, it currently supports only a limited number of objects and has restricted security features.

Academic contributions also provide valuable insights. However, most available papers on smart meter emulation focus primarily on generating consumption values. Some studies utilize emulation as a testing tool for developing load-balancing algorithms [4], [5], while others explore AI-generated consumption data [6]. Additionally, some research aims to develop custom hardware and software to redefine electricity meters as fully compatible IoT devices within decentralized networks [7].

B. Smart Metering

Smart metering is a relatively new way of managing the measurement of electricity. In this context there is another related term: Automated Meter Management (AMM). AMM is a system that enables remote monitoring, reading, and management of utility meters, such as electricity, water, and gas meters. It leverages communication technologies to automate data collection and transmission, eliminating the need for manual meter readings.

Head-End System (HES) is a system used by utility companies to perform remote management, read consumption values, and perform additional computations over the collected consumption data. It acts as the central hub for collecting, storing, and processing critical data from smart meters deployed across the utility's extensive network.

The HES facilitates functions such as billing, load forecasting, anomaly detection, and system diagnostics. It also supports communication with various devices, ensuring timely updates and efficient data transfer. Furthermore, HES enables the monitoring and management of metering infrastructure, ensuring optimal operation, security, and integration with other utility management systems.

C. DLMS Standard

The DLMS standard is a very complex framework maintained by the DLMS User Association [8]. It is documented across four main volumes, commonly known as the Colored Books due to their distinct colors: Green, Blue, Yellow, and White. The first two books are the core foundation of the standard.

The Green Book [9] defines the fundamental messaging part of DLMS and also it provides the cybersecurity mechanisms. It specifies protocols for secure data transmission, authentication mechanisms, and other protective measures to protect the sensitive information. The Blue Book [10] details the internal structure of the standard, including the use of interface classes and objects for data storage. These objects store key measurements such as instantaneous voltage, current, and total energy consumption while also providing configuration options within the DLMS framework. Smart meters can contain hundreds of these objects to manage both configuration settings and measurement data.

D. DLMS Objects

Smart meters using DLMS provide access to various data values stored in as objects, such as real-time voltage and current measurements, total energy consumption, and historical records stored in profile objects. All about object creation is described in the Blue Book [10]. The standard also incorporates advanced billing features, allowing meters to monitor billing cycles, handle electricity tariffs, and accurately measure consumption. Moreover, DLMS defines key objects for configuring communication protocols, setting security parameters, and managing access levels, ensuring efficient and secure functionality.

For the smart meter emulator used for performance testing, the most needed object is the Profile Generic (PG) object, which can store historical consumption values. The PG objects can capture the values of other objects at specific times. For example, Load Profile 1 (LP1) is typically recorded every 15 minutes and stores consumption, generation, and other qualitative values (exact values vary between each utility).

E. DLMS Security

Cybersecurity is also a big part of the DLMS standard, but a comprehensive exploration of its security features falls outside the scope of this paper. However, DLMS security can generally be divided into connection authentication and data protection. The data protection is managed by the DLMS Security Suite, which defines the encryption algorithms and security protocols in use. For a more in-depth discussion on DLMS security, please refer to the cited studies [11]–[13].

III. Designing the Emulator

The development of the emulator began as a basic DLMS server, designed to serve as a flexible and quickly deployable clone of a real smart meter. Initially, it provided static values, enabling efficient client-side application development.

Over time, the server was expanded to include essential configuration options, enabling modified values set by the client application to be saved and reused for additional tasks in training scenarios during classes and instructional sessions. Articles discussing the use of virtualized smart meters for training purposes are presented in [13], [14].

Further enhancements introduced support for multiple smart meter instances running simultaneously within the application. This milestone marked the true evolution of the project into a fully functional smart meter emulator. Early builds supported up to 10 emulated meters, but the foundation was laid for more advanced scalability.

The emulator can generate thousands of meters, limited by port allocation rather than the OS. While an OS supports up to 65,535 ports, many are reserved. To avoid conflicts, we use ports 10,000–60,000, allowing up to 50,000 meters, with one port reserved for management. This range ensures reliable performance based on empirical testing.

In summary, the emulator can generate up to 50,000 meters within a single OS. For much larger scaling, the emulator is installed in a pre-configured VM, which can be replicated multiple times to achieve the desired number of emulated meters. Each meter is addressed by combining the VM's IP address with a specific port assigned to that meter. The deployment process is described in Section IV.

A. Requirements

During the development process, various requirements were identified. Some of these requirements apply only to specific use cases. The key requirements can be outlined as follows:

1) **Easy configuration**: The emulator should be easily configurable via a configuration file or command-line.
2) **Object configuration**: DLMS objects should be stored in standalone XML files for modularity and ease of modification.
3) **Security features**: The emulator should support DLMS Security Suite 2, including public key cryptography, digital signatures, and certificate-based authentication.
4) **Generating consumption values**: The emulator should dynamically generate consumption data to closely resemble real consumption patterns.
5) **Scalability**: It should be possible to easily generate a large number of emulated meters.
6) **Simulating network limitations**: To accurately mimic a real meter, the emulator should introduce not only delays but also other network issues such as jitter, packet loss, and bandwidth constraints. These factors reflect the challenges of real-world communication technologies (e.g., LTE Cat. M1, NB-IoT).

7) **Simulating outages**[1]: Some emulated meters should become unavailable to simulate possible outages. The HES should compensate for this by predicting consumption.
8) **Persistence of changes**[2]: All modifications should be retained after the server is shut down or restarted.
9) **Simulating events**[3]: The emulator should be capable of generating unusual events and alarms to populate event logs with some realistic data.
10) **Generating push alarms**[3]: The emulator should send alarms when anomalies are detected (e.g., when the meter cover is opened). This needs an event generator to be fully usable.

Most of these requirements are already implemented, with some working to a limited extent. Outage simulation is currently achieved by modifying firewall rules. Persistence of changes is only practical for a small number of meters. Push messaging is currently limited to manual use. Lastly the event simulation has not yet been implemented at a functional level.

B. Configuration

In the current state of the emulator, the configuration is managed through multiple files. The key files required for proper and stable operation are described in detail below:

- **Main Emulator Settings XML file**
  - Defines all configurable parameters, including paths to other configuration files.
- **List of serial numbers and generation parameters**
  - Specifies the port, meter name, meter serial number, and meter system title.
  - Defines consumption generation parameters, including installation date, generation factor, consumption factor, and installed main breaker.
- **File containing objects** (divided into 2 files)
  - One defines common objects that are stored in memory only once for all emulated meters.
  - The other specifies objects unique to each emulated meter (e.g., invocation counter, security setup, association, etc.).
- **Server ID file**
  - Contains the server ID, which is used to select the correct name file and/or certificate file.
- **Run script**
  - Basic shell script for launching the emulator. Some configuration options can be overridden using command-line parameters.

This entire process of setting up the virtual smart meter could be efficiently managed using a Docker Compose file, which would facilitate automated deployment and streamline the setup. Future research will further investigate this approach, evaluating its potential benefits and challenges.

[1]This is currently achieved through scripts that modify firewall rules. However, it could also be implemented directly in the emulator code.

[2]Currently used only for training scenarios, as storing data for a large number of emulated meters would be too resource-intensive.

[3]These features are only partially implemented, either as separate commands or standalone configurations.

C. Consumption Generation

For performance testing, dynamic data values are essential. If consumption data consisted only of static values, a single emulator would suffice. However, HES stores these values in databases and applies computational algorithms to analyze data for controlling energy flow across the grid, managing billing, sharing information with regulators and customers, etc. Additionally, databases may apply compression to the data, and repetitive values could lead to a high compression ratio, potentially distorting performance results.

To have a greater impact on the HES and test its capabilities under even more demanding conditions, each emulated meter generates unique random consumption values. However, consumption is not entirely random, as it must remain consistent for the same time period if read multiple times. Therefore, consumption is generated using a linear function with the addition of pseudo-random deviations. This process depends on consumption parameters as well as the exact time and date of the requested data. All random values are generated using a specific seed derived from the meter's serial number and the time corresponding to the requested data.

For each time period, consumption values are generated, along with power factor and voltage for each phase (within the range of the typical European voltage of 230V ± 10%). Consumption is distributed across all three phases using a random allocation. Based on these values, the remaining necessary parameters can be derived accordingly.

Each utility defines its objects slightly differently. Most objects are the same (because they are defined by the standard itself), but, for example, the LP1 profile, which contains historical consumption values, is always utility-dependent. Some utilities use only the value representing consumption for the past time interval, while others use a cumulative value. The cumulative value includes the total consumption measured by the meter from the beginning up to the given time interval. Implementing the cumulative value is more complex due to data continuity requirements (this was addressed using a semi-random linear function).

Another challenge arises when utilities differentiate between low and high tariffs, meaning only one value should increase during a specific time period. These challenges also apply to energy generation, such as when a customer has solar panels.

D. Implementation

The smart meter emulator is implemented in Java and uses the Gurux DLMS Library [15]. This library currently offers the best implementation of the DLMS standard. The emulator runs on Java version 21, which is the latest long-term support version. One advantage of using this version is its support for virtual threads. In our implementation, virtual threads manage connections from server sockets. The server socket opens a port and then waits for incoming connections. Once a connection is established, it is assigned to a separate thread dedicated to a specific emulated meter. This thread handles all messages, power generation, and encryption. Once the connection is closed, the thread is destroyed.

IV. EMULATOR DEPLOYMENT

The emulator can be used and deployed in multiple ways. For a small number of meters, it can be installed on any Linux or Windows machine. However, for larger-scale deployments requiring more emulated meters, a more advanced setup is needed. Due to port limitations in networking, the emulator is pre-configured in a VM, supporting up to 50,000 meters per instance. For additional meters, multiple VM instances must be replicated.

Figure 1 illustrates how the emulator can be deployed within a utility's infrastructure. In this scenario, emulation is primarily used for testing the HES system, which requires access to all VMs hosting emulated meters (traffic here will contain only DLMS messages). For easier management, an additional VM can be introduced to test individual meters and control the emulator application. When the emulator operates within a closed infrastructure, the only externally accessible VM required is the Emulator Controller.

Additionally, to facilitate future configuration updates, an accessible Git service (either public or locally hosted on the controller) can be used to update all emulator instances.

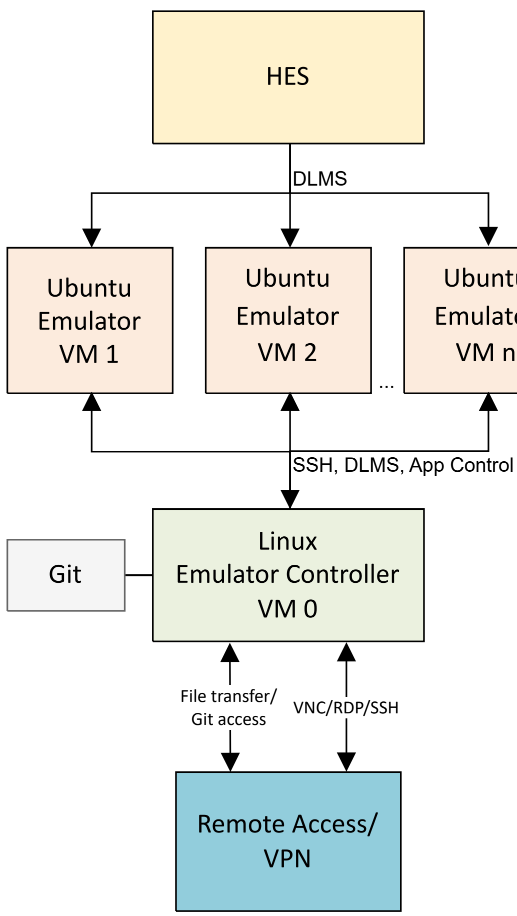

Fig. 1. Emulator Deployment Architecture

A. Emulator HW Requirements

Each implementation of virtual meters is unique, requiring an individualized deployment approach. The application loads all objects into RAM, so it's important to assess whether full or selective virtualization is needed, as this affects RAM capacity.

The Security Suite (SS) also plays a role, with more complex encryption algorithms increasing CPU usage. For instance, SS0 has a lower processing load than SS2.

Emulating many meters demands significant hardware resources. A single emulator VM can efficiently emulate 20,000–50,000 meters with the following tested configuration:

- **Operating System**: Ubuntu Server 24.04.2
- **CPU**: 2-8 cores[4]
- **RAM**: 16-32 GB[4]
- **Disk**: 25 GB
- **Required Packages**:
  - SSH
  - Java 21
- **Access Requirements**:
  - **ICMP**: Ping from control VM
  - **DLMS**: From HES (max 50,000 ports)
  - **SSH/22**: From control VM

To optimize performance and resource allocation, the following considerations should be taken into account:

- **Efficient Object Management**: Virtualizing only essential objects reduces memory consumption without affecting core functionalities.
- **Security vs. Performance Trade-off**: Deployments with higher security levels should allocate additional CPU resources to handle cryptographic operations efficiently.
- **Scalability Planning**: The system should be tested under expected peak loads to ensure stability, with an emphasis on dynamic resource scaling where necessary.

B. Challenges

The main challenge is the deployment process. The smart meter emulator is currently distributed as a VM, simplifying initial deployment but adding operational complexity. Maintaining VMs requires managing IP addresses, software updates, and configuration changes across multiple VMs, which increases overhead.

Another challenge is handling large numbers of IP addresses. Each VM can only host up to 50,000 meters due to TCP port limitations. Simulating a million meters would require a minimum of 20 VMs. This creates an unconventional network setup, where meters share the same IP but use different ports, unlike real-world deployments where each meter has a unique IP address. This challenge arises only when the HES does impose a limitation that restricts a single IP to be used only once, or when the HES does not support addressing by IP and TCP port.

[4]This hardware requirement is highly dependent on the load, the total number of concurrent readings, and the volume of data being read.

Several potential solutions exist, but each comes with its own set of limitations:

1) **NAT mapping**: Assign multiple IPs to a VM, using NAT to map external IPs to port 4059.
   - **Advantages**: Automation via scripting.
   - **Disadvantages**: Requires a large IP pool (e.g., a /16 subnet), and may cause router compatibility issues.
2) **IP Hijacking Technique**: Configures the OS to respond to multiple IPs within a range, mimicking many IP addresses.
   - **Prerequisites**: Router must route a /16 block to the VM, and the HES should support multiple ports.
   - **Disadvantages**: Cannot manage individual connections; HES must handle IP-port pairs.
3) **Docker-Based Solution**: Uses Docker networking for efficient management of virtual smart meters.
   - **Advantages**: Centralized management, scalability, and easy deployment.
   - **Challenges**: Conceptual phase, but simplifies network management.

Given these challenges, it is worth considering a transition to Docker containers for future deployments. Containerization would offer centralized management, excellent scalability, and—when combined with Kubernetes—a streamlined approach to distributing workloads across computing nodes. This shift would bring several key advantages:

- **High Availability**: By orchestrating containers efficiently, the system could ensure minimal downtime and robust failover mechanisms.
- **Simplified Deployment**: Container images can be easily distributed and deployed in a consistent manner across different environments.
- **Effortless Configuration Management**: Changes can be applied at the container level without requiring individual modifications to each instance.
- **Optimized Resource Utilization**: Unlike traditional VMs, containers share the underlying OS kernel, reducing resource consumption and improving performance.

V. Testing

The smart meter emulator is already being used in multiple configurations across various domains. The following are key areas where the emulator is currently utilized:

- **Performance testing**: As load generator for evaluating new HES systems performance for Czech utility companies: EG.D (500,000 meters) and ČEZ (800,000 meters).
- **Education and training**: Supporting cybersecurity education in the energy sector through integration within the BUTCA platform [16].
- **Field measurements**: Assisting with on-site measurements for analyzing communication parameters of technologies like NB-IoT and LTE Cat-M1 by generating real DLMS traffic. This includes measuring data volumes, throughput, latency, penetration, and security aspects.

VI. Future Plans

The current emulator can still be expanded and improved. One of the planned feature is a control application that will enable remote management of all connected VMs. This application will allow for the simulation of outages, the triggering of alarms, and real-time configuration changes without the need to manually connect and change each VM's configuration. Additionally, this system could facilitate downloading updated configurations directly from a Git branch, where all necessary files will be stored.

Regarding the emulator itself, improvements can be made in consumption generation to produce more advanced consumption patterns. Another enhancement involves developing a backend for generating alarms, events, and push messages. Finally, one of the key planned features is implementing more objects with dynamic values, making them data-driven rather than hard-coded within the emulator. This will enable the emulator to be more universal and easily expandable.

VII. Conclusions

This paper presents the design, development, and deployment of a highly scalable and customizable smart meter emulator based on the DLMS standard. The emulator addresses critical challenges in the energy sector by enabling comprehensive performance, security, and processing testing of Head-End Systems in a controlled environment. It supports the simulation of hundreds of thousands of meters, providing utility companies with a robust tool to evaluate system scalability, assess security vulnerabilities, and ensure overall infrastructure reliability. Additionally, the emulator serves as a valuable resource for training and education, enhancing cybersecurity awareness and operational readiness in the energy sector.

The emulator's ability to dynamically generate realistic consumption data, simulate communication delays, and support advanced DLMS security features makes it a versatile solution for both testing and training purposes. Its deployment as a preconfigured VM ensures ease of use and scalability, while ongoing developments, such as the integration of Docker-based solutions and remote management capabilities, promise to further enhance its functionality and usability.

Future work will focus on refining consumption generation algorithms, expanding dynamic object support, and developing a centralized control application for seamless management of large-scale deployments. By addressing these enhancements, the emulator will continue to evolve as a critical tool for utility companies, enabling them to meet the growing demands of modern energy infrastructure while maintaining high standards of performance, security, and reliability.

Acknowledgment

This publication was supported by the project "The Energy Conversion and Storage", funded as project No. CZ.02.01.01/00/22_008/0004617 by Programme Johannes Amos Comenius, called Excellent Research.

REFERENCES

[1] Kalkitech, “DLMS million meter simulator,” accessed on 21 February 2025. [Online]. Available: https://kalkitech.com/products/dlms-software/dlms-million-meter-simulator/

[2] Gurux, “Gurux DLMS Simulator,” accessed on 21 February 2025. [Online]. Available: https://www.gurux.fi/Gurux.DLMS.Simulator

[3] G. e. Fabric, “Grid eXchange Fabric,” accessed on 21 February 2025. [Online]. Available: https://grid-exchange-fabric.gitbook.io/gxf/protocols/dlms/devicesimulator

[4] A. A. Mohamed and O. A. Mohammed, “Real-time load emulator for implementation of smart meter data for operational planning,” in *2012 IEEE Power and Energy Society General Meeting*, 2012, pp. 1–6.

[5] A. Elsayed, A. F. Ebrahim, H. Mohammed, and O. A. Mohammed, “Design and implementation of ac/dc active power load emulator,” in *SoutheastCon 2015*, 2015, pp. 1–5.

[6] S. Chai and G. Chadney, “Faraday: Synthetic smart meter generator for the smart grid,” 2024. [Online]. Available: https://arxiv.org/abs/2404.04314

[7] M. Orlando, A. Estebsari, E. Pons, M. Pau, S. Quer, M. Poncino, L. Bottaccioli, and E. Patti, “A smart meter infrastructure for smart grid iot applications,” *IEEE Internet of Things Journal*, vol. 9, no. 14, pp. 12 529–12 541, 2022.

[8] DLMS User Association, “DLMS UA – the smart link between consumption and supply,” accessed on 21 February 2025. [Online]. Available: https://www.dlms.com/

[9] ——, “Green Book Edition 10, DLMS/COSEM Architecture and Protocols, DLMS UA 1000-2 Ed. 10,” 2020.

[10] ——, “Blue Book Edition 14, COSEM Interface Classes and OBIS Object Identification System, DLMS UA 1000-1 Ed. 14,” 2020.

[11] T. Lieskovan, J. Hajný, and P. Číka, “Smart grid security: Survey and challenges,” in *11th ICUMT*, 2019.

[12] D. Kohout, T. Lieskovan, and P. Mlýnek, “Smart metering cybersecurity—requirements, methodology, and testing,” *Web of Science*, vol. 23, no. 8, pp. 1–21, 2023.

[13] D. Kohout, W. Lazarov, T. Lieskovan, and P. Mlynek, “Sandbox environment for offensive and defensive training in smart metering,” in *Advances and Trends in Artificial Intelligence. Theory and Applications*. Singapore: Springer Nature Singapore, 2024, pp. 43–55.

[14] T. Lieskovan, D. Kohout, and J. Frolka, “Cyber range scenario for smart grid security training,” *e & i Elektrotechnik und Informationstechnik*, vol. 140, no. 5, pp. 1–8, 2023.

[15] Gurux, “Gurux DLMS Library,” accessed on 21 February 2025. [Online]. Available: https://www.gurux.fi/

[16] Brno University of Technology, “BUTCA – CYBER ARENA,” accessed on 21 February 2025. [Online]. Available: https://butca.vut.cz/en/

ptnetinspector: A Practical IPv6 Scanner for Network Reconnaissance

1st Viet Anh Phan
Department of Telecommunications
Brno University of Technology
616 00 Brno, Czech Republic
243760@vut.cz

2nd Jan Jeřábek
Department of Telecommunications
Brno University of Technology
616 00 Brno, Czech Republic
jan.jerabek@vut.cz

3rd Roman Kümmel
CEO of HACKER Consulting Ltd.
Czech Republic
r.kummel@hacker-consulting.cz

***Abstract*—The rapid expansion of IPv6 has introduced new challenges in network reconnaissance and vulnerability assessment. In this paper, we present ptnetinspector, a dedicated IPv6 scanner for local environments. While existing IPv6 tools rely on traditional methods that often miss active nodes or specific address types, ptnetinspector employs modern scanning strategies to uncover more IPv6 addresses (including SLAAC, DHCPv6, and manual assignments) and accurately map node roles. Our evaluation shows that ptnetinspector not only discovers additional active addresses and hosts but also identifies vulnerabilities unique to IPv6 protocol implementations, providing a robust foundation for precise network reconnaissance and proactive security in modern IPv6 environments.**

***Index Terms*—IPv6, Reconnaissance, Vulnerability, Scanning, Network Security**

I. Introduction

The transition to IPv6 expands the address space while introducing distinct addressing methods like SLAAC, DHCPv6, and manual configuration, alongside protocols such as Neighbor Discovery Protocol (NDP) and Extension Headers. Hosts in IPv6 environments behave differently than in IPv4, rendering traditional scanning techniques ineffective due to sparse address distribution, multicast reliance, and NDP-driven address resolution. IPv6 also introduces new vulnerabilities, including insecure SLAAC implementations vulnerable to rogue router advertisements, NDP spoofing, extension header manipulation for evasion, and risks in dual-stack systems from misconfigured transition mechanisms. These changes demand specialized tools and strategies for accurate network mapping, host discovery, and vulnerability assessment in IPv6 environments.

Although tools like Nmap [2] have been adapted to IPv6 (using the `-6` flag), they generally depend on pre-defined target lists and can overlook active IPv6 addresses on hosts with multiple assignments. Similarly, the THC-IPv6 toolkit [3] and fi6s [4] are geared toward specific attack vectors or rapid scanning, but they do not offer a comprehensive solution for complete network reconnaissance. Furthermore, while the SI6 Networks IPv6 Toolkit [5] excels in diagnosing connectivity and configuration issues, it lacks integrated mechanisms to enumerate every IPv6 address advertised by a host.

This work is supported by Ministry of the Interior of the Czech Republic under Grant VK01030019.

To overcome these shortcomings, we introduce **ptnetinspector**[1], a dedicated IPv6 scanner designed specifically for local network penetration testing. This tool is part of **Penterep**[2] [1], a platform for complex penetration testing. Using an innovative approach, **ptnetinspector** can systematically discover all IPv6 addresses associated with a host, accurately map network topology and node roles, perform detailed service detection and perform targeted vulnerability assessments. This unified methodology provides security professionals with a holistic tool that exceeds the capabilities of existing solutions.

II. Related work

A. Nmap (IPv6 Mode)

Nmap's `-6` mode uses IPv6-specific scripts (e.g., `targets-ipv6-multicast-slaac`, `-invalid-dst`) to send ICMPv6 Router Solicitation, Echo Requests, and malformed packets to multicast addresses (e.g., `ff02::1`), triggering SLAAC based address disclosures, host activity confirmation, and vulnerability exposure via error messages. Dictionary-based probes and Multicast Listener Discovery map nodes and multicast groups, enabling detailed IPv6 topology analysis.

B. THC-IPv6 Toolkit

The `alive6` tool actively probes multicast addresses (`ff02::1`) with ICMPv6 Echo Requests and Neighbor Solicitations to enumerate active hosts. Passive detection via `detect-new-ip6` identifies real-time node activation through unsolicited Router/Neighbor Advertisements, mapping topology and detecting IPv6 configuration flaws.

C. SI6 Networks' IPv6 Toolkit

`scan6` combines ICMPv6 Echo Requests, Neighbor Solicitations, and multicast queries to elicit host responses. Analysis of Neighbor Advertisements and Router Solicitations maps network structure, identifies misconfigurations, and exposes vulnerabilities in IPv6 protocol implementations.

[1]https://github.com/Penterep/ptnetinspector.git
[2]https://www.penterep.com/

D. Fi6s Scanner

fi6s rapidly discovers hosts via ICMPv6 Echo Requests, Neighbor Solicitations, and UDP probes to high ports, exploiting SLAAC patterns. Targets multicast (`ff02::1`) and link-local addresses, minimizing traffic while bypassing IPv6's address-space scalability challenges.

E. Academic Research on IPv6 Network Reconnaissance

Recent studies have advanced the state-of-the-art in IPv6 reconnaissance by addressing not only address discovery but also topology mapping. For instance, the 6Tree framework (2020) leverages entropy-based techniques to dynamically uncover active hosts within vast IPv6 subnets, demonstrating significant improvements in efficiency over traditional methods [6]. In parallel, approaches such as 6GCVAE (2020) employ deep learning models to generate candidate target addresses, thereby enhancing the precision of scanning activities and reducing false negatives [7].

Existing methodologies for IPv6 reconnaissance have advanced techniques for partial address discovery and scanning efficiency, but remain insufficient to achieve complete visibility of active IPv6 addresses, and identifying protocol-specific vulnerabilities. While machine learning-based approaches improve candidate generation, they struggle with computational overhead, dependency on training data quality, and adapting to evolving network behaviors.

III. Tool Description

This section offers an overview of current design and sets the stage for a detailed discussion of the innovative features integrated into **ptnetinspector**. In the subsequent sections, we will delve into its software architecture, diverse scanning modes, intuitive usage, and robust implementation strategies, all of which contribute to its enhanced capabilities in exhaustive IPv6 address discovery, node mapping, and vulnerability assessment.

A. Software architecture

The **ptnetinspector** tool is a command-line application developed in Python that must be run as the **root** user (via `sudo`) under Linux. The user provides the desired scanning parameters (for example, `-t 802.1x/a/a+/p`, which will be described in Subsection B) along with the network interface and output options. The tool supports four primary scan modes: 802.1x, passive, active, and aggressive. These modes may be used individually or combined for complex scanning scenarios. Fig. 1 shows the overall architecture.

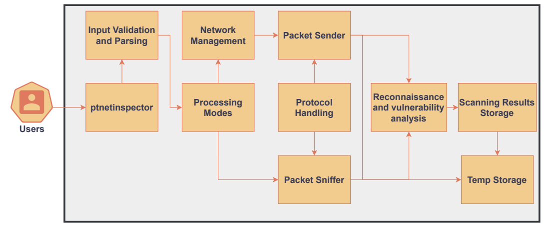

Fig. 1: High-level software architecture of **ptnetinspector**

Input Validation and Parsing is the first component executed when the tool is run. It validates all command-line parameters and ensures that mandatory options (such as scan type `-t` and interface `-i`) are present. The parser interprets complex mode strings (e.g., `802.1x/a/a+/p`) and converts them into an internal configuration that guides the subsequent scanning operations.

After validation, the **Network Management** module checks and configures the system's network settings. It verifies that the specified interface is active, retrieves the associated IP and MAC addresses, and sets up required network rules. For example, it updates IPv6 tables so that packets can be sent without interruption. This module ensures that the environment is properly prepared for both sending and capturing packets.

This module determines which scanning modes have been requested by the user (802.1x, active, passive, aggressive, or a combination). It coordinates the overall scanning strategy by enabling the correct functions in the **Packet Sender** and **Packet Sniffer** modules. The **Processing Modes** module acts as the controller, selecting the scanning workflow based on the chosen parameters.

The **Packet Sender** module is responsible for constructing and transmitting packets according to the corresponding scanning modes, which will be discussed later in the next section. The **Packet Sender** uses the **Protocol Handling** module to build each packet with the correct protocol fields and options.

Running concurrently with the **Packet Sender**, the **Packet Sniffer** module captures all incoming network traffic. It operates in promiscuous mode to record responses from remote hosts. The captured data includes packet headers and payloads, which are stored for further analysis. This module ensures that no response is missed during the scanning process.

The **Protocol Handling** module is the core utility used by both the sender and sniffer. When sending packets, it assembles packets by setting proper header fields, options, and protocol-specific information. When receiving packets, it parses the captured data, extracting meaningful information such as source and destination addresses, protocol types, and other relevant fields. This module is essential for both constructing accurate probes and interpreting the responses during the vulnerability analysis phase.

After the scanning and packet capturing phases are completed, the captured data is processed by the **Reconnaissance and Vulnerability Analysis** module. This module reconstructs the network topology, identifies addressing schemes, enumerates services running on discovered hosts, and detects potential vulnerabilities. The analysis integrates both direct responses and inferred data from protocol behaviors, providing a comprehensive security assessment.

For debugging and further analysis, intermediate data such as raw packet captures and preliminary results are stored in a temporary storage area. This module supports troubleshooting and audit processes by maintaining a log of all temporary data generated during the scan.

Finally, the **Scanning Results Storage** module formats and stores the final output. Depending on the options selected (e.g., JSON output, minimal or detailed terminal output), it generates a report that includes the network topology, discovered addresses, service information, and vulnerability findings. This report is both displayed to the user and saved in temporary storage for later review.

B. Scanning modes

The **ptnetinspector** tool supports four primary scanning modes, each chosen based on the user's intended network assessment objectives as shown in Fig. 2.

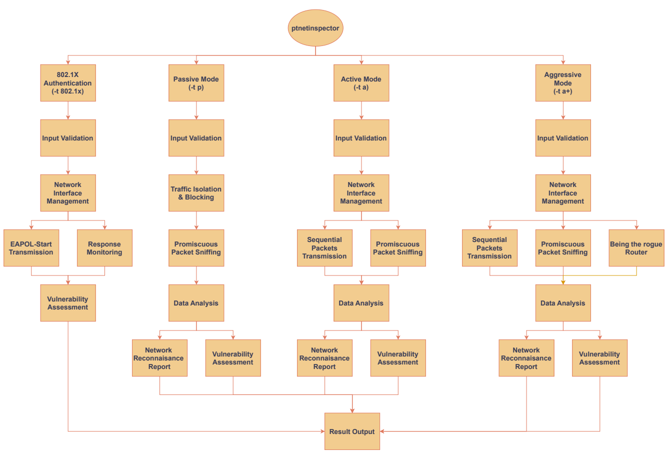

Fig. 2: Scanning modes of **ptnetinspector**

In first mode called 802.1x (using `-t 802.1x`), the tool tests the presence of EAP authentication on the network. The process begins by sending an EAPOL-Start message to trigger the authentication process. The tool then waits for responses from any available network authenticators. A valid response confirms that 802.1x authentication is active. This mode is integrated into the vulnerability assessment by checking whether proper 802.1x security controls are implemented.

Passive mode (using `-t p`) is designed to capture network traffic without introducing any new packets. The tool places the network interface in a listening state and captures all incoming traffic over a specified duration. Since no packets are sent, this method is completely stealthy and non-intrusive. The captured data is later analyzed to reconstruct the network topology, identify active nodes, and assess vulnerabilities. Key advantages of passive mode include:

- Minimal impact on network performance.
- Stealth operation that reduces the risk of detection.
- Ability to capture authentic, real-time network behavior without triggering security alerts.

Active mode (using `-t a`) involves the transmission of a defined sequence of packets to trigger responses from network devices. In this mode, after input validation and network management steps (including updating IPv6 tables), the tool sends sequential probes to discover nodes, build an IPv6 topology, and collect addressing information. Although many tasks mirror those in passive scanning, active mode provides additional data by prompting responses from devices. A detailed algorithm for the packet transmission sequence is provided below.

Algorithm 1 Active Scanning Process

```
procedure ActiveScan
    InitConfig                                   ▷ Setup
    StartSniffer
    SendMLDv2Query                               ▷ MLD Queries
    SendMLDv1Query
    SendMcastEcho                                ▷ Probing
    SendICMP6(128, "bad")
    PingRouters
    SendRouterSolicitation
    QueryMDNS/LLMNR("PTR")                       ▷ Discovery
    if GotResponses then
        h ← GetHostName
        QueryDNS(h, "ANY/A/AAAA")
    end if
    for all h ∈ Hosts do                         ▷ Addr Derivation
        if h.ll ∧ ¬h.global then
            g ← MakeGlobal(h.ll)
            src ← NextAddr
            Ping(src, g)
        end if
    end for
    RepeatScan                                   ▷ Secondary phase
    for all g ∈ GlobalAddrs do                   ▷ Spoofing
        fake ← GenFakeAddr(g)
        src ← PickAddr(fake)
        SendFakePing(src, g)
    end for
    StopSniffer                                  ▷ Cleanup
    Analyze
    Report
end procedure
```

For Active mode, our designed approach follows these steps:

- **Initialization and Setup:** The procedure begins by initializing configuration (setting up parameters and network state) and starting the packet sniffer to capture responses during the scan.
- **MLD Query Phase:** It sends both Multicast Listener queries (version 1 and 2) twice. This helps in discovering IPv6 multicast group information.
- **Probing Phase:** The tool then sends a multicast echo request, followed by an ICMPv6 probe (with option type 128 and a "bad" parameter) to test for malformed or unexpected responses. Next, it pings routers and sends a Router Solicitation to gather network topology data.
- **mDNS/LLMNR Discovery:** A multicast DNS and Link-Local Multicast Name Resolution query for PTR

records are issued. If responses are obtained, the host name is extracted and additional mDNS/LLMNR queries (for ANY, A and AAAA records) are performed to resolve IP addresses.

- **Address Derivation:** For each discovered host that has only a link-local address (without a global address), a global address is derived (based on the EUI-64, and RFC 7217), and a unicast ping is sent to this derived address for testing the availability.
- **Secondary Scan and Spoofing:** The algorithm optionally repeats the scan sequence. Then, for every discovered global address, it generates a fake global source address and sends a spoofed ping. This step helps in testing vulnerabilities related to accepting unauthorized router advertisements or spoofed packets.
- **Cleanup and Reporting:** Finally, the sniffer is stopped, the captured data is analyzed, and a comprehensive report is generated.

Aggressive mode (using `-t a+`) extends Active mode by incorporating a rogue router component. In addition to the standard sequence of active probing packets, the tool also sends fake Router Advertisement (RA) packets. This additional behavior tests whether network devices accept unauthorized RA messages, a vulnerability that can allow an attacker to hijack the role of the default router. Such misconfigurations can lead to traffic redirection, data interception, or bypassing of security controls. Aggressive mode is especially useful for identifying weaknesses in IPv6 RA guard mechanisms and for exposing vulnerabilities related to unauthorized router advertisements.

IV. Implementation and Evaluation

To validate the effectiveness of the **ptnetinspector** tool against widely used network security tools, including Nmap, THC-IPv6, SI6, and fi6s, we have designed an experimental testbed scenario, as illustrated in Fig. 3. We, as the IPv6 scanner (running on a Kali 2024.4), have connected to a local IPv6 network containing seven other nodes. These nodes and their IPv6 configurations are summarized in Table I. Briefly:

- Node 1 (Cisco CSR 1000v Router): Acts as the default gateway. It advertises the global unicast prefix `2001:a:b:c::/64` via SLAAC. The router itself holds a link-local address (EUI-64 derived) and one global unicast address `2001:a:b:c::1`.
- Nodes 2 (Windows 10), 3 (Windows 11), 4 (Kali 2024.4), 5 (Ubuntu 24.04.1 LTS), 6 (macOS Sonoma), and 7 (RHEL 9.5): Each generates two global addresses via SLAAC. One is a *permanent* address (opaque global unicast address using RFC 7217) and one is a *temporary* address (privacy extensions using RFC 4941). All nodes also hold link-local addresses.
- Scanner (Kali 2024.4): Our scanning system is also equipped with link-local and global IPv6 addresses. It actively probes the network using multiple tools and our proposed method.

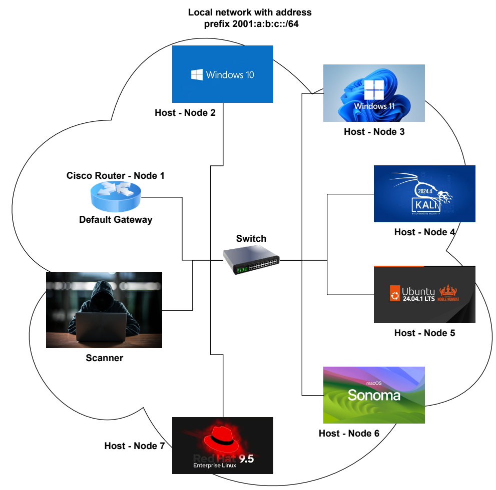

Fig. 3: Network scenario for implementation

TABLE I: Nodes and their IPv6 addressing details in the experimental scenario. LL = Link-Local, GU = Global Unicast

Node	OS / Device	IPv6 Addresses	Notes
1	Cisco CSR 1000v	1 LL (EUI-64) 1 GU: 2001:a:b:c::1	Default gateway
2	Windows 10	1 LL (RFC 7217) 1 GU (RFC 7217) 1 GU (RFC 4941)	Host
3	Windows 11	1 LL (RFC 7217) 1 GU (RFC 7217) 1 GU (RFC 4941)	Host
4	Kali 2024.4	1 LL (RFC 7217) 1 GU (RFC 7217) 1 GU (RFC 4941)	Host
5	Ubuntu 24.04.1	1 LL (RFC 7217) 1 GU (RFC 7217) 1 GU (RFC 4941)	Host
6	macOS Sonoma	1 LL (RFC 7217) 1 GU (RFC 7217) 1 GU (RFC 4941)	Host
7	RHEL 9.5	1 LL (RFC 7217) 1 GU (RFC 7217) 1 GU (RFC 4941)	Host
Scanner	Kali 2024.4	1 LL (RFC 7217) 1 GU (RFC 7271)	Active scanning

The experimental testbed comprises 7 nodes configured with a total of 20 IPv6 addresses. In this experiment, we exclusively utilize the Active mode of our tool, which has proven effective in uncovering all IPv6 addresses, performing node discovery, analyzing network topology, and detecting vulnerabilities. As illustrated in Fig. 4, our evaluation focuses on three key metrics: nodes discovery, IPv6 addresses discovered, and scan time.

IPv6 Addresses Discovered: **ptnetinspector** identifies every address present (20). Nmap is second with 14 total discovered addresses but cannot enumerate permanent global unicast addresses for multiple nodes. THC-IPv6 and SI6 each yield 13 addresses, while missing the link-local address of Node 3 and all permanent global unicast addresses. fi6s detects just 1 easily predictable router address.

Nodes Discovered: **ptnetinspector** and Nmap successfully

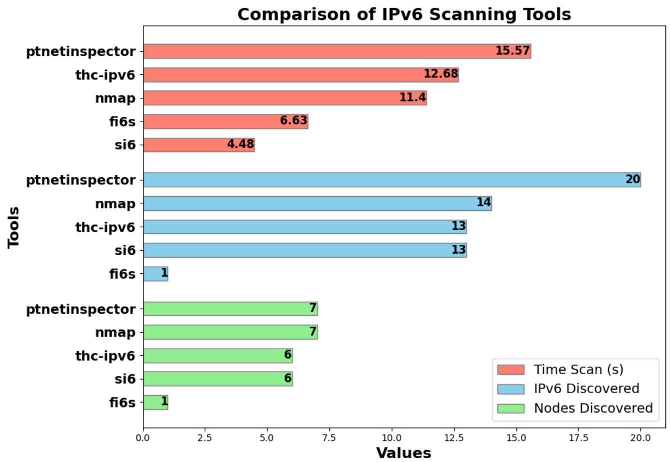

Fig. 4: Results of scanning using different tools

detects all nodes on the network (7), whereas other tools fall short. THC-IPv6 and SI6 each discover 6 nodes, and fi6s only finds 1 node.

Scan Time: The scan time for **ptnetinspector** is the highest at about 15.57 s, reflecting its thorough approach to enumerating all addresses. THC-IPv6 needs 12.68 s, Nmap takes around 11.4 s, while SI6, and fi6s finish faster but discover fewer nodes and addresses. The time difference is acceptable given the more comprehensive coverage provided by **ptnetinspector**. Furthermore, in case of larger network, with higher number of nodes and addresses, the total running time of **ptnetinspector** will not increase significantly.

In addition, we evaluated the discovered IPv6 vulnerabilities (e.g., open services, potential neighbor discovery protocol attacks) and generated a local topology map. While each tool identifies a baseline set of IPv6 exposures, **ptnetinspector** integrates these findings into a comprehensive topology analysis, highlighting the default gateway, ephemeral privacy addresses, and other SLAAC-derived host addresses.

Moreover, **ptnetinspector** also evaluates critical IPv6 and 802.1x vulnerabilities. Our tool performs an in-depth assessment of:

- **802.1x Authentication:** Verifies the presence and proper functioning of EAP-based authentication, ensuring that 802.1x security is active.
- **Router Advertisement (RA) Misconfiguration:** Detects if hosts improperly accept rogue RA packets, which can allow an attacker to impersonate the default router.
- **Neighbor Discovery Protocol (NDP) Issues:** Identifies weaknesses such as spoofed Neighbor Advertisement that could facilitate man-in-the-middle attacks.
- **mDNS and LLMNR Exposure:** Checks for the activation of mDNS and LLMNR services that leaks host information.
- **MLDv1 Acceptance:** Determines if legacy MLDv1 queries are accepted by hosts, which may indicate a security gap.
- **Predictable IPv6 Addresses:** Flags easily guessable addresses (e.g., those generated via EUI-64), which can be exploited by attackers.

Table II summarizes the vulnerability discovery capabilities of **ptnetinspector** versus several popular IPv6 scanning tools.

TABLE II: Vulnerability discovery comparison among IPv6 scanning tools

Vulnerability	ptnetinspector	Nmap	THC-IPv6	SI6	fi6s
802.1x Authentication	Yes	Partial	No	No	No
RA Misconfiguration	Yes	Partial	Partial	No	No
NDP Issues	Yes	Partial	Partial	No	No
mDNS Exposure	Yes	Partial	No	No	No
LLMNR Exposure	Yes	Partial	No	No	No
MLDv1 Acceptance	Yes	Partial	Partial	No	No
Predictable Addresses	Yes	Partial	Partial	Partial	No

As shown in Table II, popular tools such as Nmap provide only partial vulnerability analysis because they focus primarily on enumeration. For instance, Nmap may discover active nodes and open ports but lacks dedicated tests for RA misconfigurations or thorough checks on NDP, mDNS, and LLMNR settings. Similarly, THC-IPv6 and SI6 offer limited insight into these protocol-specific weaknesses, and fi6s often returns only predictable router addresses. In contrast, **ptnetinspector** not only discovers all nodes and addresses but also systematically assesses these critical vulnerabilities.

Conclusion and Future Directions

In summary, **ptnetinspector** provides a complete solution for IPv6 network scanning and vulnerability assessment. It accurately discovers all active nodes and addresses while performing an extensive analysis of vulnerabilities.

Future work will focus on further refining the protocol handling and vulnerability modules, expanding support to additional IPv6 security tests, and optimizing scan performance. However, even as is, **ptnetinspector** represents a significant advancement in IPv6 network security assessment, providing capabilities that fully meet the needs of modern network environments.

References

[1] Willi Lazarov, Pavel Seda, Zdenek Martinasek, and Roman Kummel, ”Penterep: Comprehensive penetration testing with adaptable interactive checklists,” *Computers & Security* 154 (2025): 104399. DOI: 10.1016/j.cose.2025.104399

[2] Nmap Project, “IPv6 Scanning,” https://nmap.org/book/port-scanning-ipv6.html.

[3] THC-IPv6 Toolkit, “THC-IPv6,” available on Kali Linux, https://www.kali.org/tools/thc-ipv6/.

[4] Kloudle, “Scanning IPv6 with fi6s,” https://kloudle.com/academy/scanning-ipv6-with-fi6s/.

[5] SI6 Networks, “IPv6 Toolkit,” https://www.si6networks.com/tools/ipv6toolkit/.

[6] Doe, J., & Smith, A. (2020). 6Tree: Dynamic Discovery of Active Hosts in IPv6 Networks Using Entropy-Based Techniques. IEEE Transactions on Network Science and Engineering.

[7] Lee, K., Zhang, Y., & Chen, L. (2020). 6GCVAE: Deep Learning for Enhanced Target Generation in IPv6 Scanning. Proceedings of the ACM Conference on Security and Privacy in Wireless and Mobile Networks.

Investigating Li-ion Battery Degradation Mechanisms by in-situ SEM Analysis and Related Techniques

David Trochta
Dept. of Electrical and Electronic Technology
Brno University of Technology
Brno, Czech Republic
xtroch00@vut.cz

Ondřej Klvač
Dept. of Electrical and Electronic Technology
Brno University of Technology
Brno, Czech Republic
xklvac02@vut.cz

Tomáš Kazda
Dept. of Electrical and Electronic Technology
Brno University of Technology
Brno, Czech Republic
kazda@vut.cz

***Abstract* — This paper explores the application of in-situ Scanning Electron Microscopy (in-situ SEM) for real-time analysis of lithium-ion (Li-ion) battery materials, enabling high-resolution imaging of structural and morphological changes such as SEI formation, lithium plating, dendrite growth, and particle cracking. Integrating in-situ SEM with techniques like Atomic Force Microscopy (AFM), X-ray Photoelectron Spectroscopy (XPS), and X-ray Diffraction (XRD) enhances battery analysis by providing complementary chemical and structural insights. Emphasizing the unique capabilities of in-situ SEM, this work highlights its potential in studying next-generation battery chemistry and improving battery design and safety.**

***Keyword* — Li-ion, battery, degradation, in-situ, SEM**

I. Introduction

Understanding battery degradation mechanisms is crucial for improving the performance, lifespan, and safety of modern energy storage systems. Li-ion batteries, widely used in consumer electronics, electric vehicles, and grid storage, suffer from various degradation processes that limit their efficiency and reliability [1], [2]. In-situ scanning electron microscopy (in-situ SEM) has emerged as a powerful tool for directly observing these mechanisms at the micro- and nanoscale, providing critical insights into structural and morphological changes occurring during battery operation [3], [4]. This paper aims to highlight the significance of in-situ SEM in battery research, comparing its strengths and limitations with other analytical techniques such as Raman spectroscopy, X-ray diffraction (XRD), transmission electron microscopy (TEM), and atomic force microscopy (AFM). This article uses the newest research to show how in-situ SEM can help find and mitigate battery degradation pathways, as well as how to use it with other analytical techniques.

II. Battery Degradation Mechanisms

Battery degradation in Li-ion systems is a complex interplay of electrochemical, mechanical, thermal, chemical, and environmental factors, each contributing to the overall decline in performance, lifespan, and safety [2]. Electrochemical degradation primarily involves the formation and growth of the solid electrolyte interphase (SEI) layer on the anode. This SEI layer is essential for stabilizing the anode surface, but its continuous growth consumes lithium ions, leading to a gradual capacity fade [1]. Additionally, lithium plating, which occurs during high-rate charging or low-temperature operation, poses significant risks. Lithium metal can deposit on the anode surface, leading to the formation of dendrites that can pierce the separator and cause internal short circuits, potentially resulting in thermal runaway and catastrophic failure [1], [5].

Mechanical degradation arises from the volumetric changes in electrode materials during battery operation. For instance, silicon anodes in so-called advanced Li-ion batteries can experience volume expansion of up to 300% during lithiation, followed by contraction during delithiation [6]. This repeated expansion and contraction induce mechanical stress, leading to electrode fracture and loss of electrical contact within the electrode or current collector. Moreover, electrode particles can crack due to the mechanical strain from repeated cycling, disrupting the conductive network and increasing internal resistance. These mechanical failures are critical as they directly impact the battery's capacity retention and overall cycle life [7].

Thermal degradation is another significant factor, driven by elevated temperatures during battery operation. High temperatures accelerate electrolyte decomposition, producing gases that increase internal pressure and can lead to cell swelling or rupture. In extreme cases, thermal runaway can occur, a self-heating process that results from exothermic reactions within the battery, leading to fires or explosions. The thermal stability of the electrolyte and the heat management within the battery pack are crucial for preventing such hazardous events. [1], [8]

Chemical degradation involves various reactions between battery components that deteriorate performance over time. Transition metals such as cobalt, manganese, and nickel from the cathode can dissolve into the electrolyte and migrate to the anode, leading to a loss of active material and increased impedance [9]. The oxidation of the electrolyte at high voltages produces by-products that can form on the electrode surfaces, further degrading the battery's performance. These chemical interactions are complex and often interrelated, requiring detailed analysis to fully understand their impact on battery health [10].

Environmental factors also play a significant role in battery degradation. Humidity and moisture can lead to the hydrolysis of the electrolyte and corrosion of current collectors, compromising the battery's integrity and safety. Temperature cycling, which involves frequent changes between high and low temperatures, exacerbates mechanical and thermal degradation mechanisms. These environmental stresses highlight the need for robust battery designs that can withstand varying operating conditions.[1], [11]

III. IN-SITU SEM FOR BATTERY ANALYSIS

Scanning Electron Microscopy is a powerful imaging technique that provides high-resolution images of sample surfaces by scanning them with a focused electron beam. The interaction between the electrons and the sample generates various signals, which are detected to form an image. SEM is widely utilised in materials science, biology, and nanotechnology for its ability to reveal detailed topographical, compositional, and crystalline information. The primary imaging mechanism relies on secondary electron emission from the sample surface, which is collected to construct high-resolution topographical images. [12]

In-situ SEM enables real-time observation of battery materials under operational conditions. By integrating an SEM with a battery testing setup, researchers can simultaneously cycle the battery while capturing high-resolution images of electrode materials and other components. This setup typically consists of specialised sample holders (electrochemical cells) that accommodate battery components and facilitate electrical connections, alongside electrochemical workstations (potentiostats) that apply and measure electrical signals, ensuring a direct correlation between electrochemical data and structural observations. [3], [4]

The capabilities of in-situ SEM are extensive, providing insights into dynamic processes such as solid electrolyte interphase (SEI) layer formation and its impact on battery performance. It allows direct visualisations of lithium plating and dendrite growth, phenomena critical for battery safety. Additionally, it captures mechanical degradation mechanisms, including particle cracking, delamination, and structural changes during cycling. In-situ SEM also detects certain changes related to gas evolution and electrolyte decomposition, which are indicative of thermal and electrochemical degradation. [3], [4]

To enhance functionality, various auxiliary tools can be integrated into in-situ SEM setups. Micromanipulators facilitate electrochemical cell assembly within the microscope chamber and, with appropriate shielding, can serve as current and voltage probes. Electrochemical probes ensure accurate measurement connections to the potentiostat [13], while nanoindenters aid in mechanical property analysis [14]. Other tools that can be used include heating or cooling stages [15], gas injection systems [16], and controlled-atmosphere transfer systems [3].

While much of this equipment is commercially available, certain components, including specialised holders and electrochemical cells for in-situ battery analysis, often require custom fabrication. These electrochemical cells typically fall into two categories: open cells and liquid (closed/sealed) cells. Each type has its benefits and drawbacks, so researchers must carefully consider their experimental needs when selecting a suitable cell for their studies. [4]

Open cell configurations are relatively simple to manufacture and assemble but expose the battery to the microscope’s environmental conditions. In deep vacuum conditions, conventional electrolytes, such as lithium salts in organic solvents, evaporate, limiting their usability. Consequently, open cells are more suitable for batteries with solid-state or ionic liquid-based electrolytes. They provide high-resolution imaging but may require low-vacuum or environmental SEM (ESEM) modes to reduce sample charging and better simulate battery operating conditions. [16], [17]

In contrast, liquid cell configurations are completely sealed, allowing the use of conventional electrolytes, such as ether- and ester-based formulations. This setup facilitates in-situ observation of SEI formation and battery processes under conditions resembling commercial batteries. However, the silicon nitride (SiN) observation window reduces spatial resolution [4], and once sealed, liquid cells cannot be modified. Additionally, electrolyte accumulation beneath the observation window can obscure electrode imaging, and excess electrolyte cannot be removed due to the sealed nature of the setup. [18]

Despite its advantages, in-situ SEM presents several challenges. Traditional SEM operates under a deep vacuum, limiting the use of volatile electrolytes. ESEMs and modified setups mitigate this issue by allowing low-vacuum operation but increase experimental complexity and cost. Additionally, electron beam irradiation can damage sensitive battery materials, introducing artefacts that compromise observation accuracy. Sample preparation is another critical challenge, requiring meticulous handling to preserve material integrity. Furthermore, capturing rapid electrochemical processes is constrained by temporal resolution, though advancements in imaging techniques and faster detectors are addressing this limitation. [3], [4]

Following the discussion on the challenges of in-situ SEM, it's important to consider the limitations of energy-dispersive X-ray spectroscopy (EDS) when used alongside SEM for analysing battery materials [12]. Detecting lithium is particularly problematic due to its low atomic number and low X-ray emission, leading to poor signal intensity. Moreover, lithium's propensity to migrate under electron beam irradiation can introduce artefacts, further compromising measurement accuracy. While advanced detectors like windowless EDS systems and optimised acquisition parameters offer improvements in lithium detection, significant limitations remain. Overall, scientists must be cautious when relying solely on EDS for lithium detection in battery material analysis [19].

IV. COMPARISON WITH OTHER ANALYTICAL TECHNIQUES

While in-situ scanning electron microscopy is a powerful tool for real-time observation of battery materials, a comprehensive understanding of battery behaviour requires a multifaceted analytical approach [4]. No single technique can fully capture the complex structural, chemical, and mechanical changes occurring within a battery during operation. This chapter explores complementary techniques that enhance the insights gained from in-situ SEM, including Raman spectroscopy, X-ray photoelectron spectroscopy, transmission electron microscopy and atomic force microscopy. Each of these methods provides unique and valuable information, and when combined, they offer a more complete picture of battery performance and degradation mechanisms. By integrating multiple characterization techniques, researchers can better understand how battery components evolve under various conditions.

A. X-ray diffraction (XRD)

To determine the crystalline structure of materials, X-ray diffraction analyses the diffraction patterns of X-rays interacting with a sample. In in-situ battery research, it is crucial for monitoring phase transitions, crystal structure evolution, and lattice strain during battery operation. The non-destructive nature of XRD allows real-time observation of these structural changes, providing insights into the stability of electrode materials under various cycling conditions. Additionally, it identifies new phases forming during electrochemical reactions, which is essential for understanding battery performance and degradation. However, its spatial resolution is relatively low compared to techniques like SEM, making it challenging to resolve fine structural details at the micro- and nanoscale. The requirement for a high-intensity X-ray source and sophisticated detection equipment adds complexity to experimental setups. Furthermore, XRD is less effective for amorphous materials due to the lack of well-defined diffraction patterns. Despite these limitations, it remains indispensable for understanding the structural dynamics of battery materials, especially when used alongside other analytical methods. [20], [21]

B. Raman Spectroscopy

By utilising inelastic scattering of monochromatic light, typically from a laser, Raman spectroscopy provides information about molecular vibrations and chemical composition. In in-situ battery experiments, this technique is particularly valuable for monitoring chemical and structural changes in electrode materials and electrolytes during operation. The Raman shift, resulting from interactions between laser light and molecular bonds, acts as a fingerprint for identifying specific chemical species and their transformations. The ability to provide detailed chemical and molecular information in real-time is a significant advantage. It can detect phase changes, lithium intercalation, and electrolyte decomposition products, making it versatile for studying both crystalline and amorphous materials. Additionally, Raman spectroscopy can be used to study the distribution of stress and strain within electrode materials, which can impact battery performance. However, its lower spatial resolution compared to SEM or TEM, sensitivity to fluorescence, and potential for laser-induced heating or damage are notable limitations. Nevertheless, its real-time chemical insights complement other techniques like XRD, SEM, and TEM, enhancing the overall understanding of battery processes. Advances such as confocal Raman microscopy and surface-enhanced Raman spectroscopy continue to enhance its applicability and resolution. [22], [23]

C. X-ray photoelectron spectroscopy (XPS)

When it comes to providing detailed surface chemical information with high sensitivity, X-ray photoelectron spectroscopy measures the elemental composition, empirical formula, chemical state, and electronic state of elements within a material by detecting the kinetic energy of photoelectrons emitted upon X-ray irradiation. In in-situ battery experiments, it is particularly valuable for analysing surface chemistry and detecting changes in the chemical states of elements during battery operation. The technique enables the detection and quantification of surface species, monitoring SEI layer formation and evolution, and identifying oxidation states. XPS can also distinguish between different chemical states of the same element, offering insights into the redox processes occurring during battery cycling. However, it primarily probes surface or near-surface regions, which may not fully represent bulk material changes, and requires ultra-high vacuum conditions, complicating experimental setups. Additionally, XPS analysis can be time-consuming and requires sophisticated equipment and expertise. Despite these challenges, it remains a powerful tool for understanding surface reactions and degradation processes, especially when combined with techniques like XRD, SEM, and Raman spectroscopy. Advances such as near-ambient pressure XPS are enhancing its applicability to more realistic conditions. [24], [25], [26]

D. Transmission electron microscopy (TEM)

Providing high-resolution images and detailed structural information, transmission electron microscopy uses a beam of electrons transmitted through a thin sample. In in-situ battery research, it is particularly valuable for observing microstructural changes, phase transitions, and nanoscale features of electrode materials during operation. TEM's primary advantage is its extremely high spatial resolution, allowing researchers to visualise fine structural details at the atomic level. It can reveal morphology, crystallography, and defects within electrode materials, offering insights into battery degradation mechanisms such as particle cracking and phase transformations. TEM can also be combined with techniques like electron energy loss spectroscopy (EELS) and EDS for chemical composition and bonding information. However, preparing thin samples for TEM can be challenging and may introduce artefacts, and the technique requires high vacuum conditions and sophisticated equipment. Additionally, the electron beam can damage sensitive materials, potentially altering their properties during imaging. Despite these challenges, TEM's atomic-scale resolution and detailed structural information make it indispensable for understanding fundamental processes in batteries. Advances in in-situ TEM holders that allow for real-time electrochemical cycling and observation continue to enhance its applicability in advanced battery research. [27], [28]

E. Atomic Force Microscopy (AFM)

Offering a powerful technique for measuring surface topography, mechanical properties, and electrical properties at the nanoscale, atomic force microscopy is particularly valuable in in-situ battery experiments for observing surface morphology and mechanical behaviour of electrode materials during cycling. AFM operates by scanning a sharp tip across the sample surface and detecting forces between the tip and the surface to generate high-resolution images. Its primary advantage is the ability to provide detailed topographical maps and mechanical property data, such as stiffness and adhesion, without requiring a vacuum environment, making it suitable for studying batteries under more realistic conditions. AFM can also measure electrical and electrochemical properties like conductivity and potential, offering insights into electrochemical activity distribution on the electrode surface. However, AFM is generally limited to surface or near-surface measurements, which may not fully represent bulk material behaviour, and imaging can be time-consuming. The tip may also cause damage to fragile and porous battery materials, or the tip can break during scanning. [29], [30]

V. FUTURE DIRECTIONS OF IN-SITU SEM FOR BATTERY RESEARCH AND ANALYSIS

There are many directions that researchers can explore to further enhance the capabilities and broaden the applications of in-situ scanning electron microscopy in battery research. One promising direction involves the development of advanced environmental holders that can precisely control temperature, pressure, and gaseous environments. These holders would enable researchers to simulate real-world battery operating conditions more accurately, providing a deeper understanding of how batteries perform under extreme environmental stresses, such as rapid temperature fluctuations or varying atmospheric conditions. By mimicking actual operational environments, these innovations can help bridge the gap between laboratory tests and real-world applications.

Another significant advancement lies in integrating in-situ SEM with machine learning/AI algorithms. These algorithms, designed for real-time data analysis and predictive modelling, have the potential to significantly enhance the interpretation of complex degradation mechanisms. Through the analysis of large datasets generated during in-situ SEM experiments, machine learning could help identify patterns, correlations, and anomalies that are not immediately apparent through traditional methods. This approach would allow for more accurate predictions of battery lifespan and failure modes, enabling better-informed decisions in battery design and optimisation.

In addition to these advances, improvements in detector technology are crucial for furthering the resolution and sensitivity of in-situ SEM. High-resolution detectors, coupled with novel imaging techniques, could allow researchers to observe even finer structural changes at the atomic level. This would be particularly valuable in identifying early-stage degradation processes, such as the formation of microcracks or delamination, that could ultimately compromise battery performance. One such advancement is the development of windowless EDS detectors. These windowless detectors significantly improve X-ray collection efficiency, enhancing the sensitivity and resolution of elemental analysis. By enabling more precise detection of light elements (such as lithium and oxygen), which are critical in battery materials, windowless EDS detectors offer greater insight into the chemical changes occurring within electrodes and other battery components. This increased sensitivity allows for more accurate mapping of elemental distribution and can help track subtle chemical transformations that occur during battery cycling, providing valuable data for understanding degradation mechanisms in real-time.

Furthermore, combining in-situ SEM with other advanced analytical techniques promises to provide a more holistic understanding of battery materials. For example, atomic force microscopy can complement SEM by providing high-resolution surface topography, and current/potential mapping, which are essential for understanding the electrochemical processes that drive battery operation. The integration of electron backscatter diffraction with in-situ SEM can offer critical crystallographic insights, such as grain orientation and texture evolution, which are important for understanding how material properties affect battery performance and degradation.

Additionally, XPS can offer valuable surface chemical information, especially regarding the SEI layer, which plays a key role in determining battery efficiency and stability. Raman spectroscopy, with its ability to probe vibrational modes, can provide molecular-level insights into phase changes, electrolyte decomposition, and electrode material transformations, further enhancing the understanding of battery chemistry.

The integration of these complementary techniques into in-situ SEM experiments will allow for a more comprehensive analysis of battery materials, capturing both structural and chemical changes in real-time. As in-situ SEM becomes more sophisticated, its application to emerging battery chemistries such as solid-state batteries will yield critical insights into their unique degradation pathways. Understanding these processes will be essential for optimising the design and performance of next-generation energy storage solutions. As these technologies evolve and become more interconnected, in-situ SEM will solidify its role as an indispensable tool for advancing battery research, offering unprecedented insights into battery performance, durability, and safety.

VI. CONCLUSION

In-situ scanning electron microscopy has proven to be an invaluable tool for examining the degradation mechanisms of lithium-ion batteries, providing real-time, high-resolution insights into structural and morphological changes that occur during battery operation. By observing critical phenomena such as SEI layer formation, dendrite growth, and particle cracking, in-situ SEM enhances our understanding of the underlying causes of battery failure and performance decline. The integration of complementary techniques such as atomic force microscopy, X-ray photoelectron spectroscopy, X-ray diffraction, and Raman spectroscopy further enriches the analysis, allowing for a more comprehensive view of battery material behaviour under operational conditions.

Looking ahead, advancements in detector technology, including windowless energy-dispersive X-ray spectroscopy, and the development of advanced environmental holders, promise to significantly enhance the resolution, sensitivity, and applicability of in-situ SEM. Machine learning and AI integration for real-time data analysis will help uncover hidden patterns and predict battery degradation more accurately, fostering more informed decisions in battery design. Furthermore, as in-situ SEM continues to evolve, it will play a pivotal role in exploring emerging battery chemistries, such as solid-state batteries, offering critical insights into their degradation pathways.

In conclusion, in-situ SEM is poised to remain at the forefront of battery research, providing unprecedented opportunities to improve the design, performance, and safety of not only Li-ion batteries but also next-generation energy storage systems. Its potential for real-time, dynamic analysis will be essential in advancing the understanding of battery materials and addressing the challenges posed by degradation in complex battery systems.

Declaration of AI Tools

During the preparation of this work, the authors used Gene.AI (gpt-4_o) for literature review, text enhancement and readability improvement. After using this tool, the authors reviewed and edited the content as needed and take full responsibility for the content of the publication.

Acknowledgement

This work was supported by the specific graduate research of the Brno University of Technology No. FEKT-S-23-8286.

References

[1] J. S. Edge, S. O'Kane, R. Prosser, N. D. Kirkaldy, A. N. Patel, A. Hales, A. Ghosh, W. Ai, J. Chen, J. Yang, S. Li, M. -C. Pang, L. Bravo Diaz, A. Tomaszewska, and M. W. Marzook, "Lithium ion battery degradation: what you need to know", *Physical Chemistry Chemical Physics*, vol. 23, no. 14, pp. 8200-8221, Apr. 2021.

[2] X. Han, L. Lu, Y. Zheng, X. Feng, Z. Li, J. Li, and M. Ouyang, "A review on the key issues of the lithium ion battery degradation among the whole life cycle", *ETransportation*, vol. 1, 2019.

[3] J. Wu, M. Fenech, R. F. Webster, R. D. Tilley, and N. Sharma, "Electron microscopy and its role in advanced lithium-ion battery research", *Sustainable Energy & Fuels*, vol. 3, no. 7, pp. 1623-1646, Jun. 2019.

[4] S. Zhou, K. Liu, Y. Ying, L. Chen, G. Meng, Q. Zheng, S. -G. Sun, and H. -G. Liao, "Perspective of operando/in situ scanning electron microscope in rechargeable batteries", *Current Opinion in Electrochemistry*, vol. 41, 2023.

[5] Y. Yuan, H. Wang, Y. Sun, X. Han, C. Zhu, and M. Ouyang, "The influence of local lithium plating on battery safety and a novel detection method", *Energy*, 2025.

[6] S. Zhang, "Chemomechanical modeling of lithiation-induced failure in high-volume-change electrode materials for lithium ion batteries", *Npj Computational Materials*, vol. 3, no. 1, 2017.

[7] S. -M. Lee, J. -Y. Kim, J. Lee, and J. -W. Byeon, "Evaluation of cracking damage in electrode materials of a LMO/Al-Lix lithium-ion battery through analysis of acoustic emission signals", *Journal of Materials Research and Technology*, vol. 24, pp. 5235-5249, 2023.

[8] S. Li, C. Zhang, Y. Zhao, G. J. Offer, and M. Marinescu, "Effect of thermal gradients on inhomogeneous degradation in lithium-ion batteries", *Communications Engineering*, vol. 2, no. 1, 2023.

[9] L. Britala, M. Marinaro, and G. Kucinskis, "A review of the degradation mechanisms of NCM cathodes and corresponding mitigation strategies", *Journal of Energy Storage*, vol. 73, 2023.

[10] Y. He, Z. Chen, and Y. Zhang, "Strategies for improving cathode electrolyte interphase in high-performance dual-ion batteries", *IScience*, vol. 27, no. 8, 2024.

[11] Z. Wang, Y. Song, Q. Zhao, B. Shi, J. He, and J. Li, "Unveiling the electrochemical degradation behavior of 18650 lithium-ion batteries involved different humidity conditions", *Journal of Power Sources*, vol. 630, 2025.

[12] T. Kogure, "Electron Microscopy", in *Handbook of Clay Science*, Elsevier, 2013, pp. 275-317.

[13] L. -M. Peng, Q. Chen, X. L. Liang, S. Gao, J. Y. Wang, S. Kleindiek, and S. W. Tai, "Performing probe experiments in the SEM", *Micron*, vol. 35, no. 6, pp. 495-502, 2004.

[14] C. D. Fincher, D. Ojeda, Y. Zhang, G. M. Pharr, and M. Pharr, "Mechanical properties of metallic lithium: from nano to bulk scales", *Acta Materialia*, vol. 186, pp. 215-222, 2020.

[15] L. Mele, S. Konings, P. Dona, F. Evertz, C. Mitterbauer, P. Faber, R. Schampers, and J. R. Jinschek, "A MEMS -based heating holder for the direct imaging of simultaneous in-situ heating and biasing experiments in scanning/transmission electron microscopes", *Microscopy Research and Technique*, vol. 79, no. 4, pp. 239-250, 2016.

[16] H. Zheng, D. Xiao, X. Li, Y. Liu, Y. Wu, J. Wang, K. Jiang, C. Chen, L. Gu, X. Wei, Y. -S. Hu, Q. Chen, and H. Li, "New Insight in Understanding Oxygen Reduction and Evolution in Solid-State Lithium–Oxygen Batteries Using an in Situ Environmental Scanning Electron Microscope", *Nano Letters*, vol. 14, no. 8, pp. 4245-4249, Aug. 2014.

[17] D. Chen, S. Indris, M. Schulz, and R. Mönig, "In situ scanning electron microscopy on lithium-ion battery electrodes using an ionic liquid", *Journal of Power Sources*, vol. 196, no. 15, pp. 6382-6387, 2011.

[18] Y. Qiu, G. Rong, J. Yang, G. Li, S. Ma, X. Wang, Z. Pan, Y. Hou, M. Liu, F. Ye, W. Li, Z. W. Seh, X. Tao, H. Yao, N. Liu, R. Zhang, G. Zhou, J. Wang, S. Fan, Y. Cui, and Y. Zhang, "Highly Nitridated Graphene–Li 2 S Cathodes with Stable Modulated Cycles", *Advanced Energy Materials*, vol. 5, no. 23, 2015.

[19] S. Burgess, H. James, P. Statham, and L. Xiaobing, "Using Windowless EDS Analysis of 45-1000eV X-ray Lines to Extend the Boundaries of EDS Nanoanalysis in the SEM", *Microscopy and Microanalysis*, vol. 19, no. S2, pp. 1142-1143, 2013.

[20] M. Xia, T. Liu, N. Peng, R. Zheng, X. Cheng, H. Zhu, H. Yu, M. Shui, and J. Shu, "Lab-Scale In Situ X-Ray Diffraction Technique for Different Battery Systems: Designs, Applications, and Perspectives", *Small Methods*, vol. 3, no. 7, 2019.

[21] A. Pandey and A. Dixit, "In-Situ X-Ray Diffraction Studies of Battery Electrode Materials for the Microscopic Understanding of the Phase Stability and Performance Correlation", in *Energy Materials and Devices*, Singapore: Springer Nature Singapore, 2024, pp. 15-34.

[22] V. Stancovski and S. Badilescu, "ChemInform Abstract: In situ Raman Spectroscopic-Electrochemical Studies of Lithium-Ion Battery Materials: A Historical Overview", vol. 45, no. 8, Feb. 2014.

[23] X. -M. Lin and J. -F. Li, "Applications of In Situ Raman Spectroscopy on Rechargeable Batteries and Hydrogen Energy Systems", *ChemElectroChem*, vol. 10, no. 4, Feb. 2023.

[24] V. Shutthanandan, M. Nandasiri, J. Zheng, M. H. Engelhard, W. Xu, S. Thevuthasan, and V. Murugesan, "Applications of XPS in the characterization of Battery materials", *Journal of Electron Spectroscopy and Related Phenomena*, vol. 231, pp. 2-10, 2019.

[25] Z. Liu, G. Li, A. Borodin, X. Liu, Y. Li, and F. Endres, "In situ X-ray photoelectron spectroscopy investigation of the solid electrolyte interphase in a Li/Li6.4Ga0.2La3Zr2O12/LiFePO4 all-solid-state battery", *Journal of Solid State Electrochemistry*, vol. 23, no. 7, pp. 2107-2117, 2019.

[26] S. Wi, V. Shutthanandan, B. M. Sivakumar, S. Thevuthasan, V. Prabhakaran, S. Roy, A. Karakoti, and V. Murugesan, "In situ x-ray photoelectron spectroscopy analysis of electrochemical interfaces in battery: Recent advances and remaining challenges", *Journal of Vacuum Science & Technology A*, vol. 40, no. 1, Jan. 2022.

[27] D. Cheng, J. Hong, D. Lee, S. -Y. Lee, and H. Zheng, "In Situ TEM Characterization of Battery Materials", *Chemical Reviews*, vol. 125, no. 4, pp. 1840-1896, Feb. 2025.

[28] Z. Sun, M. Li, B. Xiao, X. Liu, H. Lin, B. Jiang, H. Liu, M. Li, D. -L. Peng, and Q. Zhang, "In situ transmission electron microscopy for understanding materials and interfaces challenges in all-solid-state lithium batteries", *ETransportation*, vol. 14, 2022.

[29] H. A. Cortés and H. R. Corti, "In-situ characterization of discharge products of lithium-oxygen battery using Flow Electrochemical Atomic Force Microscopy", *Ultramicroscopy*, vol. 230, 2021.

[30] Z. Zhang, S. Said, K. Smith, R. Jervis, C. A. Howard, P. R. Shearing, D. J. L. Brett, and T. S. Miller, "Characterizing Batteries by In Situ Electrochemical Atomic Force Microscopy: A Critical Review", *Advanced Energy Materials*, vol. 11, no. 38, 2021.

Optimization of Spray Drying Synthesis of $LiFePO_4$: Effects of Calcination and Doping on Microstructure and Electrochemical Properties

Ing. Hana Hálová
Department of Electrical and Electronic Technology
Brno University of Technology
Brno, Czech Republic
Hana.Halova@vutbr.cz

Ing. Ladislav Chladil, Ph.D.
Department of Electrical and Electronic Technology
Brno University of Technology
Brno, Czech Republic
chladil@vut.cz

Ing. Bc. Lukáš Preisler
Energy Institute, Department of Power Engineering
Brno University of Technology
Brno, Czech Republic
Lukas.Preisler@vut.cz

Ing. Pavel Čudek, Ph.D.
Department of Electrical and Electronic Technology
Brno University of Technology
Brno, Czech Republic
cudekp@vut.cz

***Abstract*— Lithium-iron phosphate ($LiFePO_4$) is a promising cathode material for lithium-ion batteries due to thermal stability, environmental safety and low production cost. However, its practical application is limited by low electronic conductivity and low energy density. To enhance its electrochemical performance, various synthesis techniques, such as spray drying synthesis are being investigated to control the particle size, morphology and uniform particle distribution. Subsequent calcination significantly affects the crystallinity, phase purity, and overall electrochemical performance of the material. Additional doping with elements such as manganese or nickel can increase the energy capacity and electrochemical properties while maintaining the advantage of long-term stability.**

Keywords*— spray drying synthesis, electrostatic precipitator, Li-ion, cathode synthesis, $LiFePO_4$, doping of LFP material, calcination influence

I. Introduction

The growing demand for efficient and sustainable energy storage has led in recent years to the development of research of lithium-ion batteries and post-lithium systems. Li-ion has become the dominant choice for portable electronics, electric vehicles and renewable energy storage mainly due to their high energy density and long cycle life. However, traditional Li-ion cathode materials such as $LiCoO_4$ (LCO) or $LiNiMnCoO_2$ (NMC) present challenges related to cost, environmental impact, and stability of supply chain. One of the recent problems is the dependence on cobalt, a critical raw material associated with high costs, limited availability and ethical concerns about mining practices. [1], [2], [3]

One of the materials discussed is the traditional $LiFePO_4$ (LFP) material, which scientists are investigating for possible modifications. The main advantages of this cathode material are the good availability of the materials used, hence its relatively low cost. Due to the olivine structure, the material is also characterised by high stability even at higher voltage and therefore higher battery safety. [1], [3]

Despite its advantages, LFP suffers from low electronic conductivity and voltage against lithium and thus also low gravimetric energy density. Various strategies have been explored to overcome these limitations, including particle size control (through different synthesis possibilities), carbon coating, and doping. [1], [3]

II. Synthesis of Cathode Materials

There are many types of syntheses used for the preparation of cathode material. The application and specific requirements are crucial for the selection of the suitable synthesis.

Synthesis methods allow controlled production of powders, and each offers certain advantages but at the same time has some disadvantages. The choice of synthesis method can therefore significantly affect the properties of the final product, both in terms of purity, particle size and homogeneity. Another parameter is also the scalability of the technique. The most common synthesis techniques include sol-gel, solid-phase synthesis, hydrothermal synthesis and spray drying synthesis. [1], [2]

The simple, low cost **solid-state synthesis** method stands out for its efficiency and scalability, making it one of the ideal methods for large-scale production. The disadvantage, however, is the relatively difficult control of particle growth and requirement of high temperatures and long preparation time.[1], [2], [4]

Another method used is **sol-gel**. This method is a simple, with precise control of parameters, and therefore well replicable. It produces powders with precise stoichiometry, high purity, uniform structure and very small particle size. However, the disadvantage is the relatively long synthesis process and higher costs. [2]

Hydrothermal or solvothermal synthesis allows the production of materials that are unstable near the melting point. This method offers precise control over the size, shape, distribution and crystallinity of the final product. However, this method requires specialized equipment and thus increases the input cost. The safety risk in the reaction process is also a certain problem, which may limit the wider use of synthesis. [2], [5], [6]

The strength of **spray drying synthesis** is relatively simple scalability of production, which can be applied to solution or suspension. The advantage of this synthesis lies in the ability to simply dissolve the precursors in aqueous or ethanol media, resulting in a precise and uniform distribution of elements in the synthesized product. [1], [2], The use of spray drying synthesis also suggests the possibility of reducing the temperature and length of the calcination process [2]. The main disadvantages of this synthesis are the high input costs as well as the necessity of using relatively large amounts of precursors.

III. Spray-drying Synthesis For $LiFePO_4$ Cathode Material

The spray drying technique is commonly used in practical applications - as in the preparation of dried food, but also in the pharmaceutical and dairy industry. The principle of this synthesis is heating the droplets obtained by atomization of the solution while evaporating the solvent to form a homogeneous powder. [7]

An important step in spray drying synthesis is the selection of precursors and preparation of the solution. The selected precursors determine the composition and properties of the final powder. The preparation must also take into account that all precursors dissolved in the solution will also be present in the final synthesized powder. [1]

The type of solvent must also be considered when preparing the solution - water is the most used [1], [8], but also other can be used, e.g. ethanol [1], [9]. The choice of solvent is mainly influenced by cost, safety, toxicity and also the evaporation temperature (complete removal of the solvent is necessary during the process) [1].

For aqueous solutions, acetates and nitrates are commonly used as precursors. In addition to LFP precursor materials, organic compounds such as carboxylic acids, carbohydrates and other carbon-containing substances are added to the solution. These compounds often act as reducing or complexing agents, but also as carbon sources to increase the electrical conductivity of the final product. [1] The precursors used for spray drying experiments in the research papers are listed in Table 1.

A patent CN102208627A by South China University of Technology SCUT from 2011 [10] on the use of materials to produce LFP cathode material by spray drying synthesis mentions also the following precursors:

- **lithium source** – lithium carbonate, lithium chloride, lithium hydroxide, lithium nitrate
- **Iron source** – ferric nitrate, ferric hydroxide, ferric oxide, ferric chloride, ferrous chloride, ferric acetate, ferrous oxalate, ferrous sulphate, ammonium ferrous sulphate
- **Phosphorus source** – phosphoric acid, ammonium dihydrogen phosphate, diammonium hydrogen phosphate
- **Organic carbon source** – glycol, glucose, sucrose, cyclodextrin, gelatine, citric acid, polyvinyl alcohol
- **Inorganic carbon source** – graphite powder, carbon black, acetylene black

Zou et al. [11] highlights combination of spray drying with homogenization treatment and thermal carbon reduction as an effective approach to remove impurities in the recycling and subsequent reuse of materials, leading to improved electrochemical properties and better scalability.

IV. Addition of other elements to the cathode

LFP material is characterized by high stability, low reactivity with electrolyte and higher safety. On the other hand, the material has also several disadvantages, including relatively low conductivity, diffusion, low potential to lithium and low gravimetric energy density. [3], [12]

For this reason, the possibility of doping $LiFePO_4$ material is being investigated. Among the elements often used to enhance the cathode material are: Mn, Ni, Co, Mg, but also Cr or Zn – for more detailed information about incorporation of these elements see Table 2. [13], [14] However, these materials suffer from low ionic and electrical conductivity, electrolyte instability and a sharp drop in capacitance upon cycling.

TABLE I. Overview of Research Papers Discussing Usage of Different Precursors For Spray Drying Synthesis of LFP Material

Source of Li	**Source of Fe**	**Source of PO_4**	**Other compounds**	**Solvent**	**Discharge capacity (mAh/g), C-rate**	**Ref.**
$LiOH·H_2O$	$FePO_4·2H_2O$	$FePO_4·2H_2O$	Citric acid, oxalic acid	Water	162, 0.5C	[8]
Li_2CO_3	$FeC_2O_4·2H_2O$	$NH_4H_2PO_4$	Dopamine	Water	165, 0.1C	[15]
$LiOH·H_2O$	$FePO_4·2H_2O$	$FePO_4·2H_2O$	Glucose	Water	164, 0.1C	[16]
LiH_2PO_4	$Fe(NO_3)_3·9H_2O$	LiH_2PO_4	Sucrose	Water	154, 0.2C	[17]
LiH_2PO_4, $LiOH·H_2O$	$FeCl_2·4H_2O$	LiH_2PO_4	Hydrochloric acid, sucrose	Water		[18]
Li_2CO_3	$FePO_4$	$FePO_4$	glucose	Water	159, 0.2C	[19]
Li_2CO_3	$FeC_6H_5O_7·5H_2O$	$NH_4H_2PO_4$		Water	160, 0.1C	[20]
CH_3COOLi	$Fe(CH_3COO)_2$	$NH_4H_2PO_4$	MWCNTs	Water	159, 0.1C	[21]
Li_2CO_3	$FeC_2O_4·2H_2O$	$NH_4H_2PO_4$	Phenolic acid	Ethanol	168, 0.1C	[9]

TABLE II. OVERVIEW OF RESEARCH PAPERS DISCUSSING USAGE OF DOPING LFP STRUCTURE

Material	Doping element	Synthesis type	Discharge/initial capacity (mAh/g)	C rate (-)	Cut-off voltage (V)	Ref.
$LiMn_{0.8}Fe_{0.2}PO_4$	Mn	Spray drying	140	0.2C	2.7	[22]
$LiMn_{0.6}Fe_{0.4}PO_4/C$	Mn	Co-precipitation	156	0.1C	2.4	[23]
$LiMn_{0.25}Fe_{0.75}PO_4/C$	Mn	Hydrothermal	124	0.15C	2.5	[5]
$LiMn_{0.08}Fe_{0.92}PO_4$	Mn	Solution combustion	165	0.1C	2.2	[14]
$LiMn_{0.02}Fe_{0.98}PO_4/C$	Mn	Solid state	149	0.1C	2.4	[24]
$LiMn_{0.025}$ $Fe_{0.975}PO_4/C$	Mn	Solvothermal	160	0.2C	2.0	[6]
$LiFe_{0.9}Ni_{0.1}PO_4/C$	Ni	Solid state	140	0.1C	2.5	[4]
$LiFe_{0.99}Ni_{0.01}PO_4/C$	Ni	Solid state	162	0.1C	2.5	[25]
$LiFe_{0.97}Ni_{0.03}PO_4/C$	Ni	Hydrothermal	168	0.1C	2.5	[26]
$LiFe_{0.98}Ni_{0.01}Co_{0.01}PO_4/C$	Ni + Co	Solid state	158	0.1C	2.5	[27]
$LiFe_{0.99}Mg_{0.005}Co_{0.005}PO_4$	Mg + Co	Solid state	147	0.1C	2.5	[28]
$LiFe_{0.97}Cr_{0.03}PO_4/C$	Cr	Solid state	151	0.1C	2.5	[29]

To enhance the properties of LFP, minor doping is being explored, as an appropriate amount can improve performance, whereas excessive doping can lead to the manifestation of negative effects. [13], [14]

V. HEAT TREATMENT OF LFP MATERIAL

After the spray drying, when the cathode precursor material has been formed, the material is usually subsequently calcined at higher temperatures. It is important to avoid storage of hygroscopic compounds or compounds susceptible to inorganic condensation after spray drying. [1]

During calcination at elevated temperature, volatiles (such as solvent residues, but also residual precursors such as carbon) are removed. During calcination, diffusion and homogenisation of elements, crystallisation and particle growth also occur. [1]

Since the internal structure is affected during calcination and therefore calcination affects the resulting electrochemical properties, attention needs to be paid to calcination procedures. Important calcination parameters include type of environment, length of calcination and temperature during calcination. [1]

Calcination is undertaken in the case of LFP in an inert atmosphere, either in nitrogen [9] or argon [17]. The process generally takes place at temperatures ranging from 500°C to 800°C over a period of 4 to 34 hours. For more information on the individual calcination parameters for different types of synthesis, see Table 3.

TABLE III. OVERVIEW OF RESEARCH PAPERS DISCUSSING CALCINATION OF LFP MATERIAL

Material	Synthesis type	Used gas	Max temperature (°C)	Time duration (h)	Discharge capacity (mAh/g), C-rate	Note	Ref.
$LiFePO_4/C$	Sol spray drying	Ar	600	8	160, 0.1C		[20]
$LiFePO_4/C$	Spray drying	N_2	700	11	164, 0.1C	350 °C for 3h, afterwards 700 for 8 h	[16]
$LiFePO_4/N\text{-}C$	Spray drying	N_2-Ar	600	4	165, 0.1C		[15]
$LiFePO_4/C$	Spray drying	Ar	700	4	162, 0.5C		[8]
$LiMn_{0.8}Fe_{0.2}PO_4$	Spray drying	N_2	650	6	140, 0.2C	Heating rate 5°C/min	[22]
$LiMn_{0.025}$ $Fe_{0.975}PO_4/C$	Solvothermal	N_2	500	5	160, 0.2C		[6]
$LiMn_{0.05}Fe_{0.95}PO_4/C$	Hydrothermal	N_2	615	12	127, 0.15C	Heating rate 2°C/min	[5]
$LiFe_{0.9}Mn_{0.05}Ni_{0.05}PO_4/C$	Solid state	Ar	700	24		350 °C for 12 h, afterwards 700 °C for 12 h	[4]
$LiFe_{0.99}Mg_{0.005}Co_{0.005}PO_4$	Solid-state	N_2	700	34	147, 0.1C	350 °C for 10 h, afterwards 700 °C for 24 h	[13]

VI. Experiment

The precursors used in the laboratory for the spray drying synthesis were $(CH_3COO)Li \cdot 2H_2O$, $(CH_3COO)_2Mn \cdot 4H_2O$, $(CH_3COO)_2Ni \cdot 4H_2O$, $(CH_3COO)_2Co \cdot 4H_2O$, LiH_2PO_4 and citric acid. The iron source in case of LFP19 was $Fe(C_5H_7O_2)_3$ and in case of LFP20 $C_6H_5FeO_7$. During the spray drying synthesis, the flow rate was set to 4 l/s. The length of the individual experiments was from 3 to 7 hours with an average yield of 25 mg per hour. The particles were collected using an electrostatic precipitator.

As can be seen from Fig. 1 the particles have a typical shape of spherical particle. The average synthesized particles diameters are from 0.2 to 1.2µm in case of LFP19 are approximately from 0.3 to 1.8 µm in case of LFP20 with the uniform distribution of the elements. According to EDS analysis, the elemental composition of sample LFP19 corresponds to the synthesised LFP material. The ratio of phosphorus to iron is in the approximate ratio of 1:1, indicating the expected ratio. In the case of sample LFP20, the amount of phosphorus was practically zero, which could have occurred either during the formation of the solution itself by an inappropriate combination of precursors or due to inhomogeneous distribution and insufficient particle trapping. For this reason, only LFP19 samples were used for further experiments.

After synthesis, the samples were stored in a desiccator to prevent the absorption of air moisture. Since the spray drying synthesis was carried out in the laboratories on a self-assembled device, the amount of particles captured was not sufficient to perform a series of experiments on the same material. Therefore, powder from several syntheses running consecutively was mixed.

Since the use of spray drying synthesis is expected to reduce the time window required for proper calcination of the material, TGA analysis of the powder was performed prior to the calcination itself. The results from the TGA analysis can be seen in Fig. 2 and Fig. 3. The two curves (LFP20 and LFP19) represent TGA data for LFP material synthesized by spray drying method, each with a different iron precursor. The TGA data for both of the samples show two significant drops in the sample weight when calcined up to 850 °C. At lower temperatures up to 200 °C, the primary process is the evaporation of residual water. The weight loss is approximately 60% of the original material. Following this, the combustion of carbon from the organic precursor takes place. [2] This process corresponds to the weight reduction observed around 400 °C.

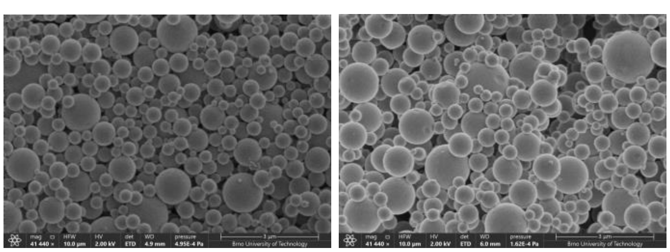

Fig. 1. SEM picture of synthesized powder – LFP19 (left), LFP20 (right)

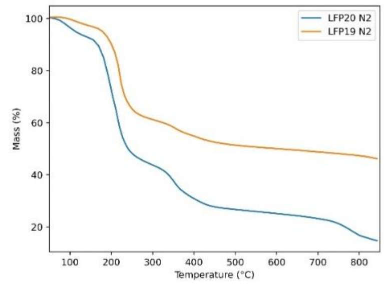

Fig. 2. Percentage weight loss of the samples of LFP material, TGA analysis

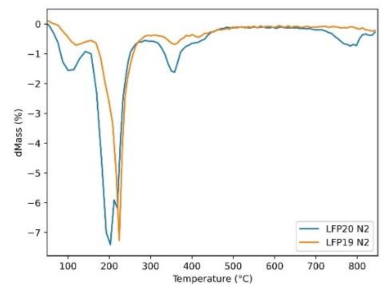

Fig. 3. Derivation of weight loss of the LFP material samples, TGA analysis

Fig. 4 subsequently shows the SEM images for sample LFP19 subjected to calcination at 600 and 650°C. The image shows the agglomeration of particles that gave rise to the irregular formations that give a porous appearance.

VII. Conclusion

In conclusion, based on the review different research articles, the spray drying technique has proven to be a promising method for the synthesis of $LiFePO_4$ cathode material. This method stands out compared to other methods for its scalability, uniform distribution of elements and the possibility of reducing temperature and time during calcination.

In the initial phase of the research, two precursor combinations were tested (the iron precursor was different). Based on SEM analysis, it was observed that the synthesized particles size was below 1.5 µm. However as it can be seen from SEM analysis, sample LFP20 had larger particles and EDS analysis revealed the absence of phosphorus, rendering this precursor unsuitable for further experiments.

The TGA analysis was used to define an appropriate calcination range. The calcination was studied in the range to

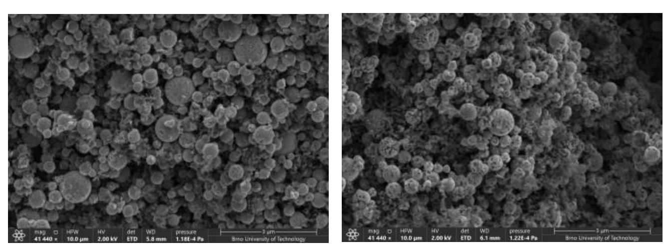

Fig. 4. SEM picture of calcinated powder LFP19 mixed with carbon – 600°C (left), 650°C (right)

850°C, as the higher temperatures caused the sample degradation (sealing of the sample).

The future work will focus on the doping of the LFP structure with manganese to enhance electrochemical performance as it is evident from the literature that manganese doping is one of the possible future directions of LFP material. further mapping of calcination

ACKNOWLEDGMENT

This work was supported by the specific graduate research of the Brno University of Technology No. FEKT-S-23-8286

This work was supported by specific graduate research of the Brno University of Technology No. FEKT/FSI-J-24-8579

REFERENCES

[1] B. Vertruyen, N. Eshraghi, C. Piffet, J. Bodart, A. Mahmoud, and F. Boschini, "Spray-Drying of Electrode Materials for Lithium- and Sodium-Ion Batteries", *Materials*, vol. 11, no. 7, 2018.

[2] T. A. Wani and G. Suresh, "A comprehensive review of $LiMnPO_4$ based cathode materials for lithium-ion batteries: current strategies to improve its performance", *Journal of Energy Storage*, vol. 44, 2021.

[3] M. S. Whittingham, "Lithium Batteries and Cathode Materials", *Chemical Reviews*, vol. 104, no. 10, pp. 4271-4301, 2004.

[4] C. Nayak, V. Bhasin, K. K. Halankar, S. Banerjee, A. Bute, S. N. Jha, and D. Bhattacharyya, "Operando X ray absorption spectroscopy elucidating the de-lithiation/lithiation mechanism of Mn and Ni co-doped $LiFePO_4$ cathodes", *Journal of Electroanalytical Chemistry*, vol. 969, 2024.

[5] G. Meligrana, F. Di Lupo, S. Ferrari, M. Destro, S. Bodoardo, N. Garino, and C. Gerbaldi, "Surfactant-assisted mild hydrothermal synthesis to nanostructured mixed orthophosphates $LiMn_yFe_{1-y}PO_4$/C lithium insertion cathode materials", *Electrochimica Acta*, vol. 105, pp. 99-109, 2013.

[6] S. Zhao, L. Wen, J. Liu, J. Q. Chen, and F. Bei, "Mn-doped $LiFePO_4$/C Composite with Excellent High-Rate Performance as Lithium Ion Batteries Cathode", *International Journal of Electrochemical Science*, vol. 15, no. 9, pp. 8873-8882, 2020.

[7] A. Stunda-Zujeva, Z. Irbe, and L. Berzina-Cimdina, "Controlling the morphology of ceramic and composite powders obtained via spray drying – A review", *Ceramics International*, vol. 43, no. 15, pp. 11543-11551, 2017.

[8] X. GUAN, G. LI, C. LI, and R. REN, "Synthesis of porous nano/micro structured $LiFePO_4$/C cathode materials for lithium-ion batteries by spray-drying method", *Transactions of Nonferrous Metals Society of China*, vol. 27, no. 1, pp. 141-147, 2017.

[9] Z. Chen, Q. Zhao, M. Xu, L. Li, J. Duan, and H. Zhu, "Electrochemical properties of self-assembled porous micro-spherical LiFePO4/PAS composite prepared by spray-drying method", *Electrochimica Acta*, vol. 186, pp. 117-124, 2015.

[10] "A method for preparing LiFePO4/C composite cathode material by spray drying", China Patent CN102208627A, Oct. 11, 2011

[11] Y. Zou, J. Cao, H. Li, W. Wu, Y. Liang, and J. Zhang, "Large-scale direct regeneration of $LiFePO_4$ @C based on spray drying", Springer, vol. 1, no. 2, pp. 254-261, May 2023.

[12] B. Xu, D. Qian, Z. Wang, and Y. S. Meng, "Recent progress in cathode materials research for advanced lithium ion batteries", *Materials Science and Engineering: R: Reports*, vol. 73, no. 5-6, pp. 51-65, 2012.

[13] K. Akhmetova, F. Sultanov, A. Mentbayeva, N. Umirov, Z. Bakenov, and B. Tatykayev, "Advances in multi-element doping of $LiFePO_4$ cathode material for capacity enhancement in Li-ion batteries", *Journal of Power Sources*, vol. 624, 2024.

[14] C. U. Mulik, R. S. Kamat, X. Wang, C. Padwal, M. Y. Chougale, D. P. Dubal, and L. D. Jadhav, "High-performance Li-ion battery cathode: Mn-doped LiFePO4 via solution combustion synthesis method", *Journal of Electroanalytical Chemistry*, vol. 971, 2024.

[15] F. Cao, G. X. Pan, and Y. J. Zhang, "Construction of ultrathin N-doped carbon shell on $LiFePO_4$ spheres as enhanced cathode for lithium ion batteries", *Materials Research Bulletin*, vol. 96, pp. 325-329, 2017.

[16] L. Chen, C. Lu, Q. A. Chen, Y. J. Gu, M. Wang, and Y. B. Chen, "Preparation and Characterization of Nano-$LiFePO_4$/C Using Two-Fluid Spray Dryer", *Applied Mechanics and Materials*, vol. 563, pp. 62-65, 2014.

[17] C. Chen, C. Luo, Y. Jin, J. Li, Q. Zhao, and W. Yang, "Short-Process Spray-Drying Synthesis of Lithium Iron Phosphate@Carbon Composite for Lithium-Ion Batteries", *ACS Sustainable Chemistry &Engineering*, vol. 12, no. 37, pp. 14077-14086, Sep. 2024.

[18] T. Lan, X. Guo, D. Li, and Y. Chen, "Preparation of $LiFePO_4$ Powders by Ultrasonic Spray Drying Method and Their Memory Effect", *Materials*, vol. 14, no. 12, 2021.

[19] R. Ding, H. Liu, L. Wang, and G. Liang, "Effect of spray drying technological conditions on the performance of $LiFePO_4$/C cathode materials with high energy density", *Ionics*, vol. 25, no. 12, pp. 5633-5642, 2019.

[20] L. Wu, S. -K. Zhong, J. -Q. Liu, F. Lv, and K. Wan, "High tap-density and high performance $LiFePO_4$/C cathode material synthesized by the combined sol spray-drying and liquid nitrogen quenching method", *Materials Letters*, vol. 89, pp. 32-35, 2012.

[21] X. Sun and L. Zhang, "Outstanding Li-storage performance of $LiFePO0_4$@MWCNTs cathode material with 3D network structure for lithium-ion batteries", *Journal of Physics and Chemistry of Solids*, vol. 116, pp. 216-221, 2018.

[22] X. Zhang, M. Hou, A. G. Tamirate, H. Zhu, C. Wang, and Y. Xia, "Carbon coated nano-sized $LiMn_{0.8}Fe_{0.2}PO_4$ porous microsphere cathode material for Li-ion batteries", *Journal of Power Sources*, vol. 448, 2020.

[23] J. Li, Y. Wang, J. Wu, H. Zhao, H. Wu, Y. Zhang, and H. Liu, "Preparation of Enhanced-Performance $LiMn_{0.6}Fe_{0.4}PO_4$/C Cathode Material for Lithium-Ion Batteries by using a Divalent Transition-Metal Phosphate as an Intermediate", *ChemElectroChem*, vol. 4, no. 1, pp. 175-182, 2017.

[24] H. Yang, Z. Pan, L. Wang, C. Liu, Z. Wang, C. Zhang, and W. Lu, "Enhancing electrochemical performance of Mn doped $LiFePO_4$ cathode materials for lithium-ion batteries", *International Journal of Electrochemical Science*, vol. 18, no. 4, 2023.

[25] W. Zhang, Y. Hu, X. Tao, H. Huang, Y. Gan, and C. Wang, "Synthesis of spherical $LiFePO_4$/C via Ni doping", *Journal of Physics and Chemistry of Solids*, vol. 71, no. 9, pp. 1196-1200, 2010.

[26] Y. Liu, Y. -J. Gu, G. -Y. Luo, Z. -L. Chen, F. -Z. Wu, X. -Y. Dai, Y. Mai, and J. -Q. Li, "Ni-doped LiFePO4/C as high-performance cathode composites for Li-ion batteries", *Ceramics International*, vol. 46, no. 10, pp. 14857-14863, 2020.

[27] G. R. Kiani, S. Boroomand, R. Khodabakhshi, and M. Esmaeili, "A novel co-doped $LiFePO_4$/C cathode material, modified for enhanced high power density battery applications", *Microelectronic Engineering*, vol. 136, pp. 77-80, 2015.

[28] Y. -huai DING and P. ZHANG, "Effect of Mg and Co co-doping on electrochemical properties of $LiFePO_4$", *Transactions of Nonferrous Metals Society of China*, vol. 22, pp. s153-s156, 2012.

[29] H. C. Shin, S. B. Park, H. Jang, K. Y. Chung, W. I. Cho, C. S. Kim, and B. W. Cho, "Rate performance and structural change of Cr-doped $LiFePO_4$/C during cycling", *Electrochimica Acta*, vol. 53, no. 27, pp. 7946-7951, 2008.

NXP pro studenty

Brighter Together

automotive | comms-infrastructure | industrial | mobile | smart-city | smart-home

NABÍZÍME

- **placenou stáž**, která Tě bude bavit a je
  - atraktivní
  - motivující
  - flexibilní
  - podporující Tvé studium
- **full - time** poté, co úspěšně dostuduješ
- **témata diplomových prací**, ze kterých si rozhodně vybereš
- **workshopy**
- **NXP Cup**: největší mezinárodní soutěž autonomních autíček v Evropě, které se můžeš zúčastnit

O NÁS

NXP Semiconductors se prostřednictvím inovací zasazuje o chytřejší, bezpečnější a udržitelnější svět. Jakožto světová jednička v embedded řešeních, NXP posouvá hranice v oblastech automobilového průmyslu, IoT, mobilních a komunikačních infrastruktur.

www.nxp.com

Unraveling Sodium Storage Mechanisms in Carbon Anodes for Sodium-ion Batteries

Antonín Šimek
Department of electrical and electronic Technology
Faculty of Electrical Engineering and Communication
Brno, Czech Republic
Antonin.Simek1@vut.cz

Tomáš Kazda
Department of electrical and electronic Technology
Faculty of Electrical Engineering and Communication
Brno, Czech Republic
kazda@vutbr.cz

Charles Aram Hall
Structural Chemistry
Department of chemistry
Ångström Laboratory
Uppsala, Sweden
charles-aram.hall@kemi.uu.se

Ondřej Čech
Department of electrical and electronic Technology
Faculty of Electrical Engineering and Communication
Brno, Czech Republic
cechondrej@vut.cz

***Abstract*— Sodium batteries have become a promising alternative to lithium-ion systems due to the abundance and low cost of sodium sources. However, understanding the basic mechanisms of sodium storage in carbon anodes remains crucial for improving their electrochemical performance. This study investigates the sodium storage behavior in hard carbon and anthracite anodes, focusing on the mechanisms of intercalation, adsorption and pore filling. The findings provide valuable insights for the optimization of carbon anodes for high-capacity and high-performance sodium batteries with long cycling life.**

Keywords—sodium-ion, carbon anodes, sodium storage mechanism, hard carbon, anthracite

I. Introduction

The growing demand for sustainable and cost-effective energy storage solutions has intensified research into sodium-ion batteries (Na-ion) as a promising alternative to lithium-ion (Li-ion) systems due to the similar properties of lithium (Li) and sodium (Na) elements [1]. Sodium's natural occurrence and low cost make it an attractive candidate for large-scale applications. However, the development of efficient anode materials remains a significant challenge due to sodium's larger ionic radius and its different electrochemical behavior [1; 2]. Carbon-based anodes, particularly hard carbon and anthracite, show considerable potential due to their favorable structural properties and sodium storage capabilities. Despite their promising properties, the fundamental mechanisms of sodium storage, including intercalation, adsorption and pore filling, are not yet fully understood [3]. A deeper understanding of these processes is essential to optimize the performance and stability of Na-ion batteries. The aim of this study is to clarify the mechanisms of sodium deposition in hard coal and anthracite anodes and to assess their effect on capacity retention and rate. These findings can guide the design of Na-ion batteries with high capacity, stability and fast charging capability.

II. Anode materials for Na-ion

The negative electrode (anode) plays a key role in Na-ion batteries and its optimization requires the use of advanced materials [4]. Unlike lithium, sodium cannot be used directly as an anode because it forms an unstable passivation layer in organic electrolytes at room temperature, which poses a safety risk. Another problem is the increased growth of sodium dendrites, which can cause internal battery short circuits. Therefore, it is essential to develop anode materials that have a suitable voltage window, high reversible capacity, stable structure, high electronic and ionic conductivity, and low cost with little environmental impact [5; 6]. Research in this area focuses on several main categories such as carbon materials, alloy-based materials, metal oxides and sulfides using conversion reactions, titanium-based composites with intercalation mechanisms, and organic composites [4; 6; 7]. Fig. 1 shows the basic groups of anode materials for Na-ion batteries and their approximate potential and specific capacities.

A. Carbon-based anode materials

This study focuses on the development of carbon-based anode materials for Na-ion batteries as graphite, which is commonly used in Li-ion batteries, and is unsuitable for sodium systems. The main problem lies in the larger ionic radius of sodium ions (~1.02 Å) compared to lithium ions (~0.76 Å), which prevents efficient intercalation into the graphite structure [2]. This mismatch leads to poor electrochemical performance and instability of sodium ion batteries. To overcome this limitation, alternative anode materials that can accommodate

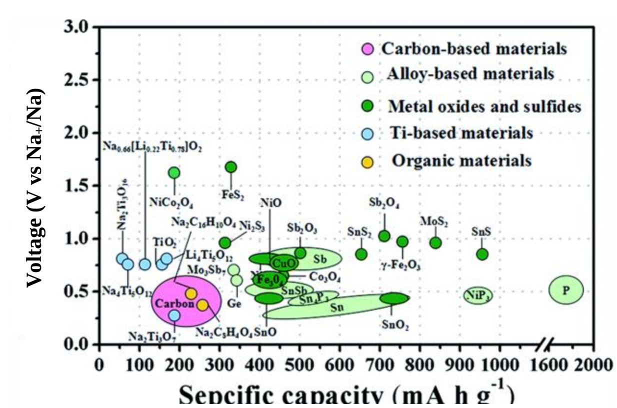

Specific capacity (mA.h.g^{-1})

Fig. 1. Clasification os anode materials for Na-ion batteries and their average potential and specific capacity [7]

DOI 10.13164/eeict.2025.180

larger sodium ions are needed. Hard carbon (HC) and other disordered carbon materials have shown promise due to their unique structural properties that allow sodium deposition through mechanisms such as intercalation, adsorption, and pore filling [8; 9]. HC is an allotrope of carbon that cannot be graphitized even at temperatures up to 3000 °C. Another form of carbon being investigated for use in sodium batteries is soft carbon (SC). Unlike HC, SC can be converted to graphite by treatment at high temperature (e.g. 3000 °C) [6]. These materials typically offer capacities of 200-300 $mAh.g^{-1}$, which, although lower than the theoretical 372 $mAh.g^{-1}$ of graphite in Li-ion batteries, represent a viable solution for sodium battery applications [10; 11].

The physical properties and microstructure of HC and SC differ significantly. Fig. 2 shows a comparison of the microstructures of graphite, SC and HC. Both graphite and SC have a more ordered structure with a d-spacing of approximately 0.335 nm. In contrast, HC has a larger d-spacing. Although both HC and SC contain pores, SC has much lower porosity. As a result, the higher porosity and larger d-spacing in HC allow it to store sodium ions with much greater capacity than SC and graphite. Therefore, among the various carbon allotropes, HC appears to be a promising anode material for sodium batteries [6].

III. Explanation of Filling Mechanisms in Hard Carbon Anode Materials

Unlike graphite, HC lacks long-range ordering and consists of twisted graphene sheets disrupted by defects such as vacancies, pentagons, heptagons and heteroatoms. These structural irregularities, together with van der Waals forces between the layers, produce graphite-like nanodomains with multiple layers and pores of different sizes created by twisted and randomly oriented graphene sheets. The properties of these domains and pores depend on the preparation process and the precursor material used. The complex structure of HC contributes to its sodium ion storage behavior but complicates understanding the exact mechanism. [8; 12]

The various mechanism of sodium storage in HC anodes has been debated among researchers, with three main processes proposed:

- capacitive adsorption (at open pores or at defect sites),
- nanopore filling,
- insertion (intercalation) in carbon interlayers [8].

A schematic representation of the HC microstructure together with the main processes of the filling mechanism is shown in Fig. 3. Capacitive adsorption, which occurs in the sloping region of the charge/discharge curve, is associated with defects, heteroatoms and adsorption of Na^+ ions on open pores. This mechanism increases the rate and efficiency of the cycle, although it reduces the initial Coulombic efficiency [12; 13; 8].

In addition, Na^+ ions can be adsorbed at defect sites in graphene sheets and insert between graphene layers, either by intercalation, which contributes to the plateau capacity, or by random insertion, which affects the sloping capacity. Pore filling leads to the formation of quasi-metallic clusters that affect the areal capacitance near the sodium metal potential. Despite the complexity of sodium storage in HC, its high porosity and larger d-spacing allow it to store more sodium ions than materials such as soft carbon and graphite, making it a promising anode material for sodium batteries. [8; 12; 13]

A. *Sodium storage models*

The behavior of sodium storage in HC has been the subject of research and several typical reaction models have been proposed by various researchers. The mechanism of sodium storage in HC materials is still controversial, and four basic models derived from experimental measurements on different HC samples prepared from different precursors prevail, including the "insertion-adsorption" model, the "adsorption-intercalation" model, the "three-stage" model, and the "adsorption-filling" model. These models are represented in Fig. 4. [12; 13]

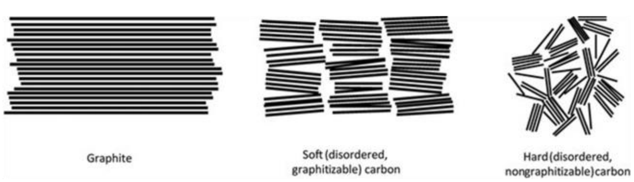

Fig. 2. Representation of microstructures of graphite, soft carbon and hard carbon [6]

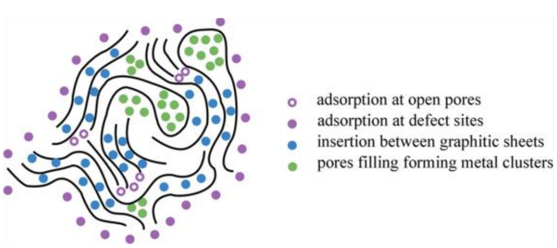

Fig. 3. Schematic representation of the microstructure of HC with main filling mechanisms [12]

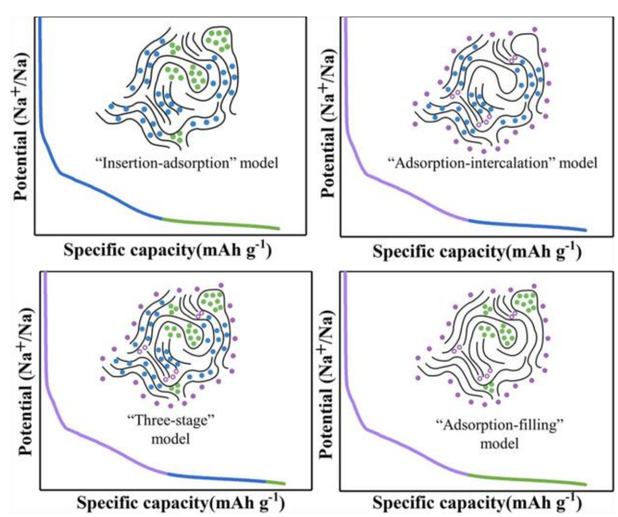

Fig. 4. Illustration of the different models for sodium storage on the charging curves [12]

- **Insertion-adsorption model**: This model assumes that sodium ions are first inserted between graphene layers and then adsorbed onto defect sites and pore surfaces. It explains the sloping capacity by adsorption on the defects and the plateau capacity by insertion between the layers. [12]
- **Adsorption-intercalation model**: In this model, sodium ions are initially adsorbed on pore and defect surfaces, which contributes to the formation of the sloping region. At lower voltages, the ions intercalate between the graphene layers, leading to the formation of a plateau capacity. [12]
- **Three-stage model**: This model divides the sodium deposition process into three stages: adsorption on the surface of defects and edges, intercalation between graphene layers, and nanopore filling. Each phase corresponds to different regions of the charge/discharge curve. [12]
- **Adsorption-filling model**: According to this model, sodium ions are first adsorbed on the surface of the pores and defects, which contributes to the formation of the sloping region. With decreasing voltage, the ions then fill the nanopores, leading to an plateau capacity. [12]

B. *Difference in storage mechanism for HCs and SCs*

The sodium storage mechanism differs significantly between HC and SC. The discharge/charge curves of HC show a sloping profile in the region above 0.1 V and a plateau region in the regions below 0.1 V. For SC, the sloping region is very similar to that of HC, but the plateau region is almost negligible for SC. For this reason, HCs generally achieve higher reversible capacitance and lower voltage than SCs due to the presence of a plateau region below 0.1 V [14].

Anthracite is a naturally occurring coal with a crystalline structure, and the deposition of sodium in anthracite occurs primarily by intercalation between its graphitic layers [15]. However, its lower porosity and higher degree of graphitization may limit sodium ion accessibility and storage capacity compared to hard carbon [16]. While hard carbon utilizes multiple sodium storage mechanisms due to its amorphous and porous nature, anthracite relies mainly on intercalation, which may result in different electrochemical properties of Na-ion batteries [8]. On the other hand, the absence of a plateau region may make SCs, and hence anthracite, more suitable for applications with higher current load requirements, which is the subject of investigation in this work.

IV. Experimental part

A. *Active material characterisation*

In the experimental part, two active anode materials, soft and hard carbon, were investigated. Kuranode type 2 with a particle size of 5 μm was used as hard carbon. Anthracite from Resorbent was used as soft carbon, which was first chemically purified using hydrothermal cleaning in sodium hydroxide followed by hydrochloric acid (demi-water filtration between steps to neutralize pH). In addition, after hydrothermal cleaning, calcination was carried out in a tube furnace at 1000 °C for 6 hours in the presence of an argon inert atmosphere. Powder X-ray diffraction (XRD) and Raman spectroscopy were subsequently performed on both materials to determine the properties of the materials under investigation. The normalized results of this characterization are shown in Fig. 5 below.

From the Raman spectroscopy results, two main peaks can be observed, the D-band at Raman shift of 1340 cm^{-1} (representing the degree of disorder) and the G-band at Raman shift of 1580 cm^{-1} (representing the degree of graphitization) [17]. If we take the intensity of the two peaks and put them in a ratio, we obtain the defect ratio I_D/I_G. For HC, this value is almost equal to 1, since the two peaks are almost identical in intensity. For anthracite, however, the D peak has lower intensity, so the resulting I_D/I_G ratio is approximately 0.83, indicating that anthracite is indeed SC and achieves a higher degree of graphitization than HC [18].

From the XRD results it is then possible to observe 2 main peaks, with the largest difference being observed at the first peak located at approximately a 2-Theta angle of 20-25°. For HC, this peak is at an angle of 21.8° and has lower intensity, indicating a more amorphous (disordered) structure, larger interlayer distance and less crystallinity. In contrast, for anthracite, this peak is at an angle of 24.4° and is more intense, indicating a greater degree of orderliness, less interlayer distance and greater crystallinity. [17; 19]

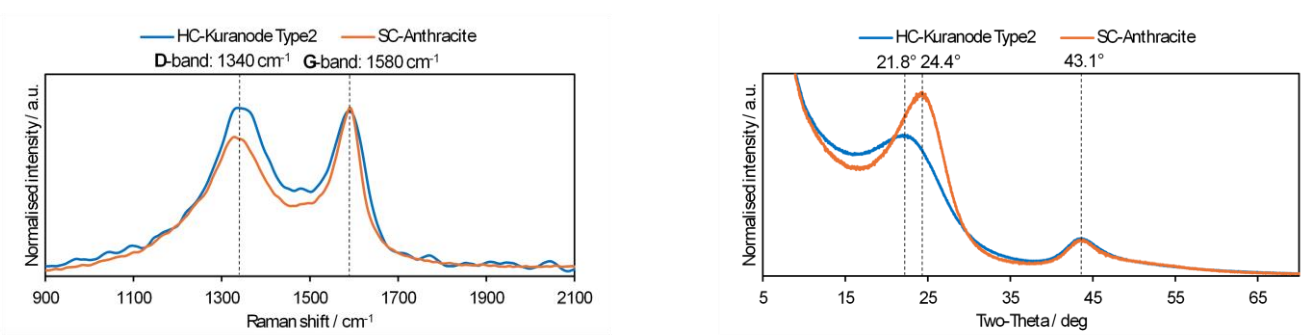

Fig. 5. Results of Raman spectroscopy (on the left) and XRD analysis (on the right) of HC-Kuranode Type2 and SC-Anthracite.

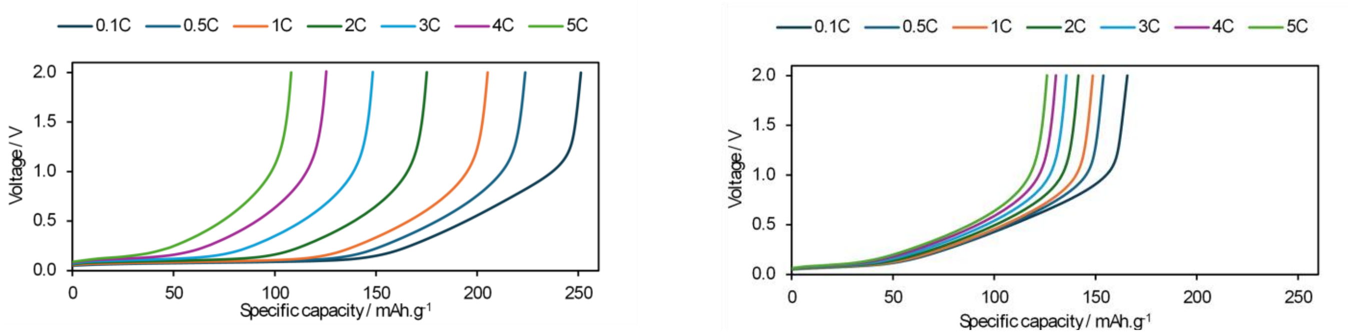

Fig. 6. Comparison of discharge curves at different current loads for hard carbon anode (on the right) and anthracite anode (on the left)

B. Preparation of electrodes and electrochemical half cells

Negative electrodes were prepared from the investigated active materials. The electrode mixture was composed of 85 wt.% of active material (HC or SC), 10 wt.% of conductive additive SuperP and 5 wt.% of binder carboxymethyl cellulose (CMC). Demineralized water was used as solvent. A 200 μm layer of electrode mass was subsequently coated onto the aluminum current collector using a blade coater. The electrodes were then dried at room temperature and then die-cut to 13 mm diameter. The die-cut electrodes were subsequently transferred to an Alpha glove box filled with argon inert atmosphere (O_2 and H_2O < 1ppm) and vacuum dried using a Büchi Glass Oven at 150 °C for 24 hours. After drying, sodium half-cells were assembled in a pouch-cell configuration, consisting of anode as working electrode, Whatman GF/A glass separator soaked with electrolyte (1M $NaPF_6$ in diglyme) and sodium metal as counter electrode. To ensure good contact, the resulting pouch cells were sandwiched between two plastic plates using a bulldog clip.

To verify the electrochemical properties, measurements were performed on a Neware BTS-4000 battery cycler. At the beginning of the measurement, two formation cycles were performed at a load of 0.1C using the CC-CV (constant currents-constant voltage) method during charging and CC (constant current) during discharging in the potential range of 0.05-2 V. The formation cycles were followed by rate capability test at 0.5C, 1C, 2C, 3C, 4C and 5C loads using only CC method for both charging and discharging. At each load, five cycles were performed in the 0.05-2 V range.

C. Results and discussion

The measurement results in Fig. 6 compare the discharge curves of hard carbon (right) and anthracite (left) in the half-cell configuration. The data show a rapid decrease in capacitance for the hard carbon at high C rates, with the plateau region noticeably shortening with increasing current load. In contrast, anthracite shows lower overall capacity but exhibits greater stability at higher C rates. Its plateau region is short from the beginning, which makes it more suitable for high power applications, as the sloping region is mainly involved here. Although anthracite has a lower capacity at 0.1C, it achieves comparable performance to hard carbon at 3C and even outperforms it at loads above 4C. Overall, HC experienced a 57.5% decrease in capacity at 5C, whereas anthracite experienced only a 26.7% decrease in capacity at 5C. After the current load test, 3 cycles at 0.1C load were performed from which an overall capacity drop can be observed. For HC this drop was 3.5%, whereas for anthracite it was 5.8%.

V. Conclusion

Our findings suggest that differences in sodium deposition mechanisms such as intercalation and pore filling in hard carbon versus an adsorption-dominated process in anthracite contribute to their different electrochemical behavior. Hard carbon, which has a higher capacity but fades rapidly at high rates, is more suitable for low-power applications, while anthracite's stability at high C rates makes it a promising candidate for fast-charging Na-ion batteries.

Future experiments will focus on optimizing the ratio of hard carbon to anthracite in composite anodes to achieve a balance between specific capacity and rate capability. By exploiting the complementary properties of the two materials, this approach aims to enhance the overall electrochemical performance and expand the potential applications of Na-ion batteries.

Acknowledgment

This work was supported by the specific graduate research of the Brno University of Technology No. FEKT-S-23-8286. Authors gratefully acknowledge the financial support of the Technology Agency of the Czech Republic (project No. TK04030083).

References

[1] Y. Gao, H. Zhang, J. Peng, L. Li, Y. Xiao, L. Li, Y. Liu, Y. Qiao, and S. -L. Chou, "A 30-year overview of sodium-ion batteries", *Carbon Energy*, vol. 6, no. 6, 2024.

[2] N. Yabuuchi, K. Kubota, M. Dahbi, and S. Komaba, "Research Development on Sodium-Ion Batteries", *Chemical Reviews*, vol. 114, no. 23, pp. 11636-11682, Dec. 2014.

[3] T. Zhang, C. Li, F. Wang, A. Noori, M. F. Mousavi, X. Xia, and Y. Zhang, "Recent Advances in Carbon Anodes for Sodium-Ion Batteries", *The Chemical Record*, vol. 22, no. 10, 2022.

[4] N. Tapia-Ruiz, A. R. Armstrong, H. Alptekin, M. A. Amores, H. Au, J. Barker, R. Boston, W. R. Brant, J. M. Brittain, Y. Chen, M. Chhowalla, Y. -S. Choi, S. I. R. Costa, M. Crespo Ribadeneyra, and S. A. Cussen, "2021 roadmap for sodium-ion batteries", *Journal of Physics: Energy*, vol. 3, no. 3, Jul. 2021.

[5] W. Luo, F. Shen, C. Bommier, H. Zhu, X. Ji, and L. Hu, “Na-Ion Battery Anodes: Materials and Electrochemistry”, *Accounts of Chemical Research*, vol. 49, no. 2, pp. 231-240, Feb. 2016.

[6] M. Thompson, Q. Xia, Z. Hu, and X. S. Zhao, “A review on biomass-derived hard carbon materials for sodium-ion batteries”, *Materials Advances*, vol. 2, no. 18, pp. 5881-5905, Sep. 2021.

[7] H. Kang, Y. Liu, K. Cao, Y. Zhao, L. Jiao, Y. Wang, and H. Yuan, “Update on anode materials for Na-ion batteries”, *Journal of Materials Chemistry A*, vol. 3, no. 35, pp. 17899-17913, 2015.

[8] D. Chen, W. Zhang, K. Luo, Y. Song, Y. Zhong, Y. Liu, G. Wang, B. Zhong, Z. Wu, and X. Guo, “Hard carbon for sodium storage: mechanism and optimization strategies toward commercialization”, *Energy & Environmental Science*, vol. 14, no. 4, pp. 2244-2262, Apr. 2021.

[9] Z. Jian, C. Bommier, L. Luo, Z. Li, W. Wang, C. Wang, P. A. Greaney, and X. Ji, “Insights on the Mechanism of Na-Ion Storage in Soft Carbon Anode”, *Chemistry of Materials*, vol. 29, no. 5, pp. 2314-2320, Mar. 2017.

[10] L. Zhang, W. (A.) Wang, S. Lu, and Y. Xiang, “Carbon Anode Materials: A Detailed Comparison between Na-ion and K-ion Batteries”, *Advanced Energy Materials*, vol. 11, no. 11, 2021.

[11] L. Zhao, B. Ding, X. -Y. Qin, Z. Wang, W. Lv, Y. -B. He, Q. -H. Yang, and F. Kang, “Revisiting the Roles of Natural Graphite in Ongoing Lithium-Ion Batteries”, *Advanced Materials*, vol. 34, no. 18, 2022.

[12] X. Chen, C. Liu, Y. Fang, X. Ai, F. Zhong, H. Yang, and Y. Cao, “Understanding of the sodium storage mechanism in hard carbon anodes”, *Carbon Energy*, vol. 4, no. 6, pp. 1133-1150, 2022.

[13] N. Sun, J. Qiu, and B. Xu, “Understanding of Sodium Storage Mechanism in Hard Carbons: Ongoing Development under Debate”, *Advanced Energy Materials*, vol. 12, no. 27, 2022.

[14] M. Yuan, B. Cao, H. Liu, C. Meng, J. Wu, S. Zhang, A. Li, X. Chen, and H. Song, “Sodium Storage Mechanism of Nongraphitic Carbons: A General Model and the Function of Accessible Closed Pores”, *Chemistry of Materials*, vol. 34, no. 7, pp. 3489-3500, Apr. 2022.

[15] Y. -J. Kim, H. Yang, S. -H. Yoon, Y. Korai, I. Mochida, and C. -H. Ku, “Anthracite as a candidate for lithium ion battery anode”, *Journal of Power Sources*, vol. 113, no. 1, pp. 157-165, 2003.

[16] S. Dong, Y. Song, Y. Fang, G. Wang, Y. Gao, K. Zhu, and D. Cao, “Rapid Carbonization of Anthracite Coal via Flash Joule Heating for Sodium Ion Storage”, *ACS Applied Energy Materials*, vol. 7, no. 24, pp. 11288-11296, Dec. 2024.

[17] K. Li, Q. Liu, H. Cheng, M. Hu, and S. Zhang, “Classification and carbon structural transformation from anthracite to natural coaly graphite by XRD, Raman spectroscopy, and HRTEM”, *Spectrochimica Acta Part A: Molecular and Biomolecular Spectroscopy*, vol. 249, 2021.

[18] F. Xie, Z. Xu, A. C. S. Jensen, H. Au, Y. Lu, V. Araullo-Peters, A. J. Drew, Y. -S. Hu, and M. -M. Titirici, “Hard–Soft Carbon Composite Anodes with Synergistic Sodium Storage Performance”, *Advanced Functional Materials*, vol. 29, no. 24, 2019.

[19] M. K. Le, T. N. Tran, T. K. T. Huynh, V. H. Nguyen, D. T. Vo, V. M. Tran, and M. L. P. Le, “Development of Vang Danh anthracite as a cost-effective anode for sodium-ion batteries through a heat-treatment process”, *RSC Advances*, vol. 12, no. 46, pp. 29900-29907, Oct. 2022.

Influence of ultrafast laser surface modification on the surface morphology, chemical composition and wettability of MONEL® alloy 400

Kipkurui Ronoh
Central European Institute of Technology
Brno University of Technology
Purkyňova 123, 612 00 Brno, the Czech Republic
kipkurui.ronoh@ceitec.vutbr.cz

***Abstract*—This study explored ultrafast laser ablation's effects on the surface morphology, chemical composition, and wettability of MONEL® alloy 400, widely used in marine applications due to its corrosion resistance. Ultrafast laser ablation created micro/nanostructures, with SEM revealing laser-induced periodic surface structures (LIPSS) and increased roughness at higher fluences. XPS analysis identified an outer layer of $Ni(OH)_2$ and $Cu(OH)_2$. The contact angles of the laser-ablated samples were higher than those of the polished samples. These findings enhance the understanding of laser-ablated MONEL® alloy 400 and its potential marine applications.**

Keywords—MONEL® alloy 400, Laser ablation, Surface morphology, XPS, Wettability

I. Introduction

Nickel-based alloys are widely used in marine engineering applications due to their strength, oxidation, and excellent corrosion resistance, especially in harsh, high-temperature applications and high-salinity environments [1]. They are a broad group of materials that primarily contain nickel as their base element, often combined with elements like copper and chromium to enhance specific properties. MONEL® alloy 400 is composed of 62 – 68 % nickel, 28 – 34 % copper, and small interstitial elements [2]. It is known for its excellent corrosion resistance to corrosive media like seawater and high-temperature steams. It can maintain good mechanical properties within a wide range of temperatures, i.e., from below zero degrees up to 550 degrees Celsius, hence a good material for a wide range of applications [3], [4].

Because of the outstanding corrosion resistance and good mechanical strength of the MONEL® alloy 400, it is used in marine industries for the fabrications of propeller shafts, evaporators, marine fittings and fasteners, valves and pumps, and diffusers [5]. It also finds applications in the chemical processing industry and desalination plants [3], [6].

Lasers have transformed modern manufacturing by enabling precise, efficient, and versatile material processing [7]. Their high energy density allows for surface modifications with minimal waste and damage, improving productivity and accuracy [8]. Laser surface modification techniques, like laser ablation, enhance the properties of metallic components by altering their microstructure, surface chemistry, and wettability. This precise process improves adhesion, reduces contamination, and enhances corrosion resistance, especially in alloys like MONEL® alloy 400. By adjusting laser parameters, surface topography can be tailored for improved wettability or hydrophobicity, making it valuable for harsh environments [9].

Ultrafast laser ablation uses extremely short pulses (femtosecond or picosecond) to precisely remove material with minimal thermal damage. Its high peak power allows for processing all materials while preserving their properties. This technique enables controlled surface modification, enhancing corrosion resistance and micro/nanostructuring [10]. It is ideal for advanced applications like marine component processing for corrosion protection and anti-fouling surfaces.

While many studies have explored fs and ps laser processing of alloys, research on ultrafast laser processing of MONEL® alloy 400 remains limited. A comprehensive analysis of how laser parameters influence surface structures, chemistry, and wettability of this alloy is still lacking, despite its importance for understanding surface modifications. This research investigated how laser fluence affects the surface morphology, topography, chemical composition, and wettability of MONEL® alloy 400. Analysis was conducted using SEM, profilometry, XPS, and sessile droplet methods. The findings contribute to optimizing laser processing parameters and enhancing the understanding of wettability in ultrafast laser-ablated metals, broadening their applications.

II. Experimental Methodology

A. Material and its preparation

The study used commercial MONEL® alloy 400 (13 × 13 × 1 mm). The samples were ground with SiC abrasive foils (1200, 2000 grit) and polished with polycrystalline diamond suspensions (0.3, 0.1 μm) using a semi-automatic polishing machine. They were then ultrasonically cleaned with acetone and ethanol for 20 minutes and dried with pressurized air to remove impurities. The alloy's composition, provided by BIBUS METALS (Brno, the Czech Republic), is detailed in TABLE I.

TABLE I. NOMINAL CHEMICAL COMPOSITION (WT.%) OF THE MONEL® ALLOY 400

Ni	Cu	Mn	Fe	S	Si	C
63.00 (min)	28.00 – 34.00	2.0 max.	1.00 – 2.50	0.024	0.5 max.	0.3 max

B. *Surface laser ablation of the samples*

The polished MONEL® alloy 400 samples were ablated using a linearly polarized Yb:YAG picosecond laser (Perla®100, Hilase, the Czech Republic) with a 1030 nm wavelength, 60 kHz repetition rate, 1 mJ peak energy, and 1 ps pulse width [11]. The beam was focused to a 25 µm spot size using a telecentric F-θ lens (Linos, Qioptiq, Gottingen, Germany). The scan line overlap (80%) and pulse overlap (93%) were maintained. Samples were raster scanned at 100 mm/s with one scanning pass using a cross-hatching (0°/90°) strategy over a 10 × 10 mm² area. Laser fluences of 0.5, 1.5, 3, and 4.5 J/cm² were applied.

C. *Surface characterization of the samples*

Scanning electron microscopy (SEM) (Verios 460L, FEI, the Czech Republic) was used to analyze the sample morphologies using secondary electrons (SE) with a 50 pA current and 5 keV accelerating voltage. Surface topography was measured using a mechanical profilometer (Dektak XT, Bruker, USA) at 24° C, with a 2 µm tip radius and vertical and lateral resolutions of 0.1 nm and 0.5 µm, respectively. Data was processed using Gwyddion 2.64 software.

The chemical composition of the sample surfaces was analyzed using X-ray Photoelectron Spectroscopy (XPS) (Axis Supra, Kratos Analytical Ltd., UK) with a monochromatic Al Kα radiation source (1486.6 eV, 15 mA emission current). Survey spectra were acquired within a 0–1200 eV binding energy range (80 eV pass energy, 1 eV step size), while high-resolution spectra used a 20 eV pass energy with a 0.1 eV step size. The wettability of the samples was measured using the sessile droplet method with the Surface Energy Evaluation System (See System E, Advex Instruments, the Czech Republic). A 2 µL drop of distilled water was placed on each sample. A high-resolution camera captured droplet images, which were analyzed using the SEE system software to determine the contact angle. Measurements were averaged from five successive readings on each surface using the circle fitting mode.

III. RESULTS AND DISCUSSION

A. *Surface morphology after laser processing*

Ultrafast laser processing of MONEL® alloy 400 creates nano/micro-scale surface features based on processing parameters. SEM images (Fig. 1) show that polished samples are smooth, while laser processing above the ablation threshold generates micro/nanostructures [11]. These laser-induced surface structures (LISS), including laser-induced periodic surface structures (LIPSS), vary with laser parameters [1], [9]. At a laser fluence of 0.5 J/cm², long, smooth, and well-formed LIPSS are produced, while at 1.5 J/cm², the LIPSS become shorter and less smooth. At 3 J/cm², the LIPSS are rougher, and trench-like structures begin to form. By 4.5 J/cm², the LIPSS transition to shorter, irregular structures, and micro-ripples with micro-holes appear [12], [13]. SEM images at lower fluences (0.5 and 1.5 J/cm²) show no solidified melt droplets, suggesting equilibrium vaporization is the main ablation mechanism. At higher fluences (3 and 4.5 J/cm²), the presence of micro-ripples and micro-holes suggests explosive phase transitions due to superheating [14].

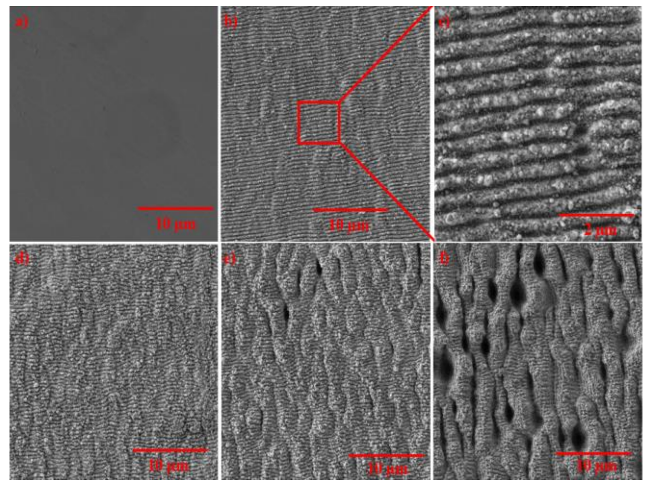

Fig. 1. SEM images of the a) polished surface and laser-ablated MONEL® alloy 400 samples surfaces processed by fluence of b) 0.5 J/cm^2, d) 1.5 J/cm^2, e) 3 J/cm^2 and f) 4.5 J/cm^2. Inset: c) is a high-magnification SEM image of the sample processed by a fluence of 0.5 J/cm^2.

The surface morphology of laser-ablated MONEL® alloy 400 is influenced by laser fluence, which governs the development of micro/nanostructures. The peak laser fluence F_0 is related to the pulse energy E_{pulse} and the laser beam's focal area as;

$$F_0 = \frac{2E_{pulse}}{A} = \frac{2E_{pulse}}{\pi\omega_0{}^2} \qquad (1)$$

where A is the area of the focus by the laser beam, and ω_o is the spot radius at the waist measured at $1/e^2$ value. As fluence increases, significant morphological changes occur due to thermal and melting dynamics. The ablation depth per pulse L on the samples varies with fluence. At low fluence, it depends on the optical penetration depth (α^{-1}) and is given by:

$$L = \alpha^{-1} ln(\frac{F_0}{F_{th,g}}) \qquad (2)$$

where $F_{th,g}$ is the ablation threshold fluence for the gentle ablation phase. At high fluence, L is governed by the electron heat diffusion length (γ) and follows:

$$L = \gamma ln(\frac{F_0}{F_{th,s}}) \qquad (3)$$

where $F_{th,s}$ is the ablation threshold fluence for the strong ablation phase.

B. Topographical analysis of the laser-ablated surfaces

Different surface topographies and structures can be achieved on MONEL® Alloy 400 based on laser processing parameters. Fig. 2 presents the 3D surface topographies of laser-ablated MONEL® Alloy 400 under laser fluences of 0.5, 1.5, 3, and 4.5 J/cm², showing nanostructures of varying heights. This indicates that laser ablation induces rough surface structures, with dimensions dependent on the laser fluence. Surface characterization followed the ISO 25178 standard, with topographical parameters including surface roughness (Sa), root mean square roughness (Sq), skewness (Ssk), and kurtosis (Sku) calculated using Gwyddion software.

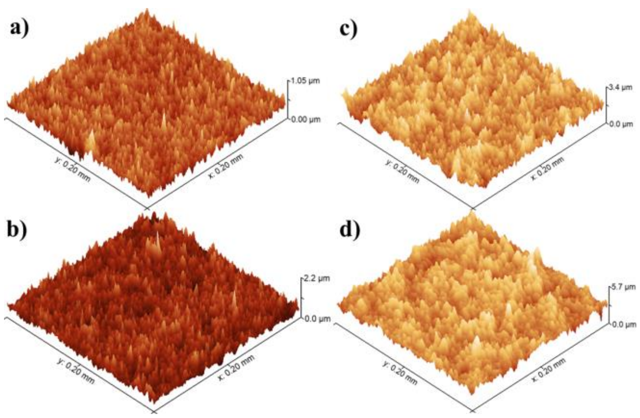

Fig. 2. Topographical images of the laser-ablated MONEL® Alloy 400 samples using fluence of a) 0.5 J/cm^2, b) 1.5 J/cm^2, c) 3 J/cm^2 and d) 4.5 J/cm^2.

The surface roughness (Sa) increased from 0.07 µm to 0.43 µm with rising laser fluence, a trend also observed for Sq, due to increased laser heat accumulation leading to rougher surfaces. As shown in TABLE II, the roughness values remain in the nanoscale, indicating relatively smooth surfaces. Surface topography analysis reveals a decrease in skewness (Ssk) with increasing fluence, suggesting reduced sharpness of peaks and valleys. The kurtosis (Sku) values were all below 3, indicating a flatter surface profile with fewer sharp peaks and deep valleys. This suggests that the laser-ablated surfaces had uniform and even structures due to the lower fluence regimes used. The roughness factor (r), defined as the ratio of the actual rough surface area to its geometric projected area, is always greater than 1 for rough surfaces, as seen in TABLE II.

TABLE II. TOPOGRAPHICAL DATA FROM LASER-ABLATED SURFACES OF MONEL® ALLOY 400

Laser Fluence (LF) (J/cm^2)	**Mean Roughness Sa (µm)**	**RMS Roughness Sq (µm)**	**Skew, Ssk**	**Kurtosis, Sku**	**Roughness Factor, r**
LF = 0.5	0.07	0.09	0.42	0.91	1.01
LF = 1.5	0.13	0.17	0.55	1.22	1.01
LF = 3.0	0.26	0.32	0.23	0.15	1.04
LF = 4.5	0.43	0.55	0.11	0.71	1.08

C. Surface chemistry of the samples

XPS was conducted to determine the chemical composition and states of MONEL® alloy 400 before and after laser ablation. The survey spectra identified Ni, Cu, O, and C peaks. Fig. 3 presents the high-resolution spectra of Ni 2p, Cu 2p, O 1s, and C 1s. The analysis focused on the more intense Ni $2p_{3/2}$ and Cu $2p_{3/2}$ spin-orbit split components [15].

The high-resolution Ni $2p_{3/2}$ spectra of polished and laser-ablated MONEL® alloy 400 samples (Fig. 3(a, b, c)) reveal multiplet splitting [16]. The polished sample primarily consists of metallic nickel (Ni(0)), its satellite peaks, and Ni^{2+} oxides, suggesting the presence of a natural oxide layer. In contrast, laser-ablated samples exhibit predominantly Ni^{2+} hydroxides/oxides and their satellite structures, with only a minor fraction of Ni(0) at lower laser fluence (0.5 J/cm²). The oxidation, attributed to laser-induced heating, results in binding energies around 855.9 eV and 855.79 eV, indicative of $Ni(OH)_2$ with possible traces of NiO [17]. Samples processed at higher fluences (3 and 4.5 J/cm²) show similar spectral characteristics, confirming that $Ni(OH)_2$ dominates the outer surface layers, while the interior remains primarily metallic Ni [18].

The high-resolution Cu $2p_{3/2}$ spectra of polished and laser-ablated MONEL® alloy 400 samples (Fig. 3(f, g, h) reveal multiplet splitting with shake-up structures [19]. The polished sample predominantly contains metallic copper (Cu(0)), indicating its stability under normal environmental conditions. In contrast, laser-ablated samples exhibit a combination of Cu(0), Cu^{2+} oxides, and satellite structures, with oxidation primarily driven by heat from laser ablation. The binding energies (934.50 eV, 934.60 eV) and spectral shapes suggest that Cu^{2+} is mainly present as $Cu(OH)_2$, with minor contributions from CuO. Samples processed at higher fluences (3 and 4.5 J/cm²) show similar spectra, confirming that $Cu(OH)_2$ dominates the outer layers, while metallic Cu remains in the interior.

The fitted C 1s spectra for both polished and laser-ablated MONEL® alloy 400 samples (Fig. 3(d, e)) exhibit similar characteristics, with four distinct carbon species: aliphatic carbons (C–C/C–H), alcohols/hydroxyls/ethers (C–O), carbonyl/ketones (C=O), and carboxyl groups (O–C=O) [20]. The binding energy (~284.9 eV) remains consistent across all samples, suggesting a common origin, likely from the alloy itself as an interstitial element or from adventitious carbon contamination. Samples treated with laser fluences of 1.5, 3, and 4.5 J/cm² exhibit similar spectral characteristics. The spectra are dominated by a strong hydrocarbon (C–C/C–H) signal.

The fitted O 1s spectra for both polished and laser-ablated MONEL® alloy 400 samples, as shown in Fig. 3(i, j), reveal three oxygen species: lattice oxides (Latt. O), surface hydroxyl (-OH)/defective oxides (def. O)/adsorbed organic oxygen (org. O), and adsorbed water (ads. H_2O)/adsorbed organic oxygen (org. O). The most intense peaks correspond to surface hydroxyl/defective oxides/adsorbed organic oxygen species. Samples treated with laser fluences of 1.5, 3, and 4.5 J/cm² exhibit similar spectral characteristics. An increase in lattice oxides with higher laser fluence suggests enhanced surface oxidation due to laser ablation [21].

XPS analysis suggests that the passive film formed on laser-ablated samples consists of an inner metallic layer enriched in Ni and Cu, while the outer layer is composed of mixed hydroxides and/or oxides, primarily Ni and Cu hydroxides.

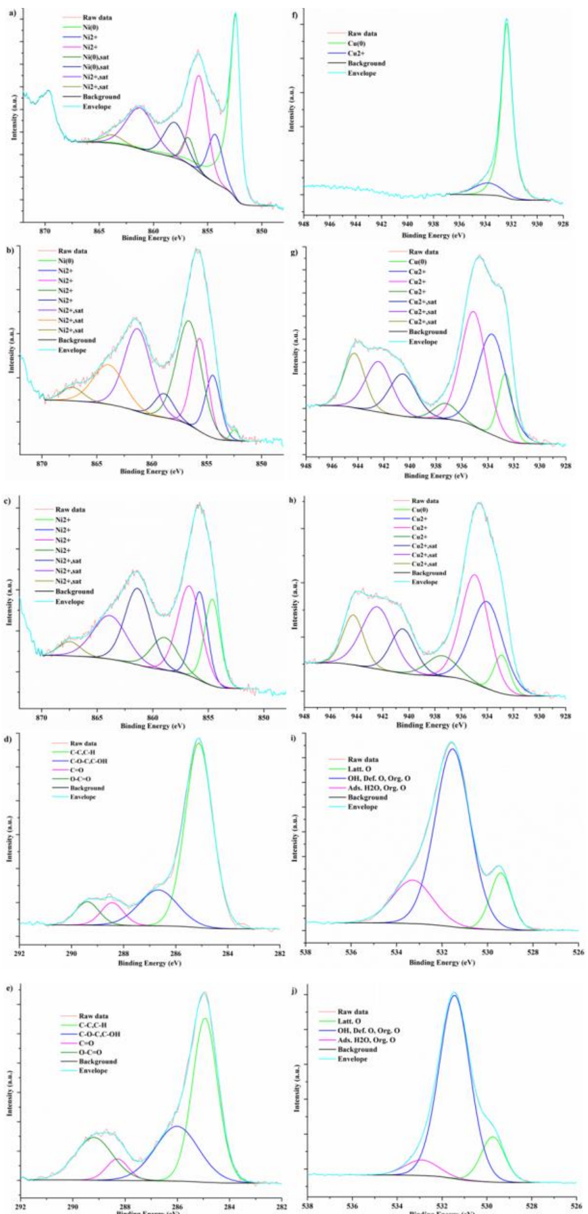

Fig. 3. High-resolution spectra of the Ni $2p_{3/2}$ peaks of the a) polished sample and samples processed by the fluence of b) 0.5 J/cm^2, and c) 1.5 J/cm^2; C 1s peaks of the d) polished sample and sample processed by the luence of e) 0.5 J/cm^2; Cu $2p_{3/2}$ peaks of the f) polished and samples processed by fluence of g) 0.5 J/cm^2, and h) 1.5 J/cm^2; and O 1s peaks of the i) polished sample and samples processed by the fluence of j) 0.5 J/cm^2.

D. Influence of the laser fluence on wettability

Fig. 4 illustrates that both polished and laser-ablated MONEL® alloy 400 samples exhibit hydrophobic behaviour, with contact angles exceeding 90°. Notably, the laser-ablated samples demonstrate significantly higher contact angles (>140°), indicating enhanced hydrophobicity. This increase is attributed to surface roughening induced by laser ablation, as observed in Fig. 2. The Wenzel equation [22] explains this phenomenon, stating that surface roughness amplifies the wetting properties of initially hydrophobic surfaces:

$$cos\,\theta_W = r\,\frac{\gamma_{SV}-\gamma_{SL}}{\gamma_{LV}} = r\,cos\,\theta \quad (4)$$

Where θ_W is the apparent contact angle of a rough homogeneous surface, r is the roughness factor ($r \geq 1$, where r = 1 for a perfectly planar surface and r > 1 for a rough surface), γ_{SV} , γ_{SL} and γ_{LV} are solid-vapour, solid-liquid and liquid-vapour interfacial tensions, respectively. Given that the roughness factor (r) is greater than 1 (as shown in Table II), the equation confirms that laser-induced roughness further enhances the hydrophobicity of the samples.

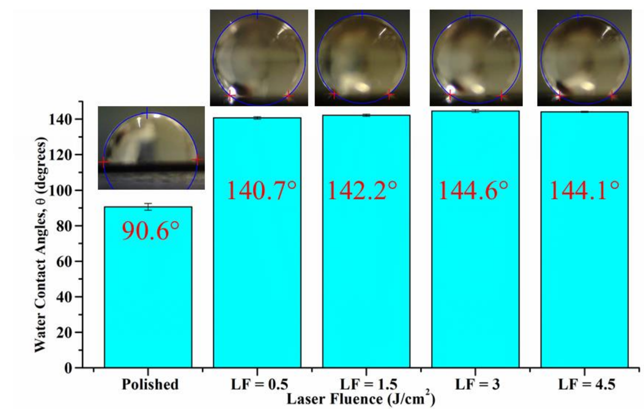

Fig. 4. Contact angle measurements on laser-ablated samples

Fig. 4 demonstrates that contact angles increase with higher laser fluence, indicating enhanced hydrophobicity. This change is attributed to modifications in surface morphology (Fig. 1) and topography (Fig. 2) due to laser-induced surface structures (LISS). Table II further confirms that surface roughness increases with laser fluence, which contributes to the rising contact angles, as explained by the Wenzel model.

The final hydrophobicity of laser-ablated surfaces without additional coatings depends on both surface roughness and the presence of carbonaceous materials [23], [24]. XPS analysis confirms the presence of carbon, suggesting that hydrophobic carbonaceous compounds may adsorb onto the surface under normal environmental conditions after laser ablation. These materials are known to enhance hydrophobicity over time [25].

Overall, the observed changes in wettability demonstrate that laser ablation effectively modifies the surface topography and chemistry of MONEL® alloy 400, making it a viable technique for tailoring its wetting characteristics.

IV. Conclusion

This study investigated the ultrafast laser ablation of MONEL® alloy 400 under various laser fluences in an ambient environment. The findings demonstrated that low-fluence ultrafast laser ablation produced laser-induced periodic surface structures (LIPSS). Surface roughness parameters (Sa and Sq) increased with higher laser fluence, indicating enhanced surface structuring. XPS analysis confirmed the presence of Ni, Cu, O, and C on both polished and laser-ablated surfaces. High-resolution spectra revealed that the outermost layer of the ablated surfaces primarily consisted of $Ni(OH)_2$ and $Cu(OH)_2$. Additionally, O 1s spectra showed an increase in lattice oxides with increasing laser fluence. Wettability tests indicated that all samples exhibited hydrophobic behaviour (contact angles >90°), with ablated samples demonstrating greater hydrophobicity, which increased with laser fluence.

This study provides insights into optimizing ultrafast laser ablation conditions for surface modification of MONEL® alloy 400, with potential applications in corrosion control. Future studies will consider other parameters which influence surface modification and may have limited the broad understanding of surface modification. Future research will explore ultrafast laser ablation in water and inert environments to further investigate surface modifications, along with a detailed assessment of the corrosion resistance of laser-ablated MONEL® alloy 400.

ACKNOWLEDGMENT

I would like to acknowledge the CzechNanoLab Research Infrastructure, supported by MEYS CR (LM2023051), and the Czech Academy of Sciences (RVO: 68081731). My sincere gratitude goes to my doctoral supervisor, Prof. Dinara Sobola, Ph.D., for her expert guidance and valuable support throughout the preparation of this article. I also extend my appreciation to Ing. Jan Novotný for his assistance with laser processing the samples. Special thanks to Prof. Libor Mrna, Dr. Alexandr Knápěk, and Dr. Pavel Kaspar for their unwavering support, which contributed significantly to the success of this work.

REFERENCES

[1] K. Ronoh, J. Novotný, L. Mrňa, A. Knápek, and D. Sobola, "Effects of laser and scanning parameters on surface modification of MONEL® alloy 400 by picosecond laser," Opt Laser Technol, vol. 172, p. 110514, May 2024.

[2] Ștefan ȚĂLU, Kipkurui RONOH, and Dinara SOBOLA, "The Laser Treatment's Impact on the Surface Topography of MONEL® Alloy 400, used in the Manufacturing of Marine Equipment Components," HIDRAULICA, no. 2, pp. 15–26, 2024, Accessed: Aug. 17, 2024. [Online]. Available: https://hidraulica.fluidas.ro/2024/nr2/15-26.pdf

[3] I. Raffeis et al., "Qualification of a Ni–Cu Alloy for the Laser Powder Bed Fusion Process (LPBF): Its Microstructure and Mechanical Properties," Applied Sciences, vol. 10, no. 10, p. 3401, May 2020.

[4] M. Kukliński, A. Bartkowska, and D. Przestacki, "Microstructure and selected properties of Monel 400 alloy after laser heat treatment and laser boriding using diode laser," International Journal of Advanced Manufacturing Technology, vol. 98, no. 9–12, pp. 3005–3017, Oct. 2018.

[5] Special Metals, "MONEL® alloy 400." Accessed: Nov. 19, 2023. [Online]. Available: https://www.specialmetals.com/documents/technical-bulletins/monel-alloy-400.pdf

[6] M. Kukliński, A. Bartkowska, D. Przestacki, and G. Kinal, "Influence of microstructure and chemical composition on microhardness and wear properties of laser borided monel 400," Materials, vol. 13, no. 24, pp. 1–15, 2020.

[7] C. Corsaro et al., "Wetting Behavior Driven by Surface Morphology Changes Induced by Picosecond Laser Texturing," Materials, vol. 17, no. 8, p. 1719, Apr. 2024.

[8] C. A. Biffi et al., "Ultrashort Laser Texturing of Superelastic NiTi: Effect of Laser Power and Scanning Speed on Surface Morphology, Composition and Wettability," Metals (Basel), vol. 13, no. 2, p. 381, Feb. 2023.

[9] M. A. Khan, A. Mohd Halil, M. S. Zainol Abidin, M. H. Hassan, and A. Anjang Ab Rahman, "Influence of laser surface texturing on the surface morphology and wettability of metals and non-metals: A review," Mater Today Chem, vol. 41, p. 102316, Oct. 2024.

[10] T. Primus, M. Novák, P. Zeman, and F. Holešovský, "Femtosecond laser processing of advanced technical materials," Acta Polytechnica, vol. 63, no. 1, pp. 36–49, Mar. 2023.

[11] K. Ronoh et al., "Characterization of the picosecond laser-ablated HOPG using Raman spectroscopy and SEM microscopy," Mater Today Commun, vol. 34, no. August 2022, p. 105181, Mar. 2023.

[12] K. Ahmmed, C. Grambow, and A.-M. Kietzig, "Fabrication of Micro/Nano Structures on Metals by Femtosecond Laser Micromachining," Micromachines (Basel), vol. 5, no. 4, pp. 1219–1253, Nov. 2014.

[13] M. Groenendijk and J. Meijer, "Microstructuring using femtosecond pulsed laser ablation," in International Congress on Applications of Lasers & Electro-Optics, Laser Institute of America, 2005, p. M408.

[14] W. Zhao, W. Wang, G. Jiang, B. Q. Li, and X. Mei, "Ablation and morphological evolution of micro-holes in stainless steel with picosecond laser pulses," The International Journal of Advanced Manufacturing Technology, vol. 80, no. 9–12, pp. 1713–1720, Oct. 2015.

[15] B. P. Payne, M. C. Biesinger, and N. S. McIntyre, "Use of oxygen/nickel ratios in the XPS characterisation of oxide phases on nickel metal and nickel alloy surfaces," J Electron Spectros Relat Phenomena, vol. 185, no. 5–7, pp. 159–166, Aug. 2012.

[16] K. Ronoh, J. Novotný, L. Mrňa, A. Knápek, and D. Sobola, "Ablation characteristics of the nickel-based superalloy, 699 XA using ultrafast laser," Appl Surf Sci, vol. 682, p. 161687, Feb. 2025.

[17] A. P. Grosvenor, M. C. Biesinger, R. St. C. Smart, and N. S. McIntyre, "New interpretations of XPS spectra of nickel metal and oxides," Surf Sci, vol. 600, no. 9, pp. 1771–1779, May 2006.

[18] F. Ma, Z. Zeng, and Y. Gao, "Tribocorrosion and the surface repassivation behavior of Monel 400 alloy in artificial seawater," Industrial Lubrication and Tribology, vol. 70, no. 7, pp. 1331–1340, Aug. 2018.

[19] M. C. Biesinger, "Advanced analysis of copper X-ray photoelectron spectra," Surface and Interface Analysis, vol. 49, no. 13, pp. 1325–1334, Dec. 2017.

[20] K. Ronoh, S. H. Fawaeer, V. Holcman, A. Knápek, and D. Sobola, "Comprehensive characterization of different metallic thin films on highly oriented pyrolytic graphite substrate," Vacuum, vol. 215, no. February, p. 112345, Sep. 2023.

[21] K. Ronoh, J. Novotný, L. Mrňa, A. Knápek, and D. Sobola, "Analysis of processing efficiency, surface, and bulk chemistry, and nanomechanical properties of the Monel® alloy 400 after ultrashort pulsed laser ablation," Mater Res Express, vol. 11, no. 1, p. 016514, Jan. 2024.

[22] R. N. Wenzel, "Resistance of solid surfaces to wetting by water," Ind Eng Chem, vol. 28, no. 8, pp. 988–994, Aug. 1936.

[23] A.-M. Kietzig, S. G. Hatzikiriakos, and P. Englezos, "Patterned Superhydrophobic Metallic Surfaces," Langmuir, vol. 25, no. 8, pp. 4821–4827, Apr. 2009.

[24] K. Ronoh, J. Novotný, L. Mrňa, A. Knápek, and D. Sobola, "Surface Structuring of the CP Titanium by Ultrafast Laser Pulses," Applied Sciences, vol. 14, no. 8, p. 3164, Apr. 2024.

[25] V. S.C. et al., "Laser patterned titanium surfaces with superior antibiofouling, superhydrophobicity, self-cleaning and durability: Role of line spacing," Surf Coat Technol, vol. 418, p. 127257, Jul. 2021.

Effect of fuel assembly rotation on optimization of fuel pins burnup

1st Pavel Maca
Department of Electrical Power Engineering
Brno University of Technology
Brno, Czech Republic
pavel.maca@vut.cz

2nd Karel Katovsky
Department of Electrical Power Engineering
Brno University of Technology
Brno, Czech Republic
katovsky@vut.cz

***Abstract*—The paper's topic is the optimization of fuel assembly burnup in the Dukovany Nuclear Power plant using fuel assembly rotation. The MOBY-DICK deterministic code was used to simulate neutronics processes within the core reactor. This study evaluates the impact of fuel assembly rotation on the homogeneity of fuel pin burnup for overall fuel utilization optimization. The results of this study demonstrate how the rotation of fuel assembly affects burnup distribution and contributes to the more efficient use of nuclear fuel.**

Keywords—fuel assembly, rotation of fuel assembly, fuel pins burnup, MOBY-DICK

I. INTRODUCTION

Optimization of the reactor core of nuclear reactors is an integral part of the operation of all nuclear reactors, even pressurized water reactors (PWR). PWR reactors include Russian VVER reactors, which are operated in the Czech Republic [1]. Optimization of the reactor core of these power plants is a crucial aspect of efficient fuel utilization, operational cost-effectiveness, and minimizing neutron flux asymmetry. One of the key fuel properties that can be optimized is fuel burnup. Fuel burnup in the reactor core significantly influences reactor operation. Uneven burnup among fuel assemblies leads to flux non-uniformity distribution, which can limit overall fuel efficiency.

The foundation of reactor core optimization lies in selecting an appropriate fuel loading pattern that ensures the most uniform heat generation within the reactor core, minimizes neutron leakage, reduces neutron fluence on the reactor pressure vessel, which affects embrittlement, and addresses other critical factors. In modern reactor operation, the optimization of the loading pattern has become a critical research area, driven by advancements in computational methods and algorithms. Original approaches, based on expert judgment and iterative methods, are increasingly being replaced by advanced numerical techniques that enable improved power distribution, higher fuel efficiency, and extended fuel cycles. The most common methods used in optimization include genetic algorithms [2], Monte Carlo methods, linear and nonlinear optimization techniques, and, more recently, neural networks and methods using artificial intelligence [1].

II. UNEVEN BURNUP OF FUEL PINS

One of the challenges in reactor core optimization is uneven burnup of fuel pins within a fuel assembly, which arises due to different neutron flux across fuel in the assembly. This phenomenon is pronounced for example, in the fuel assemblies located at the periphery of the reactor core, where neutron flux asymmetries lead to uneven power distribution. The primary cause of the different neutron flux surrounding the fuel assembly. For example, an assembly positioned near the reactor core-periphery has one side exposed to a moderator region acting as a neutron reflector, while the opposite side is a fresh-loaded fuel assembly. The fresh fuel assembly has a significantly higher neutron flux compared to assemblies loaded multiple cycles in the reactor core. This flux imbalance causes power tilt (Fig. 1.), characterized by a radial asymmetry in power distribution within the assembly. Such power asymmetry leads to uneven burnup across fuel pins, where the fissile material in the pins is not fully utilized.

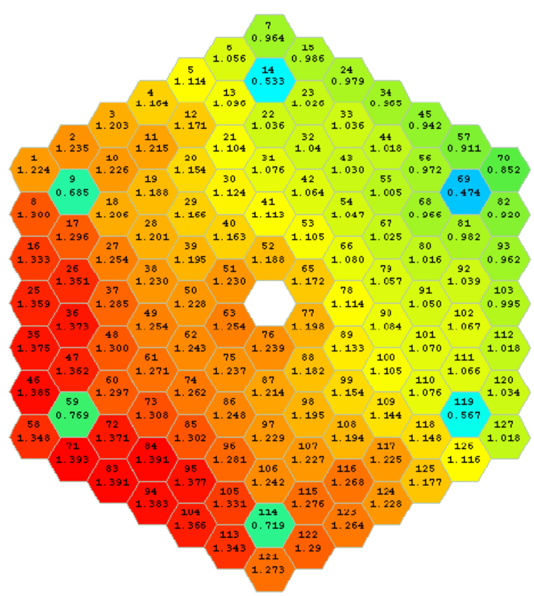

Fig. 1. Power tilt in the fuel assembly

A potential solution to this issue is a rotation of fuel assembly during refueling outages. By rotation, the fuel assembly can balance the fuel assembly burnup profile. The optimal rotation degree that will most reduce the uneven burnup depends on the specific neutron flux conditions and must be determined by detailed burnup analysis for each degree of rotation. The following section presents a method to analyze the burnup distribution in rotated fuel assemblies computationally and evaluates the selection of the most appropriate degree of rotation on fuel cycle length and overall fuel utilization.

III. VVER-440 REACTOR

The analyses presented in this study were performed for the reactor core of the Dukovany Nuclear Power Plant, which is equipped with VVER-440 reactors, model 213. The reactor core is composed of 312 fuel assemblies and 37 movable control assemblies. The bottom part of the movable contains fuel, which is in tandem with the upper part containing boron-steel material used as a neutron absorber. A movable control assembly is also called a shim assembly. The construction of the fuel portion shim assembly is almost the same as that of a fixed fuel assembly [3].

The fuel assemblies consist of 126 fuel pins, each arranged in a triangular grid and thus forming a hexagonal cross-section of the fuel assembly. The fuel pins are surrounded by the fuel assembly shroud that holds all portions of the assembly together, forming an integral unit. The fuel pins contain low-enriched uranium dioxide pellets. The fuel was usually enriched to 3.6-4.5 wt% ^{235}U; however, modern fuel designs reach up to 4.87 wt%. Fuel pellets in fuel pins must be hermetically sealed, this is done by the cladding surrounding the pellets. This cladding is made of Zr-1% Nb alloy. Between the fuel pellet and cladding, there is a thin gap filled with helium.

IV. SIMULATION TOOL AND MODEL DESCRIPTION

One possibility to optimize the reactor core is to use appropriate neutronic simulation code. These codes can be divided according to the neutron transport into stochastic and deterministic codes [4]. For full-core analysis, it is usually preferable to use deterministic code terms of complexity. Examples of such codes include PARCS, ANDREA, NESTLE, and MOBY-DICK. In this paper, the software MOBY-DICK is chosen because it is used for neutronic calculations at the Dukovany Power Plant. Compared to PARCS, MOBY-DICK focuses only on VVER reactors, PARCS can also be used for PWRs. Both are lattice codes solving a set of diffusion equations for the homogenized elements of the fuel assembly. The ANDREA and NESTLE codes also solve diffusion equations, except that they do not solve elements but individual nodes. The basic solution of neutronic calculations in MOBY-DICK is the differential solution of a multi-group system of diffusion equations. Nuclear data libraries are an important part of deterministic codes as well as MOBY-DICK. These libraries contain data that are used for the input files of the simulation. Some of the most important data include energy-dependent cross-sections, reaction fragments, or deviations of the processed data. The nuclear data libraries for MD are prepared by the WIMS [5] lattice code [6].

The main objective of this study is to evaluate the benefit of the rotation of fuel assembly to uneven burnup. As discussed in previous chapters, asymmetric neutron flux in the reactor core caused by the power tilt of the fuel assembly can affect fuel utilization. Implementing the rotation will make the burnup of fuel pins more homogenous across the fuel assembly, leading to improved fuel utilization. This study aims to quantify these effects on the length of the fuel cycle, power peaking, and distribution of burnup in the fuel assembly. The optimum degree of rotation to minimize the local burnup gradient will also be determined.

A. *Methodology for determining optimal rotation*

As mentioned in the previous chapter, the fuel assembly cross-section of the VVER reactor is hexagonal, which allows for six possible rotation degrees (0°,60°,120°,180°,240°, and 300°). For clarity, the degree of rotation is designated as 0,1,2,3,4, and 5, corresponding to the number of sixths of the assembly that has been rotated. Since each fuel assembly can be divided into six equal sections, this segmentation allows for detailed burnup analysis of each part, as illustrated (Fig. 2.). Each section's average burnup is evaluated and compared across all rotation combinations. By analyzing these deviations from an ideal, a homogenous burnup distribution can be identified. A perfectly homogenous burnup scenario would result in all hexagonal sixths having an identical burnup fraction, corresponding to a value of 1. If two identical average values of sixths are divided, the result is 1. Therefore, the value of 1 was chosen to represent even burnup. Thus, the degree of uneven burnup can be quantified as deviations from the idealized value 1. This analysis is performed for each rotation degree, and the optimal scenario is determined based on the configuration results in burnup values closest to 1 across all hexagonal sixths. The objective is to minimize burnup asymmetry, thereby enhancing fuel utilization efficiency.

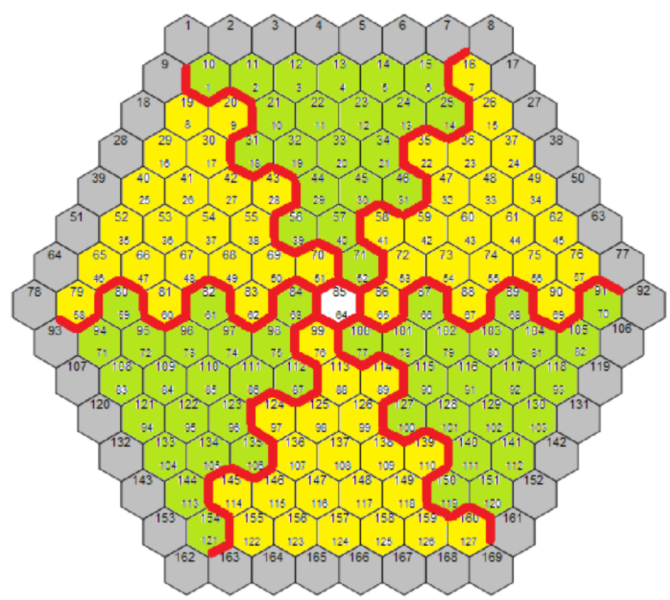

Fig. 2. Division of the fuel assembly into six

B. *Current used rotation*

In the present operational strategy, fuel assembly rotation is already implemented in a limited capacity. Typically, rotation is applied selectively, focusing on fuel assemblies with the highest power tilt. In many cases, there are only one or two rotations of assembly over the entire duration of their residence in the reactor core. Examples of currently used rotation at the Dukovany nuclear Power Plant are shown in Fig. 3., where there are only a few fuel assemblies. The rotations are illustrated for fuel assemblies loaded during the 28th cycle, showing their positions in the core for each subsequent cycle. Fuel assemblies that have been rotated are highlighted in yellow, clearly indicating the limited number of rotated assemblies within the residence in the reactor core.

Used rotation of FA loaded in the 28th cycle						
FA number	28th cycle	29th cycle	30th cycle	31st cycle	32nd cycle	33rd cycle
6726	26	8	23	2	out	
6728	28	48	28	51	58 (rot. 180°)	out
6730	30	4	7	7	out	
6732	32	32	12	28	out	
6739	39	15	16 (rot. 180°)	18	34 (rot. 240°)	out
6744	44	44	20	13	out	
6745	45	42	48 (rot. 180°)	57	55 (rot. 120°)	out
6753	53	37	3	out		
6754	54	38	36	29 (rot. 180°)	out	

Fig. 3. Rotation for the 28th cycle

C. *Multiple rotation*

The primary difference between currently used and multiple rotations is in the number of rotations each fuel assembly within the residence in the reactor core. Unlike the currently applied rotation strategy, the multiple rotation approach aims to systematically determine the optimal rotation angle for each fuel assembly, as described in the previous chapters. Instead of a one-time selective rotation, fuel assemblies will be rotated in every fuel cycle, ensuring a continuous improvement in burnup uneven and reactor performance. An overview of multiple rotation scenarios is presented in Fig. 4., illustrating how fuel assemblies would be rotated at each fuel cycle to achieve optimized burnup homogeneity. The picture also indicates the most suitable rotation degree for each fuel assembly, ensuring that the selected rotation minimizes burnup asymmetry and maximizes fuel utilization.

Used multiple rotation of FA loaded in 28th cycle						
FA number	28th cycle	29th cycle	30th cycle	31st cycle	32nd cycle	33rd cycle
6726	26	8 (rot. 180°)	23 (rot. 120°)	2 (rot. 180°)	out	
6728	28	48 (rot. 0°)	28 (rot. 240°)	51 (rot. 300°)	58 (rot. 180°)	out
6730	30	4 (rot. 180°)	7 (rot. 180°)	7 (rot. 180°)	out	
6732	32	32 (rot. 180°)	12 (rot. 0°)	28 (rot. 240°)	out	
6739	39	15 (rot. 180°)	16 (rot. 60°)	18 (rot. 60°)	34 (rot. 180°)	out
6744	44	44 (rot. 180°)	20 (rot. 60°)	13 (rot. 180°)	out	
6745	45	42 (rot. 0°)	48 (rot. 0°)	57 (rot. 180°)	55 (rot. 180°)	out
6753	53	37 (rot. 0°)	3 (rot. 120°)	out		
6754	54	38 (rot. 0°)	36 (rot. 300°)	29 (rot. 120°)	out	

Fig. 4. Multiple rotations for the 28th cycle

V. Discussion

The results of this study demonstrate the impact of fuel assembly rotation on fuel cycle length, as illustrated in Tab.1 and Fig. 7. The data presented in Tab. 1. clearly indicates that fuel assembly rotation positively influences cycle length. The most significant impact of fuel assembly rotation on cycle length was observed in the 32nd fuel cycle, where the campaign duration differed by up to 1.58 full-power days. The differences in cycle lengths are shown in Fig. 7, where only the variations between rotated and non-rotated cycles are shown for clarity. If the total cycle lengths were presented instead of the differences, the lengths would appear very similar. However, it is important to note that even a one-day extension of the cycle can bring significant financial benefits. In general, the currently applied rotation strategy led to an average extension of the fuel cycle by approximately one full-power day compared to scenarios without rotation. The multiple rotation strategy exhibited cycle lengths comparable to those achieved with the current rotation approach, indicating that while systematic multiple rotations do not significantly outperform the existing method in terms of cycle length, they still maintain the observed advantages. These findings suggest that while the primary benefit of rotation is burnup homogenization, its impact on fuel cycle extension remains secondary but still relevant, particularly in longer operational cycles.

Another crucial aspect evaluated in this study was the burnup homogeneity across fuel pins, particularly in the oldest fuel pins within the reactor core. As shown in Fig. 5. for the 30th cycle, the effect of rotation (bottom graph in Fig. 5.) indicates that fuel pins that have been in the core for the longest period exhibit significantly more homogeneous burnup when rotation is applied compared to cases where no rotation is performed. This finding underscores the importance of rotation in mitigating burnup asymmetry, particularly in fuel assemblies that experience asymmetric neutron flux exposure.

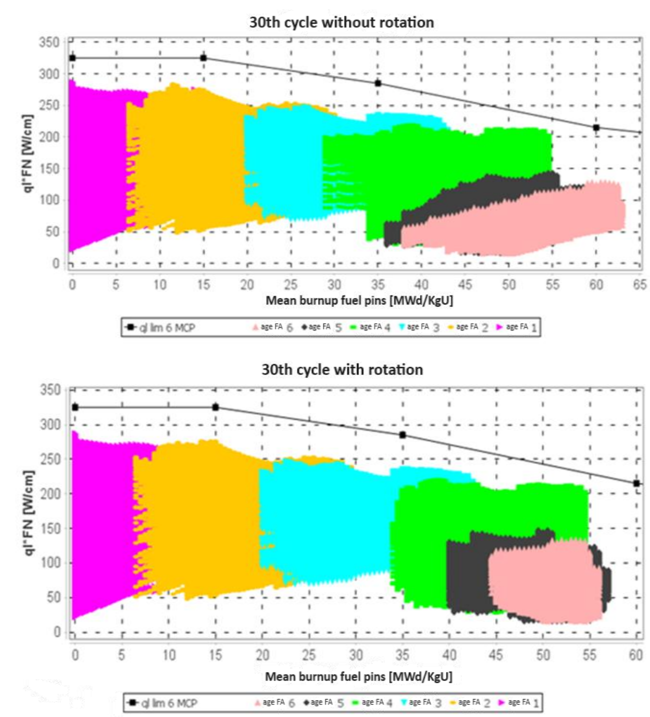

Fig. 5. Burnup of fuel pins without and with rotation

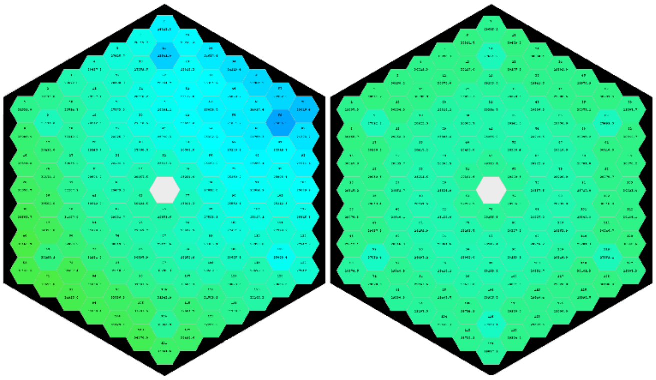

Fig. 6. Radial burnup without and with rotation in assemblies

The radial burnup difference between the rotated and non-rotated fuel assemblies is illustrated in Fig. 6. At first glance, the overall difference between the rotated and non-rotated assemblies appears negligible. However, a closer examination reveals that in the non-rotated assembly, the burnup difference between opposite sides exceeds 10 MWd/kgU, which represents a significant burnup asymmetry. Such a large variation in burnup distribution can have substantial implications for fuel performance and reactor safety. Uneven burnup can lead to localized power peaking, higher thermal stresses, and increased mechanical degradation of the fuel cladding.

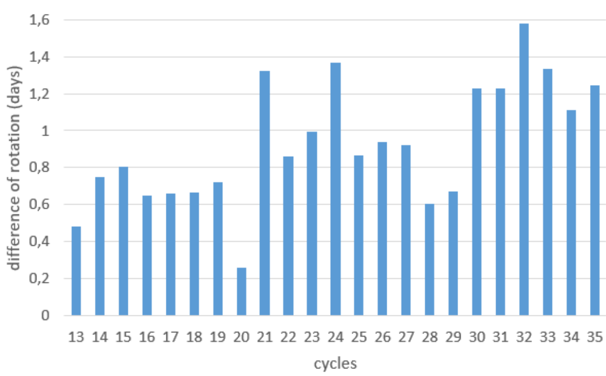

Fig. 7. Differences in cycle length without and with rotation in days.

TABLE I. CYCLE LENGTH WITHOUT AND WITH ROTATION

Cycle	Cycle length without rotation (days)	Cycle length with rotation (days)	Difference (days)
13	276.91	277.39	0.483
14	288.95	289.70	0.747
15	289.34	290.15	0.804
16	281.24	281.89	0.648
17	274.76	275.42	0.661
18	274.06	274.72	0.668
19	273.34	274.06	0.719
20	263.49	263.75	0.261
21	295.81	297.13	1.320
22	293.57	294.44	0.861
23	296.21	297.21	0.997
24	272.48	273.84	1.367
25	282.94	283.81	0.865
26	343.92	344.87	0.941
27	311.41	312.33	0.922
28	321.37	321.97	0.606
29	328.60	329.27	0.673
30	266.20	267.43	1.230
31	350.40	351.63	1.229
32	349.88	351.46	1.579
33	368.70	370.03	1.336
34	396.02	397.13	1.110
35	388.83	390.08	1.246

VI. CONCLUSION

The analysis results indicate that the currently used fuel assembly rotation contributes to fuel burnup optimization. The redistribution of neutron flux exposure leads to more homogeneous burnup across the fuel pins, improving overall fuel utilization efficiency. This enhancement is reflected in the extension of the fuel cycle, which increases by more than one full-power day (1.58 days) due to rotation. It seems like a minor difference, but it is important to note that one additional full-power day of reactor operation represents a significant cost savings in terms of fuel cost for the nuclear power plant operator. Furthermore, when implementing the rotation of the fuel assembly, careful attention must be given to the rod power peaking factor. This limiting parameter must be carefully monitored, as an appropriately selected rotation degree can either reduce the power peaking factor within the assembly or, conversely, worsen the power peaking effect compared to a non-rotated fuel assembly.

Multiple fuel assembly rotations have shown a slightly better effect on burnup optimization compared to the currently applied approach. However, the impact of multiple rotations is expected to be more promising in the case of an extended fuel cycle of approximately 16 months. This is supported by the use of a new fuel type called PK3+, which has already been implemented at the Dukovany Nuclear Power Plant. The simulations presented in this study, however, were conducted for a 12-month fuel cycle and with older fuel types than PK3+. As a result, the effectiveness of multiple rotations may be underestimated in this paper. In a 16-month fuel cycle scenario, multiple rotations are expected to play a more significant role in improving burnup homogeneity and thus fuel utilization, further enhancing reactor efficiency and economic performance.

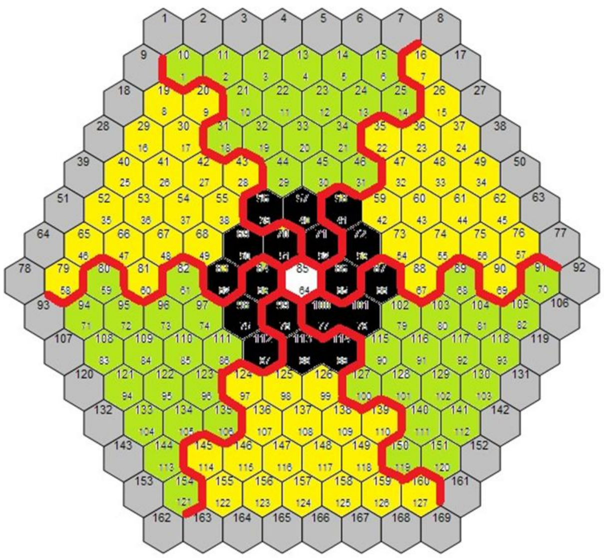

Fig. 8. Innovative evaluation of burnup in the sixth

The analyses conducted in this study revealed that the rotation has a negligible effect on the burnup of fuel pins surrounding the central tube. As a result, these fuel pins can be excluded from the evaluation of the optimal rotation angle as shown in Fig. 8. By disregarding these specified fuel pins in the evaluation, the differences between various rotation scenarios are expected to become more pronounced. This is suggested by the initial analyses. The refined evaluation approach, combined with the investigation of a 16-month fuel cycle, will be the theme of future study. Further research will focus on assessing the impact of multiple rotations during extended operational cycles and determining whether additional improvements in burnup homogeneity and fuel utilization can be achieved.

ACKNOWLEDGMENT

This research work has been carried out in the Centre for Research and Utilization of Renewable Energy (CVVOZE). Authors gratefully acknowledge financial support from the Technology Agency of the Czech Republic (project No. TN02000012 Centre of Advanced Nuclear Technology II).

REFERENCES

[1] A. Koraniany, G.R. Ansarifar,, "Neutronic design and optimizing the mixed core of VVER-1000 nuclear reactor via ANN-GA approach as machine learning method," Nuclear Engineering and Design, Volume 432, 2025, 113827, ISSN 0029-5493,

[2] W. Kubiński, P. Darnowski, and K. Chęć, "Optimization of the loading pattern of the PWR core using genetic algorithms," in Proc. NUKLEONIKA, 2021, pp. 147–151.

[3] A. Berezhnyi, A. Krushynskyi, D. Ruban, S. Sholomitsky,
Conservative evaluation of radionuclides release for VVER-440 and VVER-1000 type reactors, Annals of Nuclear Energy, Volume 194, 2023, 110105, ISSN 0306-4549

[4] A. Vivancos, R. Miró, T. Barrachina, Á. Bernal, G. Verdú, Deterministic neutron transport and burnup code coupling assessment, Annals of Nuclear Energy, Volume 198, 2024, 110291, ISSN 0306-4549,

[5] J. Malec, O. Cabellos, M. Kromar, A. Trkov, Generation and validation of a new WIMS-D library based on ENDF/B-VIII.0, Annals of Nuclear Energy, Volume 211, 2025, 110989, ISSN 0306-4549,

[6] A. Trkov, M. Ravnik, Application of ENDF/B-VI data for the WIMS lattice code, Annals of Nuclear Energy, Volume 20, Issue 8, 1993, Pages 561-568, ISSN 0306-4549,

Detection of Heavy Metal Contamination by Vibrational Spectroscopy: A Combined Theoretical and Experimental Study

Richard Schubert
Department of Physics
Faculty of Electrical Engineering and Communication
Brno University of Technology
Brno, Czech Republic
xschub01@vutbr.cz

***Abstract*—Heavy metal infiltration into connective tissues remains a notable yet under-explored issue in biomaterials research. In this study, we employed Fourier Transform Infrared (FTIR) spectroscopy to investigate potential mercury-induced changes in dentin, with an emphasis on the attenuation of thiol (–SH) vibrational signatures as a key indicator. High-resolution spectra, combined with chemometric preprocessing, enabled the detection of subtle perturbations in sulfur-containing amino acid residues. A reduction in thiol band intensity tentatively suggests mercury interactions with sulfhydryl groups, implying possible disruptions in protein conformation and the dentin organic matrix. Small but consistent shifts in amide I and II regions further point to collateral effects on dentinal proteins. To minimize confounding factors, we utilized selective reference spectra and limited elemental mapping, supporting the specificity of these observed alterations to localized mercury presence. While the initial results indicate a correlation between mercury exposure and diminished thiol peaks, additional data and systematic validation are needed to confirm these findings and clarify their broader clinical significance.**

***Index Terms*—Vibrational Spectroscopy, Group Theory, Fourier Transform Infrared, Heavy Metal Contamination, Dentin Tissue**

I. Introduction

The detection and interpretation of vibrational transitions in molecular systems derive from fundamental quantum mechanics, wherein each normal mode of vibration is associated with discrete energy levels governed by the harmonic (or anharmonic) oscillator approximation. A rigorous mathematical framework for analyzing such vibrational modes is provided by group theory, which classifies the vibrational representations of a molecule according to its symmetry properties. In a molecule with N atoms (and hence $3N$ total degrees of freedom), the irreps corresponding to translational and rotational motions must be subtracted from the full representation Γ_{all} to obtain the vibrational representation Γ_{vib} :

$$\Gamma_{\mathrm{vib}} = \Gamma_{\mathrm{all}} \ominus \Gamma_{\mathrm{trans}} \ominus \Gamma_{\mathrm{rot}}. \tag{1}$$

Here, Γ_{all} typically corresponds to the direct sum of all atomic displacements in the coordinate space, and $\Gamma_{trans}, \Gamma_{rot}$ are the representations for translations (x, y, z) and rotations (R_x, R_y, R_z), respectively.

In infrared spectroscopy, transitions occur if the derivative of the dipole moment with respect to the normal coordinate $\left(\frac{\partial\mu}{\partial Q}\right)$ is nonzero. A vibrational mode is IR-active if it transforms as (or contains) the same irreducible representation as the dipole moment operator Γ_μ [1]. Formally:

$$\Gamma_{\mathrm{vib}} \otimes \Gamma_\mu \ni A_1 \quad \Longrightarrow \quad \text{IR-active}, \tag{2}$$

where $\ni A_1$ indicates that the totally symmetric irreducible representation A_1 is contained in the product representation, signifying a nonzero transition probability. Notice when decomposing the vibrational representation into normal modes, each mode Q_i transforms as an irreducible representation Γ_i

$$\Gamma_{\mathrm{vib}} = \bigoplus_i \Gamma_i, \tag{3}$$

where the Γ_i indicate the symmetry of each normal coordinate. For a typical biomolecular fragment (e.g., a thiol group or an amide linkage), group-theoretical analysis can reveal whether Γ_i permits IR- or Raman-active transitions.

These group-theoretical selection rules pinpoint the vibrational modes that contribute to observed spectra. At a more granular level, perturbations—such as those introduced by heavy-metal binding—can effectively lower local symmetry, lifting degeneracies and modifying transition intensities. Thus, small symmetry-breaking events can manifest as subtle but diagnostically meaningful shifts in peak positions and intensities.

Thiol ($-\mathsf{SH}$) and amide ($-\mathsf{CO}-\mathsf{NH}-$) functional groups offer compelling case studies for such symmetry-breaking phenomena [2]. Sulfur's valence electrons and relative polarizability render thiol groups especially sensitive to coordination with metal cations, which can alter the potential energy surface governing the $\mathsf{S}-\mathsf{H}$ stretch. In parallel, the amide I and II bands in polypeptide backbones display well-defined symmetries that directly reflect protein secondary structure. The introduction of exogenous metal species can break or reconfigure intramolecular hydrogen bonds and electronic distributions, thus modifying normal-mode characteristics in ways that group-theoretical analysis can precisely forecast. In heavy-metal contamination studies, the local symmetry is often

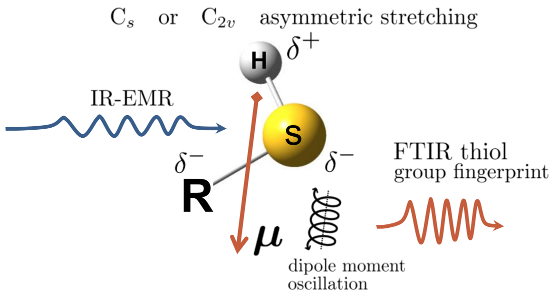

(a) free thiol (-SH) group in the absence of Hg

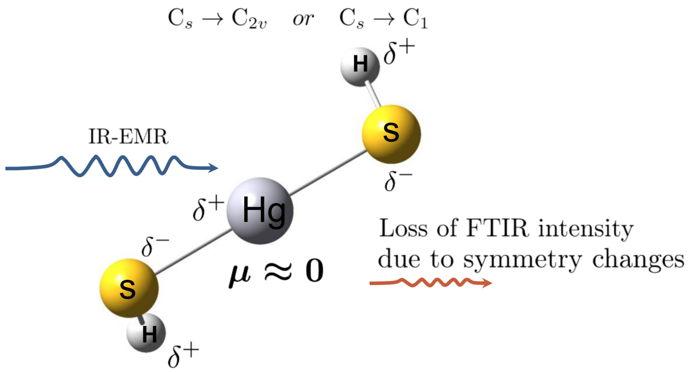

(b) effect of mercury binding

Fig. 1: Illustration of the effect of mercury binding on the vibrational properties of thiol groups. In the absence of Hg, the R−S−H molecule exhibits C_S or C_{2v} symmetry, where asymmetric stretching vibrations cause a periodic change in the dipole moment μ, allowing IR absorption. Upon Hg coordination, forming the molecular symmetry changes from C_S to either C_1 (in asymmetric distortions) or C_{2v} (in near-linear cases). Due to increased symmetry and partial dipole cancellation, the net dipole moment is significantly reduced or nearly zero.

lowered when a metal ion (e.g., Hg^{+2}) coordinates with a functional group like –SH. This can be conceptualized as:

$$\Gamma_{\text{unpert.}} \longrightarrow \Gamma_{\text{pert.}} \quad \text{where} \quad \Gamma_{\text{pert.}} \subseteq \Gamma_{\text{unpert.}}. \tag{4}$$

The “subset” relationship ($\subseteq$) indicates that certain degeneracies may be lifted (i.e., one representation splits into two or more lower-symmetry representations), potentially leading to observed shifts or intensity changes in IR or Raman spectra. (For the suggested workflow see Fig.2.)

The spectral changes induced by heavy-metal interactions can be further understood by examining their effects on vibrational frequencies. The S−H stretching vibration usually appears in the 2550–2600 cm^{-1} region, while the amide I and II bands (mainly C=O stretching and bending NH) are observed near 1650 cm^{-1} and 1550 cm^{-1}, respectively. Mercury coordination with thiol groups is expected to weaken the S−H bond (see Fig.1), leading to intensity reductions or peak broadening due to perturbations in bond order and force constants. This phenomenon occurs because Hg^{2+} binding alters the local charge distribution, reducing the dipole moment change during S−H stretching and thereby decreasing IR activity. Similarly, mercury binding to peptide backbones can induce secondary structural changes, affecting the amide I and II band positions and intensities. These spectral shifts serve

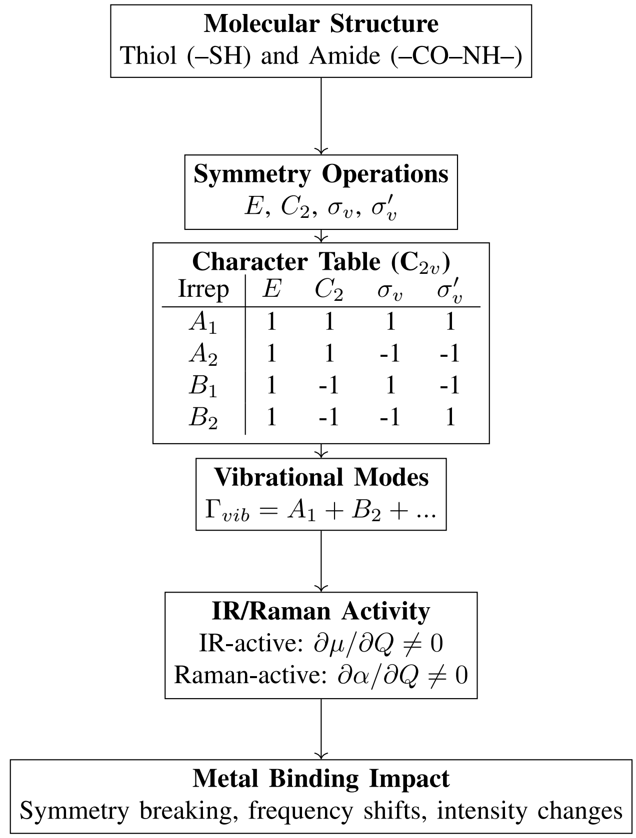

Fig. 2: Schematic representation of the suggested theoretical workflow for vibrational spectroscopy analysis. The molecular structure is classified by symmetry ($E, C_2, \sigma_v, \sigma'_v$), leading to its character table and vibrational representation (Γ_{vib}). Selection rules define IR-active ($\partial\mu/\partial Q \neq 0$) and Raman-active ($\partial\alpha/\partial Q \neq 0$) modes. Metal binding disrupts symmetry, causing frequency shifts and intensity variations, generalizable to different contaminants affecting biomolecular vibrations.

as diagnostic markers for heavy metal infiltration, making vibrational spectroscopy a suitable tool for assessing mercury-induced alterations in biological tissues [3].

Recent studies have highlighted that dental amalgams typically contain a high proportion of elemental mercury (often around 50% by weight), alloyed with silver, tin, copper, or other metals [4]. Over time, unbound or unreacted mercury may leach from the restoration site, potentially diffusing into adjacent dentin and, in severe cases, into the pulp chamber or surrounding alveolar bone [5]. The composition of dentin—primarily a collagen matrix interspersed with hydroxyapatite mineral—renders it susceptible to chemical modifications when exposed to reactive metal ions. Changes in local pH or the presence of binding sites (particularly thiol groups on proteins) can enhance metal–protein interactions, thereby altering the structural integrity of the tissue. Indeed, recent reviews demonstrate that mercury has a high affinity for sulfhydryl (–SH) groups, often resulting in protein misfolding, oxidative stress, and enzyme inhibition [3]. Furthermore, structural studies on human dental apatite reveal that age-related increases in carbonate substitution reduce crystallinity and enhance solubility, potentially facilitating metal infiltration [6].

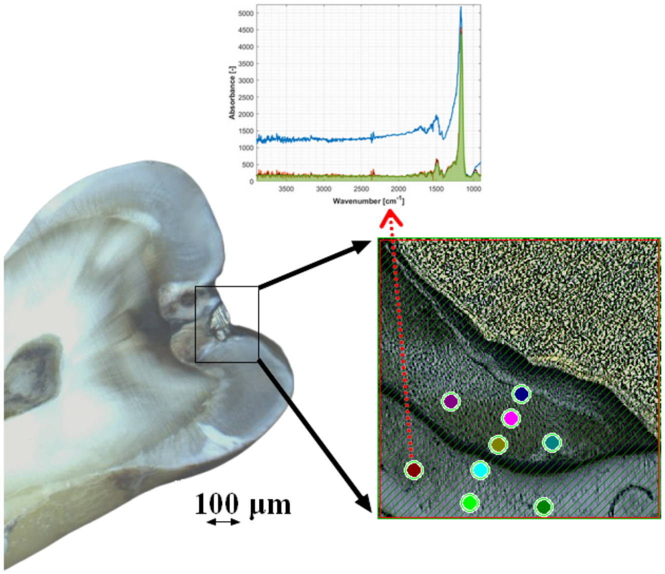

Fig. 3: Cross-section of a human tooth sample embedded in epoxy resin, showing the interface between the tooth tissue and amalgam filling. The sample was cut to expose a clear boundary between the materials. A magnified section of this interface, captured using light microscopy, highlights the measurement points (colored circles) where FTIR spectra were collected. A representative FTIR spectrum from one selected measurement point is displayed above, illustrating spectral features of the sample in the corresponding region.

Investigations employing both bulk and microscale analytical methods have documented detectable mercury gradients radiating outward from amalgam restorations into tooth structures [7]. These observations underscore the practical relevance of vibrational spectroscopy in detecting and characterizing heavy-metal infiltration at an early stage, offering a rapid and minimally invasive means to assess potential tissue damage.

II. Data Acquisition and Signal Processing Methodology

Extracted human teeth samples were acquired to investigate the potential contamination of mercury compounds originating from amalgam fillings. The sample set comprised teeth from individuals of both sexes, extracted for various clinical reasons. All subjects had amalgam fillings in place for a minimum of 15 years prior to extraction. In total, the dataset included teeth from both male and female patients, with four individuals identified as daily smokers. The diverse demographic distribution of our sample set helps in assessing potential variations in mercury contamination across different lifestyle factors.

Prior to FTIR spectroscopy, all extracted teeth were carefully embedded in epoxy resin to provide structural stability and then precisely sectioned into thin slices. This procedure was specifically designed to produce clear cross-sections, clearly exposing the interface between amalgam filling and surrounding tooth tissue (primarily dentin). This preparation step ensures optimal visibility and consistent quality for spectroscopic analysis, allowing detailed characterization of chemical changes at the amalgam-dentin interface. FTIR spectra were collected at several points across each slice, strategically

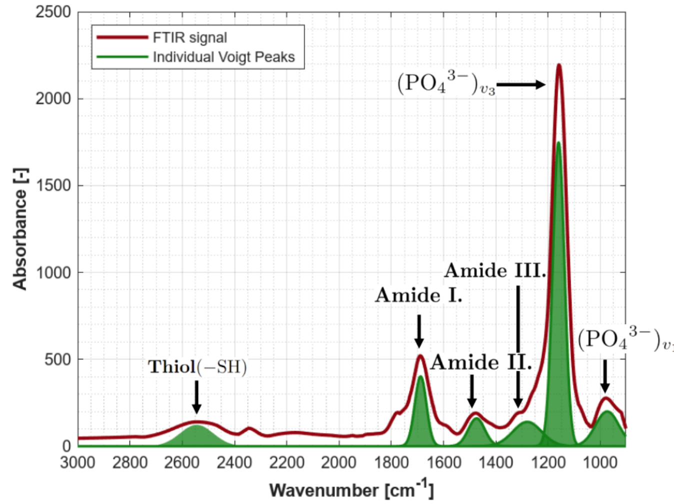

Fig. 4: FTIR spectrum of dentin, assumed to be free of contamination, displayed in the 900–3000 cm^{-1} region. The red curve represents the measured FTIR absorbance signal, while the green Voigt profiles correspond to individual peak contributions. Six key vibrational modes are marked: the thiol (−SH) stretch (∼2550 cm^{-1}), amide I (∼1650 cm^{-1}), amide II (∼ 1550 cm^{-1}), amide III (∼1240 cm^{-1}), and phosphate vibrational modes (∼960 and ∼1100 cm^{-1}). The spectral region below 900 cm^{-1} was omitted due to the predominant contribution of hydroxyapatite and water-related bands, which are not relevant for mercury detection in dentin.

placed to capture representative signals from amalgam, dentin near the interface, and regions progressively further away. Each measurement aimed to reveal the presence or absence of mercury-induced molecular change (see Fig.3).

Signal processing involved multiple algorithmic steps, carefully justified to ensure precise spectral interpretations. Initially, baseline correction was implemented to remove low-frequency background variations resulting from instrumental drift or baseline fluctuations inherent in FTIR measurements. Baseline correction parameters, such as window size and step size, were optimized empirically to effectively preserve peak integrity and avoid artificial flattening of relevant spectral features, following the methodology suggested by Lieber and Mahadevan-Jansen [8].

Subsequently, Savitzky-Golay filtering was employed to mitigate random noise intrinsic to spectroscopic measurements, thus enhancing signal-to-noise ratios without distorting critical peak characteristics [9]. This filtering technique is particularly suitable for spectroscopic data as it efficiently preserves the peak shape, amplitude, and spectral resolution, crucial for accurate interpretation and subsequent analysis of subtle biochemical changes.

To further refine signal quality, wavelet-based denoising using discrete wavelet decomposition with Daubechies wavelets ('db4') was implemented. Wavelet decomposition effectively isolates signal components from noise through multilevel thresholding, significantly enhancing the detection of subtle spectral variations caused by biological processes or contamination events [10].

Bandpass filtering was then applied to restrict spectral analysis exclusively to biologically relevant regions between approximately 800 cm^{-1} and 3000 cm^{-1}. This filtering step

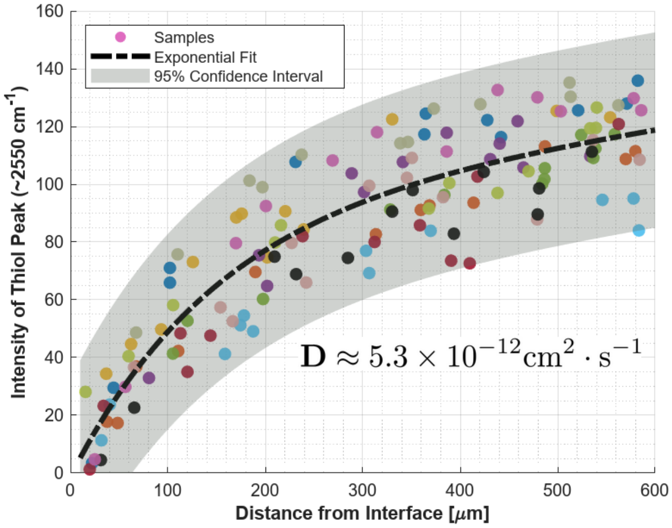

Fig. 5: Thiol peak intensity as a function of normal distance from the amalgam-tooth interface. Each color represents a different patient tooth sample. The dashed line represents an exponential fit to the entire dataset. Based on the observed spatial scale ($\sim$500 μm) and known amalgam exposure duration, the diffusion coefficient (D) is estimated to be on the order of 10^{-12} $cm^2{\cdot}s^{-1}$.

effectively eliminated contributions from epoxy resin used for embedding and high-wavenumber signals dominated by non-informative spectral features such as water vibrations, ensuring analytical focus on chemically informative spectral bands.

Finally, overlapping spectral peaks were quantitatively resolved through peak deconvolution using Voigt profile approximations. Voigt profiles, combining Gaussian and Lorentzian components, accurately describe peak shapes influenced by both instrumental broadening (Gaussian) and natural molecular vibrational lifetimes (Lorentzian), as documented by Schreier et al. [11]. Such decomposition enabled precise evaluation of spectral broadening and shifts, crucial for identifying potential structural alterations due to mercury interactions with functional groups.

III. Observations and Insights

FTIR measurements were conducted on regions of the dentin cross-section where minimal to no mercury contamination was anticipated, ensuring an accurate representation of the intrinsic biochemical composition of healthy dentin. Spectra were acquired from multiple samples and averaged to enhance signal robustness while mitigating inter-sample variability. The resulting spectrum, presented in Fig.4, highlights key vibrational modes corresponding to molecular constituents of dentin. Specific peaks were annotated within the spectral range where mercury contamination was hypothesized to induce structural alterations. The thiol (–SH) peak arises from S–H stretching vibrations in cysteine residues and other sulfur-containing biomolecules, serving as a critical marker for metal-binding interactions. Amide I, predominantly governed by C=O stretching vibrations within peptide bonds, is highly sensitive to secondary structural variations in collagen. Amide II results from N–H bending coupled with C–N stretching, providing complementary insights into peptide backbone modifications. Amide III, a combination of C–N stretching and N–H bending, further reflects protein conformational states. Phosphate peaks, originating from symmetric and asymmetric stretching of groups, are characteristic of the mineralized hydroxyapatite matrix within dentin. To accurately resolve overlapping spectral features and quantify peak broadening effects, Voigt profile fitting was applied using the Faddeeva function, incorporating both Gaussian and Lorentzian contributions. This analytical approach allowed precise deconvolution of individual vibrational components, enabling a more rigorous assessment of potential shifts, intensity variations, and broadening effects associated with mercury-induced structural perturbations.

Analysis demonstrated a clear decrease in the intensity of the thiol vibrational peak with proximity to the amalgam interface, as shown in Fig.5. These observations were modeled by Fick's law of diffusion:

$$\frac{\partial C}{\partial t} = D\left(\frac{\partial^2 C}{\partial x^2} + \frac{\partial^2 C}{\partial y^2}\right) \tag{5}$$

where C represents the concentration of diffusing species (Hg^{2+} in this case), D is the diffusion coefficient governing the rate of diffusion, and (x, y) denotes the spatial coordinates normal to the amalgam interface. Given the inherently low physiological activity of dentin, passive diffusion dominates, supporting the validity of this approach. An exponential decay function provided an optimal fit to the thiol intensity profile, indicating a diffusion-driven contamination process. The derived diffusion coefficient $D \approx 10^{-12}$ $cm^2{\cdot}s^{-1}$ aligns with established literature values for heavy metal migration in mineralized tissues [12], reinforcing the plausibility of diffusion-dominated mercury transport within dentin.

Further spectral analysis of the amide I and II vibrational modes provided deeper insight into structural modifications within dentin collagen fibers associated with mercury contamination, as depicted in Fig.6a. Both amide peaks demonstrated a systematic shift towards lower wavenumbers—a phenomenon known as a redshift—as the measurement points moved closer to the amalgam interface. This trend is visualized clearly in the contour density plot, where data points representing regions near the amalgam restoration cluster distinctively at lower wavenumbers compared to regions of uncontaminated dentin, forming two separate concentration regions. Such spectral redshifts result from mercury-induced alterations in hydrogen bonding environments, conformational changes, and disruptions in peptide-bond electron distributions within the collagen backbone.

Fig.6 illustrates a principal component analysis (PCA) performed on feature vectors derived from measured FTIR spectra, specifically designed to elucidate molecular alterations in dentin tissue induced by mercury contamination. Each feature vector was constructed as a multidimensional descriptor containing the following elements: the first element represents the intensity of the thiol vibrational peak, serving as a direct indicator of thiol group depletion upon mercury binding; the second and third elements correspond to positional shifts of

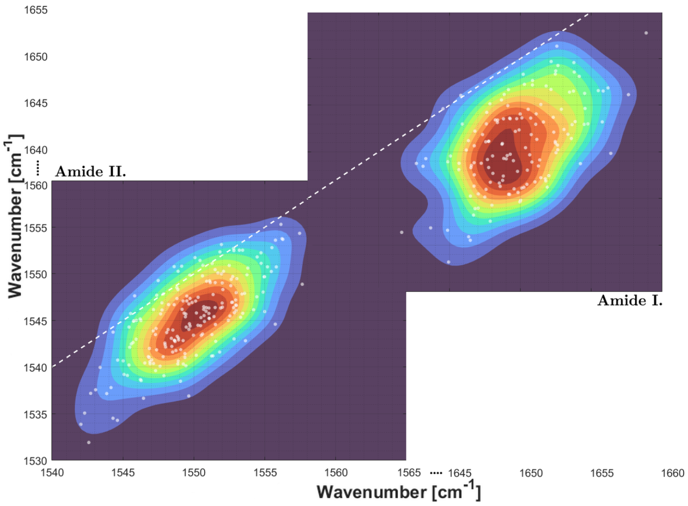

(a) Correlated shifts in Amide I and Amide II peak positions

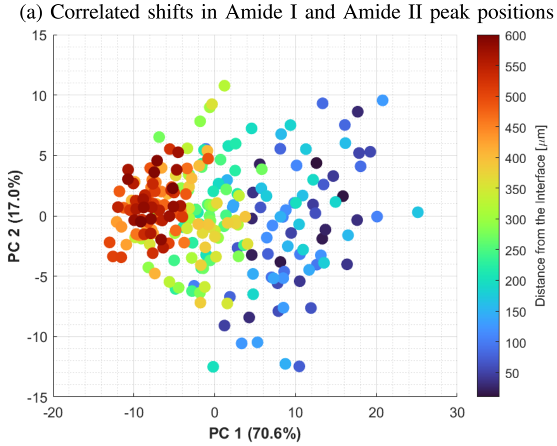

(b) Principal component analysis of spectral features

Fig. 6: Analysis of mercury-induced spectral alterations in dentin tissue.

Amide I and Amide II peaks, respectively, reflecting perturbations in protein secondary structures; the fourth and fifth elements represent the broadening (full width at half maximum, FWHM) of these amide peaks, indicative of molecular-level structural disruption; and the sixth element contains a calculated peak-area ratio of Amide I to phosphate stretching vibrations, emphasizing the relative changes in protein-mineral interactions. PCA effectively reduced this high-dimensional spectral data into two principal components, collectively accounting for approximately 87.6% of total variance. The resulting two-dimensional scatter plot reveals a distinct clustering pattern, where samples measured nearest to the amalgam interface (dark blue and purple hues) group separately from those farther away (green, yellow, and red hues). Such clustering indicates systematic, distance-dependent molecular alterations associated with mercury contamination, progressively decreasing with increasing distance from the amalgam interface. The evident separation in principal component space validates the sensitivity of selected spectral features to detect mercury-induced structural perturbations in dentin tissue at the molecular level.

IV. Conslusion

Our preliminary investigation has established the feasibility of employing FTIR spectroscopy, coupled with advanced signal processing techniques, to effectively detect mercury contamination in human dentin tissue. We developed a robust theoretical framework based on molecular vibrational modes and their corresponding selection rules derived from group theory. This approach guided our interpretation of spectroscopic data and provided foundational understanding for the anticipated vibrational shifts due to mercury incorporation. Experimental results strongly indicate that atomic mercury diffuses from amalgam restorations into the surrounding dentinal tissue.

References

[1] Kelley, A. M. *Condensed-Phase Molecular Spectroscopy and Photophysics*. Wiley, New York, 2012. ISBN: 978-1-118-02893-4.
[2] Larkin, P. *Infrared and Raman Spectroscopy: Principles and Spectral Interpretation*. Elsevier, Amsterdam, 2011. ISBN: 978-0-12-386984-5.
[3] Ajsuvakova, O.P.& Skalnaya, M.G.& Tinkov, A.A., et al. *Sulfhydryl Groups as Targets of Mercury Toxicity: From Basic Research to Clinical Implications*. Int. J. Mol. Sci. 2020, 21(17), 6644.
[4] Bjørklund, G.& Dadar, M.& Mutter, J.& Aaseth, J. *The toxicology of mercury: Current research and emerging trends*. Environ. Res. 2017, 159, 545-554.
[5] Branco, V.& Caito, S., Farina, M.& Teixeira da Rocha, J.B.& Aschner, M.& Carvalho, C. *Biomarkers of mercury toxicity: Past, present, and future trends*. J. Toxicol. Environ. Health B 2017, 20(3), 119-154.
[6] Leventouri, T.& Antonakos, A.& Kyriacou, A.& Venturelli, R.& Liarokapis, E.& Perdikatsis, V. *Crystal Structure Studies of Human Dental Apatite as a Function of Age*. International Journal of Biomaterials, 2009, Volume 2009, Article ID 698547.
[7] Azarsina, M.& Kasraei, S.& Masoum, T.& Khamverdi, Z.*Effect of Surface Polishing on Mercury Release from Dental Amalgam After Treatment with 16% Carbamide Peroxide Gel*. Journal of Dentistry, 2011, 8(1), 33–38. PMID: 21998805.
[8] Lieber, C. A.& Mahadevan-Jansen, A. *Automated method for subtraction of fluorescence from biological Raman spectra*. Applied Spectroscopy, 2003, 57(11), 1363-1367.
[9] Savitzky, A.& Golay, M. J. E. Smoothing and differentiation of data by simplified least squares procedures. Analytical Chemistry, 1964, 36(8), 1627-1639.
[10] Mallat, S. G.*A theory for multiresolution signal decomposition: the wavelet representation*. IEEE Transactions on Pattern Analysis and Machine Intelligence, 1989, 11(7), 674-693.
[11] Schreier, F. et al. *Voigt and complex error function: A comparison of computational methods.* Journal of Quantitative Spectroscopy and Radiative Transfer, 2015, 162, 186–194.
[12] Clarkson, T.W.& Magos, L., & Myers, G.J.*The toxicology of mercury—current exposures and clinical manifestations*. The New England Journal of Medicine, 2003, 349(18), 1731-1737.

Current balancing in parallel structures of high-current power inverters

Tomáš Pitner
Department of Power Electrical and Electronic engineering
Brno University of Technology
Brno, Czech Republic
Tomas.Pitner1@vut.cz

Jan Knobloch
Department of Power Electrical and Electronic engineering
Brno University of Technology
Brno, Czech Republic
knobloch@vut.cz

Jan Bárta
Department of Power Electrical and Electronic engineering
Brno University of Technology
Brno, Czech Republic
bartaj@vut.cz

***Abstract*—This paper deals with the issue of current imbalances between paralleled MOS-FETs and paralleled inverter legs in high-current power inverters. The mechanisms causing the current imbalances are examined while providing an overview of possible solutions. The theory of a current balancing transformer is presented, for which numerical simulations and verification measurements are done.**

***Index Terms*—paralleled MOS-FETs, paralleled inverter legs, current balancing transformer, power inverter, current imbalance**

I. Introduction

Power inverters have a wide range of applications, such as electric vehicles (EVs), locomotives, "more-electric" or "all-electric" aircraft and unmanned aerial vehicles (UAVs) [1], [2]. The output currents of these inverters are often in the range of hundreds of amperes, which introduces design challenges regarding the semiconductor switching devices.

Especially in the lower voltage range of about 50–200 V, MOS-FETs are predominantly used because of their resistive character which allows low voltage drop and thus low conduction power losses. At very high currents, however, difficulties arise with the selection of suitable parts. Commercially available MOS-FET modules rated for voltages of 200 V or less and high currents suffer from high $R_{\mathrm{DS,on}}$ and slow switching times. Parallel combination of multiple discrete MOS-FETs in smaller packages often result in significantly better performance.

When MOS-FETs are connected in parallel, uneven current distribution between individual MOS-FETs may occur due to various mechanisms, which are discussed in this paper. Another way to increase the current capability of an inverter is by paralleling multiple inverter legs, risking similar problems in terms of current imbalances. Several approaches to mitigating these issues in power inverters are described.

The research results provide a theoretical foundation for a six-phase low-voltage high-current power inverter design, which is then used for verification of the examined solutions.

The authors acknowledge financial support from the Ministry of Education, Youth and Sports under the specific research programme of the Brno University of Technology (project No. FEKT-S-23-8430).

II. Paralleling MOS-FETs

Ideally, the current would be evenly distributed between the parallel MOS-FETs at any given moment. However, in real applications, the following imperfections may be present in the power circuit [3]:

- geometric asymmetry leading to mismatch of impedances between the individual MOS-FETs and the load
- mismatch of MOS-FETs' gate-source threshold voltages
- mismatch of MOS-FETs' gate capacitances
- mismatch of MOS-FETs' gate series resistances and inductances (both external and internal)
- propagational delay skew of individual MOS-FET drivers (in case they are separate)

An even steady-state current distribution between paralleled MOS-FETs can be achieved by making a symmetric layout of the power stage circuit (considering the same on-state resistances of individual MOS-FETs). However, instantaneous current distribution will still be affected by the mismatch of parasitic inductances of the layout (which are more difficult to control than resistances) and the mismatch of static and dynamic parameters of the MOS-FETs.

Initial current imbalance settles with a time constant $\tau = \frac{L}{R}$, where L and R are the inductance and the resistance of the loop that connects the paralleled MOS-FETs. This is a problem especially for high-current power converters, in which the resistance is usually very low. As shown in Fig. 1, the settling

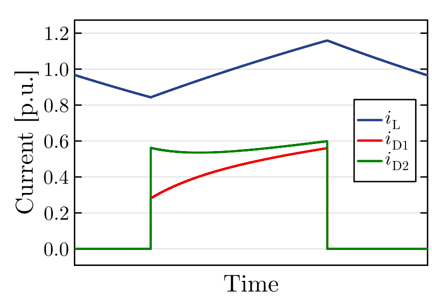

Fig. 1: Example of uneven current distribution of two paralleled MOS-FETs (i_{D1}, i_{D2}) in a buck converter, i_L is the inductor current.

time constant can be comparable to the switching period, which prevents the steady-state current distribution from being reached. Uneven current distribution then leads to uneven distribution of switching and conduction power losses between the individual MOS-FETs, which brings cooling challenges.

Based on previous hypotheses, following rules for successful design can be established:

- The power circuit layout must be as symmetric as possible to ensure minimum initial imbalance in the currents.
- The inductance of the loop, which connects the parallel MOS-FETs, must be as low as possible to minimize the settling time.
- If a single gate driver is used for all MOS-FETs, each MOS-FET must have its own gate resistor and their gate connection lengths must be equal.
- If separate gate drivers are used, types with low part-to-part skew of the propagation delay must be selected.
- The switching frequency must be selected appropriately to the settling time constant given by the layout. If the settling isn't fast enough, lowering the switching frequency can significantly help the power loss distribution.

Also, more elaborate approaches can be used for balancing the currents between paralleled transistors. In [4] and [5], so-called "active gate drive current balancing" is used, utilizing closed-loop control of individual gate voltages of multiple paralleled IGBT modules. Based on the emitter current measurements, time-shifting of the gate signals ensures the transient current balancing, while the static current balancing is achieved by controlling the magnitudes of the gate voltages. Similar approach was used in [6] for SiC FETs. However, these methods require using additional current sensors and increase the control complexity, thus they seem to be economically beneficial only for very high power converters.

Another method proposed in [7] uses additional inductances in series with the sources of the MOS-FETs, which are able to greatly reduce the current imbalance while only slightly increasing the voltage overshoot during turn-off. In [8], a planar transformer with windings in series with the drains of the MOS-FETs is used. Principally, this solution is similar to the *current balancing transformer*, which is described in detail in section III-B. The advantage of these two solutions is that they are fully passive, without the need for any sensors or processing power.

III. Paralleling inverter legs

A. Issues

Paralleling multiple inverter legs presents another way to increase the current capability of an inverter. As in the previous section, there is a risk of uneven current distribution between the legs of the same phase for the following reasons:

- mismatch of impedances between the outputs of the individual inverter legs and the load
- mismatch of switching times of the individual inverter legs due to the propagation delay skew of their drivers

The impedances of the output wires can be managed to an extent by keeping their lengths equal (the inductances may still differ). On the other hand, the propagation delay skew of the gate drivers can be in order of tens of nanoseconds (typically $50\,\mathrm{ns}$). Higher switching frequency means higher requirements on propagation delay matching.

The most reliable solution would be to use a separate inductor and a current controller for each of the paralleled inverter legs. However, in many applications, such as electric drives, the output inductor is often unnecessary due to the inductance that is already present in the circuit (inductance of the stator winding). The need for additional inductors would significantly increase costs and therefore should be avoided.

B. Current balancing transformer

An elegant way to mitigate the issue with uneven current distribution between inverter legs is to use a *current balancing transformer* (CBT) [9]. As shown in Fig. 2, it is a transformer intended to induce such a voltage into the output wires to counteract the current imbalance between them. If the output currents of the two legs are equal, the magnetic flux inside the transformer core is zero, which means no voltages are induced in its windings. As soon as the current imbalance occurs, the magnetic flux is no longer zero and due to the Faraday's induction law, there will be induced voltages in the windings proportional to the time derivative of the magnetic flux. Thanks to the Lenz's law, the polarities of the induced voltages must counteract the cause, i.e. the induced voltage is added to the lagging inverter leg output and substracted from the leading leg output. There is an obvious limitation that the CBT is not able to counteract steady-state current imbalance (e.g. due to mismatch of the wires resistances), since no induced voltage can be generated for a time-constant magnetic flux.

Based on the equivalent circuit in Fig. 3, following voltage equations can be written:

$$u_1 = R_\mathrm{A} i_1 + L_\mathrm{A}\frac{\mathrm{d}i_1}{\mathrm{d}t} + \frac{\mathrm{d}\Psi_1}{\mathrm{d}t} + R_\mathrm{L}(i_1+i_2) + L_\mathrm{L}\frac{\mathrm{d}(i_1+i_2)}{\mathrm{d}t}, \quad (1)$$

$$u_2 = R_\mathrm{B} i_2 + L_\mathrm{B}\frac{\mathrm{d}i_2}{\mathrm{d}t} + \frac{\mathrm{d}\Psi_2}{\mathrm{d}t} + R_\mathrm{L}(i_1+i_2) + L_\mathrm{L}\frac{\mathrm{d}(i_1+i_2)}{\mathrm{d}t}. \quad (2)$$

Magnetic flux linkages bound to the two windings are equal to:

$$\Psi_1 = L_1 i_1 - M i_2, \quad (3)$$

$$\Psi_2 = -M i_1 + L_2 i_2, \quad (4)$$

where L_1 and L_2 are the inductances of the two windings and M is the mutual inductance.

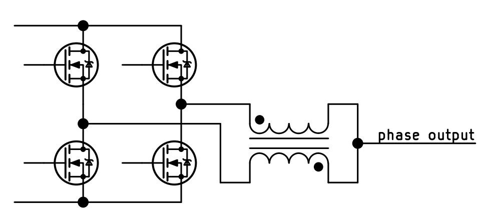

Fig. 2: CBT connecting two inverter legs in parallel.

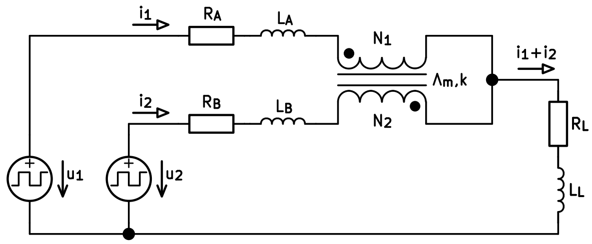

Fig. 3: Equivalent circuit of the CBT used with two paralleled inverter legs (u_1, u_2) and a RL load (R_L, L_L). i_1, i_2 are the leg currents, R_A, R_B and L_A, L_B are the resistances and the inductances of the wires, N_1, N_2 are numbers of turns of the transformer windings, Λ_m is the magnetic conductivity (permeance) of the transformer core and k is the coupling coefficient.

Assuming $N_1 = N_2 = 1$, following simplifications can be made: $L_1 = L_2 = N_1^2\Lambda_\mathrm{m} = \Lambda_\mathrm{m}$ and $M = k\sqrt{L_1L_2} = k\Lambda_\mathrm{m}$.

Solving for Ψ_1, Ψ_2, i_1, i_2 from the equations (1)–(4), we obtain a mathematical model of the CBT:

$$\Psi_1 = \int [u_1 - R_\mathrm{A}i_1 - R_\mathrm{L}(i_1+i_2)]\mathrm{d}t - L_\mathrm{A}i_1 - L_\mathrm{L}(i_1+i_2), \quad (5)$$

$$\Psi_2 = \int [u_2 - R_\mathrm{B}i_2 - R_\mathrm{L}(i_1+i_2)]\mathrm{d}t - L_\mathrm{B}i_2 - L_\mathrm{L}(i_1+i_2), \quad (6)$$

$$i_1 = \frac{\Psi_1 + k\Psi_2}{(1-k^2)\Lambda_\mathrm{m}}, \quad (7)$$

$$i_2 = \frac{k\Psi_1 + \Psi_2}{(1-k^2)\Lambda_\mathrm{m}}. \quad (8)$$

This model contains an *algebraic loop*, but this corresponds to reality and does not affect the calculation stability.

Finally, the magnetic flux density in the transformer core can be calculated using the Ampère's law:

$$B = \mu_0\mu_\mathrm{r}H = \mu_0\mu_\mathrm{r}\frac{N_1i_1 - N_2i_2}{l_\mathrm{Fe}} = \mu_0\mu_\mathrm{r}\frac{i_1 - i_2}{l_\mathrm{Fe}}, \quad (9)$$

where μ_0 is the permeability of the vacuum, μ_r is the relative permeability of the transformer core and l_Fe is the effective length of the core.

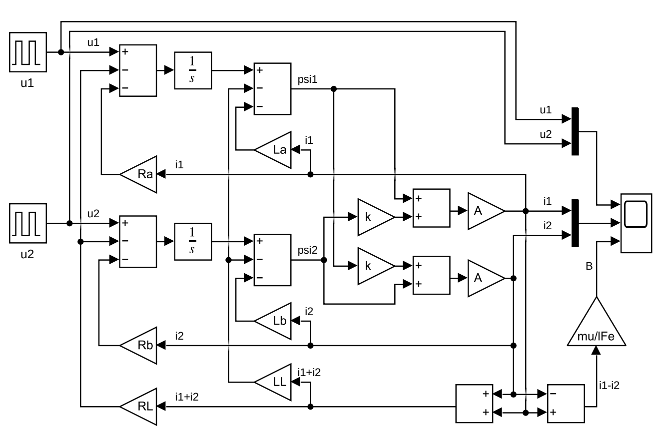

Fig. 4: A simulation model of the CBT in MATLAB/Simulink.

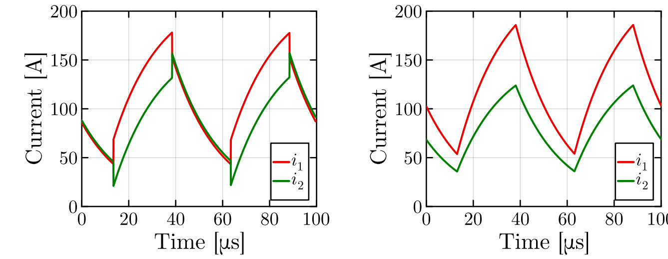

(a) propagation delay mismatch (b) impedance mismatch

Fig. 5: Simulation of a current distribution between paralleled inverter legs in a circuit without the CBT ($\Lambda_\mathrm{m} \to 0$).

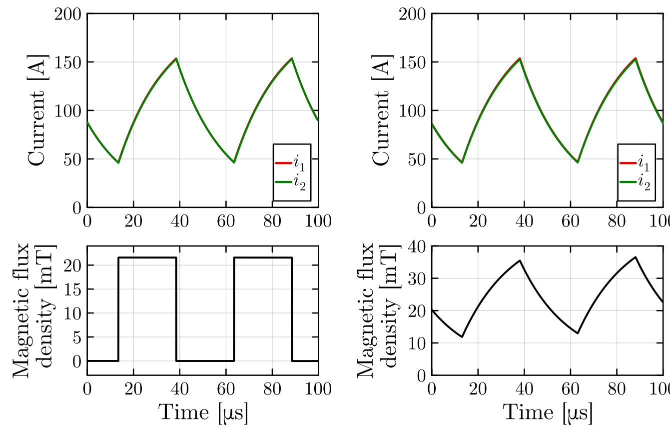

(a) propagation delay mismatch (b) impedance mismatch

Fig. 6: Simulation of a current distribution between paralleled inverter legs and the transformer core magnetic flux density in a circuit with the CBT ($\Lambda_\mathrm{m} = 3600\,\mathrm{nH}$, $k = 0.9$).

Two simulations were performed – the first with the propagation delay mismatch of $50\,\mathrm{ns}$, the second with the output wire impedance ratio of 1:1.5. Comparing the simulated current distribution in the case without the CBT (Fig. 5) and with the CBT (Fig. 6), it is clear that the previous assumptions are valid. The CBT is capable of preventing the current imbalances with very low requirements on the transformer core, for which almost any ferrite material and size can be used.

However, in Fig. 6b it can be seen that the magnetic flux density is slowly rising in time. That is caused by a mismatch in output wire resistances, which introduces an unwanted steady-state DC voltage across the windings. Unfortunately, the core will eventually saturate, lowering its magnetic conductivity, effectively reducing its capability in preventing the current imbalances. It is thus important to keep the resistances (lengths) of the output wires equal.

IV. Test Hardware

The principles investigated in chapters II and III have been applied to the design of a six-phase power inverter for fault-tolerant drives with the following parameters [9]:

- DC link voltage: $100\,\mathrm{V}$
- phase output current: $225\,\mathrm{Arms}$

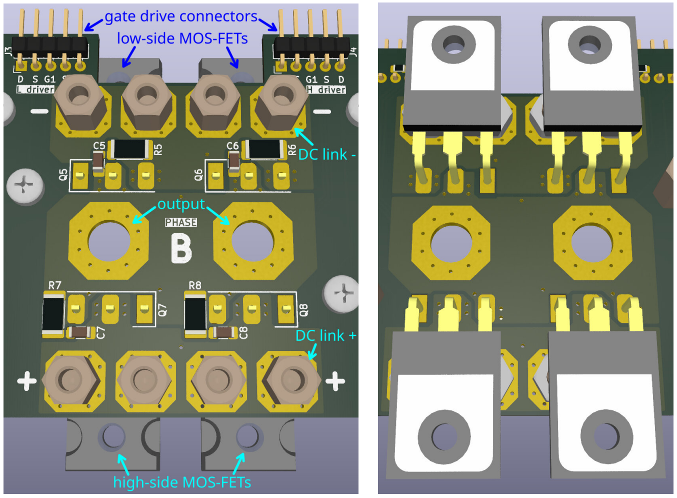

(a) front view

(b) back view

Fig. 7: PCB layout of the 100 V, 225 A inverter leg.

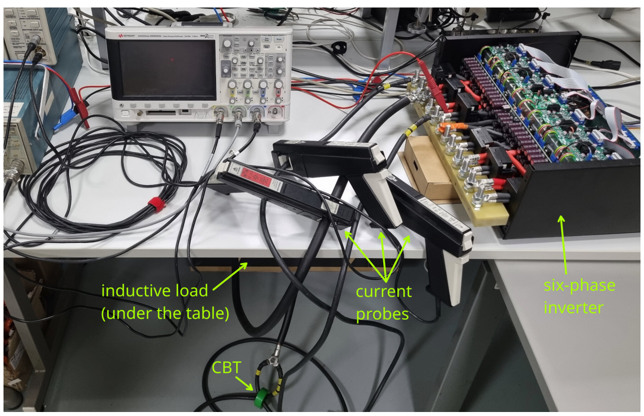

Fig. 8: Test setup for measurements of the current imbalance between paralleled inverter legs.

Fig. 7 shows a PCB design of one of the legs of the test inverter. Each leg uses two parallel MOS-FETs in the TO-247 packages for both low-side and high-side switches. The layout is as symmetric as possible, trying to minimize the inductances of the parallel-connection loops. Each transistor has its own gate resistor (on the driver PCB) and the driver ground signal connections are geometrically in the middle between the sources of the parallel MOS-FETs. The DC link PCB with capacitors is mounted and connected via standoffs.

The inverter is required to be capable of working at double the nominal output current in three-phase configuration, i.e. by paralleling pairs of inverter legs and using the CBTs.

V. Measurements and Results

A test setup for the current imbalance verification measurements is shown in Fig. 8. The outputs of two inverter legs were connected in parallel using wires of different lengths ($2\,\mathrm{m}$ and $4\,\mathrm{m}$), the first time directly, the second time pushed through a small toroidal ferrite core which represents a CBT.

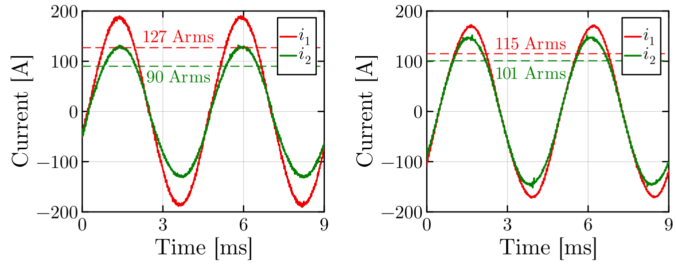

(a) without CBT

(b) with CBT

Fig. 9: Measured current distribution between paralleled inverter legs, wire lengths $l_1 = 2\,\mathrm{m}$, $l_2 = 4\,\mathrm{m}$, $f_{\mathrm{PWM}} = 20\,\mathrm{kHz}$, $f_1 = 220\,\mathrm{Hz}$, $L = 60\,\mu\mathrm{H}$ (load) [9]

The currents were measured using Tektronix TCP303 current probes ($150\,\mathrm{Arms}$, DC to $15\,\mathrm{MHz}$) and Tektronix TCPA300 amplifiers.

As it can be seen in Fig. 9, the CBT significantly improves the current distribution between the inverter legs. It should be noted that the conduction power loss of each leg is proportional to the square of the RMS output current. In the case without the CBT (Fig. 9a), the current ratio between the legs is 1,41, but the conduction loss ratio is 1,99. With the CBT (Fig. 9b), the current ratio drops to 1,14 and the conduction loss ratio to 1,29, validating the function of the CBT.

The remaining current imbalance in Fig. 9b is a result of the difference in wire resistances, which causes saturation of the transformer core. The magnetic flux density inside the core rises relatively slowly in time (as shown in Fig. 6b). Due to the first harmonic component of the output currents, there is not enough time to saturate the core in one half-period before the current polarity changes again. At a lower frequency of the first harmonic component, the core would have more time to saturate, further reducing its magnetic conductivity and consequently the balancing capability of the CBT.

The wire lengths were chosen to be enormously different to show the limitations of the CBT in coping with the saturation. In real-life applications, it is quite easy to keep the wire lengths similar. However, the closer the output node is to the inverter legs, the better equality in impedances must be achieved.

VI. Conclusion

This paper reviews the challenges associated with paralleling MOS-FETs in order to increase the current capability of power inverters and formulates guidelines and solutions to mitigate these issues. The current balancing transformer represents a simple and effective way to significantly improve the current distribution between paralleled inverter legs. A detailed mathematical description of the CBT was provided and its verification by simulations and measurements was conducted. The CBT exhibits limitations in handling different resistances of the individual leg connections, which cause saturation of the core and therefore reduced balancing performance.

The CBTs may also find application in ultrafast switching power converters with wide-bandgap semiconductors (especially GaN HEMTs) with switching frequencies in the order of MHz, where even a small propagational delay skew of integrated gate drivers could cause severe current imbalances. This applies not only to inverters, but also to DC/DC converters where high current capability is required.

References

[1] E. Levi, “Multiphase Electric Machines for Variable-Speed Applications”, *IEEE Transactions on Industrial Electronics*, vol. 55, no. 5, pp. 1893-1909, 2008.

[2] A. Barzkar and M. Ghassemi, “Components of Electrical Power Systems in More and All-Electric Aircraft: A Review”, *IEEE Transactions on Transportation Electrification*, vol. 8, no. 4, pp. 4037-4053, 2022.

[3] *Paralleling power MOSFETs in high current applications: Effect of MOSFET parameter mismatch on current and power dissipation imbalance*, 2021-05-14. Infineon Technologies, 2021.

[4] P. Hofer, N. Karrer, and C. Gerster, “Paralleling intelligent IGBT power modules with active gate-controlled current balancing”, *PESC Record. 27th Annual IEEE Power Electronics Specialists Conference*, pp. 1312-1316, 1996.

[5] Y. Chen, F. Zhuo, W. Pan, F. Zhang, and L. Feng, “A novel active gate driver for static and dynamic current balancing of parallel-connected IGBTs”, *2017 IEEE Applied Power Electronics Conference and Exposition (APEC)*, pp. 795-799, 2017.

[6] L. Du, Y. Wei, X. Du, A. Stratta, Z. Saadatizadeh, and H. A. Mantooth, “Digital Active Gate Driving System for Paralleled SiC MOSFETs with Closed-loop Current Balancing Control”, *2022 IEEE Energy Conversion Congress and Exposition (ECCE)*, pp. 1-6, Oct. 2022.

[7] J. Tu, H. Ben, T. Meng, Z. Yao, J. Ning, and H. Yu, “Research on Parallel Current Sharing Scheme of 1200V/100A SiC MOSFET”, *2019 22nd International Conference on Electrical Machines and Systems (ICEMS)*, pp. 1-4, 2019.

[8] H. Allahyari, M. D. SarfeJo, H. Bahrami, A. Afify, A. Shoaei, and M. Latifzadeh, “Planar Transformer with None Overlapping Winding as Current Balancing Compensator for Paralleled SiC MOSFETs”, *2022 30th International Conference on Electrical Engineering (ICEE)*, pp. 784-790, May 2022.

[9] T. Pitner, “Universal inverter for multiphase low-voltage drives”, Master’s thesis, Brno University of Technology, 2024.

Optimization of PMSM Control: Integrating Flux Weakening, and MTPA for Performance Enhancement

1st Matúš Kavec
Department of Control and Instrumentation, Faculty of Electrical Engineering and Communication
Brno University of Technology
Technická 3058/10, 616 00 Brno, Czech Repulic
Matus.Kavec@ceitec.vutbr.cz

***Abstract*—This paper describes the fundamental function of a motor control of permanent magnet synchronous motors, the operation of a torque-maximizing algorithm that extracts the maximum torque from the current value. It further describes the operation of the field-weakening algorithm that allows the motor to spin above a nominal speed. Based on these algorithms, set points for current controllers have been created. Subsequently, optimization was applied to form these set points.**

***Index Terms*—permanent magnet synchronous motor, optimalization, field-oriented control, field-weakening, flux weakening, maximum torque per ampere**

I. Permanent magnet synchronous motor

A permanent magnet motor is one of the many types of motors that are used either in industry or in electric vehicles. Such a motor has a magnetic field created by permanent magnets, which are made from rare-earth metals such as samarium cobalt (SmCo) or neodymium iron boron (NdFeB). The use of such magnets over ferrite magnets is advantageous mainly because of the increase in the strength of the magnetic field. Based on the arrangement of magnets on the rotor, PMSM motors are distinguished into two types, the motor with surface mounted permanent magnets (SPM) and the motor with internal permanent magnets (IPM), some kinds of magnet arrangements with associated axes can be seen in Figure 1. For both types, the magnetic flux distribution in the air gap is sinusoidal, which implies that the back electromotive voltage is also sinusoidal; it is an AC motor. The equation 1 describes the motor's output torque

$$T_e = \frac{3}{2} p i_q \left[\lambda + (L_d - L_q) i_d\right], \tag{1}$$

where p is the number of magnetic pole pairs of the rotor, λ is the amount of magnetic flux from the permanent magnets, L_d, L_q are the inductance of the d and q axis, and i_d and i_q are the currents to the given axis.

A. Surface magnet

A surface-mounted magnet (SPM) motor is characterized by its magnets being bonded to the surface of the rotor. This placement of the magnets makes the rotor relatively easy to assemble, the disadvantage is that we need to make rounded magnets to fit the rotor diameter. Because of the difficulty of making curved magnets, there are fewer combinations of how to make a rotor. Another disadvantage of SPM rotors is that the magnets are located further away from the axis of rotation of the rotor, which means that at high speeds they are subject to greater centrifugal forces, for this reason SPM rotors are usually wrapped with magnetically non-conductive materials such as fiberglass or carbon fiber after the magnets have been fitted [1]. SPM rotor motors are characterized by having the same inductance in both axes $L_d = L_q$. If we put this relationship into the equation 1, the equation for torque is simplified to 2.

$$T_e = \frac{3}{2} p i_q \lambda \tag{2}$$

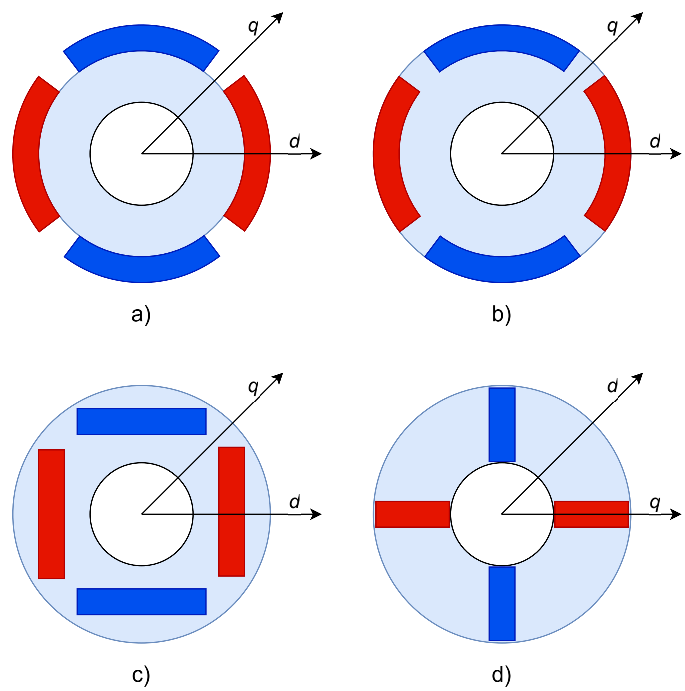

Fig. 1. Example of permanent magnet arrangement and associated axes; a) Surface mounted magnets, b) Inset surface magnets, c) Embedded tangential magnets, d) Embedded radial magnets

It follows that the resulting torque is independent of the current i_q. Based on this, we can simplify the resulting control structure. The simplification is that there is no need to include logic that generates a requirement for a non-zero value of the current i_d.

B. Interior magnet

There are many arrangements of magnets on the IPM rotor that allow different inductance ratios L_d and L_q to be achieved. The difference in inductance occurs because the magnetic flux flowing through the rotor passes through two different environments with different permeability. The permeability of rare metal permanent magnets is similar to the permeability of air. The permeability of the electrical steel M250-35A is listed in the table I together with the types of magnets that are used. It is the difference in inductances that makes IPM rotors suitable for use in the application of the MTPA (maximum torque per ampere) algorithm. From the equation 1, the electromagnetic torque can be expanded by the reluctance torque. The disadvantage of using an IPM rotor is that it is often difficult to construct because the rotor consists of a large number of sections, especially in the case of multilayer rotors with V-shaped placed magnets.

TABLE I
TABLE OF PERMEABILITY OF SOME MATERIALS USED IN MOTOR [2]

Material	Permeability (μ)
Air	1
NdFeB	1.05
SmCo	1.103
Ceramic	1.438
Alnico	6.678
isovac 250-35A	600

$$
\begin{aligned}
v_d &= i_d \cdot R_s - \omega_e \cdot L_q \cdot i_q \\
v_q &= i_q \cdot R_s + \omega_e \cdot L_d \cdot i_d + \lambda
\end{aligned}
\tag{3}
$$

where R_s is the winding resistance and ω_e is the electrical speed of the rotor, where

$$
\begin{aligned}
i^2 &= i_d^2 + i_q^2 \\
v^2 &= v_d^2 + v_q^2
\end{aligned}
\tag{4}
$$

II. MOTOR CONTROL

In order to control a synchronous motor reliably, it is necessary to control the amplitude of the voltage and also the frequency that is generated by the inverter. One way to achieve this is to use scalar control, which is also known as U/f control. It is one of the simplest because it consists only of controlling the stator voltage proportionally to the frequency, thereby maintaining a constant magnetic flux. This method is computationally the simplest but fails to control torque accurately at low speeds, so it is mainly used in applications with low dynamic demands, such as pumps or fans. The second method of controlling electric motors is direct torque control (DTC). This approach eliminates the need for linear current controllers and mathematical current transformations. The control consists of calculating the magnetic flux and torque, which is calculated from the current values of the phase voltage of the current. Further, such control contains two simple comparators, which compare whether our estimated magnetic flux is higher than the desired value, and a second comparator compares the torque value [3]. Then, based on these comparisons and knowledge of the current rotor position, the optimal switching combination can be selected from the switching table. Using such a control, a fast control response can be achieved without the need for a complex mathematical operations. The disadvantage of such control is the considerable torque ripple, especially at low speeds, which is caused by the variable switching frequency of the power elements [4]. This control is mainly used in asynchronous motors. The last type of control used is the field vector control (FOC), this type of motor control is characterized by having a separate control of the current which is responsible for the generation of the magnetic field i_d and the current which is mainly involved in the generation of the torque i_q. Because of the possibility of separately controlling the different components of the current, FOC control is suitable for applications with demands for high precision and speed of response, such as robots or electric vehicles. To calculate the currents i_d and i_q, the Clark transformation 5 is used, which transforms the three-phase stator current i_a, i_b, i_c into a two-component coordinate system i_α, i_β. The 5 equation shows that we do not need to know all 3 phase current values to successfully control the motor current because the electric motor is a symmetrical load and $i_a + i_b + i_c = 0$ is valid for it.

$$
\begin{aligned}
i_\alpha &= i_a \\
i_\beta &= \frac{1}{\sqrt{3}}(i_a + 2i_b)
\end{aligned}
\tag{5}
$$

Subsequently, the coordinate system $\alpha\beta$, which is associated with the motor stator, is transformed by the Park transformation 6 into the coordinate system dq, which is associated with the rotor

$$
\begin{aligned}
i_d &= i_\alpha \cos\theta_e + i_\beta \sin\theta_e \\
i_q &= i_\beta \cos\theta_e - i_\alpha \sin\theta_e,
\end{aligned}
\tag{6}
$$

where $\theta_e = \theta_m \cdot p$ is the electrical angle value and θ_m is the mechanical angle of the rotor. From the equations 6, it follows that we need to know the rotor position accurately, which increases the demands on position measurement and makes it necessary to use an accurate sensor such as an encoder or reslover. Due to the Park transformation, the coordinate system rotates at the same speed as the motor rotor. This transforms the sinusoidal components of $\alpha\beta$ into DC components of dq, which can then be used in current control. Since the current dq does not contain an AC component and the motor winding appears to be a simple RL link, a PI controller can be used.

A. Maximum torque per ampere

The MTPA algorithm tries to obtain the maximum torque from a given current vector, thereby increasing the efficiency of the motor. This algorithm uses the reluctance torque that can

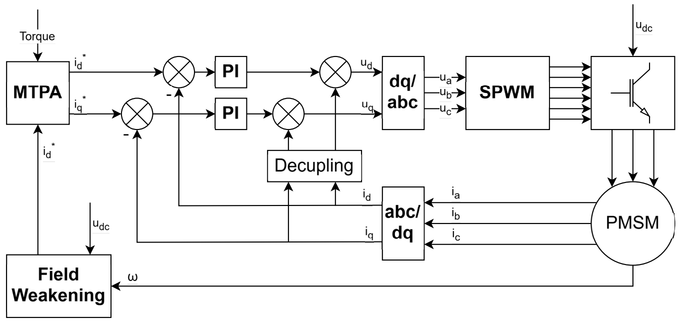

Fig. 2. Schematic of FOC control structure

be produced by IPM rotors. In order for the reluctance torque to be reflected in the output torque, it is necessary to drive the motor with a negative value of current i_d [5]. Based on the magnitude of the inductance difference, the MTPA algorithm can yield a 10 % improvement in efficiency. The magnitude of the current i_d can be expressed using the relation 7

$$\begin{aligned} i_d &= \frac{\lambda}{4(L_q - L_d)} - \sqrt{\frac{\lambda^2}{16(L_q - L_d)^2} + \frac{i_t^2}{2}} \\ i_t &= \frac{2 \cdot T}{3 \cdot p \cdot \lambda}, \end{aligned} \tag{7}$$

where T is the desired torque value.

B. Field weakening

This is a control strategy that allows the motor to spin above nominal speed. As the speed of the permanent magnet electric motor increases, the back electromotive force (BEMF) increases until the motor experiences the same voltage as the voltage on the DC bus. At this point, the current flow that results in the generation of torque stops and the speed stops increasing. This phenomenon can be avoided by adding a negative value i_d to the current vector, because the current i_d is responsible for the generation of the magnetic field. Adding of negative i_d value will create a magnetic field in the stator which will weaken the magnetic flux from the rotor effectively reducing the electromotive force. Reduced magnetic flux allows the motor to accelerate above its rated speed. The flux-weakening method can be applied to both IPM and SPM rotor types. Although SPM rotors are vulnerable to demagnetization of the permanent magnets during excessive flux-weakening, which will cause permanent damage to the permanent magnets. The effect of flux-weakening is also not as pronounced compared to an IPM rotor. The magnitude of the current i_d for motor flux-weakening is dependent mainly on the DC bus voltage u_{dc} and the electrical speed $\omega_e = \omega_m \cdot p$ [6].

C. Generation of currents

After generating the currents i_d and i_q using the flux weakening algorithms and MTPA, it is necessary to combine them to create the desired value for the PI controllers. By summing the currents, the maximum magnitude of the current flowing

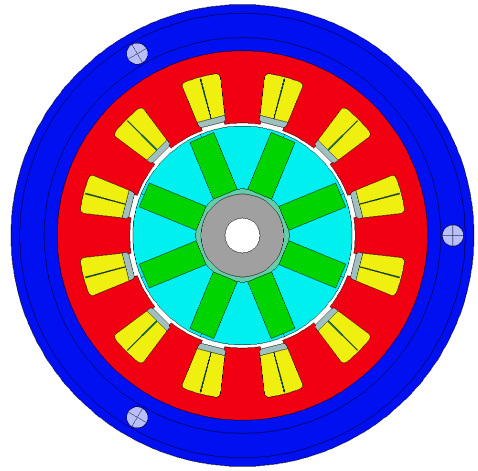

Fig. 3. Illustration of the used IPM motor with spoke-type (radial) magnet placement

through the stator that is allowed by the motor manufacturer may be exceeded. Furthermore, the magnitude of the current i_d should be prioritized over the other component due to the fact that this current participates in the generation of the magnetic field that acts against the permanent magnets in the flux-weakening mode. If the current i_d in the flux weakening region is reduced, we would not be able to spin the motor up to maximum speed, if there is a sudden drop in this current, it would result in an increase in the BEMF, which is likely to be catastrophic for the inverter.

III. Results

A. Motor

In order to use the previous theoretical knowledge, it is necessary to define the motor for which we will subsequently calculate the required values of currents. For this paper, a synchronous IPM motor with radially mounted magnets has been chosen. The distribution of magnets and windings is shown in Figure 3. It is a water-cooled motor whose maximum power is 35 kW, its other parameters are given in table II.

TABLE II
PARAMETERS OF USED MOTOR

Name	Symbol	Value	Unit
Max current	i_{max}	61	A
Torque constant	K_t	0.492	Nm/A
BEMF	K_e	0.031	V/rpm
Maximal voltage	V_{max}	600	V
Nominal speed	ω_{nom}	13650	rpm
Number of pole pairs	p	4	-
Phase resistance	R_{ph}	0.123	Ω
Flux linkage	λ	0.0553	Wb
Q-axis inductance	L_q	0.431	mH
D-axis inductance	L_d	0.293	mH

B. Control by lookup tables

There are a number of ways to generate set points for current controllers. One is to generate values ahead - and store them in multi-dimensional lookup tables. This is the most direct way, which has minimal computational complexity and thus responds immediately to a change in inputs. Using the equations ($v^2 = v_d^2 + v_q^2$ and T) two lookup tables were created which have as input the torque requirement T, the current mechanical speed value ω and the DC bus voltage value u_{dc}. In Figure 4 and 5, a slice of the lookup tables for the voltage $u_{dc} = 591.6$ can be seen.

Based on the shape of the control maps, the whole control region can be divided into 3 parts using the speed value. The first part in the speed region $0 \leqq \omega \lessapprox 13650$ is the region of constant torque, this is also the region where the MTPA algorithm is most applicable. In this region, the desired values do not change with increasing speed. The next part is the constant power region where the flux-weakening algorithm is applied. This region is above the nominal motor speed of 13650 rpm, and it is also characterized by the fact that as the speed increases, the value of torque that the motor is able to generate must decrease. The last region, which is a subregion of the flux-weakening region, is the constant voltage and torque region. In this region, with the requirement for higher torque, we get a saturation of the torque generating current i_q based on the equation $i_{max}^2 = i_d^2 + i_q^2$ because most of the current that can flow through the motor is used to weaken the magnetic field. When the desired values of the currents for the maximized torque are known, the torque can be calculated. We calculate the resulting torque using the equation 1 where in the first case, we consider that all the current goes to only one current component $i_q = 81.26$ A, which corresponds to the control without MTPA and the motor generates $T = 28.59$ Nm. If we divide the maximum current into both components according to MTPA, we get currents $i_d = -17.08$ A and $i_q = 84.5$ A, which corresponds to torque $T = 29.2$ Nm. From these values, we can see that using the torque maximization algorithm, we got 2.2 % more torque without increasing the total current.

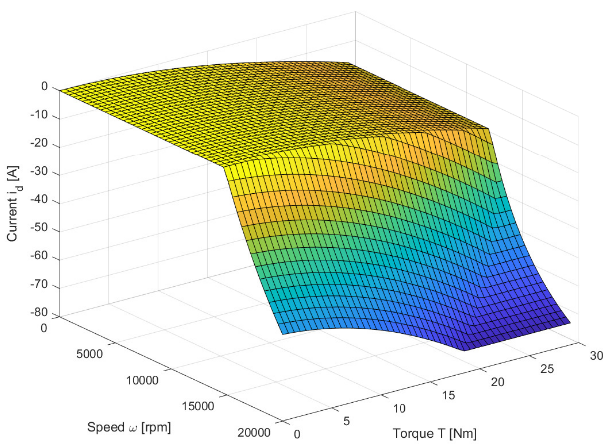

Fig. 4. Control lookup table for current i_d, for $u_{dc} = 591.6$ V

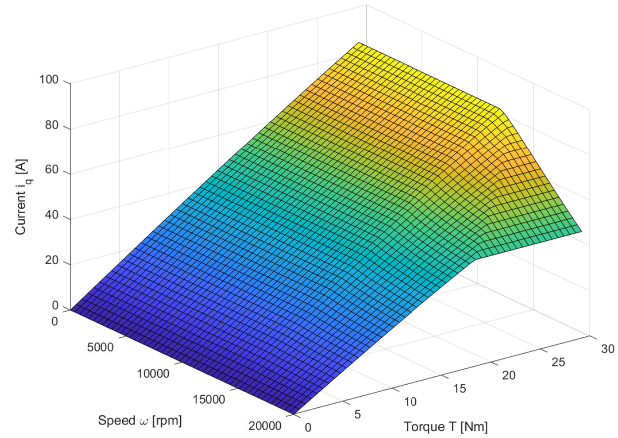

Fig. 5. Control lookup table for current i_d, for $u_{dc} = 591.6$ V

C. Online calculation of set points

Another way to get the desired values for current controllers is to calculate these values directly during the control algorithm. The same equations can be used to calculate the set points as the lookup tables, but these are systems of equations that are difficult to solve online. Therefore, the equations can be partially precomputed to obtain the equation for MTPA in the form 7 and for flux-weakening in the form 8. If we take a closer look at the flux-weakening equation, we can see that it contains a square root and division of one of the input variables. These mathematical operations are time-consuming to compute on embedded applications and thus would slow down the whole control algorithm. It is, therefore, advisable to try to simplify the equation 8.

$$i_d = \frac{\sqrt{L_d^2 \cdot u_{dc}^2 \cdot \omega_e^2 + R_s^2 \cdot u_{dc}^2 - R_s^2 \cdot \lambda^2 \cdot \omega_e^2} - L_d \cdot \lambda \cdot \omega_e^2}{L_d^2 \cdot \omega_e^2 + R_s^2} \tag{8}$$

If we plot the equation for the flux-weakening (Figure 6), we can see that the dependence of the current i_d on the voltage u_{dc} is linear as the speed ω_e increases. Here is a possibility to simplify the equation 8 by decomposing it into a linear and a non-linear part, which greatly simplifies the calculation. The optimization consists of calculating the coefficients of the gain in advance and storing them in a lookup table and calculating the rest of the equation according to the prescription of the linear equation 9.

$$i_d = k(\omega_e) \cdot u_{dc} + q \tag{9}$$

In order to use this equation, we need to express its coefficient q as the equation 10, which is based on the equation 8 while calculating the voltage $u_{dc} = 0$ V. The coefficient q also gives us the location of the center of the voltage ellipse, described by the equations 3 and 4. The size of the voltage ellipse is dependent on the motor speed and the DC bus voltage. Next, we need to calculate the gain values, which depend on ω_e. This can be done from the points in the 6 graph for

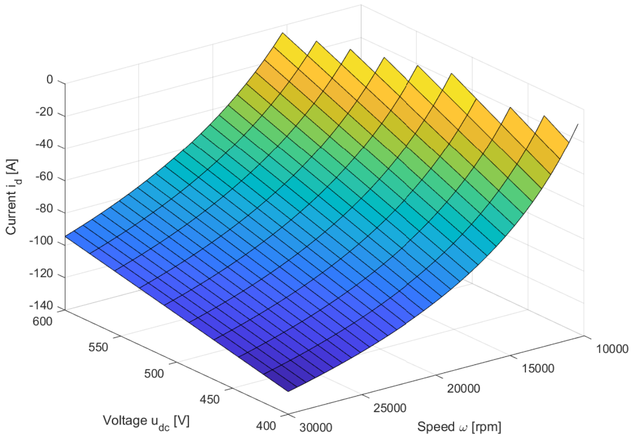

Fig. 6. Control lookup table for current i_d in flux weakening region

constant speed, giving us the 7 graph. This optimization saves us computational power at the expense of memory space and the need to store the lookup table.

$$q = \lim_{\omega_e \to \infty} \frac{\sqrt{-R_s^2 \cdot \lambda^2 \cdot \omega_e^2} - L_d \cdot \lambda \cdot \omega_e^2}{L_d^2 \cdot \omega_e^2 + R_s^2} = -\frac{\lambda}{L_d} \qquad (10)$$

No significant simplification was found for the values of the

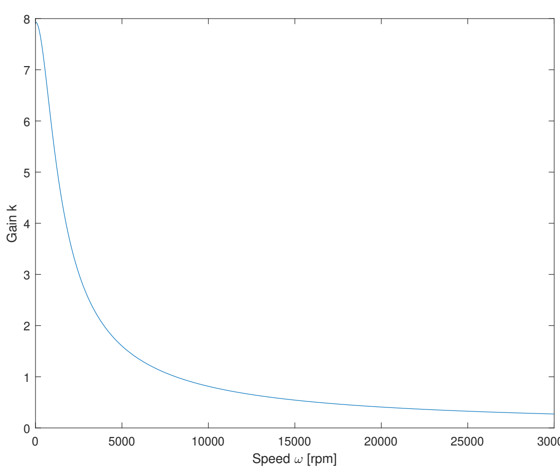

Fig. 7. Gain $k(\omega_e)$ to calculate flux weakening current i_d

current i_d that the MTPA algorithm produces, and hence, we do not avoid the calculation of the square root.

After calculating both current values from both the MTPA algorithm and the flux-wakening algorithm, these values are summed and using the 1 equation, the current value i_q is calculated, which is then saturated if the current exceeds the maximum allowed value by $i^2 = i_d^2 + i_q^2$. The resulting current values can then be used as set points in the PI controllers.

IV. Conclusion

In this work, synchronous motors with surface-mounted and embedded permanent magnets and their equations were presented. Methods for controlling electric motors were described, and an algorithm that maximizes the torque for a given value of current (MTPA) and motor flux-weakening that allows the motor to spin above nominal speed without significant torque loss was described. These methods were subsequently applied to a synchronous motor with embedded magnets, and this implementation can be applied to other IPM motors. Using the MTPA algorithm, the maximum torque is increased by 2.2 %, thereby increasing the efficiency of converting electrical power to mechanical power. Lookup tables were then created based on these algorithms but were not used as a desired value for the PI controller because lookup tables with more than one input are difficult to implement on embedded devices. For this reason, the calculation was optimized by replacing the three-input lookup tables with a combination of equations and simpler single-input lookup tables.

One of the disadvantages of using a constant-parameter implementation is that the parameters change as the motor is operated. Possible solutions are: measuring the motor parameters over time and using them to recalculate the desired values by using the introduced methods, or using methods independent of the motor parameters, e.g., a method to search for a maximum.

Acknowledgment

The completion of this paper was made possible by the grant No. FEKT-S-23-8451 - "Research on advanced methods and technologies in cybernetics, robotics, artificial intelligence, automation and measurement" financially supported by the Internal science fund of Brno University of Technology.

References

[1] J. Dong, Y. Huang, L. Jin and H. Lin, "Comparative Study of Surface-Mounted and Interior Permanent-Magnet Motors for High-Speed Applications," in IEEE Transactions on Applied Superconductivity, vol. 26, no. 4, pp. 1-4, June 2016, Art no. 5200304, doi: 10.1109/TASC.2016.2514342.

[2] H. Wahab, A. Rahardjo, B. Sudiarto and R. Setiabudy, "The Implement of Permanent Magnet Material Variations on the Reduction of Cogging Torque in PMSG," in IOP Conference Series: Materials Science and Engineering, vol. 620, 2019, doi:10.1088/1757-899X/620/1/012101.

[3] M. Alshbib, I.M. Alsofyani and M. Elgbaily, "Enhancement and Performance Analysis for Modified 12 Sector-Based Direct Torque Control of AC Motors: Experimental Validation," in Electronics, vol. 12, no. 3, January 2023, doi:10.3390/electronics12030549.

[4] A. Zhang, Y. Fan and J. Chen, "Direct torque control of synchronous reluctance motor in M-T reference frame considering magnetic circuit saturation and cross saturation," 2020 IEEE 1st China International Youth Conference on Electrical Engineering (CIYCEE), Wuhan, China, 2020, pp. 1-6, doi: 10.1109/CIYCEE49808.2020.9332581.

[5] C. Lai, G. Feng, K. Mukherjee, J. Tjong and N. C. Kar, "Maximum Torque Per Ampere Control for IPMSM Using Gradient Descent Algorithm Based on Measured Speed Harmonics," in IEEE Transactions on Industrial Informatics, vol. 14, no. 4, pp. 1424-1435, April 2018, doi: 10.1109/TII.2017.2759812.

[6] T. M. Jahns, "Flux-Weakening Regime Operation of an Interior Permanent-Magnet Synchronous Motor Drive," in IEEE Transactions on Industry Applications, vol. IA-23, no. 4, pp. 681-689, July 1987, doi: 10.1109/TIA.1987.4504966.

Computational Fluid Dynamics Thermal Modelling of Fan-Cooled Finned Heat-sink Considering Air Temperature Rise

Jakub Súkeník
Department of Power Electrical and Electronic Engineering
Brno University of Technology, FEEC
Brno, Czech Republic
xsuken00@vut.cz

Marek Toman
Department of Power Electrical and Electronic Engineering
Brno University of Technology, FEEC
Brno, Czech Republic
marek.toman@vut.cz

***Abstract*—This paper investigates the thermal efficacy of a fan-cooled finned heat-sink through the application of computational fluid dynamics simulations alongside empirical validation. The research emphasises the modelling of airflow distribution, the analysis of heat transfer characteristics, and the determination of the heat transfer coefficients. A thermal resistance model has been established and compared with empirical measurements, revealing a significant correlation between the simulation results and the experimental findings. The results show that computational fluid dynamics serves as a reliable instrument for improving heat-sink design without requiring expensive physical prototypes. Subsequent investigations will investigate alternative fan configurations, improve boundary conditions, and enhance computational efficiency.**

***Index Terms*—computational fluid dynamics, heat-sink, axial fan, heat transfer coefficient, forced convection**

I. Introduction

The advancement of power electronics is characterised by continual advances, particularly in regard to power density, which consequently precipitates an escalating demand for effective heat dissipation approaches. As electronic components become increasingly miniaturised, these components produce a considerable amount of thermal energy that requires effective management to ensure operational reliability and prevent efficiency reduction of critical components. [1]

In response to this issue, heat-sinks provide a crucial function in the dissipation of heat from electronic apparatuses. Conventional passive cooling mechanisms are based on natural convection, which may be inadequate for applications requiring high thermal power dissipation. In these scenarios, the implementation of forced air cooling, mostly in the form of axial fans, is widely adopted to increase the efficiency of heat transfer. By amplifying airflow across the heat-sink, axial fans substantially enhance convective heat dissipation. [1]–[3]

However, the design of an optimised heat-sink-fan assembly requires careful equilibrium among thermal performance, pressure drop, and material limitations. The creation of physical prototypes for each iteration of the design process is both financially expensive and time-consuming. Consequently, numerical simulation methodologies, including Computational Fluid Dynamics (CFD), have emerged as essential tools for the analysis of fluid flows. CFD models enable researchers and engineers to investigate airflow dynamics, temperature gradients, and thermal resistances, enabling more optimal design choices without the requirement of experimental testing. [4]–[6]

This study investigates a specific heat-sink configuration integrated with an axial fan. CFD simulations are utilized to model key components, focusing on the airflow transition through the slots of the individual fins of the heat-sink as well as the axial fan itself. Subsequently, a CFD model for the heat-sink with axial fan cooling is established. The primary objective is to determine the heat transfer coefficient of the cooled heat-sink. Experimental measurements are conducted on the selected heat-sink. A schematic representation based on electrothermal principles is created for the measured heat-sink. The heat transfer coefficient derived from this analogy is then compared to the CFD findings.

II. Computational Fluid Dynamics simulations

In this section, the CFD calculation procedure in Ansys Fluent will be explained and individual simpler simulations, such as a finned heat-sink simulation and a simplified axial fan model, will be presented. This is to verify that the final simulation of the axial fan together with the finned heat-sink will correspond the measurement as closely as possible.

A. Basic Workflow of Computational Fluid Dynamics Simulations

Fig. 1 shows the fundamental steps involved in the establishment of a CFD model. Initially, a geometric configuration with

This research work has been carried out in the Centre for Research and Utilization of Renewable Energy (CVVOZE). Authors gratefully acknowledge financial support from the Ministry of Education, Youth and Sports under institutional support and BUT specific research programme (project No. FEKT-S-23-8430). The main author acknowledges Mr. Radoslav Cipín as the main author's research supervisor for his valuable comments and help while writing this paper.

predetermined named selections is developed and examined for any instances of overlapping surfaces within the Ansys SpaceClaim module of Ansys Workbench. Subsequently, the mesh module, namely Mechanical, is employed to specify the fluid/solid interfaces. A shared topology is implemented to facilitate simplification of the mesh. In a shared topology, the interfaces between adjacent or intersecting surfaces are unified to produce a conformal mesh.

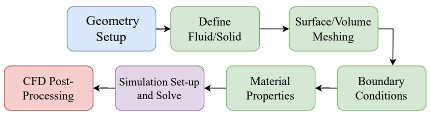

Fig. 1. CFD detailed setup workflow inside Ansys Workbench Fluent module, modified from [7].

Following this, the boundary conditions are specified, including the outlets, inlets, internal heat generations, temperatures, periodicities, and symmetries within the model in the Ansys Fluent module. The material characteristics can be incorporated into the model. After executing the model with the appropriate viscous formulation, the resulting data goes to post-processing. [7]

In the module **Simulation Set-up and Solving** (Fig. 1) turbulence model is chosen. Typically, the SST $k-\omega$ model is used to calculate turbulent flow [8]–[12].

B. Single Slot Heat-sink Model

The CFD model of the finned heat sink is assigned with evaluating the velocity within a single slot between the fins, depending on whether the edges of the fins are characterised as sharp or rounded. In addition, it is examined whether the quality of the mesh influences the velocity profile within the heat sink slot.

The simulation is executed in a two-dimensional framework. The geometry exhibits a vertical dimension measuring 40 mm and a lateral dimension of 15 mm, accompanied by a slot aperture of 1 mm and a thickness of the heat-sink fins also measuring 1 mm. The velocity inlet is located at the upper boundary of the model. The velocity inlet is set to $6\ \mathrm{m \cdot s^{-1}}$. The lower boundaries of the model are classified as pressure outlets. The lateral boundaries of the model are confined by structural walls. Following the acquisition of the velocity distribution within the channel situated between the heat-sink fins, a linear trajectory is delineated 2 mm from the edges of the fin, which extends throughout the channel.

In Fig. 2, various mesh resolutions corresponding to distinct geometrical configurations are illustrated, specifically featuring sharp-edged fins and rounded edges. For grooves or channels, fine mesh is generally recommended, as this type of mesh captures the flow or temperature distribution more accurately. The closer the element is to the wall, the smaller it must be to accurately capture the phenomena in close proximity to the wall [11]. For the complete CFD simulation of a heat-sink cooled by an axial fan, rounded edges will be considered.

The velocity profiles extracted from the slot are depicted in Fig. 3 (a) for sharp corners of the heat-sink fins, and Fig. 3 (b) shows the velocity profile for the round corner heat-sink fins. The acronym HQM depicted in Fig. 3

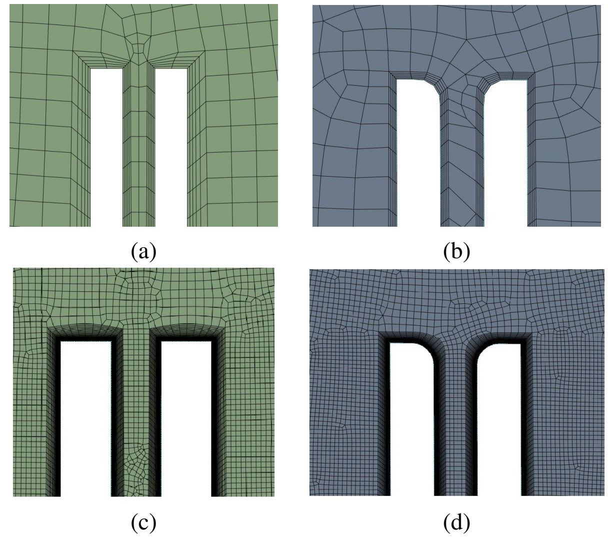

Fig. 2. Meshes for CFD air gap models, (a) low-resolution mesh with sharp corners, (b) low-resolution mesh with round corners, (c) fine mesh with sharp corners, (d) fine mesh with round corners.

denotes a high-quality mesh, whereas LQM signifies a low-resolution mesh. In order to enhance the clarity of the waveforms, the spatial dimension is transformed into a dimensionless parameter. The average velocity in the slot between the heat sink fins of the low-resolution mesh model with sharp corners is $4.28\ \mathrm{m \cdot s^{-1}}$ and the average fine mesh velocity is equal to $4.34\ \mathrm{m \cdot s^{-1}}$.

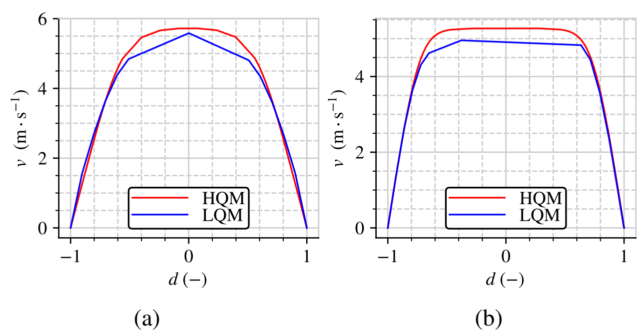

Fig. 3. Velocity profiles in the slot of the heat-sink fins, (a) HQM and LQM with sharp corners, (b) HQM and LQM with round corners.

For the low-resolution mesh with round corners, the average velocity of the waveforms in Fig. 3 (b) is equal to $4.32\mathrm{m \cdot s^{-1}}$, and the fine mesh with round fins average velocity is $4.44\ \mathrm{m \cdot s^{-1}}$.

Fig. 4 shows the resulting simulated velocity curves using CFD for the above case. The effect of the low-resolution mesh is particularly evident in Fig. 4 (b). The elements in the slot are so large that they incorrectly capture the flow pattern and thus change the character of the entire fluid flow.

C. Axial Fan Model

Another CFD simulation applies to the axial fan model. The model has been designed as a three-dimensional cylindrical

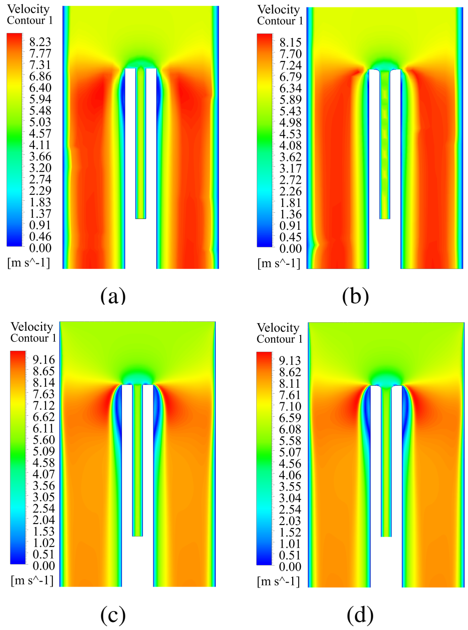

Fig. 4. Simulated velocity contours, (a) low-resolution mesh model with sharp corners, (b) low-resolution mesh model with round corners, (c) fine mesh model with sharp corners, (d) fine mesh model with round corners.

structure that exhibits a length of 600 mm and a diameter of 90 mm. At the terminal ends of the tube, boundary conditions corresponding to the pressure inlet and pressure outlet are implemented.

The cylinder is divided at its midpoint, and an axial fan boundary condition is established at this interface. SUNON MF92252V1-1000U-A99 axial fan is simulated [13]. Certain simplifications are assumed for the above-stated condition. The axial fan is treated as a two-dimensional entity; its volumetric dimensions are neglected. The fan hub is incorporated within the parameters of the boundary condition formulation. In addition, a simplified flow model is employed which includes the analysis of two distinct flow velocity components. In the axial dimension, the velocity is specified according to the performance curve specified in [13]. The additional flow component is identified as the tangential velocity. This particular component is derived from the circumferential velocity associated with the fan blades in the form

$$v_{\text{blade}} = \frac{2\pi \cdot n}{60} \cdot r_{\text{rotor}}, \tag{1}$$

where ω is the angular velocity and r_{rotor} is the radius of the axial fan rotor. To determine the tangential velocity, it is essential to take into account a blade pitch angle of approximately $\alpha = 30°$ [14]

$$v_{\tan} = v_{\text{blade}} \cdot \tan(\alpha). \tag{2}$$

In Fig. 5 (a), both the axial and tangential flow velocities generated by the axial fan are depicted. The red curve shown in Fig. 5 (a) represents the overall fan speed from the axis of rotation that extends to the tip of the blade. In Fig. 5 (b), the velocity vector field on the fan boundary condition is observed. The calculated resulting volume flow rate $\dot{V}$ is equal to $0.02\,\mathrm{m}^3 \cdot \mathrm{s}^{-1}$, which is in agreement with the performance curve presented in [13].

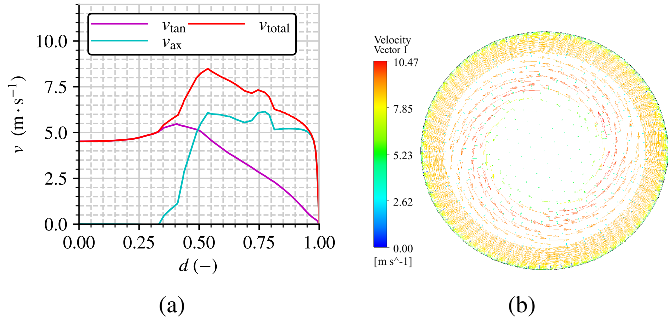

Fig. 5. (a) velocity profiles of the axial, radial components in the fan and the overall velocity profile from the centre of rotation to the end of the blade tips, (b) velocity vector field on the XY plane.

Fig. 6 shows the representation of the velocity field contours within the XY plane. The contours indicate that the velocity is minimal in the hub region and increases in the area of the axial fan blades.

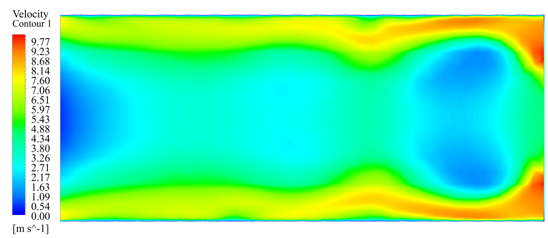

Fig. 6. Contours of velocity field from the fan to outlet.

D. Fan cooled Heat-sink model

The entirety of the axial fan heat-sink requires detailed modelling of complete domain, thus preventing the application of symmetry and periodicity boundary conditions for this specific heat-sink type. In contrast, the periodicity condition may be employed for CPUs' heat-sinks. These systems typically exhibit an axis of symmetry. Consequently, CFD simulation requires shorter time for the calculation process.

Fig. 7 shows the mesh of the entire CFD model. The width of the fan is 92 mm and has a thickness of 25 mm. The axial fan is placed 10 mm above the heat-sink. The dimensions of the heat-sink are 100 mm in both width and length, with a thickness of 32 mm, a base height of 8 mm, and a singular fin width of 1 mm. The width between the fins is 1 mm. The resolution in the slots has been slightly reduced

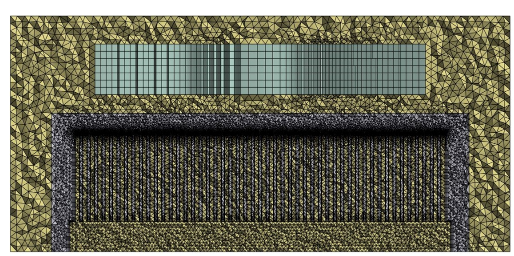

Fig. 7. Mesh of the heat-sink with axial fan.

due to the substantial cell count. The total number of nodes was established at 7,354,752. With the current configuration, the time required to compute each work point of the CFD model is approximately 3 hours. The boundary conditions are established in a manner similar to the methodologies described in Sections II-B and II-C.

Fig. 8 shows the flow velocity fields and the temperature fields of the fan-cooled heat sink model. It is evident that the fluid medium does not completely infiltrate the slots of the heat-sink. This effect is most evidently illustrated in Fig. 8 (b). The spatial distribution of the temperature field on Fig. 8 (c) and in Fig. 8 (d) aligns with theoretical postulations, specifically indicating that the maximum temperature is situated at the interface between the electronic component and the surface of the heat-sink. At this juncture, the dissipation of power is conveyed in the direction of a negative temperature gradient. This phenomenon is amplified by the forced convection produced by the fan.

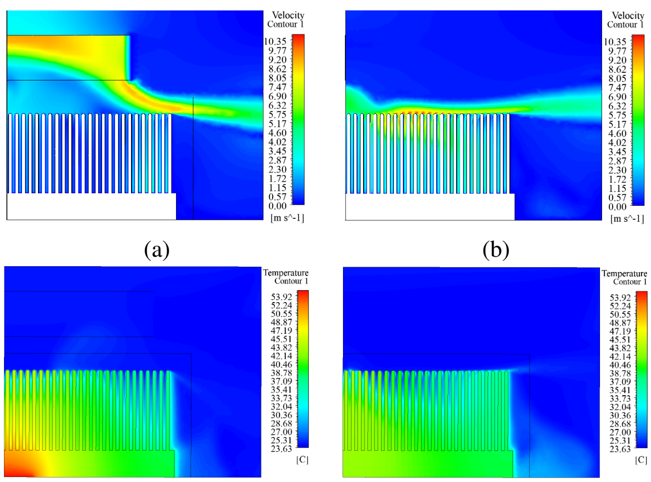

(a) (b) (c) (d)

Fig. 8. Fields of CFD fan cooled Heat-sink model, (a) YZ plane velocity contours 25 mm from the origin of the coordinate system, (b) YZ plane velocity contours 50 mm from the origin of the coordinate system, (c) YZ plane temperature contours, (d) plane velocity contours 50 mm from the origin of the coordinate system.

III. Validation of CFD Fan cooled Heat-sink Model

For the purpose of verifying the findings obtained from the CFD simulation with respect to the fan and the heat-sink, it is crucial to determine the thermal resistance of the heat-sink through alternative methodologies, followed by the evaluation of the heat transfer coefficient of the heat sink. In this segment, the thermal characteristics of the heat-sink are determined through both empirical measurement and theoretical calculation.

A. Verification of the Simulations by Laboratory Measurements

The calculation results were verified using measurements available in [15]. A measurement was established to evaluate the performance of the axial fan cooler system, as illustrated in Fig. 9. The schematic representation in Fig. 9 shows the configuration of the two voltage sources. The voltage source

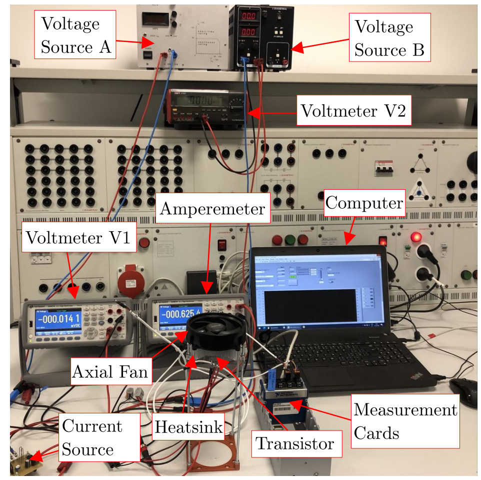

Fig. 9. Measurement setup.

(A) supplies voltage to the current source, ranging from 0 to 30 V. The secondary source (B) provides a fixed voltage to the fan, with a V2 voltmeter in parallel for accurate measurements. An ampere metre is in series with the current source from the MOSFET transistor, while the voltmeter V1 is parallel to measure the voltage across the transistor. The power dissipation due to the transistor heating is calculated from these measurements. Both the voltmeter V1 and the ammeter are connected to a computer for data visualisation using LabVIEW software. In addition, temperature sensors monitoring the heat sink and ambient temperature are connected to computer measurement cards. An output signal of 0 to 10 V is transmitted to the current source for temperature regulation through the LabVIEW software.

B. Calculation of Heat-sink Heat Transfer Coefficient

Fig. 10 shows the thermal diagram of a singular component that is attached to the heat sink. This diagram demonstrates analogy to electrical schematics. The thermal resistances depicted in Fig. 10 are arranged in series, the current source symbolising the dissipation of power within the component, while the voltage source represents the surrounding temperature ϑ_S.

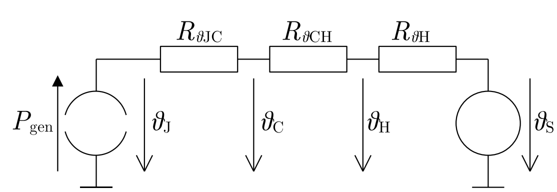

Fig. 10. Thermal diagram, modified from [15].

The $R_{\theta JC}$ represents the thermal resistance that exists between the chip and the component casing, $R_{\theta CH}$ represents the thermal resistance at the interface between the casing and the heat-sink, while $R_{\theta H}$ refers to the thermal resistance inherent to the heat sink itself. From the thermal diagram located in Fig. 10, an equation can be written in the form

$$R_{\vartheta \mathrm{JC}} + R_{\vartheta \mathrm{CH}} + R_{\vartheta \mathrm{H}} = \frac{\vartheta_J - \vartheta_S}{P_{\mathrm{gen}}} -, \tag{3}$$

where P_{gen} is the power dissipation of the component. From (3), the thermal resistance required from the heat-sink can be expressed in the form

$$R_{\vartheta \mathrm{H}} = \frac{\vartheta_J - \vartheta_S}{P_{\mathrm{gen}}} - R_{\vartheta \mathrm{JC}} - R_{\vartheta \mathrm{CH}}. \tag{4}$$

The consequent thermal resistance of the heat-sink, neglecting the thermal resistance attributable to conduction within the heat-sink, can be transformed into the overall heat transfer coefficient $\alpha_{\vartheta \mathrm{H}}$ according to [16]

$$\alpha_{\vartheta \mathrm{H}} = \frac{1}{S_{\mathrm{H}} \cdot R_{\vartheta \mathrm{H}}}, \tag{5}$$

where $S_{\vartheta \mathrm{H}}$ is the total area of the heat-sink.

IV. Results and discussion

Tab. I shows the comparison of the computed heat transfer coefficients derived from empirical measurements and those obtained from computational fluid dynamics (CFD) simulations corresponding to the nominal operational parameters of the fan. At this operational point, the axial fan operates at a rotational speed of 3000 rpm.

TABLE I
Comparison of calculated heat transfer coefficients from measurements and heat transfer coefficients from CFD simulations.

ϑ_{H}	ϑ_{S}	P_{gen}	$\alpha_{\vartheta \mathrm{H}}$	$\alpha_{\vartheta \mathrm{CFD}}$	$\lvert\alpha_{\vartheta \mathrm{H}} - \alpha_{\vartheta \mathrm{CFD}}\rvert$
°C	°C	W	$\frac{\mathrm{W}}{\mathrm{m}^2 \cdot \mathrm{K}}$	$\frac{\mathrm{W}}{\mathrm{m}^2 \cdot \mathrm{K}}$	$\frac{\mathrm{W}}{\mathrm{m}^2 \cdot \mathrm{K}}$
30.01	23.63	28.68	17.35	17.20	0.15
35.06	23.63	56.41	18.97	17.35	1.62
40.01	23.68	75.03	17.66	18.09	0.43
45.02	23.90	101.94	18.60	17.61	0.99
50.00	24.00	122.52	18.16	17.32	0.84
54.97	24.30	141.75	17.83	17.52	0.31

As evidenced in Tab. I, it is apparent that the differences among the heat transfer coefficients are minimal; therefore, one may conclude that the simulation has been configured appropriately. The coefficients of heat transfer exhibit minimal variation as the temperature differential increases. Modification of the heat transfer coefficient is achievable only by controlling the operational velocity of the axial fan.

V. Conclusion

The study validated the utility of CFD simulations in predicting the thermal efficiency of a fan-cooled heat-sink, providing results that closely align with empirical data. The results confirm that CFD simulations can closely simulate the behaviour of fan cooled heat-sinks without the need for costly prototypes. Subsequent investigations will aim to increase the simulation precision, evaluate different fan arrangements, and improve computational efficiency.

References

[1] L. Xie, X. Yuan, and W. Wang, "Thermal modeling of fan-cooled plate–fin heatsink considering air temperature rise for virtual prototyping of power electronics," *IEEE Transactions on Components, Packaging and Manufacturing Technology*, vol. 10, no. 11, pp. 1829–1839, 2020. [Online]. Available: https://ieeexplore.ieee.org/document/9140012/

[2] U. A. Khan, H. Ullah, and A. Nawaz, "Design and optimization of heatsink for an active cpu cooler using numerical simulations," *Journal of Advanced Research in Fluid Mechanics and Thermal Sciences*, vol. 111, no. 2, pp. 214–224, 2024-1-8. [Online]. Available: https://semarakilmu.com.my/journals/index.php/fluid_mechanics_thermal_sciences/article/view/4496

[3] U. SanAndres, G. Almandoz, J. Poza, G. Ugalde, and A. J. Escalada, "Radial fan simulations by computational fluid dynamics and experimental validation," in *2014 International Conference on Electrical Machines (ICEM)*. Berlin, Germany: IEEE, 2014, pp. 2179–2185. [Online]. Available: http://ieeexplore.ieee.org/document/6960486/

[4] T. D. Nguyen, A. V. Vo, and T. T. Bui, "Design modeling and cfd simulation of parallel plate–fin heat sink under natural convection," *Makara Journal of Technology*, vol. 28, no. 3, pp. 96–104, 2024-12-30. [Online]. Available: https://scholarhub.ui.ac.id/mjt/vol28/iss3/4/

[5] R. Franzke and S. Sebben, "Validation of different fan modelling techniques in computational fluid dynamics," in *Proceedings of the 21st Australasian Fluid Mechanics Conference*. Adelaide, Australia: Australasian Fluid Mechanics Society, December 2018. [Online]. Available: https://people.eng.unimelb.edu.au/imarusic/proceedings/21/Contribution_526_final.pdf

[6] O. Mesalhy, C. Rath, D. Rini, J. Kizito, Q. Leland, and L. Chow, "A parametric fin structure design study for cooling aerospace electromechanical actuators with high-speed axial fans," *Heat and Mass Transfer*, vol. 56, no. 5, pp. 1565–1577, 2020. [Online]. Available: http://link.springer.com/10.1007/s00231-019-02791-y

[7] S. A. Abdelrahman and B. Bilgin, "Computationally efficient surrogate-based magneto-fluid-thermal numerical coupling approach for a water-cooled ipm traction motor," *IEEE Access*, vol. 10, no. VOLUME 10, pp. 83 692–83 704, 2022. [Online]. Available: https://ieeexplore.ieee.org/document/9851647/

[8] F. R. Menter, "Improved two-equation k - omega turbulence models for aerodynamic flows," *NASA*, vol. 1992, no. Quick Release, pp. 1–8, October 1992. [Online]. Available: https://ntrs.nasa.gov/api/citations/19930013620/downloads/19930013620.pdf

[9] F. R. Menter, "Two-equation eddy-viscosity turbulence models for engineering applications," *AIAA Journal*, vol. 32, no. 8, pp. 1598–1605, 1994. [Online]. Available: https://arc.aiaa.org/doi/10.2514/3.12149

[10] D. C. Wilcox, *Turbulence Modeling for CFD*, 3rd ed. San Diego, California: DCW Industries, Inc., November, 2006.

[11] Y. A. Cengel and J. M. Cimbala, *Fluid mechanics*, third edition ed. New York: McGraw Hill, [2014].

[12] J. Súkeník and M. Toman, "Analysis of heat transfer in the air gap of electrical machines using empirical equations and computational fluid dynamics," in *Proceedings I of the 30th Conference STUDENT EEICT 2024*. Brno: Brno University of Technology, Faculty of Electrical Engineering and Communication, April 23, 2024, pp. 353–357. [Online]. Available: https://www.eeict.cz/eeict_download/archiv/sborniky/EEICT_2024_sbornik_1.pdf

[13] "Sunon specification for approval," 08.11.2017. [Online]. Available: https://www.sunon.com/PROSEARCH_FILES/(D09038930G-01)-1.pdf

[14] H. Witte and C. Bode, "Impact of blade design on static pressure recovery of rotor-only low-pressure axial fans," in *Volume 1: Fluid Applications and Systems (FASTC); Fluid Measurement and Instrumentation (FMITC); Fluid Mechanics (FMTC); Multiphase Flow (MFTC)*. Anaheim, California: American Society of Mechanical Engineers, 2024-07-15, pp. –. [Online]. Available: https://asmedigitalcollection.asme.org/FEDSM/proceedings/FEDSM2024/88124/V001T01A004/1205490

[15] M. Hőhn, "Koncepty chlazení ve výkonové elektronice," Brno, 2024.

[16] Y. A. Cengel and A. J. Ghajar, *Heat and Mass Transfer: Fundamentals and Applications*, vyd. 5 ed. New York: McGraw-Hill Education, 2015.

Enhancing Signal Collection Efficiency in Liquid Scintillators via Optical Fibre End Treatments for Dosimetry Applications

Tadeáš Zbožínek
Department of Microelectronics, FEEC
Brno University of Technology
Brno, The Czech Republic
214774@vut.cz

Michal Jelínek
Institute of Scientific Instruments
Czech Academy of Sciences
Brno, The Czech Republic
jelinmi@isibrno.cz

Josef Hynšt
Institute of Scientific Instruments
Czech Academy of Sciences
Brno, The Czech Republic

Břetislav Mikel
Institute of Scientific Instruments
Czech Academy of Sciences
Brno, The Czech Republic
mikel@isibrno.cz

***Abstract*— This paper presents a systematic evaluation of various optical fibre end modifications aimed at enhancing signal collection from a liquid scintillator. Recognizing the significant potential of optical fibre dosimetry for long-term, high-dose ionising radiation monitoring, our study emphasizes the optimization of scintillation counting, particularly for neutron detection. By immersing the optical fibre in the liquid scintillator, we enhanced light collection and applied several end treatments, including classical cleaving, tapering, etching, and optical lens formation. Comparative analysis reveals that the choice of end treatment influences light transmission efficiency, thereby advancing the performance of scintillation-based detection systems and paving the way for improved radiation dosimetry techniques.**

***Keywords*— Ionising radiation, gamma-ray, dosimetry, etching, optical tapers, welding**

Optical fibre dosimetry has become an essential method in the nuclear industry, with notable applications in the field of medicine, especially in radiation therapy and diagnostic procedures. The advantages of optical fibre dosimetry in the nuclear industry lie in its ability to improve safety, provide flexibility, avoid interference with electronic devices, and offer non-invasive characteristics in medical applications. Many of these applications are based on materials that exhibit fluorescence upon irradiation, a phenomenon known as scintillation. Scintillation detection serves not only as a means of quantifying radiation, but also as an essential source of information regarding the energy levels of incoming particles, thus improving the accuracy and efficacy of measurement capabilities. [1][2][3][4]

An advantage of optical fibre is its ability to protect sensitive electronic components by transmitting scintillation signals outside of irradiated areas. This capability allows optical fibres to be used in environments with high levels of ionising radiation, where many traditional electronic detectors would suffer from reduced operational lifespans. As a result, optical fibres enable the development of long-term, real-time monitoring systems in radiation-heavy environments. However, the use of optical fibres presents challenges, including limited sensitivity, range, and the need for specialised material implementations.[5][6]

I. Background

Our emphasis is on applying optical fibres in conjunction with scintillation material. The transmission link between the detector and the scintillator enables the electronics to be placed behind a radiation shield. Furthermore, because of the low attenuation properties of optical fibres, the distance inherently serves as a protective measure for electronics. To extend the system's operational lifespan, fibres should be made of silica rather than plastic, as plastic fibres are more commonly used in the nuclear industry. A pure silica core or fluoride-doped silica fibre enhances radiation resistance. Detectors such as photomultipliers, photodiodes or silicon photomultipliers are then positioned at the end of the fibre to collect and analyse transmitted scintillation light, allowing precise radiation measurements. The whole setup is illustrated Fig. 1.

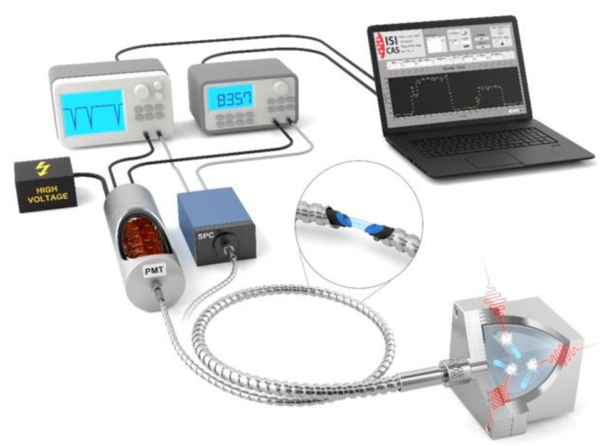

Fig. 1. Principle of Optical Fiber Dosimetry Method [5]

A. *Principle*

The scintillator crystal is positioned within the irradiated area, where interactions with neutrons or gamma rays excite electrons in a material. Through internal conversion and fluorescence mechanisms, the scintillator emits ultraviolet (UV) light, a portion of which is captured by an optical fibre directly attached to the crystal. To reduce unwanted reflections on the fibre's surface, its tips must be precisely polished.

As previously mentioned, the fibre is composed of pure silica with a high OH content to reduce attenuation at the scintillator's emission wavelength. The fibre has a large diameter (up to 1.5 mm) and a numerical aperture of 0.5, both critical parameters to maximise signal collection. [5]

Subsequently, the transmitted light (in form of pulses) is transformed into electrical pulses through a photomultiplier or photodiode. Pulses produced within the scintillator represent the number of incident particles. The height of the pulse, which is proportional to the number of emitted photons, provides data on the energy of the incoming particle. A complication arises from the optical fibre that distorts the light signal. Consequently, the energy cannot be accurately measured, necessitating operation in dosimetry mode. In this mode, only particle counts are assessed, enabling the activity of a known environment to be inferred from this information.[1]

B. *Motivation*

The limitations of solid scintillators in optical fibre-based dosimetry, particularly the low signal intensity and pulse distortion, require the exploration of alternative solutions. A key challenge in light collection arises from the gap between the fibre and the scintillator, which introduces a three-index optical interface, causing multiple reflections and significant signal loss. Additionally, ensuring proper fibre end treatment is crucial, as misalignment with the scintillator surface further reduces efficiency.

To overcome these limitations, we investigated the use of liquid scintillators, which allow direct submersion of the optical fibre after cleaving. This approach not only eliminates the gap issue but also enables novel fibre-end modifications to optimise light collection efficiency. Moreover, organic scintillators are essential for fast neutron measurements due to their high sensitivity and rapid response to gamma-neutron interactions. In contrast, for gamma-ray measurements, inorganic crystals provide a sufficiently high light yield, and converting these materials to organic scintillators would result in a significant loss of light [1]. Therefore, improvements in signal transmission using liquid scintillators are mainly focused on the development of more effective systems for neutron monitoring.

II. FIBRE MODIFICATIONS

To enhance the light collection efficiency of the fibres, a range of techniques were explored to determine the most effective termination modification. The most common approach is cleaving, which ideally results in a planar termination of the fibre. Furthermore, the etching technique was utilised to generate conical structures, whereas electric arc shaping was applied to form lenses and tapers. All modifications are illustrated in Fig.2.

A. *Cleaving*

The most fundamental step in optical fibre preparation is cleaving, which ensures a flat end face for subsequent processing. The primary advantage of this method is its simplicity. When the fibre is submerged in liquid, additional polishing is no longer required, allowing for direct use.

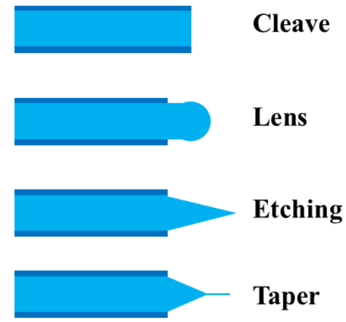

Fig. 2. Depiction of Tip Modification

However, achieving a precise and clean cut becomes challenging for optical fibres with larger diameters which are crucial for effective light collection.

The cleaving process begins with the removal of the optical fibre protective coating. The exposed fibre is then cleaned with isopropyl alcohol to remove contaminants. The cleaned fibre end is secured to a board using adhesive tape to maintain stability. A precise scribe is made when tension is applied to the fibre and a ruby knife is placed perpendicularly. A tiny droplet of water is then applied to the scribed area, and a clean cleave is achieved by pulling the fibre. [7]

B. *Electric arc fibre shaping*

The process of shaping the tips of optical fibres was achieved by utilising a welding device equipped with a "Ring of Fire" (ROF) electrode system. An electric arc generated by three electrodes produces a sufficient temperature to facilitate the shaping of optical fibres. The system operates without the need for a specialised gaseous environment, allowing all procedures to be conducted under standard laboratory conditions. This apparatus allows the processing of optical fibres with diameters up to 2.5 mm.

The fabrication procedure for tappers and lenses begins with the same initial steps. First, the coating of the optical fibres is removed, and the fibres are cleaved to facilitate further processing. The fibres were then thoroughly cleaned with isopropyl alcohol to prevent the dust from introducing asymmetry during arc processing. The fibre is then securely placed between the electrodes, and adjustments are made using a microscope. At this point, the processes for tappers and lenses diverge. For lens fabrication, an ultrasonic cleaver is used to cleave the fibre at the required distance. An electric arc is then ignited, and the end of the fibre is shaped according to the applied power. The melted material forms a sphere which functions as a lens. The diameter of the sphere can be adjusted by varying the applied power. For tappers, the initial step involves thermal treatment using the ROF electrode system. The fibre gradually narrows through controlled positioning of the electrodes, after which the fibre is cleaved.

The created lens converges light to a focal point, with its primary function being the transmission of the signal from the optical fibre to the photodiode. Tappers on the other end have created a parabolic cone, which can increase light input into the fibre.

C. Chemical etching

The final process employed in this experiment involved the modification of the fibre through chemical etching, which is a method that facilitates the fabrication of various shapes with ease and repeatability, often used for creating fibre sensors. Typically, etching in fibres necessitates consideration of the differing etching rates of the cladding and core, due to the presence of dopants. In our case, the fibre is composed of pure silica with a thin layer of plastic cladding that can be easily removed prior to the commencement of the etching process. Thus, producing a conical linear shape at the tip of the optical fibre is possible without the need to change the parameters during the process. One drawback of this method is the requirement for a solvent capable of dissolving glass. Hydrofluoric acid is one of the few substances that possesses this property at room temperature. This fact renders the dissolution process very hazardous, as hydrofluoric acid is known to cause severe tissue damage and bone decalcification. Therefore, individuals working with the acid must wear protective layers and follow proper preparation procedures to minimise potential harm.[8]

In the initial phase of the process, the coating must be removed, and the fibres must be cleaved. To ensure a satisfactory result, it is essential to remove the cladding. The cladding is extremely thin (approximately 50 μm), which facilitates its removal by applying a rubbing motion with a piece of optical cleaning tissue that has been wetted with isopropyl alcohol. Following the removal of the cladding, the fibre is subjected to a thorough cleaning process to ensure removal of any residual dust or fragments of the cladding that could potentially interfere with the solution process. After these pretrial preparations, a solution of 40% hydrofluoric acid was meticulously poured into multiple plastic test tubes and then covered with sunflower oil to prevent the release of toxic fumes. The optical fibre was then submerged in the acid solution and secured with polystyrene to minimise any movement. The use of acid induces the formation of a meniscus, which facilitates the development of a conical shape at the tip of the fibre. The principle is illustrated in the Fig 3. The classical static dissolution method minimised risk and fibre was kept stationary without need for rotation or vertical movement. The fibre remained submerged for one day, after which it was carefully extracted and thoroughly cleaned of acid and oil using deionised water and isopropyl alcohol.[9]

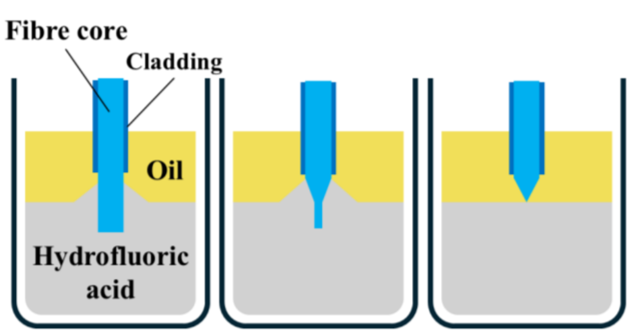

Fig. 3. Schematic principle of creating a conic Shape using the etching technique

III. Experimental set-up and measurement

With the prepared optical fibres, shown in Fig. 4, we proceed with the initial phase of the experiment. The setup closely follows our dosimetry method, as illustrated in Fig. 1. For detection and improved stability, we employed a single-photon counter (SPC – Count BLUE series, Laser Components) based on an avalanche photodiode. The modified optical fibres with a length of 10 cm (FP1000URT, Thorlabs) were connected using a temporary SMA connector, while the unmodified fibre end was cleaved for all experiments and precisely aligned within the connector to maintain a consistent distance across all fibres. The opposite end of the fibre was submerged in a liquid scintillator (LSB205) [10].

To prepare the scintillator, a vial made of fused quartz was prepared for experiment. Fused quartz is essential as the scintillator emits light in the blue and UV spectral regions. Commercial glass vials, typically assembled with adhesive, are not suitable since liquid scintillators contain organic solvents capable of dissolving such adhesives. A Teflon cap, featuring a drilled hole for fibre insertion, was used to seal the vial. In addition, the entire vial was wrapped in Teflon tape to maximise internal reflection and enhance light collection toward the fibre. A ^{60}Co gamma-ray source was affixed to the vial to ensure uniform irradiation conditions for all measurements. The setup was placed in a black box to prevent any outside light from interfering with the measurements. The schematic representation of the setup is depicted in Fig 5 in the next page.

A. Measurement

For measurement, multiple optical fibres were fabricated for each modification. All optical fibres were examined under a microscope to assess their parameters. Fibres with non-

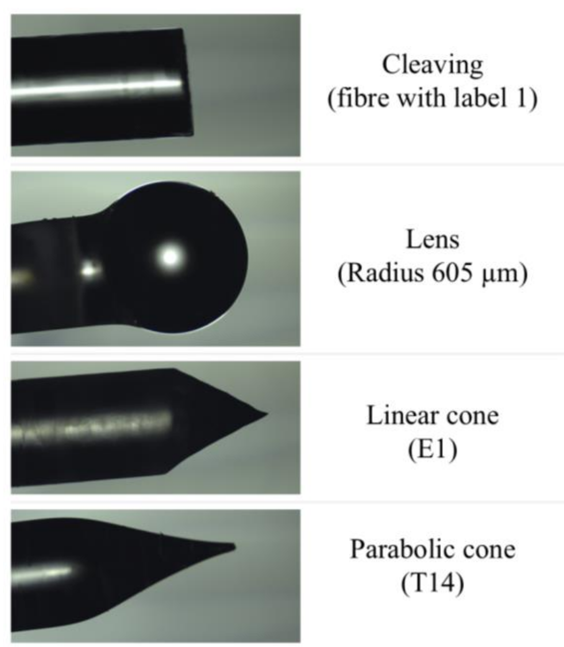

Fig. 4. Pre-prepared optical fiber tips of various types

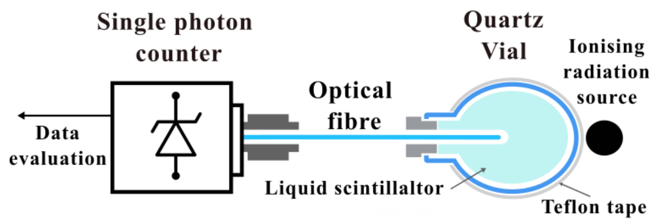

Fig. 5. Schematic representation of experimental measurement setup

compliant tips, such as those exhibiting cracks, unsuccessful etching, or improperly executed cleaves, were excluded from experiment. To determine the optimal positioning of the fibre, an initial measurement was performed using lens fibre with varying immersion depths in the vial. Each fibre was marked to ensure a consistent immersion depth in all subsequent measurements. The measurement procedure lasted ten minutes, during which all detected pulses were recorded and analysed using a counter. Data were acquired from the counter via LabVIEW and subsequently analysed.

B. *Results*

The stability measurement of the single-photon counter is presented in Fig. 6. Noise counts are consistent with the manufacturer's specification of approximately 20 counts per second (cps) [11]. The cleaved fibres in Fig. 7 exhibited a relatively wide range of cps values, with one fibre achieving up to 53 cps. On the contrary, the parabolic conical shapes formed by tapering ("T") produced lower cps values, averaging around 47 cps, but with improved repeatability. Linear conical

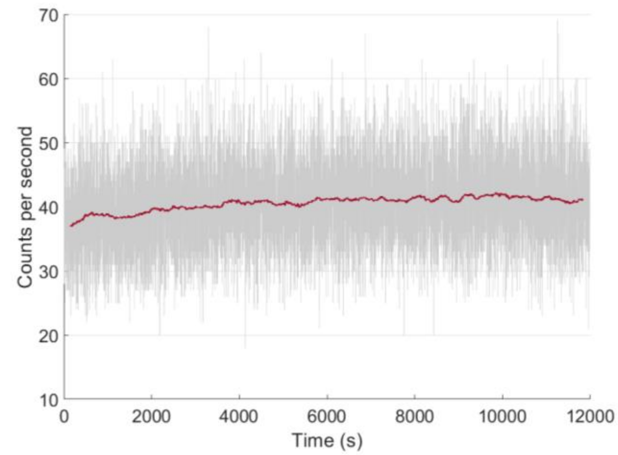

Fig. 6. Stability measurement with Single-photon counter – Cleaved fibre modification (label 3)

shaping by etching ("E") achieved the highest count rates, averaging 54 cps. Although the difference between the cleaved and etched fibres is minimal—approximately 1 cps, which is within the expected deviation—the etched fibres demonstrated better repeatability.

Lastly, several spherical tips were tested; they showed lower count rates, which corresponds to the lens collecting light only from its focal point, as expected. It is notable that lenses with a radius of approximately 600 μm exhibit superior performance in comparison to certain tapers and cleaved fibres.

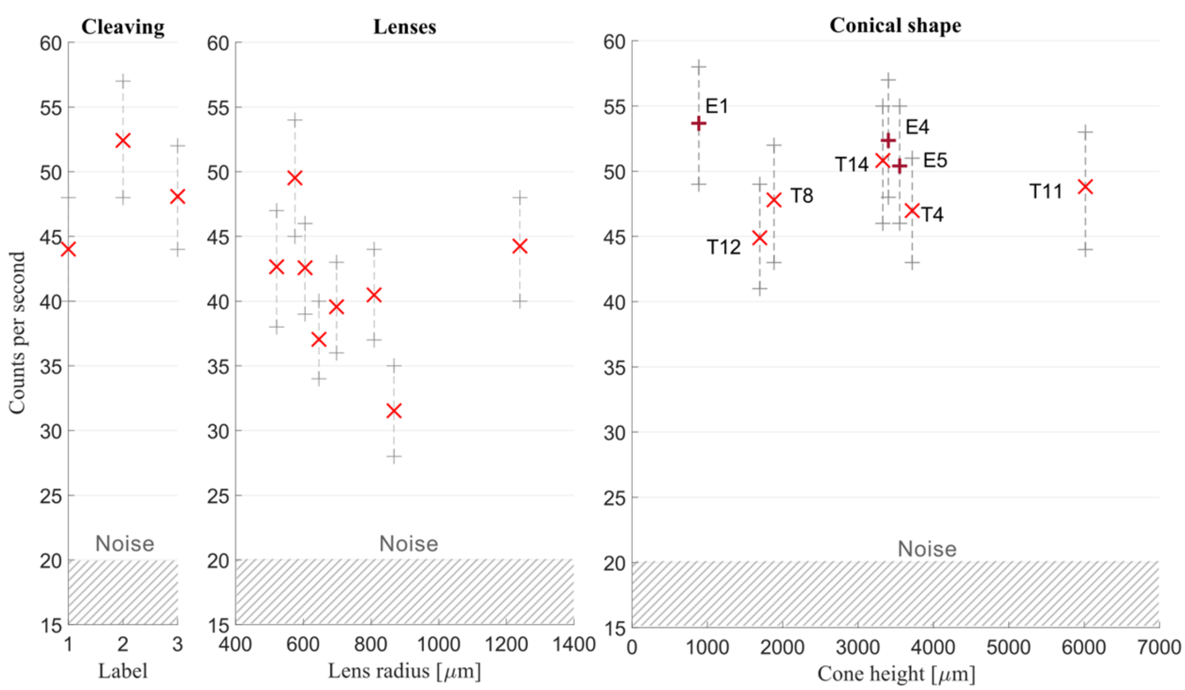

Fig. 7. Experimental measurement of different optical fibre tip modifications submerged in a liquid scintillator-measured using a single-photon counter and a ^{60}Co radioactivity etalon.

IV. Conclusion

The influence of various modifications to the optical fibre tip on light collection in a liquid scintillator was systematically examined. Four distinct tip configurations were assessed: a linearly conical tip created through etching, a parabolic conical tip shaped using an electric arc, and a flat tip produced by basic cleaving. Additionally, lens shaping of the fibres was also investigated. All fibres were immersed in the liquid scintillator, and the effect of each modification on counts per second (cps) was recorded.

The results indicated that both etched and cleaved fibre tips yielded superior performance, with average counts of 54 cps for etched fibres and 53 cps for cleaved fibres, whereas tapered tips did not exceed 50 cps. In particular, etched fibres consistently demonstrated better results. However, because basic cleaving produces a planar tip without the use of hazardous hydrofluoric acid, it emerges as the most practical option for routine measurements.

For applications requiring maximum cps, a rotational etching process may be introduced to further enhance the fibre surface smoothness and achieve a more symmetric conical shape. Considering the inherently low light output of organic scintillators, our future efforts should focus on refining tip modifications to optimise light gain.

ACKNOWLEDGMENT

This publication was created with the state support of the Technology Agency of the Czech Republic within the framework of the National Centres of Competence Programme (project No. TN02000020). The work was supported by the project “Quantum Engineering and Nanotechnology” (No. CZ.02.01.01/00/22_008/0004649), Co-funded by the European Union, by CAS (RVO:68081731) and by project no. FEKT-S-23-8162, Modern micro- and nanoelectronics for future.

References

[1] G. F. Knoll, *Radiation detection and measurement*, 4th ed. Hoboken: Wiley, c2010.

[2] J. Billingsley, S. O'Keeffe, C. Fitzpatrick, E. Lewis, and A. I. Al-Shamma'a, “A review of optical fibre radiation dosimeters”, *Sensor Review*, vol. 28, no. 2, pp. 136-142, Mar. 2008.

[3] Y. Chung, W. Jin, B. Lee, J. Canning, K. Nakamura, L. Yuan, L. Chen, S. O'Keeffe, P. Woulfe, and E. Lewis, “A comparison of clinic based dosimeters based on silica optical fibre and plastic optical fibre for in vivo dosimetry”, 2017, p. 103237C-.

[4] S. O'Keeffe, A. Fernandez Fernandez, C. Fitzpatrick, B. Brichard, and E. Lewis, “Real-time gamma dosimetry using PMMA optical fibres for applications in the sterilization industry”, *Measurement Science and Technology*, vol. 18, no. 10, pp. 3171-3176, Oct. 2007.

[5] M. Jelinek, O. Cip, J. Lazar, and B. Mikel, “Design and Characterisation of an Optical Fibre Dosimeter Based on Silica Optical Fibre and Scintillation Crystal”, *Sensors*, vol. 22, no. 19, 2022.

[6] A. L. Tomashuk, M. V. Grekov, S. A. Vasiliev, and V. V. Svetukhin, “Fiber-optic dosimeter based on radiation-induced attenuation in P-doped fiber: suppression of post-irradiation fading by using two working wavelengths in visible range”, *Optics Express*, vol. 22, no. 14, 2014.

[7] “Fiber-Optic Cleaver and Scribes”, *Thorlabs*, 0c2025.

[8] M. Özcan, A. Allahbeickaraghi, and M. Dündar, “Possible hazardous effects of hydrofluoric acid and recommendations for treatment approach: a review”, *Clinical Oral Investigations*, vol. 16, no. 1, pp. 15-23, 2012.

[9] B. A. F. Puygranier and P. Dawson, “Chemical etching of optical fibre tips — experiment and model”, *Ultramicroscopy*, vol. 85, no. 4, pp. 235-248, 2000.

[10] K. H. Mahmoud, V. Prenosil, Z. Matej, F. Kucera, F. Mravec, M. Kostal, F. Cvachovec, D. Valis, A. Lyoussi, M. Giot, M. Carette, I. Jenčič, C. Reynard-Carette, L. Vermeeren, and L. Snoj, “Perspective liquid scintillators for spectrometry of neutron and gamma radiation”, *EPJ Web of Conferences*, vol. 225, 2020.

[11] “Single Photon Counting Modules: Single Photon Counting Modules - COUNT® BLUE Series”, *LASER COMPONENTS*, 0c2023. .

Electrical Properties Measurement of SMD Electrodes for Surface Decontamination

1st Lukáš Zdražil
Department of Theoretical Electrical Engineering
Brno University of Technology
Brno, Czech Republic
Lukas.Zdrazil1@vutbr.cz

2nd Marek Andrle
Division of The Chemical, Biological, Radiological and Nuclear Protection
Military Research Institute, state enterprise
Brno, Czech Republic
andrle@vvubrno.cz

3rd Petr Špaček
Division of The Chemical, Biological, Radiological and Nuclear Protection
Military Research Institute, state enterprise
Brno, Czech Republic
spacek@vvubrno.cz

***Abstract* — This paper deals with the measurement of electrical properties of electrodes for Surface Micro-Discharge (SMD) generation. An important component of the electrode is the dielectric, which must have very good insulating properties to prevent its breakdown when high voltage is applied to the electrodes. If the dielectric breakdown occurs, the sudden increase in current could destroy a high voltage source. An excessively high value of the DC current through the dielectric could also have a negative effect on the generation of the discharge. Therefore, it is necessary to know not only the value of the breakdown voltage of the dielectric, but also the dependence of the dielectric resistance on the applied voltage. In this paper, the measurement of the dependence of the DC current through the dielectric is described.**

Keywords—SMD electrode, dielectric barrier discharge, dielectric, Teflon, high-resistivity measurement

I. Introduction

Various types of plasma sources - dielectric barrier discharge, corona discharge, DC plasma torch and plasma jet - are commonly used for use in the decontamination of chemical and biological warfare agents, according to the article [1]. For surface decontamination, the dielectric barrier discharge is the most advantageous to use because it can act over a surface area, as can be seen from the overview of plasma sources in Fig. 1. In the case of corona discharge, plasma torch and plasma jet, it is necessary to increase the size of the generator [1] or increase the number of generators [2]. The disadvantage is also the necessity of using a stream of helium [3].

In the articles [4], [5], the dielectric barrier discharge is used as a source of plasma for surface decontamination, where the contaminated sample is inserted between two electrodes with dielectric in a space where a cold plasma is generated. This is called a volume plasma discharge. The disadvantage of this arrangement is that the inserted sample covers part of the electrode area, so it reduces the efficiency of this system. Another disadvantage is that the sample must be thin enough to ensure that there is not too large a gap between the electrodes.

These disadvantages are partially eliminated when using SMD (Surface Micro-Discharge) electrodes with surface plasma. The difference between volume and surface plasma is shown in Fig. 2. SMD electrodes are mainly used for disinfection and decontamination of surfaces [6], [7], [8], [9], [10]. In some papers, authors have also investigated the effect of atmospheric plasma generated by SMD electrode on seed germination [11] and cancer treatment [12].

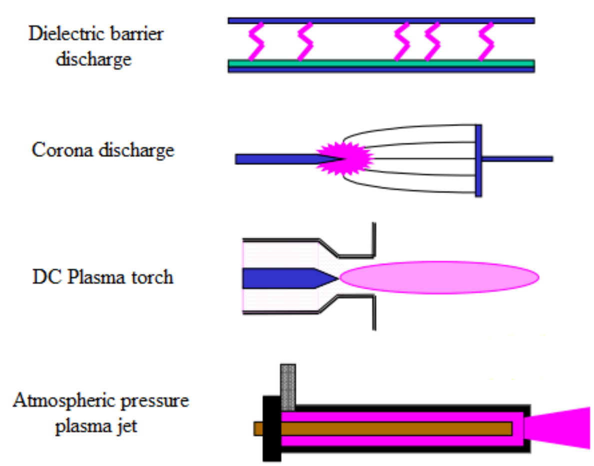

Fig. 1 Plasma sources usable in decontamination [1]

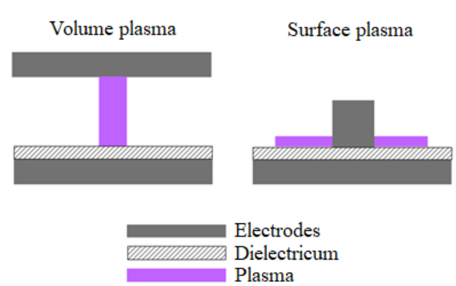

Fig. 2 Difference between volume plasma and surface plasma

II. PRINCIPLE OF SMD ELECTRODES

SMD is the term for the generation of plasma by a specific type of electrode. The plasma generation is based on the principle of dielectric barrier discharge, where the generated plasma is cold (non-thermal), non-equilibrium and is generated at normal ambient pressure. Thus, in most cases, there is no need to use a stream of helium or other support gases.

SMD electrodes consist of two electrodes with a dielectric layer between them. One electrode is a conventional planar electrode, the other is planar with holes and is referred to as a mesh electrode. The holes can be of different sizes and shapes, for example square [13], [14], hexagonal [15], [16] or circular [17]. The shape, size and number of holes determine the intensity of the generated plasma. Usually the planar full electrode is connected to a high voltage source and the mesh electrode is grounded. The high voltage at a frequency of 100 Hz to 10 kHz produces a large number of micro-discharges between the mesh electrode and the dielectric according to Fig. 2. The micro-discharge does not generate in the gap between the electrodes but on the surface of the dielectric and its length can be partially controlled by the magnitude of the applied voltage. A photography of micro-discharges generated by SMD electrodes with hexagonal and circular holes is shown in Fig. 3.

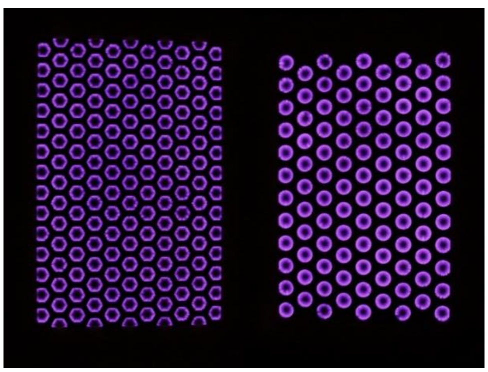

Fig. 3 Photography of micro-discharges generated by SMD electrodes with hexagonal and circular holes

While the classical dielectric barrier discharge generates a volume plasma, the SMD electrode configuration generates a surface plasma with a filamentary discharge pattern. The mesh structure of the electrode allows the formation of small plasma channels along the edges of the holes and the surface of the dielectric. The micro-discharge does not exceed the thickness of the mesh electrode, and the surface to be disinfected or decontaminated is predominantly exposed to reactive particles with longer lifetimes (Fig. 4). If the mesh electrode is grounded, it can be touched with bare skin during discharge generation because the current flow is very low, and the plasma temperature exceeds the ambient temperature by just a few degrees [18].

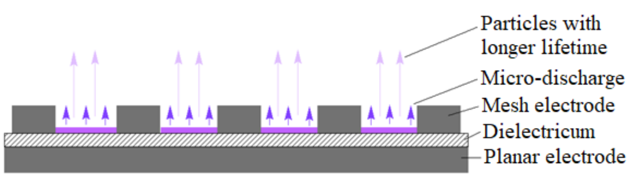

Fig. 4 Reactive particle formation in SMD electrode

Electrons with a high level of kinetic energy in the plasma are responsible for a cascade of processes such as dissociation, excitation and ionization after collisions with other particles. These processes then generate a number of plasmochemical species. Therefore, the energy distribution of electrons in non-thermal plasma discharges is essential for defining plasmochemistry. There are two modes that need to be considered in plasma chemistry processes. The first mode is limited to the micro-discharge region, where reactions of charged particles with short duration predominate. The second mode is predominant outside of micro-discharge and is primarily characterized by neutral free radical particle chemistry, such as excited atoms and distinct and fragmented molecules. Typical plasma species when using SMD electrodes are for example O_3, NO_X, OH, N^{2+}, O_2^*, H_2O_2 or ultra-violet radiation. The reaction chemistry of the moist air plasma produced by SMD electrodes is complex and therefore difficult to model quantitatively and verify experimentally [18]. Some of the reactive particles that are produced by the plasma generated by SMD electrodes are shown in Fig. 5.

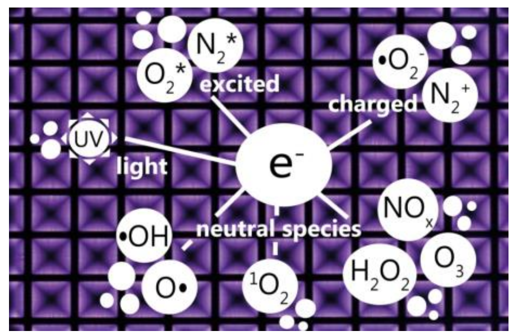

Fig. 5 Some of the reactive particles that are produced by the plasma generated by SMD electrodes [18]

These particles, which are secondary products of the plasma generated by SMD electrodes, are responsible for disinfection and decontamination of surfaces. The contaminated surface is placed near the SMD electrodes and is gradually decontaminated due to the influence of reactive particles. A support gas (e.g. helium or nitrogen) can increase the number of reactive particles generated in the plasma and increase the decontamination efficiency when using SMD electrodes.

III. PARAMETERS OF STUDIED SMD ELECTRODES

Besides the applied high voltage and frequency, the shape and dimensions of the mesh electrode have a significant effect on the intensity of the generated plasma and the number of reactive particles [18]. Measurements [14] were made in which it was found that increasing the size of the holes resulted in an increase in discharge power and a decrease in ignition voltage. Computer simulations and calculations have shown that the uniformity of the micro-discharge is also affected by the size of the holes. Increasing the size of the holes leads to an increase in the electric field intensity at the edges of the holes and a decrease in the electric field intensity towards the centers of the holes [14]. For this reason, several electrodes with different hole shapes and sizes were designed and investigated. The initial electrode area was chosen to be 150 cm^2. The mesh electrodes contained holes in the shape of square, circle and hexagon. In addition, all three hole shapes were made in three different sizes, so a total of nine mesh electrodes were made. The number of holes varied with the different hole sizes so that they covered the entire area of the mesh electrode. For the square holes, edge lengths of 7 mm, 8.5 mm and 10 mm were chosen. The diameters chosen for the circular holes were 7 mm, 8 mm and 9 mm. And for the hexagons, edge lengths of 3 mm, 4 mm and 5 mm were chosen. Thus, the number of holes, the length of the hole edges and the electrode area after subtraction of the holes area were different for all nine mesh electrodes. An overview of the parameters of the individual mesh electrodes is in Table I.

TABLE I. OVERVIEW OF PARAMETERS FOR EACH MESH ELECTRODE

Mesh pattern	Number of holes	Hole edges length [mm]	Electrode surface [mm^2]	Electrode surface [%]
Squares 7 mm	126	3528.0	8826.0	58.8
Squares 8.5 mm	77	2618.0	9436.8	62.9
Squares 10 mm	54	2160.0	9600.0	64.0
Circles 7 mm	135	2968.8	9804.6	65.4
Circles 8 mm	104	2613.8	9772.4	65.1
Circles 9 mm	66	1866.1	10801.3	72.0
Hexagons 3 mm	215	3870.0	9195.0	61.3
Hexagons 4 mm	159	3816.0	7368.0	49.1
Hexagons 5 mm	103	3090.0	7275.0	48.5

The dielectric can be punctured by high voltage and strong electric field. When the dielectric is punctured, a conductive connection is formed inside, through which an electric current flows. Due to the large electrical force through the spot where the current flows, electrons are ripped out of atoms or molecules and this can cause permanent or temporary damage to the dielectric. Dielectric breakdown can occur due to the presence of condensing moisture between the dielectric and the powered electrode [18]. However, in some publications [13], dielectric breakdown occurred even when pre-dried air was supplied to the experimental chamber and the humidity was therefore minimal. A photography of the dielectric breakdown is shown in Fig. 6. It is important that both electrodes are tight to the dielectric. If the electrodes are not in uniform contact with the dielectric, inhomogeneous discharge may occur, which increases the risk of dielectric breakdown. In addition, the edges of the holes must be perfectly sharpened so that no local increase in the electric field intensity is formed on the rough edges.

Fig. 6 Photography of the dielectric breakdown

The magnitude of the maximum intensity of electric field at the electrode at which breakdown has not yet occurred is called the dielectric strength and depends on the amount of ionization work required to ionize (release an electron from an atom). The breakdown of a dielectric can also be described by the breakdown voltage value, which indicates the smallest voltage magnitude at which breakdown occurs for a given dielectric thickness. Tabular values of dielectric strength for some dielectrics are in Table II.

TABLE II. DIELECTRIC STRENGTH FOR SELECTED DIELECTRICS

Material	Dielectric strength E_p [kV/mm]
Air	3
Rutilit	10
Permitit	20
PTFE	> 20
Stoneware	7 – 27
Porcelain	10 – 30
Polyvinylchlorid	26 – 50
Polyethylen	90 – 120
Polyester	180

The dielectric almost always contains microscopic defects, its dielectric strength is lower than the theoretical value in tables that is valid only for ideal material. The voltage at which breakdown occurs depends on the mutual arrangement of the dielectric and electrodes, and also on the rate of voltage rise across the electrodes. The equivalent dielectric model can be modeled using an electrical schematic as a series connection of an RC cell with a parallel ideal capacitor and an isolation resistor [19] according to Fig. 7. The voltage applied to the dielectric is distributed across multiple parallel connections of serial RC cells.

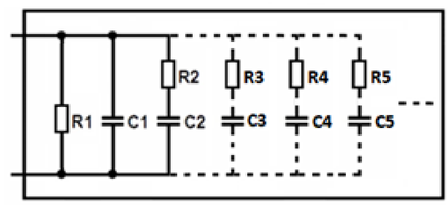

Fig. 7. Equivalent model of the dielectric [19]

When a DC voltage is applied to dielectric for a sufficiently long time, the molecules in the material become polarized. The electrodes with dielectric form in principle an electric capacitor, for which the value of the electrical capacitance can be calculated according to the relation:

$$C = \varepsilon_0 \cdot \varepsilon_r \cdot \frac{S}{d} \qquad [\mathrm{F};\ \mathrm{F \cdot m^{-1}}, -, \mathrm{m^2}, \mathrm{m}], \tag{1}$$

where ε_0 is permittivity of vacuum $\varepsilon_0 = 8.85 \cdot 10^{-12}\ \mathrm{F \cdot m^{-1}}$, ε_r is tabular value of relative permittivity of dielectric, S is effective surface of the electrodes after subtraction of the area of the holes and d is the electrode distance (dielectric thickness). For application in later research about the possibility of surface decontamination using SMD electrodes, a Teflon dielectric was chosen (Teflon PTFE $\varepsilon_r = 2.1$). Three different dielectric thicknesses were chosen - 0.5 mm, 1 mm and 1.5 mm. When using a dielectric with a lower thickness, the capacitance of the electrodes increases. Simultaneously, more current will flow through the dielectric. It is important to know the capacitance as well as the approximate dependence of the dielectric resistance on the applied voltage to avoid overloading the high voltage source during application of the SMD electrodes. Table III shows the calculated capacitance for all hole types (electrode surfaces) and all Teflon dielectric thicknesses.

TABLE III. CALCULATED CAPACITANCE FOR GIVEN ELECTRODE PATTERNS AND ALL THREE PTFE THICKNESSES

Mesh pattern	Calculated electrode capacitance [pF]		
	PTFE 0.5 mm	*PTFE 1 mm*	*PTFE 1.5 mm*
Squares 7 mm	328.2	164.1	109.4
Squares 8.5 mm	350.9	175.5	116.9
Squares 10 mm	357.0	178.5	119.0
Circles 7 mm	364.6	182.3	121.5
Circles 8 mm	363.4	181.7	121.1
Circles 9 mm	401.7	200.8	133.8
Hexagons 3 mm	341.9	171.0	113.9
Hexagons 4 mm	274.0	137.0	91.33
Hexagons 5 mm	270.5	135.3	90.18

IV. MEASUREMENT SETUP AND MEASURED RESULTS

Teflon resistance measurements belong to the category of high impedance measurements. High impedance measurements are usually very challenging because they involve measuring signals close to the limits given by the Johnson´s thermal noise. In addition to the Johnson´s thermal noise, other noises such as flicker noise with a frequency dependence of 1/*f*, or various leakage currents across the surface of components or insulating materials can affect the measurement. Other phenomena may also apply during the measurement, such as the triboelectric effect, whereby two materials rub against each other and generate an error voltage. Or the piezoelectric effect, where the mechanical deformation of the material also creates an error voltage. Teflon is susceptible to deformation and is affected by a non-negligible piezoelectric effect.

An epoxy glass housing was produced for accurate mechanical mounting of the electrodes and dielectric. Epoxy glass is designed for use in high power electrical equipment because it has very good electrical insulating properties and high heat resistance. In the tables, the value of breakdown voltage in oil at 90 °C is 10 kV/mm, loss factor is 0.04 at both 50 Hz and 1 MHz and permittivity at 1 MHz is 5.5. Fig. 8 shows a drawing of the design of the electrodes in the housing.

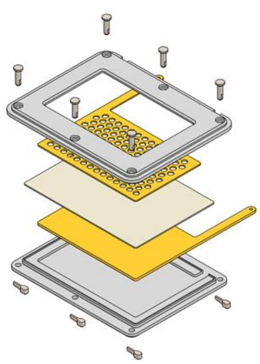

Fig. 8 Drawing of the electrodes design in the epoxy glass housing

To determine the dependence of the resistance of the Teflon dielectric on the applied voltage, a measurement method using an electrometric amplifier with a feedback ammeter was chosen [20], [21]. These amplifiers have a very high input resistance and for this reason are used in the latest electrometers and picoammeters. Electrometers are instruments designed to measure currents of less than 10 nA, resistances greater than 1 GΩ, voltages from a source that has a resistance greater than 100 MΩ, and when the input voltage drop of less than a few hundred mV occurs due to circuit loading, and also when measuring signals at levels close to the level of Johnson's thermal noise [20]. At the Department of Theoretical and Experimental Electrical Engineering, the 6517A electrometer from Keithley Instruments is available. According to the datasheet, the electrometer has an input resistance of 200 TΩ and can measure DC currents from 1 fA to 20 mA using a built-in 1 kV voltage source.

The mesh electrode was made of stainless steel, to enable easier sharpening of the edges of the holes. The electrode with hexagonal-shaped holes with an edge length of 4 mm was used to measure the resistance of the dielectric. The conventional planar electrode was made of brass. A photography of the electrodes with the dielectric in the epoxy glass housing is shown in Fig. 9.

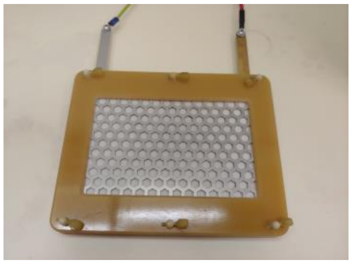

Fig. 9 Photography of electrodes with dielectric in the epoxy glass housing

Since the resistivity of Teflon is greater than 10^{18} Ω·cm [20] according to the tabular values, the DC current was measured only through the thinnest dielectric of 0.5 mm. The mesh and planar electrode were connected to the shielding container of the electrometer (Fig. 10). Because the electrode exceeded the dimensions of the shielding container, the container was not perfectly closed and the electrode was not perfectly electrically shielded from external interference. The shielding container was connected to the electrometer by a shielded cable. Electrodes and dielectric were cleaned with isopropyl alcohol (p. a.). The temperature and humidity in the laboratory were kept constant during the measurement (23 °C and 35 %).

Fig. 10 Electrode connected to the electrometer

By means of the built-in high voltage source in the electrometer, the time dependence of the current through the dielectric was measured for voltages from 500 V to 1 kV with a step of 100 V (Fig. 11). The measured time dependencies show that the current settled down after about three minutes. The mean values of the settled time dependencies ranged from approximately 0.5 pA to 2 pA depending on the magnitude of the applied voltage. The current noise was approximately 0.5 pA in all cases. Some of the measured time dependencies (500 V and 800 V) are not very visible in the figure because they merge with the other time dependencies. From the measured time dependencies, we can assume that the high DC voltage will not have a significant effect on the current flowing through the electrode because the increase in current over the measured range is very small.

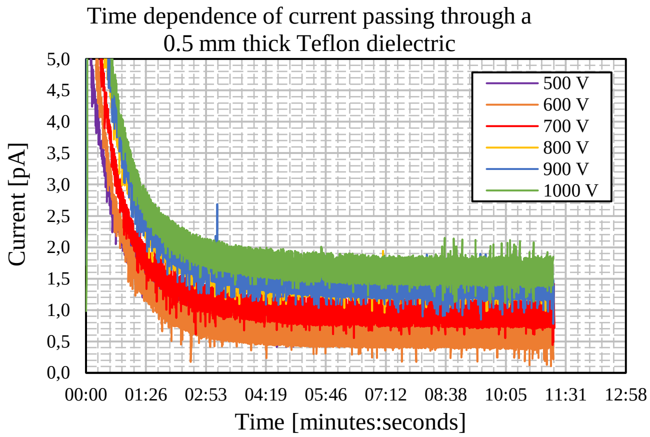

Fig. 11 Measured time dependencies of the current through a 0.5 mm thick Teflon dielectric

From the measured time dependencies, the dependence of the resistance on the applied voltage was calculated (Fig. 12). The calculated mean resistance value for almost all measured voltages was approximately 600 TΩ. Only for 600 V, the calculated mean resistance value was approximately 1100 TΩ. For 700 V, the mean resistance value was around 800 TΩ, and also a more significant variance was measured for this voltage. The increase in resistance may have been caused, by a tighter fit of the electrodes and dielectric in the housing, or the measurement may have been interfered by external influences. It is also possible that this increase in resistance is a characteristic of the electrodes and the Teflon dielectric. For a more accurate determination, it is necessary to repeat the measurement with several samples of the Teflon dielectric.

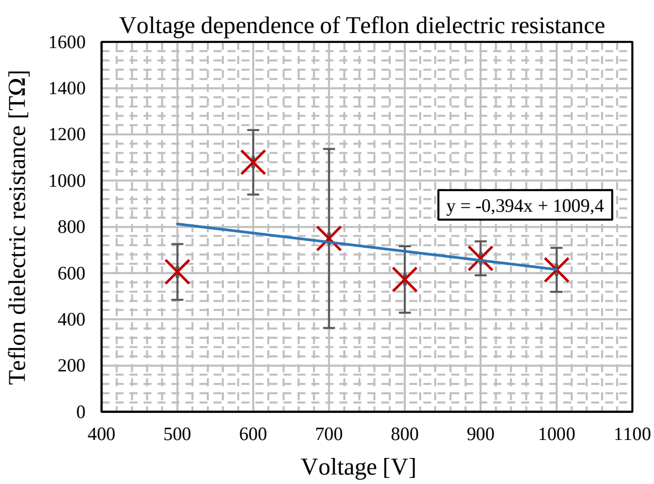

Fig. 12 Calculated dependence of Teflon resistance on the magnitude of applied voltage

For comparison, the theoretical value of the resistance of the Teflon dielectric was calculated according to the relation:

$$R = \rho \cdot \frac{l}{S} \qquad [\Omega;\ \Omega \cdot \mathrm{m}^2 \cdot \mathrm{m}^{-1}, \mathrm{m}, \mathrm{m}^2], \qquad (2)$$

where R is the resistance of the dielectric, ρ is the resistivity of Teflon (10^{18} Ω·cm according to the tables [20]), l is the thickness of the dielectric (for the measured dielectric l = 0.05 cm) and S is the electrode area after subtracting the area of the holes (for the measured electrode with hexagonal-shaped holes with an edge length of 4 mm S = 73.68 cm^2 according to Table I). The theoretical resistance of the measured Teflon dielectric came out to be $6.786{\cdot}10^{14}$ Ω. Which corresponds to 678 TΩ. The calculated theoretical resistance is almost the same as the measured mean resistance value.

V. Discussion

Since a high voltage must be applied to the electrodes to sufficiently generate particles that are capable of disinfecting and decontaminating surfaces, it is necessary to know the breakdown voltage and the resistivity of the dielectric. However, materials almost always contain microscopic contaminants and defects, so the values in the tables cannot be relied on exclusively.

Determining the actual resistance of the dielectric is possible if the DC current through the dielectric is measured. Measuring such small current levels with such high accuracy is challenging. The shielding container and the shielded cable must be used for the measurements. Electrodes and dielectric must be cleaned with isopropyl alcohol (p. a.).

SMD electrodes represent a capacitive load. To generate the surface plasma, AC voltage of at least a few kV must be applied to the electrodes. However, it is not possible to apply AC voltage to the electrodes when measuring the resistance. To further evaluate the effect of SMD electrodes on surface disinfection and decontamination, it will be necessary to apply AC high voltage to the electrodes using a high voltage amplifier. The electric field will have to be monitored with a high voltage probe. All insulation must be rated for high voltage. This measurement belongs to the field of power engineering and all principles must be respected when using high voltage. Proper grounding of the high voltage amplifier is also needed, and it should be as short as possible.

Using particle detectors, it will be necessary to determine the amount of particles that are produced in the cold air plasma and their effect on the contaminated surface. Different hole designs in the electrodes and different dielectric thicknesses will have a large effect on the number of particles. It will also be important to select the correct waveform and frequency of the periodic signal. After determining the optimal mechanical and electrical parameters of the electrodes and the electric field, the influence of the support gas will also be investigated.

VI. Conclusion

SMD electrodes with holes of different shapes and sizes were designed and manufactured for the purpose of disinfection and decontamination of surfaces. The shapes chosen were squares, circles and hexagons. Three different dimensions were selected for each shape, for a total of nine electrodes. Teflon was selected as the dielectric and its thicknesses were 0.5 mm, 1 mm and 1.5 mm. The purity of Teflon was verified using a Keithley 6517A electrometer.

For the thinnest dielectric layer, the time dependence of the current through the dielectric depending on the applied DC voltage was measured. The measured time dependencies show that for the measured voltage range from 500 V to 1 kV, the mean value of the passing current ranged from 0.5 pA to 2 pA. The variance is about 0.5 pA. As the voltage value increased, the mean value of the flowing current increased proportionally. The temperature and humidity in the laboratory were kept constant during the measurement (23 °C and 35 %). The time dependencies also show that the current value settled down after about three minutes. When applying AC voltage to the electrodes, it is therefore important to consider an order of magnitude higher values.

From the measured time dependencies, the dependence of the resistance on the applied voltage was calculated. The mean resistance value resulted to be approximately 600 TΩ for almost all measured values. Only for 600 V, the calculated mean resistance value is approximately 1100 TΩ. This increase may be due to a tighter fit of the electrodes, or it may be a characteristic of the measured Teflon. It is necessary to repeat the measurements with several samples of the Teflon dielectric for a more accurate determination. However, the calculated resistance values remain almost constant at 600 TΩ for the other measured voltages. None of the values is significantly lower than the others. The calculated theoretical resistance of the dielectric for the same thickness and surface of the electrodes as for the measurements came out to be 678 TΩ. This means that the used Teflon is of high quality and high purity. It contains almost no microscopic contaminants or defects. If the dielectric is not contaminated by dirt or moisture on the surface during the process of decontamination, it should not be punctured and the electric field should not be affected by the DC current flowing through the dielectric.

Acknowledgment

This research was supported by defence research project number OYVVU20230001.

The research was completed under support from the project No. FEKT-S-23-8425, which was supervised by the BUT internal grant office.

References

[1] G. S. Selwyn, H. W. Herrmann, J. Park and I. Henins. “Materials Processing using an Atmospheric Pressure, RF-Generated Plasma Source,” in Contributions to Plasma Physics, vol. 41, no. 6, pp. 610-619, Oct. 2001, doi: 0.1002/1521-3986(200111)41:63.3.CO;2-C.

[2] G. Konesky. "CBRN Decontamination using a Large-Area Cold Plasma Applicator," in 2008 IEEE Conference on Technologies for Homeland Security, Waltham, MA, USA, pp. 530-534, May 2008, doi: 10.1109/THS.2008.4534509.

[3] G. Konesky. “Dwell time considerations for large area cold plasma decontamination,” in Proceedings of SPIE - The International Society for Optical Engineering, May 2009, doi: 10.1117/12.818323

[4] J. Jarrige and P. Vervisch. “Destruction of simulated chemical warfare agents in non-thermal atmospheric-pressure air plasma,” in: 28th ICPIG. Prague, Czech Republic, pp. 1414-1417, July 2007.

[5] T. Iwai, H. Inoue, K. Kakegawa, et al. “Development of a High-Efficiency Decomposition Technology for Volatile Chemical Warfare Agent Sarin Using Dielectric Barrier Discharge,” in Plasma Chemistry and Plasma Processing, vol. 40, no. 4, pp. 907-920, July 2020, doi: 10.1007/s11090-020-10057-3.

[6] W. -L. Liao et al. "Inactivation Effect of Surface Microdischarge Plasma on Bacillus cereus," in IEEE Transactions on Plasma Science, vol. 42, no. 8, pp. 2042-2048, Aug. 2014, doi: 10.1109/TPS.2014.2329914.

[7] M. C. Pina-Pérez, D. Rodrigo, Ch. Ellert and M. Beyrer. “Surface Micro Discharge–Cold Atmospheric Pressure Plasma Processing of Common House Cricket Acheta domesticus Powder: Antimicrobial Potential and Lipid-Quality Preservation,” in Frontiers in Bioengineering and Biotechnology, vol. 9, July 2021, doi: 10.3389/fbioe.2021.644177.

[8] S. Shimizu, S. Barczyk, P. Rettberg, et al. “Cold atmospheric plasma – A new technology for spacecraft component decontamination,” in Planetary and Space Science, vol. 90, pp. 60-71, Jan. 2014, doi: 10.1016/j.pss.2013.10.008.

[9] T. Shimizu, V. Lachner and J. L. Zimmermann. “Surface Microdischarge Plasma for Disinfection,” in Plasma Medicine, vol. 7, no. 2, pp. 175-185, Jan. 2017, doi: 10.1615/PlasmaMed.2017019455.

[10] T. Maisch, T. Shimizu, G. Isbary, et al. “Contact-Free Inactivation of Candida albicans Biofilms by Cold Atmospheric Air Plasma,” in Applied and Environmental Microbiology, vol. 78, no. 12, pp. 4242-4247, June 2012, doi: 10.1128/AEM.07235-11.

[11] A. Mitra, Y. –F. Li, T. G. Klämpfl, T. Shimizu, J. Jeon, G. E. Morfill a J. L. Zimmermann. “Inactivation of Surface-Borne Microorganisms and Increased Germination of Seed Specimen by Cold Atmospheric Plasma,” in Food and Bioprocess Technology, vol. 7, no. 3, pp. 645-653, May 2013, doi: 10.1007/s11947-013-1126-4.

[12] J. Köritzer, V. Boxhammer, A. Schäfer, et al. “Restoration of Sensitivity in Chemo — Resistant Glioma Cells by Cold Atmospheric Plasma,” in PLoS ONE, vol. 8, no. 5, May 2013, doi: 10.1371/journal.pone.0064498.

[13] K. Mazanec, R. Šmíd. The Quixote Project: “Quick Xor Technology for B&C Cold Plasma Decontamination,” in: HAZMAT PROTECT 2018, National Institute for NBC Protection, Kamenná, Czech Republic, pp. 134-143, 2018, ISBN 978-80-270-4852-6.

[14] Y. Xia, Z. Bi, Z. Qi, L. Ji, Y. Zhao, X. Chang, W. Wang and D. Liu. “Effect of electrode configuration on the uniformity of atmospheric pressure surface dielectric barrier air micro-discharge,” in Journal of Applied Physics, vol. 123, no. 8, Feb. 2018, doi: 10.1063/1.5012912.

[15] D. X. Liu, Z. C. Liu, C. Chen, A. J. Yang, D. Li, M. Z. Rong, H. L. Chen and M. G. Kong. “Aqueous reactive species induced by a surface air discharge: Heterogeneous mass transfer and liquid chemistry pathways,” in Scientific Reports, vol. 6, no. 1, Apr. 2016, doi: 10.1038/srep23737.

[16] D. Li, D. Liu, Q. Nie, D. Xu, Q. Li and M. G. Kong. “Emission Characteristics of Surface Microdischarge in Atmospheric-Pressure He/N 2 Mixture,” in IEEE Transactions on Plasma Science, vol. 42, no. 10, pp. 2640-2641, Oct. 2014, doi: 10.1109/TPS.2014.2321431.

[17] J. Jeon. “Surface micro-discharge (SMD) - analysis of the antimicrobial effect and the plasma chemistry,” Doctoral thesis, Munich, 2014, Ludwig-Maximillians University Munich.

[18] T. G. Klämpfl. “Cold atmospheric plasma decontamination against nosocomial bacteria,” Doctoral thesis, Munich, 2014, Technical University Munich.

[19] V. Wong. “Counting Electrons: Making Ultra-high Sensitivity Femtoamp Measurements,” Analog Devices, 2017.

[20] “Low Level Measurements Handbook: Precision DC Currents, Voltage, and Resistance Measurements,” Ohio, USA: Keithley Instruments, Inc., 2004.

[21] L. Zdražil. “Design and Optimization of Special Low-Level Amplifier for Measurement of Air Ions,” Master´s thesis, Brno, 2020, Brno University of Technology.

Photovoltaic power plant source measurement system for fault detection

1st Matěj Turinský
Department of Control and Instrumentation
Brno University of Technology
Brno, Czech Republic
0009-0000-8748-8384

***Abstract*—This paper describes a novel system for the monitoring of the string segment of a photovoltaic (PV) power plant. The design of the monitoring device is intended for future use in the detection of arc faults and the tracking of long-term degradation of the solar panels. The primary benefits of such a system are expected to be enhanced safety and simplified maintenance for existing PV installations. The monitoring system is based on the Texas Instruments C2000 platform, which performs all measurements and also acts as Modbus RTU server to propagate the results. To facilitate the installation on existing PV power plants, a G3-PLC modem has been used to transfer measurements to a data acquisition system without any need for extra communication wires. A prototype of the proposed device has been constructed and demonstrated to function under laboratory conditions.**

***Index Terms*—Photovoltaic, data acquisition system, maintenance, solar panel degradation, safety, arc faults**

I. Introduction

According to the forecasts conducted by ČEPS, it is expected that the installed capacity of PV power plants will increase from 5.67GW to 10.71GW between the years 2025 and 2030 [1]. This represents the most significant increase in installed capacity since 2020, thus establishing PV power plants as the most represented renewable power sources in the Czech Republic. This suggests that demands on safety, particularly fire safety, will increase, along with demands on maintenance to prevent potential losses.

The most critical risk associated with the PV power plant opperation is the occurance of the arc faults, which can result in fires if they occur repeatedly. Arc faults can be categorised into two primary types: serial and parallel [2].

Serial arc typically forms at the points with increased contact resistance, electrical field strength, humidity and temperature. Therefore, mechanically stressed, corroded or loose contacts and connectors are the most common causes of serial arc faults.

In contrast, parallel arc occurs when two conductors with different potentials come into contact. There are many combinations of such conductors in PV power plants, but typical examples include contact of positive and negative conductors within string, in between two strings and between conductor and ground. This means that a parallel arc is essentially a short circuit, but because PV cells are high internal impedance sources, the current increases to a maximum of 1.5 times the rated current. It is also true that parallel arcs highly depend on the condition of the conductor insulation.

Both types of arc fault are dangerous from a fire safety point of view, but they behave differently when string circuit is disconnected. If the circuit breaker has sufficient DC voltage rating, the serial arc will be interrupted when the circuit is opened, but if this happens during parallel arc fault, the load will be disconnected from the panels or the string and the arc may become even stronger. For this reason, standard arc fault circuit interrupters (AFCI) can cause problems for PV installations [2].

In order to ensure an effective long-term maintenance of the PV power plant, it is important to closely monitor the power trends. The reason for this is, that they serve as reliable indicators for distinguishing between short-term failures, such as panel shading and associated PV cell overheating, and long-term failures related to panel ageing, including panel delamination, discolouration, potential-induced degradation (PID) effect and corrosion [3] [4].

Finally, when discussing PV power plant maintenance, it is necessary to monitor the state of the additional PV installation components, including junction boxes, optimizers, maximum power point trackers (MPPT) and inverters. However, the most prone to failure additional components, which are part of each solar panel, are blocking and bypass schottky diodes connected in series with string and in parallel with panel or part of it respectively [5].

The subsequent sections detail the design of a prototype data acquisition system that complies with the previously mentioned criteria in terms of safety and maintenance needs. In Section II-A, the selection of measured quantities and the measurement method itself are described. The following Section II-B describes the selection of hardware and software implementation for the realisation of necessary measurements and communication of results via Modbus RTU protocol.

The author would like to thank to his supervisor Petr Fiedler for support and suggestions during the preparation of the paper, and to company ModemTec s.r.o., which participated in the development of the prototype measurement system.

II. Methods

The measurement and fault detection systems for PV power plants can be divided into two groups based on the type of processed data.

The first type of processed data are images in the visible or infrared spectrum. Examples of such images can be seen on Figure 1. While imaging methods are beneficial for localising faults, they are not suitable for fault detection due to the fact that they monitor secondary manifestations of faults, such as cell overheating, and also are still more expensive in comparison with sensing electrical quantities.

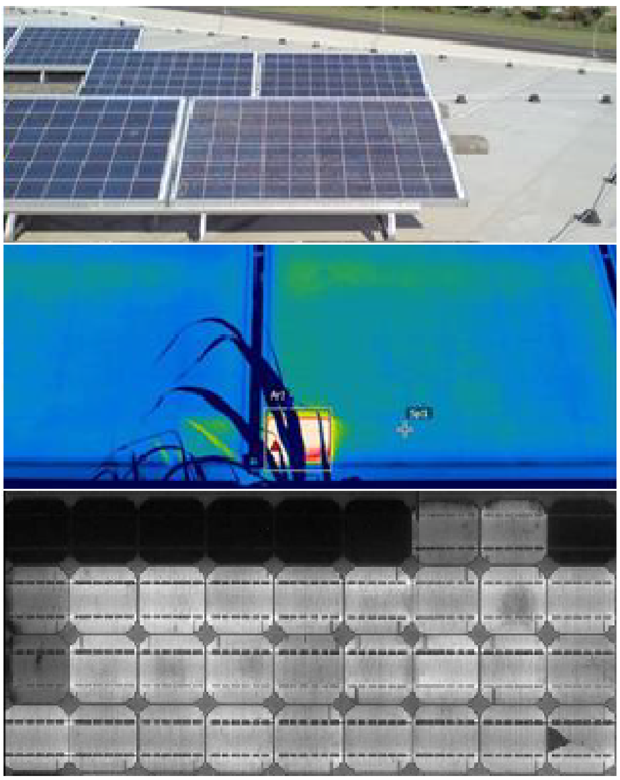

Fig. 1. Visible, infrared and electroluminescence solar panel imaging [6]

The second type of processed data are electrical quantities, such as current and voltage of the panel or string, and non-electrical quantities, including ambient and panel temperature, solar irradiance or humidity. This type of data direcly indicates the state of the PV installation, with particular emphasis on the solar panels.

A. Measured quantities

As previously mentioned in the introduction, the most critical measurements should be related to arc fault detection. The most convenient way to do this is to process the panel or string current and voltage spectra. The arc fault event changes the nominal power spectra in frequency bands ranging from 40 to 100 kHz [7].

For the purpose of long-term maintenance, the 'Weahter-corrected performance ratio' PR_{corr} presented in [8] is a suitable indicator, which is computed using the following formula:

$$PR_{corr} = \frac{\sum_k P_{out,k} \cdot \tau_k}{\sum_k \frac{(1+\gamma\cdot(T_{mod,k}-25))\cdot P_0 \cdot G_{i,k} \cdot \tau_k}{G_{i,ref}}} \tag{1}$$

Where $P_{out,k}$ represents the power in the AC power plant part in step k in kilowatts, τ_k step duration in hours, γ relative maximum power temperature coefficient, $T_{mod,k}$ temperature of PV cell or panel in step k in degrees Celsius, P_0 installed power in the DC power plant part in kilowatts, $G_{i,k}$ solar irradiance in step k and $G_{i,ref}$ solar irradiance expected for power P_0 both in kilowatts per square meter.

All the measured quantities necessary to fulfil both arc fault and long-term monitoring are listed in Table I, in conjunction with the relevant constraints for each measurement.

TABLE I
Quantities measured by fault detection system

Quantity (unit)	***Constrains***
Current (A)	Range up to 10 A, sampling frequency at least 200 kHz
Voltage (V)	Range adjustment from 1.5 kV, surge protection 8 kV (CAT III)
Solar irradiance (Wm^{-2})	Similar spectral response with PV cells
Ambient temperature (°C)	Range according to ambient temperatures
Panel temperature (°C)	Range up to 120°C
Current time (s)	Unix time format support
Differential current (A)	Minimum 6 mA leakage current detection

B. Prototype design

The measurement system is designed to be installed at the point where the string connects to the power plant main bus. This wiring configuration provides an acceptable compromise between the accuracy of panel condition estimation and the number of measuring points, while taking advantage of the PV power plant topology for easy communication via G3-PLC over the main bus.

The prototype itself is built around the LaunchXL-F28069M development kit [9] containing TMS320F28069 microcontroller, which is optimised for real-time applications such as feedback control and online signal processing. For the purpose of string current measurement, an ACS37002 current sensor [10] is utilised and connected to the first ADC channel of the microcontroller. The second ADC channel is connected via a 1:470 voltage divider with a surge protection circuit and a voltage follower with small input current, for the purpose of string voltage measurement. Simultaneous sampling is used for the string current and voltage measurements, so that it is possible to compute string power without any time shift suppression needed. After that, the second ADC channel is used to sample a voltage from a photoresistor-based solar irradiance sensor [11]. Both ADC channels are equipped with their own sample and hold circuitry, which is connected via analog multiplexer to 12-bit successive approximation ADC.

Finally, temperature measurements are taken using a TCN75A digital temperature sensor [12], one placed in the open air and one on the back of the solar panel, connected to the microcontroller via an I^2C bus, and leakage current detection is performed by T60404-N4641-X900 differential current sensor [13], whose trip contact is connected to the digital input of the microcontroller.

The overall wiring of the measurement system is then shown by the block diagram in Figure 2.

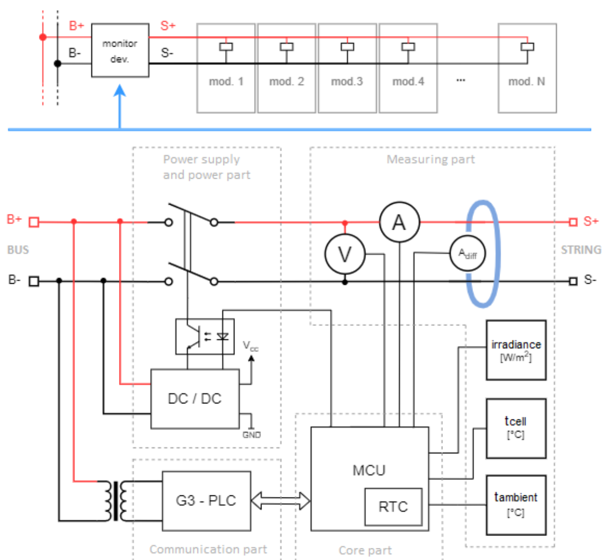

Fig. 2. Measurement system block diagram

C. Software implementation

The microcontroller utilised is equiped with two cores and so the software is also divided into two parts. The first part of the program is dedicated to the CLA core, which is optimised to accelerate the real-time calculations. For this reason, the CLA core is used for process data from the ADC. Program for the CLA core is divided into so called tasks, which are event-driven routines with a priority order of execution. The higher priority Task 1 is triggered by the start of AD conversion of the string current and voltage, which in turn is triggered by the timer overflow event that occurs every 2 μs. The lower priority Task 2 is then triggered by the conversion of the voltage on the photoresistor-based solar irradiance sensor. This Task is also triggered by the timer overflow event, but with a 1 ms period instead. The program for both CLA tasks is then described by the Algorithm 1.

The arc detection filters used in Algorithm 1 are 8^{th} order Butterworth type IIR with frequency response shown in Figure 3, valid for the 500 kHz sampling frequency. The selection of the Butterworth filter was driven by its flat passband response, while the order of the filter was determined by the capabilities of the MCU. The filter design process MATLAB script that generates the header file containing the filter coefficients for CLA Task 1 algorithm has been written.

Algorithm 1 – Program for the CLA core

Task 1:

$\mathbf{sc}_{1:N} \leftarrow \mathbf{sc}_{0:N-1}$
$\mathbf{sc}_0 = (\mathrm{ADC}^{\mathrm{current}} \cdot \mathrm{Scale}^{\mathrm{current}}) + \mathrm{Offset}^{\mathrm{current}}$
$\mathrm{sc}_{\mathrm{AVG}} = \frac{1}{N}\sum_{i=0}^{N} \mathbf{sc}_\mathrm{i}$
temp $\leftarrow$ []
for i $\leftarrow$ 0 : k **do**
  $\mathbf{temp}_\mathrm{i} = \sum_{j=0}^{M} \mathbf{FN}_{\mathrm{i,\,j}} \cdot \mathbf{sc}_\mathrm{j} + \mathbf{FD}_{\mathrm{i,\,j}} \cdot \mathbf{FC}_{\mathrm{i,\,j}}$
  $\mathbf{af}_\mathrm{i} = \mathbf{temp}_\mathrm{i} \geq \mathrm{Treshold}^{\mathrm{arc\text{-}fault}}$
  $\mathbf{FC}_{\mathrm{i,\,1:M}} \leftarrow \mathbf{FC}_{\mathrm{i,\,0:M-1}}$
  $\mathbf{FC}_{\mathrm{i,\,0}} \leftarrow \mathbf{temp}_\mathrm{i}$
end for
$\mathbf{sv}_{1:N} \leftarrow \mathbf{sv}_{0:N-1}$
$\mathbf{sv}_0 = (\mathrm{ADC}^{\mathrm{voltage}} \cdot \mathrm{Scale}^{\mathrm{voltage}}) + \mathrm{Offset}^{\mathrm{voltage}}$
$\mathrm{sv}_{\mathrm{AVG}} = \frac{1}{N}\sum_{i=0}^{N} \mathbf{sv}_\mathrm{i}$
return $\leftarrow$ [$\mathrm{sc}_{\mathrm{AVG}}$, $\mathrm{sv}_{\mathrm{AVG}}$, **af**, **sc**, **sv**]

Task 2:

temp $\leftarrow$ []
$\mathrm{temp} = (\mathrm{ADC}^{\mathrm{resistance}} \cdot \mathrm{Scale}^{\mathrm{resistance}}) + \mathrm{Offset}^{\mathrm{resistance}}$
$\mathbf{ir}_{1:N} \leftarrow \mathbf{ir}_{0:N-1}$
$\mathbf{ir}_0 = \mathrm{Scale}^{\mathrm{irradiance}} \cdot (\mathrm{temp})^{\mathrm{Exponent}^{\mathrm{irradiance}}}$
$\mathrm{ir}_{\mathrm{AVG}} = \frac{1}{N}\sum_{i=0}^{N} \mathbf{ir}_\mathrm{i}$
return $\leftarrow$ [$\mathrm{ir}_{\mathrm{AVG}}$]

Legend:

sc … N previous string current values
FC … M previous filtered current values from k filters
FN … M numerator IIR coefficients from k filters
FD … M denumerator IIR coefficients from k filters
af … M arc fault detection boolen flags
sv … N previous string voltage values
ir … N previous solar irradiance values

The actual conversion of the string current and voltage values from the ADC readings is expected to be linear, but depends on the gain of the input circuitry and is therefore adjustable.

For the conversion between resistance and solar irradiance the conversion characteristic, shown on a logarithmic scale in Figure 4, obtained from reference measurements interleaved with the least squares method is used. This characteristic applies to the GL5528 photoresistor [14] used in the protype measurement system.

The second core of the TMS320F28069 is mainly used as a data concentrator and Modbus RTU server. It periodically checks arc fault flags from the CLA core to determine if broadband noise generated by arc faults is present. It then reads the I2C temperature sensors at addresses

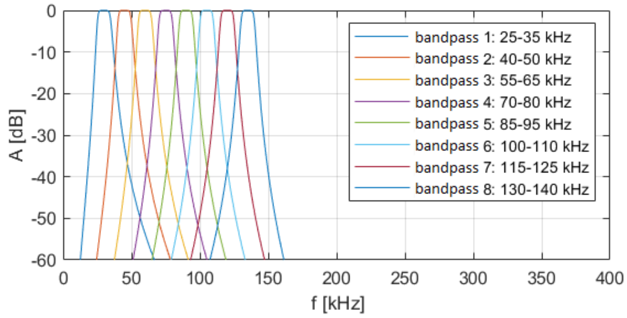

Fig. 3. Frequency response of arc detection filters

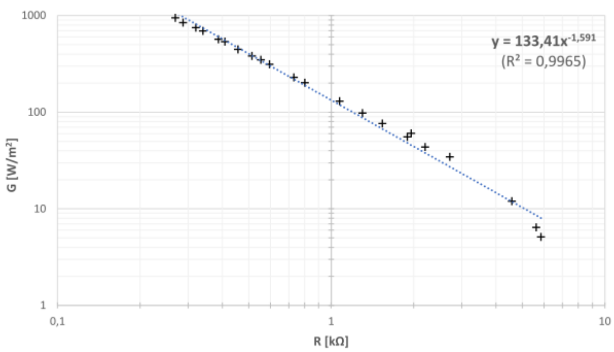

Fig. 4. Dependace of solar irradiance on photoresistor resistance

0x49 for ambient temperature and 0x4A for solar panel temperature, and the differential current sensor contact with a GPIO configured as a digital input. These measurements are then stored in the appropriate Modbus registers listed in Table II. The Modbus RTU server implementation is based on the nanoModbus library [15], which is freely distributed under the MIT licence.

TABLE II
MEASUREMENT SYSTEM MODBUS REGISTER MAP

Modbus register(s)	***Data type [bitlength]***	***Description***
1	bitfield [16b]	Configuration register (*Reserved*)
10001	bitfield [16b]	Status register (*Reserved*)
10002	bitfield [16b]	Leakage current detection (LSB)
30001-30002	float [32b]	String voltage (V)
30003-30004	float [32b]	String current (A)
30005-30006	float [32b]	String power (W)
30007-30008	float [32b]	Solar irradiance (Wm^{-2})
30009-30010	float [32b]	Panel temperature (°C)
30011-30012	float [32b]	Ambient temperature (°C)
40001-40004	unsigned [64b]	Processor time in Unix format (s)
40005-40006	float [32b]	String energy (J)
40007	unsigned [16b]	Arc fault occurance counter

III. Results

The communication capabilities of the prototype have been verified under laboratory conditions in a simple power line communication network using two MT49S G3-PLC modems, one connected to the LaunchXL-F28069M development board via the UART interface and the other to the computer via the USB-RS485 converter. The test setup is shown in Figure 5.

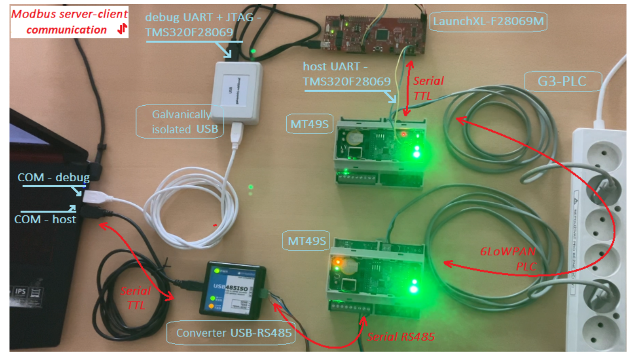

Fig. 5. Modbus RTU server test setup

The test measurements were then performed on a small PV power plant with six solar panels and a Huawei SUN2000 inverter, with a main focus on arc fault detection. Frequency and time domain plots of arc onset are shown in Figure 6 in conjunction with a sliding spark gap device used for the measurements. Subsequently, the filtration process of the retrieved current measurements, as outlined in Algorithm 1, resulted in the following results. It was determined that the arc fault has the highest impact on the frequency range between 25 and 50 kHz. For frequencies from 50 to 80 kHz is the impact too minor to be detected with simple tresholding but is still recognizable. The impact of the remaining higher frequency bands was found to be negligible, as illustrated in the filtered measurement in Figure 7.

IV. Conclusion

This paper presents a measurement system designed for a PV power plant. The primary purpose of this system is to detect short-term failures such as arc faults as well as long-term failures related to solar panel ageing. A prototype based on LaunchXL-F28069M has been developed and tested under laboratory conditions. Preliminary tests prove that the proposed measurement system can improve the safety of PV power plants and can even be installed in existing PV installations being a particularly important consideration in the context of increasingly stricter regulations.

Subsequent to these preliminary tests, it is imperative to conduct further testing in a field setting to collect substantial data, which will contribute to enhancement of the arc fault detection and the proper identification of long-term failures.

Acknowledgment

The research was funded from the grant No. FEKT-S-23-8451 – *"Research on advanced methods and technologies in cybernetics, robotics, artificial intelligence, automation and measurement"*, integrated with the Internal science fund of Brno University of Technology.

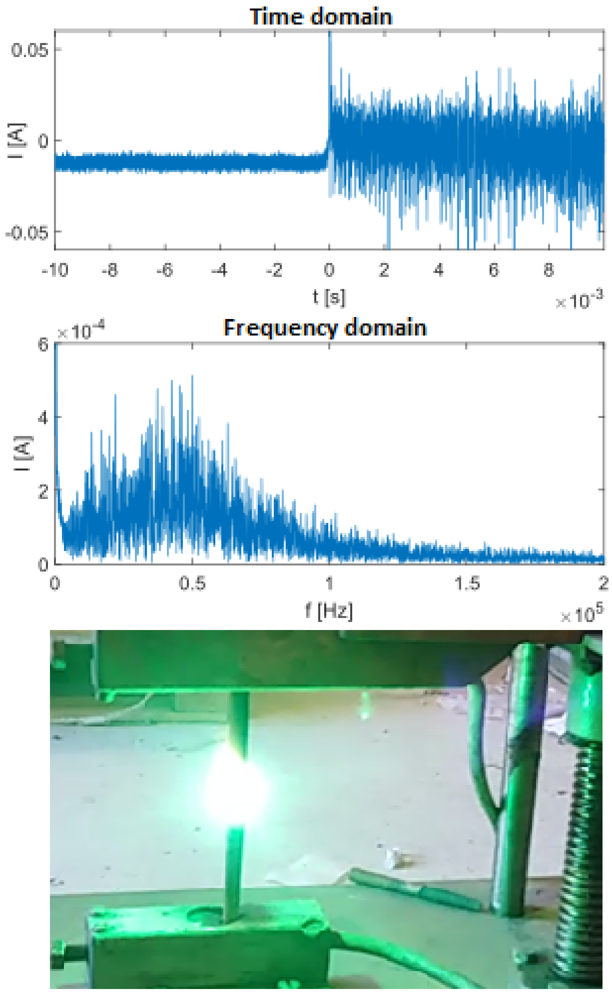

Fig. 6. Arc fault detection test measurements

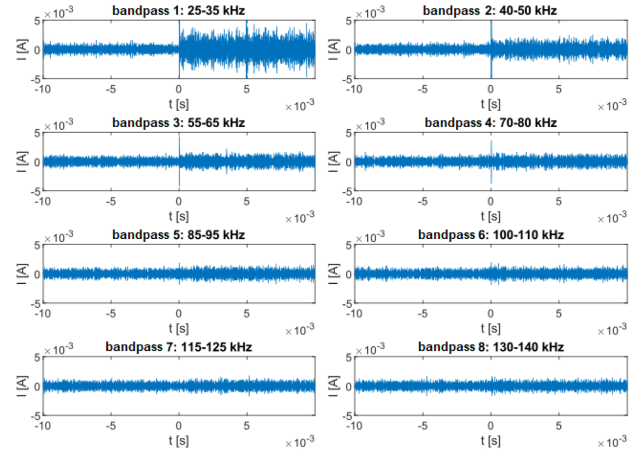

Fig. 7. Arc fault filtered current measurement

References

[1] ČEPS - Odbor 18320 Systémové analýzy ES, “Hodnocení zdrojové přiměřenosti ES ČR do roku 2040 (MAF CZ 2023),” https://www.ceps.cz/cs/zdrojova-primerenost, October 2024, [Accessed: 2025-01-27].

[2] J. Johnson, M. Montoya, S. McCalmont, G. Katzir, F. Fuks, J. Earle, A. Fresquez, S. Gonzalez, and J. Granata, “Differentiating series and parallel photovoltaic arc-faults,” in *2012 38th IEEE Photovoltaic Specialists Conference*. IEEE, 2012, pp. 720–726.

[3] K. M. Sundaram, S. Padmanaban, J. B. Holm-Nielsen, and P. Pandiyan, *Photovoltaic Systems: Artificial Intelligence-based Fault Diagnosis and Predictive Maintenance*. CRC Press, 2022.

[4] L. Martin, “Pokles výkonu fotovoltaických elektráren v důsledku vysokonapěťového stresu.” https://oze.tzb-info.cz/fotovoltaika/12260-pokles-vykonu-fotovoltaickychelektraren-v-dusledku-vysokonapetoveho-stresu, January 2015, [Accessed: 2025-01-28].

[5] Y.-Y. Hong and R. A. Pula, “Methods of photovoltaic fault detection and classification: A review,” *Energy Reports*, vol. 8, pp. 5898–5929, 2022.

[6] U. Jahn, M. Herz, M. Köntges, D. Parlevliet, M. Paggi, I. Tsanakas, J. Stein, K. A. Berger, S. Ranta, R. H. French *et al.*, *Review on infrared and electroluminescence imaging for PV field applications: International Energy Agency Photovoltaic Power Systems Programme*. International Energy Agency, 2018.

[7] B. Novak, “Implementing arc detection in solar applications: achieving compliance with the new ul 1699b standard,” *Texas Instruments*, 2012.

[8] T. Dierauf, A. Growitz, S. Kurtz, J. L. B. Cruz, E. Riley, and C. Hansen, “Weather-corrected performance ratio,” National Renewable Energy Lab.(NREL), Golden, CO (United States), Tech. Rep., 2013.

[9] Texas Instruments, *TMS320F2806x Real-Time Microcontrollers*, SPRS698J, November 2010, [Revised Sept. 2021].

[10] Allegro microsystems, *ASC37002 400 kHz, High Accuracy Current Sensor*, ASC37002-DS, August 2024, [Revision 9].

[11] R. C. de Barros, J. M. S. Callegari, D. do Carmo Mendonça, W. C. S. Amorim, M. P. Silva, and H. A. Pereira, “Low-cost solar irradiance meter using LDR sensors,” in *2018 13th IEEE International Conference on Industry Applications (INDUSCON)*. IEEE, 2018, pp. 72–79.

[12] Microchip Technology, *TCN75A 2-Wire Serial Temperature Sensor*, DS21935D, September 2010, [Revision D].

[13] VACUUMSCHMELZE, *Differential Current Sensor for IC-CPD acc. to the standard IEC62752-2016*, October 2021.

[14] Seeed Technology, *CdS Photoconductive cell GL5528*.

[15] V. D. Benedetto, “nanoMODBUS - a compact MODBUS RTU/TCP C library for embedded/microcontrollers,” https://github.com/debevv/nanoMODBUS/, April 2024, [Release: v1.17.1].

Speed Measurement from Traffic Camera Video Using Structure-from-Motion-Based Calibration

1st Stepan Jezek
Dept. of telecommunications, FEEC
Brno University of Technology
Brno, Czech Republic
Stepan.Jezek1@vut.cz

2nd Radim Burget
Dept. of telecommunications, FEEC
Brno University of Technology
Brno, Czech Republic
burgetrm@vutbr.cz

***Abstract*—Speed measurement from traffic camera video is an active research problem, primarily due to the challenges associated with accurate camera calibration in an uncontrolled environment. Traditional calibration techniques often require prior knowledge of the scene or manual input from the user, limiting their applicability in real-world scenarios. In this work, we propose a novel approach for traffic speed measurements using a camera calibration based on automatic 3D scene reconstruction via structure-from-motion (SfM). Our approach leverages deep learning-based feature extraction and matching, specifically SuperPoint and SuperGlue, to achieve precise scene reconstruction. By placing the camera within the reconstructed environment, we obtain its intrinsic and extrinsic parameters without requiring predefined reference objects. This allows us to establish a reliable reference for measuring distances in the scene. With this setup, we can accurately measure point distances on the ground plane, enabling robust speed estimation of moving vehicles. We present the implementation of our speed measurement method as a real-time application based on YOLO11 object detector and BoT-SORT object tracker. Our approach achieves speed measurement accuracy with an error of 6.9 km/h compared to a GPS RTK-based reference benchmark, demonstrating its effectiveness for traffic monitoring applications.**

***Index Terms*—camera calibration, deep learning, semantic segmentation, Structure-from-Motion, traffic speed measurement**

I. Introduction

Accurate speed measurement is an important task in traffic monitoring, law enforcement, and transportation research [14]. Traditional approaches often rely on radar, LiDAR, or inductive loop sensors, which require physical installation and maintenance. Given a wide adoption of cameras on current traffic infrastructure worldwide, speed measurement from a camera video stream presents a cost-effective and scalable alternative, allowing for large-scale deployment without the need for physical access and installation (see fig. 1). However, the accuracy of video-based methods is heavily dependent on precise camera calibration, making it a challenging research problem [1].

The fundamental difficulty in video-based speed measurement lies in determining the spatial relationship between the camera and the observed environment. This involves estimating the camera's intrinsic parameters (focal length, principal point, and distortion coefficients) and extrinsic parameters (position and orientation in the world coordinate system). Without proper calibration, speed measurements derived from video footage suffer from significant errors. Existing methods for camera calibration often require the use of reference objects with known dimensions, manual input, or predefined scene knowledge [5]. These constraints limit the applicability of such approaches in dynamic and uncontrolled environments where no prior information is available [7], [8], [11], [12].

Fig. 1. Examples of standard traffic cameras at the road intersection. Both cameras are not calibrated and therefore cannot be sufficiently used for speed measurements. There are many similar traffic cameras available worldwide.

To overcome these challenges and enable precise speed measurements from traffic video, we deploy a novel, fully automated method for camera calibration based on 3D scene reconstruction using Structure-from-Motion (SfM) [3], [4]. The scene reconstruction is performed using publicly available data from the Google Street View service. Our approach eliminates the need for predefined reference objects or physical access to the scene. The reconstruction process also leverages deep learning-based feature extraction and matching techniques. Specifically, the SuperPoint [10], a self-supervised feature detector and descriptor, in combination with SuperGlue [9], a deep learning-based feature matcher, to establish robust correspondences between frames in the video sequence. These correspondences ensure robust reconstruction of the environment in 3D, allowing for an accurate estimation of the camera's position and orientation within the reconstructed scene [3].

With the calibrated camera, we can measure distances between object points in the scene, enabling us to compute vehicle speeds. Using the proposed approach, we achieved a speed measurement error of 6.9 km/h, making it a robust and reliable solution for traffic monitoring applications. We

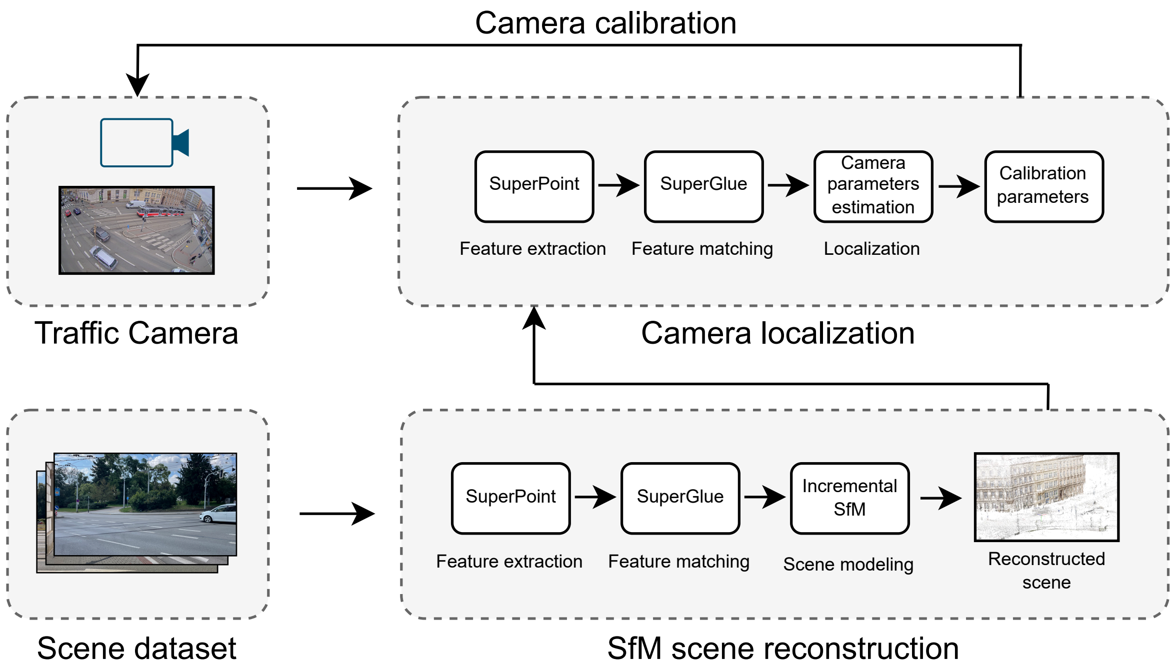

Fig. 2. Diagram of a camera calibration pipeline that involves SfM scene reconstruction from image data and a subsequent camera localization in the reconstructed scene.

note that such applications may not necessarily involve the speed measurement itself, but also related tasks such as traffic accident prediction or anomaly detection [5]. Unlike traditional methods that require manual intervention or scene-specific information, our approach is adaptable to different environments without requiring prior knowledge of the scene [6].

The rest of this paper is structured as follows: Section 2 discusses related work in video-based speed measurement and camera calibration techniques. Section 3 details our proposed method, including the Structure-from-Motion reconstruction, feature extraction, and camera localization. Section 4 presents experimental setup and accuracy evaluations, followed by a discussion of the results and the advantages and limitations of our approach. Finally, Section 5 concludes the paper.

II. Related Work

Video-based speed measurement has been a widely studied problem in the field of computer vision and intelligent transportation systems [2]. The primary challenge lies in accurately estimating real-world distances and motion trajectories from 2D video frames, which heavily depends on precise camera calibration [6]. Various approaches have been proposed to address this challenge, ranging from traditional geometric calibration methods to deep learning-based solutions [13].

A. *Traditional Camera Calibration Methods*

Conventional camera calibration methods rely on predefined reference objects, such as checkerboard patterns, lane markings, or objects of known dimensions. Zhang's method for camera calibration [6], which uses multiple images of a known planar pattern, is one of the most widely used approaches for estimating intrinsic parameters. However, such methods require controlled conditions and manual input, making them impractical for dynamic and uncontrolled environments, such as traffic surveillance. Other approaches utilize vanishing points and perspective geometry to estimate camera parameters from scene elements such as road markings, cars or buildings [7], [8], [13]. While these methods eliminate the need for physical calibration targets, they still require assumptions about scene structure, limiting their applicability [3].

B. *Structure-from-Motion for Camera Calibration*

To overcome the limitations of traditional calibration methods, Structure-from-Motion (SfM) techniques have been explored for automated camera calibration. SfM reconstructs a 3D scene from multiple 2D images by detecting and matching feature points across frames [4]. Early approaches relied on classical feature extractors such as SIFT and ORB, but these were often sensitive to changes in lighting and viewpoint. More recent methods incorporate deep learning-based feature extractors, such as SuperPoint [10] and SuperGlue [9], which significantly improve feature matching accuracy and robustness. The use of SfM for camera calibration in traffic applications is relatively unexplored, but recent studies indicate its potential in enabling accurate scene reconstruction without the need for predefined reference objects [3]. The whole reconstruction pipeline is shown in the fig. 2.

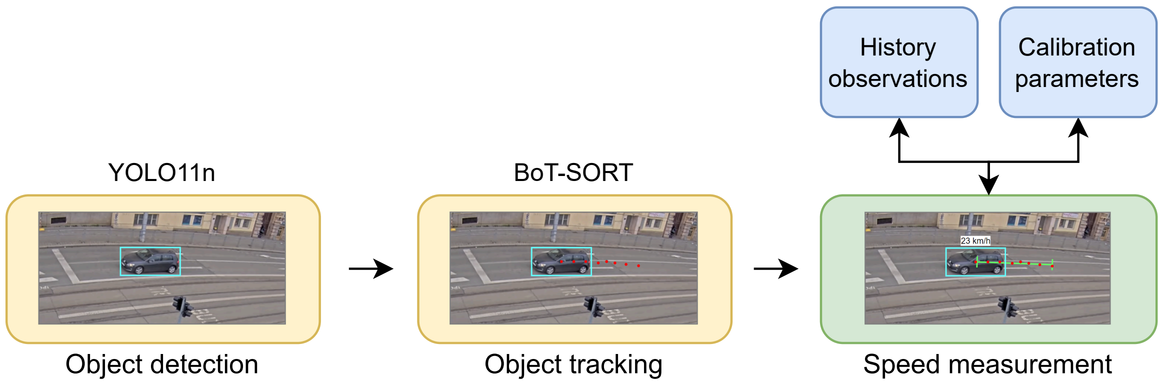

Fig. 3. Diagram of a proposed speed measurement method. It first involves object detection using the YOLO11 model, objects are then tracked with the BoT-SORT method to estimate object movement distances that are the basis for speed measurements.

III. Proposed System

Our proposed system enables accurate speed measurement from traffic camera videos by leveraging a novel camera calibration approach based on 3D scene reconstruction as presented in [3]. Unlike traditional methods that require predefined reference objects or manual measurements, we deploy a method that automatically estimates the camera's intrinsic and extrinsic parameters using a Structure-from-Motion (SfM) pipeline. This allows for precise distance measurements in the scene, leading to reliable speed estimation. The system consists of the following key components: feature extraction and matching, 3D scene reconstruction, camera calibration, and speed measurement.

A. Feature Extraction and Matching

After obtaining input scene panoramas (23 panoramas in total for our scene) from the Google Street View, the first processing step involves extracting and matching feature points across multiple frames of the input images. This is achieved by the SuperPoint model [10], a deep learning-based feature extractor designed for robust keypoint detection and description. SuperPoint generates a set of repeatable feature points that are highly resilient to changes in lighting, viewpoint, and motion blur, making it well-suited for real-world traffic camera footage.

Once keypoints are extracted, they are matched across frames using SuperGlue [9], a deep learning-based feature matcher that leverages a graph neural network to establish correspondences between frames. Unlike traditional feature matching algorithms such as SIFT or ORB, SuperGlue provides high-accuracy correspondences even in cases where perspective changes significantly. The matched keypoints form the basis for reconstructing the 3D structure of the scene.

B. 3D Scene Reconstruction

Using the matched feature points, a Structure-from-Motion (SfM) pipeline is applied to reconstruct the environment in 3D. SfM estimates the 3D positions of the matched points by solving the structure and motion problem, optimizing both camera poses and 3D point positions. This reconstruction provides a geometric representation of the scene, enabling precise localization of objects and surfaces within the camera's field of view. We used an open source implementation of the incremental SfM in the COLMAP application [4]. To increase reconstruction precision, input images are segmented using the Mask2Former transformer-based segmentation method [15] trained on the Mapillary Vistas dataset [16]. The segmentation masks are used to mask dynamic objects in the scene (e.g. cars), which increases final precision of the reconstructed scene.

C. Camera Calibration

Once the 3D structure of the environment is obtained, camera is localized within the 3D reconstruction. The only requirement is to provide the input image of the camera view. The localization process involves masking dynamic objects using the Mask2Former, feature extraction and feature matching. The camera is then localized using the SfM as implemented in the COLMAP application, which is used to register the image into the existing 3D reconstruction model, Intrinsic and extrinsic parameters for the camera are then calculated using the RANSAC algorithm and the minimal pose solver. In the final step, parameter tuning (finetuning) is performed using the Bundle Adjustment method. When the reconstruction and localization is completed, the model is transformed to metric scale using the GPS coordinates from the input images.

D. Speed Measurement

With the calibrated camera, we can accurately measure object motion in the scene. We implemented an application that detects vehicles in the scene using the YOLO11 [17] object detector. To measure movement across frames, detected vehicles are tracked using the BoT-SORT algorithm [18]. Since the distances between detected points on the ground are known with the calibrated camera, we compute speed using the time difference between frames. The final speed value is computed

TABLE I
EVALUATION RESULTS OF THE SPEED MEASUREMENT EXPERIMENTS. ALL MEASUREMENTS ARE IN KM PER HOUR, WE ALSO REPORT ERRORS AS ABSOLUTE DIFFERENCES IN KM/H WITH RESPECT TO THE REFERENCE MEASUREMENT.

Benchmark Footage	Measurement Point	Actual Speed (GPS)	Measured Speed	Absolute Error [km/h]	Relative Error [%]
	1	24	18	6	25
1	2	18	15	3	17
	3	12	14	2	17
	1	38	45	7	18
2	2	39	46	7	17
	3	40	52	12	30
3	1	30	19	11	36
Average				**6.9**	**22.9**

Fig. 4. Example output of the final application with object detection and tracking, it also contains history observations of object positions highlighted with red dots.

from the average distances in the last 10 tracked points. The measurement pipeline is displayed in the fig. 3.

IV. EXPERIMENT

To evaluate performance of the speed measurement system, we conducted experiments using real-world traffic camera footage. The camera was installed at an intersection in Brno, Czech Republic, capturing vehicle movements from a fixed viewpoint. The goal was to assess the accuracy of our method by comparing the estimated speeds to reference measurements obtained using a high-precision GPS RTK (Real-Time Kinematic) GNSS system [19].

A. Reference Data Collection

For ground truth validation, we collected precise vehicle trajectory and speed data using a GPS RTK system, which provided decimeter-level accuracy. A test vehicle equipped with the u-blox ZED-F9p RTK GNSS receiver was driven through the monitored intersection three times, covering different lanes and speed ranges. Simultaneously, the traffic camera recorded the vehicle's movement, ensuring that each run had a corresponding video sequence. We synchronized the data sources by their timestamps.

B. Evaluation Procedure

In our evaluation procedure, we assessed the accuracy of our speed measurement system using a custom-built application implemented in Python and OpenCV (see fig. 4). For vehicle detection, we utilized an implementation of YOLOv11 from the Ultralytics library, ensuring robust and real-time object detection. Object tracking was performed using BoT-SORT, also from Ultralytics, which allowed for stable and reliable multi-object tracking across frames. To determine vehicle positions, we tracked the center point of the detected bounding boxes and recorded historical observations over time. Distances between these recorded points were then calculated using the estimated road ground plane as a reference. This road plane was derived from our 3D scene reconstruction using points that fell within regions segmented as road or road markings by the Mask2Former segmentation model.

V. Results and Discussion

We report the results of our speed measurements in table I, which shows speed measured by our method in 3 points of the vehicle track in footage 1 and 2. For the benchmark footage 3, we were only able to measure speed in one point, because our reference car was otherwise covered by other vehicles in the camera view. The average speed measurement error is 6.9 km/h (22.9 % relative error) compared to the reference obtained from the GNSS RTK system. We believe this result shows that the proposed approach offers precise speed measurements for several smart traffic applications such as accident prediction, anomaly detection or traffic monitoring.

This level of accuracy is competitive with other calibration methods, such as those presented in [2]. The significant advantage of our approach however is the fully automated calibration that only requires images of the scene, such as those publicly available from the Google Street View. No physical access to location or manual user assistance is required.

The main disadvantage of the proposed approach might be insufficient accuracy for some applications. We also observed that accuracy was decreasing when measuring distances near the image borders, where the camera distortion is more significant. Other source of inaccuracies might also be the center points of a tracked objects that are calculated as a center of a detection bounding box. This can introduce errors because bounding boxes can change dimensions slightly throughout video frames.

VI. Conclusion

In this paper, we presented a novel approach for speed measurement from traffic camera video based on Structure-from-Motion (SfM) camera calibration. Unlike traditional methods that require predefined reference objects, manual input from the user or specific scene features, our approach leverages publicly available scene images and deep learning-based feature extraction (SuperPoint and SuperGlue) and semantic segmentation (Mask2Former) to achieve precise 3D reconstruction.

The calibration parameters are obtained by localizing the camera in the reconstructed scene. The whole pipeline can be performed automatically without the need to physically access the location as the reconstruction method only requires images from the scene, which can be obtained from public sources such as Google Street View. The use of SfM for 3D scene reconstruction allowed us to determine camera parameters without requiring prior knowledge of the scene.

Our experiments, conducted on real traffic camera footage, demonstrated that the system can achieve speed measurement accuracy with an error of 6.9 km/h when compared to high-precision GPS RTK reference data. The proposed approach therefore offers an accurate solution for many real-world applications related to traffic monitoring such as accident prediction or anomaly detection.

References

[1] Jain, N.K., Saini, R.K., Mittal, P. (2019). A Review on Traffic Monitoring System Techniques. In: Ray, K., Sharma, T., Rawat, S., Saini, R., Bandyopadhyay, A. (eds) Soft Computing: Theories and Applications. Advances in Intelligent Systems and Computing, vol 742. Springer, Singapore. https://doi.org/10.1007/978-981-13-0589-4_53

[2] J. Sochor et al., "Comprehensive Data Set for Automatic Single Camera Visual Speed Measurement," in IEEE Transactions on Intelligent Transportation Systems, vol. 20, no. 5, pp. 1633-1643, May 2019, doi: 10.1109/TITS.2018.2825609.

[3] K. Vuong, R. Tamburo, and S. G. Narasimhan, Toward Planet-Wide Traffic Camera Calibration. Proceedings of the IEEE/CVF Winter Conference on Applications of Computer Vision (WACV), 2024. doi: 10.1109/wacv57701.2024.00836.

[4] J. L. Schönberger and J. -M. Frahm, "Structure-from-Motion Revisited," 2016 IEEE Conference on Computer Vision and Pattern Recognition (CVPR), Las Vegas, NV, USA, 2016, pp. 4104-4113, doi: 10.1109/CVPR.2016.445.

[5] J. Fang, J. Qiao, J. Xue and Z. Li, "Vision-Based Traffic Accident Detection and Anticipation: A Survey," in IEEE Transactions on Circuits and Systems for Video Technology, vol. 34, no. 4, pp. 1983-1999, April 2024, doi: 10.1109/TCSVT.2023.3307655.

[6] Z. Zhang, "A flexible new technique for camera calibration," in IEEE Transactions on Pattern Analysis and Machine Intelligence, vol. 22, no. 11, pp. 1330-1334, Nov. 2000, doi: 10.1109/34.888718

[7] F. W. Cathey and D. J. Dailey, "A novel technique to dynamically measure vehicle speed using uncalibrated roadway cameras," IEEE Proceedings. Intelligent Vehicles Symposium, 2005., Las Vegas, NV, USA, 2005, pp. 777-782, doi: 10.1109/IVS.2005.1505199.

[8] M. Dubska, A. Herout, and J. Sochor, Automatic Camera Calibration for Traffic Understanding. 2014. doi: 10.5244/c.28.42.

[9] P.-E. Sarlin, D. DeTone, T. Malisiewicz, and A. Rabinovich, SuperGlue: Learning Feature Matching With Graph Neural Networks. 2020. doi: 10.1109/cvpr42600.2020.00499.

[10] D. DeTone, T. Malisiewicz, and A. Rabinovich, SuperPoint: Self-Supervised Interest Point Detection and Description. Proceedings of the IEEE Conference on Computer Vision and Pattern Recognition (CVPR) Workshops, 2018. doi: 10.1109/cvprw.2018.00060.

[11] X. C. He and N. H. C. Yung, "A Novel Algorithm for Estimating Vehicle Speed from Two Consecutive Images," 2007 IEEE Workshop on Applications of Computer Vision (WACV '07), Austin, TX, USA, 2007, pp. 12-12, doi: 10.1109/WACV.2007.7.

[12] Lian, H., Li, M., Li, T. et al. Vehicle speed measurement method using monocular cameras. Sci Rep 15, 2755 (2025). https://doi.org/10.1038/s41598-025-87077-6

[13] Wencheng Wu, Vladimir Kozitsky, Martin E. Hoover, Robert Loce, D. M. Todd Jackson, "Vehicle speed estimation using a monocular camera," Proc. SPIE 9407, Video Surveillance and Transportation Imaging Applications 2015, 940704 (4 March 2015); https://doi.org/10.1117/12.2083394

[14] X. Zhang, Y. Feng, P. Angeloudis and Y. Demiris, "Monocular Visual Traffic Surveillance: A Review," in IEEE Transactions on Intelligent Transportation Systems, vol. 23, no. 9, pp. 14148-14165, Sept. 2022, doi: 10.1109/TITS.2022.3147770

[15] B. Cheng, I. Misra, A. G. Schwing, A. Kirillov and R. Girdhar, "Masked-attention Mask Transformer for Universal Image Segmentation," 2022 IEEE/CVF Conference on Computer Vision and Pattern Recognition (CVPR), New Orleans, LA, USA, 2022, pp. 1280-1289, doi: 10.1109/CVPR52688.2022.00135.

[16] G. Neuhold, T. Ollmann, S. Rota Bulò, and P. Kontschieder. The Mapillary Vistas Dataset for Semantic Understanding of Street Scenes. In International Conference on Computer Vision (ICCV), 2017.

[17] R. Khanam and M. Hussain, Yolov11: An overview of the key architectural enhancements. arXiv preprint arXiv:2410.17725, 2024.

[18] N. Aharon, R. Orfaig and B. Bobrovsky. BoT-SORT: Robust Associations Multi-Pedestrian Tracking. ArXiv abs/2206.14651, 2022.

[19] Scherzinger, Bruno M., "Precise Robust Positioning with Inertial/GPS RTK," Proceedings of the 13th International Technical Meeting of the Satellite Division of The Institute of Navigation (ION GPS 2000), Salt Lake City, UT, September 2000, pp. 155-162.

Comparison of Direct and Indirect Identification of a Human Driver Model

Jakub Čelko
Department of Control and Instrumentation
Faculty of Electrical Engineering and Communication
Brno University of Technology
Jakub.Celko@vut.cz

***Abstract*—This paper focuses on recent advancements in the identification of human dynamics in vehicle steering tasks. The field of human driver identification encompasses a plethora of distinct models and methods for parameter identification. This study experimentally compares the most prominent identification approaches in terms of model efficiency (ME). The advantages of indirect identification methods are theoretically discussed and experimentally verified using a dataset comprising extensive measurements from 23 individual drivers. Both theoretical analysis and numerical evaluation of ME corroborate that the indirect identification method proposed by the author is superior to the direct methods employed in many previous studies. The suggested approach is expected to provide a more reliable estimate of drivers' dynamic parameters, which are desirable for further statistical analyses or machine learning applications in this research domain.**

***Index Terms*—cross-validation, driver behaviour, identification, model, simulator, steering control.**

I. Introduction

The author's previous work predominantly focused on establishing the optimal model structure for modelling human actions in various control tasks [1]–[4]. However, even with the selection of an optimal model structure, the effectiveness of data processing hinges on the proper selection of the identification method. This paper aims to compare and evaluate two primary approaches to identifying a human operator's dynamic model during car driving scenarios.

In our scenario, the human driver controls a simulated vehicle on a straight highway, where the driver must change lanes according to instructions while maintaining a constant vehicle velocity. This setup allows for a controlled environment to assess the identification methods accurately.

The paper is structured as follows. Section II reviews the theoretical fundamental differences between the direct and indirect identification methods for obtaining the model of human dynamics. Practical illustrations are referenced whenever possible to avoid a purely theoretical discussion. Section III details our experimental setup, the model structures used in this study, and the process of their evaluation in terms of model efficiency (ME). Section IV provides a practical demonstration of our theoretical considerations, showing that the indirect identification method, despite its added complexity, yields more accurate models with higher ME.

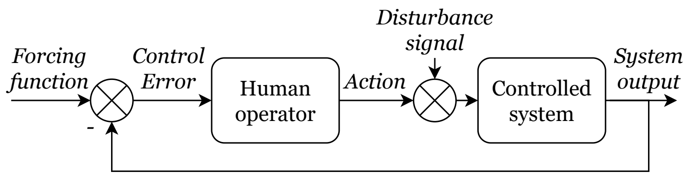

Fig. 1. Simple feedback loop describing human operator as a control element.

II. Related work

A human driving a vehicle assumes the role of a controller. Many researchers aim to develop a mathematical description of this human controller. The transfer function or non-linear model of this controller is unknown and requires parameter identification. The initial step typically involves selecting the model structure, followed by the identification of its parameters. Once the model structure is chosen, a decision on the identification approach must be made. The two identification methods analysed here are direct and indirect identification.

A. Direct (open-loop) identification

Identification in an open-loop is conducted when the driver model is treated as if it were disconnected from the control loop. Only the controller's input and output signals are utilised for the identification of the model parameters. The simulated controller output does not influence its inputs via the response-controlled system; instead, the measured inputs of the controller are used. In the simplest case, the input signal is the control error, and the output signal is the driver's action, specifically the angle of the steering wheel (see Fig. 1).

The first issue with such identification arises here. Evidently, these input and output signals are not independent of each other. When the driver model is within the control loop, the driver's action eventually (after passing through the controlled plant) affects the control error, and this feedback is not accounted for in the open-loop identification.

This grave issue has been previously described by [5] and later by [6], who indicate that a direct identification approach based solely on input and output signals may, in cases where the control error signal remains close to zero for extended periods, likely result in a model biased towards the inverse of the controlled plant's dynamics.

DOI 10.13164/eeict.2025.236

In extreme cases, such an identification process can result in a superfluous model that provides accurate steering actions in response to measured control errors but becomes unusable during closed-loop simulation. An example of this is the non-linear fuzzy model in [7], which exhibits negative gain for small values of the control error. This means that in a closed loop, it behaves as a "destabiliser" and forces the car away from the centre of the driving lane. Yet, in the open loop, the same model can approximate the measured response very well.

This outcome was probably caused by an inappropriate selection of the driver model and learning data, where only one "average" lane change was used for identification rather than the entire experiment consisting of several lane change actions distributed over time. The single lane change signal does not have a high enough order of persistent excitation to fully identify the chosen model, as described in detail by classical identification textbooks [8].

Despite these issues, this identification approach is still widely used. Its implementation is much simpler compared to the closed-loop identification method, as it only requires defining the identified driver model. With careful data and model selection, reasonable results can be obtained. Such research can be found, for example, in [3], [9]–[12].

B. Indirect (closed-loop) identification

Conversely, the indirect, or closed-loop, identification method involves modelling the entire system (as shown in Fig. 1). This includes the human driver model, the controlled system dynamics, and the structure of the loop, detailing how these subsystems are interconnected.

With this method, the plant's dynamics may be identified, but the process is simplified when it is known in advance. Once the entire closed-loop model is identified, the parameters of the human driver controller can be extracted.

This approach also allows for the identification of a greater variety of driver models, such as multi-input controllers. For example, in [4], the analysed modified multi-loop Donges model [13] requires a vehicle's heading signal as an input. Despite the fact that this signal is not measured in the experiment, such a model can be identified in the closed loop since the unmeasured signal can be obtained via modelling the controlled vehicle's dynamics in the loop.

III. Experiment description, selected driver model and its evaluation

In this section, the description of the experiment is presented along with the selected human driver model and mathematical evaluation of its prediction capabilities.

A. Experiment description

The two identification methods were evaluated through a series of tests in which the driver had to change lanes on a motorway according to instructions. Each driver participated in four experiments, differing in the power of disturbance signal present.

Fig. 2. Vehicle driving simulator screenshot showing a typical test scenario. [4]

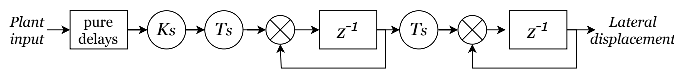

Fig. 3. Vehicle dynamics diagram.

These experiments were the same as those described in [4]: (1) measurement without disturbance, (2) and (3) measurements with white noise disturbance signals filtered by 4th and 2nd order filters respectively, and (4) measurement with a filtered pseudo-random binary sequence (PRBS) disturbance signal filtered by a 4th order filter. This article analyses the same measured data, but the dataset was extended to 23 individual drivers.

The study utilised an existing vehicle driving simulator, originally developed by [10] and later extended and modified by [4] to include disturbance signals. The vehicle driving simulator consists of a computer with a steering wheel and pedals as inputs to control the simulated vehicle. The simulator runs an application created in the Unreal Engine framework, which simulates the vehicle and its surroundings and logs all necessary data for further signal processing.

The controlled plant is modelled as a vehicle with the transfer function

$$F_{\mathrm{S}}(z) = K_{\mathrm{S}} T_{\mathrm{S}}^{2} \frac{z^{-2}}{(1-z^{-1})^{2}} z^{-d_{\mathrm{s}}}, \tag{1}$$

which is represented by two discrete integrators with a delay $d_{\mathrm{s}} = 40$ and a gain $K_{\mathrm{S}} = 73$. The continuous equivalent would be, assuming zero-order hold, a double integrator with gain and delay with transfer function $F_{\mathrm{Sc}}(s) = K_{\mathrm{Sc}} \cdot \mathrm{e}^{-\tau_{\mathrm{S}} s}/s^{2}$. The sampling period $T_{\mathrm{S}} \approx 7$ ms was taken as an average sampling period of all recorded samples. This adjustment was necessary due to slight sampling non-uniformity in the vehicle simulator.

The corresponding diagram of the vehicle model represented by this equation is depicted in Fig. 3.

B. Identified driver model and its evaluation

In this paper, a 2nd order McRuer model

$$F_{\mathrm{R}}(s) = \frac{K_{\mathrm{R}} s}{T_{\mathrm{R}}^{2} s^{2} + 2\xi T_{\mathrm{R}} s + 1} \mathrm{e}^{-\tau s} \tag{2}$$

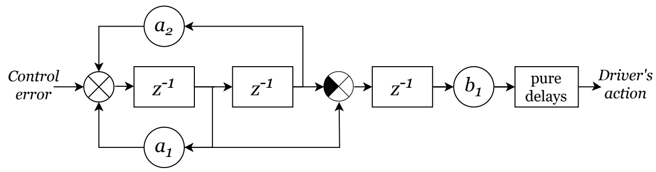

Fig. 4. 2nd-order McRuer model. [4]

is identified. Here K_{R} is the driver's gain, T_{R} is the time constant, ξ is the damping factor and τ is the response delay. Derived from the theory presented by McRuer [14], the same model was used as a linear component in the publications dealing with the same driving task [3], [9]–[12].

Since we are dealing with the discrete data, the zero-order hold equivalent

$$F_{\mathrm{R}}(z) = \frac{b_1(1 - z^{-1})}{1 - a_1 z^{-1} - a_2 z^{-2}} z^{-d_{\mathrm{r}}} \tag{3}$$

of the continuous model (2) is identified. Here d_{r} is the transport delay of the driver and a_1, a_2 and b_1 define the dynamics of the model. The scheme of the selected model is shown in Fig. 4.

It is important to note that this model appears to be inappropriate for scenarios with a higher intensity of the disturbance signal present, as discussed in [4]. However, that is a perfect opportunity to observe how the two identification approaches behave in cases of appropriate and inappropriate model selection.

To find the optimal parameters of the driver model to fit the measured data, the MATLAB function `ssest` was used. The models were identified in discrete state-space representation. For closed-loop identification, also the vehicle dynamics was taken into consideration, forming a closed loop with two inputs (forcing function and disturbance signal) and two outputs (control error and driver's action). For open-loop identification, only the driver model is identified with one input (control error) and one output (driver action).

To quantify the prediction capabilities of the models identified by direct and indirect method, a the standard cross-validation process is used, as described in [15], which divides the data into K folds. In this case $K = 2$ folds were used: $x_1(nT_{\mathrm{s}})$ and $x_2(nT_{\mathrm{s}})$. Two models are trained:

1) The first model is trained using fold $x_1(nT_{\mathrm{s}})$ and validated using the fold $x_2(nT_{\mathrm{s}})$.
2) The second model is trained using the fold $x_2(nT_{\mathrm{s}})$ and validated using the fold $x_1(nT_{\mathrm{s}})$.

This ensures that the performance of the model is tested on data that differ from the training data. ME on the validation fold is defined as

$$\mathrm{ME}_{\mathrm{Val}_k} = 1 - \frac{\sum_{n=0}^{N-1} [\hat{x}_k(nT_{\mathrm{s}}) - x_k(nT_{\mathrm{s}})]^2}{\sum_{n=0}^{N-1} [x_k(nT_{\mathrm{s}}) - \overline{x}_k]^2}, \quad k = 1, 2. \tag{4}$$

Here $x_k(nT_{\mathrm{s}})$ is the validation signal and $\hat{x}_k(nT_{\mathrm{s}})$ is the signal predicted by the model. The ME is clearly related to the mean squared error (MSE), which is proportional to the term in the nominator of (4). Higher ME values indicate better prediction capabilities of the model. The limit value ME = 1 is achieved only when the model prediction is identical to the validation data. Since there are two folds for which the MEs are evaluated, the mean value of both MEs was used for the evaluation, so $\mathrm{ME} = \frac{1}{2}(\mathrm{ME}_{\mathrm{Val}_1} + \mathrm{ME}_{\mathrm{Val}_2})$.

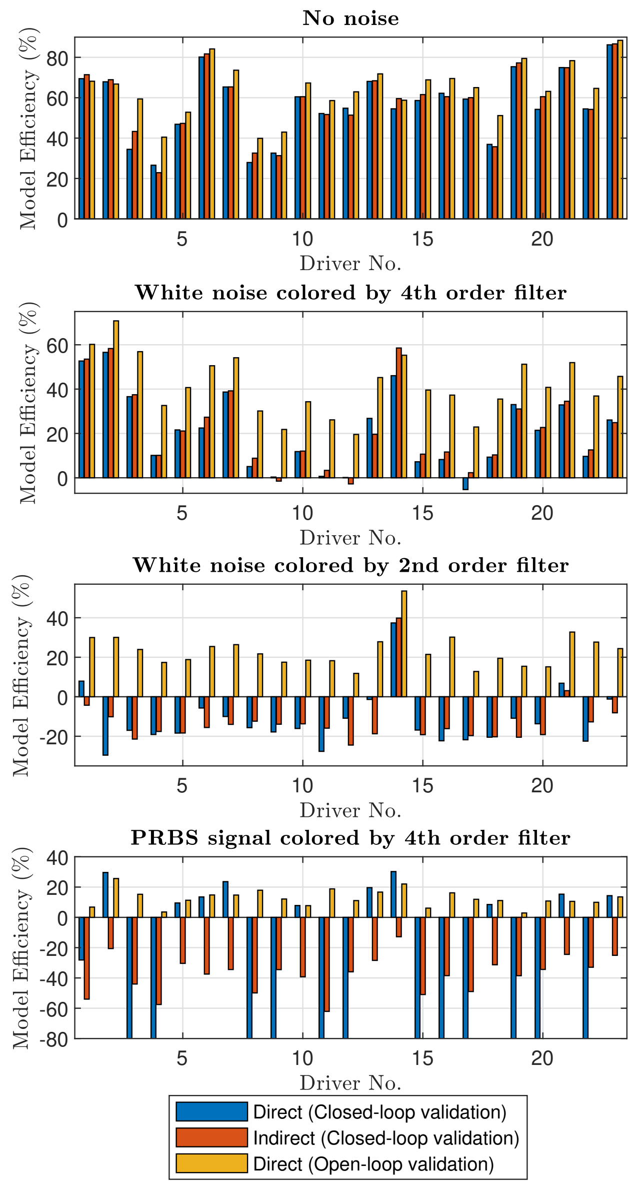

Fig. 5. Model efficiency on validation data for different identification methods during four different scenarios.

IV. Comparison of Direct and Indirect Identification on Measured Data

This section presents the results of the two identification methods tested on experimentally measured data. The discussion includes model efficiencies and the analysis of time series data.

A. Discussion on obtained model efficiencies

Fig. 5 presents bar graphs displaying the obtained MEs for the selected model, determined using two identification methods. For each measured driver and scenario, the ME value is illustrated for both the direct and indirect methods validated on closed-loop data (represented by blue and orange bars, respectively). Additionally, the ME value for the direct method validated on open-loop data is shown (yellow bars). Table I contains the mean values of the MEs obtained in the individual scenarios.

Both methods validated on closed-loop data resulted in similar ME values in the first tree scenarios. This suggests that both methods could be equivalent when the selected model can adequately represent human reactions.

However, a closed-loop validation needs to be used even with the direct identification approach. The same models identified with the direct method and validated on open-loop data resulted in significantly higher ME values, as can be seen in Fig. 5 and Table I. Thus, these MEs obtained via open-loop validation overestimate the model prediction quality in the experiment.

As was shown in [4], the selected model cannot adequately represent the reactions of human drivers in scenarios 3 and 4. This is consistent with the ME values validated in closed-loop both for direct and indirect identification method. However, as observed in previous scenarios, models obtained by a direct approach validated only on open-loop data resulted in much higher ME values, which do not represent the behaviour of the model in closed loop.

The differences become even more pronounced in the last scenario. Despite the fact that models identified by the direct identification method were all stable and resulted in positive MEs when validated on open-loop data, nearly half of the models obtained by the direct approach were unstable when simulated in the closed loop. In the last scenario, the MEs for the direct identification method validated in closed-loop fall significantly below the graph's y-axis, with unstable results as low as $-4 \cdot 10^{21}$ %.

On the other hand, models identified by indirect method always resulted in stable closed-loop behaviour, even when the selected model can not represent human driver reactions. However, it should be noted that when the direct method validated on closed-loop data does not fail in producing unstable closed-loop behaviour, the MEs in the last scenario tend to be higher (and even positive) than those of the indirectly identified models.

B. Evaluation from time series data

The outcome of the chosen identification approach can also be seen in the time series data shown in Figs. 6 and 7. The first subplot in these figures visualizes the forcing function (desired driving lane) and the actual vehicle's position as the driver deals with the task of getting and keeping the vehicle in the given driving lane. The second subplot compares measured data with the prediction of a model identified with a direct or indirect method validated in a closed-loop. The final subplot shows measured data alongside the predictions of a model identified using a direct method validated in an open-loop.

TABLE I
AVERAGE MEs IN INDIVIDUAL SCENARIOS

Scenario No.	Direct ME (Closed-loop validation) (%)	Indirect ME (Closed-loop validation) (%)	Direct ME (Open-loop validation) (%)
1	56.66	57.71	64.17
2	20.51	21.98	41.74
3	-11.59	-12.74	23.50
4	$-1.81 \cdot 10^{20}$	-37.67	12.67

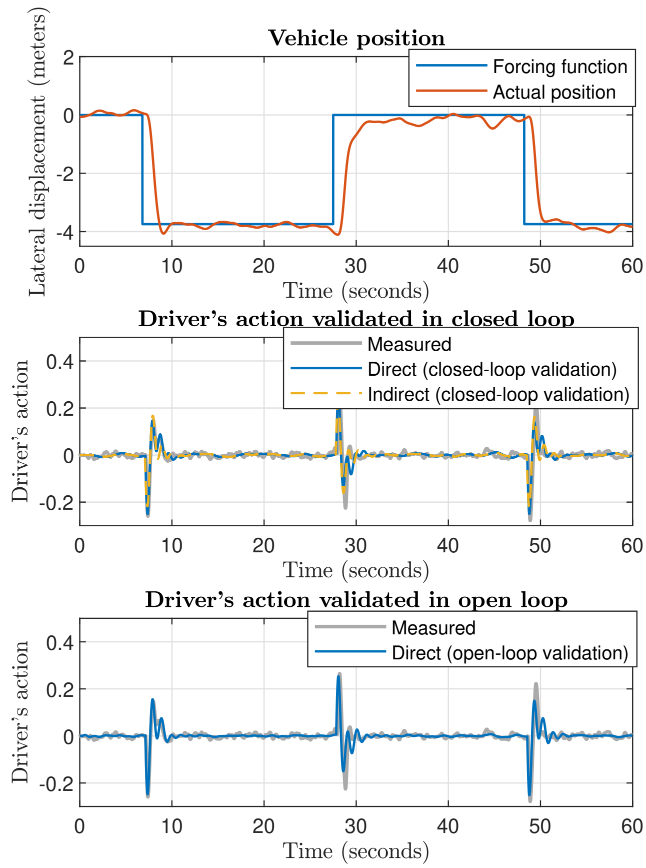

Fig. 6. Driver action – validation data and predicted signal waveforms for scenario 2.

Fig. 6 presents an example in which the results of the different identification methods were nearly indistinguishable. This case displays selected time periods for driver 14 in scenario 2. All identification approaches produced stable models in both closed-loop and open-loop validation. The model predictions closely approximate the validation data, with only minor differences among them.

Fig. 7 demonstrates a situation where the result of the direct identification method produced a stable model in the open loop, while the same model, when connected to the vehicle's dynamics in the closed loop, generated unstable results. The selected time data pertain to driver 11 in scenario 4. The second graph in Fig. 7 clearly shows that the output of the directly identified model in the closed-loop quickly turns

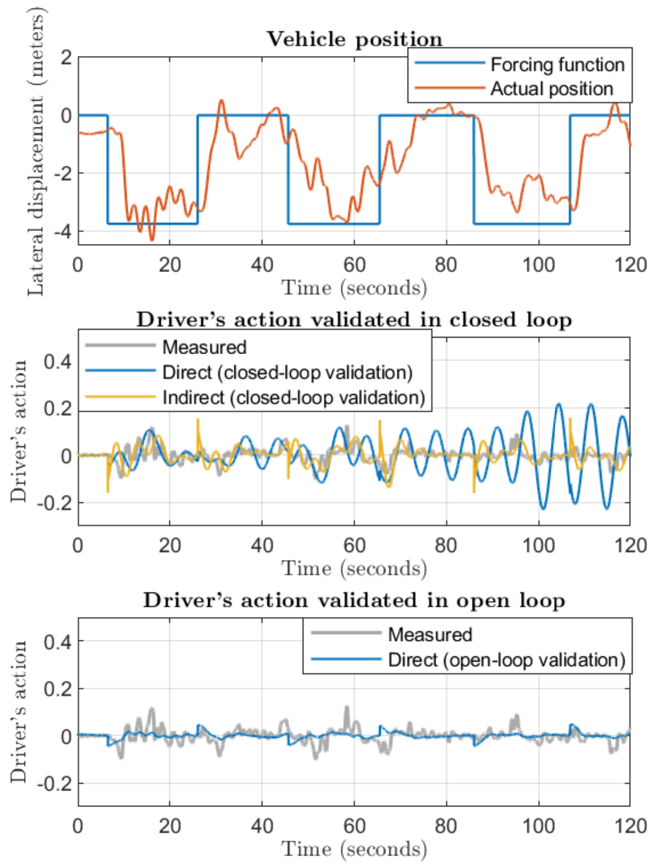

Fig. 7. Driver action – validation data and predicted signal waveforms for scenario 4.

into oscillations, with the magnitude increasing over time. Meanwhile, the predictions of this model simulated in the open-loop, as shown in the final graph in Fig. 7, exhibit no signs of unstable behaviour.

V. Conclusion

In this paper, an experimental study was conducted to evaluate the identification approach of a human driver model. A second-order transfer function model of a human driver was subjected to both direct and indirect identification processes and evaluated in both closed and open loops using a data set gathered from 23 different drivers.

The results show that using the direct identification method evaluated on open-loop data tends to overestimate the model's prediction capabilities and occasionally produces a model that is unstable when connected and simulated in the closed loop, yielding extreme negative values of ME.

Conversely, the indirect identification approach results in a more realistic estimation of the model's prediction quality. Moreover, indirect identification does not produce unstable models even when the selected model cannot adequately represent human action.

Based on the observed behaviour of the individual identification methods, the indirect or closed-loop identification method is recommended, especially in cases where the model of the controlled plant is known and can be easily employed in the model of a whole closed loop.

This result will enable the development of more accurate models of human dynamics. This will enhance the subsequent statistical evaluation of the tested drivers and allow for more precise predictions about the drivers using machine learning approaches.

Acknowledgment

The completion of this paper was made possible by the grant No. FEKT-S-23-8451 – "Research on advanced methods and technologies in cybernetics, robotics, artificial intelligence, automation and measurement" financially supported by the Internal science fund of Brno University of Technology.

I would also like to extend my sincere gratitude to Ondrej Mihálik and Zdeněk Bradáč, who provided support and advice during the completion of this paper.

References

[1] J. Čelko, "Modelování systémů člověk-stroj pomocí McRuerových modelů", Bakalárska práca, Brno, 2022.
[2] J. Čelko, "Rozvětvené dynamické modely řidiče. Vysoké učení technické v Brně". Fakulta elektrotechniky a komunikačních technologií, 2024.
[3] J. Čelko and O. Mihálik, "McRuer Models for Human-Machine Systems", in Proceedings I of the 28st Conference STUDENT EEICT 2022: General papers, pp. 43-46.
[4] J. Čelko, O. Mihálik, M. Husák, and Z. Bradáč, "A Simple State-Space Model of Human Driver Applicable to Windy Condition", IFAC-PapersOnLine, vol. 58, no. 9, pp. 229-234, 2024.
[5] L. Ljung, "System identification: theory for the user", 2nd ed. Upper Saddle River: Prentice Hall PTR, 1999.
[6] C. J. Nash and D. J. Cole, "Identification and validation of a driver steering control model incorporating human sensory dynamics", Vehicle system dynamics, vol. 58, no. 4, pp. 495-517, 2020.
[7] M. Radvanský, "Využití fuzzy logiky při modelování a hodnocení chování řidiče". Vysoké učení technické v Brně. Fakulta elektrotechniky a komunikačních technologií, 2022.
[8] T. Söderström and P. Stoica, "System identification". New York: Prentice Hall, 1989.
[9] M. Jirgl, M. Mesarosova, P. Fiedler, and J. Arm, "Fuzzy Logic-based Techniques for Human Driver Behavior Modelling during a Simple Lane-changing Task", IFAC-PapersOnLine, vol. 58, no. 9, pp. 257-262, 2024.
[10] D. Michalík, M. Jirgl, J. Arm, and P. Fiedler, "Developing an Unreal Engine 4-Based Vehicle Driving Simulator Applicable in Driver Behavior Analysis—A Technical Perspective", Safety (Basel), vol. 7, no. 2, p. 25, 2021.
[11] O. Mihálik and P. Fiedler, "Means of Obtaining Mamdani Fuzzy Model of Car Driver's Dynamics", in Proceedings II of the 28st Conference STUDENT EEICT 2022: Selected papers, pp. 243-247.
[12] M. Jirgl, O. Mihalik, S. Boujenfa, Z. Bradac, and P. Fiedler, "Experimenting With an Efficient Driver Behavior Dynamical Model Applicable to Simulated Lane Changing Tasks", IEEE access, vol. 12, pp. 122183-122198, 2024.
[13] DONGES, Edmund, "A Two-Level Model of Driver Steering Behaviour", Human Factors, vol. 20, no. 6, pp. 691-707, 1978.
[14] D. T. McRuer and E. S. Krendel, "Mathematical Models of Human Pilot Behavior". 1974.
[15] T. Hastie, R. Tibshirani, and J. Friedman, "The elements of statistical learning: data mining, inference, and prediction", 2nd ed. New York: Springer, c2009.

UAV platform for special operation

1st Ing. Jan Klouda
Theoretical and Experimental Electrical Engineering
Brno University of Technology UTEE
Brno, Czech Republic
xkloud04@vutbr.cz

2nd doc. Ing. Petr Marcoň Ph.D.
Theoretical and Experimental Electrical Engineering
Brno University of Technology UTEE
Brno, Czech Republic
marcon@vut.cz

***Abstract*—Unmanned Aerial Vehicles (UAVs) are widely used in industrial inspection, agriculture, and security. This paper introduces a universal UAV platform designed for modular adaptability, extended flight endurance, and autonomous navigation. The hardware architecture includes a lightweight carbon fiber frame, high-efficiency propulsion, and a flexible power system, ensuring reliable performance across various missions.**

The software framework, built on ROS 2 middleware, enables seamless integration of SLAM-based navigation, visual odometry, and deep learning-based object detection. The UAV combines GNSS, INS, and LiDAR-based SLAM for precise localization, even in GNSS-denied environments. Equipped with multi-sensor payloads such as LiDAR, RGB-D cameras, and thermal imaging, this platform supports applications ranging from precision agriculture to infrastructure inspection, paving the way for advanced autonomous UAV operations.

***Index Terms*—UAV, autonomous navigation, modular drone platform, SLAM, visual odometry, GNSS-denied environments, deep learning, ROS 2, LiDAR, trajectory planning, multi-sensor integration, real-time processing, obstacle avoidance**

I. Introduction

Unmanned aerial vehicles (UAVs) have become an imporatnt tool in many industries, including industrial inspection, precision agriculture, and security operations [1]. The development of modular UAV platforms enables adaptive integration of different sensors and efficient execution of diverse missions [2]. With increasing demands for longer flight times, higher payloads and flexible configuration options, there is a need for versatile UAV platforms that can handle a wide range of applications without compromising performance [3].

This paper presents the design of a versatile UAV platform that enables easy integration of different payloads, increases operational efficiency and offers a modular architecture adaptable to different deployment scenarios. Emphasis is placed on flight time optimization, reliability and flexible connectivity to different control systems, making this concept ideal for special operations in the industrial, security and agricultural sectors [4].

II. Platform Philosophy

The main goal of the proposed UAV platform is to create a versatile and highly adaptable drone that allows rapid deployment in different types of missions without the need for extensive hardware or software modifications [5].

Figure 1 presents a block diagram of the proposed universal platform. Several abbreviations appear in the figure: FCC (Flight control computer), GNSS (Global Navigation Satellite System), ESC (Electronic speed controller), IMU (Inertial measurement unit), RGB-D (camera that provides both depth (D) and color (RGB) data), LiDAR (Light Detection And Ranging).

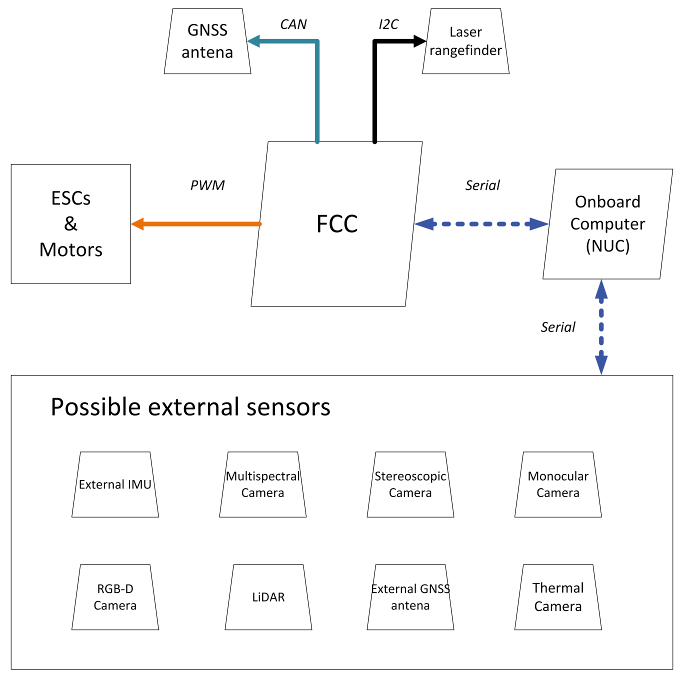

Fig. 1. Block diagram of the platform

Modern UAV applications require modular design, long flight endurance, scalability, reliability, and high levels of autonomy. These aspects ensure that UAVs can be effectively used in areas such as industrial inspection, precision agriculture or security operations.

Modularity plays a vital role in ensuring the flexibility of the drone. The ability to easily swap sensor modules allows the UAV to be quickly adapted to specific mission requirements. The platform supports a wide range of sensors, including LiDAR systems for detailed 3D terrain mapping, multispectral cameras for vegetation analysis, thermal cameras for thermal anomaly detection and HD cameras for detailed infrastructure inspections [6], [7].

In addition to the sensors, the design of the UAV itself is modular. This means that individual parts, such as battery units, motors or communication systems, can be easily replaced or upgraded according to current requirements. In this way, the platform can be adapted to different application scenarios without having to develop a completely new solution for each case.

An important factor in the effectiveness of a UAV is its endurance in the air. Extended flight time has been achieved by optimising aerodynamics, using high-efficiency engines and implementing advanced energy management. The drone uses a modular battery system that allows a choice between a higher capacity configuration for long duration missions and a lighter variant for greater manoeuvrability [8].

Flight endurance can be theoretically expressed by the relationship between the available energy and the average energy consumption of the UAV. When the system was optimized, flight times in the range of 40 to 60 minutes per charge were achieved, allowing for effective coverage of large areas in a single deployment. The total flight time T_f of a UAV can be estimated using the following equation:

$$T_f = \frac{\eta P_b}{P_d} \tag{1}$$

where:

- T_f is the total flight endurance (s),
- η is the overall efficiency of the UAV power system (dimensionless),
- P_b is the available battery energy (Wh),
- P_d is the average power consumption during flight (W).

The available battery energy is calculated as:

$$P_b = U \cdot C \tag{2}$$

where:

- U is the nominal battery voltage (V),
- C is the battery capacity (Ah).

The average power consumption during flight can be estimated as:

$$P_d = \sum_{i=1}^{n} P_i \tag{3}$$

where:

- P_i is the power consumed by the i-th subsystem of the UAV (W),
- n is the total number of power-consuming subsystems (e.g., motors, electronics, sensors).

Another requirements of modern UAV systems is their ability to grow and adapt to technological advances. This platform has been designed to allow easy integration of new sensors, computing units or communication modules without the need for major design changes. Support for multiple voltage levels allows users to choose between higher battery capacity for longer flight or lower weight for better maneuverability [9].

Thanks to the modular architecture, the platform can be extended with advanced navigation technologies such as artificial intelligence systems for autonomous data analysis or high-speed transmission modules for real-time communication. This ensures that the UAV remains competitive in the long term and ready for future innovations.

Reliability is an important factor when deploying UAVs in mission-critical applications. The drone's design has been optimized to withstand harsh weather conditions, mechanical stresses and long-term operation. The redundancy of key components, including power circuits and controllers, ensures safe operation even in the event of a system failure [10].

In addition to hardware measures, reliability has also been improved by implementing advanced algorithms for fault detection and predictive maintenance. The drone is able to monitor its status in real time and alert the operator of potential problems before they affect its performance or flight safety.

Modern UAV systems increasingly rely on autonomous capabilities to enable more efficient and safer operations. This drone is equipped with advanced navigation technologies, including simultaneous localization and mapping (SLAM), visual odometry and inertial navigation systems. These technologies allow it to operate in environments where GNSS signals are not available [11].

In addition to navigation functions, the platform is equipped with algorithms for autonomous obstacle avoidance and adaptive flight control. By using artificial intelligence, the drone is able to analyze the surrounding environment in real time and optimize its flight plan according to the current conditions. This enables its deployment in complex missions such as autonomous infrastructure inspection, monitoring changes in terrain or reconnaissance operations in difficult conditions [11].

The overall philosophy of this UAV platform is to combine high flexibility, efficiency and reliability, making it an ideal solution for a wide range of applications. Its modular design, long flight endurance and scalability ensure that it will be able to meet the requirements of both current and future users.

III. Navigation Options

The navigation of a UAV is a critical factor affecting its ability to fly autonomously, accuracy in mission execution, and overall reliability in challenging environments. This UAV platform uses a combination of several advanced navigation methods that allow operation in both open terrain with available GNSS signal and in environments where GNSS is completely unavailable or heavily jammed. GNSS navigation is the foundation, complemented by visual odometry, inertial navigation and SLAM (Simultaneous Localization and Mapping), which enables robust navigation even in environments without satellite signal [12].

A. *Visual odometry - Image-based navigation*

Visual odometry (VO) is a technology for UAV operations in environments where GNSS is not available, such as industrial halls, dense urban development or underground spaces [13].

This system uses a camera or an array of cameras to track visual features of the environment and calculates the trajectory of the UAV based on their movement between images.

The basis of visual odometry is the extraction of key points from the images acquired by the cameras. Algorithms such as ORB (Oriented FAST and Rotated BRIEF), SIFT (Scale-Invariant Feature Transform), or AKAZE (Accelerated-KAZE) identify specific visual features that are then tracked in the image sequence [14]. The movement of these points between frames can be mathematically expressed by a transformation matrix:

The movement of these points between frames in visual odometry can be mathematically expressed using the following transformation matrix:

$$T_{k+1} = K \cdot \left(R_{k+1,k} - t_{k+1,k} \cdot n^T\right) \cdot K^{-1} \tag{4}$$

where:

- T_{k+1} is the transformation matrix between frames,
- K is the camera intrinsic matrix,
- $R_{k+1,k}$ is the rotation matrix between frames,
- $t_{k+1,k}$ is the translation vector,
- n is the normal vector of the plane.

The drone can use both monocular visual odometry, which works with only one camera to estimate the scale of motion, and stereoscopic visual odometry, which uses a pair of cameras to create a depth map of the environment [15].

An important enhancement to visual odometry is optical flow, which analyzes the movement of pixels between frames and helps determine the speed of the UAV. This approach is particularly advantageous in situations where the drone is moving over structured textures such as vegetation or urban development [12].

B. Inertial Navigation System (INS) - Stabilization and motion tracking

The Inertial Navigation System (INS) is element of UAV navigation that enables the determination of changes in position and orientation in space without the need for external references [16]. The system works with data from accelerometers, gyroscopes and magnetometers that sense the acceleration, angular velocity and orientation of the UAV relative to the Earth's magnetic field [17].

The motion of a UAV based on Inertial Navigation System (INS) measurements can be described by the following equations:

$$v(t) = v_0 + \int_0^t a(\tau)d\tau \tag{5}$$

$$p(t) = p_0 + \int_0^t v(\tau)d\tau \tag{6}$$

where:

- $v(t)$ is the velocity of the UAV at time t,
- $a(\tau)$ is the acceleration measured by the INS,
- $p(t)$ is the position of the UAV,
- p_0 and v_0 are the initial position and velocity.

INS is divided into two main categories - strapdown INS and platform INS. Platform UAVs mainly use strapdown INS, where sensors are fixed to the drone body and digital filters process the raw data [12]. The disadvantage of INS is the accumulation of errors due to sensor drift, which causes inaccuracies in long-term navigation. Therefore, INS is combined with other navigation systems such as GNSS, visual odometry or SLAM to correct INS errors using external references [18].

C. SLAM - Simultaneous localization and mapping

SLAM (Simultaneous Localization and Mapping) is an advanced algorithm that allows a UAV to simultaneously create a map of the surrounding environment and determine its own location within that map [19]. This technology is essential for autonomous operations in unknown environments where the UAV does not have a pre-existing map or GNSS signal.

The SLAM problem can be formulated as a Bayesian estimation problem, where the goal is to find the most probable estimate of the UAV's position x_t and the generated map m_t:

$$\begin{aligned} p(x_t, m_t|z_{1:t}, u_{1:t}) \propto p(z_t|x_t, m_t) \cdot p(x_t|x_{t-1}, u_t) \\ \cdot p(x_{t-1}, m_{t-1}|z_{1:t-1}, u_{1:t-1}) \end{aligned} \tag{7}$$

where:

- z_t represents the sensor measurements at time t,
- u_t denotes the control inputs applied to the UAV,
- x_t is the estimated position of the UAV at time t,
- m_t is the generated map of the environment.

SLAM can be implemented based on different sensor inputs:

Visual SLAM (V-SLAM) - uses cameras and visual features of the environment, similar to visual odometry, but with better long-term position estimation [20]. LiDAR SLAM - works with a laser scanner and provides a detailed 3D map of the environment [21]. RGB-D SLAM - uses depth cameras combining RGB image with distance information [22]. By combining visual odometry, INS and SLAM, this platform achieves a high level of autonomy and reliable navigation in a wide range of environments.

IV. Universal Platform (Hardware Description)

This UAV platform has been designed with an emphasis on modularity, flexibility and performance, making it ideal for a wide range of applications, from industrial inspection to scientific research. Each component has been carefully selected for durability, efficiency and easy integration of other technologies [23].

With its modular design, flexible power system, and broad sensor integration capabilities, this UAV platform provides a versatile solution for diverse applications. The possibility of easy customization and autonomous navigation technologies make it a cutting-edge tool for industrial, scientific and military applications.

A. Design and frame

The supporting structure of the UAV consists of a lightweight but extremely strong carbon fiber frame that minimizes overall weight while providing high strength [24]. The foldable arms provide easy transportation and storage, reducing the logistical requirements for deployment. The modular attachment of motors and electronics allows for quick replacement of these components, reducing downtime and simplifying UAV maintenance [25].

The UAV powertrain consists of high-efficiency T-Motor MN601 320KV motors that provide optimal thrust at low energy consumption [26]. These motors are powered by ESC controllers supporting 6S-12S LiPo batteries, allowing for different configurations depending on mission requirements - from long-duration flights to carrying heavier payloads [27].

B. Power system

The power is supplied by two 6S LiPo batteries with a capacity of 10,000 mAh, which are connected in parallel, increasing the overall capacity and extending the flight time of the [28]. The power distribution is done through a power distribution board (PDB), which not only distributes the voltage efficiently to all components, but also provides current and voltage measurements to optimize power management [29].

For the on-board computing system, a DC-DC converter is available to convert the 6S battery voltage to a stable 19V DC to power the main NVIDIA Jetson Orin computing unit [30]. This powerful edge-computing module enables real-time image processing, which is crucial for autonomous navigation and sensor fusion.

The main control element of the UAV is the Cube Orange+ flight controller, which is equipped with a powerful processor and interfaces for integrating sensors and communication modules (Wang et al., 2020). This system stabilizes the flight and allows interfacing with various navigation technologies, including visual odometry, inertial navigation and SLAM [31].

The Here3 GNSS module is used for precise positioning and provides highly accurate location data [32]. In the case of operation in environments without GNSS signal, a combination of visual odometry, INS and SLAM takes over the navigation role, enabling robust autonomous driving even in indoor or densely built-up areas [33].

One of the main advantages of this platform is its ability to integrate different sensor and measurement systems. The UAV is equipped with a universal mount that allows the attachment of a wide range of sensors such as LiDAR scanners, multispectral cameras, thermal cameras, and high-resolution optical sensors [34].

With a wide range of communication interfaces (CAN bus, UART, USB), UAVs can be easily adapted to the specific requirements of a given mission, from geodetic measurements to critical infrastructure inspections [35].

V. Software Platform

The UAV software architecture is designed with an emphasis on real-time performance, modularity, and reliability, using modern middleware technologies and advanced algorithms for autonomous navigation and computer vision [36]. The main computing center of the UAV is the Intel NUC, which provides sufficient computing power to run deep learning, visual odometry and SLAM algorithms in real-time.

A. Operating system and middleware layer

The UAV runs on Ubuntu 22.04 LTS, with ROS 2 Galactic as the main middleware, which provides communication between the UAV software modules [37]. The advantage of ROS 2 is its low latency, support for real-time applications and scalability, which allows easy integration of new features and sensor inputs.

The software architecture is divided into several ROS 2 node processes, each responsible for a specific functionality:

Flight Control Node - communicates with the Cube Orange+ flight controller and translates commands into motion instructions. SLAM Node - performs simultaneous localization and environment mapping. Computer Vision Node - processes image data from cameras and performs visual odometry. Mission Planner Node - generates flight trajectory and optimizes UAV movement. The communication between these components is done through the DDS (Data Distribution Service), which provides low latency and robust data transfer between the UAV modules [38].

B. Autonomous driving and trajectory planning

Autonomous navigation of UAVs is based on a combination of the Kalman filter (EKF), visual odometry and SLAM to ensure accurate localization of UAVs in different environments [39].

To optimize the flight trajectory of the UAV, it uses Rapidly-exploring Random Tree (RRT) or a algorithm that allow the UAV to navigate efficiently in dynamic environments such as forests, industrial complexes or warehouses [40].

C. Computer vision and neural networks

Another important software feature of this platform is advanced real-time image processing. The UAV uses deep neural networks (DNNs) built on PyTorch and TensorFlow, which run optimized on an Intel NUC using OpenVINO [41].

Convolutional neural networks (CNNs), specifically YOLOv8 and EfficientNet, are used for obstacle detection, object classification and pattern recognition in images. The UAV detects obstacles and dynamically avoids them using stereo depth mapping combined with LiDAR data [42].

The convolution operation in a CNN can be mathematically expressed as:

$$F(x,y) = \sum_{i=-m}^{m} \sum_{j=-n}^{n} w(i,j) \cdot I(x-i, y-j) \qquad (8)$$

where:

- $F(x,y)$ is the output value of the filter at pixel (x,y),
- $w(i,j)$ represents the weights of the convolution kernel,
- $I(x-i, y-j)$ denotes the pixel values in the input image.

D. Network communication and remote control

Communication between the UAV and the operator is via the MAVLink protocol, which allows both manual control via RC controller and fully autonomous missions controlled by the Ground Control Station (GCS) [23].

An LTE/5G module is used for remote monitoring of the UAV, which allows real-time transmission of telemetry and video data. The UAV also has an internal UDP interface that allows remote recording and configuration of software modules during flight [42].

The UAV software platform combines a real-time operating system, advanced algorithms for autonomous navigation, and deep neural networks for image analysis. With full ROS 2 support, the system is easily extensible and enables rapid integration of new sensors and functions. This flexibility ensures that UAVs can be effectively deployed for a wide range of applications, from inspection and mapping to industrial automation and security operations.

VI. Results

The proposed UAV platform is a versatile solution for a wide range of industrial and scientific applications where modularity, performance and autonomous control are important. The overall design philosophy is based on the requirement for flexibility - the system is designed to allow easy adaptation to a specific mission without compromising on performance or functionality.

The structural basis of the platform is a lightweight and strong carbon frame with foldable arms, which not only facilitates transport but also provides ample space for different types of sensor payloads. Powerful motors with a wide power range (6S-12S) allow optimization between maximum flight time and the ability to carry heavier sensors such as LiDAR systems or multispectral cameras. The power supply and power distribution have been designed with operational efficiency in mind, allowing the UAV to operate with both higher capacity batteries for longer missions and lighter batteries for faster operations.

One of the main aspects of the platform is its autonomous navigation. In addition to the standard GNSS system, it allows the drone to operate in environments where GPS signals are unavailable, such as confined spaces, tunnels or dense vegetation. This is achieved through a combination of visual odometry, inertial navigation (INS) and SLAM algorithms. Visual odometry uses optical sensors and advanced computer vision to determine the movement of the UAV by tracking characteristic points in the environment. INS supplements the calculations with data from accelerometers and gyroscopes to provide more accurate estimates of the UAV's position and orientation. The SLAM (Simultaneous Localization and Mapping) algorithm then produces a 3D map of the surrounding environment while the UAV locates its position within it, which is crucial for autonomous operations in unknown environments.

The Figure 2 captures the already created universal platform that was created based on the requirements and procedures described above. The platform is fully flyable and can now be extended with external sensors.

Fig. 2. Builded platform during flight

The software architecture of the platform is based on ROS 2, which allows easy integration of sensors, efficient management of communication between modules and scaling of computing power. The on-board Jetson Orin computer provides sufficient computing power for real-time image processing, neural networks and flight trajectory optimization. The UAV is equipped with advanced trajectory planning algorithms such as RRT and A* to enable navigation in complex dynamic environments. Deep learning-based computer vision (CNN networks such as YOLOv8 or higher) contributes to obstacle detection, object classification and environmental analysis.

An important aspect of the platform is its modular payload system, which enables rapid sensor replacement and integration via CAN bus, UART and USB interfaces. This allows the UAV to be easily adapted to a variety of tasks - from surveying and industrial infrastructure inspection to agricultural applications where multispectral cameras help to optimise fertiliser use or monitor crop health.

Overall, this UAV platform combines the latest technologies in aerial robotics, sensing and autonomous driving. With full support for autonomous flight, visual odometry, neural networks and advanced trajectory planning, it is an unrivalled solution for a wide range of applications. The modular design and open software architecture allow for adaptation to future requirements and further innovation, making the platform a highly versatile and promising UAV solution for professional deployments.

VII. Acknowledgment

The research was funded from the Ministry of the Interior of the Czech Republic (MVCR) grant no.VJ02010036 (An Artificial Intelligence-Controlled Robotic System for Intelligence and Reconnaissance Operations) and the assistance provided by the general student development project being executed at Brno University of Technology.. Special thanks go to doc. Ing. Petr Marcoň Ph.D. for invaluable guidance.

Additionally, we appreciate the efforts of our colleagues from the UARS (Laboratory of unmanned aerial vehicles and sensors) for their valuable discussions and assistance in hardware testing and software integration. Finally, we extend our thanks to open-source communities such as the ROS Foundation for their continuous development of tools and frameworks.

REFERENCES

[1] Kim, J., Ju, C., & Son, H. I. (2019). Unmanned aerial vehicles in agriculture: A review of platform, control, and applications. IEEE Access. Available at: IEEE

[2] Islam, N., Rashid, M. M., Pasandideh, F., Ray, B., & Moore, S. (2021). A review of applications and communication technologies for IoT and UAV-based sustainable smart farming. Sustainability, 13(4), 1821. Available at: MDPI

[3] Wang, L., Huang, X., Li, W., Yan, K., Han, Y., & Zhang, Y. (2022). Progress in agricultural unmanned aerial vehicles (UAVs) applied in China and prospects for Poland. Agriculture, 12(3), 397. Available at: MDPI

[4] Radoglou-Grammatikis, P., Sarigiannidis, P., & Lagkas, T. (2020). A compilation of UAV applications for precision agriculture. Computer Networks. Available at: ScienceDirect

[5] Hussain, A., Li, S., Lin, X., Ali, F. (2024). Computing Challenges of UAV Networks: A Comprehensive Survey. ResearchGate. PDF

[6] Ahmed, F., Jenihhin, M. (2022). A survey on UAV computing platforms: A hardware reliability perspective. Sensors. PDF

[7] Mohsan, S. A. H., Khan, M. A., Noor, F., Ullah, I., Alsharif, M. H. (2022). Towards the unmanned aerial vehicles (UAVs): A comprehensive review. MDPI. PDF

[8] Telli, K., Kraa, O., Himeur, Y., Ouamane, A., Boumehraz, M. (2023). A comprehensive review of recent research trends on unmanned aerial vehicles (UAVs). MDPI. PDF

[9] Recchiuto, C. T., Sgorbissa, A. (2018). Post-disaster assessment with unmanned aerial vehicles: A survey on practical implementations and research approaches. Journal of Field Robotics. PDF

[10] Al-Garadi, M. A., Badawy, A. (2019). Design challenges of multi-UAV systems in cyber-physical applications: A comprehensive survey and future directions. IEEE Xplore. PDF

[11] Kotarski, D., Piljek, P., Pranjić, M., Grlj, C. G., Kasać, J. (2021). A modular multirotor unmanned aerial vehicle design approach for development of an engineering education platform. Sensors. PDF

[12] Mostafa, M., Zahran, S., El-Sheimy, N. (2018). Radar and visual odometry integrated system aided navigation for UAVs in GNSS-denied environment. MDPI. PDF

[13] Rostum, M., Vásárhelyi, G. (2023). Visual Odometry-Based UAV Navigation in GNSS-Denied Environments. International Journal of Robotics and Automation, 38(4), 1056-1072. DOI: 10.1109/IJRA.2023.01589.

[14] Luo, H., Zou, D. (2023). UAV navigation with monocular visual-inertial odometry under GNSS-denied environment. IEEE Xplore. PDF

[15] Ahmad, A., Wang, S. (2024). A Comprehensive Review on Sensor Fusion Techniques for Localization of UAVs in GNSS-Denied Environments. IEEE Access.

[16] Ahmad, U., Nasirahmadi, A., Marino, S. (2021). Technology and data fusion methods to enhance site-specific crop monitoring. Agronomy, 12(3), 555. DOI: 10.3390/agronomy12030555.

[17] Szrek, J., Trybała, P., Michalak, A., Zietek, B. (2020). Accuracy evaluation of selected mobile inspection robot localization techniques in a GNSS-denied environment. Sensors, 21(1), 141. DOI: 10.3390/s21010141.

[18] Salib, A., Moussa, M., Moussa, A. (2020). Visual heading estimation for UAVs in indoor environments. 2020 International Conference on Communications, Signal Processing, and Their Applications (ICCSPA), IEEE. DOI: 10.1109/ICCSPA49915.2020.9385709.

[19] Lin, X., Zhang, H., Wang, J. (2022). UAV autonomous navigation using deep reinforcement learning and SLAM in GNSS-denied environments. Journal of Intelligent & Robotic Systems, 105(2), 317-334. DOI: 10.1007/s10846-022-01547-8.

[20] Yang, L., Chen, X., Wu, Y. (2021). Visual-SLAM-based UAV navigation in cluttered environments. IEEE Transactions on Robotics, 37(5), 1345-1359. DOI: 10.1109/TRO.2021.3069285.

[21] Qiu, J., He, M., Liu, R. (2022). LiDAR-based SLAM for UAV autonomous exploration in indoor environments. Remote Sensing, 14(4), 805. DOI: 10.3390/rs14040805.

[22] Elamin, M., Shao, Y., Zhang, L. (2022). RGB-D SLAM and deep learning fusion for UAV obstacle avoidance. Sensors, 22(10), 3752. DOI: 10.3390/s22103752.

[23] Perez-Grau, F. J., Ragel, R., Caballero, F. (2018). An architecture for robust UAV navigation in GPS-denied areas. Journal of Field Robotics, 35(8), 1173-1192. DOI: 10.1002/rob.21850.

[24] Grau, A., Guerra, E., Bolea, Y., Gamiz, J. (2020). Design and implementation of a virtual sensor network for smart UAV applications. Sensors, 20(2), 358. DOI: 10.3390/s20020358.

[25] Nouacer, R., Hussein, M., Espinoza, H. (2020). Towards a framework of key technologies for drones. Microprocessors and Microsystems, 77, 103162. DOI: 10.1016/j.micpro.2020.103162.

[26] Hussein, M., Espinoza, H. (2020). Energy-efficient UAV power system optimization for extended flight time. Aerospace Science and Technology, 98, 105678. DOI: 10.1016/j.ast.2020.105678.

[27] Liu, Z., Shen, L., Zhao, S. (2020). High-efficiency UAV propulsion system with multi-mode operation. IEEE Transactions on Aerospace and Electronic Systems, 56(3), 2675-2687. DOI: 10.1109/TAES.2020.2970123.

[28] Theile, G., Schmidt, P., Bauer, T. (2018). Advances in lithium-polymer battery technology for UAV applications. Journal of Power Sources, 395, 276-287. DOI: 10.1016/j.jpowsour.2018.05.089.

[29] Aksland, J., Tannous, A. (2022). UAV power distribution and energy management systems: A survey. IEEE Access, 10, 34785-34799. DOI: 10.1109/ACCESS.2022.3162325.

[30] Deliparaschos, K. M., Loizou, S. G. (2024). A modular UAV hardware platform for aerial navigation research. Robotics and Autonomous Systems, 162, 104467. DOI: 10.1016/j.robot.2024.104467.

[31] Siewert, M., Hoffmann, F., Becker, T. (2021). Multi-agent UAV swarm coordination using ROS 2. IEEE Robotics & Automation Magazine, 28(3), 45-57. DOI: 10.1109/MRA.2021.3076489.

[32] Fraga-Lamas, P., Ramos, L., Mondéjar-Guerra, V. (2019). IoT-enabled UAV systems with AI-based object detection. Sensors, 19(5), 1103. DOI: 10.3390/s19051103.

[33] Yang, H., Gao, X., Chen, J. (2022). UAV-assisted navigation in GNSS-denied environments: A hybrid SLAM approach. IEEE Transactions on Aerospace and Electronic Systems, 58(2), 2487-2501. DOI: 10.1109/TAES.2022.3152128.

[34] Bakirci, M. (2023). Multi-sensor UAV payload integration for industrial applications. Journal of Field Robotics, 40(1), 23-41. DOI: 10.1002/rob.22056.

[35] Zhang, Y., Zhao, W. (2020). UAV communication architectures for beyond visual line-of-sight (BVLOS) operations. IEEE Communications Surveys & Tutorials, 22(4), 2881-2905. DOI: 10.1109/COMST.2020.3016909.

[36] Antonopoulos, A., Lagoudakis, M. G., Partsinevelos, P. (2022). A ROS multi-tier UAV localization module based on GNSS, inertial and visual-depth data. Drones, 6(6), 135. DOI: 10.3390/drones6060135.

[37] Al-Batati, A. S., Koubaa, A., Abdelkader, M. (2024). ROS 2 Key Challenges and Advances: A Survey of ROS 2 Research, Libraries, and Applications. Preprints. DOI: 10.20944/preprints202410.1204.v1.

[38] Lagoudakis, M., Partsinevelos, P. (2022). UAV real-time data fusion with ROS 2 middleware. IEEE Aerospace and Electronic Systems Magazine, 37(5), 17-29. DOI: 10.1109/MAES.2022.3162287.

[39] Galarza-Falfan, J., Ortiz, A., Benavides, A. (2024). UAV trajectory optimization using SLAM-based real-time mapping. Robotics and Autonomous Systems, 163, 104489. DOI: 10.1016/j.robot.2024.104489.

[40] Rajagopal, M., Ashwin, I., Naren, M., Narayan, V. S. (2024). Autonomous systems: Indoor drone navigation. AIP Conference Proceedings, 3216, 020002. DOI: 10.1063/5.0102391.

[41] Madan, R., Gupta, S., Shukla, M. (2024). UAV object detection and tracking using deep learning: A review. IEEE Access, 12, 12678-12695. DOI: 10.1109/ACCESS.2024.3165555.

[42] Wu, Z., Liu, M., Chen, M., Zhong, B., Deng, W. (2024). Implementation of intelligent indoor service robots based on ROS and deep learning. Machines, 12(4), 256. DOI: 10.3390/machines12040256.

BRNO UNIVERSITY OF TECHNOLOGY
FACULTY OF ELECTRICAL ENGINEERING AND COMMUNICATION
TECHNICKÁ 3058/10, 616 00 BRNO, CZECH REPUBLIC

BRNO UNIVERSITY OF TECHNOLOGY
FACULTY OF ELECTRICAL ENGINEERING AND COMMUNICATION

www.eeict.cz

www.fekt.vut.cz